



Università degli Studi di Cagliari

PhD Degree in Chemical Science and Technology

XXXIII cycle

**Design, synthesis and characterization of novel
building blocks for supramolecular assemblies.**

Scientific Disciplinary Sector:

CHIM/03 – General and Inorganic Chemistry

PhD Candidate:

Enrico Podda

Supervisor:

Prof.ssa M. Carla Aragoni

PhD Coordinator:

Prof. Stefano Enzo

Final Exam. Academic Year 2019 - 2020

Thesis defence: May 2021

Acknowledgments

The first person I would like to thank is Prof. M. Carla Aragoni for being an extraordinary mentor since our first journey started with my bachelor's degree, for guiding me in my professional career and for have always believed in me. I would like to thank her for the invaluable contribute to the present work, not only professionally speaking, but also for her endless patience and empathy.

A huge thank you goes to Prof. Massimiliano Arca and Dr. Anna Pintus to whom I am immensely grateful. Thanks for all we shared in the last years.

I cannot fail to express my gratitude to all the other members of my research group including Prof. Vito Lippolis, Prof. Claudia Caltagirone, Prof. Francesco Isaia, Dr. Alessandra Garau and Dr. Giacomo Picci.

I am most grateful to Dr. Rob Davies and all his group for the great support during my stay at the Imperial College London. Thanks to Drs. Lisa Haigh, Peter Haycock and Andrew J. P. White for MS, NMR, XRD services that I have had the chance to use at the Imperial College.

Thanks to Prof. Simon Coles and all the staff from the UK National Crystallography Service in Southampton for the knowledge they have passed on to me in the field of crystallography. A special thanks goes to James for his infinite patience and continuous support throughout all my PhD. Thanks to Peter, Graham, Wim and Wilma for making my visit so special. I will always remember the time spent struggling solving crystal structures and the Friday lunches at The Crown Inn.

I would like to acknowledge Prof. John Derek Woollins, Prof. Alexandra MZ Slawin and Dr. Cameron Carpenter-Warren from the University of St. Andrews for the XRD analysis they carried on some of the samples reported in the present thesis.

The Centro Servizi di Ateneo per la Ricerca (CeSAR) in Cagliari is kindly acknowledged for the NMR services and the technical support provided by Dr. Sandrina Lampis for both analysis in solution and in the solid state. The CeSAR is also thanked for the SC-XRD facilities made available for the characterization of some of the research products presented herein.

Summary

1. Introduction to Supramolecular Chemistry	1
1.1. Supramolecular interactions	1
1.1.1. π - π Interactions	1
1.1.2. Hydrogen bonds	5
1.1.3. Boron-Nitrogen bonds.....	9
1.1.4. Halogen bonds.....	12
1.2. Supramolecular Architectures	20
1.2.1. Coordination Polymers and Metal-Organic Frameworks.	20
1.2.2. Co-crystals and Hydrogen-Bonded Organic Frameworks.	29
1.2.3. Covalent Organic Frameworks (COFs).....	34
2. Aim and objectives.....	39
3. Results and discussion.....	42
3.1. Neutral pyridyl-based building blocks.	42
3.1.1. Interaction between N-donors L1-L6 with metal ions: CPs and MOFs.....	42
3.1.1.1. Interaction between N-donors L1 and L2 with metal ions	42
3.1.1.2. Interaction between N-donors L3 and L4 with metal ions	57
3.1.1.3. Interaction between N-donors L5 and L6 with metal ions	81
3.1.2. Interaction between N-donors and carboxylic acids	94
3.1.2.1. Interaction between L1 and L2 with carboxylic acids.....	96
3.1.2.2. Interaction between L7 with H ₂ TER	114
3.1.3. Interaction between N-donors and borasiloxanes: COFs.....	117
3.1.3.1. Design of cyclic borasiloxanes R1-R3	117
3.1.3.2. Interaction between L1 and the cyclic borasiloxane R3.....	122
3.1.3.3. Interaction between L3 and the cyclic borasiloxanes R2 and R3.....	123
3.1.3.4. Interaction between L5 and the cyclic borasiloxane R3.....	130
3.1.4. Interaction between N-donors and halogens	132

3.1.4.1.	Interaction between L1 and L2 and halogens	132
3.1.4.2.	Interaction between L3 and halogens	135
3.1.4.3.	Interaction between L11 and halogens	140
3.1.4.4.	Interaction between L12-L14 and halogens	146
3.2.	Charged carboxylate-based building blocks: bifluorene derivatives.....	160
3.2.1.	Bifluorene derivatives L15, L16 and H ₄ L17	161
3.2.2.	Interaction between H ₄ L17 and metal ions	167
3.2.2.1.	[(Cd ₂ L17·3H ₂ O)·3H ₂ O] _∞ and [(Cd ₂ L17·6H ₂ O)·2H ₂ O] _∞	167
3.2.2.2.	[(Cu ₂ L17)·3DMF] _∞	178
3.2.3.	Interaction between H ₄ L17 and pyridyl derivatives.....	179
3.2.4.	Three components supramolecular architectures: H ₄ L17, metal ions and pyridyl derivatives	182
3.2.4.1.	[(Co ₂ L3 ₂ L17·H ₂ O)·2DMF] _∞	182
3.2.4.2.	[(Zn ₂ L3L17·3H ₂ O·DMF)·3.5DMF] _∞	186
4.	Conclusions	191
4.1.	Outlook and future perspectives	195
5.	Experimental	196
5.1.	Methods and materials.....	196
5.2.	Synthesis.....	199
5.2.1.	Preparation of 3,5-di(pyridin-3-yl)-1,2,4-thiadiazole (L1)	199
5.2.2.	Preparation of 3,5-di(pyridin-4-yl)-1,2,4-thiadiazole (L2)	200
5.2.3.	Preparation of 2,5-bis(pyridin-3-ylethynyl)thiophene (L3)	200
5.2.4.	Preparation of 2,5-bis(pyridin-4-ylethynyl)thiophene (L4)	201
5.2.5.	Preparation of 2,7-bis(pyridin-3-ylethynyl)-9H-fluorene (L5)	201
5.2.6.	Preparation of 2,7-bis(pyridin-4-ylethynyl)-9H-fluorene (L6)	202
5.2.7.	Preparation of 1,3-bis(pyridin-3-ylethynyl)benzene (L7).....	202
5.2.8.	Preparation of 1,3-bis(pyridin-4-ylethynyl)benzene (L8).....	203

5.2.9.	Preparation of 2,7-bis(pyridin-3-ylethynyl)fluoren-9-one (L9).....	203
5.2.10.	Preparation of 2-(2,7-bis(pyridin-3-ylethynyl)fluoren-9-ylidene)malononitrile (L11)	204
5.2.11.	Preparation of bis(2,7-dibromo-9H-fluoren-9-yl)methane (L15).....	204
5.2.12.	Preparation of bis(2,7-dibromo-9-methylfluoren-9-yl)methane (L16)	205
5.2.13.	Preparation of 9,9'-methylenebis(9-methylfluorene-2,7-dicarboxylic acid) (H ₄ L17)	205
5.2.14.	Preparation of C ₃₆ H ₃₀ B ₂ O ₄ Si ₂ (R1).	206
5.2.15.	Preparation of C ₃₆ H ₂₈ B ₂ F ₂ O ₄ Si ₂ (R2).....	206
5.2.16.	Preparation of C ₃₆ H ₂₆ B ₂ F ₄ O ₄ Si ₂ (R3).....	207
5.2.17.	Preparation of 1	207
5.2.18.	Preparation of 2	207
5.2.19.	Preparation of 3	208
5.2.20.	Preparation of [AgL1(OTf)·((CH ₃) ₂ CO) _{0.5}] _∞	208
5.2.21.	Preparation of [ZnL1(NO ₃) ₂ ·CH ₃ CN] ₂	209
5.2.22.	Preparation of (ZnL1Cl ₂) _∞	209
5.2.23.	Preparation of (1·L1) ₂	209
5.2.24.	Preparation of (1·L2) _∞	210
5.2.25.	Preparation of [AgL3(OTf)((CH ₃) ₂ CO) _{2.5}] _∞	210
5.2.26.	Preparation of [CdL3(NO ₃) ₂ (H ₂ O) ₂ ·1.5H ₂ O] _∞	210
5.2.27.	Preparation of [CuL3(NO ₃) ₂ ·CH ₃ CN] ₂ ·2CH ₃ CN	211
5.2.28.	Preparation of [Co(L4) ₂ Cl ₂] _∞	211
5.2.29.	Preparation of (2·L5·CHCl ₃) _∞	211
5.2.30.	Preparation of (3·L5) _∞	211
5.2.31.	General method for the preparation of co-crystals with L1, L2 and benzenedicarboxylic acids.....	212
5.2.32.	Preparation of L1·H ₂ TER	212
5.2.33.	Preparation of (L1·H ₂ TER-Br) _∞	212

5.2.34.	Preparation of $(L1 \cdot H_2TER-(OH)_2)_\infty$	212
5.2.35.	Preparation of $(L1 \cdot H_2TER-F_4)_\infty$	212
5.2.36.	Preparation of $L1 \cdot H_2ISO$	213
5.2.37.	Preparation of $(L1 \cdot H_2ISO-F_4)_\infty$	213
5.2.38.	Preparation of $(L1 \cdot H_2PyDC)_\infty$	213
5.2.39.	Preparation of $(L2 \cdot H_2TER)_\infty$	213
5.2.40.	Preparation of $(L2 \cdot H_2TER-Br)_\infty$	213
5.2.41.	Preparation of $(L2 \cdot H_2TER-(OH)_2)_\infty$	214
5.2.42.	Preparation of $(L2 \cdot H_2TER-F_4)_\infty$	214
5.2.43.	Preparation of $(L2 \cdot H_2ISO)_\infty$	214
5.2.44.	Preparation of $(L2 \cdot H_2ISO-F_4)_\infty$	214
5.2.45.	Preparation of $(L2 \cdot H_2PyDC)_\infty$	214
5.2.46.	Preparation of $(L1)_2 \cdot R3$	214
5.2.47.	Preparation of $(L3 \cdot R2)_\infty$	215
5.2.48.	Preparation of $(L3 \cdot R3)_\infty$	215
5.2.49.	Preparation of $(L5 \cdot R2)_\infty$	215
5.2.50.	Preparation of $(L2 \cdot 1,4-DITFB)_\infty$	216
5.2.51.	Preparation of $(HL3)I_3 \cdot I_2$	216
5.2.52.	Preparation of $(H_2L3Br_4)BrBr_3 \cdot 0.5 CHCl_3$	216
5.2.53.	Preparation of $(L11 \cdot I_2) \cdot 0.5 I_2$	216
5.2.54.	Preparation of $(HL12)I \cdot 2.5 I_2$	216
5.2.55.	Preparation of $HpyTeI_2$	217
5.2.56.	Preparation of $HpyTeBr_2$	217
5.2.57.	Preparation of $HpyTeBr_4$	217
5.2.58.	Preparation of $[(HL14)I_2Cl]_3 \cdot 0.5I_2$	218
5.2.59.	Preparation of $[(Cd_2L17 \cdot 3H_2O) \cdot 3H_2O]_\infty$ and $[(Cd_2L17 \cdot 6H_2O) \cdot 2H_2O]_\infty$	218
5.2.60.	Preparation of $(H_4L17 \cdot Py_2Et)_\infty$	218

5.2.61.	Preparation of $[(\text{Co}_2\text{L}_3\text{L}17 \cdot \text{H}_2\text{O}) \cdot 2\text{DMF}]_\infty$	218
5.2.62.	Preparation of $[(\text{Zn}_2\text{L}_3\text{L}17 \cdot 3\text{H}_2\text{O} \cdot \text{DMF}) \cdot 3.5\text{DMF}]_\infty$	218
References	219
Appendix 1: NMR spectra	243
Appendix 2: FT-IR spectra	271
Appendix 3: Mass spectra	295
Appendix 4: Diffuse reflectance spectra	297
Appendix 5: Computational data	298
Appendix 6: Crystal data and refinement parameters	312
Appendix 7: Supplementary Information	354

List of figures

Figure 1 Schematic representation of the tetrahedral arrangement found in the crystal structure of ice (left) and of its hexagonal packing (right).....	6
Figure 2 Distribution of three coordinated boron derivatives reported in the CSD. Subclasses are divided according to the number of nitrogen or oxygen atoms included in the fragment. $R \neq N, O$	10
Figure 3 Distribution of tetra-coordinated boron derivatives reported in the CSD. Subclasses are divided according to the number of nitrogen or oxygen atoms included in the fragment. $R \neq N, O$. The BR_4 fragment is intentionally removed for clarity.....	12
Figure 4 Molecular electrostatic potential $V(r)$ calculated for the series CF_3X ($X = F, Cl, Br, I$). Reproduced from ref. ^[107]	13
Figure 5 Examples of different products generated by reacting chalcogenated species with dihalogens. Thermal ellipsoids are drawn at the 50 % probability level. Hydrogen atoms have been omitted for clarity.....	14
Figure 6 Structural data for T-shaped insertion adducts ($X-E-Y$) according to their elongation values ($\delta_1 = \delta_{XE}$; $\delta_2 = \delta_{EY}$). The solid black curve is the product of the least square fit of all data (adopting equation 2) except those included in the red circle. Fitted parameter $k = 0.157$; rmsd = 0.050; normalized rmsd = 0.067. Reproduced from ref. ^[115]	16
Figure 7 Structural data of $N \cdots I-X$ ($X = Cl, Br, I$) fragments overlapped with those related to chalcogen-halogen three-body systems depicted as blue dots (reproduced from ref. ^[131]).....	16
Figure 8 The reactivity of 1,4-bis(pyridin-3-ylethynyl)benzene towards I_2 and Br_2 . The molecular unit of the CT bis I_2 adduct is depicted along with the iodine molecule intercalated in the 2D network (LEWKOP). The pyridinium tribromide salt resulted from the bromine addition to the organic linker is represented (OQUYAB). Hydrogen atoms are omitted for clarity except the one involved in the protonated pyridine fragment.....	17
Figure 9 Helical iodonium complex held together by means of $[N-I-N]^+$ interactions (NOMCAW). X-ray crystal structure representations along a (left) and b axis (right). Iodine and nitrogen atoms are depicted in purple and light blue balls, respectively. BF_4^- units and hydrogen atoms have been omitted for clarity. Reproduced from ref. ^[141]	18
Figure 10 Schematic representation of ligand L and crystal packing of the double stranded cationic interwound polymeric chains of the type $[AgL]_\infty^+$. H atoms and perchlorate anions are omitted for clarity. Reproduced from ref. ^[171] (refcode: ABOKAD).....	21

Figure 11 View along the <i>c</i> axis of linear chains rotated and stacked to produce virtual hexagonal cavities. H atoms and H ₂ O molecules have been omitted for clarity. Reproduced from ref. ^[172] (refcode: FAKQEN).....	22
Figure 12 Supramolecular construct: a) zig-zag arrangement of a Zn(II)-based CP; b) helical arrangement of a Zn(II)-based CP. Reproduced from ref. ^[172] and ^[173] , respectively (refcodes: DOHJES, POXVIK).....	23
Figure 13 Isoreticular series of IRMOF-1. Linker functionalities and lengths yield isoreticular networks with different pore size and functionalities but featuring the parent pcu topology. See refcodes: MIBQAR, EDUSOL, EDUSUR, EDUTIG, EDUTOM, EDUVAA.....	24
Figure 14 Topology table reproducing possible nets constructed with a two-component approach. Reproduced from ref. ^[189]	26
Figure 15 a) examples of selected SBUs with variable number of metal nodes and connectivity (reproduced from refcodes: FIQCEN, ALEJAE, FAZPON and CUFHIX, respectively). b) schematic representation of linker with different shapes and topologies.....	27
Figure 16 Honeycomb arrangement found in the crystal structure of H ₃ BTC (left). Two component co-crystals prepared by the self-assembly of H ₃ BTC and 4,4'-bipy (middle) and 1,2-di(pyridin-4-yl)ethane (right). Refcodes: BTKOAC, RAPHUR and SAYMUB, respectively. H atoms have been omitted for clarity and H-bonds (D–A) are depicted in turquoise.....	30
Figure 17 Ternary co-crystals: a) assembled through hydrogen-bond of different strength; b) cooperativity of hydrogen bond and halogen bond. Refcodes: BUFBIP and OQIJJ, respectively. Hydrogen bonds are depicted in turquoise and halogen bonds in green. H atoms not involved in hydrogen bonding have been omitted for clarity.	31
Figure 18 The five edge-transient topologies in 2D-COFs. Both simple and augmented nets are reported for each topology.	37
Figure 19 Kohn–Sham frontier orbital energies (Hartree) of free pyridine (Py) and ligands I–IV [1-pyridyl-4-(4'-pyridyl-ethynyl)-benzene (I), 4,4'-bipyridine (II), 3,6-bis(4-pyridyl)-1,2,4,5-tetrazine (III), and 3,6-bis(3-pyridyl)-1,2,4,5-tetrazine (IV)]. In the inset, the sketches of the molecular orbitals are depicted (Contour value = 0.05 e). (a) = LUMO+1, (b) = LUMO, (c) = HOMO, (d) = HOMO–1, (e) = HOMO–2, (f) = HOMO–3. Reproduced from ref ^[289] ..	42
Figure 20 Iso-surface drawings of Kohn–Sham HOMO–3 (left) and HOMO (right) calculated for L2 . Cutoff value = 0.05 e. Reproduced from ref ^[134]	43
Figure 21 Representation of the asymmetric unit of [Ag L1 (OTf)·((CH ₃) ₂ CO) _{0.5}] _∞ (left) and of the polymeric zig-zag chain (right). Hydrogen atoms and acetone molecules in the right-hand side have been omitted for clarity. Symmetry codes: ¹ -1/2+x, 3/2-y, 1-z; ² 1/2-x, 3/2-y, 1-z.	44

Figure 22 Chelating bridging triflate anions arranged into a dimeric network that stabilize two adjacent zig-zag chains. Ag–O distances = 2.680(4) and 2.877(4) Å for Ag1–O2 and Ag1–O1, respectively. Symmetry codes: ¹ 1/2-x, 3/2-y, 1-z; ² -x, +y, 1/2-z; ³ -1/2+x, 3/2-y, -1/2+z. H atoms, acetone molecules and disorder have been omitted for clarity.	45
Figure 23 Perspective view of the intermolecular Ag···Ag and π-π interactions along the [100] and [011] directions in a) and b) respectively. Centroid-centroid distances are reported in Å.	45
Figure 24 Crystal packing diagrams of [AgL1(OTf)·((CH ₃) ₂ CO) _{0.5}] _∞ along [101] and [010] directions from left to right, respectively. Counterions, solvent molecules and hydrogen atoms have been omitted for clarity reasons.....	46
Figure 25 Perspective view of the asymmetric unit with atom numbering scheme for [ZnL1(NO ₃) ₂ ·CH ₃ CN] ₂ (left). Paddle wheel arrangement (right); disorder at the thiadiazol ring and hydrogen atoms have been omitted for clarity. Symmetry code: ¹ 1-x, 1-y, 1-z.	47
Figure 26 View of the hydrogen bonded network found in [ZnL1(NO ₃) ₂ ·CH ₃ CN] ₂ . Only H-atoms involved in intermolecular interactions are shown. Interactions are labelled according to Table 3.....	48
Figure 27 Packing diagrams for [ZnL1(NO ₃) ₂ ·CH ₃ CN] ₂ along the [110] direction. Interactions are labelled according to Table 3.	48
Figure 28 Asymmetric unit and atom numbering scheme for (ZnL1Cl ₂) _∞ (left); staircase polymeric network (right).	49
Figure 29 Intermolecular interactions found in (ZnL1Cl ₂) _∞ . Intermolecular π-π interactions between parallel pyridyl rings are highlighted in green c) d _{centroid-centroid} = 3.801 Å. Interactions a and b are labelled according to Table 4.	50
Figure 30 (a) Tetracoordinated <i>bis</i> (<i>O,O</i> -diethyldithiophosphato)nickel complex and 4,4'-bipyridine building blocks; (b) [Ni((OEt) ₂ PS ₂) ₂ (4,4'-bipy)] _∞ CP.	52
Figure 31 Structure and numbering scheme of the dimer (1·L1) ₂ ; symmetry code: ¹ 1-x, -y, 1-z.	53
Figure 32 Packing views of (1·L1) ₂ showing the (a) layers formed by interacting dimers along 010 and (b) intercalating layers along 100. All the hydrogen atoms with the exception of those involved in the showed interactions have been omitted. Interactions: a : C4 ¹ –H4 ¹ ···N8, 2.62, 3.153(5), 116; b : C5 ² –H5 ² ···S2, 3.01, 3.633(8), 120; c : C42–H42a···N11 ³ , 2.42, 3.365(5), 164; d : C52b ⁴ –H52b ⁴ ···S9, 2.83 Å, 3.548(5) Å, 131°. Symmetry codes: ¹ 2-x, -y, 2-z; ² 2-x, -y, 1-z; ³ x, 0.5-y, -0.5+z; ⁴ x, 0.5-y, 0.5+z.	55

- Figure 33** Perspective view along the propagation axis and numbering scheme of the helix $(\mathbf{1}\cdot\mathbf{L2})_\infty$; symmetry codes: ¹ $x, 3/2-y, 1/2-z$; ² $3/2-x, 2-y, z$ 56
- Figure 34** View along the crystallographic a axis of a polymeric helix $(\mathbf{1}\cdot\mathbf{L2})_\infty$ (a) and an undulated chain of the analogous $(\mathbf{1N}\cdot\mathbf{L2})_\infty$ (b). For clarity reasons, H-atoms are omitted, and only one orientation of the penta-atomic ring depicted. Symmetry code: ¹ $x, 1+y, z$ 56
- Figure 35** Packing view along the [100] crystallographic direction of helices $(\mathbf{1}\cdot\mathbf{L2})_\infty$ showing the interactions described in the discussion. For clarity, H-atoms not involved in the showed interactions are omitted and only one orientation of the penta-atomic ring depicted..... 57
- Figure 36** UV-Vis and Luminescent emission spectra ($C_{\mathbf{L3-L4}} = 10^{-5}$ M; $\lambda_{\text{ex}} = 350$ nm) of **L3** (black) and **L4** (red) in CHCl_3 depicted in solid and dashed line, respectively (left); Normalized diffuse reflectance and Luminescence emission spectra ($\lambda_{\text{ex}} = 350$ nm) of **L3** (black) and **L4** (red) measured in the solid state depicted in solid and dashed line, respectively (right)..... 59
- Figure 37** Representation of the asymmetric unit of **L3** (orthorhombic). Ellipsoids are drawn at 50 % probability level. 61
- Figure 38** View along the [100] direction of the hydrogen bonding interactions in the orthorhombic polymorph of **L3**. $\text{C3}^2\text{-H3}^2\cdots\text{N1}^1$ ($d_{\text{D}\cdots\text{A}} = 3.412(5)$ Å; $d_{\text{H}\cdots\text{A}} = 2.61(3)$ Å; $\alpha_{\text{D-H}\cdots\text{A}} = 142.9(2)$ °); $\text{C16}^1\text{-H16}^1\cdots\text{N2}$ ($d_{\text{D}\cdots\text{A}} = 3.428(5)$ Å; $d_{\text{H}\cdots\text{A}} = 2.48(3)$ Å; $\alpha_{\text{D-H}\cdots\text{A}} = 172.8(2)$ °). Symmetry codes: ¹ $3/2-x, 1/2-y, 1/2+z$; ² $3/2-x, -3/2+y, +z$ 61
- Figure 39** Views of the hydrogen-bonded folded grid found in **L3** (orthorhombic) along a (left) and c (right) axis, respectively. 2D-grid display openings of approximately 8.2×15.3 Å. $d_{\text{Py1} - \text{Py2}} = 27.752$ Å; $d_{\text{Py2} - \text{Py3}} = 28.682$ Å; $\alpha_{\text{Py1} - \text{Py2} - \text{Py3}} = 46.62^\circ$. Symmetry codes: ¹ $-1/2+x, -3/2-y, 1-z$; ² $-1/2+x, -1/2+y, 3/2-z$; ³ $1-x, -y, 1-z$ 62
- Figure 40** Capped sticks representation of the 3-fold interpenetrated network of **L3** (orthorhombic). **L3** molecules depicted in red represent an element of the grid that can accommodate two more grids represented as single **L3** units in green and blue for clarity reasons. Symmetry codes: ⁱ $1-x, -y, 1-z$; ⁱⁱ $3/2-x, -1/2+y, +z$; ⁱⁱⁱ $+x, -y, -1/2+z$; ^{iv} $+x, -2+y, +z$; ^v $+x, -y, 1/2+z$; ^{vi} $+x, -1+y, +z$ 62
- Figure 41** Packing diagram of the orthorhombic polymorph of **L3** along the c axis showing a 3-fold interpenetration of 2D-grids. Interaction **a**: $\text{C17-H17}\cdots\text{N1}^1$ ($d_{\text{D}\cdots\text{A}} = 3.497(5)$ Å; $d_{\text{H}\cdots\text{A}} = 2.681(3)$ Å; $\alpha_{\text{D-H}\cdots\text{A}} = 144.4(2)$ °). Symmetry codes: ¹ $1/2+x, -1/2+y, 1/2-z$ 63
- Figure 42** Representation of the asymmetric unit of **L3** (monoclinic) along the c axis. Ellipsoids are drawn at 50 % probability level. 63

Figure 43 Capped sticks representation of the packing diagram for the modulated layered network along the [110] direction in the crystal structure of L3 (monoclinic). Hydrogens are omitted for clarity.....	64
Figure 44 Relative total electronic energy variation (ΔE) calculated as a function of the pyridine ring rotation (τ) for L3	64
Figure 45 Isosurface drawings of selected frontier Kohn–Sham molecular orbitals calculated for L3 . Hydrogen atoms were omitted for clarity. Cutoff value = 0.05 e	65
Figure 46 Perspective view of the asymmetric unit for $[\text{AgL3}(\text{OTf})((\text{CH}_3)_2\text{CO})_{2.5}]_\infty$	65
Figure 47 View of the zig-zag CP $[\text{AgL3}(\text{OTf})((\text{CH}_3)_2\text{CO})_{2.5}]_\infty$. Ag...Ag distances: (a) $d_{\text{Ag}1 \cdots \text{Ag}11} = 17.714 \text{ \AA}$; (b) $d_{\text{Ag}2 \cdots \text{Ag}21} = 17.694 \text{ \AA}$; (c) $d_{\text{Ag}1 \cdots \text{Ag}2} = 3.385 \text{ \AA}$. Symmetry code: $^1 -1/2+x, -y, 1/2+z$. Disorder and hydrogen atoms are not shown for clarity.	66
Figure 48 Schematic representation of the coordination environment around silver(I) nodes in $[\text{AgL3}(\text{OTf})((\text{CH}_3)_2\text{CO})_{2.5}]_\infty$. L3 molecules are depicted as single pyridyl rings, disorder, H atoms and solvent molecules have been omitted for the sake of clarity. Symmetry code: $^1 1/2+x, -y, -1/2+z$	67
Figure 49 Intermolecular π - π interactions in the crystal structure of $[\text{AgL3}(\text{OTf})((\text{CH}_3)_2\text{CO})_{2.5}]_\infty$: (a) Py1-Py3 ($d = 3.640(2) \text{ \AA}$; $\alpha = 172.75(14)^\circ$); (b) Py1 ¹ -Py2 ($d = 3.722(2) \text{ \AA}$; $\alpha = 168.83(14)^\circ$); (c) Py2-Py4 ($d = 3.597(2) \text{ \AA}$; $\alpha = 176.12(13)^\circ$); (d) Tph1 ¹ -Tph2 ($d = 3.831(4) \text{ \AA}$; $\alpha = 176.1(2)^\circ$); (e) Tph1- Tph1 ¹ ($d = 3.653(2) \text{ \AA}$; $\alpha = 168.67(14)^\circ$). Symmetry code: $^1 1/2-x; +y; 3/2-z$	68
Figure 50 Packing diagrams for $[\text{AgL3}(\text{OTf})((\text{CH}_3)_2\text{CO})_{2.5}]_\infty$ along <i>a</i> and <i>b</i> axis in a) and b), respectively. Disorder, H atoms and solvent molecules are not shown for clarity.	68
Figure 51 Asymmetric unit for the crystal structure of $[\text{CdL3}(\text{NO}_3)_2(\text{H}_2\text{O})_2 \cdot 1.5\text{H}_2\text{O}]_\infty$. Displacement ellipsoids are drawn at 50 % probability level.	69
Figure 52 View of the polymeric chain of $[\text{CdL3}(\text{NO}_3)_2(\text{H}_2\text{O})_2 \cdot 1.5\text{H}_2\text{O}]_\infty$ along the <i>c</i> axis. Disorder at nitrile functionalities is not shown for clarity. Symmetry code: $^1 1/2+x, -1/2+y, -z$	70
Figure 53 Packing views along [100] (a) and [001] (b) of $[\text{CdL3}(\text{NO}_3)_2(\text{H}_2\text{O})_2 \cdot 1.5\text{H}_2\text{O}]_\infty$ evidencing π - π interactions between pyridyl and Tph rings depicted in dashed green lines. Py1 ring is depicted in brick red, Py2 ring is depicted in blue, and Tph ring is depicted in green. Interactions a : Py2-Py2 ¹ (centroid-centroid distance = $3.596(9) \text{ \AA}$; $\alpha = 0.7(3)^\circ$); b : Tph-Py1 ² (centroid-centroid distance = $3.821(4) \text{ \AA}$; $\alpha = 4.2(2)^\circ$); c : Py1-Tph ² (centroid-centroid distance = $3.719(4) \text{ \AA}$; $\alpha = 4.2(2)^\circ$). Disorder and H-atoms have been omitted for clarity. Symmetry codes: $^1 +x, 3/2-y, 1/2+z$; $^2 1/2-x, +y, 1/2+z$	71

Figure 54 Hydrogen-bonded network in the crystal structure of $[\text{CdL3}(\text{NO}_3)_2(\text{H}_2\text{O})_2 \cdot 1.5\text{H}_2\text{O}]_\infty$ along the <i>b</i> axis. Interactions are labelled according to Table 8.	72
Figure 55 Packing diagrams of $[\text{CdL3}(\text{NO}_3)_2(\text{H}_2\text{O})_2 \cdot 1.5\text{H}_2\text{O}]_\infty$ along the <i>a</i> , <i>b</i> and <i>c</i> axis, in a), b) and c), respectively. Adjacent layers are depicted in red and green. Light blue and gold boxes in c) represent the solvent-accessible voids present in the crystal structure.	72
Figure 56 Perspective views of the asymmetric unit (left) and the paddle wheel arrangement (right) for $[\text{CuL3}(\text{NO}_3)_2 \cdot \text{CH}_3\text{CN}]_2 \cdot 2\text{CH}_3\text{CN}$. Displacement ellipsoids are drawn at 50 % probability level. Symmetry code: $^1 2-x, 1-y, 1-z$	73
Figure 57 View along the <i>a</i> axis of the hydrogen bonding interactions found in $[\text{CuL3}(\text{NO}_3)_2 \cdot \text{CH}_3\text{CN}]_2 \cdot 2\text{CH}_3\text{CN}$. Only hydrogens involved in H-bonds are shown for clarity. H-bonds are depicted in dashed blue lines.	74
Figure 58 Packing diagrams of $[\text{CuL3}(\text{NO}_3)_2 \cdot \text{CH}_3\text{CN}]_2 \cdot 2\text{CH}_3\text{CN}$ along the <i>a</i> (left) and <i>b</i> (right) axis, respectively.	75
Figure 59 Normalized diffuse reflectance (left) and luminescent emission spectra (right) for $[\text{AgL3}(\text{OTf})((\text{CH}_3)_2\text{CO})_{2.5}]_\infty$ (blue line), $[\text{CdL3}(\text{NO}_3)_2(\text{H}_2\text{O})_2 \cdot 1.5\text{H}_2\text{O}]_\infty$ (green line) and $[\text{CuL3}(\text{NO}_3)_2 \cdot \text{CH}_3\text{CN}]_2 \cdot 2\text{CH}_3\text{CN}$ (red line). Absorption and emission properties of L3 are depicted in black dashed lines for comparison.	76
Figure 60 View of the asymmetric unit of $[\text{Co}(\text{L4})_2\text{Cl}_2]_\infty$ along the [011] direction. H atoms are omitted for clarity.	79
Figure 61 View of the 2D square-grid network of $[\text{Co}(\text{L4})_2\text{Cl}_2]_\infty$ along the <i>b</i> axis. Disorder and H atoms are omitted for clarity.	79
Figure 62 Packing diagrams of $[\text{Co}(\text{L4})_2\text{Cl}_2]_\infty$ showing a) the connectivity between adjacent layers; b) view of parallel layers along the propagation direction of interlayer crossing of L4 molecules.	80
Figure 63 Overlapped views of $[\text{Co}(\text{L4})_2(\text{NCS})_2]_\infty$ (refcode: ALANOQ) and $[\text{Co}(\text{L4})_2\text{Cl}_2]_\infty$ depicted in blue and red, respectively.	80
Figure 64 View of the 5-fold interpenetrated network of $[\text{Co}(\text{L4})_2\text{Cl}_2]_\infty$	81
Figure 65 Absorption (solid line) and emission (dashed line) spectra for L5 (black) and L6 (red) measured in CHCl_3 (left) ($C_{\text{L5-L6}} = 10^{-5} - 10^{-6}$ M, $\lambda_{\text{ex}} = 347\text{-}351$ nm) and in the solid state (right) ($\lambda_{\text{ex}} = 370$) nm.	82
Figure 66 Crystal structure representation of L5 (top); Packing diagrams along the <i>a</i> (right) and <i>b</i> axis (bottom left). Intermolecular π - π interactions are depicted in dashed black lines. Interactions: a) centroid-centroid distance of 4.741(9) Å, $\alpha = 58.2(5)^\circ$; b) centroid-centroid	

distance 4.862(8) Å, $\alpha = 57.7(5)^\circ$. H-atoms have been removed from packing diagrams for clarity.....	83
Figure 67 Perspective view of the dimeric arrangement found in the crystal structure of complex 3 . Displacement ellipsoids are drawn at 50 % probability level.	85
Figure 68 Numbering scheme of the asymmetric unit for $(\mathbf{2}\cdot\mathbf{L5}\cdot\mathbf{CHCl}_3)_\infty$. Displacement ellipsoids are drawn at 50 % probability level.	86
Figure 69 Helicoidal assembly of $(\mathbf{2}\cdot\mathbf{L5}\cdot\mathbf{CHCl}_3)_\infty$. Thermal ellipsoids are drawn at 50 % probability level. Solvent molecules and H-atoms have been omitted for clarity.	87
Figure 70 Intermolecular interactions between adjacent helices depicted in different colours. The intermolecular π - π stacking are experienced between planes highlighted in purple (centroid-centroid distance = 3.844(2) Å, $\alpha = 4.0(2)^\circ$	87
Figure 71 View of the intermolecular interactions between adjacent helices along the <i>c</i> axis. Intermolecular hydrogen bonding interactions and contacts are depicted in dashed red lines and labelled according to Table 11.	88
Figure 72 Packing diagrams for $(\mathbf{2}\cdot\mathbf{L5}\cdot\mathbf{CHCl}_3)_\infty$ along the <i>c</i> (left) and <i>a</i> (right) axis. Adjacent helices are depicted in different colours. Co-crystallized chloroform molecules and H-atoms have been omitted for clarity.....	89
Figure 73 Asymmetric unit for $(\mathbf{3}\cdot\mathbf{L5})_\infty$. Displacement ellipsoids are drawn at 50 % probability level.	90
Figure 74 Helicoidal assembly of $(\mathbf{3}\cdot\mathbf{L5})_\infty$. Thermal ellipsoids are drawn at 50 % probability level. H-atoms have been omitted for clarity.	90
Figure 75 Packing diagrams of $(\mathbf{3}\cdot\mathbf{L5})_\infty$ along <i>c</i> (left) and <i>b</i> (right) axis, respectively. Adjacent helices are depicted in different colours for clarity.....	91
Figure 76 Diffuse reflectance (left) and solid state emission spectra (right) for $(\mathbf{2}\cdot\mathbf{L5}\cdot\mathbf{CHCl}_3)_\infty$ (red), $(\mathbf{3}\cdot\mathbf{L5})_\infty$ (green) and L5 (dashed black) ($\lambda_{\text{ex}} = 350 - 370$) nm.....	93
Figure 77 Asymmetric unit in the crystal structure of HL1Cl·3H₂O . Thermal ellipsoids are drawn at 50 % probability level.	97
Figure 78 View along the <i>c</i> axis of the hydrogen bonded network built upon the interactions between water molecules with chloride anions. Interactions are labelled according to Table 15.	97
Figure 79 Packing diagram of HL1Cl·3H₂O along the <i>c</i> axis. Interactions are labelled according to Table 15.....	98
Figure 80 Asymmetric unit and atom numbering scheme for $(\mathbf{L1}\cdot\mathbf{H}_2\mathbf{TER})_\infty$	100

Figure 81 View of the intermolecular hydrogen bonding in $(\mathbf{L1}\cdot\mathbf{H2TER})_{\infty}$ along the [111] direction. Interactions are labelled according to Table 18. Disorder at thiadiazol ring is not shown for clarity.....	101
Figure 82 Packing diagrams views of $(\mathbf{L1}\cdot\mathbf{H2TER})_{\infty}$ showing a) hydrogen bonded sheets running parallel to the <i>a</i> axis; b) overlapped sheets along the [111] direction.	102
Figure 83 Asymmetric unit and atom labelling scheme for $(\mathbf{L2}\cdot\mathbf{H2TER}\cdot\mathbf{Br})_{\infty}$. Thermal ellipsoids are drawn at 50 % probability level.	103
Figure 84 View of the polymeric hydrogen bonded network in $(\mathbf{L2}\cdot\mathbf{H2TER}\cdot\mathbf{Br})_{\infty}$ along the [100] direction. Interactions are labelled according to Table 19.....	103
Figure 85 View of intermolecular interactions in the co-crystal $(\mathbf{L2}\cdot\mathbf{H2TER}\cdot\mathbf{Br})_{\infty}$ along the <i>a</i> axis according to Table 19.	104
Figure 86 Intermolecular π - π interaction in $(\mathbf{L2}\cdot\mathbf{H2TER}\cdot\mathbf{Br})_{\infty}$: f) Py \cdots Ph (centroid-centroid distance: 3.765(5) Å; α = 3.5(5) °).....	104
Figure 87 Asymmetric unit and atom labelling scheme for $(\mathbf{L2}\cdot\mathbf{H2TER}\cdot(\mathbf{OH})_2)_{\infty}$. Thermal ellipsoids are drawn at 50 % probability level.	105
Figure 88 View along the <i>c</i> axis of a H-bonded polymeric chain in $(\mathbf{L2}\cdot\mathbf{H2TER}\cdot(\mathbf{OH})_2)_{\infty}$. Symmetry code: ¹ 1 -x, +y, 3/2-z. Interactions are labelled according to Table 20.	105
Figure 89 Intra- and intermolecular hydrogen bonding in $(\mathbf{L2}\cdot\mathbf{H2TER}\cdot(\mathbf{OH})_2)_{\infty}$ labelled according to Table 20.....	106
Figure 90 Intermolecular π - π interaction in $(\mathbf{L2}\cdot\mathbf{H2TER}\cdot(\mathbf{OH})_2)_{\infty}$: e) Py \cdots Py ¹ (centroid-centroid distance: 3.703(18) Å; α = 0 °); f) Py \cdots Ph ² (centroid-centroid distance: 3.652(12) Å; α = 3.67(8) °). Symmetry codes: ¹ 1/2-x, 1/2-y, 1-z; ² 1-x, +y, 2-z.	106
Figure 91 View and atom labelling scheme of the asymmetric unit of $(\mathbf{L2}\cdot\mathbf{H2ISO})_{\infty}$. Thermal ellipsoids are drawn at 50 % probability level.	107
Figure 92 View of the hydrogen bonded undulated 1D chain in the co-crystal $(\mathbf{L2}\cdot\mathbf{H2ISO})_{\infty}$ along the <i>b</i> axis. Ph: C14-C15-16-C17-C18-C19; Py1: N1-C1-C2-C3-C4-C5; Py2: N4-C8-C9-C10-C11-C12. Interactions are labelled according to Table 22.....	108
Figure 93 View along the <i>b</i> axis of interacting chains in $(\mathbf{L2}\cdot\mathbf{H2ISO})_{\infty}$. Intermolecular hydrogen bonding labelled according to Table 22. Disorder at thiadiazol ring is not shown for clarity.	108
Figure 94 Packing diagrams showing a) hydrogen bonded undulated sheets running parallel to the <i>a</i> axis; b) overlapped sheets along the <i>b</i> axis.	109
Figure 95 Asymmetric unit and atom labelling scheme for $(\mathbf{L2}\cdot\mathbf{H2ISO}\cdot\mathbf{F4})_{\infty}$	109

Figure 96 View of the polymeric hydrogen bonded network in the co-crystal $(\mathbf{L2}\cdot\mathbf{H2ISO}\cdot\mathbf{F4})_{\infty}$ along the c axis. Interactions are labelled according to Table 23.	110
Figure 97 Intermolecular hydrogen bonding in $(\mathbf{L2}\cdot\mathbf{H2ISO}\cdot\mathbf{F4})_{\infty}$ labelled according to Table 23. a) shows interactions found in a single sheet along the b axis. b) shows additional interactions along the a axis g and h which stabilize adjacent sheets. Disorder at thiadiazol ring is not shown for clarity.	111
Figure 98 Asymmetric unit and atom numbering scheme for $(\mathbf{L2}\cdot\mathbf{H2PyDC})_{\infty}$. Thermal ellipsoids are drawn at 50 % probability level.	112
Figure 99 View along the c axis of the polymeric chain in $(\mathbf{L2}\cdot\mathbf{H2PyDC})_{\infty}$. Disorder is not shown for clarity. Interactions are labelled according to Table 24.	112
Figure 100 Views of intermolecular interaction in the co-crystal $(\mathbf{L2}\cdot\mathbf{H2PyDC})_{\infty}$ along the c (a) and a (b) axis, labelled according to Table 24.	113
Figure 101 View and atom numbering scheme for $(\mathbf{L7}\cdot\mathbf{H2TER})_{\infty}$	115
Figure 102 Views of the undulated polymeric 1D chain in $(\mathbf{L7}\cdot\mathbf{H2TER})_{\infty}$. Interactions are labelled according to Table 26.	115
Figure 103 Packing views of $(\mathbf{L7}\cdot\mathbf{H2TER})_{\infty}$ showing the intermolecular interactions a) along the [101] direction; b) intermolecular π - π interactions between parallel undulated 2D sheets. Interactions labelled according to Table 26.	116
Figure 104 Crystal structure and numbering scheme of R2 . Ellipsoids are drawn at 30 % probability level.	119
Figure 105 Crystal structure and numbering scheme of R3 . Ellipsoids are drawn at 30 % probability level.	120
Figure 106 Intermolecular interactions found in R2 : $\text{C3}^1\text{-H3}^1\cdots\text{F1}$ ($d_{\text{D}\cdots\text{A}} = 3.238(3) \text{ \AA}$; $d_{\text{H}\cdots\text{A}} = 2.5922(2) \text{ \AA}$; $\alpha_{\text{D-H}\cdots\text{A}} = 125.57(17)^\circ$); $\text{C10}^2\text{-H10}^2\cdots\text{F1}$ ($d_{\text{D}\cdots\text{A}} = 3.433(3) \text{ \AA}$; $d_{\text{H}\cdots\text{A}} = 2.5377(3) \text{ \AA}$; $\alpha_{\text{D-H}\cdots\text{A}} = 157.0(2)^\circ$). Only H atoms involved in intermolecular interactions are shown for clarity. Symmetry codes: ¹ $2-x, 2-y, 1-z$; ² $1+x, 1+y, 1+z$	121
Figure 107 View along the a axis of the intermolecular hydrogen bonds in R3 showing the cyclic dimeric pattern R22(8) formed between $(\text{C35-F4}\cdots\text{H36-C36})_2$ along with other hydrogen bonds according to Table 29.	121
Figure 108 Representation of the asymmetric unit of adduct $(\mathbf{L1})_2\cdot\mathbf{R3}$. Displacement ellipsoids are drawn at 50 % probability level.	122
Figure 109 Ball and stick representation of the 2:1 adduct found in $(\mathbf{L1})_2\cdot\mathbf{R3}$. Disorder and H atoms are not shown for clarity. Symmetry code: ¹ $1-x, 1-y, 1-z$	123

Figure 110 Asymmetric unit and numbering scheme for helices $(\mathbf{L3}\cdot\mathbf{R2})_\infty$ and $(\mathbf{L3}\cdot\mathbf{R3})_\infty$ in a) and b), respectively. Hydrogen atoms are omitted for clarity.	124
Figure 111 View of the polymeric helices of $(\mathbf{L3}\cdot\mathbf{R2})_\infty$ (top) and $(\mathbf{L3}\cdot\mathbf{R3})_\infty$ (bottom). Phenyl substituents at Si atoms are depicted as single carbon atoms for clarity.	125
Figure 112 Packing diagram of $(\mathbf{L3}\cdot\mathbf{R3})_\infty$ along <i>c</i> axis showing symmetry related chains in different colours to evidence rotation (yellow: <i>x</i> , <i>y</i> , <i>z</i> , and $-x$, $-y$, $\frac{1}{2} + z$; light blue: <i>y</i> , <i>x</i> , $\frac{1}{4} + z$, and $-y$, <i>x</i> , $\frac{3}{4} + z$). H-atoms and disorder at thiophene rings are omitted for clarity.	126
Figure 113 Solid-state photoluminescent spectra for borasiloxanes R2 and R3 , ligand L3 , helices $(\mathbf{L3}\cdot\mathbf{R2})_\infty$ and $(\mathbf{L3}\cdot\mathbf{R3})_\infty$. Excitation wavelength: 250 nm (R2 , R3); 350 nm (L3 , $(\mathbf{L3}\cdot\mathbf{R2})_\infty$, $(\mathbf{L3}\cdot\mathbf{R3})_\infty$)	127
Figure 114 Experimental (red) and calculated (blue) PXRD patterns <i>I</i> vs 2θ for $(\mathbf{L3}\cdot\mathbf{R2})_\infty$ and $(\mathbf{L3}\cdot\mathbf{R3})_\infty$ in the region 5-30 °	128
Figure 115 Isosurface drawings of selected frontier Kohn–Sham molecular orbitals calculated for L3 , R2 , and R3 at the optimized geometry. Hydrogen atoms were omitted for clarity. Cutoff value = 0.05 e	128
Figure 116 Optimized geometries for cisoid and transoid adducts of $(\mathbf{L3})_2\cdot\mathbf{R2}$ and $(\mathbf{L3})_2\cdot\mathbf{R3}$	129
Figure 117 Crystal structure and numbering scheme for polymer $(\mathbf{L5}\cdot\mathbf{R2})_\infty$. H atoms are omitted for clarity. Symmetry codes: ¹ $-x$, $1-y$, $-z$; ² $2-x$, $-y$, $1-z$; ³ $-2+x$, $1+y$, $-1+z$	130
Figure 118 Polymeric 1D chain of $(\mathbf{L5}\cdot\mathbf{R2})_\infty$. Disorder and H atoms are not shown for clarity.	131
Figure 119 Packing diagrams of $(\mathbf{L5}\cdot\mathbf{R2})_\infty$. π - π interactions are shown in the top image. The slipped packing of 1D chain is shown in the bottom figures. H atoms and disorder are omitted for clarity.	131
Figure 120 Crystal structure of $(\mathbf{L2}\cdot\mathbf{1,4-DITFB})_\infty$. Thermal ellipsoids are drawn at 50 % probability level.	134
Figure 121 Packing diagrams of $(\mathbf{L2}\cdot\mathbf{1,4-DITFB})_\infty$ along [101] direction (left) showing a single layer and [110] direction (right) showing layers in different colours. Halogen bonds are depicted as dashed purple lines. Hydrogen atoms have been omitted for clarity.	134
Figure 122 Preliminary crystal structure of $(\mathbf{HL3})\mathbf{I}_3\cdot\mathbf{I}_2$. Crystal data: <i>a</i> = 3.5862(12); <i>b</i> = 9.6320(9); <i>c</i> = 32.929 Å; β =90.068(12) °; <i>V</i> = 2089.0(5) Å ³ ; Space group: <i>P2/c</i>	136
Figure 123 Cationic head-to-tail arrangement of $(\mathbf{HL3})^+$, counterbalanced by disordered triiodide anions.	136

Figure 124 Asymmetric unit and numbering scheme of $(\text{H}_2\text{L3Br}_4)\text{BrBr}_3 \cdot 0.5\text{CHCl}_3$. Thermal ellipsoids are drawn at 50 % probability level.	137
Figure 125 View of intermolecular interactions of $(\text{H}_2\text{L3Br}_4)\text{BrBr}_3 \cdot 0.5\text{CHCl}_3$ along the <i>c</i> axis. Interactions are labelled according to Table 31.	138
Figure 126 Packing diagrams of $(\text{H}_2\text{L3Br}_4)\text{BrBr}_3 \cdot 0.5\text{CHCl}_3$. along the <i>b</i> and <i>c</i> axis from top to bottom, respectively.	140
Figure 127 Representation of the asymmetric unit of the crystal structure of L11 along the <i>a</i> axis. Thermal ellipsoids are drawn at 50 % probability level. Hydrogen atoms have been omitted for clarity reasons.	142
Figure 128 Intra- and inter-molecular hydrogen bonds found in the crystal structure of L11 , labelled according to Table 33.	142
Figure 129 Packing diagrams of L11 along [100] and [101] directions showing undulated sheets in a) and b), respectively. Adjacent layers are coloured in different colours for the sake of clarity. Hydrogen bonds are represented as dashed lines, interaction i is depicted as dashed black line. Non interacting hydrogens have been omitted for clarity.	143
Figure 130 View of the crystal structure of $(\text{L11} \cdot \text{I}_2) \cdot 0.5\text{I}_2$ along the <i>a</i> axis. Thermal ellipsoids are drawn at 30 % probability level. Symmetry code: ¹ -x, 1-y, -z.	144
Figure 131 View of the CT adduct $(\text{L11} \cdot \text{I}_2) \cdot 0.5\text{I}_2$ showing the Z-shaped assembly formed by three I_2 molecules. Thermal ellipsoids are drawn at 30 % probability level. Symmetry codes: ¹ 2-x, 1-y, z; ² 1-x, 1-y, -z; ³ 1+x, 1+y, +z.	145
Figure 132 Intra- and inter-molecular hydrogen bonds found in the crystal structure of $(\text{L11} \cdot \text{I}_2) \cdot 0.5\text{I}_2$, labelled according to Table 33.	145
Figure 133 Representation of dimers $(\text{L11})_2\text{Z}$ found in the crystal structure of $(\text{L11} \cdot \text{I}_2) \cdot 0.5\text{I}_2$. The crystal packing features multiple hydrogen bonds labelled according to Table 33. Weak π - π interactions occurring between fluoren-9-ylidene cores are coloured in light blue.	146
Figure 134 Asymmetric unit of compound $(\text{HL12})\text{I} \cdot 2.5\text{I}_2$. N-H is displaced over the two N atoms with fractional occupancy of 50 %. Only one position is shown for clarity. Displacement ellipsoids are drawn at 50 % probability level.	147
Figure 135 View of $\Gamma \cdot 5\text{I}_2$ nodes, arranged into a distorted square pyramidal geometry in the crystal structure of $(\text{HL12})\text{I} \cdot 2.5\text{I}_2$. Symmetry codes: ¹ 1/2-x, 1/2+y, 1/2-z; ² -1+x, +y, +z; ³ -x, 1-y, 1-z.	148

Figure 136 Parallelepiped-like box found in (HL12)I·2.5I₂ . Two cations are enclosed in the 3D-polyiodide network. Symmetry codes: ¹ 1/2-x, 1/2+y, 1/2-z; ² -1+x, +y, +z; ³ -x, 1-y, 1-z.	148
Figure 137 Overlapped crystal structures of compounds (HL12)I·2.5I₂ (blue) and (HL12s)I·2.5I₂ (red).	149
Figure 138 Crystal structure of HPyTeI₂ . Displacement ellipsoids are drawn at 50 % probability level.	151
Figure 139 Asymmetric unit with numbering scheme of HPyTeBr₂ along the [101] direction. Thermal ellipsoids are drawn at 50 % probability level.	153
Figure 140 View of intra- and inter-molecular interactions in HPyTeBr₂ along the [101] direction. Interactions are labelled according to Table 35.	154
Figure 141 Packing diagrams showing the herringbone arrangement of HPyTeBr₂ molecules along the <i>a</i> and <i>c</i> axis. Interactions are labelled according to Table 35.	154
Figure 142 Molecular view of HPyTeBr₄ along the <i>b</i> axis. Thermal ellipsoids are drawn at 50 % probability level.	155
A search in the CDS database showed several structures containing Ph–TeBr ₄ anions with similar square pyramidal penta-coordinated tellurium atoms with tellurium-bromine bond lengths and angles similar to those found in HPyTeBr₄ . ^[419–423] The terminal Br atoms of HPyTeBr₄ are involved in several intermolecular Te··Br and C–H··Br interactions showed in Figure 143, along with a packing view.	155
Figure 144 Views of the intermolecular interactions found in HPyTeBr₄ , labelled according to Table 36, along the [101] and [010] directions from left to right.	156
Figure 145 Crystal structure and atom numbering scheme for HL14Cl·2H₂O . Thermal ellipsoids are drawn at 50 % probability level.	156
Figure 146 Hydrogen bonding interactions found in [(HL14)I₂Cl]₃·0.5I₂ . Thermal ellipsoids are drawn at 50 % probability level. Only interacting hydrogens are shown for clarity.	157
Figure 147 View along the <i>a</i> axis and numbering scheme of the asymmetric unit of [(HL14)I₂Cl]₃·0.5I₂ . Thermal ellipsoids are drawn at 50 % probability level. Symmetry code: ¹ 2-x, 2-y, 2-z.	158
Figure 148 Unique H-shaped polyhalide I ₁₀ Cl ₄ ⁴⁻ network formed in [(HL14)I₂Cl]₃·0.5I₂ . I··I interactions are depicted as a and b (I6A ¹ -I2A ⁶ : 3.641(6) Å; I6A ¹ -I7: 3.289(12) Å; I6B ¹ -I2B ⁶ : 3.685(8) Å; I6B ¹ -I7: 3.585(11) Å). Disorder is not shown for clarity reasons. Symmetry codes: ¹ 1+x,+y,+z; ² 2-x,2-y,1-z; ³ +x,+y,1+z; ⁴ 1-x,2-y,2-z; ⁵ 1+x,1+y,+z; ⁶ 1-x,1-y,2-z; ⁷ 2-x,2-y,2-z.	158

Figure 149 Balls and sticks representation of the crystal packing along the <i>a</i> (top) and <i>b</i> (bottom) axis. Hydrogen atoms and disordered fragments have been omitted for clarity.	159
Figure 150 Crystal structure of L16 . Torsional angles, intra- and intermolecular π - π interactions are represented.	162
Figure 151 Packing diagram of L16 along the <i>a</i> axis. Displacement ellipsoids are drawn at 50 % probability level. Hydrogen atoms have been omitted for clarity.	162
Figure 152 Mass spectra of the (a) mixture of tetra- (H4L17), tri- (H3L17Br) and di-substituted (H4L17Br2) derivatives and (b) of the fully carboxylated H4L17	163
Figure 153 Absorption (solid line) and emission (dashed line) spectra for H4L17 measured in DMSO (left) ($[\text{H}_4\text{L17}] = 10^{-5} \text{ M}$, $\lambda_{\text{ex}} = 303 \text{ nm}$) and in the solid state (right) ($\lambda_{\text{ex}} = 350 \text{ nm}$).	164
Figure 154 Crystal structure of H4L17 . Thermal ellipsoids are drawn at 50 % probability level. Hydrogen atoms have been omitted for clarity.	165
Figure 155 View of the mono-dimensional hydrogen bonded chain in the crystal structure of H4L17 . H-bonds are depicted in dashed red lines and are labelled accordingly to Table 38.	165
Figure 156 View of the layered structure in the crystal structure of H4L17 along the <i>c</i> axis. Intramolecular π - π interactions and hydrogen bonds are depicted in dashed lines and labelled according to Table 38.	166
Figure 157 Interlayer hydrogen bonding network found in H4L17 . H-bonds are depicted in dashed red lines and are labelled accordingly to Table 38. Aryl protons are not shown for clarity reasons.	166
Figure 158 Asymmetric unit of the crystal structure of MOF $[(\text{Cd}_2\text{L17}\cdot 3\text{H}_2\text{O})\cdot 3\text{H}_2\text{O}]_\infty$	168
Figure 159 Balls and sticks representation of the Cd-SBU found in MOF $[(\text{Cd}_2\text{L17}\cdot 3\text{H}_2\text{O})\cdot 3\text{H}_2\text{O}]_\infty$. Only carboxylate functionalities are shown for clarity reasons. Interactions are labelled according to Table 39 along with the relevant symmetry codes.	169
Figure 160 View of the crystal structure of $[(\text{Cd}_2\text{L17}\cdot 3\text{H}_2\text{O})\cdot 3\text{H}_2\text{O}]_\infty$ along the <i>c</i> axis. Hydrogen atoms have been omitted for clarity. Thermal ellipsoids are drawn at 50 % probability level.	170
Figure 161 View of intermolecular π - π edge to face interactions in $[(\text{Cd}_2\text{L17}\cdot 3\text{H}_2\text{O})\cdot 3\text{H}_2\text{O}]_\infty$ along the [110] direction. T-shaped: $d\text{C}241 \cdots \text{centroid} = 4.02 \text{ \AA}$, $d\text{H}241 \cdots \text{centroid} = 3.18 \text{ \AA}$; Y-shaped: $d\text{C}271 \cdots \text{centroid} = 4.41 \text{ \AA}$, $d\text{H}271 \cdots \text{centroid} = 3.78 \text{ \AA}$; $d\text{C}281 \cdots \text{centroid} = 4.36 \text{ \AA}$, $d\text{H}281 \cdots \text{centroid} = 3.66 \text{ \AA}$. Symmetry code: $^1 3/2-x, 3/2-y, -1/2+z$	171
Figure 162 Packing diagram of $[(\text{Cd}_2\text{L17}\cdot 3\text{H}_2\text{O})\cdot 3\text{H}_2\text{O}]_\infty$ along the <i>c</i> axis. Hydrogen atoms have been omitted for clarity reasons.	171

Figure 163 Numbering scheme in the asymmetric unit of $[(\text{Cd}_2\text{L17}\cdot 6\text{H}_2\text{O})\cdot 2\text{H}_2\text{O}]_\infty$. Displacement ellipsoids are drawn at 50 % probability level.	173
Figure 164 Perspective views of the SBUs present in $[(\text{Cd}_2\text{L17}\cdot 6\text{H}_2\text{O})\cdot 2\text{H}_2\text{O}]_\infty$. Interactions are described in Table 41. Symmetry codes: ¹ 1-x, 2-y, -z; ² -x, -y, 1-z.	173
Figure 165 Polymeric network of $[(\text{Cd}_2\text{L17}\cdot 6\text{H}_2\text{O})\cdot 2\text{H}_2\text{O}]_\infty$ along the [111] direction. Hydrogen atoms and co-crystallized water molecules have been omitted for clarity. Symmetry codes: ¹ -x, 2-y, -z; ² -x, -y, 1-z.	174
Figure 166 Intermolecular hydrogen bonding in the crystal structure of $[(\text{Cd}_2\text{L17}\cdot 6\text{H}_2\text{O})\cdot 2\text{H}_2\text{O}]_\infty$. Interactions are labelled according to Table 41. Only interacting H atoms are shown for clarity.	175
Figure 167 Packing diagrams of $[(\text{Cd}_2\text{L17}\cdot 6\text{H}_2\text{O})\cdot 2\text{H}_2\text{O}]_\infty$ along the <i>c</i> and <i>a</i> axis. Only interacting H atoms are depicted for clarity.	175
Figure 168 Experimental and simulated PXRD patterns of solvent exchange attempts on as-synthesized material. From the bottom to the top: simulated pattern from SC-XRD data of $[(\text{Cd}_2\text{L17}\cdot 6\text{H}_2\text{O})\cdot 2\text{H}_2\text{O}]_\infty$ (orange) and $[(\text{Cd}_2\text{L17}\cdot 3\text{H}_2\text{O})\cdot 3\text{H}_2\text{O}]_\infty$ (black); experimental pattern from as-synthesized sample (red); experimental patterns after 24 soaking in DCM (light blue), n-hexane (purple), acetonitrile (blue) and toluene (green).	176
Figure 169 DSC analysis on the as-synthesised sample ramping the temperature from RT to 150 °C (blue) and two more consecutive cooling-heating cycles in the range (-50 to 150 °C).	177
Figure 170 Photoluminescence excitation (dashed line) and emission (solid line) for H4L17 (blue) and the as-synthesized material (red) in the solid state. Emission spectra were recorded with $\lambda_{\text{ex}} = 350$ and 370 nm for H4L17 and the polymeric product, respectively.	177
Figure 171 Perspective view of the connectivity of MOF $[(\text{Cu}_2\text{L17})\cdot 3\text{DMF}]_\infty$ along <i>c</i> and <i>a</i> axis. Disordered moieties are shown in both diagrams.	178
Figure 172 Numbering scheme in the asymmetric unit of $(\text{H}_4\text{L17}\cdot \text{Py}_2\text{Et})_\infty$. Thermal ellipsoids are drawn at 50 % probability level.	179
Figure 173 Intra- and inter-molecular interactions in the crystal structure of $(\text{H}_4\text{L17}\cdot \text{Py}_2\text{Et})_\infty$. Only interacting hydrogen atoms are shown for clarity. Interactions are labelled according to Table 43.	180
Figure 174 View of the hydrogen-bonded staircase packing in $(\text{H}_4\text{L17}\cdot \text{Py}_2\text{Et})_\infty$ along the <i>b</i> axis. Only interactions a , d and f are shown for clarity.	181

Figure 175 Packing diagrams of $(\text{H}_4\text{L17}\cdot\text{Py}_2\text{Et})_\infty$ along the a (top) and c (bottom) axis. Interactions are labelled according to Table 43.	181
Figure 176 Perspective view along the [101] direction and atom labelling scheme of the asymmetric unit of $[(\text{Co}_2\text{L3}_2\text{L17}\cdot\text{H}_2\text{O})\cdot 2\text{DMF}]_\infty$. Thermal ellipsoids are drawn at 50 % probability level. The disordered units of L17^{4-} are showed in dark and light grey.....	182
Figure 177 Schematic representation of the SBUs found in $[(\text{Co}_2\text{L3}_2\text{L17}\cdot\text{H}_2\text{O})\cdot 2\text{DMF}]_\infty$. Only the major component (A) of L17^{4-} unit is shown for clarity. Interactions are labelled according to Table 44.....	183
Figure 178 Views of the polymeric arrangement of $[(\text{Co}_2\text{L3}_2\text{L17}\cdot\text{H}_2\text{O})\cdot 2\text{DMF}]_\infty$ along the a and b axis, respectively. Disorder at L17^{4-} units and hydrogen atoms are omitted for clarity.	185
Figure 179 Packing diagram of $[(\text{Co}_2\text{L3}_2\text{L17}\cdot\text{H}_2\text{O})\cdot 2\text{DMF}]_\infty$. Solvent accessible channels are represented in light blue.	185
Figure 180 Asymmetric unit of $[(\text{Zn}_2\text{L3L17}\cdot 3\text{H}_2\text{O}\cdot \text{DMF})\cdot 3.5\text{DMF}]_\infty$. Thermal ellipsoids are drawn at 50 % probability level. H atoms have been omitted for clarity.....	187
Figure 181 Representation of the SBUs found in $[(\text{Zn}_2\text{L3L17}\cdot 3\text{H}_2\text{O}\cdot \text{DMF})\cdot 3.5\text{DMF}]_\infty$. Zn1-SBU (left) and Zn2-SBU (right). Interactions are labelled according to Table 47.	187
Figure 182 Perspective view of the polymeric network in $[(\text{Zn}_2\text{L3L17}\cdot 3\text{H}_2\text{O}\cdot \text{DMF})\cdot 3.5\text{DMF}]_\infty$. Only H-atoms involved in the interactions (labelled according to Table 47) are depicted; co-crystallized DMF molecules are not shown for clarity.	188
Figure 183 Packing diagram of $[(\text{Zn}_2\text{L3L17}\cdot 3\text{H}_2\text{O}\cdot \text{DMF})\cdot 3.5\text{DMF}]_\infty$ along the [111] direction. Interactions are labelled according to Table 47.	189
Figure 184 Packing diagram of $[(\text{Zn}_2\text{L3L17}\cdot 3\text{H}_2\text{O}\cdot \text{DMF})\cdot 3.5\text{DMF}]_\infty$ showing solvent accessible voids along the b axis.....	190

List of schemes

Scheme 1: Schematic interaction geometries for benzene dimers. Centroids are displayed in red dots. Distances calculated in the gas phase: $R_1 \sim 3.7\text{--}4.0 \text{ \AA}$, $d \sim 3.5 \text{ \AA}$, $r \sim 1.5\text{--}1.8 \text{ \AA}$, $R_3 \sim 5.0 \text{ \AA}$, and $R_4 \sim 5.0 \text{ \AA}$. ^[11,12]	2
Scheme 2 Aromatic substituents commonly employed to prepare functional materials based on $\pi\text{--}\pi$ interactions.	5
Scheme 3 Hydrogen-bonded patterns: a) dimeric arrangement typical of carboxylic acids; b) dimeric arrangement typical of amides; c) polymeric chain stabilized <i>via</i> hydrogen bonds; d) tetrameric pattern adopted by <i>N</i> -phenylformamide.	7
Scheme 4 Generic graph set motif.	8
Scheme 5 Examples of graph set assignments for selected hydrogen bonded motifs.	9
Scheme 6 Three-coordinated boron derivatives employed as building blocks in supramolecular chemistry.	11
Scheme 7 Selected molecular moieties employed in the preparation of HOFs. From top to bottom: carboxylic acid, amide, amidinium, boronic acid, pyrazole, imidazole, pyridine, resorcinol, 2,4-diaminotriazine, 2,6-diaminopurine.	32
Scheme 8 Selected ligand used for the preparation of HOFs.	33
Scheme 9 a) self-condensation of 1,4-benzenediboronic acid (BDBA) into COF-1. b) condensation between BDBA and hexahydroxy tetraphenylene (HHTP) to produce COF-5. Reproduced from ref. ^[244]	35
Scheme 10 Reaction mechanism for an acid catalysed Schiff-base formation from a generic aldehyde and an amine. Schiff-base derivatives employed in the formation of COFs are represented in the bottom.	36
Scheme 11 Pyridyl-based building blocks.	39
Scheme 12 Pyridyl-based substrates containing chalcogen atoms.	40
Scheme 13 Co-facial bifluorene derivatives.	41
Scheme 14 The two periplanar and the antiperiplanar arrangements of L1 from left to right, respectively.	43
Scheme 15 Phosphor-1,1-dithiolates derivatives: A-D = dithiophosphato, dithiophosphinato, dithiophosphonato, and amidodithiophosphonato.	51
Scheme 16 Sonogashira coupling reactions for the preparation of ligand L3 and L4 . i) Pd(PPh ₃) ₂ Cl ₂ , CuI, NHEt ₂ , N ₂ , reflux, 48 h.	58
Scheme 17 Sonogashira coupling reactions for the preparation of ligand L5 and L6 . i) Pd(PPh ₃) ₂ Cl ₂ , CuI, NHEt ₂ , N ₂ , reflux, 48 h.	81

Scheme 18 Building blocks used in the formation of the luminescent CPs $(2\cdot L5\cdot CHCl_3)_\infty$ and $(3\cdot L5)_\infty$	84
Scheme 19 Organic benzenedicarboxylic acids used for the formation of co-crystals. Terephthalic acid (H_2TER), 2-bromoterephthalic acid ($H_2TER-Br$), 2,5-dihydroxyterephthalic acid ($H_2TER-(OH)_2$), tetrafluoroterephthalic acid (H_2TER-F_4), isophthalic acid (H_2ISO), tetrafluoroisophthalic acid (H_2ISO-F_4), 2,5-pyridinedicarboxylic acid (H_2PyDC).	94
Scheme 20 Sonogashira coupling reactions for the preparation of ligand L7 and L8 . i) $Pd(PPh_3)_2Cl_2$, CuI , $NHEt_2$, N_2 , reflux, 48 h.	114
Scheme 21 Formation of eight-membered cyclic borasiloxanes R1-R3 <i>via</i> cyclocondensation reactions of diphenylsilanediol and boronic acids.	118
Scheme 22 Formation of $(HL3)I_3\cdot I_2$ and $(H_2L3Br_4)BrBr_3\cdot 0.5 CHCl_3$. i) $L3:I_2$ (1:1) CH_3CN ; ii) $L3:Br_2$ (1:5) $CHCl_3$	135
Scheme 23 Synthetic approach for the preparation of L9 , L10 and L11	141
Scheme 24 Hypervalent tellurium compounds prepared from L13 : $HPyTeI_2$, $HPyTeBr_2$, $HPyTeBr_4$	150
Scheme 25 Hypervalent tellurium compounds prepared from dipyrid-4-yltelluride. Refcodes are indicated in parenthesis.	152
Scheme 26 Selected fluorene-based building blocks from literature. Compounds numbers are listed below with the relevant reference reported as superscripts. 1F , ^[436] 2F where: $R = H$, ^[438] $R = Me$, Et , ^[442] $R = Pr$, ^[443] 3F , ^[440] 4F , ^[439] 5F , ^[441] 6F , ^[444] 7F , ^[437] 8F-9F , ^[445] 10F . ^[430]	160
Scheme 27 Three-step synthetic approach for H₄L17	161
Scheme 28 Different coordination modes of $L17^{4-}$ in $[(Cd_2L17\cdot 3H_2O)\cdot 3H_2O]_\infty$: chelating (η^2), chelating/bridging ($\mu_2-\eta^2-\eta^1$), bridging ($\mu_2-\eta^2$).	170

List of tables

Table 1 Hydrogen bond classification and features.....	7
Table 2 CT adducts classification according to the extent of perturbation induced by the donor on the diiodine fragment.	14
Table 3 Hydrogen bonding interactions in $[\text{ZnL1}(\text{NO}_3)_2 \cdot \text{CH}_3\text{CN}]_2$	47
Table 4 Intermolecular interactions in $(\text{ZnL1Cl}_2)_\infty$	50
Table 5 Selected bond lengths (Å), bond and torsion angles (°) and angles between pyridyl ring mean planes (°) for $(\mathbf{1} \cdot \mathbf{L1})_2$ and $(\mathbf{1} \cdot \mathbf{L2})_\infty$	54
Table 6 Crystal data and refinement parameters for the two L3 polymorphs.....	60
Table 7 Selected bond lengths (Å), and angles (°) for $[\text{AgL3}(\text{OTf})((\text{CH}_3)_2\text{CO})_{2.5}]_\infty$	67
Table 8 Hydrogen bonding interactions in $[\text{CdL3}(\text{NO}_3)_2(\text{H}_2\text{O})_2 \cdot 1.5\text{H}_2\text{O}]_\infty$	71
Table 9 Hydrogen bonding interactions in $[\text{CuL3}(\text{NO}_3)_2 \cdot \text{CH}_3\text{CN}]_2 \cdot 2\text{CH}_3\text{CN}$. D···A distances (Å) and D–H–A angles (°). Symmetry code: $^1 +x, -1+y, +z$	74
Table 10 Geometrical features including angles, dihedral angles (°) and distances (Å) of L3 molecules in the crystal structures of L3 (orthorhombic), $[\text{AgL3}(\text{OTf})((\text{CH}_3)_2\text{CO})_{2.5}]_\infty$, $[\text{CdL3}(\text{NO}_3)_2(\text{H}_2\text{O})_2 \cdot 1.5\text{H}_2\text{O}]_\infty$ and $[\text{CuL3}(\text{NO}_3)_2 \cdot \text{CH}_3\text{CN}]_2 \cdot 2\text{CH}_3\text{CN}$. Centroids and planes are identified by numbers (1-3) and letters (a-c), respectively. Atoms have been renumbered for clarity reasons accordingly to the molecular structure given below.	77
Table 11 List of intermolecular interactions and contacts for $(\mathbf{2} \cdot \mathbf{L5} \cdot \text{CHCl}_3)_\infty$	89
Table 12 Selected bond lengths (Å) and angles (°) for compounds 3 , $(\mathbf{2} \cdot \mathbf{L5} \cdot \text{CHCl}_3)_\infty$ and $(\mathbf{3} \cdot \mathbf{L5})_\infty$	91
Table 13 Geometrical features including angles, dihedral angles (°) and distances (Å) of L5 molecules in the crystal structures of L5 , $(\mathbf{2} \cdot \mathbf{L5} \cdot \text{CHCl}_3)_\infty$ and $(\mathbf{3} \cdot \mathbf{L5})_\infty$. Centroids and planes are identified by numbers (1-5) and letters (a-e), respectively. Atoms have been renumbered for clarity reasons accordingly to the molecular structure given below.	92
Table 14 Predicted pKa values for the selected substrates.....	95
Table 15 Hydrogen bonding in the crystal structure of HL1Cl·3H₂O	97
Table 16 Crystal data and refinement parameters for HL1Cl·3H₂O , $(\mathbf{L1} \cdot \mathbf{H}_2\text{TER})_\infty$, $(\mathbf{L2} \cdot \mathbf{H}_2\text{TER} \cdot \text{Br})_\infty$, $(\mathbf{L2} \cdot \mathbf{H}_2\text{TER} \cdot (\text{OH})_2)_\infty$, $(\mathbf{L2} \cdot \mathbf{H}_2\text{ISO})_\infty$, $(\mathbf{L2} \cdot \mathbf{H}_2\text{ISO} \cdot \text{F}_4)_\infty$, $(\mathbf{L2} \cdot \mathbf{H}_2\text{PyDC})_\infty$..	99
Table 17 Angles (°) between different planes in the crystal structure of $(\mathbf{L1} \cdot \mathbf{H}_2\text{TER})_\infty$	100
Table 18 Intermolecular hydrogen bonding found in $(\mathbf{L1} \cdot \mathbf{H}_2\text{TER})_\infty$	101
Table 19 Intermolecular hydrogen bonding found in $(\mathbf{L2} \cdot \mathbf{H}_2\text{TER} \cdot \text{Br})_\infty$	103
Table 20 Intra- and intermolecular hydrogen bonding found in $(\mathbf{L2} \cdot \mathbf{H}_2\text{TER} \cdot (\text{OH})_2)_\infty$	105

Table 21 Bond lengths (Å) and angles (°) of the carboxylic groups in (L2·H2TER-(OH)2)_∞ and (L2·H2TER-Br)_∞	107
Table 22 Intermolecular hydrogen bonding found in (L2·H2ISO)_∞	108
Table 23 Intermolecular hydrogen bonding found in (L2·H2ISO-F4)_∞	110
Table 24 Intermolecular hydrogen bonding found in (L2·H2PyDC)_∞	112
Table 25 Bond lengths (Å) and angles (°) of the carboxylic groups in (L2·H2ISO)_∞ , (L2·H2ISO-F4)_∞ and (L2·H2PyDC)_∞	113
Table 26 Intermolecular hydrogen bonding found in (L7·H2TER)_∞	116
Table 27 Bond lengths (Å) and angles (°) of the carboxylic groups in (L7·H2TER)_∞ , (L1·H2TER)_∞ , (L2·H2TER-Br)_∞ and (L2·H2TER-(OH)2)_∞	117
Table 28 Selected bond lengths (Å) and angles (°) for R1-R3	120
Table 29 Intermolecular hydrogen bonding interactions found in R3	122
Table 30 CT adducts and ionic compounds obtained from N-donors L1 and L2	132
Table 31 Hydrogen bonds and contacts found within the crystal structure of (H2L3Br4)BrBr3·0.5 CHCl3	138
Table 32 Selected bond lengths (Å) and angles (°) for the cationic fragments (H2L3Br4)²⁺ in (H2L3Br4)BrBr3·0.5CHCl3	139
Table 33 Intra and intermolecular hydrogen bonding interactions in L11 and (L11·I2)·0.5I2	143
Table 34 Selected bond lengths (Å) and angles (°) for (HL12)I·2.5I2 and (HL12s)I·2.5I2	147
Table 35 Intra- and inter-molecular interactions found in HPyTeBr2	153
Table 36 Intramolecular interactions found in HPyTeBr4	155
Table 37 Hydrogen bonding interactions found in [(HL14)I2Cl]3·0.5I2 . Calculated distances (Å) and angles (°) are summarized below.	157
Table 38 Hydrogen bonding network in the crystal structure of H4L17	167
Table 39 Intermolecular hydrogen bonds found in the crystal structure of [(Cd2L17·3H2O)·3H2O]_∞	169
Table 40 Crystal data and structure refinement parameters for [(Cd2L17·3H2O)·3H2O]_∞ and [(Cd2L17·6H2O)·2H2O]_∞	172
Table 41 Intermolecular interactions found in [(Cd2L17·6H2O)·2H2O]_∞	174
Table 42 Unit cell parameters for [(Cu2L17)·3DMF]_∞	179
Table 43 Summary of the hydrogen bonding interactions in (H4L17·Py2Et)_∞	180
Table 44 Intermolecular hydrogen bonds in [(Co2L32L17·H2O)·2DMF]_∞	183

Table 45 Selected bond lengths (Å) and angles (°) for [(Co ₂ L ₃ L ₁₇ ·H ₂ O)·2DMF] _∞	184
Table 46 Geometrical features including angles, dihedral angles (°) and distances (Å) of L ₃ molecules in the crystal structures of [(Co ₂ L ₃ L ₁₇ ·H ₂ O)·2DMF] _∞ , [CuL ₃ (NO ₃) ₂ ·CH ₃ CN] ₂ ·2CH ₃ CN and [(Zn ₂ L ₃ L ₁₇ ·3H ₂ O·DMF)·3.5DMF] _∞ (§3.2.4.2). Centroids are identified by numbers (1-3). Atoms have been renumbered for clarity reasons accordingly to the molecular structure presented in Table 10.	186
Table 47 Intermolecular interactions found in the SBUs of [(Zn ₂ L ₃ L ₁₇ ·3H ₂ O·DMF)·3.5DMF] _∞	188
Table 48 Summary of the supramolecular networks obtained from ligand L ₁ -L ₁₁	191
Table 49 Products obtained from the reactions between L ₁₂ -L ₁₄ and halogens/interhalogens.	193

List of abbreviations

1,4-DITFB	1,4-diiidotetrafluorobenzene
4,4'-bipy	4,4'-bipyridine
AIE	Aggregation Induced Emission
CN	Coordination Number
COFs	Covalent Organic Frameworks
CPs	Coordination Polymers
CSD	Cambridge Structural Database
CT	Charge-Transfer
DFT	Density Functional Theory
DMF	<i>N,N</i> -Dimethylformamide
DMSO	Dimethyl sulfoxide
DSC	Differential Scanning Calorimetry
E	eclipsed
EDG	Electron-donating group
EWG	Electron-withdrawing group
H ₂ adc	Acetylenedicarboxylic acid
H ₃ BTC	Benzene(1,3,5-tricarboxylic acid) (trimesic acid)
H ₂ ISO	Benzene(1,3-dicarboxylic acid) (isophthalic acid)
H ₂ ISO-F ₄	tetrafluoroisophthalic acid
HOFs	Hydrogen-bonded Organic Frameworks
H ₂ PyDC	2,5-pyrdinedicarboxylic acid
H ₂ TER	Benzene(1,4-dicarboxylic acid) (terephthalic acid)
H ₂ TER-Br	2-bromoterephthalic acid

H ₂ TER-F ₄	tetrafluoroterephthalic acid
H ₂ TER-(OH) ₂	2,5-dihydroxyterephthalic acid
KS	Kohn-Sham
LP	lone pair
MOFs	Metal-Organic Frameworks
NBO	Natural Bond Orbital
NLO	Non-Linear Optics
NMR	Nuclear Magnetic Resonance
OTf	Trifluoromethanesulfonate
PCPs	Porous Coordination Polymers
PD	parallel-displaced
PES	Potential Energy Surface
PXRD	Powder X-ray diffraction
RCSR	Reticular Chemistry Structure Resources
SAPT	Symmetry-adapted perturbation theory
T	T-shaped
XB	Halogen bonding
XRD	X-ray diffraction
Y	Y-shaped

1. Introduction to Supramolecular Chemistry

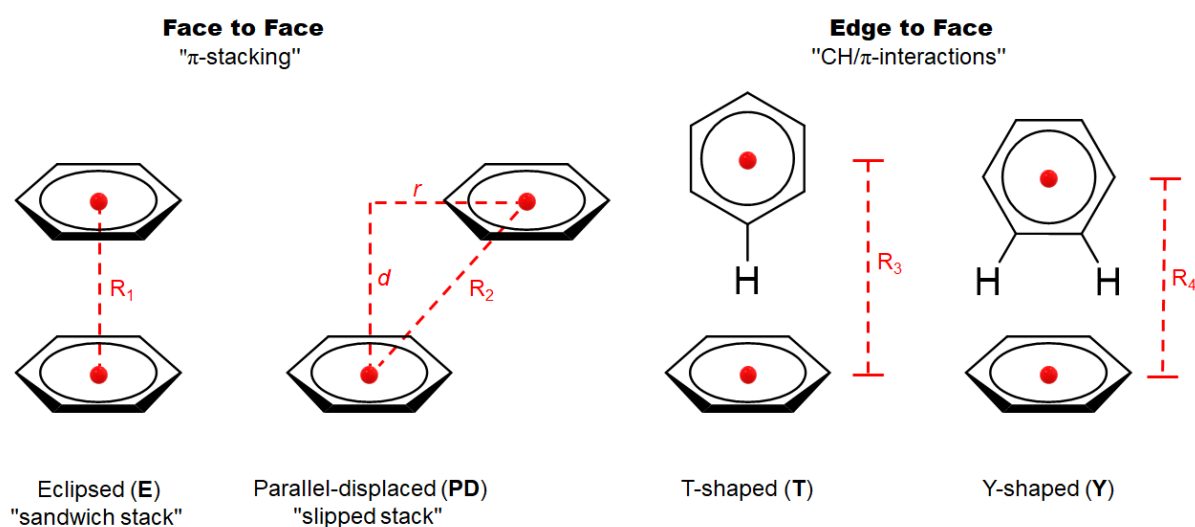
Supramolecular chemistry deals with the study of complex systems organized and held together by means of intermolecular interactions.^[1] Molecular building blocks are meticulously designed and selected according to their chemical and physical properties, and complementarity. In fact, the organization of building units into complex patterns occurs along spontaneous association or self-assembly driven by means of non-covalent interactions. In the last thirty years, a plethora of interactions including coordinative bonds,^[2] dynamic covalent bonds,^[3] π - π interactions,^[4] hydrogen-bonds,^[5] boron-nitrogen bonds,^[6] halogen-bonds,^[7] and van der Waals interactions,^[8] have been used to construct predictable networks by inorganic and organic supramolecular chemists. In the following sections the key concepts of non-covalent interactions are discussed in order to show the reader the actual state of the art in the field of supramolecular chemistry. Intermolecular interactions, although presented and treated separately, work in a synergic manner, following known hierarchies, so that the overall features of each supramolecular system are determined by the strong synergic behaviour of all the observed intermolecular interactions.

1.1. Supramolecular interactions

1.1.1. π - π Interactions

Benzene, the quintessential aromatic molecule, is in the spotlight since the born of organic chemistry and served as a benchmark to investigate the nature of π - π interactions in both gaseous, liquid and solid state. The need to understand and interpret such non-covalent interactions arises from the myriad of systems where π - π interactions play a predominant role leading to materials with sophisticated physical and chemical properties. The π - π interactions can be described by considering two benzene units interacting to form non-covalent dimers. As showed in Scheme 1, benzene units can adopt either parallel or perpendicular orientations leading to “face-to-face” or “edge-to-face” arrangements, respectively. Among them, four limit interaction geometries can be envisaged: eclipsed (**E**), also known as “sandwich stack”, and parallel-displaced (**PD**) or “slipped stack” for the face-to-face arrangement, and the T-shaped (**T**) and Y-shaped (**Y**) for the edge-to-face geometries (Scheme 1). When benzene rings are parallel, as in the **E** and **PD** configurations, the interaction is usually referred as π -stacking. These arrangements can be described by taking into account the parameters described in

Scheme 1, namely the centroid-centroid distances R_1 and R_2 , and the displacement (r) and interplanar (d) distances in the case of **PD** arrangement. In the edge-to-face arrangement benzene rings are orthogonally disposed, and the interaction can be rationalized in terms of CH/ π interaction aroused from the hydrogen of a benzene ring pointing towards the electron cloud of the second benzene ring. Moreover, it is worth noting that the just presented geometries are often found distorted in more complex systems and the resultant arrangements need to be described considering various rotations, twists and tilts.^[9,10]



Scheme 1: Schematic interaction geometries for benzene dimers. Centroids are displayed in red dots. Distances calculated in the gas phase: $R_1 \sim 3.7\text{--}4.0 \text{ \AA}$, $d \sim 3.5 \text{ \AA}$, $r \sim 1.5\text{--}1.8 \text{ \AA}$, $R_3 \sim 5.0 \text{ \AA}$, and $R_4 \sim 5.0 \text{ \AA}$.^[11,12]

In order to quantify the nature and the extent of $\pi\text{--}\pi$ interactions in the solid-state, X-ray diffraction (XRD) analysis on single crystals is certainly the most used experimental technique. Although the structural determination is essential to rationalize such non-covalent interactions, the determined morphology not always reflects the lowest energy system. In fact, different polymorphs can be obtained by varying the crystal growth conditions as suggested by the three isolated benzene polymorphs, two monoclinic and one orthorhombic, reported in the Cambridge Structural Database (CSD) up to now.^[13–21]

With this in mind, it is of particular interest to rely on computational methods in order to quantify the kinetic and thermodynamic contributes which govern the crystal packing. Density functional theory (DFT) calculations have led to crucial outcomes in the evaluation of electrostatic and steric components in $\pi\text{--}\pi$ interactions. Calculations carried out in the gas-phase for the possible interaction geometries of benzene dimers suggested that the **PD** and **T** are low-energy configurations and have similar energies.^[22] In contrast, the **E** arrangement has the

highest energy and is located on a maximum on the potential energy surface.^[22] Turning to the broader picture, other key aspects must be considered in the computing of the electronic properties of more complicated systems such as: the presence of substituents and/or heteroatoms, the presence of fused rings, and the solvent effect. One of the first computational models used for understanding π - π interactions was proposed by Hunter and Sanders^[23] with the scope to rationalize porphyrins association. The energies involved in π - π interactions were evaluated considering arenes as molecular quadrupoles and their interaction based on two main electrostatic contributes: repulsion (π - π) and attraction (π - σ).^[24] Among benzene dimers, a lower stability of **E** conformation was also confirmed by the Hunter and Sanders model as well as a higher stability of slipped and edge-to-face configurations. The work was then extended beyond the dimeric environment revealing a herringbone arrangement of arenes, which is often experimentally observed in the solid-state.^[24] Moreover, the influence in polarization of the electronic clouds along the aromatic systems by the introduction of substituents was computed.^[25] To streamline substituent effect, electron-withdrawing groups (EWGs) such as NO₂ were considered and the consequent decrease repulsion between arenes calculated. On the other hand, in the presence of electron-donating groups (EDGs) such as NR₂ (R = alkyl), an increased π -electron repulsion was found. Nevertheless, generally speaking, it was demonstrated that substituents preferentially stabilize **PD** configuration. When multiple EWGs and/or EDGs were introduced in both rings the energetically most stable arrangements were found to be the complementary configuration between one electron poor and one electron rich arene disposed along an anti-parallel rings' orientation.^[12,26-28]

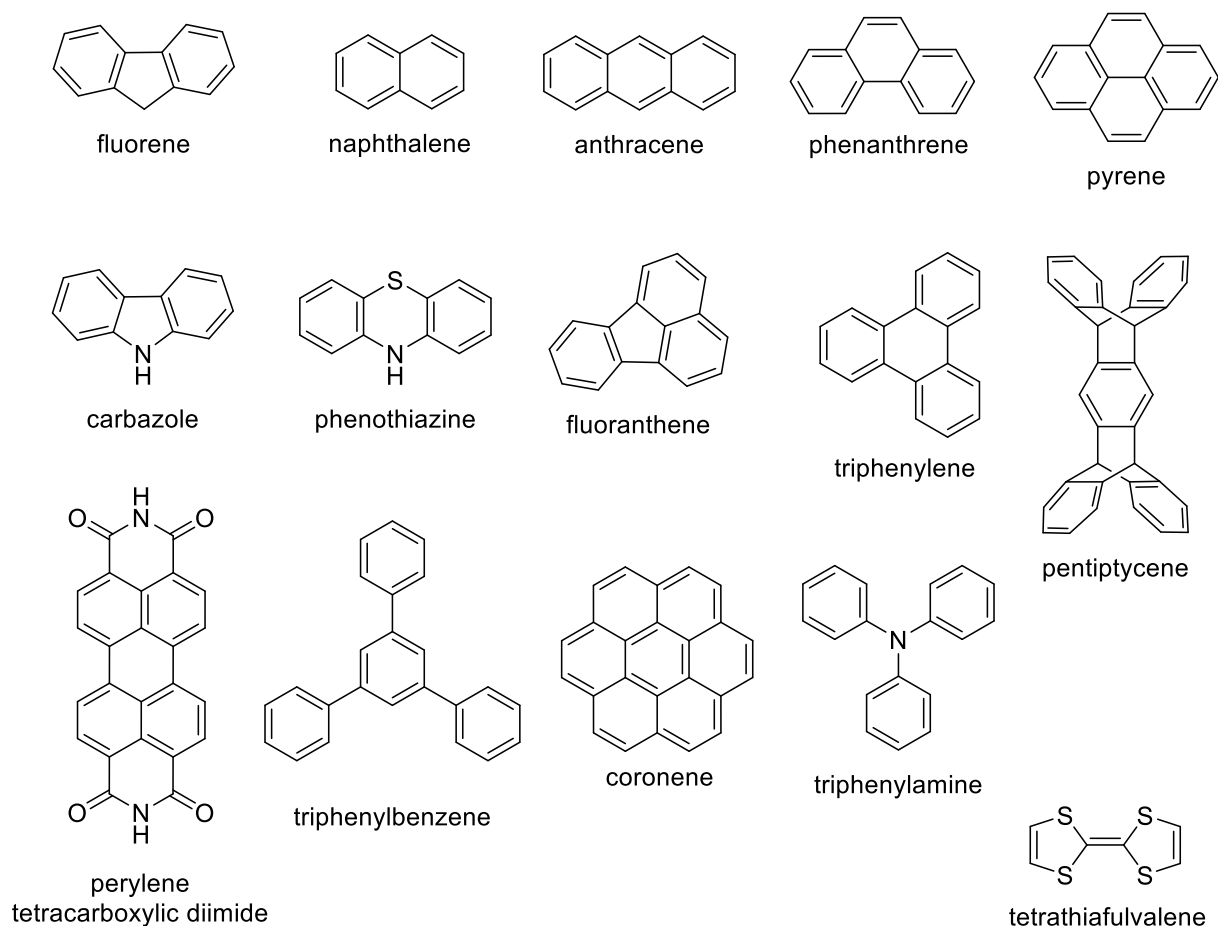
Since the Hunter-Sanders model was introduced, dozens of other studies were carried out with more and more sophisticated computational approaches such as the symmetry-adapted perturbation theory (SAPT)^[29-32] which evidenced the role of forces such as dispersion and exchange-repulsion ones in determining the total binding energy of substituted arenes.^[33]

Theoretical studies extended to aromatic rings containing heteroatoms, revealed that heterocycles such as pyridine are willing to form dimers of the type benzene-pyridine and pyridine-pyridine according to the most stable **PD** configuration.^[34,35] The dimers stability has been attributed to three main effects: contraction of the pyridinyl π -cloud resulting in a decreased exchange-repulsion contribute; direct interaction between an electron rich N-atom and an electron deficient H-atom of adjacent aromatic rings; the presence of complementary electrostatic interactions. Moreover, the inclusion of more than one nitrogen in the arene system often results in strengthening of the π - π interaction and decrease of the interplanar distance.^[36,37] It is worth to note that the presence of N-H groups in the aromatic ring can

improve the stability of the final system.^[38,39] In fact, N–H groups are expected to establish hydrogen bonds with complementary species leading to shorter interplanar distances thus strengthening π – π interactions and benefiting both stacking interactions and hydrogen bonds.^[40] Other studies demonstrated that in aromatic heterocycles functionalization of N-atoms by methylation led to enhanced stacking interactions.^[41]

Computational approaches were also employed to estimate solvent effects in both water and organic media.^[42,43] In this challenging context, dispersion contributes and solvophobic effects not always can be discriminated from the other factors that drive π – π interactions.^[44] In fact, the arene size also influences the balance between dispersion and solvophobic effects. In addition, solvent effects in heterocycles were studied, confirming the greater stability of the **PD** arrangement compared to the other geometries.^[45]

The knowledge acquired on the role of π – π interactions moved the scientific community towards their use in developing novel materials and systems with potential applications in chemistry, biology and material science.^[46] It is well known that π – π interactions are responsible for the thermal stability and folding of proteins.^[47–49] Moreover, biological applications of such non-covalent interactions surely concern the field of drug design and their delivery in biological systems.^[50] Among the applications more related to the field of molecular science we can cite the study of luminescent materials,^[51,52] ranging from fluorescence sensing and switching, to the Aggregation Induced Emission (AIE) phenomenon.^[53–57] Moreover, π – π interactions are exploited to prepare energetic salts^[58] and to develop nitroaromatic explosive detectors.^[59] Furthermore, π – π interactions are essentials for the design of electronic and optoelectronic devices,^[60,61] molecular shuttles,^[62] and photoconductive devices.^[63] A recent application of supramolecular polymers includes the study of the peculiar “self-healing” process, made possible by the presence of π – π interactions.^[64] An overview of the most common groups employed in the design of such interesting materials is provided in Scheme 2.



Scheme 2 Aromatic substituents commonly employed to prepare functional materials based on π - π interactions.

1.1.2. Hydrogen bonds

The hydrogen bonding is undoubtedly one of the most important non-covalent interactions in chemistry, biology and medicine. IUPAC defines the hydrogen bond as: "an attractive interaction between a hydrogen atom from a molecule or a molecular fragment $X-H$ in which X is more electronegative than H , and an atom or a group of atoms Y in the same or a different molecule, in which there is the evidence of bond formation".^[5] In other words, it is the result of a dipole-dipole interaction between two species and is usually depicted as $X-H\cdots Y$ or $D-H\cdots A$ where a proton donating species $D-H$ interacts with a proton acceptor A . Although D and A are typically electronegative elements, it is worth noting that also the fragment $C-H$, where the electronegativity difference between carbon and hydrogen is not very large, can act as donating species and its role in the construction of supramolecular networks spans from hydrogen bonding to $C-H\cdots\pi$ interactions.^[65] Early studies on hydrogen bonds date back to the first half

of the 20th century culminating in 1939 with the publication of the book "*The Nature of the Chemical Bond and the Structure of Molecules and Crystals*" written by Linus Pauling.^[66] The quintessential hydrogen bond is that found in the most important molecule which is water and is responsible of its unique physical and structural properties such as high boiling point, high surface tension, solid phase less dense than liquid phase, ice-clathrate formation, and so on. The first studies on the crystal structure of ice revealed that oxygen atoms interact with the hydrogen atoms of adjacent molecules forming puckered layers of fused hexagons where oxygens are alternatively raised and lowered.^[67] The layers interact each other so that each oxygen is surrounded by four other hydrogen-bonded molecules in an overall tetrahedral geometry along the hexagonal lattice (Figure 1).

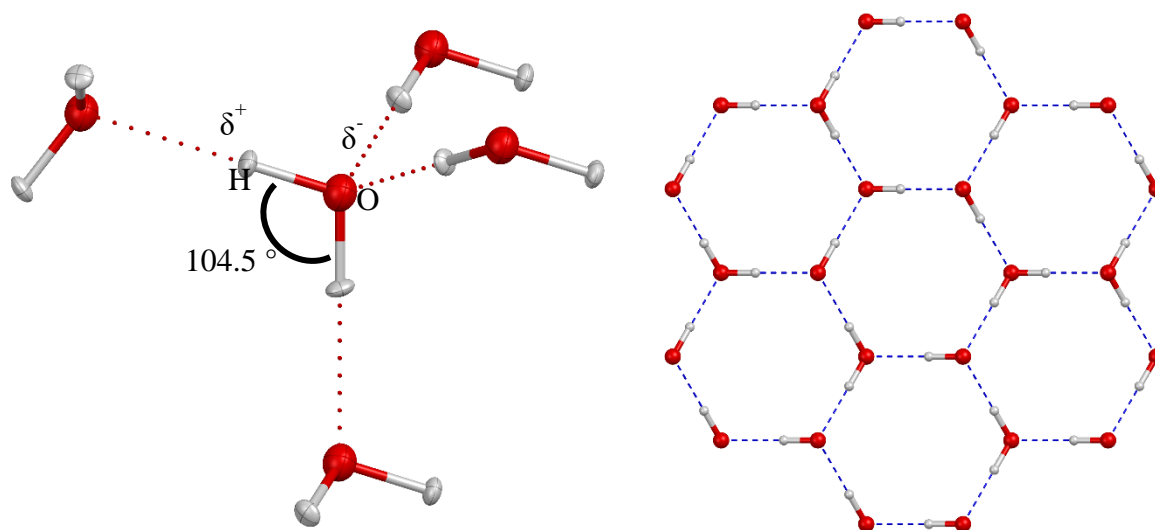


Figure 1 Schematic representation of the tetrahedral arrangement found in the crystal structure of ice (left) and of its hexagonal packing (right).

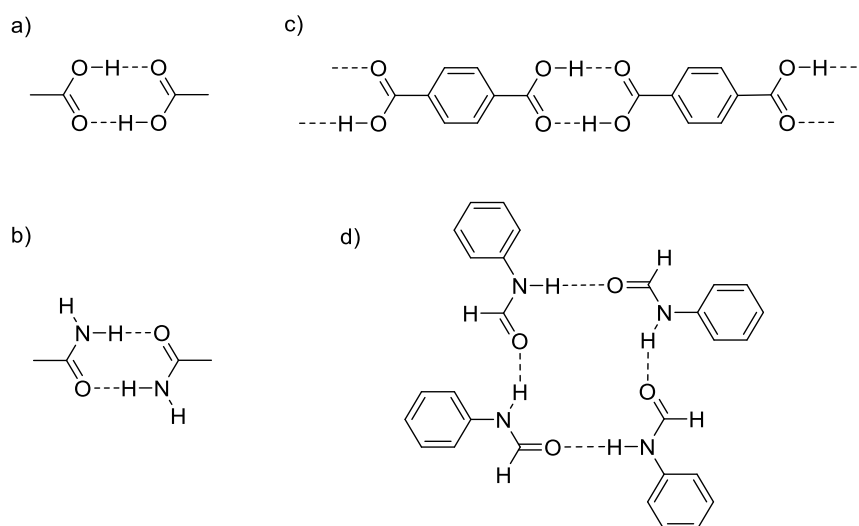
Hydrogen bonds can be classified according to the strength of the involved interaction expressed in binding energy, E_{HB} and are commonly referred as strong, moderate and weak depending on the bond distances and angle within the fragment D–H...A (Table 1).^[68]

Among others, carboxylic acids, amides, alcohols, and amines are the class of compounds which have been more widely investigated for their ability to engage hydrogen bonds following predictable interaction patterns.^[69]

Table 1 Hydrogen bond classification and features.

H-bond	Weak	Moderate	Strong
D–H···A	electrostatic	electrostatic-covalent	mostly covalent
Bond lengths	D–H \ll H···A	D–H $<$ H···A	D–H \approx H···A
H···A (Å)	3.2 - 2.2	2.2 - 1.5	1.5 - 1.2
D···A (Å)	4.0 - 3.2	3.2 - 2.5	2.5 - 2.2
D–H–A angle (°)	90 - 150	130 - 180	165 - 180
Bond energy, E_{HB} (kcal mol ⁻¹)	1 - 4	4 - 15	15 - 45

Carboxylic acids and amides are willing to form eight-membered dimeric patterns held together by two hydrogen bonds of the type O–H···O=C and N–H···O=C, respectively (a and b in Scheme 3). More complex patterns can be obtained for example by introducing more than one hydrogen-bondable moiety in the molecular structure or by the presence of substituents as empathized by terephthalic acid and *N*-phenylformamide which form a linear polymer and a tetrameric arrangement, respectively (c and d in Scheme 3).^[70,71]



Scheme 3 Hydrogen-bonded patterns: a) dimeric arrangement typical of carboxylic acids; b) dimeric arrangement typical of amides; c) polymeric chain stabilized *via* hydrogen bonds; d) tetrameric pattern adopted by *N*-phenylformamide.

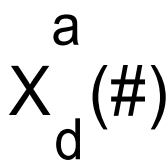
As can be intuitively understood, the strength and thus the stability of the overall system is directly proportional to the number of hydrogen bonds established. Therefore, the complexity of patterns that can be formed has almost no limit and is extremely high in biological systems. Another factor that drastically influences the strength of interaction is the presence of a solvent. Polar aprotic solvents such as dimethyl sulfoxide (DMSO), *N,N*-dimethylformamide (DMF) and acetonitrile are strong hydrogen bond acceptors and negatively influence the formation of hydrogen bonds between solute molecules. Polar protic solvents such as water or alcohols can engage hydrogen bonds with solute molecules and compete in the formation of the expected pattern. The solvent effect must be also taken into consideration when apolar media such as chloroform and dichloromethane are used. For example, while studying the hydrogen binding constant of two species in solution by means of ¹H Nuclear Magnetic Resonance (NMR) experiments, the water content in the organic solvent used, could potentially affect and interfere in the determination of the searched parameter.^[69]

Other classes of compounds have been extensively investigated for their unique features in hydrogen bond formation such as urea^[72] and thiourea^[73] derivatives, triazole^[74], pyridine^[75–79] and other analogue heterocycles.^[80,81]

Ground-breaking studies on the predictability of hydrogen bond patterns date back to the 1990s.^[82] By comparing and rationalising the crystalline structures for hydrogen bonded systems reported at the time, M. Etter enounced some empirical rules that proved successful in determining design and predictability of the final networks:

- 1) All good proton donors and acceptors are used in hydrogen bonding.
- 2) Intramolecular hydrogen bonds are favoured over intermolecular ones if they result in six-membered rings.
- 3) Once the intramolecular pattern is defined, all remaining donors and acceptors are likely to engage intermolecular hydrogen bonds.

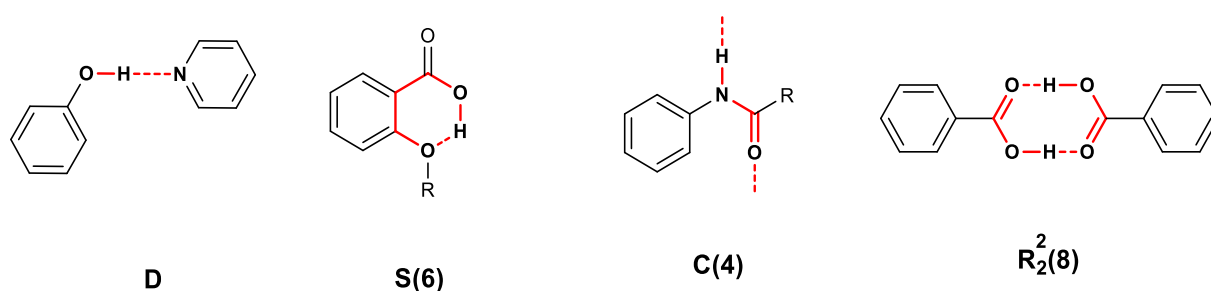
Even if the abovementioned rules have a general character, additional rules for specific functional groups were reported.^[82] Alongside the Etter's rules, the Graph Sets analysis for



Scheme 4
Generic graph
set motif.

hydrogen bond patterns was introduced.^[83,84] The first step to assign a graph set in a specific structure, is to define the different motifs generated by hydrogen bonds that can be classified according to the topology of the involved pattern as self (**S**), chain (**C**), ring (**R**) and discrete (**D**), generically **X** in Scheme 4.^[69] In addition to the motif designator **X**, the graph set indicates the number of donors (**d**) and acceptors (**a**) atoms involved as subscript and superscript, respectively, omitted when equal to one. The overall number of

atoms within the motif is reported in parenthesis (#) as shown in Scheme 4. Some examples of graph set assignments for different hydrogen bonding motifs are given in Scheme 5. According to the graph set analysis is therefore possible to define the morphology of a certain hydrogen bonded array regardless of the nature of the atoms involved. In this respect, the dimeric association of acetic acid and acetamide shown in Scheme 3 can be described as $R_2^2(8)$ as they are arranged into eight-member rings through the hydrogen bonds generated from the interaction of two donors and two acceptors. Similarly, the tetrameric arrangement of *N*-phenylformamide previously discussed, generates a $R_4^4(16)$ pattern.



Scheme 5 Examples of graph set assignments for selected hydrogen bonded motifs.

1.1.3. Boron-Nitrogen bonds

The interaction between boron and nitrogen was observed for the first time more than 150 years ago during the studies on the formation of adducts between ammonia and trimethylborane.^[85] The coordinative or dative $N \rightarrow B$ bond is nowadays of particular interest due to its peculiar property of being isoelectronic with C–C bond. The main difference between B–N and C–C bond lies in the ionic nature of the heteroatomic couple which is reflected in unique electronic and optical properties of the system.^[86] In 1926, borazine (B_3N_3), the first inorganic benzene analogue, was reported, paving the way to a new branch of boron chemistry (Scheme 6).^[87] Since then, hundreds of compounds containing B–N bonds have been isolated and their interesting biological, catalytic, photoluminescent and electronic properties, studied.^[6] The Lewis acidic nature of the three-coordinated boron atom can be easily explained by taking into account the presence of six electrons in its valence shell and therefore its consequent tendency to accept two more electrons to reach the octet. Three-coordinated boron atom is sp^2 -hybridized and adopt a trigonal planar geometry which is converted into tetrahedral upon tetra-coordination. Consequently, the Lewis acidity strength of B atom is influenced by the steric hindrance and electronic properties of the substituents.^[88] The strength of dative $N \rightarrow B$

interaction has been the subject of theoretical and experimental investigations, that confirmed that the stability of B–N bonds strongly depends on the electronic environments of both the Lewis base and the Lewis acid involved.^[89] In particular, Electron-Withdrawing Groups (EWGs) increase boron atom acidity thus favouring the formation of B–N interactions, whilst an opposite effect was observed to affect the basicity of the Lewis bases.^[89] NMR analyses have shown that in many cases B–N bonds are only stable in solid state, since undergo cleavage in solution and established again when solvent is removed.^[90,91] Such dynamic behaviour can be exploited in the field of supramolecular chemistry and B–N bonds are a useful construction tool for the preparation of self-assembled materials through non-covalent interactions. Although a large variety of Lewis bases are known to interact with coordinatively unsaturated boron species, nitrogen donors and in particular pyridine derivatives show a peculiar affinity and have been largely employed for the preparation of luminescent materials.^[92]

Trivalent boron-based compounds can be classified in different classes depending on the nature of the atoms bound to the boron atom. A search on the Cambridge Structural Database (CSD, updated to December 2020) extended to all the possible subclasses constructed by varying the number of heteroatoms from 0 to 3, shows 9902 crystalline structures of whom 75 % (7467) features one or more nitrogen or oxygen atoms. The results are shown in Figure 2 and provide a clear view of the most studied moieties.

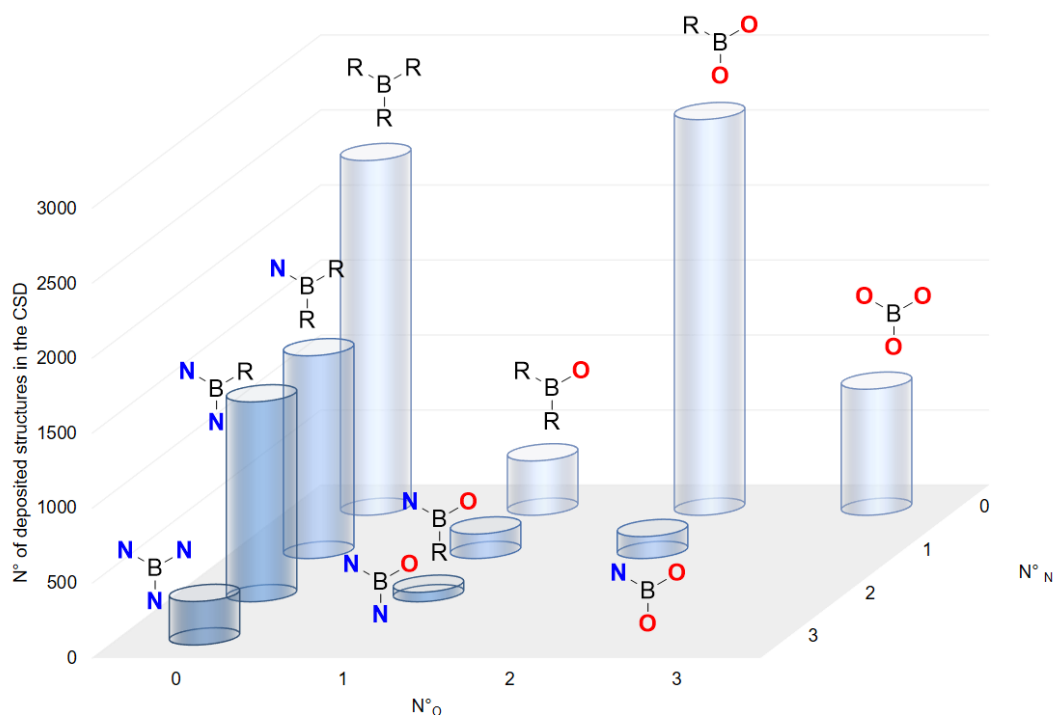
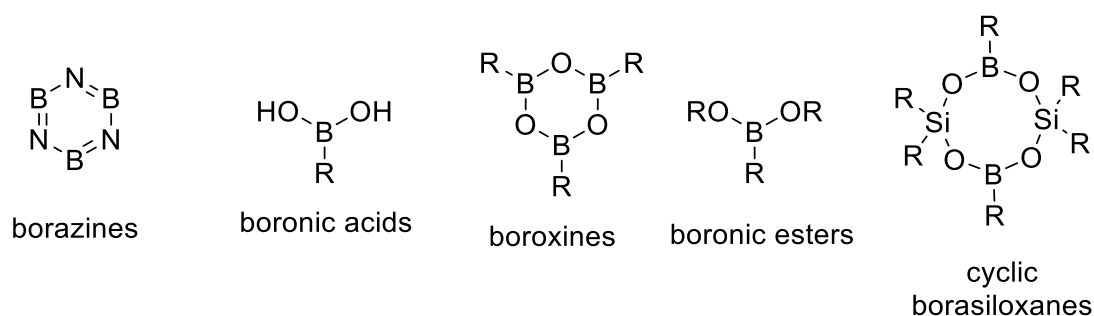


Figure 2 Distribution of three coordinated boron derivatives reported in the CSD. Subclasses are divided according to the number of nitrogen or oxygen atoms included in the fragment. $R \neq N, O$.

Among the different classes of trivalent boron compounds, boronic acids, $\text{RB}(\text{OH})_2$ gained much attention in the last decades (Scheme 6) since the report of Suzuki and Miyaura in 1979 that illustrated their use in cross-coupling reactions,^[93,94] and due to their applications in drug delivery, anion recognition and material science.^[95,96] Furthermore, boronic acids easily undergo self-condensation leading to the formation of boroxine derivatives, compounds containing six-membered ring of the type $\text{R}_3\text{B}_3\text{O}_3$ (Scheme 6), and to boronic esters upon condensation with alcohols (Scheme 6). The abovementioned classes of three-coordinated boron derivatives have been reacted with nitrogen donors for the design of discrete macrocycles,^[97] rotaxanes,^[98] cages,^[88] and supramolecular polymers.^[99,100]



Scheme 6 Three-coordinated boron derivatives employed as building blocks in supramolecular chemistry.

Another class of precursors that is recently gaining increasing attention is that of borasiloxanes, characterized by B–O–Si motifs and unique thermal and chemical stability.^[101] Cyclic-borasiloxanes and cages have also been reported and represent a family of cutting-edge synthons in supramolecular chemistry which find application as sensors and non-linear optical materials.^[102–104] The potential of cyclic-borasiloxanes featuring eight-membered rings of the type $\text{Si}_2\text{B}_2\text{O}_4$ (Scheme 6) and their role as building blocks in supramolecular chemistry will be further discussed in more detail.

In order to evaluate the number of tetra-coordinated boron derivatives potentially deriving by addition of N-bases to three-coordinated boron systems, we performed a search on CSD on the fragment BX_4 and compared the results with those found on three-coordinated BX_3 derivatives. The majority of crystal structures reported until now (32783 out of 54130), do not feature nitrogen or oxygen atoms directly bound to boron, and are not reported here. The complementary set of data was analysed according to the number of oxygen and nitrogen atoms included in the fragment and is summarized in Figure 3. In the present thesis we will mainly focus on the fragment BNOOR (highlighted in green in Figure 3), as it can be generated by the reaction of borasiloxanes with pyridine derivatives.

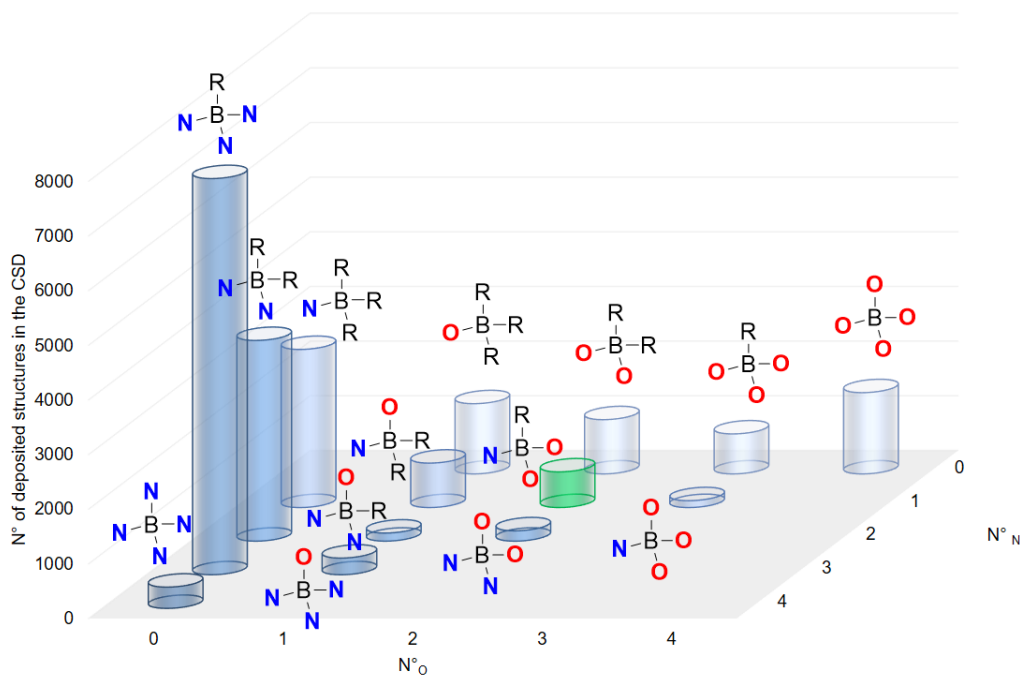


Figure 3 Distribution of tetra-coordinated boron derivatives reported in the CSD. Subclasses are divided according to the number of nitrogen or oxygen atoms included in the fragment. $R \neq N, O$. The BR_4 fragment is intentionally removed for clarity.

1.1.4. Halogen bonds

“A halogen bond occurs when there is evidence of a net attractive interaction between an electrophilic region associated with a halogen atom in a molecular entity and a nucleophilic region in another, or the same, molecular entity.”^[7] One of the first evidence of the interaction between halogens and Lewis bases dates back to the beginning of the 19th century from the studies of the interaction between ammonia and molecular iodine.^[105] Nowadays, the halogen bonding (XB) interaction is usually depicted as $X \cdots B$ where X is the halogen bond donor (Lewis acid) and B is the halogen bond acceptor (Lewis base). However, its nature is still under debate.^[106] In a generic $R-X$ species, the presence of an electrophilic region on a halogen atom can be explained by the anisotropic distribution of electrons localized towards the bonding region resulting in an electron-deficient region on the halogen atom (σ -hole). Consequently, XB is highly directional due to the geometric restraints dictated by the σ -hole. The extent of polarization of the electrostatic potential can be well evaluated by theoretical calculation as demonstrated by Politzer in 2007.^[107] In his seminal theoretical study on the series CF_3X ($X = F, Cl, Br, I$), Politzer evidenced how the chemical environment around the halogen atom heavily influences its polarization (Figure 4).

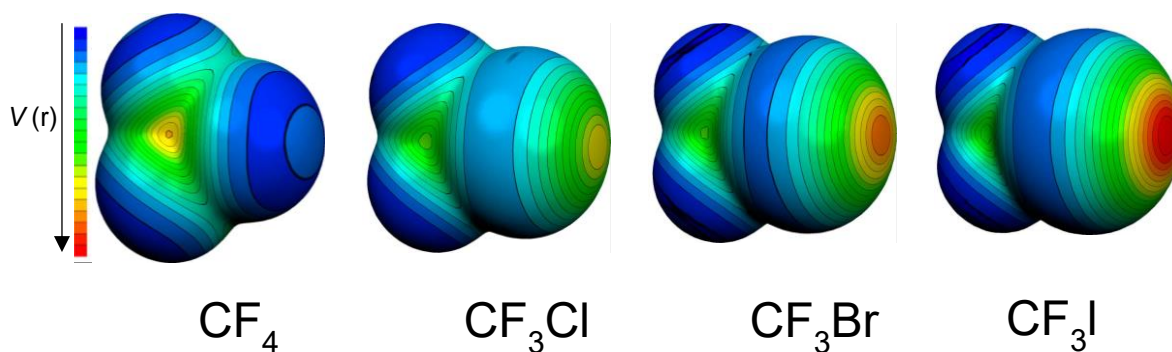


Figure 4 Molecular electrostatic potential $V(r)$ calculated for the series CF_3X ($X = F, Cl, Br, I$). Reproduced from ref. ^[107]

When a halogen atom is bonded to an alkyl or aryl moiety, the presence of EWGs at the organic skeleton enhances its tendency to establish XB. Moreover, the intrinsic polarizability of the element is reflected in the extent of the σ -hole along the series $F < Cl < Br < I$, that goes hand in hand with the trend of polarizability of the halogen atoms. As a result, XB is more likely to occur in CF_3I than in CF_4 . It is worth to note that the σ -hole is localized at the end of R-X bond and is surrounded by a belt of negative potential as showed in Figure 4. The strength of XB is found to be similar to that of hydrogen bond and was computed to have energies up to 50 kcal mol^{-1} .^[108] In contrast to the mainly electrostatic nature of hydrogen bond, the XB nature was deeply studied by means of computational and theoretical approaches. Several studies have investigated the electrostatic and charge transfer characters of XB suggesting that they vary with the nature of the halogen bond donor.^[109–112] Others have evidenced the importance of dispersion forces in some systems.^[113,114]

Interestingly, Devillanova and co-workers, introduced another school of thought, suggesting that the classical description of XB should be extended to a widest definition.^[115] Their consideration was based on the meticulous study on the crystallographic evidences for a generic three body system. When the three atoms are halogens, as in the case of I_3^- or Br_3^- , the system is properly described by the 3-center 4-electron model (3c-4e) by Rundle-Pimentel.^[116,117] The linear geometry of these fragments can be easily explained by the combination of the p_z atomic orbitals into three molecular orbitals which are filled by four electrons localized in the bonding and non-bonding orbitals. Hence, the overall bond order is 1, which divided for the number of bonds gives the value of 0.5 for a symmetric trihalide. Another interesting approach to describe such systems was introduced by Martin and Arduengo, that described a trihalide as a 10-X-2 system,^[118,119] with a hypervalent central halogen formally associated with five electron pairs (10 electrons) with only two bond pairs localized at the axial positions in a pseudo-trigonal-

bipyramidal (tbp) geometry. Both the above-mentioned approaches can be successfully extended to chalcogen-containing three body systems. It is renowned that the reaction between dihalogens X–Y (X = Y = I, Br; X = I, Y = Br, Cl) and chalcogen-containing donor species (RE) can generate different classes of products.^[120,121] Among them, Charge-Transfer (CT) “spoke” adducts, featuring an almost linear E–X–Y moiety usually described as 10-X-2 system (see QAQTAE in Figure 5,^[122] can be obtained by reacting thionated or seleniated species with molecular diiodine and can be classified according to the extent of perturbation induced by the donor on the I₂ fragment.^[115]

Table 2 CT adducts classification according to the extent of perturbation induced by the donor on the diiodine fragment.

		n_{I-I}	d_{I-I} (Å)
Weak or medium-weak	E⋯I–I	$n_{I-I} > 0.6$	$d_{I-I} < 2.86$
Strong	E–I–I	$0.4 < n_{I-I} < 0.6$	$2.86 < d_{I-I} < 3.00$
Very strong	E–I ^{δ+} ⋯I ^{δ-}	$n_{I-I} < 0.4$	$d_{I-I} > 3.01$

The ensuing three classes of CT adducts, summarized in Table 2, differ for the (n_{I-I}) bond order and the (d_{I-I}) interatomic distance within the I–I fragment: in the case of very strong adducts, the di-halogen moiety is heavily polarized and the terminal halogen atom acts as a Lewis base. The reaction of a simple “spoke” adduct with another di-halogen molecule can lead to amphoteric adducts (E–X–Y–X–Y) (see DISDOB in Figure 5) and bridging amphoteric adducts [E–(X–Y)_n–E], featuring a *n* number of di-halogen bridges capped by chalcogen atoms at both ends (see IRABAE in Figure 5).^[123–126]

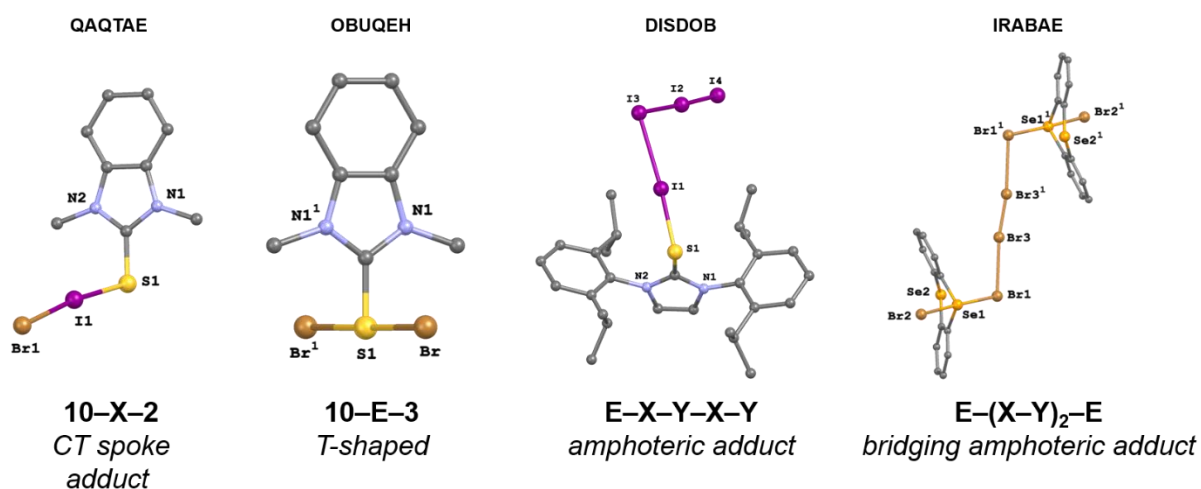


Figure 5 Examples of different products generated by reacting chalcogenated species with di-halogens. Thermal ellipsoids are drawn at the 50 % probability level. Hydrogen atoms have been omitted for clarity.

The oxidative addition of di-halogens to chalcogenone donors leads to the insertion adducts X–E–Y, also called “T-shaped” (see OBUQEH in Figure 5). According to the Martin’s notation, these three-body systems are described as 10-E-3, in which the chalcogen species is in a hypervalent state, surrounded by five electron pairs, three of which are bond pairs.^[118,119]

Devillanova and co-workers, demonstrated that all the three-body systems previously described are strictly correlated and share the same chemical bonding nature.^[115] In fact, taking into exam a generic A–B–C fragment, the normalized elongations δ_{AB} and δ_{BC} can be calculated by the following equations:

$$\delta_{AB} = \frac{d_{AB} - (r_A + r_B)}{r_A + r_B}; \quad \delta_{BC} = \frac{d_{BC} - (r_B + r_C)}{r_B + r_C} \quad (1)$$

Where r_A , r_B and r_C are the covalent radii of the involved atoms and d_{AB} and d_{BC} their experimental distance within the fragment. According to the bond-valence model, the relationship can be simplified into the following equation:

$$\delta_{AB} = -k \ln \left[1 - e^{\frac{-\delta_{BC}}{k}} \right] \quad (2)$$

where δ_{AB} and δ_{BC} depend on the single adimensional parameter k and are independent on the nature of the atomic species A, B and C. As an example, the scatter plot for T-shaped (X–E–Y) systems is reported in Figure 6 showing the good match between the structural data reported in the CDS and their least-square fit obtained by equation 2.

The main outcome that can be extrapolated from the chart in Figure 6 is that there is a continuous variation from balanced to unbalanced three-body systems. Thus, there is not any evidence of critical distances at which the essentially covalent character of the interaction become governed by the electrostatic contribute.

The study was extended to three-body systems containing N···I–X (X = Cl, Br, I) fragments from CT-adducts coming from the interaction of homonuclear^[127,128] and heteronuclear^[129,130] di-halogens with molecules containing pnicoen atoms, especially N-containing species.

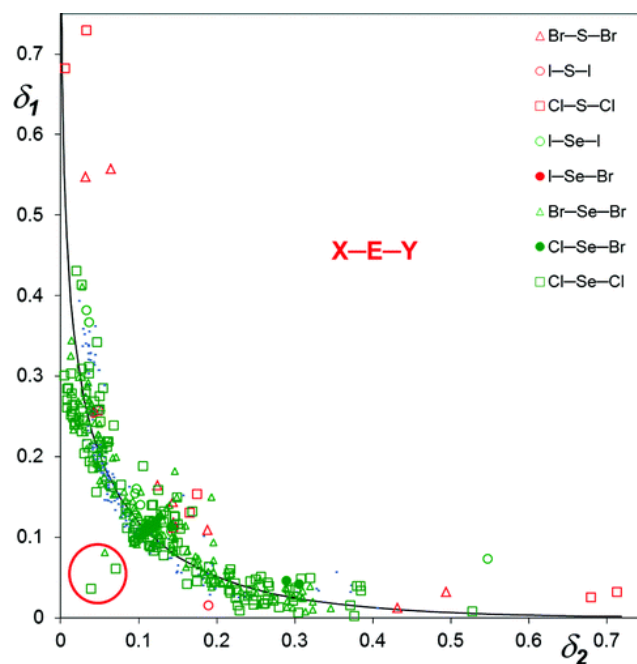


Figure 6 Structural data for T-shaped insertion adducts (X-E-Y) according to their elongation values ($\delta_1 = \delta_{XE}$; $\delta_2 = \delta_{EY}$). The solid black curve is the product of the least square fit of all data (adopting equation 2) except those included in the red circle. Fitted parameter $k = 0.157$; $rmsd = 0.050$; normalized $rmsd = 0.067$. Reproduced from ref.^[115]

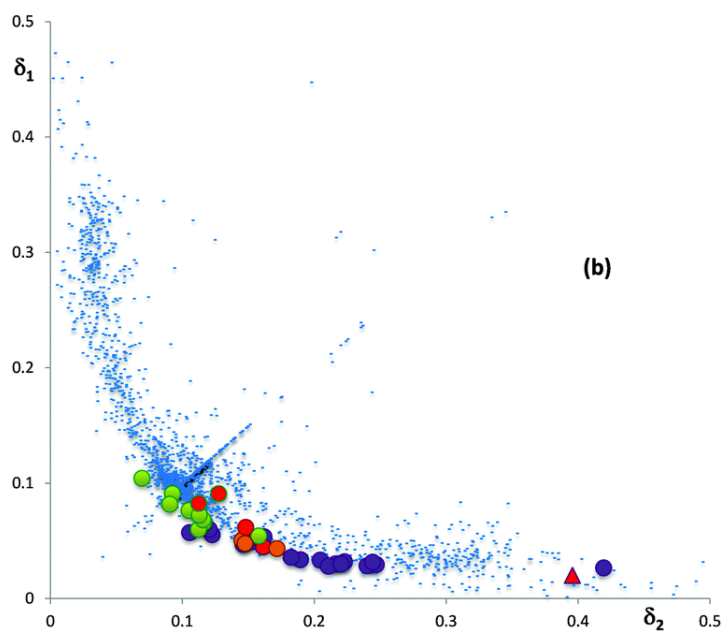


Figure 7 Structural data of $N \cdots I-X$ ($X = Cl, Br, I$) fragments overlapped with those related to chalcogen-halogen three-body systems depicted as blue dots. Reproduced from ref.^[131]

Figure 7 shows that the relative elongations (δ) of the $N \cdots I$ and $I-X$ bonds for $N \cdots I-X$ ($X = Cl, Br, I$) fragments retrieved from CSD follows the trend found for the other three body systems previously considered. The reaction between di-halogens and substrates containing pnictogen

atoms also produces a variety of discrete or polymeric supramolecular assemblies,^[131–136] moreover, in contrast to chalcogenated derivatives, pyridine nitrogen can easily undergo protonation (Py-H)⁺, forming cationic head-to-tail assemblies in polypyridine systems which are counterbalanced by halides and polyhalides, strongly depending on the experimental conditions.^[134] An interesting example that well explains the reactivity of N-containing species with halogens is represented by the ligand 1,4-bis(pyridin-3-ylethynyl)benzene.^[137] This rigid linear polypyridine linker can adopt two different conformations depending on the positions of the heterocyclic atoms. It was found that, when the ligand is reacted with I₂ in a dichloromethane medium, a CT adduct is formed, in which the pyridine derivatives coordinate two iodine molecules in a periplanar fashion (see LEWKOP in Figure 8). The central phenyl ring of a ligand unit interacts with a pyridyl ring of a slipped adjacent molecule by means of intermolecular π - π interactions establishing a 2D-layered structure. The centroid-centroid distance is about 3.715 Å, leaving enough space to accommodate an extra iodine molecule. As a consequence, an infinite chain of iodine molecules along the *a* vector dominate the crystal packing.

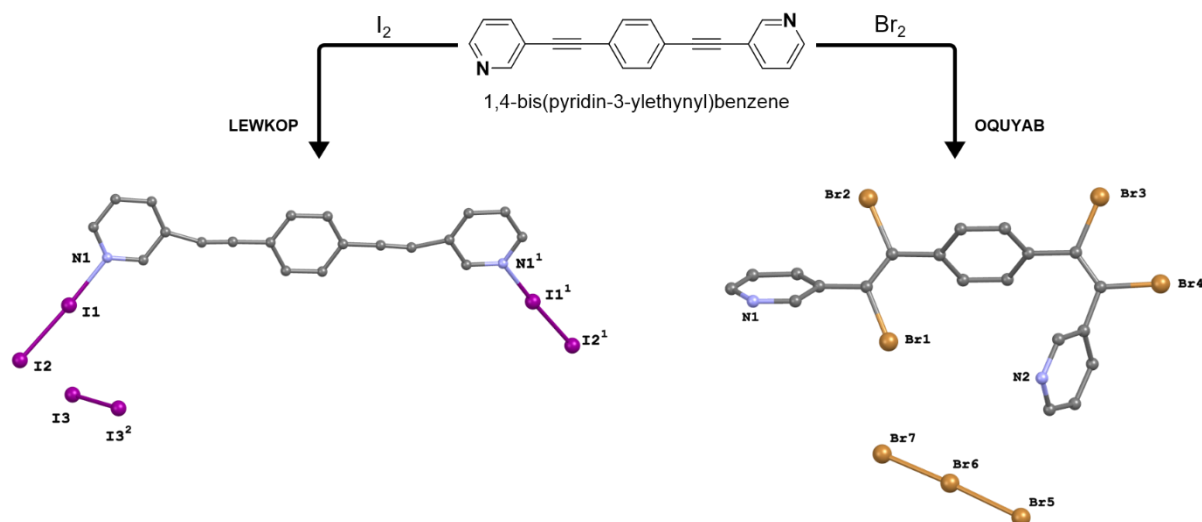


Figure 8 The reactivity of 1,4-bis(pyridin-3-ylethynyl)benzene towards I₂ and Br₂. The molecular unit of the CT bis I₂ adduct is depicted along with the iodine molecule intercalated in the 2D network (LEWKOP). The pyridinium tribromide salt resulted from the bromine addition to the organic linker is represented (OQUYAB). Hydrogen atoms are omitted for clarity except the one involved in the protonated pyridine fragment.

On the other hand, it was shown that the reaction of the same organic linker towards molecular bromine produced a very different result leading to a non-stereospecific bromine addition at the triple bonds (see OQUYAB in Figure 8), even if the starting donor molecule exhibited both *Z*

and *E* isomers. Moreover, N-protonation resulted in a positively charged fragment, (Py-H)⁺, counterbalanced by a linear asymmetric Br₃⁻ anion.

It is well known that the tendency to catenate of halogens, thus forming polyhalides, decreased along the series I > Br > Cl.^[132,138] Therefore, discrete polyiodides and polybromides are more common and are found up to I₂₉³⁻ and Br₂₀¹⁰⁻, respectively.^[139,140] Remarkably, only one example of an infinite polybromide network has been reported, in which Br–Br distances are found shorter than those found in the crystalline structure of solid Br₂ (*d*_{Br–Br} = 3.04–3.20 and 3.31–3.79 Å, respectively).^[138]

Although (Py-H)⁺ are by far the most common cationic derivatives of pyridyl groups coming from the reactions with halogens, pyridyliodonium (Py-I)⁺ cations can also be obtained. The most adopted synthetic route for their preparation is based on the reaction between Ag(I) pyridine complexes with I₂ to generate (Py-I)⁺ cations, as the result of the homolytic breaking of the I–I bond.^[141] A famous example of these system is the bis(pyridine)iodonium tetrafluoroborate also called the Barluenga's reagent, a mild iodinating agent used in organic synthesis.^[142] Erdélyi *et al.* recently reported on the implementation of iodonium functionalities in supramolecular helicates.^[141]

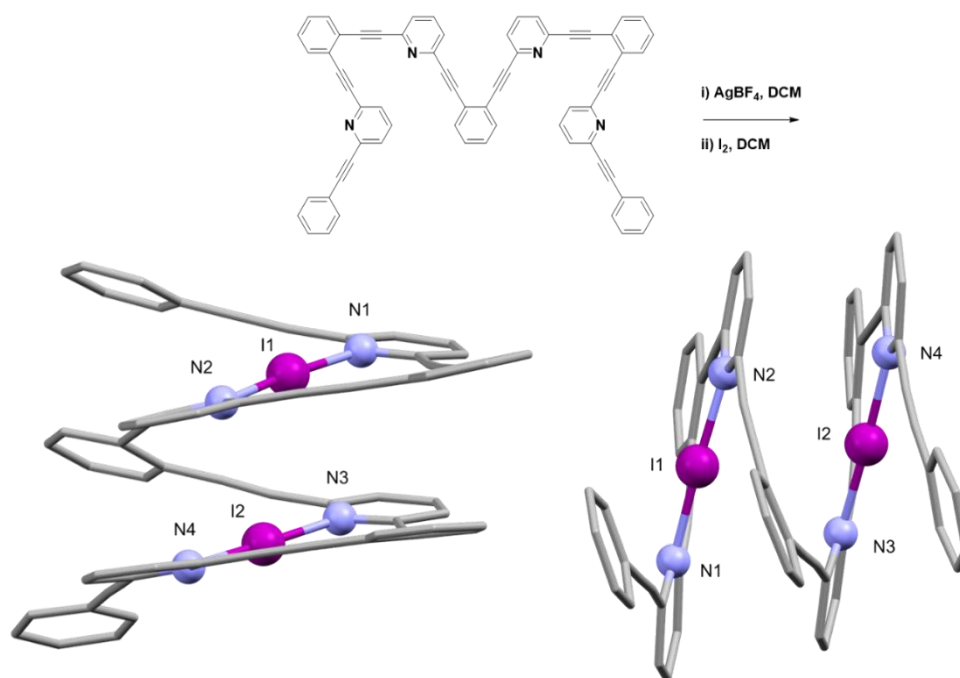


Figure 9 Helical iodonium complex held together by means of [N–I–N]⁺ interactions (NOMCAW). X-ray crystal structure representations along *a* (left) and *b* axis (right). Iodine and nitrogen atoms are depicted in purple and light blue balls, respectively. BF₄⁻ units and hydrogen atoms have been omitted for clarity. Reproduced from ref.^[141]

The rigid tetrapyridyl linker (Figure 9) was firstly reacted with silver(I) tetrafluoroborate leading the corresponding metal complex. Subsequently, reaction with molecular diiodine successfully produced the dicationic halonium helicate, counterbalanced by two BF_4^- anions (Figure 9). The halogen-bonded system is stabilized by $[\text{N}-\text{I}-\text{N}]^+$ interactions, as well as by PD and T $\pi-\pi$ interactions (§1.1.1). The measured $\text{I}^+\cdots\text{I}^+$ distance is 3.862 Å, resulting slightly shorter than the sum of the cationic radii ($r = 2.21$ Å).^[143] Despite the unusual short distance between the two haloniums, the Mayer bond order^[144] was computed to be equal to 0.01, suggesting a negligible interaction between them.

Alongside the foremost characterization technique is based on crystallographic studies by means of XRD analysis, FT-Raman spectroscopy plays an important role due to the high polarizability of the involved species that implies remarkable variations in the X–X stretching frequencies depending on the nature of the XB interaction involved. Weak and medium-weak CT adduct of the type $\text{E}\cdot\text{X}_2$ ($\text{E} = \text{S}, \text{Se}; \text{X} = \text{I}, \text{Br}, \text{Cl}$) mainly preserve the di-halogen bond and present only one peak attributable at the X–X stretching vibration,^[137] falling at values as lower than those found for the free di-halogen as stronger is the XB involved.^[123] When poly-halides are present in the crystal lattice, the FT-Raman spectroscopy can be used to get structural information on the building blocks (typically X_2 and X_3^- moieties)^[122] since asymmetric trihalides such as I_3^- typically show three distinct peaks aroused by the symmetric stretching, antisymmetric stretching and bending deformation modes, whilst X_2 moieties present single peaks, as mentioned above.^[134] On the other hand, T-shaped hypervalent systems are often characterized by a single peak in the Raman spectrum due to symmetric stretching of the fragment. A more complex panorama is observed when different or disordered halogen fragments are present in the molecule.^[124]

XB has been in the focus of supramolecular chemistry and crystal engineering, albeit is certainly one of the less exploited intermolecular interaction in these fields.^[108] XB has been employed by crystal engineers for the construction of 1D, 2D, and 3D architectures also by combination with other supramolecular interactions.^[145–148] Hydrogen bonds demonstrated either cooperative or antagonist behaviour with XB, depending on the nature of species involved and on the experimental conditions.^[149–151] For example, the nature of the solvent can influence the formation of both halogen and hydrogen bonds leading to different materials characterized by a single type of intermolecular interaction or by the coexistence of both at the same time.^[152]

Halogen bonded materials show great potential in supramolecular chemistry^[108,153] and in material science.^[154] Furthermore, XB was used for the preparation of phosphorescent materials^[155], and in other fields such as organocatalysis,^[156,157] membrane transport,^[158] and solar cells.^[159] Other important applications of XB involve medicinal chemistry and chemical biology.^[160] It is worth to note that other supramolecular interactions similar to hydrogen and halogen bonding, based on tetrels, pnicogens and chalcogens, are emerging in supramolecular chemistry for the preparation of predictable architectures.^[121,161–164]

1.2. Supramolecular Architectures

Supramolecular chemistry deals with systems of different shape, size and dimensionality and comprises aggregates as different as clathrates, host-guest species, and extended networks produced by self-assembly of two or more molecular components dependent only on the information contained within the interacting chemical building blocks. Notwithstanding the final result depends on all the involved no-covalent interactions mentioned in the above paragraph, on solvation effects and on the experimental condition used to conduct the synthesis, the chemist can decide to employ specific complementary interactions in order to design and prepare specific self-assembling systems. Metal–ligand interactions are among the most widely used interactions in synthetic self-assembly processes due to their high degree of predictability of metal-ion coordination environments, that lead to infinite supramolecular architectures known as Coordination Polymers (CPs) and Metal-Organic Frameworks (MOFs). The highly directional nature of hydrogen bonds also leads to many examples of self-assembled hydrogen bonded materials such as co-crystals and Hydrogen-Bonded Organic Frameworks (HOFs). Recently, covalent coordinative interactions such as N–B bonds were also used to design supramolecular architectures known as Covalent Organic Frameworks (COFs). In the following paragraphs, we will provide an overview of these three categories of self-assembled supramolecular architectures on which the presented PhD project was mainly developed.

1.2.1. Coordination Polymers and Metal-Organic Frameworks.

Coordination Polymers (CPs) are infinite arrays extended in one, two or three dimensions built up through coordination bonds.^[165] In other words, organic molecules called spacers, link metal nodes such as ions or clusters through coordinative bonds leading to crystalline networks of

different dimensionality. When the crystal structure of a CP presents portions or channels occupied by solvent molecules, that could be eventually removed and/or replaced, the material is considered potentially porous and the term CP is replaced by Metal-Organic Framework (MOF). CPs and MOFs are certainly the most investigated classes of crystalline materials in supramolecular chemistry. The directionality and strength of coordination bond have been a key construction tool since 1990s. CPs are designed by taking into account the coordination environment of the metal ion together with the structural features that can be provided by the organic linkers such as geometry, topology, number and nature of donor sites. In such a way, a large variety of supramolecular architectures can be obtained starting from the simplest 1D networks which can be categorized into linear, zig-zag, undulated, helical, ladder, rotaxane and ribbon, depending on the final geometry,^[166] and, notwithstanding an apparent structural simplicity, have shown interesting magnetic,^[167] electrical,^[168] mechanical,^[169] and optical properties.^[170] Even though mono-dimensional linear CPs could be considered easy to design and realize by reacting a linear linker with a linear coordinating metal ion, the resulting packing is certainly less predictable as intermolecular interactions between linear chains can drastically modify the overall structure. An example is the work published by Hosseini *et al.* reporting a silver(I)-based CP constructed using as spacer a bidentate pyridyl donor featuring a hexaethylene glycol moiety connecting at *para* position the two pyridyl ring through ester functionalities (Figure 10).^[171] As expected, the metal ions are coordinated by nitrogen atoms into a linear arrangement. Surprisingly, the ether fragment was arranged into loops adopting a pseudo-crown ether arrangement which surrounded a metal ion from an adjacent chain resulting in an unusual double stranded interwound packing (Figure 10).

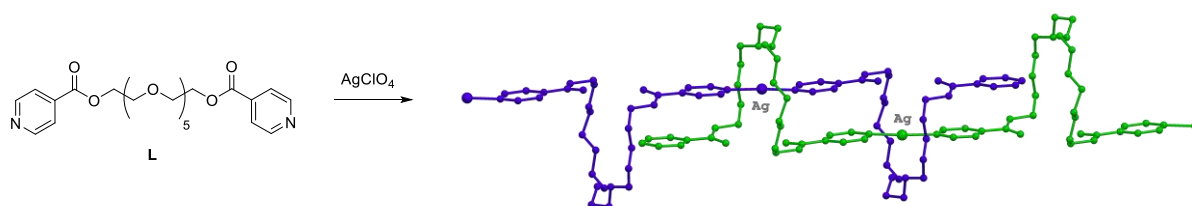


Figure 10 Schematic representation of ligand L and crystal packing of the double stranded cationic interwound polymeric chains of the type $[\text{AgL}]_{\infty}^{+}$. H atoms and perchlorate anions are omitted for clarity. Reproduced from ref. ^[171] (refcode: ABOKAD).

Another interesting example on how linear chains can be arranged into more complex networks was reported by the group of Zubieta.^[172] A copper(II)-based CP was hydrothermally prepared

by reacting $\text{Cu}(\text{SO}_4)_2 \cdot 5\text{H}_2\text{O}$ with the well-known linear 4,4'-bipyridine (4,4'-bipy). In the packing parallel $\{\text{Cu}(4,4'\text{-bipy})(\text{H}_2\text{O})_3\}_\infty^{2+}$ chains along the [101] direction feature the interchain space occupied by sulphate anions forming a layer. Adjacent layers are stacked and rotated by 60° along the c axis producing virtual hexagonal cavities which are filled by solvent molecules (Figure 11).

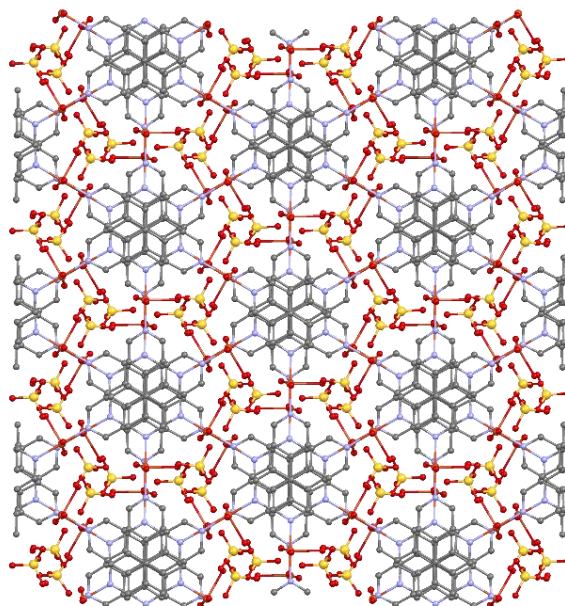


Figure 11 View along the c axis of linear chains rotated and stacked to produce virtual hexagonal cavities. H atoms and H_2O molecules have been omitted for clarity. Reproduced from ref.^[172] (refcode: FAKQEN).

Another interesting example regards the zig-zag zinc(II) CP obtained from the self-assembly of $\text{Zn}(\text{NO}_3)_2 \cdot 6\text{H}_2\text{O}$, acetylenedicarboxylic acid (H_2adc) and a terpyridine-based auxiliary ligand.^[173] Zinc ions are penta-coordinated into a distorted square pyramidal geometry by two monodentate carboxylate ligands and a chelating terpyridine unit. The 1D-zigzag main motif resulted by the bridging of the linear anionic spacer adc^{2-} to adjacent metal nodes (Figure 12a). The mono-dimensional chains interact through hydrogen bonds involving carboxylate units and water molecules trapped in the lattice and by means of intermolecular π - π stacking interactions among adjacent terpyridine ligands, leading to a 3D extended network with unusual high photosensitivity behaviour and potential application in the field of optoelectronics and solar cells development.

More challenging is the design of helical systems due to the possibility to obtain intrinsically chiral helices starting from achiral building blocks.^[174] Huan *et al.* recently reported a nice example of helically assembled CP designed by means of a semi-rigid polypyridyl derivative (Figure 12b),^[175] that was tested for cell imaging applications due to the high thermal stability and interesting photophysical properties showed.

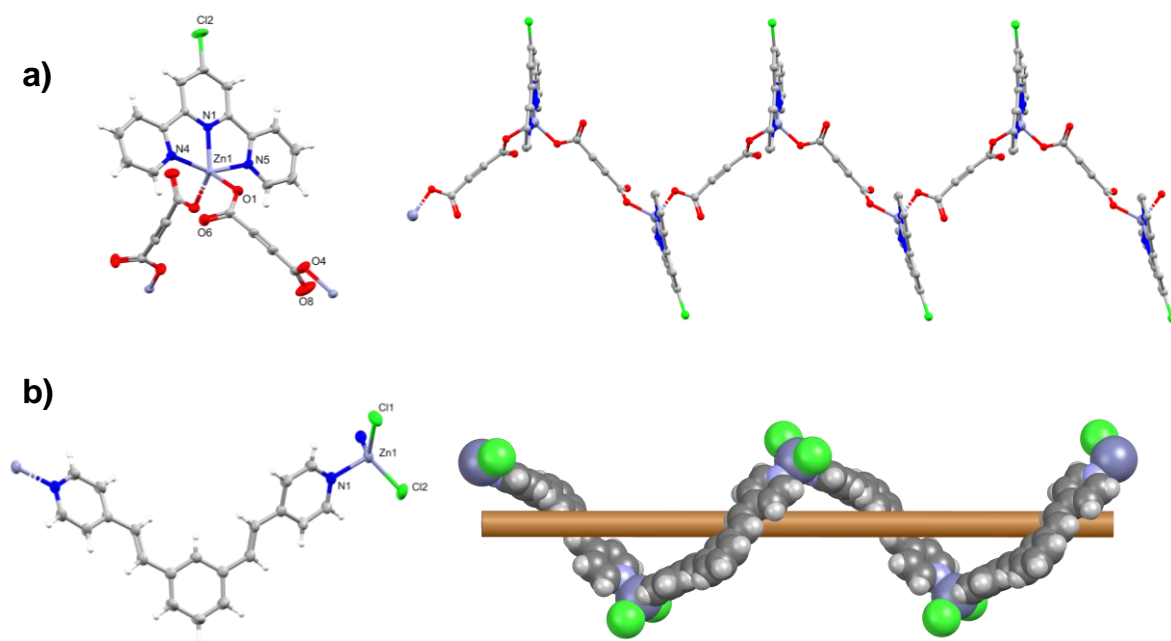


Figure 12 Supramolecular construct: a) zig-zag arrangement of a Zn(II)-based CP; b) helical arrangement of a Zn(II)-based CP. Reproduced from ref. ^[172] and ^[173], respectively (refcodes: DOHJES, POXVIK).

The design of CPs is nowadays more centred on the preparation of crystalline materials featuring large cavities, defined as Porous CPs (PCPs) or MOFs. This is not an obvious task to achieve due to the natural tendency of crystalline systems to reduce the presence of voids maximizing packing efficiency by intercalation, interdigitation and interpenetration.^[176] The intercalation usually refers to solvent molecules that are trapped or co-crystallized in the crystalline structure. Interdigitation occurs when specific moieties protrude from the main skeleton intruding an adjacent net. In contrast, the interpenetration phenomenon is observed when two or more polymeric networks are interlaced and cannot be separated without bond breaking.^[1] Up to now, the highest degree of interpenetration refers to a 54-fold interpenetrated network constructed by means of (4-imidazolylphenyl)amine and silver(I) ions as building blocks.^[177] Interpenetration of nets has always been considered a side effect in the preparation of porous materials such as MOFs and numerous strategies have been developed aimed to avoid such phenomenon.^[178,179] However, recent reports have reassessed its potential especially in small molecules separation and storage,^[180,181] due to the flexibility that such networks can exhibit leading to shared movements of the nets in response to an external stimulus or by dynamic structural transformations induced by guest inclusion.^[182,183]

As mentioned before, at the end of the 20th century the chemistry of MOFs exploded, when the papers of S.S.Y. Chui and O.M. Yaghi, now considered milestones in supramolecular and

reticular chemistry, demonstrated that the presence of potential voids, evidenced by XRD analysis, could be converted in permanent porosity upon guest removal.^[184,185] Since then, the major issue experienced was the collapsing of the structure in the activation process. Developments in this field led to several key aspects that must be considered in the design of MOFs. For example, it was demonstrated that charged ligands such as carboxylate form more stable networks by interaction with metal ions than those obtained by using neutral ligands such as pyridyl derivatives,^[186] and metal clusters, also called Secondary Building Units (SBUs) confer more stability to the overall network than naked metal ions. Based on these principles is MOF-5, one of the most famous porous networks, prepared by diffusion of triethylamine into a solution of zinc(II) nitrate and terephthalic acid (H₂BDC) in DMF/chlorobenzene.^[185] The amine induces the deprotonation of H₂BDC increasing its binding affinity towards Zn²⁺ ions, and small amounts of hydrogen peroxide facilitate the formation of O²⁻ required for the formation of the tetranuclear SBU. The resulting Zn₄O fragments possess a tetrahedral arrangement with metal ions located on the vertices and the O²⁻ in the core. The coordination environment along Zn²⁺ ions is filled by carboxylate units to form a Zn₄(O)(CO₂)₆ cluster (Figure 13).

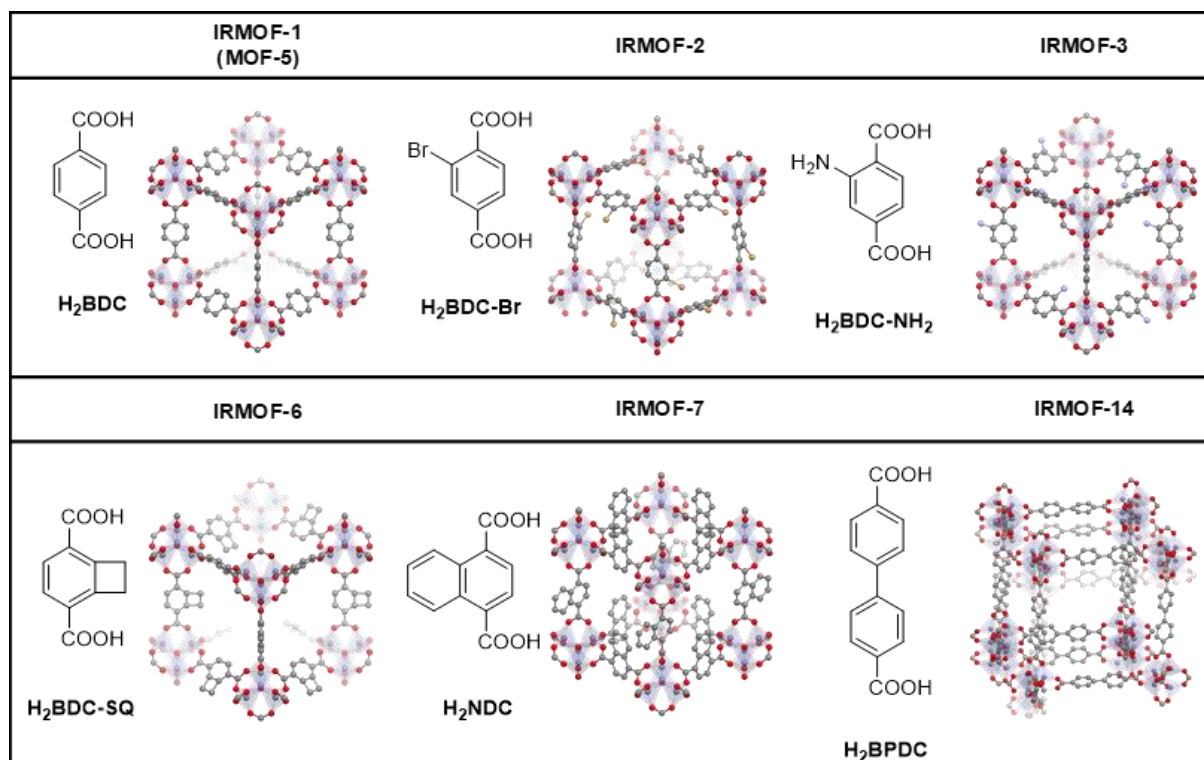


Figure 13 Isoreticular series of IRMOF-1. Linker functionalities and lengths yield isoreticular networks with different pore size and functionalities but featuring the parent **pcu** topology. See refcodes: MIBQAR, EDUSOL, EDUSUR, EDUTIG, EDUTOM, EDUVAA.

The cubic structure formed by linking zinc SBUs and BDC units can be deconstructed into the basic **pcu** net.

The elongation and/or functionalization of the linker without altering its shape and connectivity allowed to obtain a series of isorecticular MOFs (IRMOF) based on the MOF-5 structure with different pore size and functionalities,^[186] as IRMOF-2 and IRMOF-3, for example, which feature –Br and –NH₂ substituents that functionalize the resulting network (Figure 13).^[187] A similar approach and reaction conditions were used for the preparation of IRMOF-6 and IRMOF-7 bearing fused ring cores as shown in Figure 13. The elongation of the ligand skeleton gave rise to porous networks with larger apertures and accessible voids, even if in some cases net interpenetration was observed as in IRMOF-14, prepared using 1,4-biphenyldicarboxylic acid (H₂BPDC) as building block, in which two-fold interpenetration occurred (Figure 13).

Starting from the IRMOF series based on the **pcu** topology of MOF-5, a vast number of examples based on other topologies have been reported (Figure 14). Information about thousands of different nets can be found in the Reticular Chemistry Structure Resources (RCSR) database.^[188,189]

Building unit 1 \ Building unit 2	2-c Linear	3-c Triangle	4-c Square	4-c tet	6-c Hexagon	6-c oct
3-c Triangle	srs	bwt, pyo, srs-b, lhs-b	fjh, fmj, gee, iab, yac, yao	asn, ept, ofp	cys, dnf*	anh, ant, apo, brk, cep*, cmi, czz, eea, gom, rli, tsx, zzz
4-c Square	nbo, lvt, rhr	pto, tbo	cev, cdl, cdm, cdm, cds, cdz, mot, muo, qdl, qzd, ssd, sse, ssf, sst	pts	nts	myd, ybh
4-c tet	dia, lcs, qtz, sod	bor, ctn	fgl, mog, pds, pth, pli, ptr, ptt	bni, byl, cag, cbt, coe, crb, fel, icm, kea, lon, pcl, qtz-b, sca, tpd, ucn	-	alw, bix, cor, ing, spl, toc
6-c Hexagon	hxg	cys, dnf	she	-	hxg-b	-
6-c oct	pcu, bcs, crs, reo	pyr, spn	soc	gar, iac, ibd, toc	-	pcu-b, bcs-b
6-c trp	lcy, acs	ceq, dag, fmz, hwx, moo, sab, sit, ydq	stp	fsi, hea, tpt	htp	nia
8-c cub	bcu	the	scu, csq, sqc	flu	-	ocu
12-c cuo	fcu	sky	ftw	edc	-	-
12-c ico	-	-	-	ith	-	-
12-c hpr	-	aea	shp	-	-	-
12-c tte	-	ttt	-	-	mgc	-
24-c tro	-	-	-	twf	-	-

Figure 14 Topology table reproducing possible nets constructed with a two-component approach. Reproduced from ref.^[189]

The SBUs usually employed for the design of novel MOFs include different clusters featuring a variable number of metal ions (typically from three to twelve) connected by simple organic molecules, such as carboxylate anions (Figure 15a). The SBUs are linked by organic spacers generally classified by their skeleton shape (e. g. linear, bent, trigonal, tetragonal) and number of points of extension such as ditopic, tritopic, tetratopic and so on (Figure 15b).

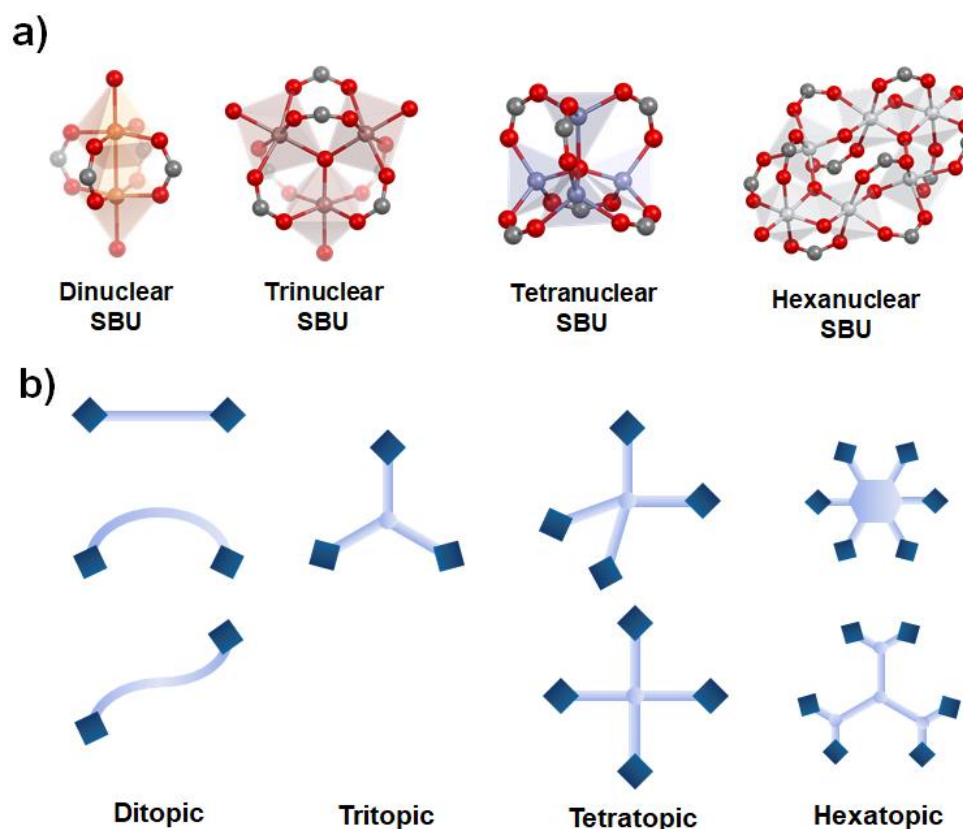


Figure 15 a) examples of selected SBUs with variable number of metal nodes and connectivity (reproduced from refcodes: FIQCEN, ALEJAE, FAZPON and CUFHIX, respectively). b) schematic representation of linker with different shapes and topicities.

The design and synthesis of the used SBU strongly depend on the nature and oxidation state of the embedded metal ion and are typically carried out under well-known approaches such as hydrothermal/solvothermal methods, layering and slow evaporation techniques. SBUs containing bivalent metal ions such as Ca^{2+} , Be^{2+} , Zn^{2+} and Cu^{2+} are typically prepared in DMF or other amide-based solvents by placing the metal source, typically nitrate salts, and the organic connector in borosilicate glass vials or special pressure tubes (e.g. Ace Pressure tubes) along with the solvent/s and heating at temperatures ranging from room temperature to 140 °C. Trivalent group 3 elements require experimental condition which vary from Al^{3+} , Ga^{3+} to In^{3+} : In-MOFs are generally prepared under reaction conditions similar to those just discussed for

divalent metal ions, Al- and Ga-MOFs require harsh conditions and are typically carried out in aqueous solution heating up to 220 °C, instead.

It is worth pointing out that the appropriate choice of reaction conditions such as temperature, concentration, solvent or mixture of solvents, is crucial for obtaining a crystalline material and in order to avoid or favour solvent decomposition. For example, DMF at high temperatures decomposes into the strong base dimethylamine ($pK_b = 3.29$) which causes the deprotonation of the polytopic carboxylic acid used as building block, and formic acid ($pK_a = 3.77$) which acts as modulator, a chemical species intentionally introduced or generated *in situ*, with the same functionality of the linker but with lower toxicity.^[186] The main role of the modulator is that of compete with the linker in the metal coordination and thus slowing down the formation of the network which is only possible *via* binding induced by the desired ligand.^[190,191] When carboxylate-based ligands are used, typical modulators are formic, acetic, benzoic, and oxalic acids. The use of modulators in MOFs preparation has been demonstrated to be a key factor to optimize physical properties such as crystallinity, particle size, morphology, porosity, defectivity, and surface chemistry.^[192] An extensive use of modulators can be found in the preparation of Zr-based MOFs.^[193–195] Moreover, the introduction of modulators is vital in the preparation of MOFs from trivalent transition metal ions such as Fe^{3+} , which are willing to form a crystalline phase only in strongly acidic pH environments due to their tendency to form oxides and hydroxides at higher pH values.^[186]

The following optimization process in MOFs preparation is often difficult since requires different steps such as purification, activation, and guest removal from the network. The first step is a treatment of the synthesized MOF with the same solvent used in the synthesis in order to separate unreacted starting materials and eventual side products from the desired product. The solvent-exchange process is then repeated several times to ensure a fully solvent exchanged sample. Since organic amides such as DMF have a high boiling point and are difficult to be removed completely by vacuum approaches preserving the crystallinity of the product, low boiling point solvents such as methanol, dichloromethane, chloroform and acetone are used to this aim. Since these processes can lead to crystal cracking and loss of crystallinity, the appropriate solvent-exchange conditions must be determined and optimized for each system. In order to preserve crystal features, the use of supercritical CO_2 is now becoming of common use.^[196]

The number of structurally characterized MOFs reported in the CSD is very high (around 75000)^[197] and many of them show porosity higher than zeolites and activated carbons with astonishing experimental surface areas reaching up to $\sim 7000 \text{ m}^2 \text{ g}^{-1}$,^[198,199] that allowed their

employment in hydrogen and methane storage,^[200] carbon dioxide capture and conversion,^[201] and separation of gas mixtures.^[202] Networks designed with specific pore size/shape and functionalities found applications in catalysis,^[203] luminescent MOFs^[204] in the fields of sensing and switching,^[205] explosives detection,^[206] and biomedical applications including bioimaging, biosensing and drug-delivery.^[207]

1.2.2. Co-crystals and Hydrogen-Bonded Organic Frameworks.

Co-crystals have been defined as *solids that are crystalline single-phase materials composed of two or more different molecular and/or ionic compounds generally in a stoichiometric ratio which are neither solvates nor simple salts.*^[208] The components assembled into a co-crystal are termed co-formers. In this respect, the design of novel co-crystals, especially by means of hydrogen bonds, have attracted much attention in the last years due to the lucrative application in drugs development.^[209] In fact, pharmaceutically active co-formers are co-crystallized in order to impart better chemical and physical properties to the resulting co-crystals such as stability, solubility, dissolution and bioavailability.^[210] In particular, the main drawback in drug-design is the poor water solubility of biologically active compounds and it has been estimated that a 2/3 of the novel potential pharmaceuticals and drugs cannot be marketed for this reason.^[211] The formation of co-crystals in this field is therefore aimed to overtake these issues and prepare novel drugs with suitable optimized properties. The design of co-crystals through hydrogen bonds and/or halogen bonds is performed by the accurate choice of complementary functional groups to be included in the starting building blocks, following a hierarchy between the selected interactions.^[212–215] Among the nicest examples of two components co-crystals is the 2D-honeycomb pattern of benzene(1,3,5-tricarboxylic acid) (H₃BTC) featuring six H₃BTC molecules aligned on the vertices of a distorted hexagonal pattern with apertures of 14 x 14 Å in which acid molecules engage hydrogen bonds along eight-member dimers (Figure 16; § 1.1.2).^[216] Co-crystallization of H₃BTC with 4,4'-bipy and 1,2-di(pyridin-4-yl)ethane yielded two similar self-assembled materials retaining the mother

hexagonal pattern but displaying much larger apertures of 26 x 35 Å and 33 x 33 Å, respectively (Figure 16).^[217,218]

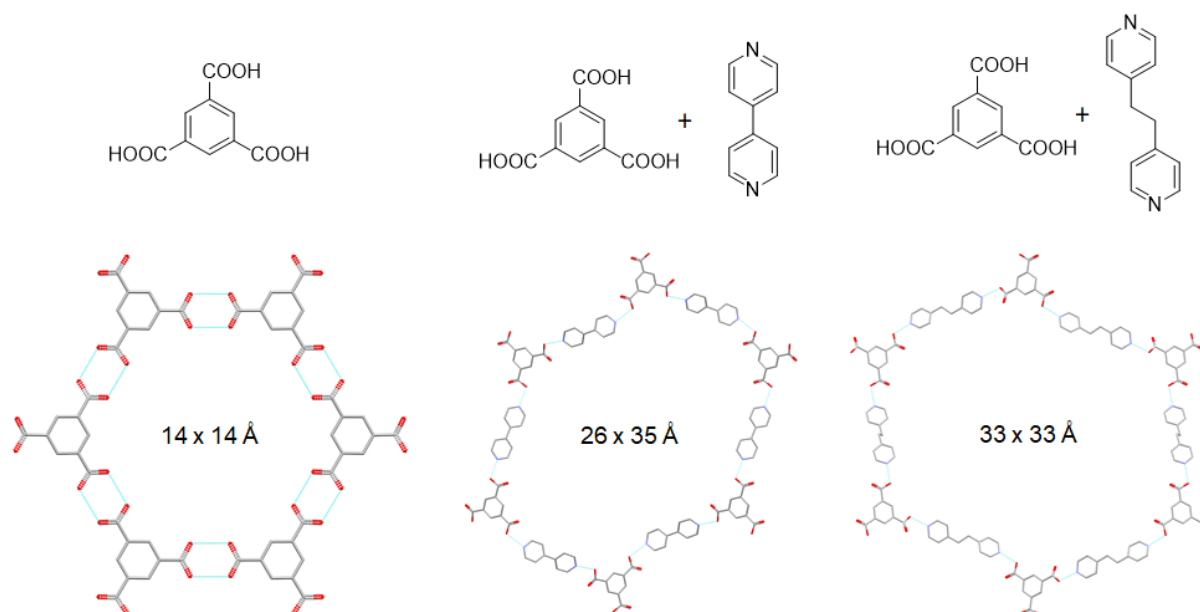


Figure 16 Honeycomb arrangement found in the crystal structure of H₃BTC (left). Two component co-crystals prepared by the self-assembly of H₃BTC and 4,4'-bipy (middle) and 1,2-di(pyridin-4-yl)ethane (right). Refcodes: BTCOAC, RAPHUR and SAYMUB, respectively. H atoms have been omitted for clarity and H-bonds (D–A) are depicted in turquoise.

By increasing the number of co-formers the complexity of the system increases drastically. Ternary co-crystals have been prepared exploiting a deep knowledge of the hierarchy of interactions, in particular, it was demonstrated that acid-pyridine interaction is favoured over acid-amide interaction and can be used to engineer crystals with predicted architectures. Helfrich, reported one of the first examples of ternary co-crystals in which co-formers engage hydrogen bonds of different strength.^[219] Rissanen *et al.* recently reported a ternary co-crystals formed by the synergic establishment of hydrogen and halogen bonds using a crown ether as hydrogen bond acceptor, thiourea as hydrogen bond donor, and perfluorohalocarbons capable to interact with sulphur atom of thiourea resulting in halogen bonding interactions (Figure 17).^[220]

Desiraju recently reported the synthesis of a series of multicomponent co-crystals including up to six components which is the highest number of co-formers included into a supramolecular solid to date.^[221]

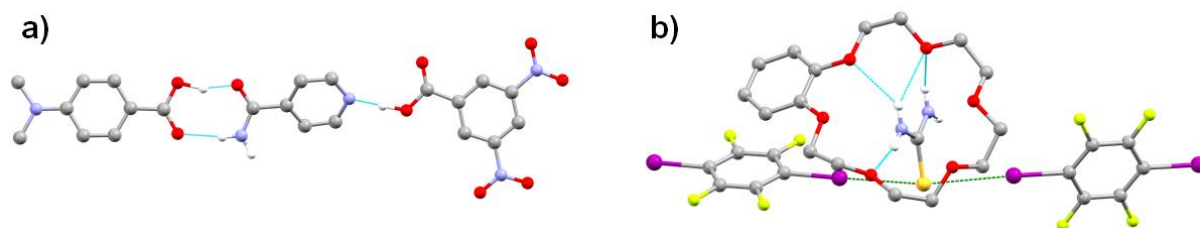
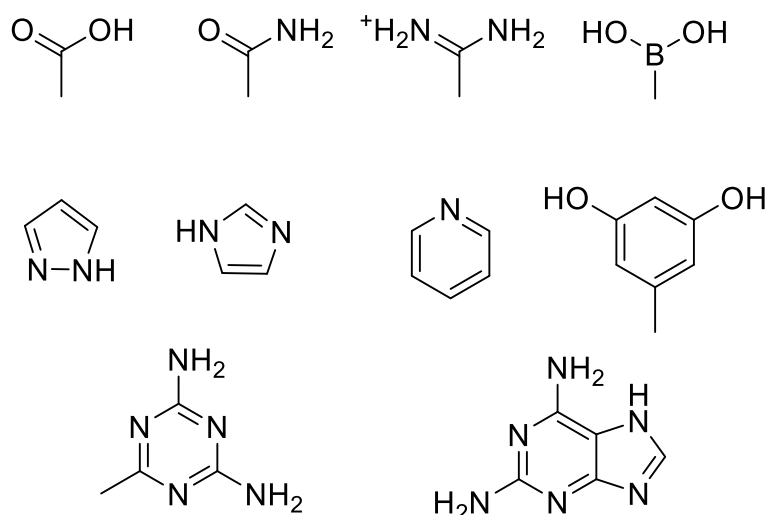


Figure 17 Ternary co-crystals: a) assembled through hydrogen-bond of different strength; b) cooperativity of hydrogen bond and halogen bond. Refcodes: BUFBIP and OQIJJ, respectively. Hydrogen bonds are depicted in turquoise and halogen bonds in green. H atoms not involved in hydrogen bonding have been omitted for clarity.

Co-crystals are to CPs, as Hydrogen-bonded Organic Frameworks (HOFs) to MOFs. HOFs are crystalline frameworks held together by hydrogen bonds which possess permanent porosity. The first report of porous hydrogen-bonded materials was published in 2010 by Yang.^[222] The reversibility of hydrogen bonds allows self-assembly and error correction during crystallization yielding highly crystalline products that can be structurally characterized by means of XRD analysis which give fundamental understanding of the intermolecular interactions within the network. Not surprisingly, these systems often lack permanent porosity due to the weakness of hydrogen bonds, and potential voids observed in the crystal structure are often lost upon activation because of collapsing of the framework. For this reason, HOFs have been poorly investigated if compared to other classes of porous materials such as zeolites and MOFs. Solvent removal on as-synthesized HOFs *via* vacuum approaches is too harsh for many frameworks and milder condition need to be applied to this aim. This notwithstanding, the crystalline framework can be often restored once the solvent is added back,^[223] an unique feature not observed for other classes of porous materials that makes HOFs particularly intriguing for potential applications. Moreover, HOFs are more light-weight materials if compared to MOFs and the absence of metal ions in their structures guarantees good biocompatibility.

Although a common strategy for preparation of HOFs is still to be developed, ground-breaking works have provided some guidelines,^[223–225] such the use of building blocks with rigid backbones to favour the formation of permanent porosity. Since other intermolecular interactions such as π - π interactions play crucial roles in providing robustness to the final framework, the design of suitable linkers must be carried out including aromatic moieties and other functional groups capable to meet this demand. Additionally, networks interpenetration significantly benefits the resilience of the system increasing the chance to retain permanent porosity.

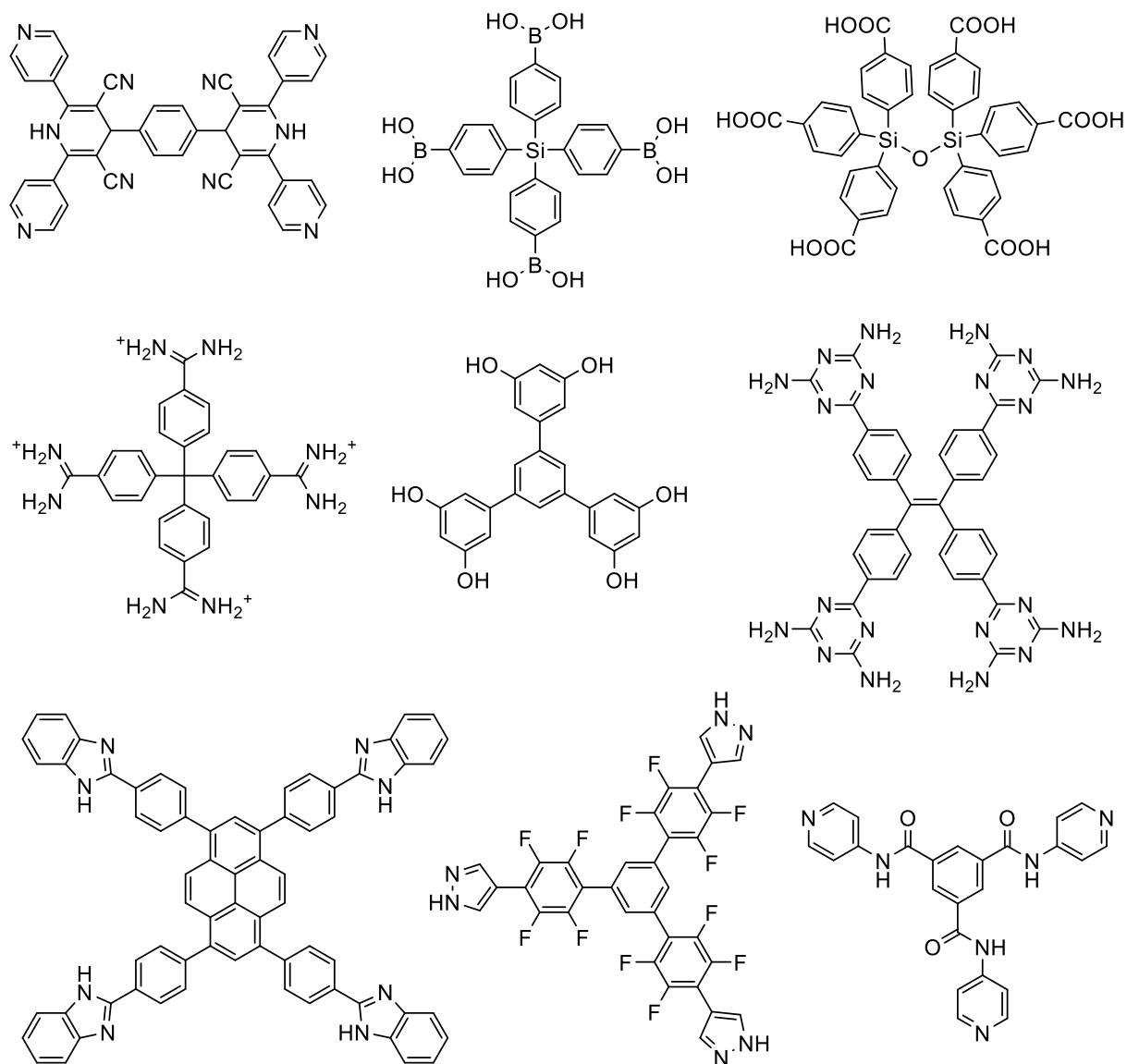


Scheme 7 Selected molecular moieties employed in the preparation of HOFs. From top to bottom: carboxylic acid, amide, amidinium, boronic acid, pyrazole, imidazole, pyridine, resorcinol, 2,4-diaminotriazine, 2,6-diaminopurine.

The most frequently used molecular moieties in the production of HOFs are carboxylic acid,^[226,227] amide,^[228] amidinium,^[229] boronic acid,^[230] pyrazole,^[231] imidazole,^[232] pyridine,^[222] resorcinol,^[233] 2,4-diaminotriazine (DAT),^[234] and 2,6-diaminopurine^[235] (Scheme 7). Given that different binding fashions can be engaged between the aforementioned functional groups, polymorphs formation is not a negligible problem in this field, even if computational studies suggest that the most energetically favoured frameworks are usually formed.^[236] Theoretical investigation is an important tool and a good guide for the design of novel HOFs, since it helps to understand known networks and to predict new ones. The first step in HOF preparation is the synthesis of the ligands which are properly designed with different shapes, number and kind of hydrogen-bondable groups, and with additional substituents capable of impart extra functionalities, few examples of organic ligands taken from recent literature are depicted in Scheme 8.

Although their challenging synthesis, HOFs have demonstrated enormous potential applications due to the flexibility and resilience of the frameworks that have been proven capable to gas storage and separation of mixture of gases. It has been reported that many HOFs are able to selectively incorporate small molecules such as H₂, CH₄, CO₂, C₂H₂ and C₄H₄ which are important in industrial applications.^[237,238] Yang *et al.* reported the self-assembly of 9,10-bis(4-((3,5-dicyano-2,6-dipyridyl)-dihydroxypyridyl)phenyl)anthracene) resulting in a flexible HOF stable up to 400 °C,^[222] with temperature-dependent porosity behaviour and dynamic gas uptake. The ligand molecules are assembled through multiple N–H⋯N hydrogen bonds into a

2D-layered structure extended into a 3D fashion upon intermolecular π - π interactions and weak C-H \cdots N contacts, and the resulting activated framework showed a BET surface area of 474 m² g⁻¹, high gas uptake and selectivity.



Scheme 8 Selected ligand used for the preparation of HOFs.

As far as the porosity features are regarded, it is worth noting that the actual pore volume record of 1.36 cm³ g⁻¹ and relatively high BET value was recently reported by Chen with an exceptional mesoporous HOF,^[239] and the HOF with highest BET value and lowest density was reported by Cooper.^[236]

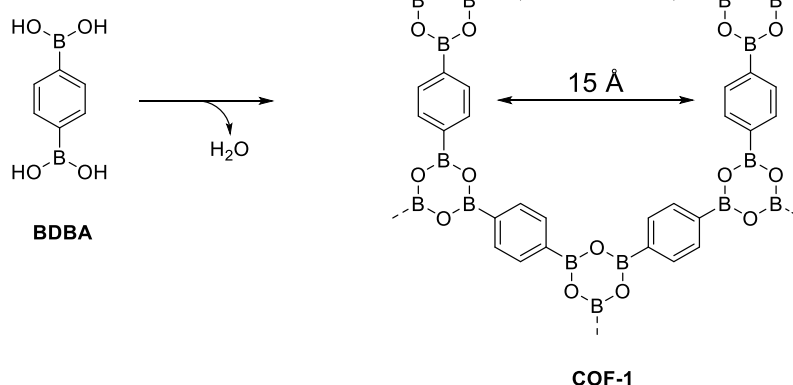
Another interesting feature of HOFs is their stability in aqueous media sometimes even in acidic conditions, resulting in promising biomedical applications, as reported by Cao and co-workers which successfully encapsulated Doxorubicin, a drug employed in chemo-photodynamic therapy, into a hydrogen-bonded framework, providing therapeutic efficiency comparable to the free drug, but lower toxicity.^[240]

Very promising, but still largely unexplored is the preparation of luminescent HOFs prepared by inserting fluorescent and/or phosphorescent dyes within the ligands that provide interesting properties to the final material. Few examples are reported showing potential application in the preparation of optical devices and sensing.^[234,241–243]

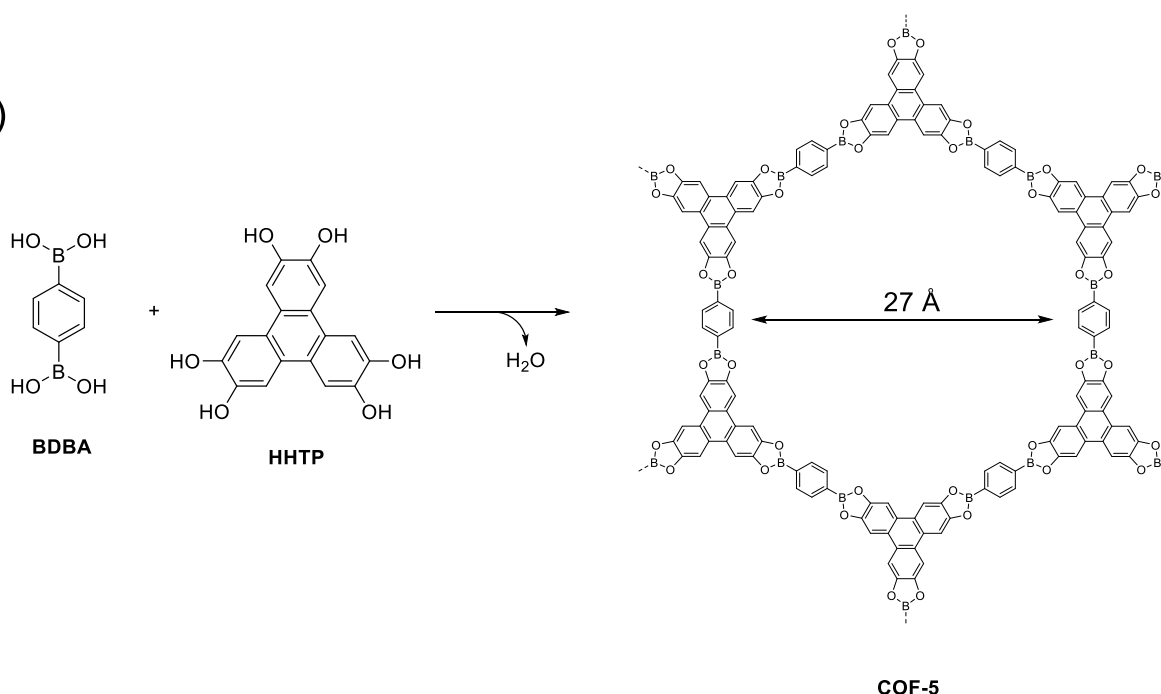
1.2.3. Covalent Organic Frameworks (COFs)

Another interesting class of porous solids is that of Covalent Organic Frameworks (COFs) formed by covalent bonds, stronger and less reversible forces compared to those just described for MOFs and HOFs. The strong nature of the implied bonds determines a more difficult crystallization process since error correction and reorganization of molecules into a crystalline phase, typical of MOFs and HOFs, is difficult to govern in a covalently assembled material, resulting in the so called “crystallization problem” of COFs.^[186] In 2005, Yaghi and co-workers reported the first examples of COFs synthesized by self-condensation of boronic acids to obtain boroxine cycles (B_3O_3) (§1.1.3) (COF-1 Scheme 9a) and condensation between boronic acids and vicinal diols yielding boronate esters (§1.1.3) (COF-5, Scheme 9b).^[244] Although single crystals of the products were not isolated, their 2D honeycomb structure was determined by means of powder XRD, and confirmed by means of computational approaches. Porosity measurements were carried out by gas sorption and BET approach, akin to what is generally done for the characterization of MOFs and HOFs.

a)



b)

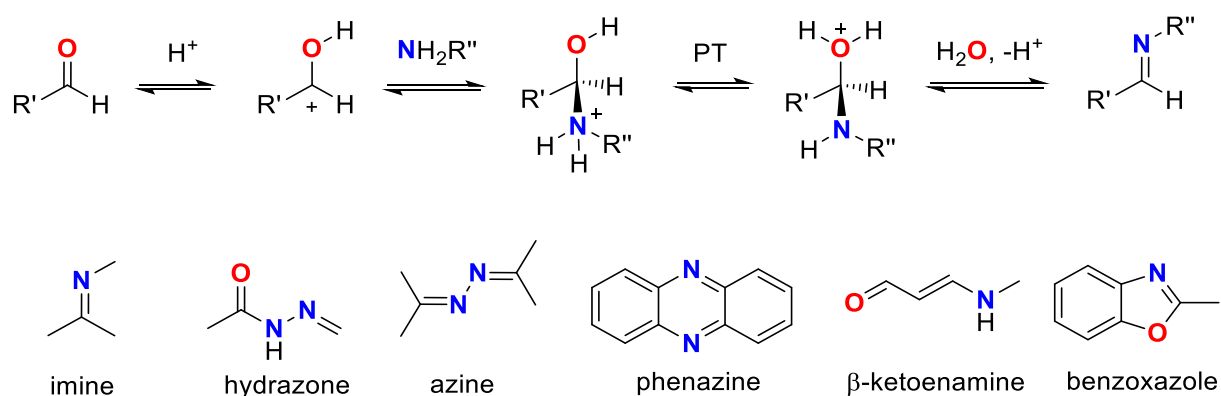


Scheme 9 a) self-condensation of 1,4-benzenediboronic acid (BDBA) into COF-1. b) condensation between BDBA and hexahydroxy tetraphenylene (HHTP) to produce COF-5. Reproduced from ref. [244].

Pore size distributions were modelled by means of DFT calculations revealing an average pore aperture of 15 and 27 Å for COF-1 and COF-5, respectively. The authors pointed out how reaction conditions are important in order to ensure a microscopic reversibility of the reactions necessary to impart crystallinity to these materials. In particular, COF-1 was prepared by self-condensation of 1,4-benzenediboronic acid (BDBA) at 120 °C for 72 h in a mesitylene-dioxane mixture in a sealed Pyrex tube, thus preventing water removal from the reaction vessel and slowing down the dehydration. Moreover, the selected solvent mixture in which BDBA is

sparingly soluble, helped crystallite growth. Similarly, COF-5 was prepared by reacting BDBA with hexahydroxy triphenylene (HHTP) in a 3:2 stoichiometric ratio. These methods differ from those previously reported for boroxine's synthesis where boronic acids are reacted in toluene and the eliminated water generally removed by azeotropic distillation.^[245]

The reversible formation of covalent bonds has been steadily investigated in the field of mechanically interlocked molecules and molecular machines and has resulted in the Nobel Prize in Chemistry awarded to Stoddart, Sauvage and Feringa in 2016.^[246] The so-called Dynamic Covalent Chemistry (DCvC) principles have been applied in the design of COFs.^[186] The library of transformations used in DCvC includes diverse synthetic tools based on the formation of C–C, C–O, C–N, C=N, C–Si, B–O and B–N bonds: imine and aminal formation,^[247] disulfide bond formation,^[248] cycloaddition reactions (Diels-Alder),^[249] condensation reactions and so on. Among them, the chemistry of Schiff-base reactions has led numerous examples of COFs:^[250] the reaction mechanism generally starts with the protonation of the carbonyl group of an aldehyde or a ketone, hence increasing the electrophilicity of the carbon atom (Scheme 10), followed by the nucleophilic attack by an amine group and intramolecular proton transfer resulting in the formation of a hemiaminal intermediate, which is converted into a Schiff-base upon elimination of water.^[251] The key to make this transformation reversible is to employ an acid as a catalyst.



Scheme 10 Reaction mechanism for an acid catalysed Schiff-base formation from a generic aldehyde and an amine. Schiff-base derivatives employed in the formation of COFs are represented in the bottom.

Depending on the substrates used, several classes of compounds were obtained including imines, hydrazones, azines, β -ketoenamines, phenazines and benzoxazoles, which have been employed for the preparation of 2D and 3D COFs.^[252–259]

Most of the reported COFs adopt 2D layered structures which are stabilized by π - π interactions through extended aromatic systems included in the building units. These 2-periodic

arrangements can be rationalized, from a topological point of view, in the five edge-transitive nets **hcb**, **sql**, **hxl**, **kgm** and **kgd**, reported in Figure 18. The nets can be discriminated on the base of their transitivity which is given by the $[pqr]$ notation that describes the different types of vertex (p), edge (q), and rings (r) in the net. The “regular nets” have transitivity $[111]$ (**hcb**, **sql** and **hkl**), “quasiregular” nets $[112]$ (**kgm**), and binodal nets $[211]$ (**kgd**). The simple nets can be converted in the so-called augmented nets which are more common and are obtained by replacing the simple nodes with the corresponding polygons or polyhedra. Both simple nets and the corresponding augmented version for 2D layered structures are illustrated in Figure 18.

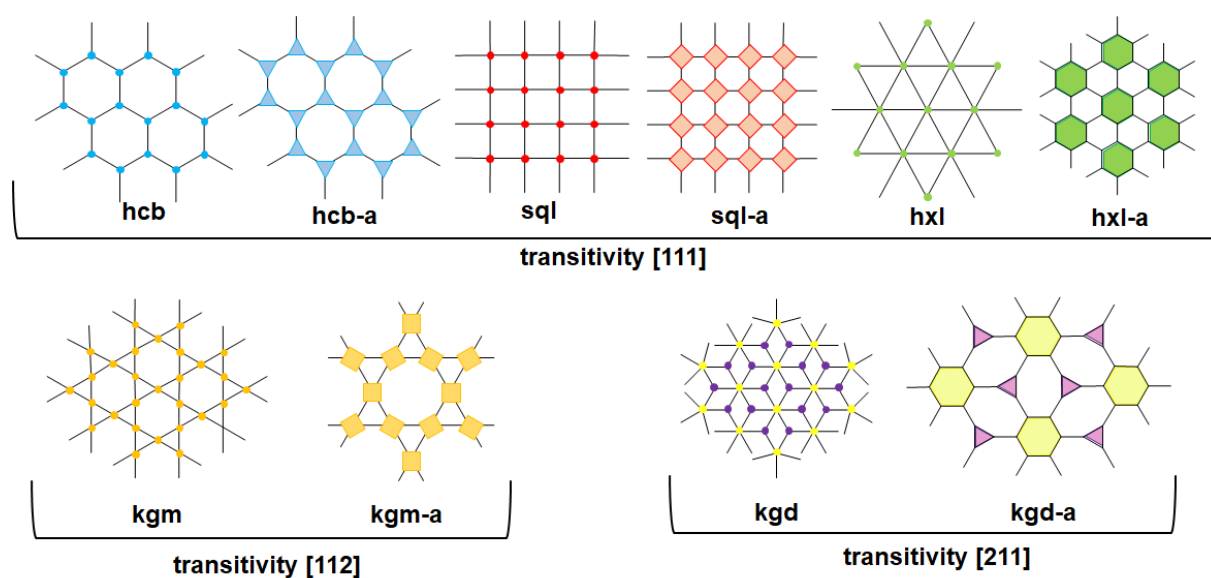


Figure 18 The five edge-transient topologies in 2D-COFs. Both simple and augmented nets are reported for each topology.

Passing from polygonal to polyhedral linkers it is possible to increase the dimensionality of COFs from 2D to 3D albeit their synthesis is even more challenging. Nowadays, only four topologies are reported for 3D-COFs: the use of tetrahedral linkers yields **dia** topology, the combination of tetrahedral and trigonal linkers led **ctn** or **bor** nets, and the concurrent presence of tetrahedral and square planar linkers produce **pts** net.^[260–262]

An example of 3D-COF is that prepared upon imine condensation of tetra-(4-anilyl)-methane and terephthalaldehyde leading to a five-fold interpenetrated diamond network,^[253] that showed permanent porosity with experimental BET surface area of $1360 \text{ m}^2 \text{ g}^{-1}$ and thermal stability up to $490 \text{ }^\circ\text{C}$.

In addition to those based on Schiff-base chemistry, other important linkages that have been reported to be suitable in COFs preparation are the coordination bonds between triazine and borazine. In contrast to the conventional solvothermal approach employed in COFs formation,

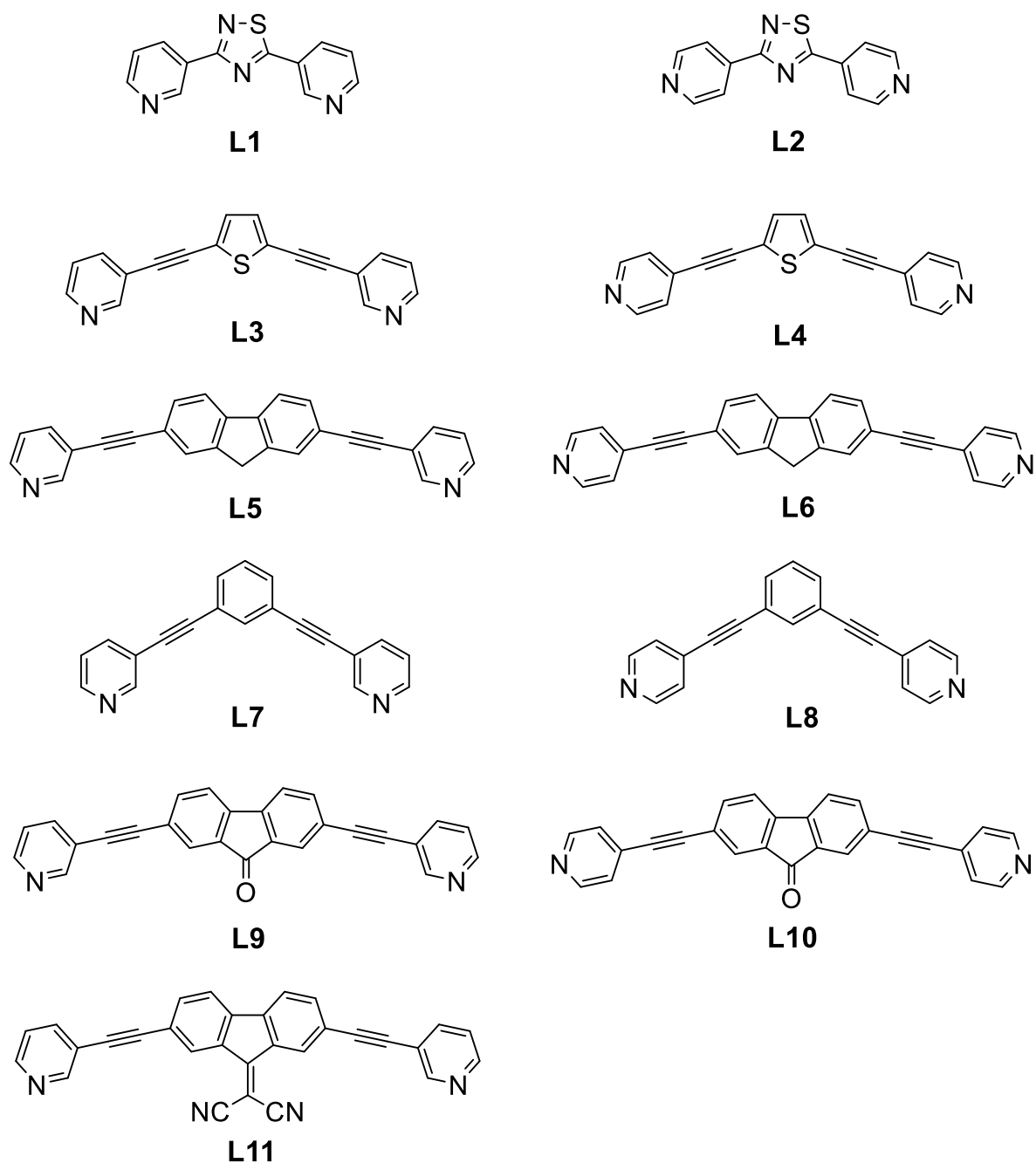
triazine based COFs can be obtained ionothermally. Their synthesis consists of a [2+2+2] cycloaddition of nitrile derivatives in liquid $ZnCl_2$ at 400 °C, very harsh experimental conditions that also guarantee for the microscopic reversibility needed to ensure crystallinity in the final.^[263]

Borazine rings (B_3N_3) (§1.1.3) and triazine rings are generally prepared by thermal decomposition of arylamine-borane complexes or -boron trihalide adducts in aprotic solvents.^[264] Borazine have been widely studied in the fields of ceramics and optoelectronics,^[265,266] but their use in porous polymer science is still largely unexplored due to their challenging synthesis.^[267] El-Kaderi *et al.* recently reported the synthesis of a borazine-based COF featuring **hcb** net prepared by decomposition of the trigonal 1,3,5-(*p*-aminophenyl)-benzene-borane carried out in a mixture of mesitylene/toluene at 120 °C in a sealed tube for three days,^[264] in order to prevent the dispersion of the hydrogen produced as by-product this providing reversibility to the system.

COFs have showed interesting properties such as permanent porosity, high thermal stability (up to 600 °C) and surprising low density with potential applications in the fields of gas sorption and separation,^[268–273] catalysis,^[274–277] proton conductivity,^[278,279] sensors,^[280,281] drug delivery,^[282] energy storage,^[283,284] optoelectronic and photovoltaics,^[285,286] and chromatography separation.^[287]

2. Aim and objectives

Objective of the work is the design and construction of supramolecular networks based on different intermolecular interactions starting from the organic molecules outlined in Scheme 11, Scheme 12 and Scheme 13.

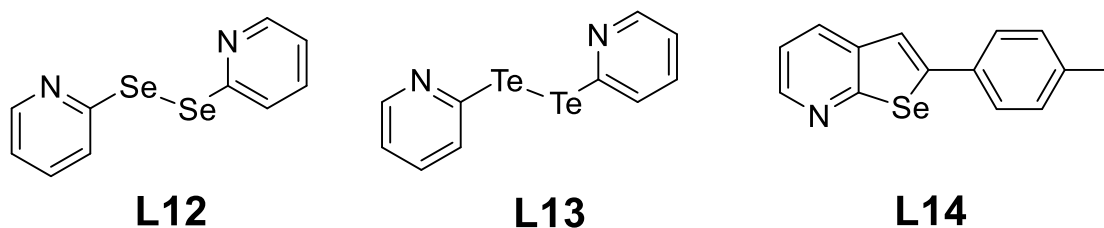


Scheme 11 Pyridyl-based building blocks.

The organic ligands **L1-L11** are pyridyl-based building blocks which present similar structural features with a central core constituted by one (either penta-atomic or hexa-atomic) or more fused rings having pyridyl substituents in divergent positions directly connected to the central core (**L1** and **L2**) or separated by a triple carbon-carbon bond (**L3-L11**). The ligands were always prepared in pairs featuring 3- and 4-pyridyl substituents, respectively, in order to evaluate the effect of the orientation of the donor on the final network. The central cores of **L3-L10** were chosen in order to impart fluorescence properties to the ligands and test possible luminescence changes in the resulting networks in order to subsequently evaluate ensuing potential applications of the investigated systems as molecular sensors.

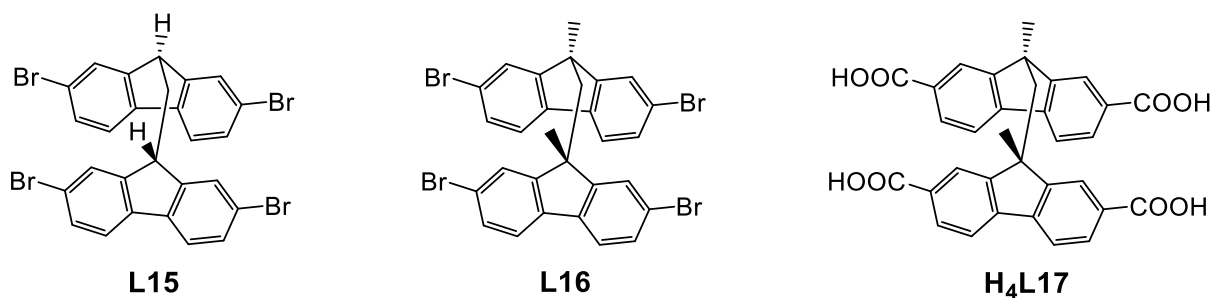
In the following sections the synthesis and characterization of the ligands are reported along with the results obtained by their reactions with selected complementary building blocks.

The versatile nature of pyridyl donors allowed to test the reactivity of the selected donors with a wide range of different Lewis acids such as metal ions (§3.1.1), coordinatively-unsaturated metal complexes (§3.1.1), carboxylic acids (§3.1.2), borasiloxanes (§3.1.3), molecular halogens and interhalogens (§3.1.4), halogenated substrates (§3.1.4), and combined systems containing two different Lewis acids (§3.2.4).



Scheme 12 Pyridyl-based substrates containing chalcogen atoms.

Ligands **L12-L14** (Scheme 12) are pyridyl based substrates containing chalcogen atoms and were appositely prepared in collaboration with the research group of prof. K. K. Bhasin of the University of Panjab, India and with the group of prof. Eder J. Lenardao of the Universidade Federal de Pelotas, Brazil to investigate their reactions with molecular halogens and interhalogens (§3.1.4.4).



Scheme 13 Co-facial bifluorene derivatives.

Ligand **H₄L17** and the relative intermediate products (**L15** and **L16**) were designed in order to extend the library of fluorene derivatives **L5**, **L6**, **L9**, **L10**, and **L11** to co-facial bifluorenes in order to investigate the different extent of overlap between the two chromophore units in the resulting networks, and the ensuing fluorescence variations.

Co-facial bifluorene **H₄L17** characterized by the presence of four carboxylic groups was reacted with metal ions (§3.2.2, §3.2.4) and dipyriddy-based derivatives (§3.2.3).

Among the huge number of obtained products, a choice was made to present here only those structurally characterized by means of SC-XRD in order to compare the resulting networks and rationalize them on the base of the different building blocks and experimental conditions used.

3. Results and discussion

3.1. Neutral pyridyl-based building blocks.

3.1.1. Interaction between *N*-donors L1-L6 with metal ions: CPs and MOFs

3.1.1.1. Interaction between *N*-donors L1 and L2 with metal ions

Pyridine and bipyridyl donors are known to react with metal ions through σ -type interactions involving centrosymmetric a_g combinations of the HOMO's or suitable orbitals at lower energy values (i.e. HOMO-1, HOMO-2, and HOMO-3) of the pyridine units mainly made up of the in-plane p orbitals of the nitrogen atoms (Figure 19).^[288,289]

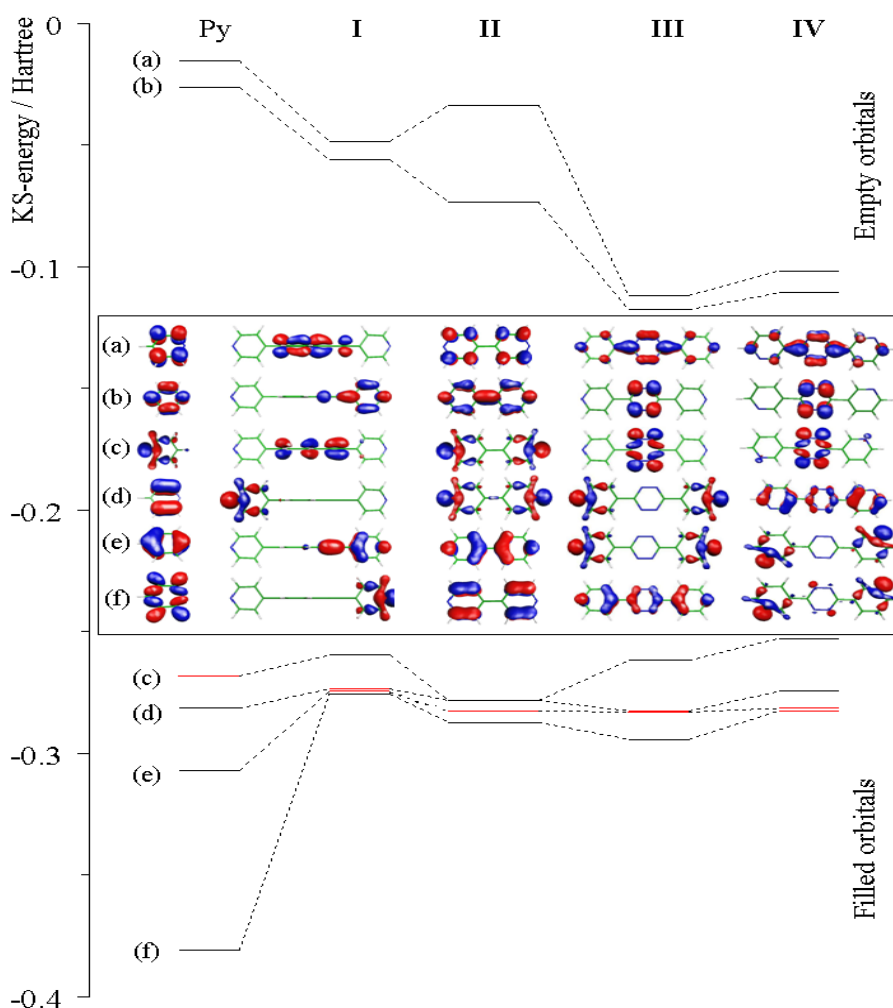


Figure 19 Kohn–Sham frontier orbital energies (Hartree) of free pyridine (Py) and ligands I–IV [1-pyridyl-4-(4'-pyridyl-ethynyl)-benzene (I), 4,4'-bipyridine (II), 3,6-bis(4-pyridyl)-1,2,4,5-tetrazine (III), and 3,6-bis(3-pyridyl)-1,2,4,5-tetrazine (IV)]. In the inset, the sketches of the molecular orbitals are depicted (Contour value = 0.05 e). (a) = LUMO+1, (b) = LUMO, (c) = HOMO, (d) = HOMO-1, (e) = HOMO-2, (f) = HOMO-3. Reproduced from ref ^[289].

As expected, among the occupied frontier molecular orbitals (MOs) calculated for 3,5-di(pyridin-3-yl)-1,2,4-thiadiazole (**L1**) and 3,5-di(pyridin-4-yl)-1,2,4-thiadiazole (**L2**), orbitals mainly made up of nitrogen lone pairs (LPs) of the pyridine rings were found (Figure 20 for **L2**).^[134]

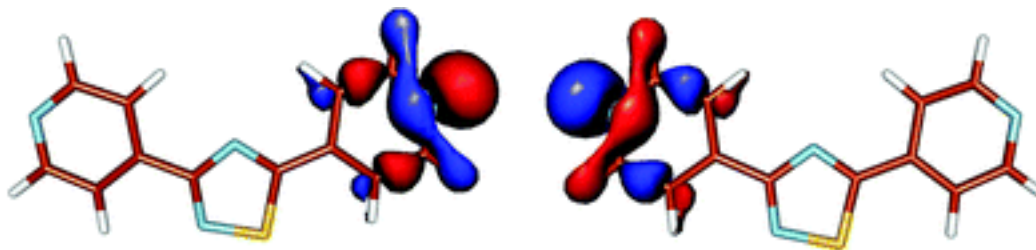
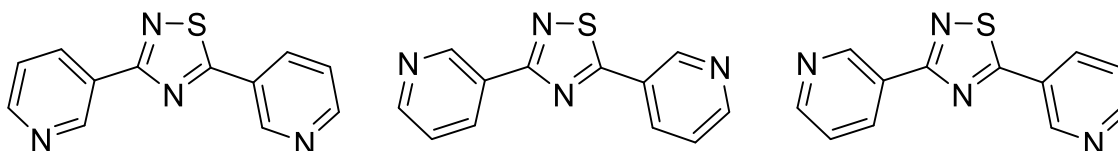


Figure 20 Iso-surface drawings of Kohn–Sham HOMO–3 (left) and HOMO (right) calculated for **L2**. Cutoff value = 0.05 e. Reproduced from ref ^[134].

In contrast, the central thiadiazol core is unreactive towards Lewis acids as evidenced by the examples reported in the present thesis. The optimised structures of the free ligands predicted the central 1,2,4-thiadiazole coplanar with the pyridine rings.^[134] In the case of **L1**, the periplanar (cisoid) and antiperiplanar (transoid) conformations (Scheme 14) differ in energy by less than 1 kcal mol⁻¹ and feature very similar metric parameters.^[134] Moreover, depending on the orientation of pyridyl rings in **L1**, three limit conformations can be envisaged, shown in Scheme 14.



Scheme 14 The two periplanar and the antiperiplanar arrangements of **L1** from left to right, respectively.

Two different periplanar conformations are possible when N-atoms point at the same side, and one antiperiplanar when N-atoms are facing towards opposite sides. It is interesting to note that since there is not an energetically preferred arrangement for **L1**, the adopted conformation is driven by other factors such as the coordination geometry of the metal ion, the counterion and the experimental conditions used in the self-assembly process.

L1 and **L2** were reacted with several monovalent (Ag⁺) and bivalent (Zn²⁺, Cd²⁺, Cu²⁺, Ni²⁺) metal ions differing for the dⁿ configuration and for the expected coordination geometry. Along with the reactivity with “naked” metal ions, that with coordinative unsaturated dithiophosphonato and dithiophosphato Ni^{II} and Cd^{II} complexes was also explored. Due to the huge amount of data collected, only the results of the CPs and MOFs structurally characterized

are here reported. Reaction between **L1** and silver(I) triflate (trifluoromethanesulfonate = OTf) in acetone led to the immediate formation of the product $[\text{AgL1}(\text{OTf})\cdot((\text{CH}_3)_2\text{CO})_{0.5}]_\infty$ as a white solid. Recrystallisation of the product from hot acetone yielded colourless prisms that were isolated and analysed by means of single crystal X-ray diffraction. Compound $[\text{AgL1}(\text{OTf})\cdot((\text{CH}_3)_2\text{CO})_{0.5}]_\infty$ is a coordination polymer crystallized in the monoclinic $C2/c$ space group (structural data refinement parameters in Table S119, bond lengths and angles in Table S120).

L1 units are slightly tilted with the two pyridyl rings angled of about 20° and arranged in a periplanar conformation. Pyridyl units from different **L1** ligands coordinate silver(I) ions in an almost linear geometry ($\text{N}-\text{Ag}-\text{N} = 170^\circ$) with $\text{Ag}-\text{N}$ distances ($d_{\text{Ag}-\text{N}}$) of 2.156(3) and 2.165(3) Å, for $\text{Ag1}-\text{N1}$ and $\text{Ag1}-\text{N4}$, respectively (Figure 21). The experimental values are in line with those observed for similar pyridyl-Ag(I) systems.^[290,291] The pentatomic thiadiazole ring is disordered over two positions with occupancies of 65 and 35 % and was modelled using RIGU and SIMU restraints. The positive charge is counterbalanced by chelating bridging triflate anions that interacts with the metal nodes along a dimeric arrangement shown in Figure 22.

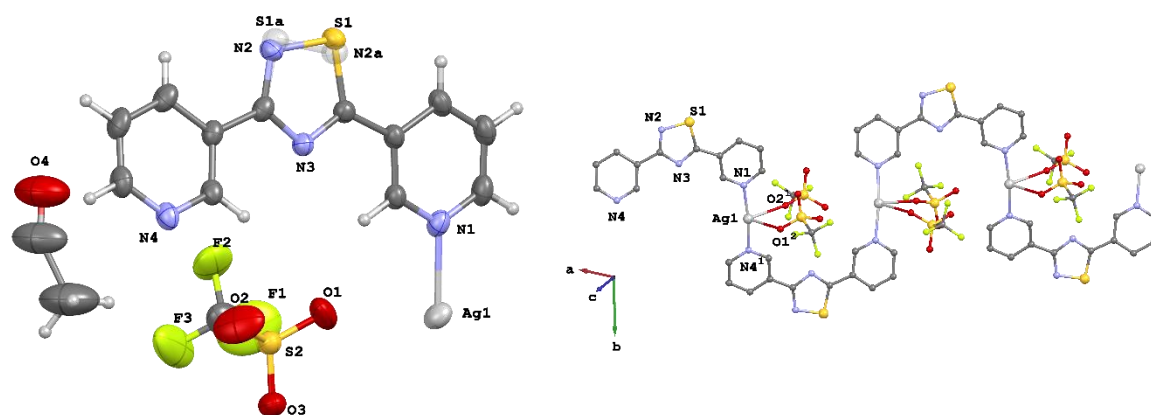


Figure 21 Representation of the asymmetric unit of $[\text{AgL1}(\text{OTf})\cdot((\text{CH}_3)_2\text{CO})_{0.5}]_\infty$ (left) and of the polymeric zig-zag chain (right). Hydrogen atoms and acetone molecules in the right-hand side have been omitted for clarity. Symmetry codes: ¹ $-1/2+x, 3/2-y, 1-z$; ² $1/2-x, 3/2-y, 1-z$.

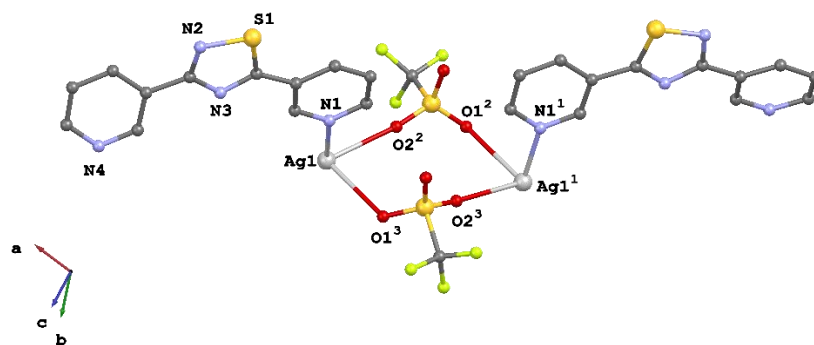


Figure 22 Chelating bridging triflate anions arranged into a dimeric network that stabilize two adjacent zig-zag chains. Ag–O distances = 2.680(4) and 2.877(4) Å for Ag1–O2 and Ag1–O1, respectively. Symmetry codes: ¹ 1/2-x, 3/2-y, 1-z; ² -x, +y, 1/2-z; ³ -1/2+x, 3/2-y, -1/2+z. H atoms, acetone molecules and disorder have been omitted for clarity.

A co-crystallized acetone molecule lying on a symmetry element is present in the packing. **L1** units bridge silver nodes in undulated polymeric chains with Ag⋯Ag distances of about 8.21 Å (Figure 23). Adjacent chains are staggered and stabilized by π – π stacking between pyridyl rings (centroid-centroid $d = 3.74$ Å) and thiadiazol rings (centroid-centroid $d = 3.69$ Å), along with silver-silver interactions ($d_{\text{Ag-Ag}} = 3.388$ Å) that enforce the cohesion between adjacent zig-zag chains (Figure 23).

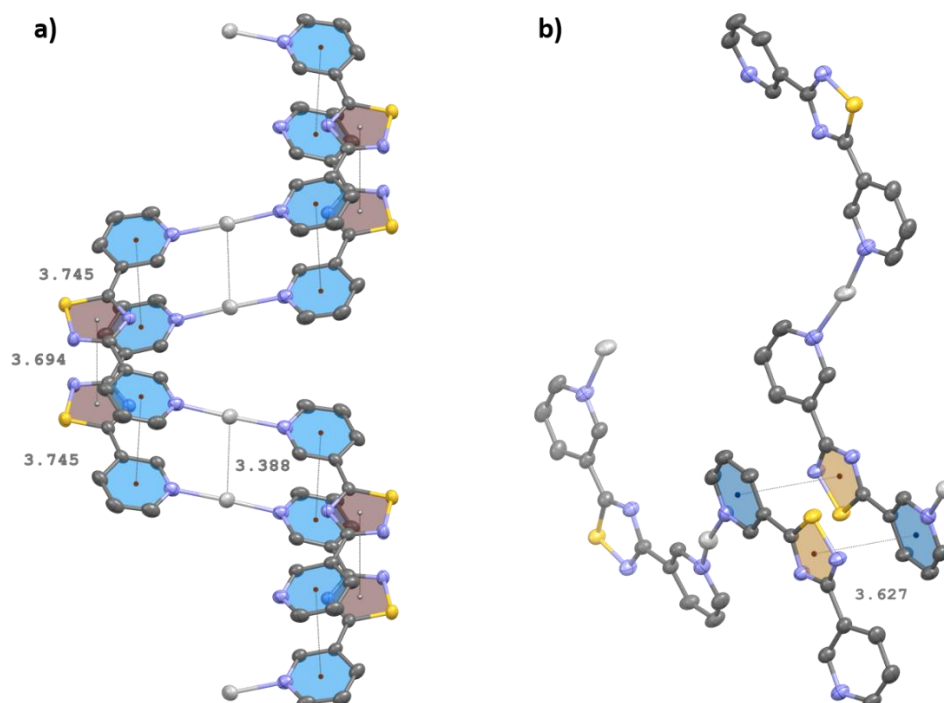


Figure 23 Perspective view of the intermolecular Ag⋯Ag and π – π interactions along the [100] and [011] directions in a) and b) respectively. Centroid-centroid distances are reported in Å.

The crystal packing is extended along the *c*-axis by an unusual 2D arrangement of **L1** units which are turned upside down every two adjacent chains, stabilized by an intermolecular π – π interaction involving a pyridyl and a thiadiazol ring belonging to different molecules (centroid-centroid distance of 3.627 Å, Figure 23b). As a result, quasi-hexagonal channels are formed along the [101] direction filled by triflate and co-crystallized acetone molecules (Figure 24).

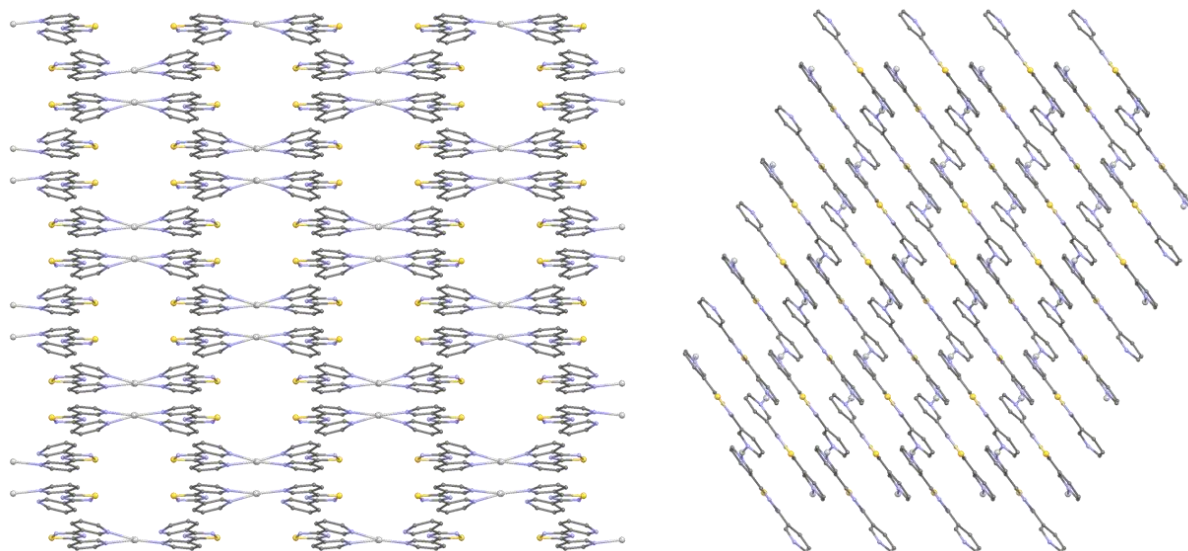


Figure 24 Crystal packing diagrams of $[\text{AgL1}(\text{OTf})\cdot((\text{CH}_3)_2\text{CO})_{0.5}]_\infty$ along [101] and [010] directions from left to right, respectively. Counterions, solvent molecules and hydrogen atoms have been omitted for clarity reasons.

The reactions of **L1** with bivalent cations were performed under solvothermal conditions starting from two different zinc salts, namely $\text{Zn}(\text{NO}_3)_2\cdot 6\text{H}_2\text{O}$ and ZnCl_2 , in order to evaluate the role of the counterion. The reaction of **L1** with $\text{Zn}(\text{NO}_3)_2\cdot 6\text{H}_2\text{O}$ in CH_3CN produced a white crystalline product which was characterized by means of single-crystal XRD analysis showing a dimeric arrangement with formula $[\text{ZnL1}(\text{NO}_3)_2\cdot \text{CH}_3\text{CN}]_2$ crystallized in the triclinic *P*-1 space group (structural data refinement parameters in Table S121, bond lengths and angles in Table S122). **L1** units are almost planar with the two pyridyl rings angled of about 178° and arranged in a periplanar conformation. The thiadiazol ring is disorder over two positions with partial occupancies of 75 and 25%, and was modelled using RIGU and SIMU restrains. In contrast to the previously discussed $[\text{AgL1}(\text{OTf})\cdot((\text{CH}_3)_2\text{CO})_{0.5}]_\infty$ coordination polymer, a couple of **L1** ligands bridges a couple of metal ions in a dimeric paddle wheel arrangement with $\text{Zn}\cdots\text{Zn}$ distance of 7.81 Å. The zinc nodes are hepta-coordinated by two neutral N-atoms from two **L1** units, four O-atoms from two bidentate nitrate fragments, and a co-crystallized acetonitrile molecule (Figure 25a).

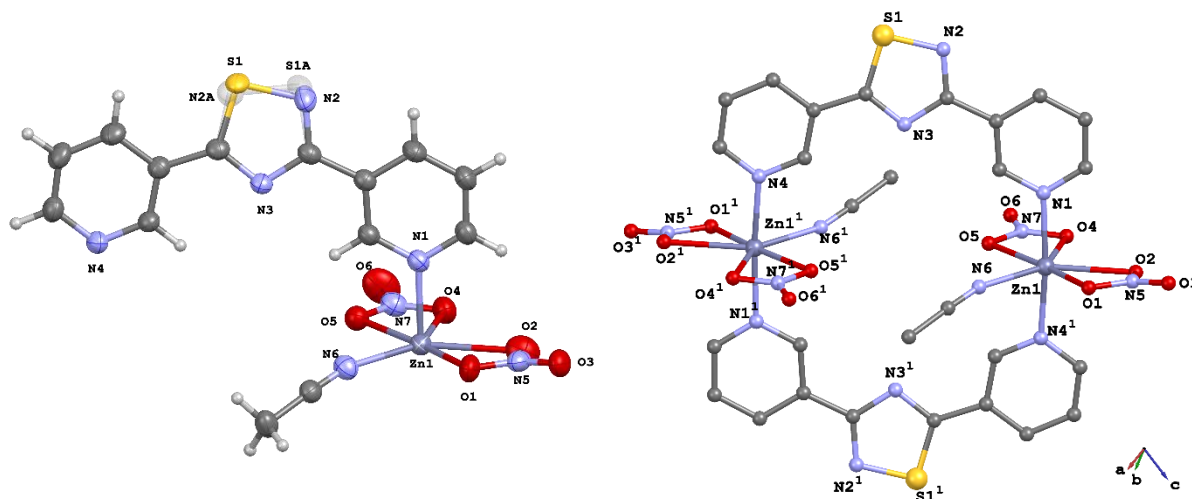


Figure 25 Perspective view of the asymmetric unit with atom numbering scheme for $[\text{ZnL1}(\text{NO}_3)_2 \cdot \text{CH}_3\text{CN}]_2$ (left). Paddle wheel arrangement (right); disorder at the thiadiazol ring and hydrogen atoms have been omitted for clarity. Symmetry code: $^1 1-x, 1-y, 1-z$.

Bond distances between Zn(II) cations and O-atoms range from 2.171(2) to 2.423(3) Å and are in agreement with those found in the literature. In addition, Zn–N distances are 2.108(2), 2.118(2) and 2.202(2) Å for Zn1–N1, Zn1–N4 and Zn1–N6, respectively. Intramolecular H-bonds occur between pyridyl protons of **L1** fragments and adjacent nitrates (interaction **a** and **b** in Figure 26 and Table 3). The crystal packing in $[\text{ZnL1}(\text{NO}_3)_2 \cdot \text{CH}_3\text{CN}]_2$ is mainly governed by moderate-weak hydrogen bonding interactions (§1.1.2) involving the CH₃ moieties of acetonitrile molecules and nitrate anions (interaction **c** and **d** in Figure 26, Figure 27 and Table 3).

Table 3 Hydrogen bonding interactions in $[\text{ZnL1}(\text{NO}_3)_2 \cdot \text{CH}_3\text{CN}]_2$.

	D	H	A	$d_{\text{D}\cdots\text{A}}$ (Å)	$d_{\text{H}\cdots\text{A}}$ (Å)	D–H \cdots A (°)
a	C1	H1	O2	3.243(4)	2.550(3)	129.94(17)
b	C11	H11	O2 ¹	3.225(4)	2.579(3)	125.56(19)
c	C14 ²	H14B ²	O3	3.209(4)	2.424(2)	136.75(18)
d	C14	H14A	O5 ¹	3.246(4)	2.493(2)	133.5(2)

Symmetry codes: $^1 1-x, 1-y, 1-z$; $^2 1-x, -y, 2-z$.

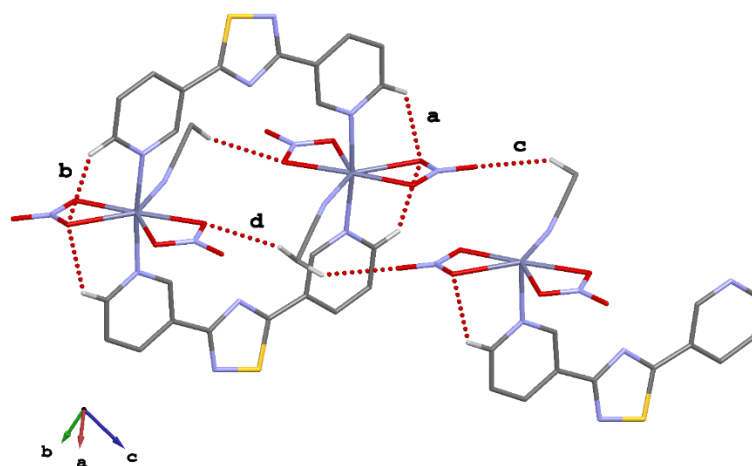


Figure 26 View of the hydrogen bonded network found in $[\text{ZnL1}(\text{NO}_3)_2 \cdot \text{CH}_3\text{CN}]_2$. Only H-atoms involved in intermolecular interactions are shown. Interactions are labelled according to Table 3.

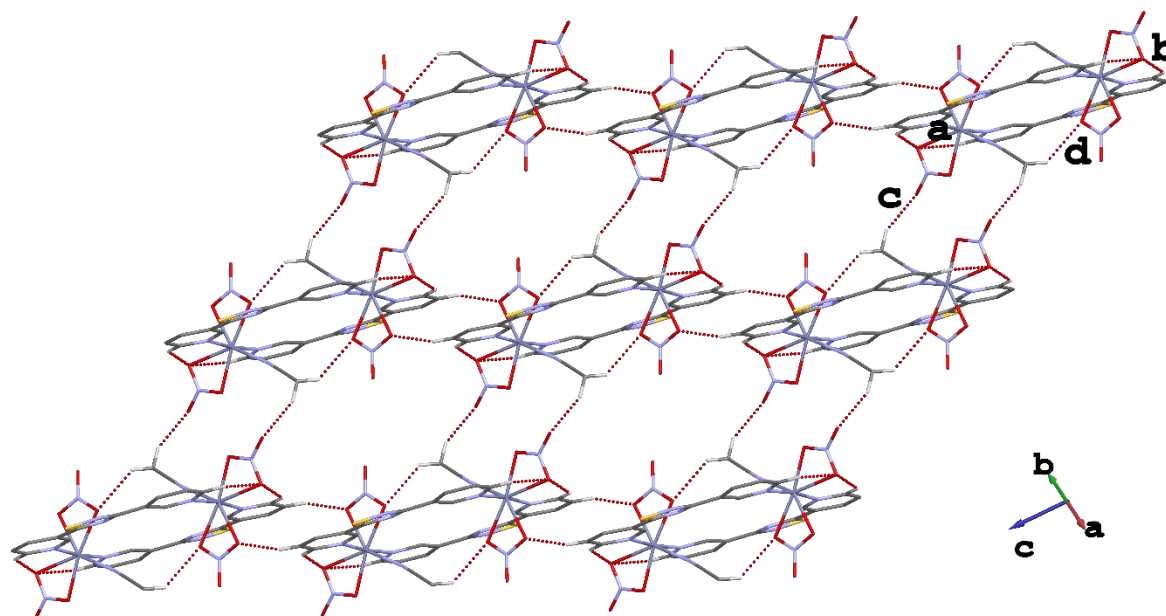


Figure 27 Packing diagrams for $[\text{ZnL1}(\text{NO}_3)_2 \cdot \text{CH}_3\text{CN}]_2$ along the $[110]$ direction. Interactions are labelled according to Table 3.

The solvothermal reaction between **L1** and ZnCl_2 in a 2:1 mixture of $\text{CH}_3\text{CN}:\text{CHCl}_3$ produced the crystalline product $(\text{ZnL1Cl}_2)_\infty$ which was characterized by means of single-crystal XRD analysis showing a polymeric nature. The CP crystallized in the monoclinic space group $P2_1/n$ (structural data and refinement parameters in Table S123, bond lengths and angles in Table S124). **L1** units are slightly tilted with the two pyridyl rings angled of about 24° and arranged in an antiperiplanar conformation. Zinc nodes show a tetrahedral coordination

geometry comprised by two chlorine and two nitrogen atoms belonging to the dipyrindyl ligand (Figure 28), with bond distances of Zn–N 2.061(3) Å, for both Zn–N1 and Zn–N4, resulting slightly shortened if compared to those previously observed for $[\text{ZnL1}(\text{NO}_3)_2 \cdot \text{CH}_3\text{CN}]_2$. Zn–Cl distances are 2.209(1) and 2.234(1) Å for Zn1–Cl1 and Zn1–Cl2, in line with the mean value of 2.26(6) Å found in the literature for similar systems.

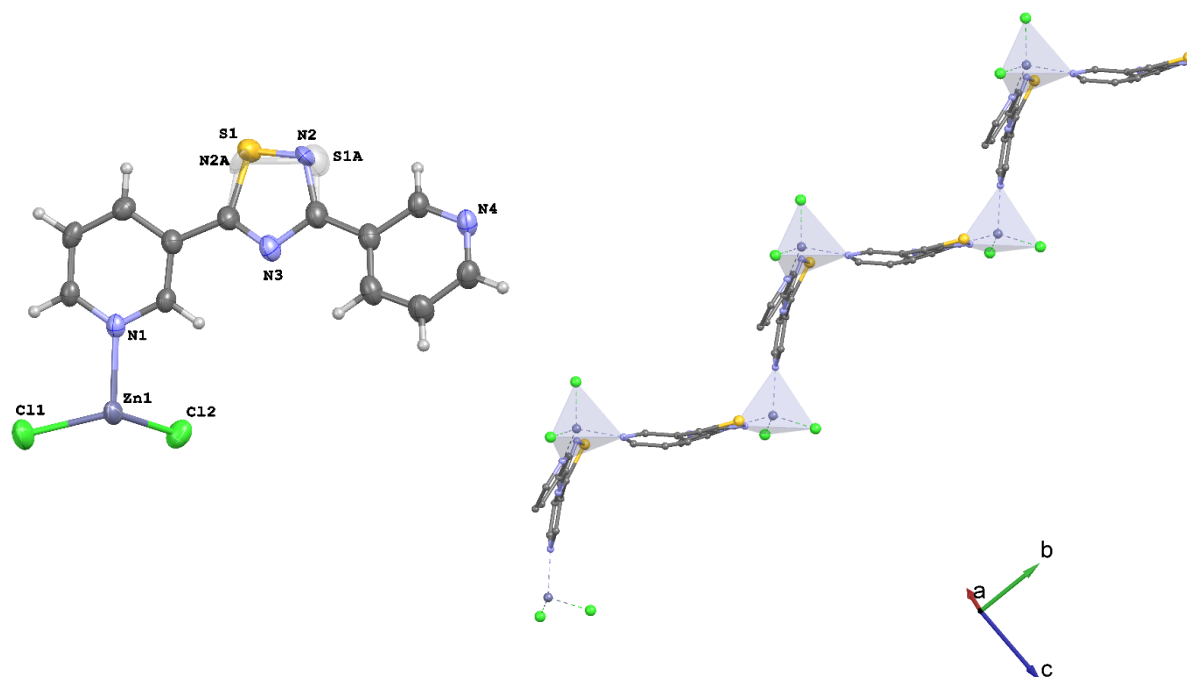


Figure 28 Asymmetric unit and atom numbering scheme for $(\text{ZnL1Cl}_2)_\infty$ (left); staircase polymeric network (right).

The angle Cl1–Zn1–Cl2 is 122.12(6) ° slightly wider than the value of 109.5 ° for an ideal tetrahedron. As a consequence, the other three angles defined by the metal node as the middle point are found narrower and thinly squeezed. L1 units bridge zinc nodes in undulated polymeric chains with Zn···Zn distances of about 11.77 Å, resulting much longer if compared with the analogue distance found in the case of $[\text{ZnL1}(\text{NO}_3)_2 \cdot \text{CH}_3\text{CN}]_2$. This is mainly due to the different conformation adopted by the pyridyl spacer in the two cases of study. The chains pack generating a staircase architecture (Figure 28). The crystal packing is governed by moderate-weak hydrogen bonds between chlorines and CH moieties of adjacent pyridyl rings (Figure 29, Table 4). Moreover, weak π - π stacking occur between aromatic rings as shown in Figure 29.

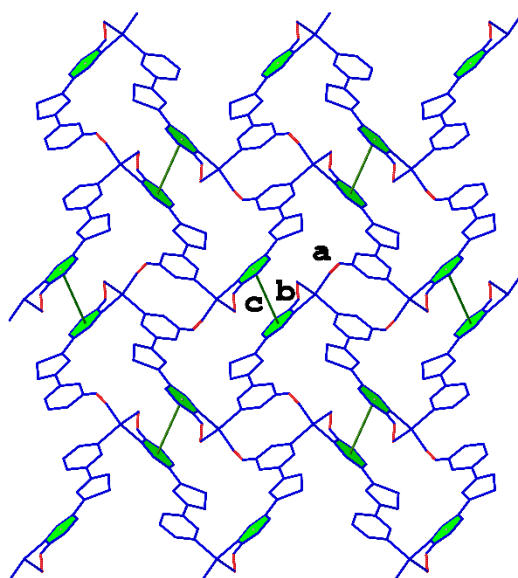


Figure 29 Intermolecular interactions found in $(\text{ZnL1Cl}_2)_\infty$. Intermolecular π - π interactions between parallel pyridyl rings are highlighted in green c) $d_{\text{centroid-centroid}} = 3.801 \text{ \AA}$. Interactions **a** and **b** are labelled according to Table 4.

Table 4 Intermolecular interactions in $(\text{ZnL1Cl}_2)_\infty$.

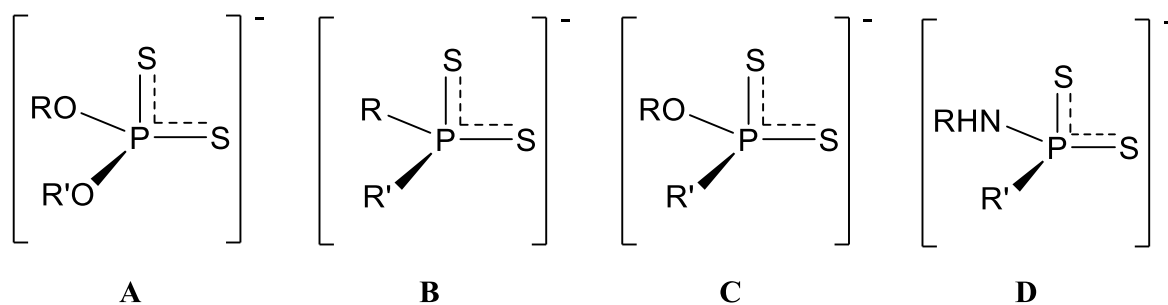
	D	H	A	$d_{\text{D}\cdots\text{A}}$ (\AA)	$d_{\text{H}\cdots\text{A}}$ (\AA)	$\text{D-H}\cdots\text{A}$ ($^\circ$)
a	C10 ¹	H10 ¹	Cl1	3.509(5)	2.84(3)	128.3(3)
b	C1 ²	H1 ²	Cl2	3.554(4)	2.82(3)	135.2(2)

Symmetry codes: ¹ $-3/2+x, 1/2-y, -1/2+z$; ² $1+x, y, +z$

In the aforementioned examples we discussed the supramolecular networks formed by reacting the dipyrrolic linker **L1** with “naked” metal ions. It is interesting to note that polymeric networks were obtained in both $[\text{AgL1}(\text{OTf})\cdot((\text{CH}_3)_2\text{CO})_{0.5}]_\infty$ and $(\text{ZnL1Cl}_2)_\infty$ where the spacer adopt a periplanar and antiperiplanar conformation, respectively. On the other hand, a discrete paddle-wheel arrangement was found in $[\text{ZnL1}(\text{NO}_3)_2\cdot\text{CH}_3\text{CN}]_2$ with the ligand featuring the same periplanar configuration encountered in $[\text{AgL1}(\text{OTf})\cdot((\text{CH}_3)_2\text{CO})_{0.5}]_\infty$. Therefore, we can deduce that the conformation adopted by the ligand is not the prior driving force in the formation of a discrete or polymeric arrangement. Other factors, such as the nature of the metal ion and its chemical environment heavily influence the resulting scaffold. It can be clearly seen by comparing the Zn(II)-based supramolecular networks $[\text{ZnL1}(\text{NO}_3)_2\cdot\text{CH}_3\text{CN}]_2$ and $(\text{ZnL1Cl}_2)_\infty$. The presence of nitrate anions in the former are responsible of forming an intricate hydrogen bonded network which stabilize the discrete crystal structure. When nitrate anions were replaced by chlorides as in the latter case, the coordination number at the zinc nodes

decreases from seven to four. As a consequence, the lower coordination geometry at metal nodes rules out the chance to form a discrete arrangement, favouring the formation of a polymeric network. Moreover, nitrate proficiency in the formation of multiple hydrogen bonds is much higher than that of chlorides, sweeping away other supramolecular interactions as showed by the crystal packing of $[\text{ZnL1}(\text{NO}_3)_2 \cdot \text{CH}_3\text{CN}]_2$. In contrast, the crystal packing of $(\text{ZnL1Cl}_2)_\infty$ features the synergistic action of hydrogen bonds and π - π interactions.

The reactivity of pyridyl derivatives **L1** and **L2** with coordinatively unsaturated metal complexes was also investigated. Since many years our research group has been working on the synthesis and coordination properties of a class of phosphor-1,1-dithiolates comprising dithiophosphato, dithiophosphinato, dithiophosphonato, and amidodithiophosphonato anions (**A-D** in Scheme 15).



Scheme 15 Phosphor-1,1-dithiolates derivatives: **A-D** = dithiophosphato, dithiophosphinato, dithiophosphonato, and amidodithiophosphonato.

In particular, tetra-coordinated metal complexes of derivatives **A-C** have been used as building blocks in the design of supramolecular systems based on their self-assembly with neutral ligands. The coordination of suitable bridging ligands on the tetra-coordinated metal centre of the complex led to coordination polymers featuring increased coordination numbers (usually 5 or 6) around the metal node. Figure 30 shows the formation of the CP $[\text{((OEt)}_2\text{PS}_2)_2(4,4'\text{-bipy})]_\infty$ between the *bis*(*O,O*-diethyldithiophosphato)nickel complex $[\text{Ni}(\text{(OEt)}_2\text{PS}_2)_2]$ and 4,4'-bipyridine.^[292]

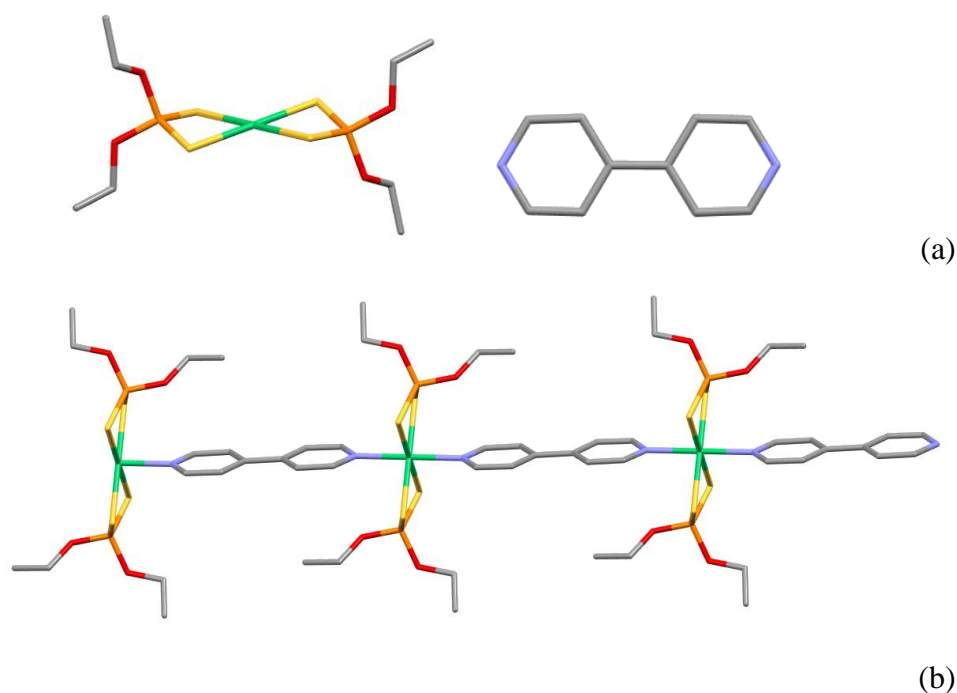


Figure 30 (a) Tetracoordinated *bis*(*O,O*-diethyldithiophosphato)nickel complex and 4,4'-bipyridine building blocks; (b) $[\text{Ni}((\text{OEt})_2\text{PS}_2)_2(4,4'\text{-bipy})]_\infty$ CP.

Following our previous study on the reactivity of dithiophosphato and dithiophosphonato Ni(II) complexes towards **L1** and **L2**,^[293] we decided to perform the reaction with the analogous cadmium complexes, in order to investigate the effect of the metal ion on the final structure. Dithiophosphato, dithiophosphito and dithiophosphonato cadmium(II) complexes are known to interact with N-donors to form molecular or polymeric frameworks in which metal nodes can feature different coordination numbers, typically five or six.^[294–297] Here, we report on the reaction products obtained by reacting the dithiophosphato Cd(II) complex $[\text{Cd}((\text{MeO})_2\text{PS}_2)_2]$ (**1**) towards **L1** and **L2**. Complex **1** was prepared in excellent yield by reacting $\text{Cd}(\text{NO}_3)_2 \cdot 4\text{H}_2\text{O}$ with P_2S_5 in methanolic solution (§5.2.17). Solvothermal reaction between **1** and **L1** in a 1:1 mixture of MeOH/ CHCl_3 produced a colourless crystalline solid in good yield (§5.2.23). The crystals were characterized by means of single-crystal XRD analysis showing a dimeric arrangement $(\mathbf{1} \cdot \mathbf{L1})_2$ crystallized in the monoclinic $P2_1/c$ space group with half-dimeric structure in the asymmetric unit (structural data and refinement parameters in Table S125, bond lengths and angles in Table 5). **L1** units are tilted with the two pyridyl rings angled of about $18.62(12)^\circ$ and arranged in a periplanar conformation. The thiadiazol ring features incommensurate disorder therefore the thermal parameters of N8 and S9 were constrained using EADP. The structure closely resemble that previously described for $[\text{ZnL1}(\text{NO}_3)_2 \cdot \text{CH}_3\text{CN}]_2$, and that recently reported for **L1** and the analogous dithiophosphato nickel complex.^[298] The

Cd^{II} coordination environment in **(1·L1)₂** displays a distorted octahedral geometry in which two OMe-dithiophosphato units coordinate the metal ion at the equatorial positions and the axial positions are occupied by pyridyl rings belonging to two different **L1** spacers (Figure 31).

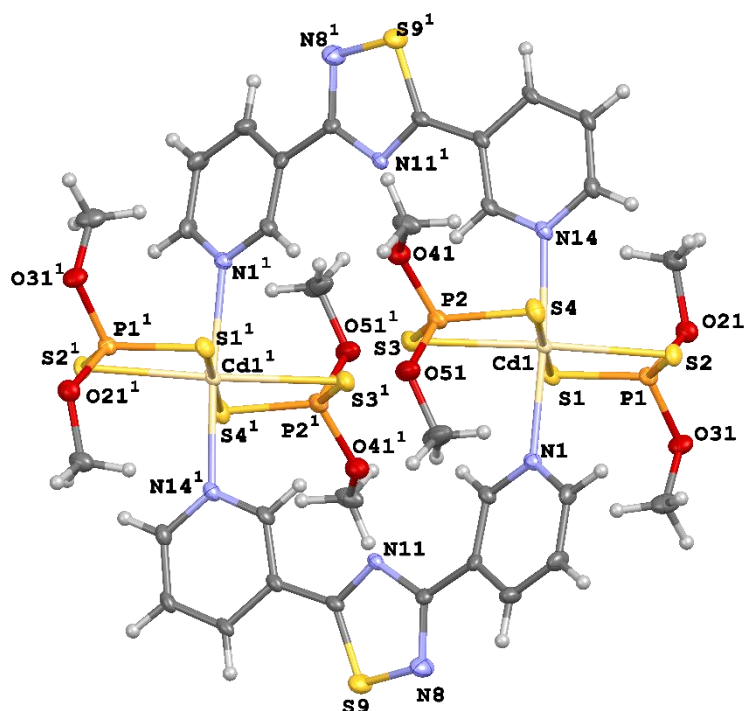


Figure 31 Structure and numbering scheme of the dimer **(1·L1)₂**; symmetry code: ¹ 1-x, -y, 1-z.

Cd–S distances range from 2.664 to 2.722 Å, whilst Cd–N distances are 2.372(3) and 2.386(2) Å, as summarized in Table 5. The inter-wheel Cd···Cd distance is 7.95 Å, resulting slightly longer with respect to what found for Zn···Zn in the dimeric structure of **[ZnL1(NO₃)₂·CH₃CN]₂**, but shorter if compared with Ag···Ag distances in **[AgL1(OTf)·((CH₃)₂CO)_{0.5}]_∞**, as expected due to the different cationic radii of the involved metal ions. The crystal packing of **(1·L1)₂** features dimers arrayed in regular-perforated layers assembled *via* N···H and S···H interactions (Figure 32). Similarly to what found in the Ni-based analogue **(1_{Ni}·L1)₂** previously reported,^[293] symmetry related parallel layers pack in an off-set compact arrangement along the *b* axis.

Table 5 Selected bond lengths (Å), bond and torsion angles (°) and angles between pyridyl ring mean planes (°) for (1·L1)₂ and (1·L2)_∞.

	(1·L1) ₂		(1·L2) _∞
Cd1-S1	2.6981(10)	Cd1-S1	2.6873(9)
Cd1-S2	2.6638(10)	Cd1-S2	2.7532(10)
Cd1-S3	2.7223(11)		
Cd1-S4	2.6836(10)		
Cd1-N1	2.386(2)	Cd1-N1	2.388(3)
Cd1-N14	2.372(3)		
P1-S1	1.9922(14)	P1-S1	1.9868(12)
P1-S2	1.9958(14)	P1-S2	1.9706(12)
P2-S3	1.9761(15)		
P2-S4	2.0020(16)		
N1-Cd1-S1	87.03(7)	N1-Cd1-S1	98.55(7)
N1-Cd1-S2	92.34(7)	N1-Cd1-S2	88.37(7)
N1-Cd1-S3	85.01(7)		
N1-Cd1-S4	94.99(7)		
N14-Cd1-S1	89.06(7)		
N14-Cd1-S2	91.69(7)		
N14-Cd1-S3	90.98(7)		
N14-Cd1-S4	88.90(7)		
N1-Cd1-N14	173.62(11)	N1-Cd1-N1 ¹	82.18(14)
S1-Cd1-S2	76.85(3)	S1-Cd1-S2	75.06(3)
S3-Cd1-S4	76.66(3)		
S1-P1-S2	114.29(6)	S1-P1-S2	113.76(5)
S3-P1-S4	114.87(6)		
C13-C10-C12-N11	168	C5-C7-C4-N2	169
C2-C3-C7-N11	21	Py1^Py2	140
Py1^Py2	20		

Symmetry code: ¹ x, 1+y, z

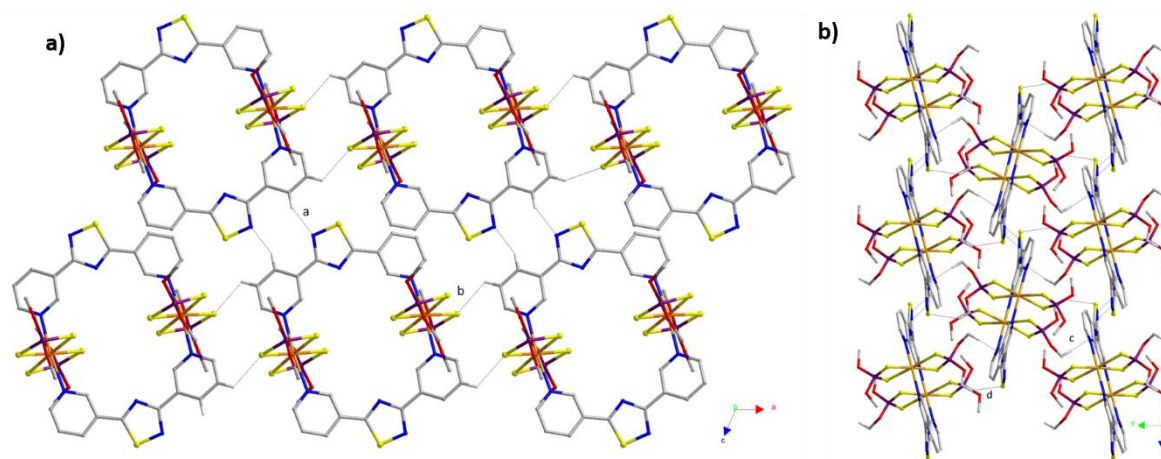


Figure 32 Packing views of $(\mathbf{1}\cdot\mathbf{L1})_2$ showing the (a) layers formed by interacting dimers along 010 and (b) intercalating layers along 100. All the hydrogen atoms with the exception of those involved in the showed interactions have been omitted. Interactions: **a**: $C4^1-H4^1\cdots N8$, 2.62, 3.153(5), 116; **b**: $C5^2-H5^2\cdots S2$, 3.01, 3.633(8), 120; **c**: $C42-H42a\cdots N11^3$, 2.42, 3.365(5), 164; **d**: $C52b^4-H52b^4\cdots S9$, 2.83 Å, 3.548(5) Å, 131°. Symmetry codes: ¹ 2-x, -y, 2-z; ² 2-x, -y, 1-z; ³ x, 0.5-y, -0.5+z; ⁴ x, 0.5-y, 0.5+z.

Solvothermal reaction between **1** and **L2** in a 1:1 mixture of MeOH/CHCl₃ produced a colourless crystalline solid in good yield (§5.2.24). The crystals were characterized by means of single-crystal XRD analysis showing a helicoidal coordination polymer with formula $(\mathbf{1}\cdot\mathbf{L2})_\infty$ crystallized in the orthorhombic space group *Pnna* with an asymmetric unit consisting of a single Cd(II) cation coordinated by two sulphur atoms of a dithiophosphato fragment and one nitrogen atom from half **L2** unit (structural data and refinement parameters in Table S125, bond lengths and angles in Table 5, Figure 33). Similarly to what observed for the crystal structures containing **L1**, $(\mathbf{1}\cdot\mathbf{L2})_\infty$ contains **L2** units arranged in two different but essentially superimposable orientations, which determine a positional disorder of the fragment N–S. This can be taken into account by considering a 180 ° rotation of the spacer passing through the midpoint of the N–S bond and through the remaining nitrogen atom of the thiadiazol functionality. Therefore, adjacent N and S atoms are found disordered over two positions with fractional occupancies of 50 %. The overall octahedral environment at the cadmium atoms is slightly distorted: main distances and angles are listed in Table 5. Cd–S distances are 2.7532(10) and 2.6873(9) Å are slightly longer with respect to the average value of 2.606 Å calculated for the structures of similar Cd complexes found in the CCDC, and the Cd–N distance is 2.388(3) Å, in line with those found in similar CPs.^[294]

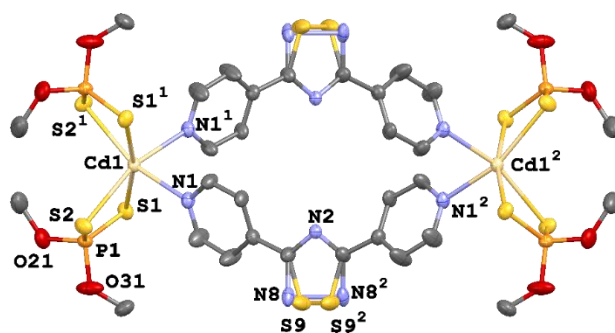


Figure 33 Perspective view along the propagation axis and numbering scheme of the helix $(\mathbf{1}\cdot\mathbf{L2})_\infty$; symmetry codes: ¹ $x, 3/2-y, 1/2-z$; ² $3/2-x, 2-y, z$.

The polymeric structure shaped by **L2** spacers, consists of infinite right-handed helices running along the [010] direction with a $\text{Cd}\cdots\text{Cd}^1$ pitch of 14.25 Å, equivalent to the b axis length. The metal-metal distance strongly resembles the $d_{\text{Ni}\cdots\text{Ni}}$ of 13.70 Å found in the analogue CP $(\mathbf{1Ni}\cdot\mathbf{L2})_\infty$,^[299] confirming the pivotal role of the spacer in determining the prime structure of CPs. However, the self-assembly along the Cd(II) ions occurs with **L2** units arranged in *cis* configuration with a $\text{N}-\text{Cd}-\text{N}^1$ bond angle of 82.18(14) °, whilst the analogue Ni(II) CP $(\mathbf{1Ni}\cdot\mathbf{L2})_\infty$, exhibits **L2** spacers *trans* disposed with an $\text{N}-\text{Ni}-\text{N}^1$ angle of 180.0 °. The different configuration around the metal ion is reflected in the different final shape of the resulting CPs: helicoidal for $(\mathbf{1}\cdot\mathbf{L2})_\infty$ and undulated for $(\mathbf{1Ni}\cdot\mathbf{L2})_\infty$ (Figure 34).

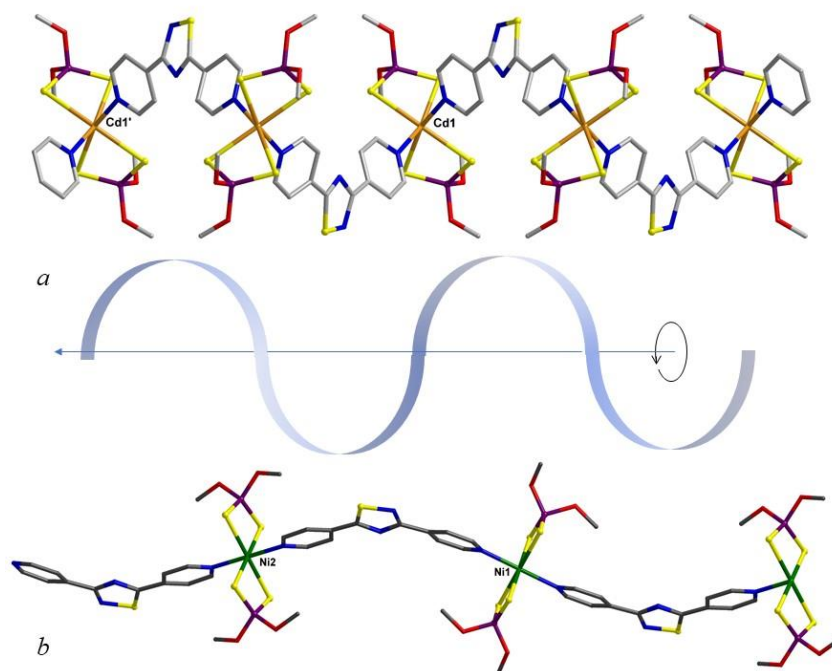


Figure 34 View along the crystallographic a axis of a polymeric helix $(\mathbf{1}\cdot\mathbf{L2})_\infty$ (a) and an undulated chain of the analogous $(\mathbf{1Ni}\cdot\mathbf{L2})_\infty$ (b). For clarity reasons, H-atoms are omitted, and only one orientation of the penta-atomic ring depicted. Symmetry code: ¹ $x, 1+y, z$.

The crystal packing in $(\mathbf{1}\cdot\mathbf{L2})_\infty$ shows helices running along [010] and [0-10] directions interacting in a 2D-layered network built up by C–H \cdots O bonds between OMe moieties (C32b–H32d \cdots O21¹ 2.52, 2.974(9) Å, 180 °; ¹ 0.5 + x, y, 1-z interaction **a** in Figure 35; and C–H \cdots S short contacts between pyridyl rings and coordinating sulphur atoms C6–H6 \cdots S1² 2.81, 3.489(4), 129 °, ² x, 1.5-y, 0.5-z interaction **b** in Figure 35.

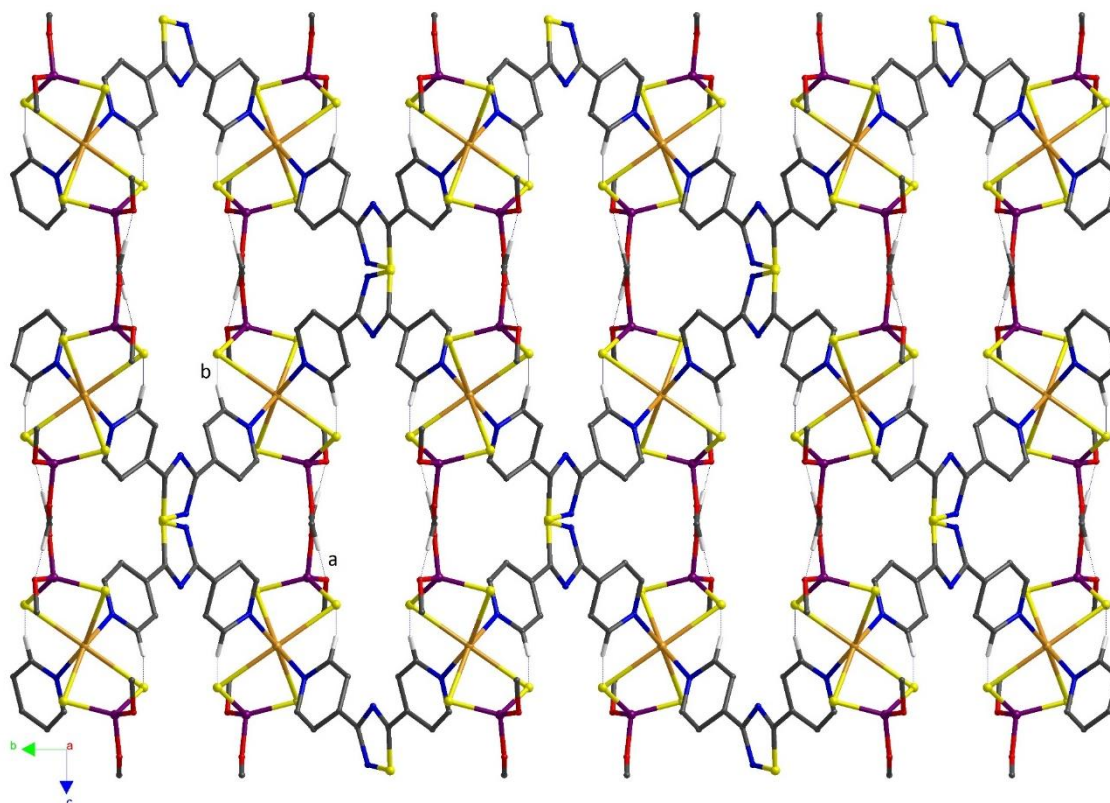


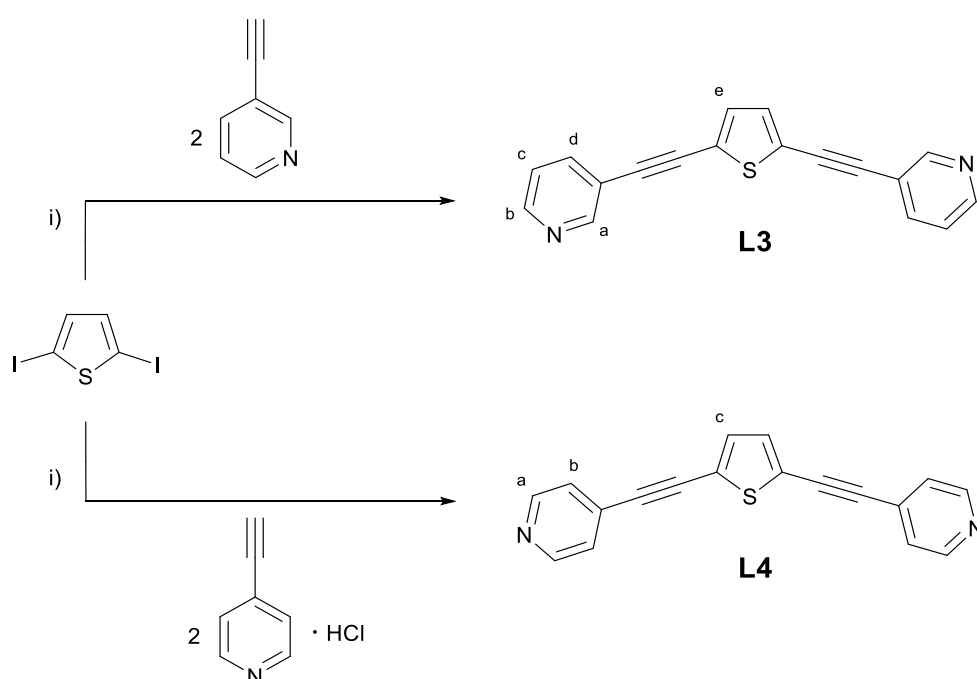
Figure 35 Packing view along the [100] crystallographic direction of helices $(\mathbf{1}\cdot\mathbf{L2})_\infty$ showing the interactions described in the discussion. For clarity, H-atoms not involved in the showed interactions are omitted and only one orientation of the penta-atomic ring depicted.

A comparison between the crystal packing of $(\mathbf{1}\cdot\mathbf{L2})_\infty$ and that of the analogous $(\mathbf{1}_{\text{Ni}}\cdot\mathbf{L2})_\infty$, show similar features, thus confirming that the overall packing for these type of CPs strongly depend on the nature of the P-substituents, as discussed in the case study of Ni(II) CPs.^[299]

3.1.1.2. Interaction between N-donors L3 and L4 with metal ions

Ligands 2,5-bis(pyridin-3-ylethynyl)thiophene (**L3**) and 2,5-bis(pyridin-4-ylethynyl)thiophene (**L4**) present structural features similar to those of ligands **L1** and **L2** with a central penta-atomic ring having two pyridyl substituents in positions 2 and 5. The differences reside in the length of the pyridyl arms, with mean N–thiophenyl centroid distances of 7.433(5) and 7.492(8)

Å for the orthorhombic and monoclinic polymorphs of **L3** and 8.117(2) Å for **L4** (refcode: LEDBAY). Not surprisingly, **L3** and **L4** differ also in the overall ligand lengths, with N1–N2 distances ranging from 13.228(2) to 14.885(7) Å for **L3** arranged along the three possible conformations, and a slightly longer distance of 15.807(3) Å, observed for **L4**. In contrast to **L1** and **L2**, the presence of triple carbon-carbon bonds in **L3** and **L4** confer some rigidity and result in interesting fluorescent properties of these last couple of ligands thanks to their highly conjugated skeleton. The dipyridyl linkers were prepared in one step by Sonogashira coupling reaction between 2,5-diiodothiophene and 3-ethynylpyridine or 4-ethynylpyridine hydrochloride and isolated in good yield (Scheme 16, see §5.2.3 and §5.2.4 for experimental details).



Scheme 16 Sonogashira coupling reactions for the preparation of ligand **L3** and **L4**. i) Pd(PPh₃)₂Cl₂, CuI, NHEt₂, N₂, reflux, 48 h.

The spacers **L3** and **L4** were characterized by elemental analysis, FT-IR, NMR. The FT-IR spectra shows a medium vibrational band at 2197 and 2206 cm⁻¹ for **L3** and **L4**, assigned to the alkyne stretching mode. ¹H NMR analysis recorded in DMSO-d₆ features signals in the range 8.79 - 7.47 and 8.65 – 7.54 ppm for **L3** and **L4**, respectively (Figure S7, Figure S10). According to the *meta*-substitution at the pyridyl rings, the spectrum of **L3** appears more complex than that of **L4**. Two doublets of doublets centred at 8.78 and 8.62 ppm can be assigned to the protons in 2 and 6 at the pyridyl rings, respectively (*a* and *b* in Scheme 16). The multiplet resonating in the range 8.06 - 7.98 ppm is attributed to the pyridyl's protons in 4 (*d* in Scheme 16), and that

centred at lower frequencies (7.51 – 7.47 ppm) to the overlap of thiophene moiety protons and pyridine residual ones (*c* and *e* in Scheme 16). The ^1H NMR spectrum of **L4** features a doublet of doublets centred at 8.65 ppm, assigned to protons *a* in Scheme 16. The signals for protons *b* and *c* of the same scheme are found overlapped into a multiplet enclosed in the region 7.58 – 7.52 ppm. $^{13}\text{C}\{^1\text{H}\}$ spectra were recorded in the same solvent (Figure S8, Figure S11) and signals resonating at 91.3 and 84.7 and 91.9 and 85.7 ppm are attributed to the *sp*-hybridized carbons of **L3** and **L4**, respectively. ^1H - ^1H COSY was used in the proton assignment of **L3** and is reported in Figure S9. The nature of the donor **L3** was also confirmed by means of TOF MS ES(+) spectrometry ($\text{M}+\text{H}^+$ $\text{C}_{18}\text{H}_{11}\text{N}_2\text{S}^+$ (m/z): calcd 287.0643; found 287.0651); the spectrum is given as supplementary material (Figure S107).

The electronic transitions of **L3** and **L4** were studied by means of UV-Vis spectrophotometry both in solution and in the solid state. The spectra recorded in chloroform, shown in Figure 36, display two absorption bands in the case of **L3** at 268 and 278 nm with ϵ values equal to 19416 and 19810 $\text{M}^{-1} \text{cm}^{-1}$, respectively. A very intense and asymmetric band is observed at 353 nm for both **L3** and **L4** ($\epsilon = 40971$ and 37823 $\text{M}^{-1} \text{cm}^{-1}$, respectively) along with a low energy band falling in the visible region of the spectrum in the case of **L3** ($\lambda_{\text{max}} = 460 \text{ nm}$; $\epsilon = 1463 \text{ M}^{-1} \text{cm}^{-1}$). An intense absorption was observed in the solid-state reflectance in the region 200 – 400 nm for both **L3** and **L4** (Figure 36). The luminescent emission properties of the N-donors were analysed both in solution (chloroform) and in the solid state.

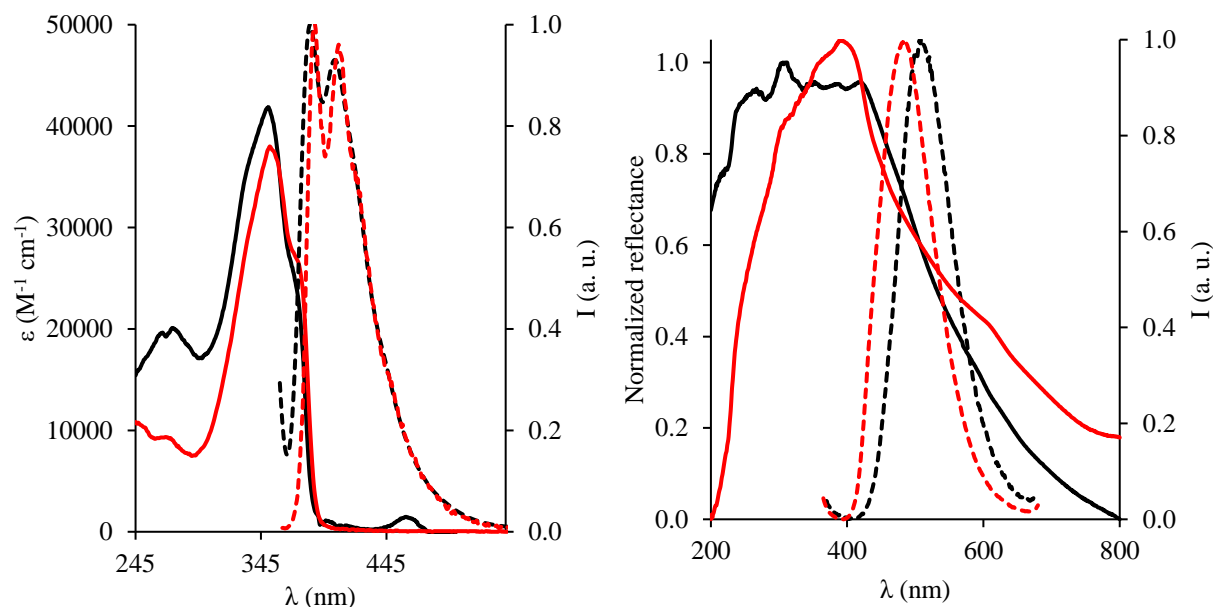


Figure 36 UV-Vis and Luminescent emission spectra ($C_{\text{L3-L4}} = 10^{-5} \text{ M}$; $\lambda_{\text{ex}} = 350 \text{ nm}$) of **L3** (black) and **L4** (red) in CHCl_3 depicted in solid and dashed line, respectively (left); Normalized diffuse reflectance and Luminescence emission spectra ($\lambda_{\text{ex}} = 350 \text{ nm}$) of **L3** (black) and **L4** (red) measured in the solid state depicted in solid and dashed line, respectively (right).

A nice profile is observed in solution with two emission maxima at 384 and 404 nm, and at 388 and 407 nm for **L3** and **L4**, respectively. The luminescent emission in the solid state is found centered at 508 and 483 nm, for **L3** and **L4**, respectively (Figure 36). **L3**, single crystals were grown by slow evaporation techniques as follows. Interestingly, **L3** crystallizes in two distinct orthorhombic and monoclinic polymorphs. Single crystals of the former were isolated by slow evaporation from CH₃CN; whilst single crystals of the latter were grown by slow evaporation of a 4:1 mixture CH₃CN/H₂O. The crystal data and refinement parameters for the two polymorphs are given in Table 6.

Table 6 Crystal data and refinement parameters for the two **L3** polymorphs.

Compound	L3_{Orthorhombic}	L3_{Monoclinic}
Formula	C ₁₈ H ₁₀ N ₂ S	C ₁₈ H ₁₀ N ₂ S
<i>D</i> _{calc.} / g cm ⁻³	1.356	1.331
μ /mm ⁻¹	1.980	1.943
Formula Weight	286.34	286.34
Colour	colourless	colourless
Shape	plate	block
Size/mm ³	0.15×0.08×0.02	0.17×0.17×0.17
<i>T</i> /K	100(2)	100(2)
Crystal System	orthorhombic	monoclinic
Space Group	<i>Pbcn</i>	<i>C2</i>
<i>a</i> /Å	34.6428(11)	29.8336(4)
<i>b</i> /Å	7.5712(2)	22.4772(3)
<i>c</i> /Å	10.6915(2)	21.5506(3)
α /°	90	90
β /°	90	98.6120(10)
γ /°	90	90
<i>V</i> /Å ³	2804.25(13)	14288.4(3)
<i>Z</i>	8	40
<i>Z'</i>	1	10
Wavelength/Å	1.54178	1.54178
Radiation type	CuK α	CuK α
θ _{min} /°	5.102	2.471
θ _{max} /°	136.47	68.246
Measured Refl's.	13192	64111
Indep't Refl's	2556	23377
Refl's $I \geq 2 \sigma(I)$	2277	20884
<i>R</i> _{int}	0.0589	0.0477
Parameters	190	1947
Restraints	0	62
Largest Peak	0.56	1.484
Deepest Hole	-0.56	-0.310
Goof	1.162	1.042
<i>wR</i> ₂ (all data)	0.1965	0.1558
<i>wR</i> ₂	0.1914	0.1510
<i>R</i> ₁ (all data)	0.0848	0.0653
<i>R</i> ₁	0.0767	0.0582

Note: the monoclinic polymorph was an inversion twin and appeared to be modulated.

Similarly to **L1**, the luminescent thiophene derivative **L3** can adopt three limit conformations, due to the *meta*-substituted pyridyl rings. The orthorhombic polymorph of **L3** crystallizes in the *Pbcn* space group with one molecule in the asymmetric unit.

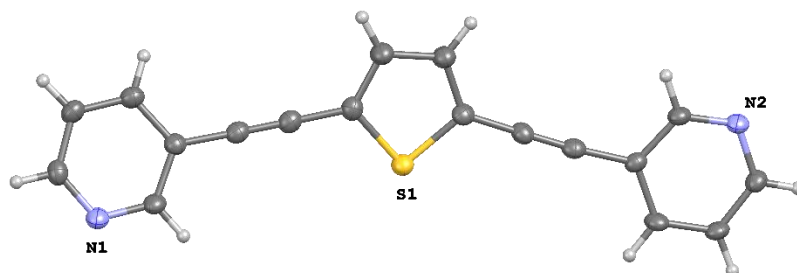


Figure 37 Representation of the asymmetric unit of **L3** (orthorhombic). Ellipsoids are drawn at 50 % probability level.

The spacer is arranged along its antiperiplanar configuration with N1–N2 distance of 14.530(4) Å. Pyridyl rings are almost coplanar with an angle of 172.0(1)°. However, the ligand features an overall bent geometry as evidenced by the angle of 155.1(3)° calculated between the centroids of both thiophenyl and pyridyl rings. **L3** molecules are involved in hydrogen bonding with adjacent molecules through intermolecular Ar–H···N interactions as showed in Figure 38.

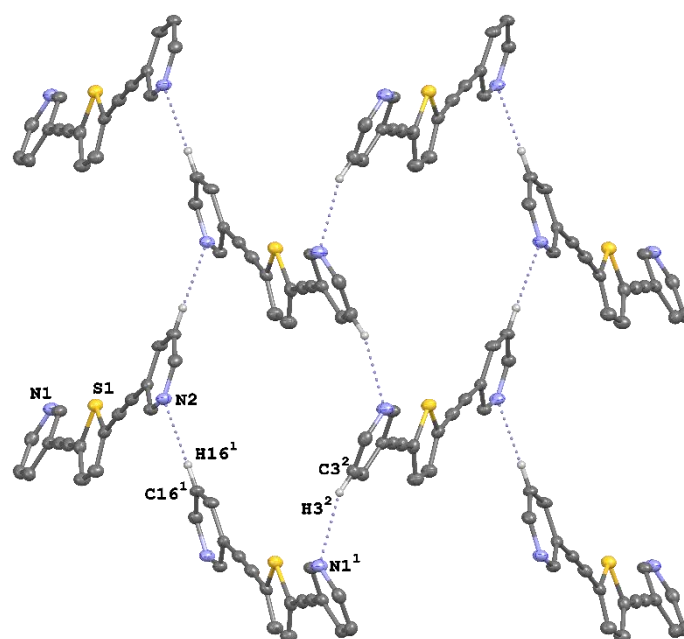


Figure 38 View along the [100] direction of the hydrogen bonding interactions in the orthorhombic polymorph of **L3**. C3²–H3²···N1¹ ($d_{D\cdots A} = 3.412(5)$ Å; $d_{H\cdots A} = 2.61(3)$ Å; $\alpha_{D-H\cdots A} = 142.9(2)$ °); C16¹–H16¹···N2 ($d_{D\cdots A} = 3.428(5)$ Å; $d_{H\cdots A} = 2.48(3)$ Å; $\alpha_{D-H\cdots A} = 172.8(2)$ °). Symmetry codes: ¹ 3/2-x, 1/2-y, 1/2+z; ² 3/2-x, -3/2+y, +z.

The interaction between four **L3** units gives rise to a 2D hydrogen-bonded network with openings of $8.2 \times 15.3 \text{ \AA}$ (Figure 39). Interestingly, the 2D-grid is not planar and is folded every two elements perpendicularly to the *c* axis as showed in Figure 39 (relevant distances and angles are reported in the figure caption). Figure 40 shows that every single net is interlaced by two more nets resulting in a 3-fold interpenetrated network, stabilized by inter-net hydrogen bonds between adjacent nets (interaction **a** in Figure 41).

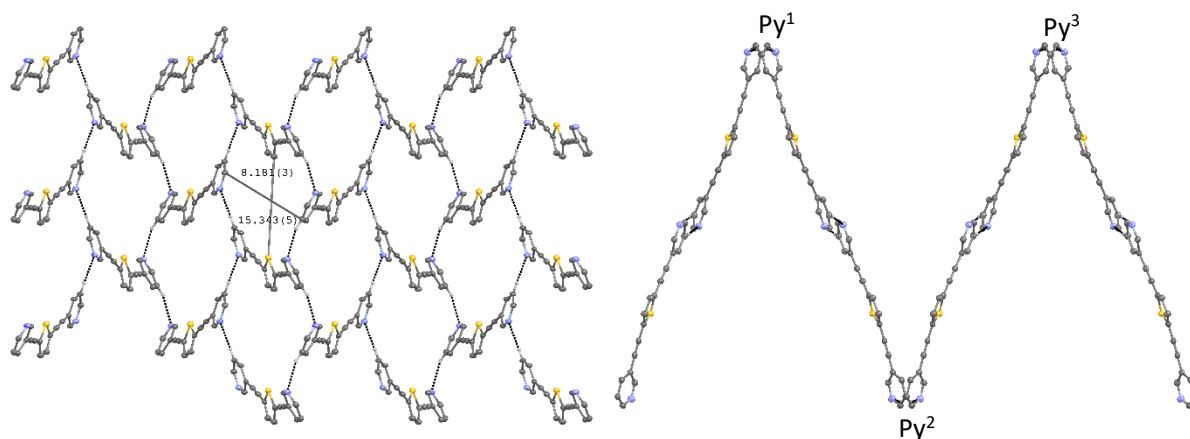


Figure 39 Views of the hydrogen-bonded folded grid found in **L3** (orthorhombic) along *a* (left) and *c* (right) axis, respectively. 2D-grid display openings of approximately $8.2 \times 15.3 \text{ \AA}$. $d_{Py^1-Py^2} = 27.75(2) \text{ \AA}$; $d_{Py^2-Py^3} = 28.68(2) \text{ \AA}$; $\alpha_{Py^1-Py^2-Py^3} = 46.6(2)^\circ$. Symmetry codes: ¹ $-1/2+x, -3/2-y, 1-z$; ² $-1/2+x, -1/2+y, 3/2-z$; ³ $1-x, -y, 1-z$.

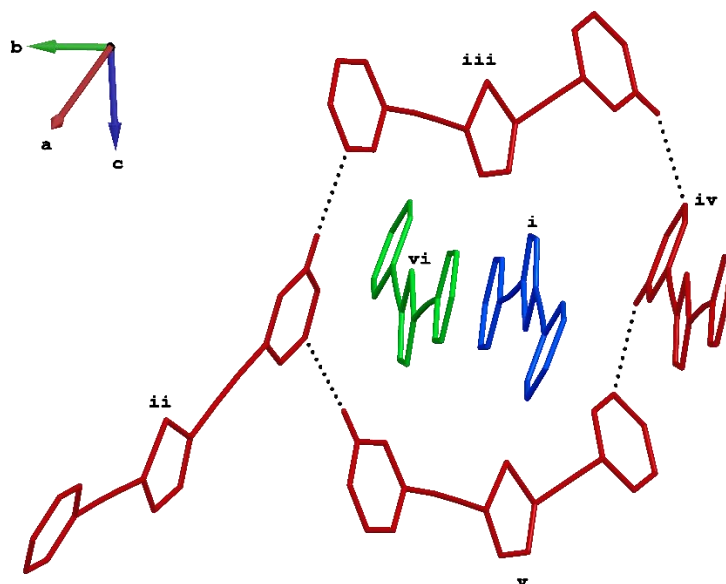


Figure 40 Capped sticks representation of the 3-fold interpenetrated network of **L3** (orthorhombic). **L3** molecules depicted in red represent an element of the grid that can accommodate two more grids represented as single **L3** units in green and blue for clarity reasons. Symmetry codes: ⁱ $1-x, -y, 1-z$; ⁱⁱ $3/2-x, -1/2+y, +z$; ⁱⁱⁱ $+x, -y, -1/2+z$; ^{iv} $+x, -2+y, +z$; ^v $+x, -y, 1/2+z$; ^{vi} $+x, -1+y, +z$.

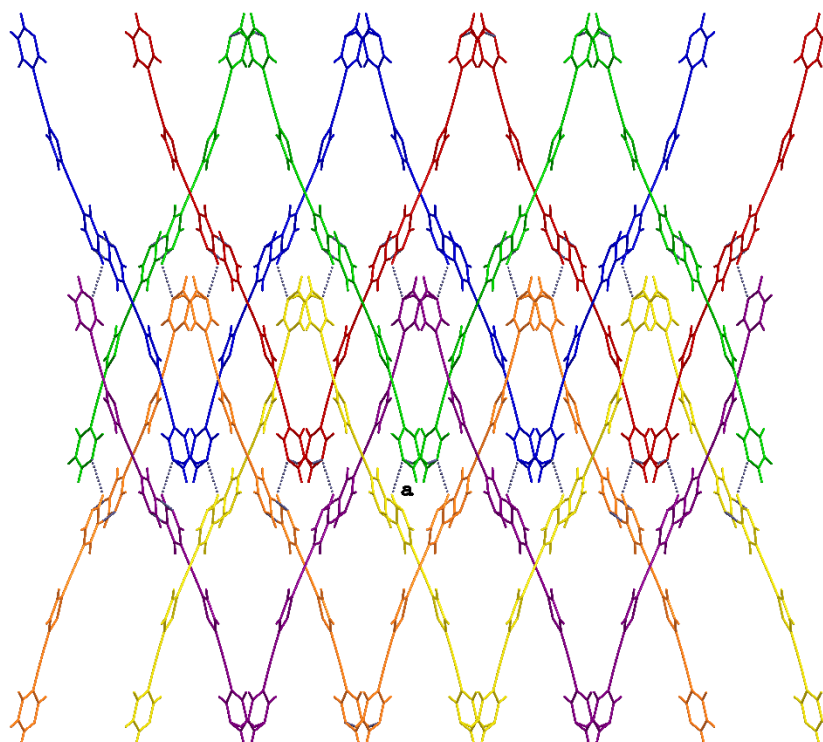


Figure 41 Packing diagram of the orthorhombic polymorph of **L3** along the *c* axis showing a 3-fold interpenetration of 2D-grids. Interaction **a**: C17–H17···N1¹ ($d_{D\cdots A} = 3.497(5) \text{ \AA}$; $d_{H\cdots A} = 2.681(3) \text{ \AA}$; $\alpha_{D-H\cdots A} = 144.4(2)^\circ$). Symmetry codes: ¹ $1/2+x, -1/2+y, 1/2-z$.

The monoclinic polymorph of **L3** crystallize in the non-centrosymmetric space group *C2* with ten crystallographically independent molecules in the asymmetric unit (Figure 42). The complex scenario aroused from the fact that all the screened crystals were twinned and appeared to be modulated. Therefore, we decided to collect the best dataset possible extending the collection strategy for overnight (see the high number of collected reflections in Table 6).

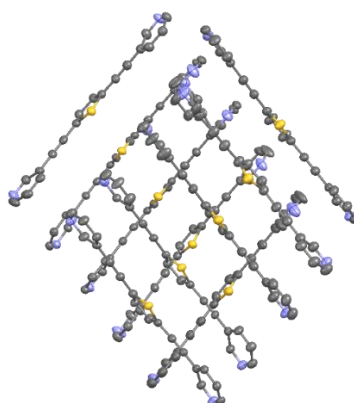


Figure 42 Representation of the asymmetric unit of **L3** (monoclinic) along the *c* axis. Ellipsoids are drawn at 50 % probability level.

L3 molecules are arranged in both the cisoid and transoid configuration with N1–N2 distances ranging from 14.854(7) – 14.920(8) and 14.379(8) – 14.543(7) Å for the former and the latter, respectively. **L3** exhibit some flexibility as suggested by the angle between pyridyl rings that ranges from 162.80(18) to 179.6(2) °. Moreover, the overall bent geometry of the linker features the Py1-Tph-Py2 angle in the range 148.64(7) - 151.42(5) °, similarly to what observed for the orthorhombic polymorph of **L3**. The crystal packing features **L3** molecules arranged into a modulated layered network along the [110] direction as shown in Figure 43.

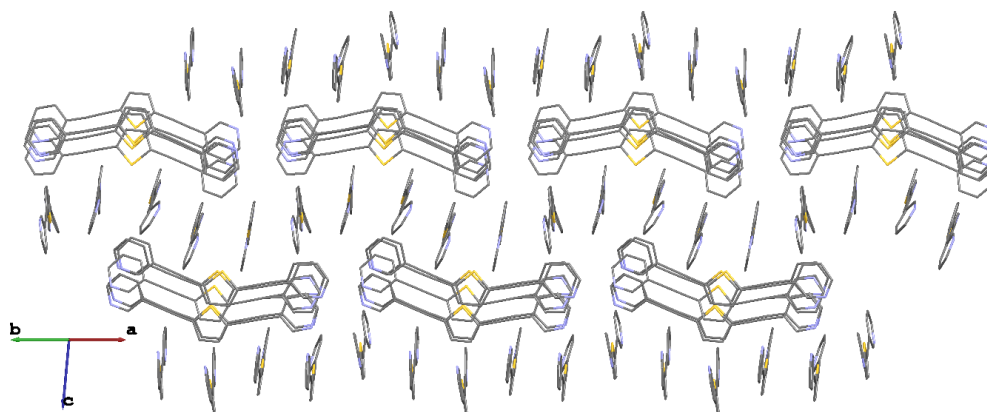


Figure 43 Capped sticks representation of the packing diagram for the modulated layered network along the [110] direction in the crystal structure of **L3** (monoclinic). Hydrogens are omitted for clarity.

Calculations at the density-functional (DFT)^[300] level of theory were carried out to investigate the electronic structure of ligand **L3** (see: experimental (§5) for computational details; appendix 4 for coordinates of optimized geometries). A scan of the potential energy surface (PES) was performed on ligand **L3** at different frozen angles of the pyridyl rings, showing a negligible rotational barrier (~ 1 kcal mol⁻¹) thus confirming a flexible nature for **L3** (Figure 44).

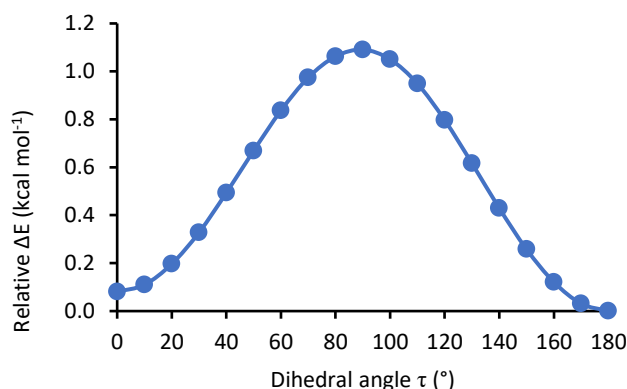


Figure 44 Relative total electronic energy variation (ΔE) calculated as a function of the pyridine ring rotation (τ) for **L3**.

As expected, the di-pyridyl ligand **L3** features a Kohn-Sham (KS) HOMO-3 and KS-HOMO-2 corresponding to the lone pair (LP) of electrons localized on the nitrogen atoms (Natural Bond Orbital (NBO) charges $Q_N = -0.481$ |e|; Figure 45),^[301] available to react with metal ions in the formation of coordination bonds.

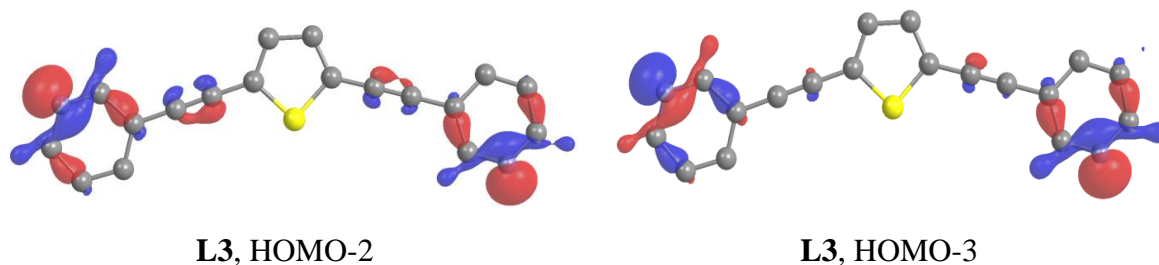


Figure 45 Isosurface drawings of selected frontier Kohn-Sham molecular orbitals calculated for **L3**. Hydrogen atoms were omitted for clarity. Cutoff value = 0.05 |e|.

In order to compare the reactivity of **L1** and **L3** towards silver(I) ions, the reaction between **L3** and AgOTf was performed in acetone and the instantaneous formation of a white solid observed (§5.2.25). Single-crystals suitable for XRD analysis were grown by layering a solution of silver(I) triflate in acetone over a dichloromethane solution of **L3** separated by a buffer of methanol (2 mL) and keeping the test tube in the dark for one week. Colorless crystals formed on the walls of the test tube and structurally characterized by means of single crystal XRD. The monoclinic lattice was solved in the centrosymmetric space group $P2/n$ featuring two crystallographically independent **L3** molecules in the asymmetric unit (structural data and refinement parameters in Table S126, bond lengths and angles in Table S127, Figure 46), belonging to a CP with formula $[\text{AgL3}(\text{OTf})((\text{CH}_3)_2\text{CO})_{2.5}]_{\infty}$.

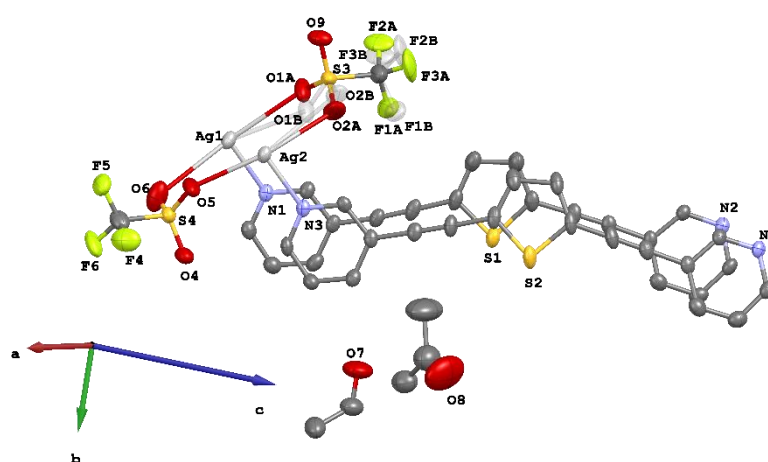


Figure 46 Perspective view of the asymmetric unit for $[\text{AgL3}(\text{OTf})((\text{CH}_3)_2\text{CO})_{2.5}]_{\infty}$.

Two and a half acetone molecules are found co-crystallized in the CP: one lies on a symmetry element and is half occupied and could be reliably included in the refinement along with a second one. The third solvent molecule featured incommensurate disorder and a solvent mask was applied in the refinement by means of PLATON/SQUEEZE routine. Both the independent **L3** units are slightly tilted with the two pyridyl rings angled of about 15.6 and 14.2 ° and arranged in a periplanar conformation. The geometrical features of **L3** molecules are very similar featuring: equal N–N distances of 14.826(5) Å for both N1–N2 and N3–N4; and pretty much the same Py–Tph–Py angles as summarized in Table 7. **L3** molecules bridge silver(I) ions forming positively charged 1D zig-zag chains with Ag···Ag distances of 17.70(4) and 17.69(4) Å for the two independent chains, longer to those found for $[\text{AgL1}(\text{OTf})\cdot((\text{CH}_3)_2\text{CO})_{0.5}]_\infty$ where the analogue distance was 8.21(4) Å as the result of the shorted pitch of the spacer. The Ag(I) ions are linearly coordinated by the **L3** ligands with angles of N1–Ag1–N2¹ 175.8(2) and N3–Ag2–N4¹ 169.2(2) °, and Ag–N distances ranging from 2.136(3) for Ag1–N1 to 2.174(3) Å for Ag1–N4¹, similar to those found for the analogous CP with **L1**. The relevant bond lengths and angles for $[\text{AgL3}(\text{OTf})\cdot((\text{CH}_3)_2\text{CO})_{2.5}]_\infty$ are summarized in Table 7.

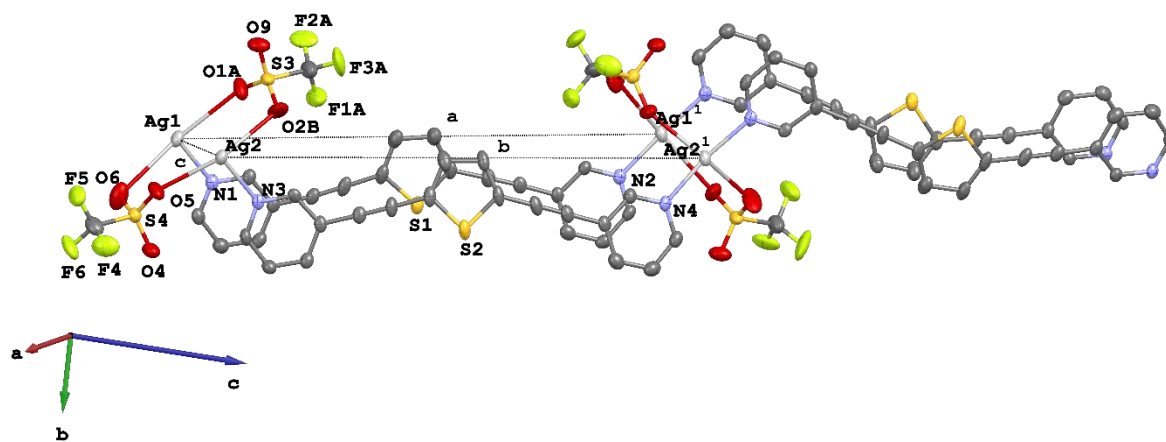


Figure 47 View of the zig-zag CP $[\text{AgL3}(\text{OTf})\cdot((\text{CH}_3)_2\text{CO})_{2.5}]_\infty$. Ag···Ag distances: (a) $d_{\text{Ag1}\dots\text{Ag1}^1} = 17.71(4)$ Å; (b) $d_{\text{Ag2}\dots\text{Ag2}^1} = 17.69(4)$ Å; (c) $d_{\text{Ag1}\dots\text{Ag2}} = 3.38(5)$ Å. Symmetry code: ¹ $-1/2+x,-y,1/2+z$. Disorder and hydrogen atoms are not shown for clarity.

Figure 47 highlights the presence of argentophilic interactions (labelled as (c)) between Ag1···Ag2 with distance 3.381(5) Å, similarly to what observed in the case of $[\text{AgL1}(\text{OTf})\cdot((\text{CH}_3)_2\text{CO})_{0.5}]_\infty$ (3.388(6) Å). The positive charge of the complex is counterbalanced by two chelating bridging triflate anions, one of which is disordered over two positions and was modelled using RIGU and SADI restraints. The displacement ellipsoids of

disordered fluorine fragments were constrained using EADP. The interaction between triflates and silver cations features Ag–O distances ranging from 2.636(3) to 3.09(4) Å, resulting in a pseudo square planar final coordination geometry around the Ag⁺ cations (Figure 48). Bond lengths and angles are listed in Table 7 and Table S127.

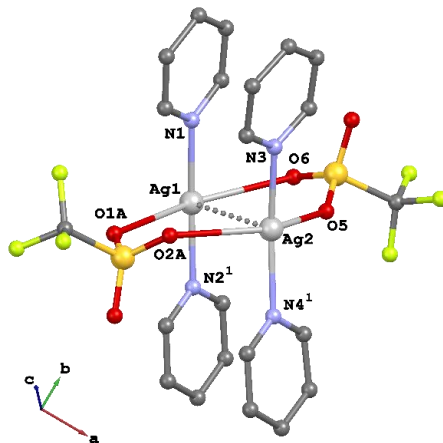


Figure 48 Schematic representation of the coordination environment around silver(I) nodes in $[\text{AgL3}(\text{OTf})((\text{CH}_3)_2\text{CO})_{2.5}]_\infty$. **L3** molecules are depicted as single pyridyl rings, disorder, H atoms and solvent molecules have been omitted for the sake of clarity. Symmetry code: $^1 1/2+x, -y, -1/2+z$.

Table 7 Selected bond lengths (Å), and angles (°) for $[\text{AgL3}(\text{OTf})((\text{CH}_3)_2\text{CO})_{2.5}]_\infty$.

Ag1–O1A	2.895(4)	N3–Ag2–O2A	92.3(8)
Ag1–O1B	2.843(14)	N3–Ag2–O2B	83.59(16)
Ag1–N1	2.136(3)	N3–Ag2–N4 ¹	169.18(12)
Ag1–N2 ¹	2.142(3)	N3–Ag2–O5	99.79(12)
Ag1–O6	3.005(5)	N4 ¹ –Ag2–O2A	84.5(8)
Ag2–O2A	3.09(4)	N4 ¹ –Ag2–O2B	94.57(17)
Ag2–O2B	2.822(6)	N4 ¹ –Ag2–O5	87.17(12)
Ag2–N3	2.165(3)	O5–Ag2–O2A	154.8(5)
Ag2–N4 ¹	2.172(3)	O5–Ag2–O2B	149.91(19)
Ag2–O5	2.636(3)	Py1 ¹ Py2	172.36(13)
O1A–Ag1–O6	164.79(15)	Py3 ³ Py4	169.35(13)
O1B–Ag1–O6	144.9(8)	Py1 ¹ Tph1 ¹ Py2	152.47(4)
N1–Ag1–O1A	89.36(14)	Py3 ³ Tph2 ² Py4	152.38(4)
N1–Ag1–O1B	80.5(5)		
N1–Ag1–N2 ¹	175.84(12)		
N1–Ag1–O6	89.68(12)		
N2 ¹ –Ag1–O1A	88.26(13)		
N2 ¹ –Ag1–O1B	96.1(5)		
N2 ¹ –Ag1–O6	91.72(12)		

Symmetry codes: $^1 1/2+x, -y, -1/2+z$; Py1 = N1–C1–C2–C3–C4–C5; Py2 = N2–C14–C15–C16–C17–C18; Py3 = N3–C19–C20–C21–C22–C23; Py4 = N4–C32–C33–C34–C35–C36; Tph1 = S1–C8–C9–C10–C11; Tph2 = S2–C26–C27–C28–C29.

Adjacent chains interact through intermolecular π - π interactions between pyridyl and thiophene rings featuring centroid-centroid distances ranging from 3.597(2) to 3.831(2) Å as showed in Figure 49.

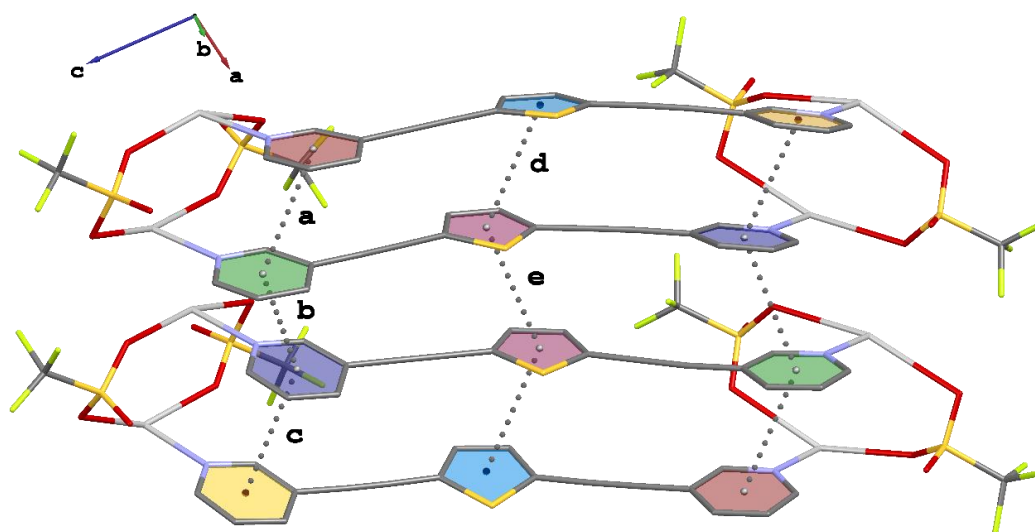


Figure 49 Intermolecular π - π interactions in the crystal structure of $[\text{AgL3}(\text{OTf})((\text{CH}_3)_2\text{CO})_{2.5}]_\infty$: (a) Py1-Py3 ($d = 3.640(2)$ Å; $\alpha = 172.75(14)^\circ$); (b) Py1¹-Py2 ($d = 3.722(2)$ Å; $\alpha = 168.83(14)^\circ$); (c) Py2-Py4 ($d = 3.597(2)$ Å; $\alpha = 176.12(13)^\circ$); (d) Tph1¹-Tph2 ($d = 3.831(4)$ Å; $\alpha = 176.1(2)^\circ$); (e) Tph1- Tph1¹ ($d = 3.653(2)$ Å; $\alpha = 168.67(14)^\circ$). Symmetry code: ¹ $1/2-x; +y; 3/2-z$.

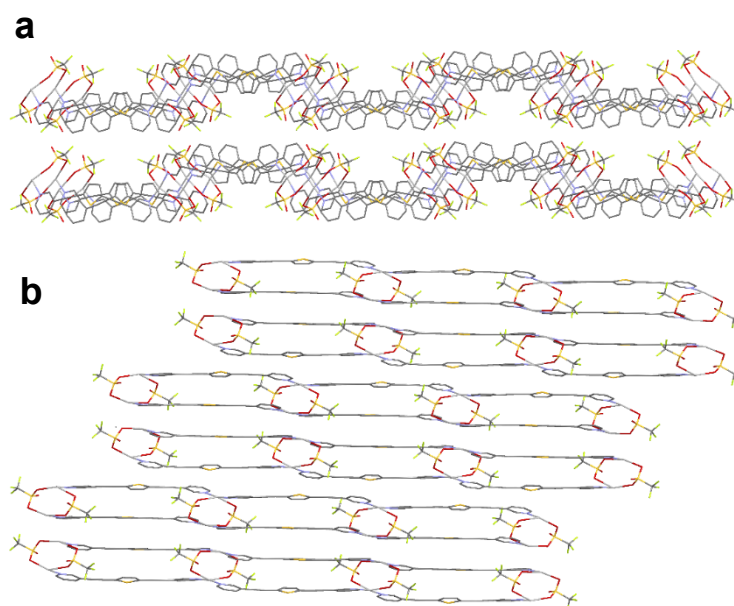


Figure 50 Packing diagrams for $[\text{AgL3}(\text{OTf})((\text{CH}_3)_2\text{CO})_{2.5}]_\infty$ along a and b axis in a) and b), respectively. Disorder, H atoms and solvent molecules are not shown for clarity.

The crystal packing consists of a 2D-layered structure along the *b* axis featuring intermolecular π - π interactions (Figure 50). Moreover, solvent molecules are arranged into channels developing along the *a* vector (Figure 50).

The study of the reactivity of **L3** with bivalent cations were performed starting from different metal nitrates, but only the reactions with $\text{Cd}(\text{NO}_3)_2 \cdot 4\text{H}_2\text{O}$ and $\text{Cu}(\text{NO}_3)_2 \cdot 2.5\text{H}_2\text{O}$ yielded crystalline products and will be here discussed.

L3 was reacted with $\text{Cd}(\text{NO}_3)_2 \cdot 4\text{H}_2\text{O}$ in a 4:1 mixture of $\text{CH}_3\text{CN}:\text{H}_2\text{O}$ and a yellowish clear solution formed (§5.2.26). Single crystals suitable for XRD analysis of the resulting $[\text{CdL3}(\text{NO}_3)_2(\text{H}_2\text{O})_2 \cdot 1.5\text{H}_2\text{O}]_\infty$ CP were obtained by slow evaporation of the solvents. The orthorhombic crystal system was solved in the centrosymmetric space group *Pccn* (structural data refinement in Table S128, bond lengths and angles in Table S129) and the asymmetric unit consisting in one **L3** unit connected to an hepta-coordinated Cd(II) ion is shown in Figure 51.

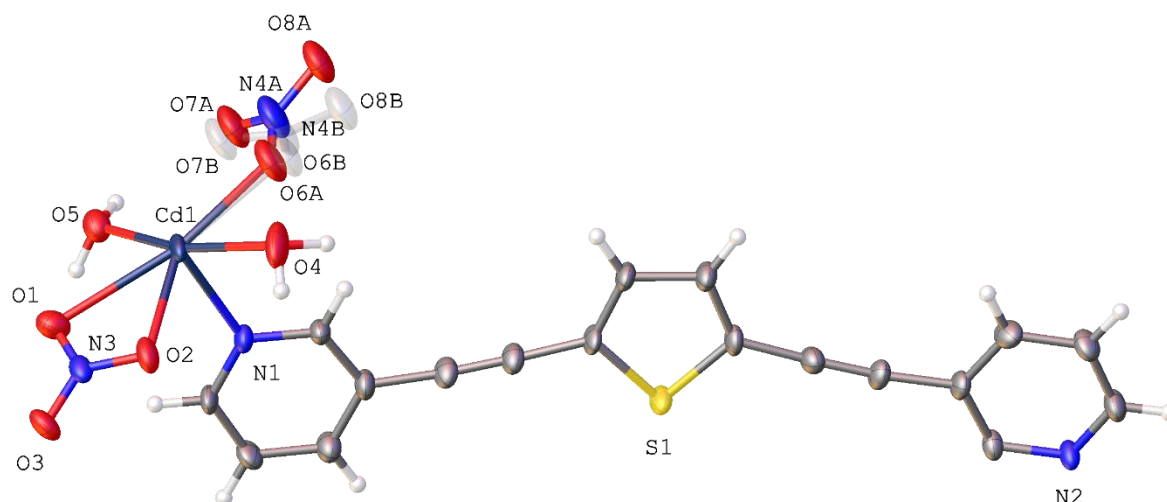


Figure 51 Asymmetric unit for the crystal structure of $[\text{CdL3}(\text{NO}_3)_2(\text{H}_2\text{O})_2 \cdot 1.5\text{H}_2\text{O}]_\infty$. Displacement ellipsoids are drawn at 50 % probability level.

L3 units are almost planar with the two pyridyl rings angled of about 10° and arranged in an antiperiplanar conformation. Cadmium nodes show a distorted pentagonal bipyramidal coordination geometry with the two N-atoms from bridging **L3** ligands occupying the axial positions. The equatorial positions are occupied by two water molecules, a bidentate nitrate and a second nitrate unit coordinating the cadmium center in a monodentate fashion (Figure 51).

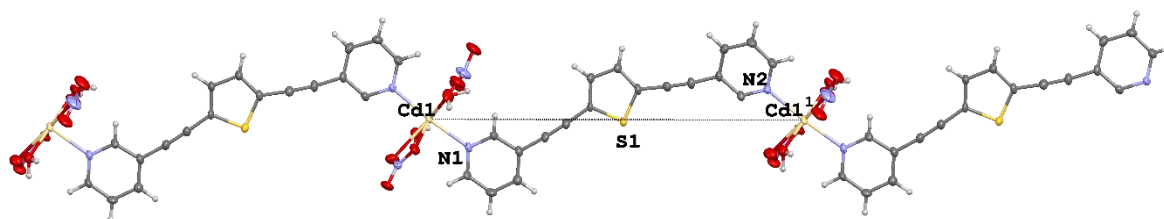


Figure 52 View of the polymeric chain of $[\text{CdL3}(\text{NO}_3)_2(\text{H}_2\text{O})_2 \cdot 1.5\text{H}_2\text{O}]_\infty$ along the c axis. Disorder at nitrile functionalities is not shown for clarity. Symmetry code: $^1 \frac{1}{2}+x, -\frac{1}{2}+y, -z$.

The monodentate nitrate fragment is disordered over two positions with fractional occupancy of approximately 50 %, and was modelled using SIMU, RIGU, SADI, FLAT restraints. Moreover, disordered 1.5 H_2O molecules per unit cell were found and have been masked using PLATON/SQUEEZE routine. Cd–O distances range from 2.316(5) to 2.571(5) Å, in line with the mean value of 2.4(1) calculated for structures containing a generic Cd– NO_3 fragment deposited in the CCDC. Cd–N distances are 2.285(4) and 2.271(4) Å for Cd1–N1 and Cd1–N2¹, respectively ($^1 \frac{1}{2}+x, \frac{1}{2}+y, -z$), slightly shorter than those found in $(\mathbf{1} \cdot \mathbf{L1})_\infty$ and $(\mathbf{1} \cdot \mathbf{L2})_\infty$. **L3** units bridge cadmium nodes in undulated polymeric chains propagated along the a axis with Cd \cdots Cd distances of 17.93(4) Å, very similar to the Ag \cdots Ag mean distance of 17.70 Å observed in $[\text{AgL3}(\text{OTf})((\text{CH}_3)_2\text{CO})_{2.5}]_\infty$, notwithstanding the different ligand conformation (Figure 51). The packing is governed by H-bondings involving the nitrate anions and water molecules, and π - π interactions between pyridyl and thiophene rings of **L3**. Figure 53 shows three main intermolecular π - π interactions packing the chains along [100] and [001] directions.

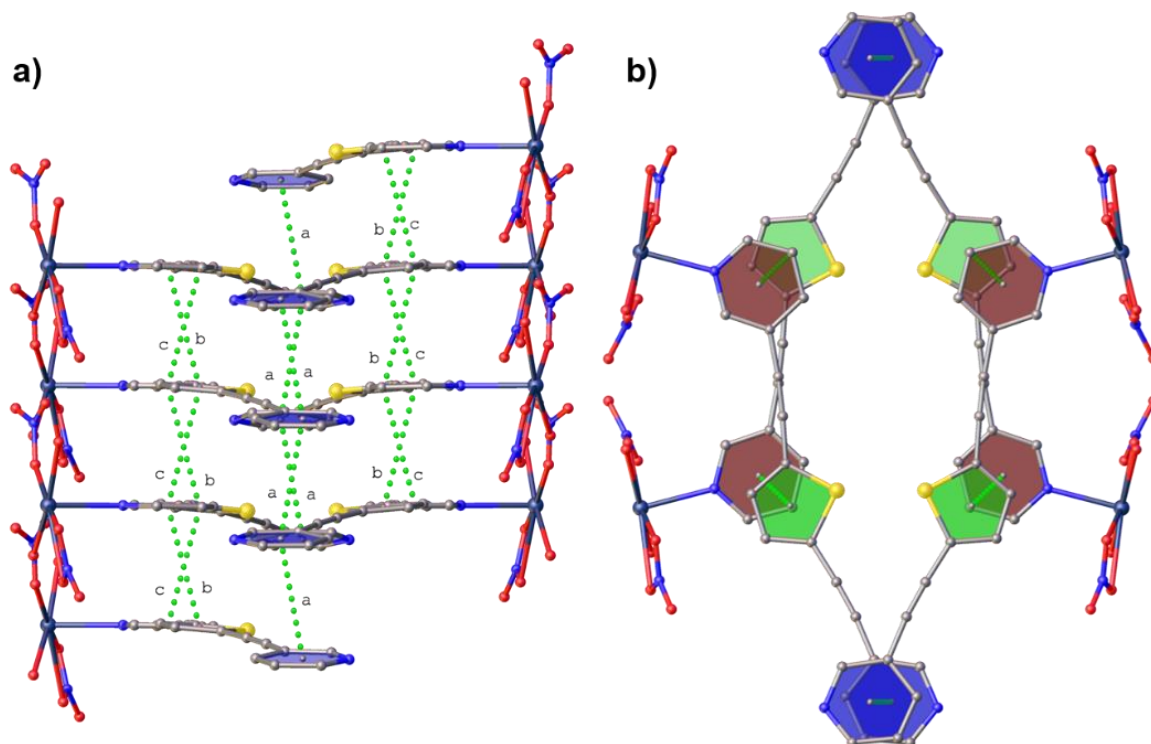


Figure 53 Packing views along [100] (a) and [001] (b) of $[\text{CdL3}(\text{NO}_3)_2(\text{H}_2\text{O})_2 \cdot 1.5\text{H}_2\text{O}]_\infty$ evidencing π - π interactions between pyridyl and Tph rings depicted in dashed green lines. Py1 ring is depicted in brick red, Py2 ring is depicted in blue, and Tph ring is depicted in green. Interactions **a**: Py2-Py2¹ (centroid-centroid distance = 3.596(9) Å; $\alpha = 0.7(3)^\circ$); **b**: Tph-Py1² (centroid-centroid distance = 3.821(4) Å; $\alpha = 4.2(2)^\circ$); **c**: Py1-Tph² (centroid-centroid distance = 3.719(4) Å; $\alpha = 4.2(2)^\circ$). Disorder and H-atoms have been omitted for clarity. Symmetry codes: ¹ $+x, 3/2-y, 1/2+z$; ² $1/2-x, +y, 1/2+z$.

Figure 54 shows the main interactions involving water molecules and adjacent nitrate anions.

Table 8 Hydrogen bonding interactions in $[\text{CdL3}(\text{NO}_3)_2(\text{H}_2\text{O})_2 \cdot 1.5\text{H}_2\text{O}]_\infty$.

	D	H	A	d_{D...A} (Å)	d_{H...A} (Å)	D-H...A (°)
a	O4	H4A	O8A ²	2.878(6)	2.198(6)	128.3(3)
b	O4	H4A	O8B ²	2.775(5)	1.882(6)	157.4(3)
c	O4	H4B	O7A ¹	2.633(7)	1.743(2)	156.7(3)
d	O4	H4B	O7B ¹	2.828(7)	1.931(2)	158.8(3)
e	O5 ³	H5B ³	O2	2.963(7)	2.036(5)	150.6 (3)
f	O5 ¹	H5A ¹	O3	2.868(6)	1.977(4)	171.2(3)

Symmetry codes: ¹ $-x, 2-y, -z$; ² $+x, +y, 1+z$; ³ $-x, 2-y, 1-z$.

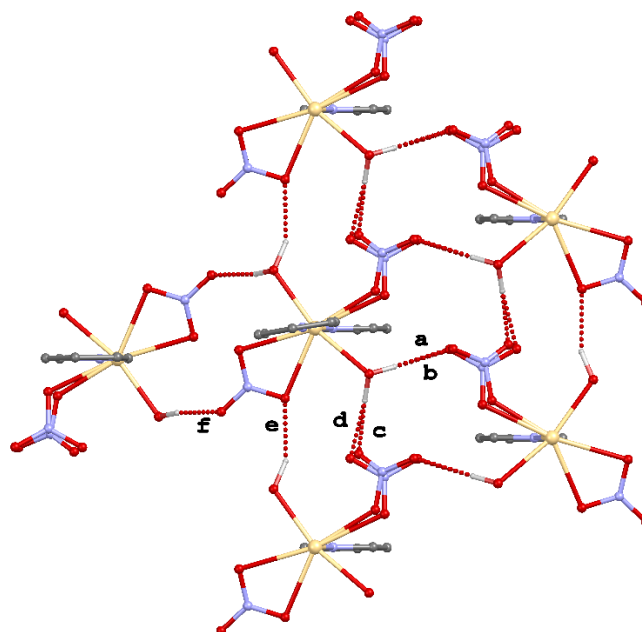


Figure 54 Hydrogen-bonded network in the crystal structure of $[\text{CdL3}(\text{NO}_3)_2(\text{H}_2\text{O})_2 \cdot 1.5\text{H}_2\text{O}]_\infty$ along the b axis. Interactions are labelled according to Table 8.

The overall crystal packing evidences as the polymeric chains pack in order to maximize the hydrophilic and hydrophobic interactions creating a 3D-network where perforated layers are formed, with two solvent-accessible channels present in the structure (Figure 55).

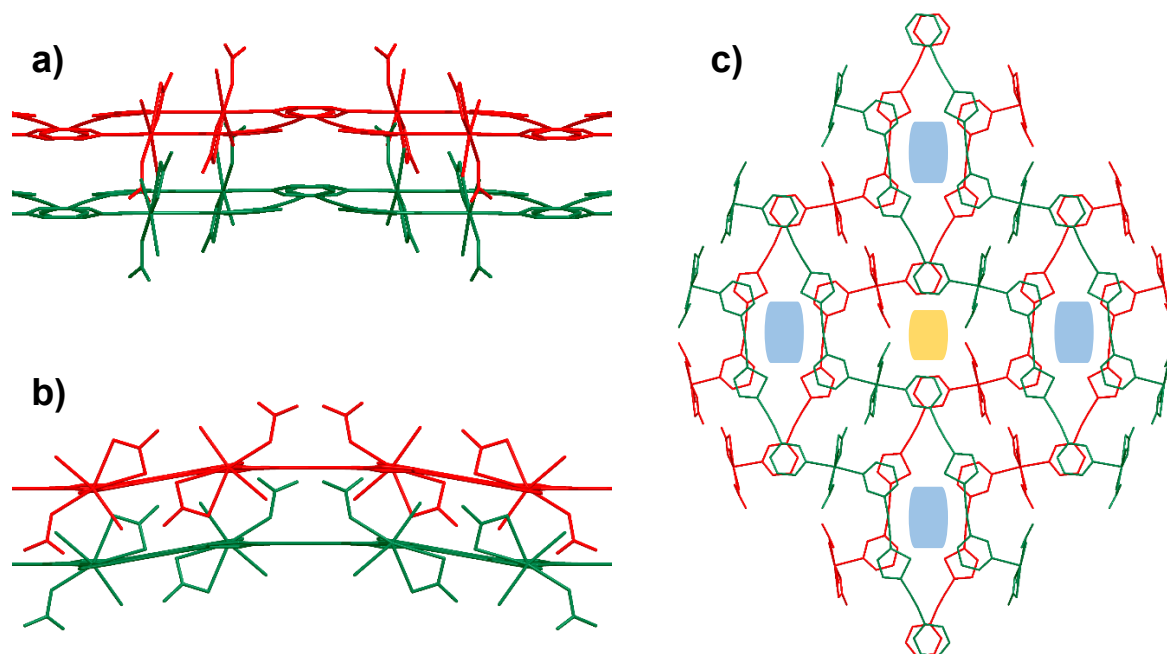


Figure 55 Packing diagrams of $[\text{CdL3}(\text{NO}_3)_2(\text{H}_2\text{O})_2 \cdot 1.5\text{H}_2\text{O}]_\infty$ along the a , b and c axis, in a), b) and c), respectively. Adjacent layers are depicted in red and green. Light blue and gold boxes in c) represent the solvent-accessible voids present in the crystal structure.

The reaction of **L3** with $\text{Cu}(\text{NO}_3)_2 \cdot 2.5\text{H}_2\text{O}$ in 4:1 mixture of a $\text{CH}_3\text{CN}/\text{H}_2\text{O}$ produced a clear green solution (§5.2.27) from which single crystals of the product were obtained by slow evaporation within 24 h. Single crystal XRD revealed the formation of a discrete supramolecular assembly (Figure 56) with formula $[\text{CuL3}(\text{NO}_3)_2 \cdot \text{CH}_3\text{CN}]_2 \cdot 2\text{CH}_3\text{CN}$ crystallized in the triclinic space group $P-1$ (structural data refinement parameters in Table S130, bond lengths and angles in Table S131).

L3 units are almost planar with the two pyridyl rings angled of about 12° and arranged in a periplanar conformation. Alike the previously discussed case of $[\text{ZnL1}(\text{NO}_3)_2 \cdot \text{CH}_3\text{CN}]_2$ dimer, a couple of **L3** ligands bridges a couple of copper ions in a dimeric paddle wheel arrangement with $\text{Cu} \cdots \text{Cu}$ distance of 13.80 \AA quite longer than that found for the Zn dimer of **L1** of 7.81 \AA , as expected (Figure 56). The copper nodes are *penta*-coordinated by two monodentate nitrate anions, one of which, results disordered over two positions with fractional occupancy close to 50 % and $\text{Cu}-\text{O}$ distances of 2.004 \AA . The disordered fragment was modelled by means of SADI and FLAT restraints. The third equatorial position is filled by an acetonitrile molecule with $\text{Cu}-\text{N}$ distance of $2.257(2) \text{ \AA}$. The axial positions are occupied by pyridyl rings featuring shorter $\text{Cu}-\text{N}$ distances of $2.006(2)$ and $2.010(2) \text{ \AA}$ for $\text{Cu1}-\text{N1}$ and $\text{Cu1}-\text{N2}^1$, respectively with $\text{N1}-\text{Cu1}-\text{N2}^1 = 162.19(6)^\circ$ (Symmetry code: $^1 2-x, 1-y, 1-z$)

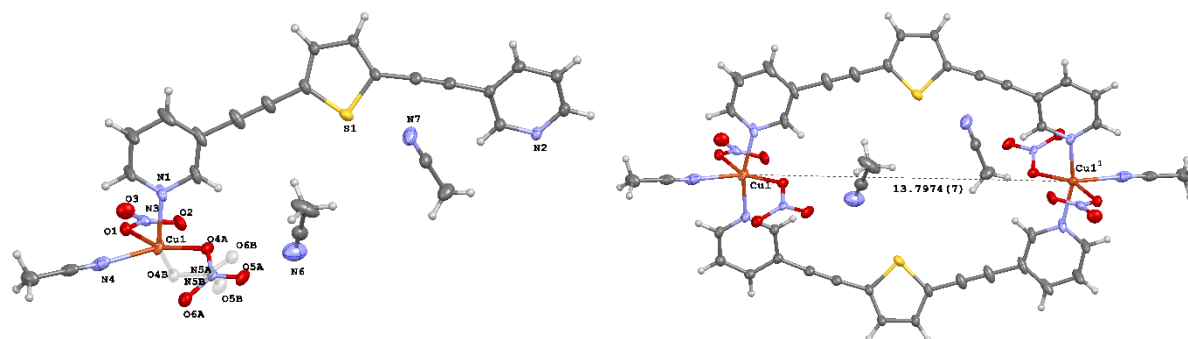


Figure 56 Perspective views of the asymmetric unit (left) and the paddle wheel arrangement (right) for $[\text{CuL3}(\text{NO}_3)_2 \cdot \text{CH}_3\text{CN}]_2 \cdot 2\text{CH}_3\text{CN}$. Displacement ellipsoids are drawn at 50 % probability level. Symmetry code: $^1 2-x, 1-y, 1-z$.

The $[\text{CuL3}(\text{NO}_3)_2 \cdot \text{CH}_3\text{CN}]_2 \cdot 2\text{CH}_3\text{CN}$ dimeric units pack staggered along the a axis, slightly slipped along the c vector, interacting through intermolecular hydrogen bonds between the thiophene ring hydrogen atoms, nitrate anions and the co-crystallized acetonitrile molecules (Figure 57). The $\text{D} \cdots \text{A}$, $\text{H} \cdots \text{A}$ distances and angles are summarized in Table 9 and shown in Figure 57. The crystal packing is shown in Figure 58.

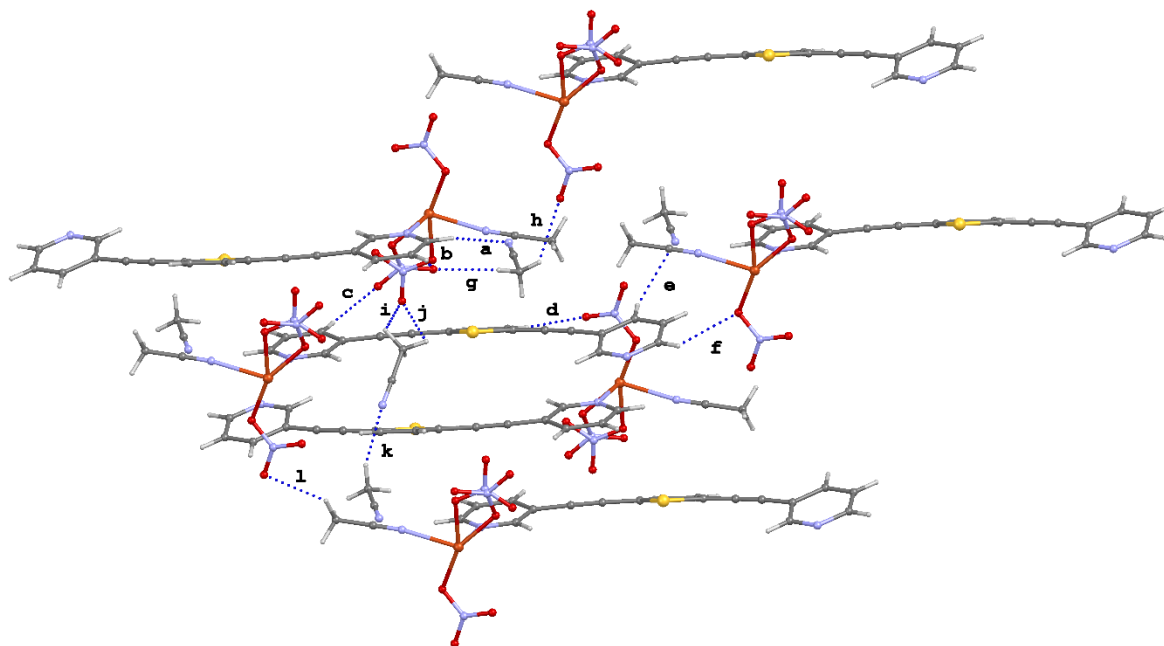


Figure 57 View along the *a* axis of the hydrogen bonding interactions found in $[\text{CuL3}(\text{NO}_3)_2 \cdot \text{CH}_3\text{CN}]_2 \cdot 2\text{CH}_3\text{CN}$. Only hydrogens involved in H-bonds are shown for clarity. H-bonds are depicted in dashed blue lines.

Table 9 Hydrogen bonding interactions in $[\text{CuL3}(\text{NO}_3)_2 \cdot \text{CH}_3\text{CN}]_2 \cdot 2\text{CH}_3\text{CN}$. $\text{D} \cdots \text{A}$ distances (\AA) and $\text{D}-\text{H} \cdots \text{A}$ angles ($^\circ$). Symmetry code: $^1 +x, -1+y, +z$.

#	D	H	A	$d_{\text{D} \cdots \text{A}}$ (\AA)	$d_{\text{H} \cdots \text{A}}$ (\AA)	$\text{D}-\text{H} \cdots \text{A}$ ($^\circ$)
a	C2 ¹	H2 ¹	N7	3.324(2)	2.4972(17)	145.54(12)
b	C3	H3	O6A	3.271(4)	2.413(3)	150.11(17)
c	C4	H4	O5A ¹	3.361(4)	2.495(3)	151.58(14)
d	C10	H10	O2 ¹	3.239(3)	2.37(3)	155(2)
e	C15	H15	N7 ¹	3.314(3)	2.22(2)	120.50(10)
f	C17	H17	O1 ¹	3.260(2)	2.6012(11)	126.78(11)
g	C24	H24A	O6A ¹	3.341(4)	2.48(3)	150(3)
h	C24	H24B	O3 ¹	3.218(3)	2.56(3)	131(2)
i	C22	H22A	O5B ¹	2.861(4)	2.428(3)	96.2(2)
j	C22	H22C	O5B ¹	2.861(4)	2.584(3)	106.3(2)
k	C24 ¹	H24C ¹	N6	3.318(3)	2.45(3)	161(4)
l	C20 ¹	H20A ¹	O3	3.292(3)	2.5450(15)	133.01(13)

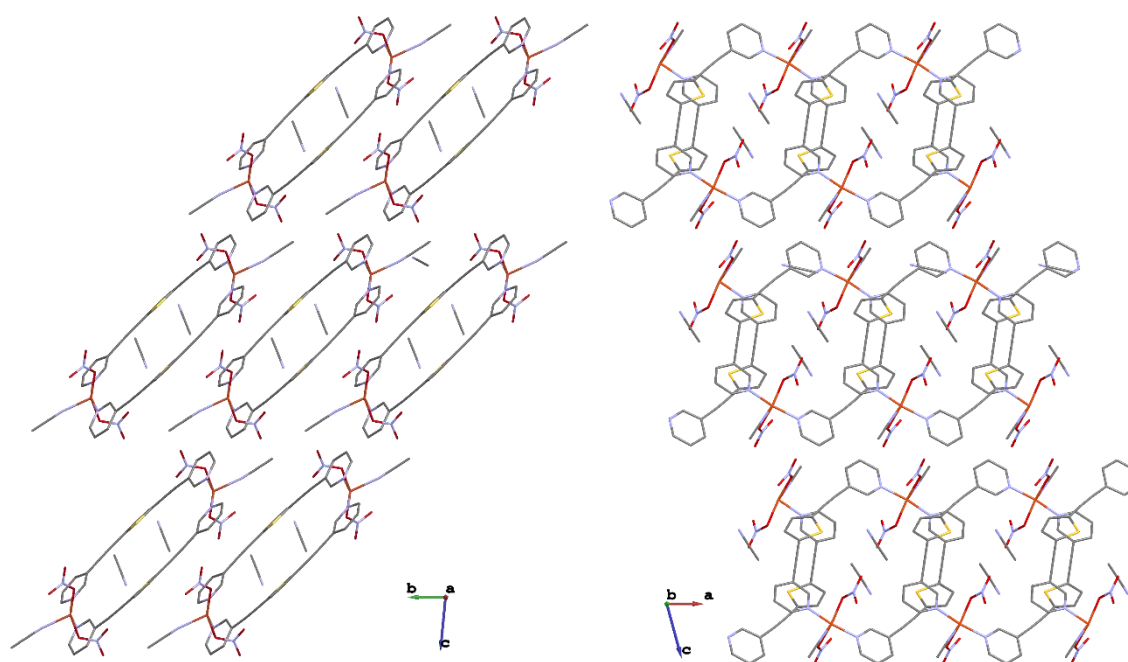


Figure 58 Packing diagrams of $[\text{CuL3}(\text{NO}_3)_2 \cdot \text{CH}_3\text{CN}]_2 \cdot 2\text{CH}_3\text{CN}$ along the a (left) and b (right) axis, respectively.

A comparison of the supramolecular assemblies obtained starting from **L3** and the shorter but similar **L1** allows to confirm the importance of the shape of the spacer in determining the primary structure of the ensuing assembly. When different ligand conformations are permitted, either convergent or divergent coordination modes can be experimented depending on the nature of the counter ions and on the solvent used and on their capability of interacting with the metal ion and participate to its coordination sphere, see for example the case of $[\text{ZnL1}(\text{NO}_3)_2 \cdot \text{CH}_3\text{CN}]_2$ and $[\text{CuL3}(\text{NO}_3)_2 \cdot \text{CH}_3\text{CN}]_2 \cdot 2\text{CH}_3\text{CN}$, compared to the CP $[\text{AgL1}(\text{OTf}) \cdot ((\text{CH}_3)_2\text{CO})_{0.5}]_\infty$, $[\text{AgL3}(\text{OTf}) \cdot ((\text{CH}_3)_2\text{CO})_{2.5}]_\infty$, and $[\text{CdL3}(\text{NO}_3)_2(\text{H}_2\text{O})_2 \cdot 1.5\text{H}_2\text{O}]_\infty$. Due to very small energy differences between the limit conformations of the ligands, an important role is also played by the intermolecular packing interactions that can drive the ligand to assume the conformation which maximize either π - π or hydrophilic H-bonding interactions.

The supramolecular assemblies $[\text{AgL3}(\text{OTf}) \cdot ((\text{CH}_3)_2\text{CO})_{2.5}]_\infty$, $[\text{CdL3}(\text{NO}_3)_2(\text{H}_2\text{O})_2 \cdot 1.5\text{H}_2\text{O}]_\infty$ and $[\text{CuL3}(\text{NO}_3)_2 \cdot \text{CH}_3\text{CN}]_2 \cdot 2\text{CH}_3\text{CN}$, were fully characterized by means of elemental analysis, SC-XRD measurements, FT-IR spectroscopy and optical measurements (§5.2.25, §5.2.26, §5.2.27, Figures S77, S78, S79).

In particular, the middle infrared spectrum of $[\text{AgL3}(\text{OTf}) \cdot ((\text{CH}_3)_2\text{CO})_{2.5}]_\infty$ features bands typical of triflate anions falling at 1279 and 1024 cm^{-1} for $\nu_{\text{asym}}(\text{SO}_3)$ and $\nu_{\text{sym}}(\text{SO}_3)$, respectively,

and two bands at 1250 and 1165 cm^{-1} are assigned to the $\nu_{\text{sym}}(\text{CF}_3)$ and $\nu_{\text{asym}}(\text{CF}_3)$, respectively.^[302] FT-IR spectra for $[\text{CdL3}(\text{NO}_3)_2(\text{H}_2\text{O})_2 \cdot 1.5\text{H}_2\text{O}]_\infty$ and $[\text{CuL3}(\text{NO}_3)_2 \cdot \text{CH}_3\text{CN}]_2 \cdot 2\text{CH}_3\text{CN}$ exhibit a very strong absorption band typical of the asymmetric NO_3^- stretching falling at 1387 and 1385 cm^{-1} , respectively, and a medium absorption band due to N–O stretching vibration at 825 and 810 cm^{-1} for $[\text{CdL3}(\text{NO}_3)_2(\text{H}_2\text{O})_2 \cdot 1.5\text{H}_2\text{O}]_\infty$ and $[\text{CuL3}(\text{NO}_3)_2 \cdot \text{CH}_3\text{CN}]_2 \cdot 2\text{CH}_3\text{CN}$, respectively.^[303] The **L3**-alkyne stretching was found at 2210 cm^{-1} for both $[\text{AgL3}(\text{OTf})((\text{CH}_3)_2\text{CO})_{2.5}]_\infty$ and $[\text{CuL3}(\text{NO}_3)_2 \cdot \text{CH}_3\text{CN}]_2 \cdot 2\text{CH}_3\text{CN}$, and at 2212 cm^{-1} for $[\text{CdL3}(\text{NO}_3)_2(\text{H}_2\text{O})_2 \cdot 1.5\text{H}_2\text{O}]_\infty$, slightly shifted if compared with the value of 2197 cm^{-1} observed for free ligand. The observed trend is reflected in a small but appreciable shortening of the $\text{C}\equiv\text{C}$ bond distances passing from the free ligands (1.204(10) Å) to the metal containing products (1.193(13) Å).

Diffuse reflectance measurements were performed on the same samples, showing a broad absorption band in the region 200–400 nm similarly to that found for the free ligand (Figure 59, left). The spectrum of $[\text{CuL3}(\text{NO}_3)_2 \cdot \text{CH}_3\text{CN}]_2 \cdot 2\text{CH}_3\text{CN}$ features an additional band in the visible region at 680 nm, probably due to the Cu^{II} d-d transitions (Figure 59).

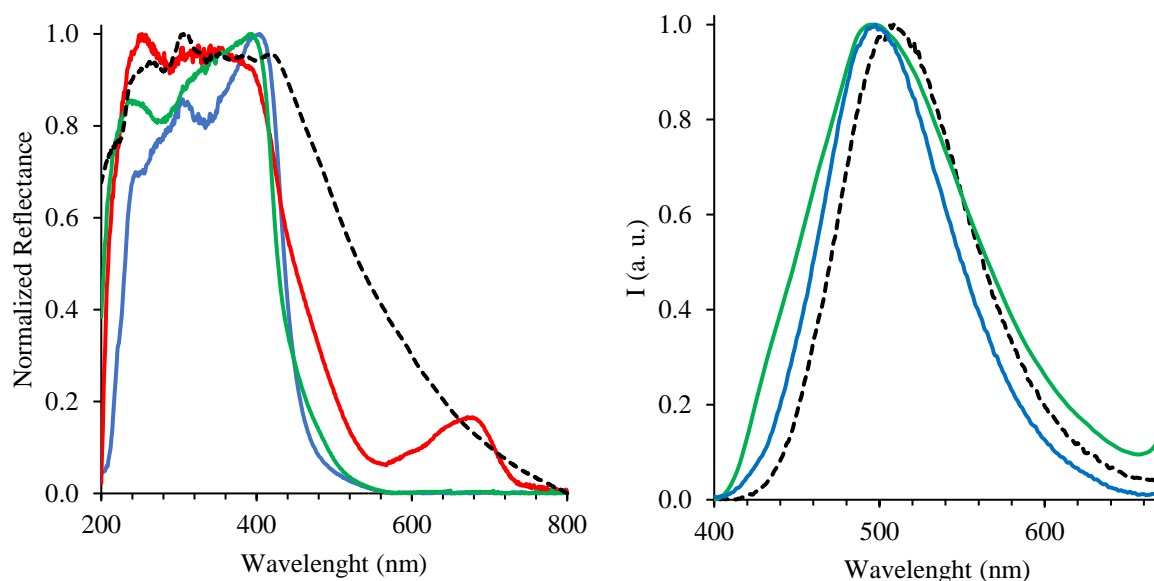
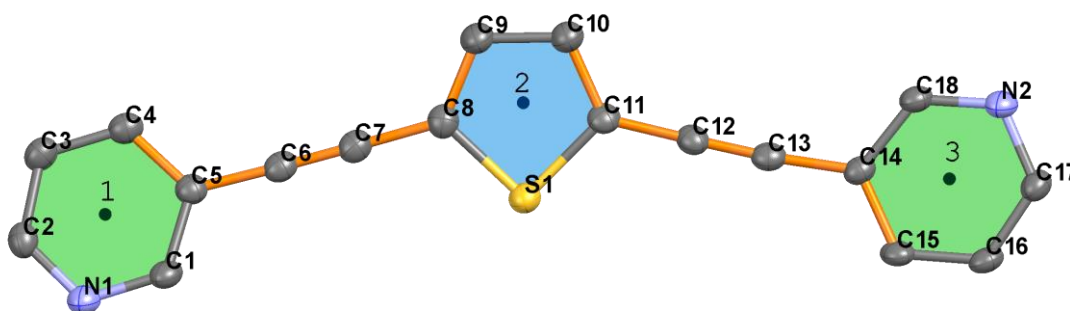


Figure 59 Normalized diffuse reflectance (left) and luminescent emission spectra (right) for $[\text{AgL3}(\text{OTf})((\text{CH}_3)_2\text{CO})_{2.5}]_\infty$ (blue line), $[\text{CdL3}(\text{NO}_3)_2(\text{H}_2\text{O})_2 \cdot 1.5\text{H}_2\text{O}]_\infty$ (green line) and $[\text{CuL3}(\text{NO}_3)_2 \cdot \text{CH}_3\text{CN}]_2 \cdot 2\text{CH}_3\text{CN}$ (red line). Absorption and emission properties of **L3** are depicted in black dashed lines for comparison.

In order to evaluate the effect of complexation on the solid-state luminescence properties, fluorescence emission spectra of compounds $[\text{AgL3}(\text{OTf})((\text{CH}_3)_2\text{CO})_{2.5}]_\infty$, $[\text{CdL3}(\text{NO}_3)_2(\text{H}_2\text{O})_2 \cdot 1.5\text{H}_2\text{O}]_\infty$, and $[\text{CuL3}(\text{NO}_3)_2 \cdot \text{CH}_3\text{CN}]_2 \cdot 2\text{CH}_3\text{CN}$ were recorded (Figure

40). The silver and cadmium assemblies show a strong band emission at 497 and 495 nm, with Stoke shifts of 93 and 101 nm, respectively. In particular, the emission band recorded for $[\text{CdL3}(\text{NO}_3)_2(\text{H}_2\text{O})_2 \cdot 1.5\text{H}_2\text{O}]_\infty$ results sensibly broadened if compared with the emission of **L3**. On the contrary, the reaction with copper led to a complete quenching of the ligand-based emission, and $[\text{CuL3}(\text{NO}_3)_2 \cdot \text{CH}_3\text{CN}]_2 \cdot 2\text{CH}_3\text{CN}$ is not fluorescent. These differences can be attributed to the different electronic configuration of the three metal ions. In fact, Ag(I) and Cd(II) are isoelectronic with a complete outer shell $4d^{10}$ which prevents metal centered (MC) transitions between d-d orbitals and then the chance to engage a non-radiative decay. On the other hand, Cu(II) features a $3d^9$ electronic configuration and an unpaired electron which is known to be responsible of a rapid non-radiative decay, with a consequent quenching of the fluorophore emission.^[304]

Table 10 Geometrical features including angles, dihedral angles ($^\circ$) and distances (\AA) of **L3** molecules in the crystal structures of **L3** (orthorhombic), $[\text{AgL3}(\text{OTf})((\text{CH}_3)_2\text{CO})_{2.5}]_\infty$, $[\text{CdL3}(\text{NO}_3)_2(\text{H}_2\text{O})_2 \cdot 1.5\text{H}_2\text{O}]_\infty$ and $[\text{CuL3}(\text{NO}_3)_2 \cdot \text{CH}_3\text{CN}]_2 \cdot 2\text{CH}_3\text{CN}$. Centroids and planes are identified by numbers (1-3) and letters (a-c), respectively. Atoms have been renumbered for clarity reasons accordingly to the molecular structure given below.



	L3 (orthorhombic)	$[\text{AgL3}(\text{OTf})((\text{CH}_3)_2\text{CO})_{2.5}]_\infty$	$[\text{CdL3}(\text{NO}_3)_2(\text{H}_2\text{O})_2 \cdot 1.5\text{H}_2\text{O}]_\infty$	$[\text{CuL3}(\text{NO}_3)_2 \cdot \text{CH}_3\text{CN}]_2 \cdot 2\text{CH}_3\text{CN}$
1-2-3	155.07	152.48 152.37	159.37	146.17
a-b	17.57	5.37 9.02	4.60	18.79
a-c	12.05	15.64 14.19	10.13	11.90
b-c	5.53	10.27 8.40	8.74	29.72
C5-C6-C7	178.17	177.17 177.92	175.85	178.68
C8-C7-C6	178.58	179.11 178.29	177.48	178.16

C7-C8-S1	121.35	120.20 120.88	121.49	120.60
C12-C11-S1	121.67	121.24 121.29	121.22	119.89
C14-C13-C12	176.02	174.90 178.98	174.24	176.36
C11-C12-C13	178.44	179.34 178.32	176.58	177.04
C4-C5-C8-C9	17.49	171.07 177.09	178.43	19.16
C10-C11-C14-C15	173.64	174.56 169.68	5.64	31.02
d _{N1-N2}	14.530	14.826 14.827	14.701	13.228

Chung and co-workers reported on the preparation of a CP $[\text{Co}(\mathbf{L4})_2(\text{NCS})_2]_\infty$ formed by the self-assembly between **L4** and $\text{Co}(\text{NCS})_2$.^[305] The authors evidenced how the linker features an unusual flexibility showing two conformation: linear and bent. In order to investigate the role of the counterion in the final polymeric networks, **L4** was reacted with a bench of cobalt(II) salts including nitrate, sulphate, tetrafluoroborate, acetate and chloride. Slow diffusion of a methanolic solution of **L4** to aqueous CoCl_2 solution yielded orange crystals in 48 h. Structural elucidation by means of XRD revealed the formation of a CP $[\text{Co}(\mathbf{L4})_2\text{Cl}_2]_\infty$ (crystal data and refinement parameters in Table S132. Bond lengths and angles are reported in Table S133). The asymmetric unit comprises two octahedrally coordinated cobalt ions, each of which features two chloride anions at their axial positions (Figure 60). The equatorial positions are fulfilled by N-atoms coming from the pyridyl rings of **L4**. There are four crystallographically independent **L4** units, two of which feature disordered thiophene fragments. All the screened crystals revealed to be twinned and the disorder was modelled over two positions treating the thiophene rings as rigid groups. The thermal ellipsoids at the disordered fragments were constrained using EADP.

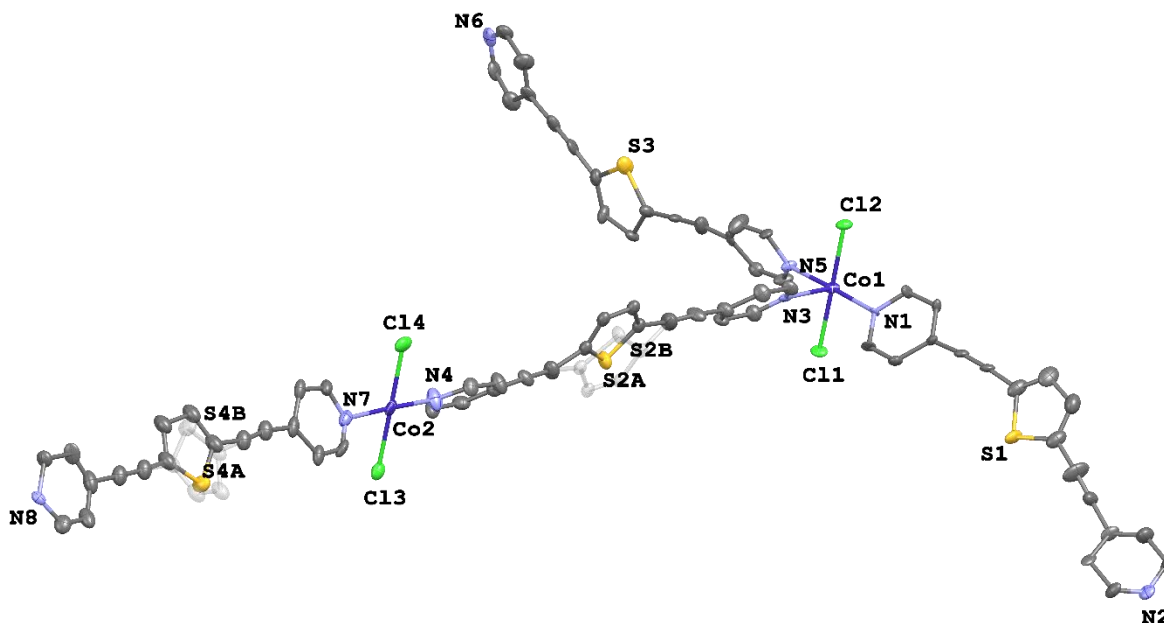


Figure 60 View of the asymmetric unit of $[\text{Co}(\text{L4})_2\text{Cl}_2]_\infty$ along the $[011]$ direction. H atoms are omitted for clarity.

Alike $[\text{Co}(\text{L4})_2(\text{NCS})_2]_\infty$, a 2D square-grid network with openings of about $19.9 \times 20.5 \text{ \AA}$ is observed in $[\text{Co}(\text{L4})_2\text{Cl}_2]_\infty$ (Figure 61).

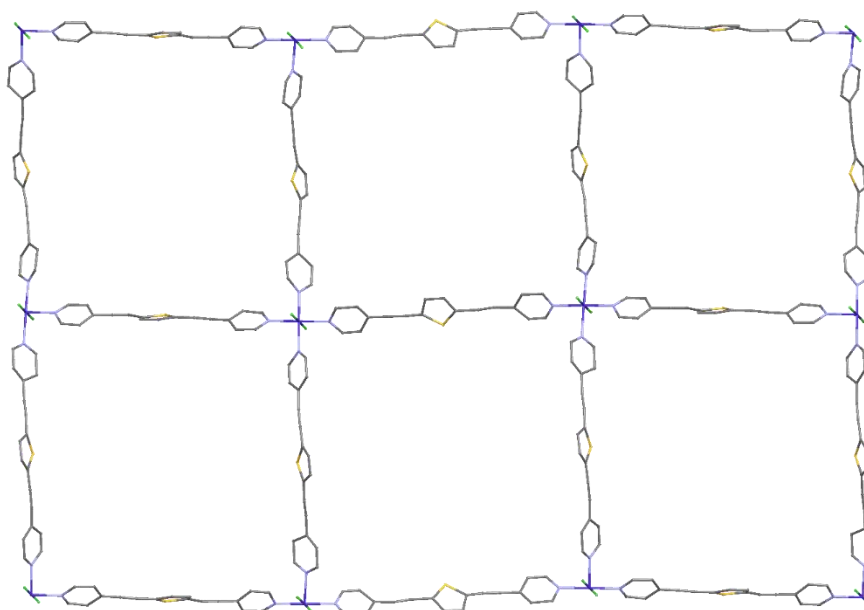


Figure 61 View of the 2D square-grid network of $[\text{Co}(\text{L4})_2\text{Cl}_2]_\infty$ along the b axis. Disorder and H atoms are omitted for clarity.

In contrast to $[\text{Co}(\text{L4})_2(\text{NCS})_2]_\infty$ where each layer is independent from the adjacent ones, the 2D square-grid network of $[\text{Co}(\text{L4})_2\text{Cl}_2]_\infty$ is generated by interlayer crossing of **L4** molecules as showed in Figure 62.

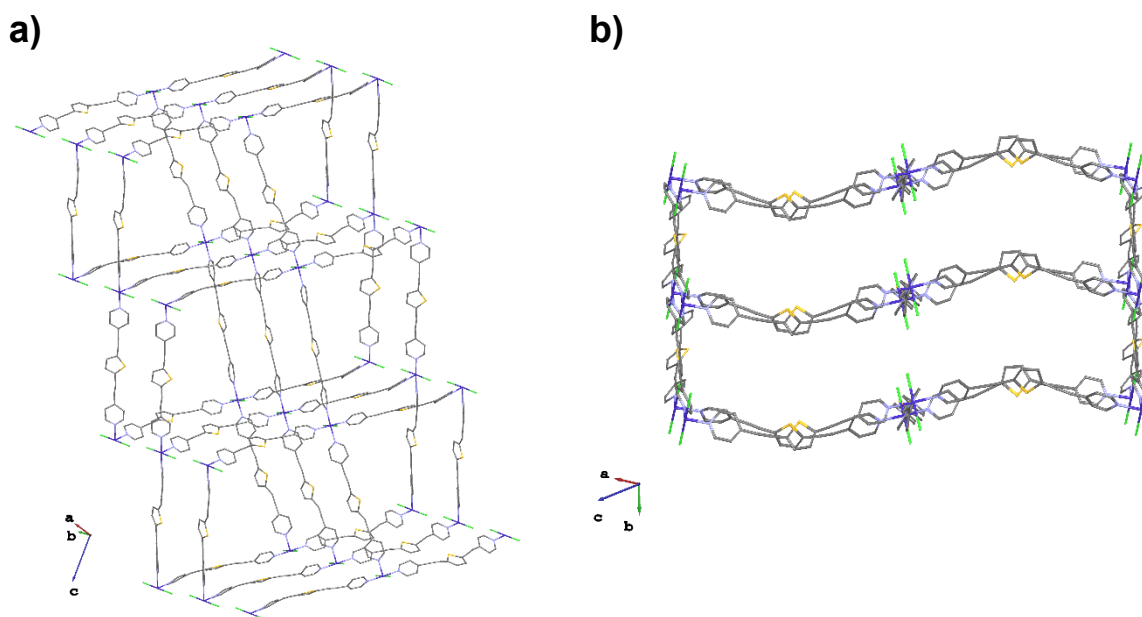


Figure 62 Packing diagrams of $[\text{Co}(\text{L4})_2\text{Cl}_2]_\infty$ showing a) the connectivity between adjacent layers; b) view of parallel layers along the propagation direction of interlayer crossing of **L4** molecules.

The geometrical similarities and differences between $[\text{Co}(\text{L4})_2(\text{NCS})_2]_\infty$ and $[\text{Co}(\text{L4})_2\text{Cl}_2]_\infty$ are clearly visible from the overlapped views of the two structures in Figure 63.

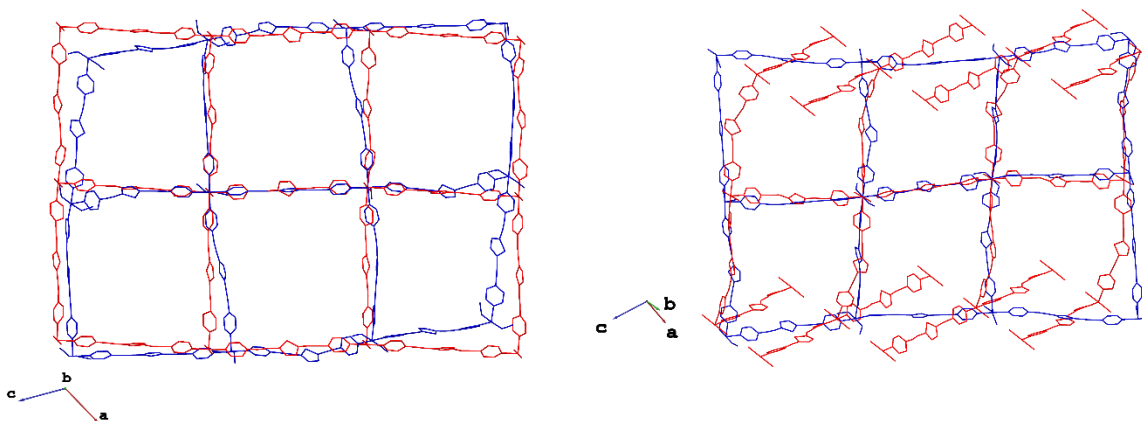


Figure 63 Overlapped views of $[\text{Co}(\text{L4})_2(\text{NCS})_2]_\infty$ (refcode: ALANOQ) and $[\text{Co}(\text{L4})_2\text{Cl}_2]_\infty$ depicted in blue and red, respectively.

Both CPs feature a 5-fold interpenetration and that of $[\text{Co}(\text{L4})_2\text{Cl}_2]_\infty$ is shown in Figure 64.

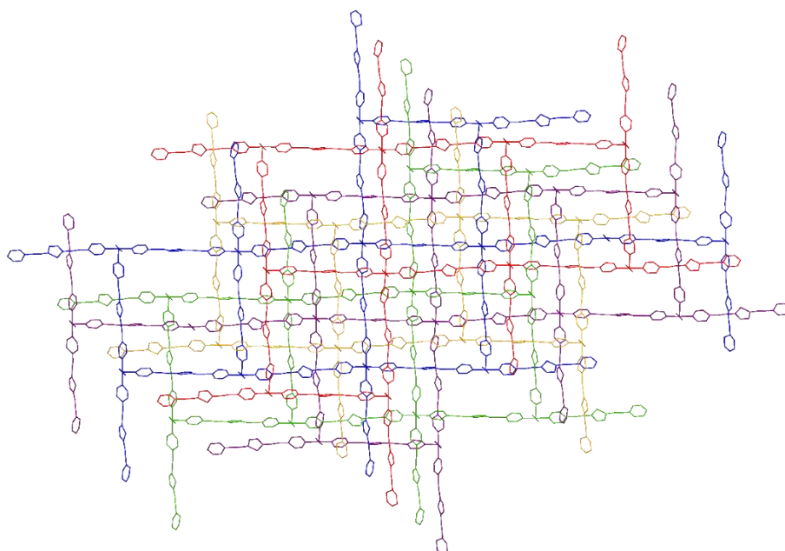
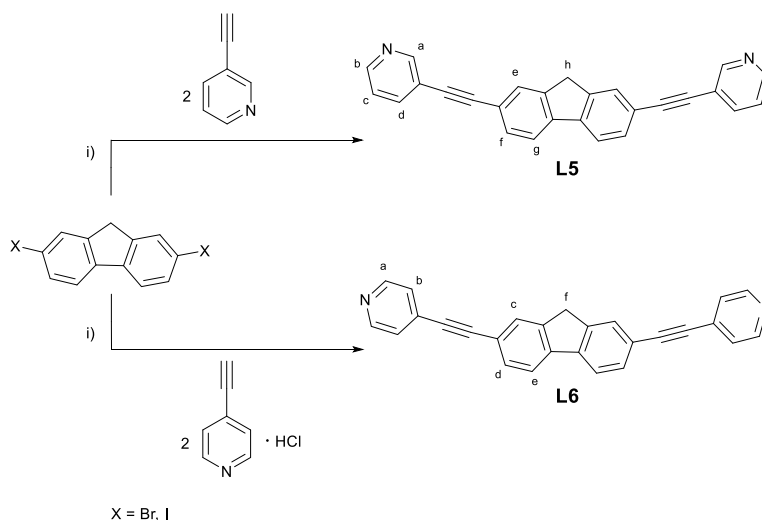


Figure 64 View of the 5-fold interpenetrated network of $[\text{Co}(\text{L4})_2\text{Cl}_2]_\infty$

3.1.1.3. Interaction between *N*-donors **L5** and **L6** with metal ions

Ligands **L5** and **L6** feature the same ethynyl-pyridyl arms of **L3** and **L4** but differ for the presence of a central 9H-fluorene unit in place of the thiophene one. In this case also the isomer with the *meta*-substituted pyridyl sites produced a higher number of crystalline items compared with the analogous with *para*-substituted pyridines. The synthesis of **L5** and **L6** was carried out by one-step Sonogashira coupling reaction between 3-ethynylpyridine or 4-ethynylpyridine hydrochloride and 2,7-dibromofluorene or 2,7-diiodofluorene (§5.2.5 and §5.2.6).



Scheme 17 Sonogashira coupling reactions for the preparation of ligand **L5** and **L6**. i) $\text{Pd}(\text{PPh}_3)_2\text{Cl}_2$, CuI , NH_4Et_2 , N_2 , reflux, 48 h.

The ligands were fully characterized by means of elemental analysis, FT-IR and NMR spectroscopy. In addition, MS spectrometry and XRD characterization were performed for **L5** (§5.2.5). The FT-IR spectra of both **L5** and **L6** show a band at 2208 and 2210 cm^{-1} respectively, assigned to the alkyne stretching, similarly to that found for **L3** and **L4**. The ^1H NMR spectrum of **L5** recorded in DMSO-d_6 shows four signals at 8.60, 8.01, 7.85 and 7.49 ppm typical for *meta*-substituted pyridyl fragment (a, b, c, d in Scheme 17, respectively). Three more signals centred at 8.05, 7.85 and 7.66 ppm from the fluorene ring are present in the aromatic region, and the singlet resonating at 4.03 ppm was assigned to the 9H protons of the fluorene units (g, e, f, h in Scheme 17, respectively). Complete NMR characterization of **L5**: ^1H , $^{13}\text{C}\{^1\text{H}\}$, and ^1H - ^{13}C HMQC sequences is reported in Figures S12, S13 and S14. The TOF MS ES(+) spectrum of **L5** shows $(\text{M}+\text{H})^+$ $\text{C}_{27}\text{H}_{17}\text{N}_2^+$ (m/z): 369.1402 and is given as supplementary material (Figure S108). The ^1H NMR spectrum of **L6** is in agreement with the spectrum reported in the literature and will not be discussed here (Figure S15).^[306] The electronic transitions of **L5** and **L6** were studied by means of UV-Vis spectrophotometry both in solution and in the solid state. The spectrum of **L5** recorded in chloroform, shown in Figure 65, displays an absorption band at $\lambda_{\text{max}} = 347 \text{ nm}$ ($\epsilon = 72607 \text{ M}^{-1} \text{ cm}^{-1}$) to whom corresponds an emission band centred at 432 nm, with a Stokes shift of 85 nm. The UV-Vis spectrum of **L6** in the same solvent feature a similar pattern with a maximum absorption band at 351 nm ($\epsilon = 67986 \text{ M}^{-1} \text{ cm}^{-1}$). However, the emission spectrum of **L6** displays two maxima at 378 and 399 nm.

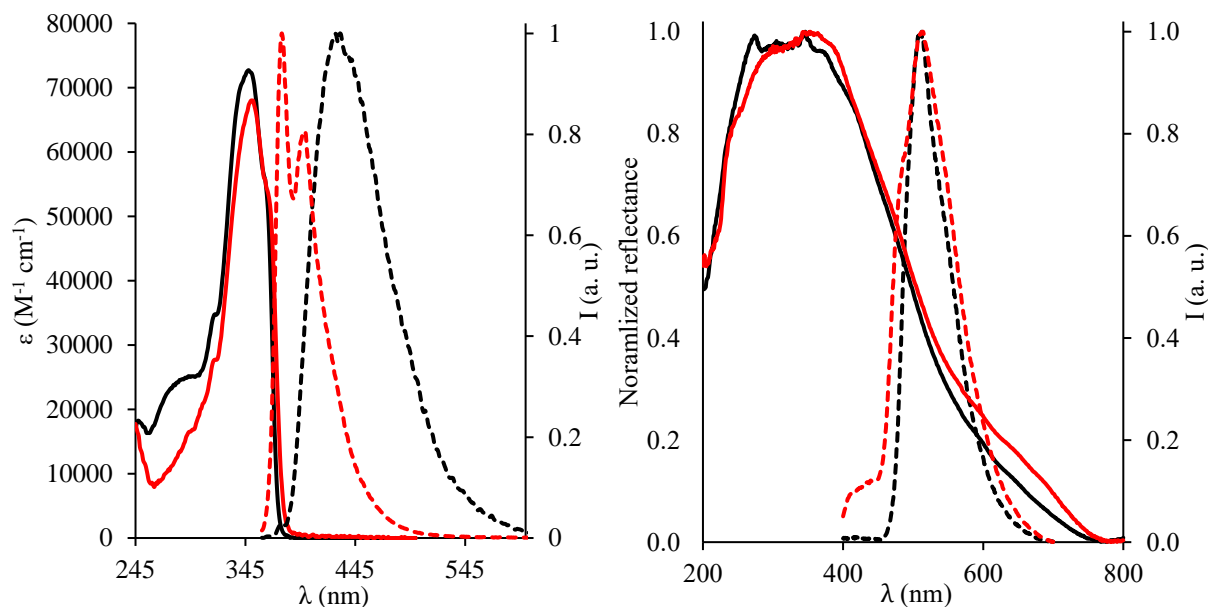


Figure 65 Absorption (solid line) and emission (dashed line) spectra for **L5** (black) and **L6** (red) measured in CHCl_3 (left) ($C_{\text{L5-L6}} = 10^{-5} - 10^{-6} \text{ M}$, $\lambda_{\text{ex}} = 347\text{-}351 \text{ nm}$) and in the solid state (right) ($\lambda_{\text{ex}} = 370 \text{ nm}$).

Diffuse reflectance measurements in the solid state displayed a strong absorption in the UV region of the spectrum for both linkers. When the linkers were excited at 370 nm, a sharp emission was obtained in both cases with maximum at 512 nm (Figure 65). Single crystals of **L5** were grown from DMSO and characterized by means of XRD. The organic linker crystallizes in the monoclinic space group $C2/c$ with half of the molecule in the asymmetric unit (structural data refinement in Table S134). The pseudo-rigid ligand is not planar with an angle between the pyridyl rings of about 72° . The spacer **L5** is notably longer than previously discussed ligands **L1** and **L3**, with intramolecular N \cdots N distance of 18.72 Å. **L5** units pack through intermolecular edge to face π - π interactions (§1.1.1) as shown in Figure 66.

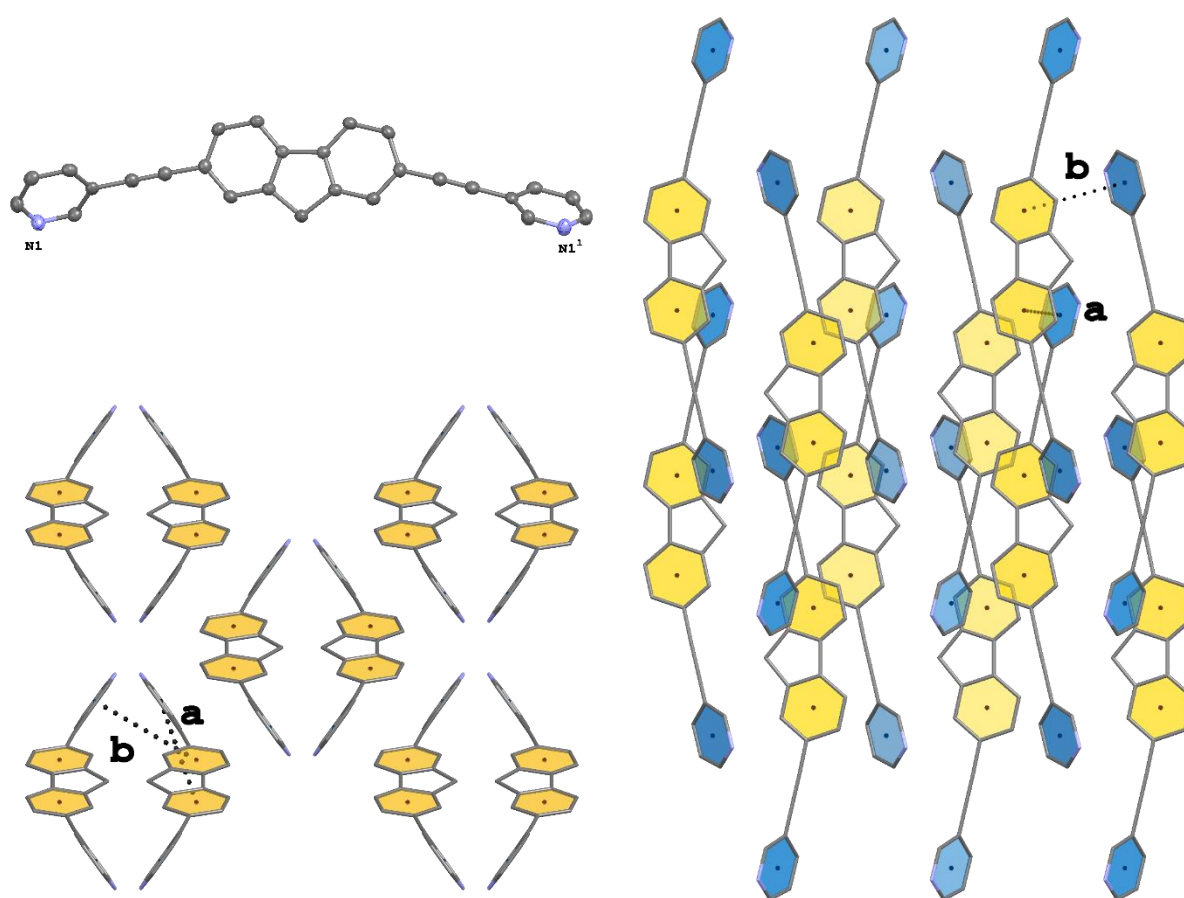
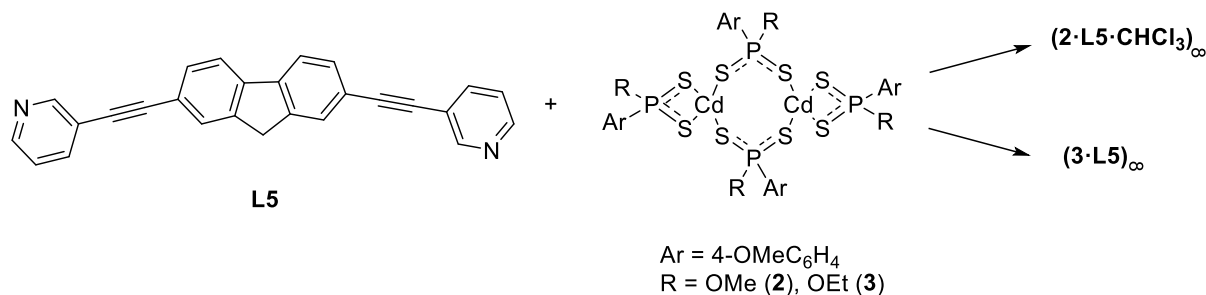


Figure 66 Crystal structure representation of **L5** (top); Packing diagrams along the *a* (right) and *b* axis (bottom left). Intermolecular π - π interactions are depicted in dashed black lines. Interactions: a) centroid-centroid distance of 4.741(9) Å, $\alpha = 58.2(5)^\circ$; b) centroid-centroid distance 4.862(8) Å, $\alpha = 57.7(5)^\circ$. H-atoms have been removed from packing diagrams for clarity.

Ligands **L5** and **L6** were reacted with several metal salts and with dithiophosphato and dithiophosphonato complexes. In fact, notwithstanding the large number of crystal structures deposited in the CCDC for dithiophosphonato derivatives embracing salts and complexes with

metal ions from group 1,^[307,308] 3,^[309,310] 6,^[311,312] 7,^[313] 8,^[314,315] 9,^[316,317] 10,^[289,292,293,313,317–346] 11,^[343,347–360] and 12^[297,307,324,361–373] elements, few reports can be found on the inclusion of dithiophosphonates into luminescent materials.^[312,313,316,352]

Despite the high number of reactions performed, crystals suitable for X-ray diffractions were obtained only from the reactions of **L5** with the two dithiophosphonato complexes *bis*(*O*-alkyl(4-methoxyphenyl)phosphonodithioato)-cadmium(II) [(C₇H₇OPS₂)₂(RO)₂Cd] [R = Me (**2**), Et (**3**), Scheme 18].



Scheme 18 Building blocks used in the formation of the luminescent CPs (**2**·**L5**·CHCl₃)_∞ and (**3**·**L5**)_∞.

The synthesis of complexes **2** and **3** was carried by the one-step reaction of Lawesson's reagent and Cd(NO₃)₂·4H₂O in the relevant alcohol (MeOH and EtOH, respectively) used as solvent (§5.2.18 and §5.2.19).^[374] Upon recrystallization of **2** and **3**, colourless crystals were obtained and the crystal structures determined by means of XRD analysis. Both complexes displayed a dimeric arrangement as showed in Figure 67, resembling what previously reported in the literature.^[324,364,371,375] XRD data collected on different crystals of **2** and using various X-ray sources (MoK_α and CuK_α), always yielded solutions with an incommensurate disorder on the aryl and methoxy P-substituents, thus preventing a reliable model for complex **2** (at least at the time of writing) but allowing to determine a connectivity very similar to that found in **3**. The good data collected on crystals of compound **3** are presented below and are summarized in Table S135. Complex **3** crystallizes in the monoclinic space group *P2*₁/*c* with half of the dimeric assembly in the asymmetric unit and the remaining half being symmetry generated. The main distances and angles in **3** are in perfect agreement with those previously reported for similar cadmium(II) complexes (refcodes: HAHDEA,^[324] MERXUD,^[307] QIDKOG,^[364]) listed in Table S136 for the sake of comparison.

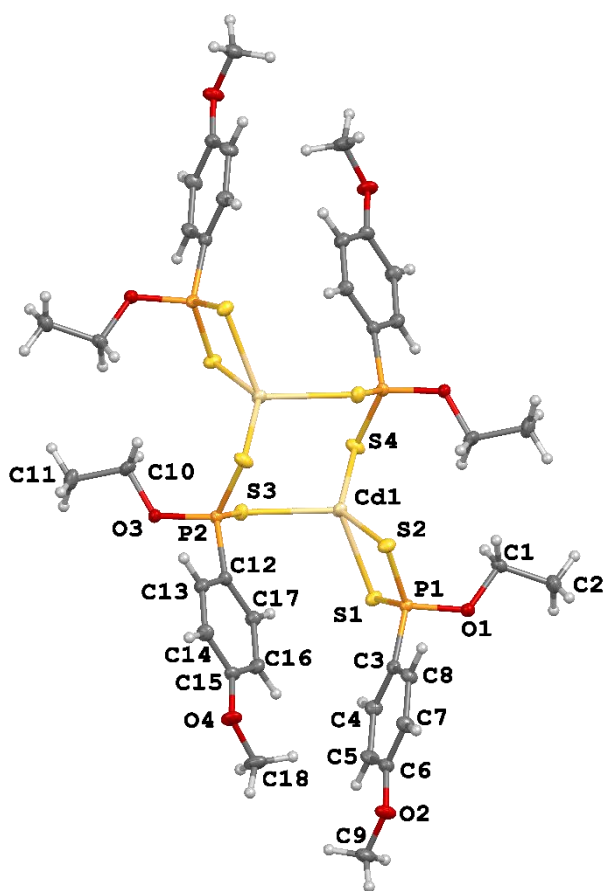


Figure 67 Perspective view of the dimeric arrangement found in the crystal structure of complex **3**. Displacement ellipsoids are drawn at 50 % probability level.

The solution $^1\text{H-NMR}$ spectra of **2** and **3**, collected by dissolving the crystalline products in DMSO-d_6 (Figures S51 and S53), show the signals of the aromatic protons at 7.88 and 6.99–7.00 ppm, featuring peculiar J_{PH} and J_{HH} scalar coupling constants.^[324,370] The singlet signal at 3.80 and 3.78 ppm, for compound **2** and **3** respectively, was assigned to the methoxy substituent of the aryl dithiophosphonate moieties. The doublet falling at 3.63 ppm was assigned to the protons of the methoxy P-substituent in **2**. Similarly, the ethoxy moieties in complex **3** generate two signals, a doublet of quartet resonating at 4.09 ppm for the CH_2 , and a triplet centred at 1.22 ppm for the CH_3 fragment. The $^{13}\text{C}\{^1\text{H}\}$ NMR spectra for both complexes **2** and **3** feature signals resonating at 131.6 and 113.3 ppm attributable to their aromatic protons (Figures S52 and S54). FT-IR spectra of **2** and **3** display the asymmetric and symmetric P–S stretching modes at around 650 and 540 cm^{-1} for, respectively (Figures S72, S73).^[324,370]

The reaction between **L5** and neutral cadmium complexes **2** and **3** in a 1:1 and 1:2 alcohol/chloroform mixture, yielded the two luminescent CPs of formula $(\mathbf{2}\cdot\mathbf{L5}\cdot\text{CHCl}_3)_\infty$ and $(\mathbf{3}\cdot\mathbf{L5})_\infty$ (§5.2.29 and §5.2.30). The former crystallizes in the monoclinic non-centrosymmetric space group Cc (structural data refinement in Table S137, Figure 68) with an asymmetric unit consisting of one cadmium ion, one **L5** molecule, two dithiophosphonato anions and a co-crystallized chloroform molecule (Figure 68). The central cadmium(II) ion in complex **2** changes its coordination geometry, from tetrahedral to octahedral, upon formation of two Cd–N bonds with the bridging **L5** ligands.

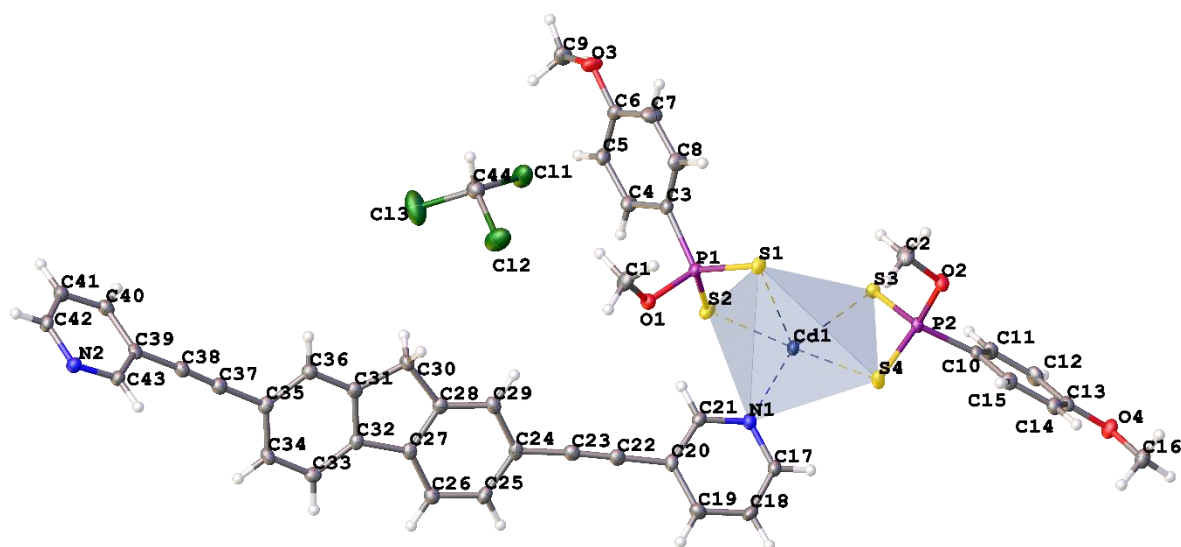


Figure 68 Numbering scheme of the asymmetric unit for $(\mathbf{2}\cdot\mathbf{L5}\cdot\text{CHCl}_3)_\infty$. Displacement ellipsoids are drawn at 50 % probability level.

L5 units are not planar with the two pyridyl rings angled of about 33° and arranged in an antiperiplanar conformation. The overall octahedral environment at the cadmium atoms is slightly distorted: main distances and angles are listed in Table 12.

The cadmium ions are coordinated by two nitrogen from the pyridyl rings in a *cis* fashion with Cd–N distances of 2.400(3) and 2.434(3) Å for Cd1–N1 and Cd1–N2, respectively, in line with those found in $(\mathbf{1}\cdot\mathbf{L1})_\infty$ and $(\mathbf{1}\cdot\mathbf{L2})_\infty$ and in similar CPs; the N1–Cd1–N2 angle is about 81.7° and the pyridyl rings are rotated of about 66.5° . Cd–S distances range from 2.6244(10) and 2.7984(10) Å showing values similar to those reported for $(\mathbf{1}\cdot\mathbf{L1})_\infty$ and $(\mathbf{1}\cdot\mathbf{L2})_\infty$, and slightly longer than those found for the starting **3** and the other similar dithiophosphonato cadmium complexes (Table S136); the P–S distances and the corresponding S–P–S angles remain unchanged when the coordination polymer $(\mathbf{2}\cdot\mathbf{L5}\cdot\text{CHCl}_3)_\infty$ is formed (Table 12).

Ligand **L5** bridges metal nodes generating polymeric helices running along the *a* axis with a pitch of 42.3 Å and Cd···Cd distances of about 22.0 Å, quite longer than those found for $(\mathbf{1}\cdot\mathbf{L1})_\infty$ and $(\mathbf{1}\cdot\mathbf{L2})_\infty$, as expected due the longer **L5** lengths (Figure 69).

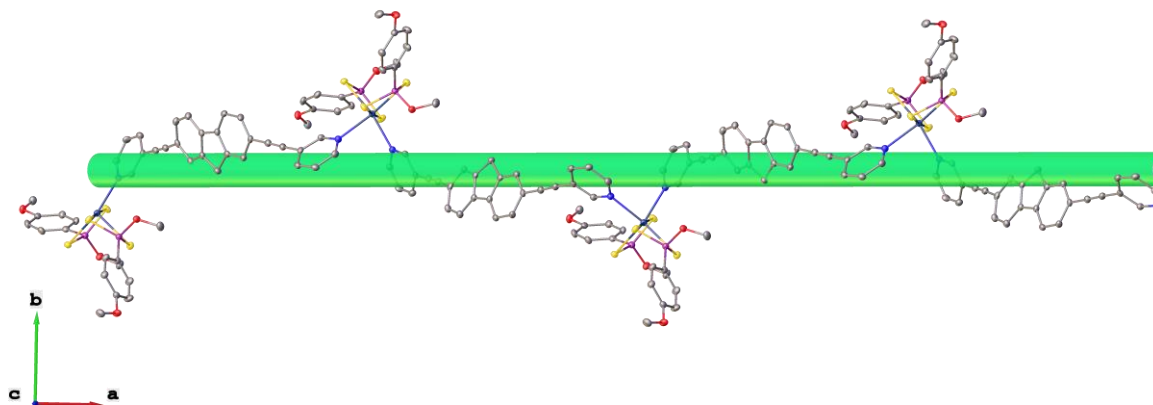


Figure 69 Helicoidal assembly of $(\mathbf{2}\cdot\mathbf{L5}\cdot\mathbf{CHCl}_3)_\infty$. Thermal ellipsoids are drawn at 50 % probability level. Solvent molecules and H-atoms have been omitted for clarity.

The crystal packing is held together by intermolecular π - π stacking interactions between the fluorenyl and pyridyl rings of adjacent helices (Figure 70) and intermolecular hydrogen bonds involving the O atoms and the aromatic protons of both fluorenyl and pyridyl rings (Figure 71). The overall packing present alternated left- and right-handed helices closely interwoven as showed in the crystal packing diagrams in Figure 72.

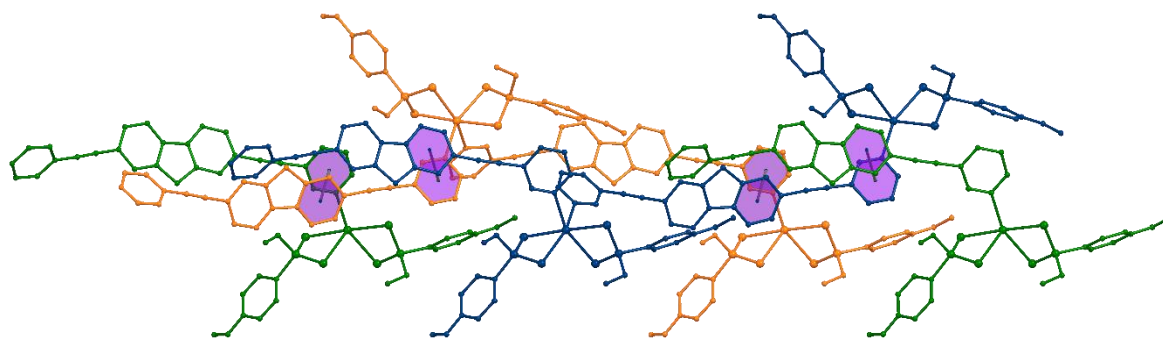


Figure 70 Intermolecular interactions between adjacent helices depicted in different colours. The intermolecular π - π stacking are experienced between planes highlighted in purple (centroid-centroid distance = 3.844(2) Å, $\alpha = 4.0(2)^\circ$).

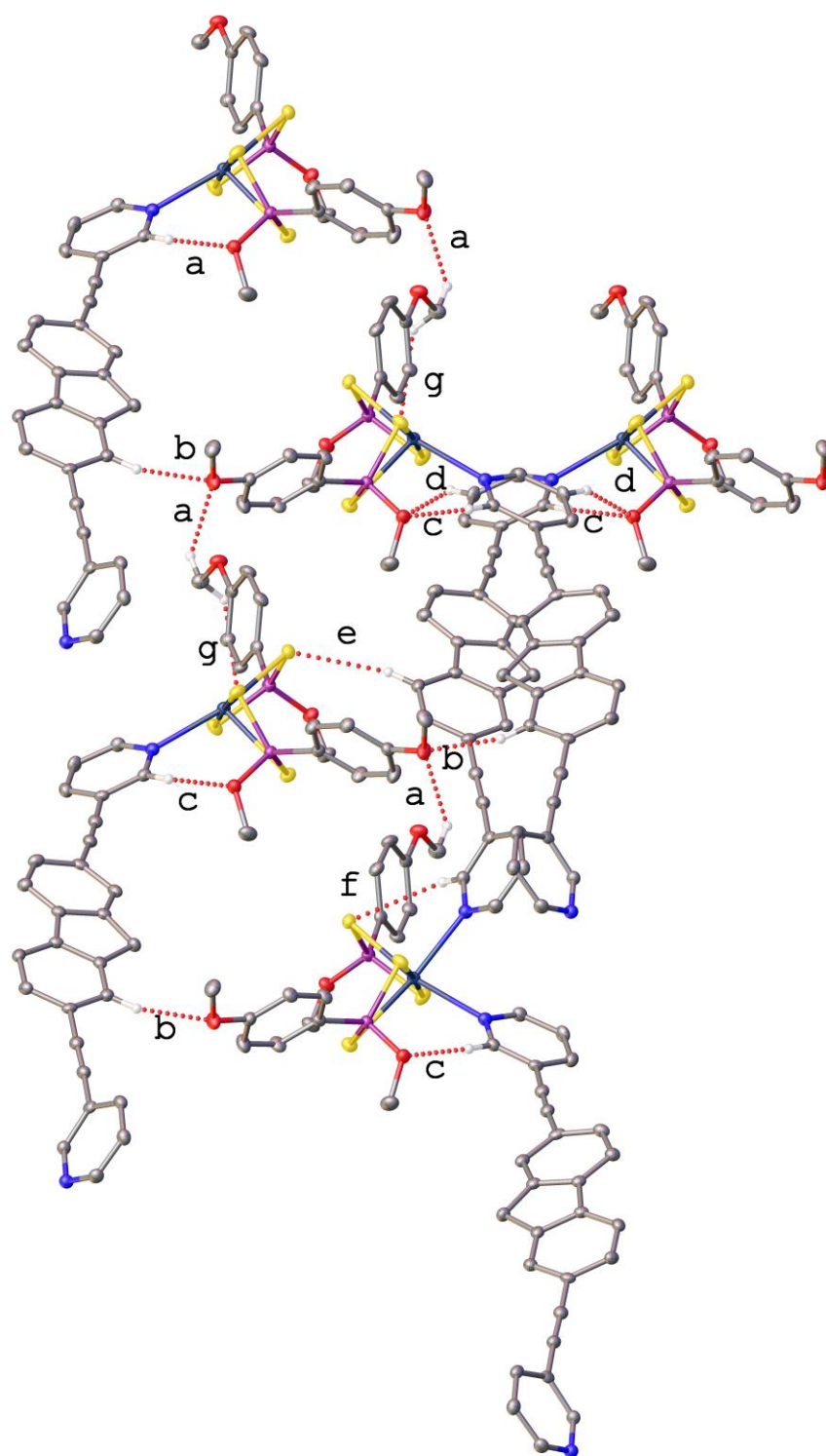
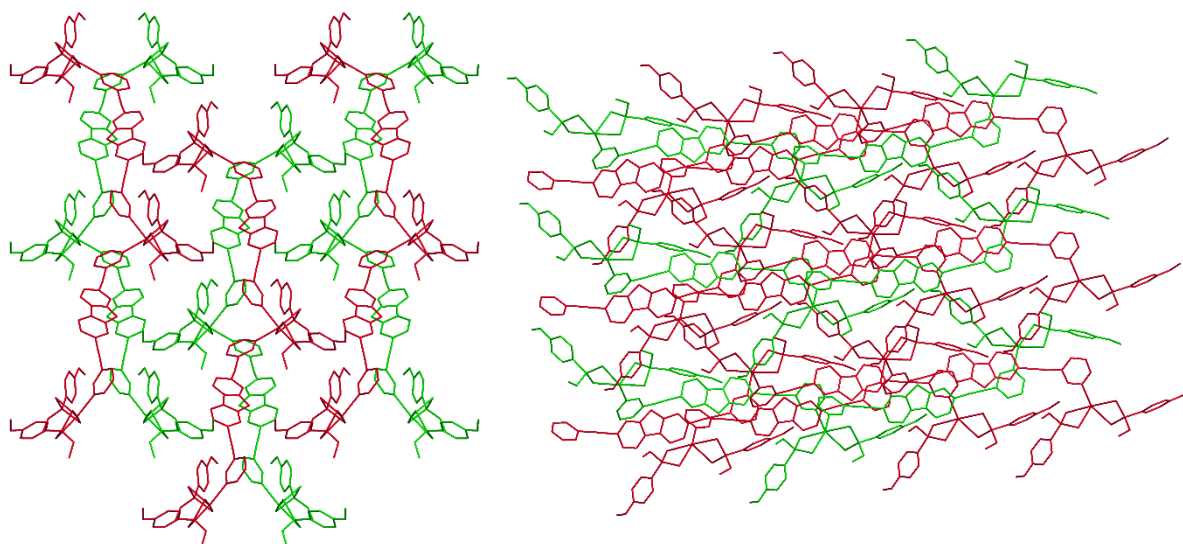


Figure 71 View of the intermolecular interactions between adjacent helices along the *c* axis. Intermolecular hydrogen bonding interactions and contacts are depicted in dashed red lines and labelled according to Table 11.

Table 11 List of intermolecular interactions and contacts for $(2\cdot\mathbf{L5}\cdot\text{CHCl}_3)_\infty$

Interaction	D	H	A	$d_{D\cdots A}$ (Å)	$d_{H\cdots A}$ (Å)	D-H \cdots A (°)
a	C16	H16B	O3 ¹	3.266(5)	2.432(3)	142.7(3)
b	C36	H36	O3 ²	3.238(5)	2.314(3)	164.0(2)
c	C21	H21	O1	3.266(5)	2.321(3)	173.2(2)
d	C18 ³	H18 ³	O1	3.363(5)	2.493(3)	152.3(3)
e	C33	H33	S3 ⁴	3.887(4)	2.956(3)	166.8(3)
f	C43	H43	S3 ⁵	3.543(4)	2.958(3)	121.0(2)
g	C16	H16A	S2 ⁶	3.682(5)	2.883(3)	139.2(3)

Symmetry codes: ¹ $-1/2+x, 3/2-y, -3/2+z$; ² $1/2+x, 3/2-y, 1/2+z$; ³ $+x, 1-y, 1/2+z$; ⁴ $1/2+x, -1/2+y, 1+z$; ⁵ $1+x, 1-y, 3/2+z$; ⁶ $+x, +y, -1+z$.

**Figure 72** Packing diagrams for $(2\cdot\mathbf{L5}\cdot\text{CHCl}_3)_\infty$ along the c (left) and a (right) axis. Adjacent helices are depicted in different colours. Co-crystallized chloroform molecules and H-atoms have been omitted for clarity.

The reaction between **L5** and complex **3** in a 1:2 ethanol/chloroform mixture, yielded the coordination polymer $(\mathbf{3}\cdot\mathbf{L5})_\infty$, that crystallizes in the monoclinic centrosymmetric space group $P2_1/c$ (structural data and refinement parameters in Table S137) with an asymmetric unit consisting of one cadmium ion, one **L5** molecule, and two dithiophosphonato anions (Figure 73).

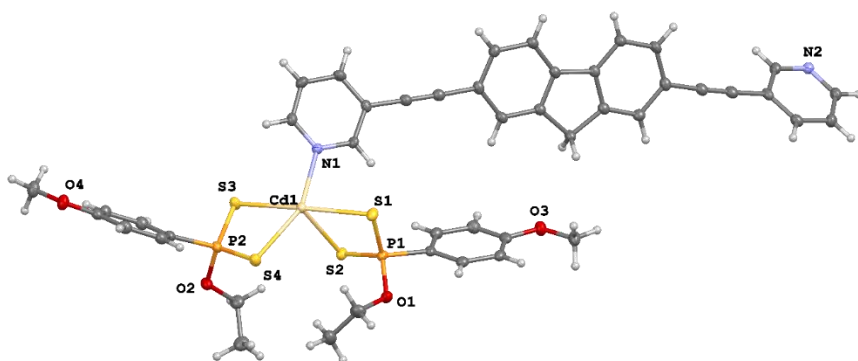


Figure 73 Asymmetric unit for $(\mathbf{3}\cdot\mathbf{L5})_{\infty}$. Displacement ellipsoids are drawn at 50 % probability level.

The structure closely resembles that described for $(\mathbf{2}\cdot\mathbf{L5}\cdot\mathbf{CHCl}_3)_{\infty}$, with a central cadmium(II) ion coordinated in a pseudo-octahedral geometry by two dithiophosphonate anions and two nitrogen atoms from bridging **L5** (Figure 74). The bond lengths and angles are very similar (Table 12). The two CPs share similar helicoidal chains with almost identical Cd \cdots Cd distances and helical pitches, 21.91(2) and 21.99(2), and 41.91(2) and 42.29(2) Å for $(\mathbf{3}\cdot\mathbf{L5})_{\infty}$, and $(\mathbf{2}\cdot\mathbf{L5}\cdot\mathbf{CHCl}_3)_{\infty}$, respectively.

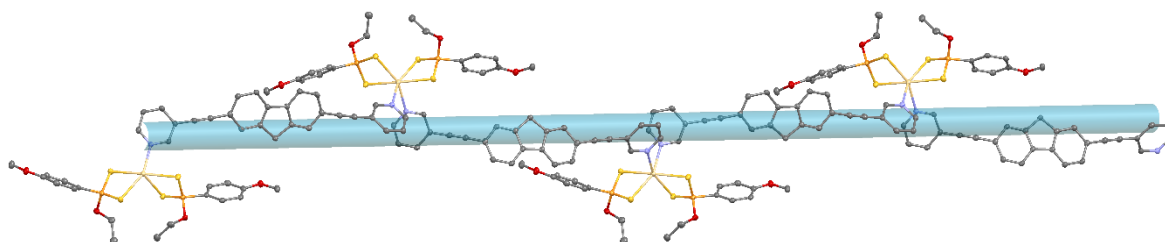


Figure 74 Helicoidal assembly of $(\mathbf{3}\cdot\mathbf{L5})_{\infty}$. Thermal ellipsoids are drawn at 50 % probability level. H-atoms have been omitted for clarity.

Notwithstanding the absence of co-crystallized solvent molecules, interactions similar to those described for $(\mathbf{2}\cdot\mathbf{L5}\cdot\mathbf{CHCl}_3)_{\infty}$, govern the crystal packing of $(\mathbf{3}\cdot\mathbf{L5})_{\infty}$ (Figure 75).

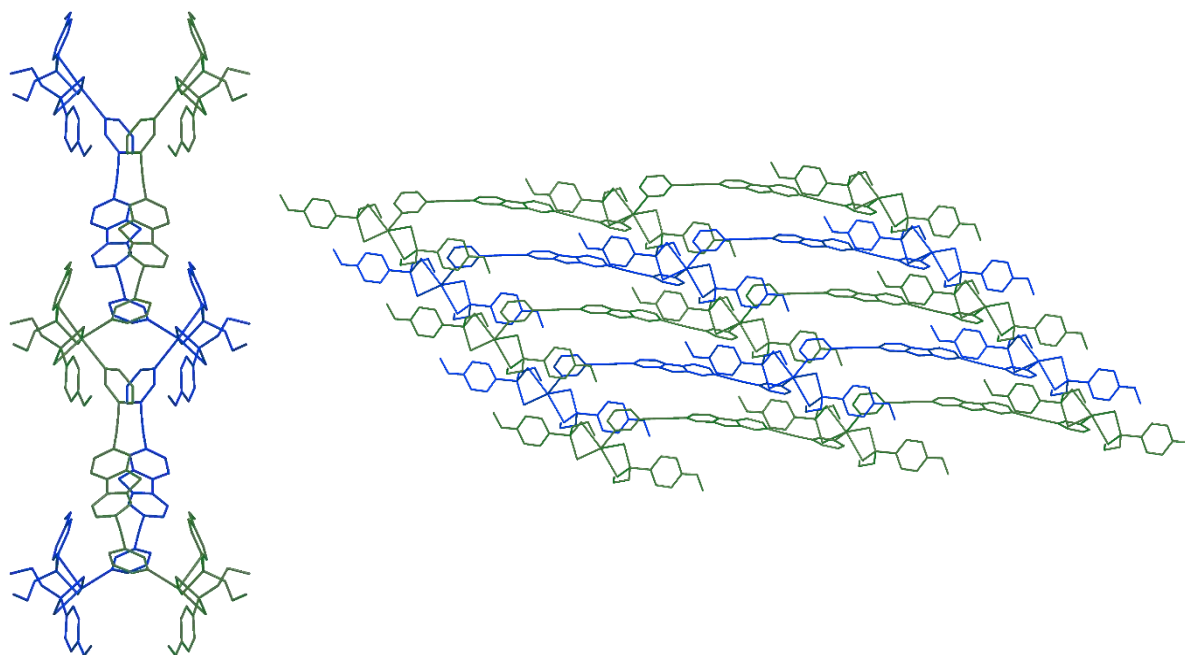


Figure 75 Packing diagrams of $(\mathbf{3}\cdot\mathbf{L5})_\infty$ along c (left) and b (right) axis, respectively. Adjacent helices are depicted in different colours for clarity.

Table 12 Selected bond lengths (Å) and angles (°) for compounds **3**, $(\mathbf{2}\cdot\mathbf{L5}\cdot\mathbf{CHCl}_3)_\infty$ and $(\mathbf{3}\cdot\mathbf{L5})_\infty$.

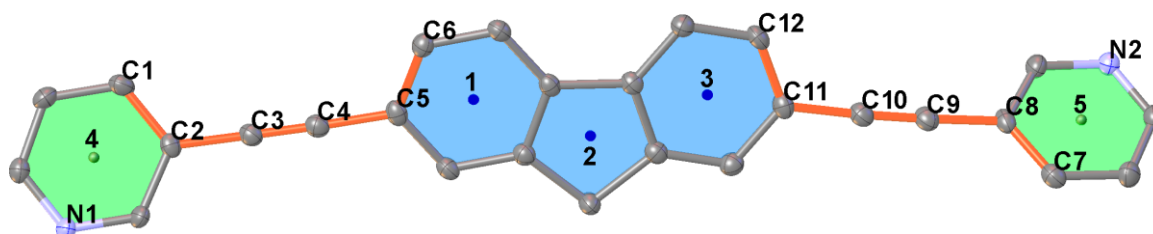
3		$(\mathbf{2}\cdot\mathbf{L5}\cdot\mathbf{CHCl}_3)_\infty$		$(\mathbf{3}\cdot\mathbf{L5})_\infty$	
Cd1–S1	2.6417(5)	Cd1–S1	2.7984(10)	Cd1–S1	2.6908(7)
Cd1–S2	2.5246(5)	Cd1–S2	2.6698(10)	Cd1–S2	2.7271(6)
Cd1–S3	2.5508(5)	Cd1–S3	2.7666(10)	Cd1–S3	2.6784(7)
Cd1–S4	2.5402(5)	Cd1–S4	2.6244(10)	Cd1–S4	2.6875(6)
		Cd1–N1	2.400(3)	Cd1–N1	2.3613(19)
		Cd1–N2 ²	2.434(3)	Cd1–N2 ³	2.454(2)
P1–S1	2.0030(6)	P1–S1	1.9809(13)	P1–S1	2.0063(9)
P1–S2	2.0216(6)	P1–S2	1.9980(14)	P1–S2	1.9891(9)
P2–S3	2.0174(6)	P2–S3	1.9924(14)	P2–S3	2.0032(9)
P2–S4 ¹	2.0036(6)	P2–S4	2.0019(14)	P2–S4	1.9987(9)
P1–O1	1.5959(13)	P1–O1	1.616(3)	P1–O1	1.6009(17)
P2–O3	1.5913(13)	P2–O3	1.608(3)	P2–O2	1.6009(18)
P1–C3	1.7908(18)	P1–C3	1.795(4)	P1–C5	1.802(2)
P2–C12	1.7872(18)	P2–C10	1.803(4)	P2–C12	1.796(2)
S1–Cd1–S2	79.670(15)	S1–Cd1–S2	74.88(3)	S1–Cd1–S2	74.452(19)
S3–Cd1–S4	100.100(16)	S3–Cd1–S4	76.17(3)	S3–Cd1–S4	74.401(19)
		N1–Cd1–N2 ²	81.73(11)	N1–Cd1–N2 ³	79.57(7)
S1–P1–S2	110.69(3)	S1–P1–S2	113.41(6)	S1–P1–S2	110.25(7)
S3–P2–S4 ¹	112.86(3)	S3–P2–S4	112.82(6)	S3–P2–S4	112.03(4)
O1–P1–C3	97.95(7)	O1–P1–C3	103.13(16)	O1–P1–C5	99.05(10)
O3–P2–C12	99.50(7)	O2–P2–C10	99.92(15)	O2–P2–C12	109.60(7)

Symmetry codes: ¹ -x, -y, -z+1; ² -1+x, 1-y, -3/2+z; ³ 1+x, 3/2-y, 3/2+z.

The lack of solvent molecules co-crystallized in the structure of $(\mathbf{3}\cdot\mathbf{L5})_{\infty}$ can be likely attributed to the bulkier ethoxy substituent compared to the methoxy groups found in $(\mathbf{2}\cdot\mathbf{L5}\cdot\mathbf{CHCl}_3)_{\infty}$.

A comparison between the structure of the free spacer $\mathbf{L5}$ and that of the CPs $(\mathbf{2}\cdot\mathbf{L5}\cdot\mathbf{CHCl}_3)_{\infty}$ and $(\mathbf{3}\cdot\mathbf{L5})_{\infty}$, shows a flexibility of the ligand and a consequent structural adaptability as demonstrated by the dihedral angles reported in Table 13.

Table 13 Geometrical features including angles, dihedral angles ($^{\circ}$) and distances (\AA) of $\mathbf{L5}$ molecules in the crystal structures of $\mathbf{L5}$, $(\mathbf{2}\cdot\mathbf{L5}\cdot\mathbf{CHCl}_3)_{\infty}$ and $(\mathbf{3}\cdot\mathbf{L5})_{\infty}$. Centroids and planes are identified by numbers (1-5) and letters (a-e), respectively. Atoms have been renumbered for clarity reasons accordingly to the molecular structure given below.



	$\mathbf{L5}$	$(\mathbf{2}\cdot\mathbf{L5}\cdot\mathbf{CHCl}_3)_{\infty}$	$(\mathbf{3}\cdot\mathbf{L5})_{\infty}$
1-2-3	142.95	142.64	142.16
4-2-5	169.74	169.28	170.50
4-1-3-5	29.62	7.74	18.71
a-c	2.00	7.64	7.77
a-d	55.67	34.18	29.37
c-e	55.67	60.24	54.97
d-e	107.95	33.00	31.57
C2-C3-C4	179.27	177.32	178.13
C5-C4-C3	177.45	176.50	177.89
C8-C9-C10	179.27	177.27	178.03
C11-C10-C9	177.45	178.06	177.22
C1-C2-C5-C6	53.54	32.28	28.427
C1-C2-C8-C7	127.95	161.97	160.61
C7-C8-C11-C12	53.54	119.33	124.647
$d_{\text{N1-N2}}$	18.721	18.956	18.935

In addition to the structural XRD analysis, the CPs were characterized by means of elemental analysis, FT-IR (Figures S80 and S81) and optical spectroscopies. The FT-IR spectra of $(\mathbf{2}\cdot\mathbf{L5}\cdot\mathbf{CHCl}_3)_{\infty}$ and $(\mathbf{3}\cdot\mathbf{L5})_{\infty}$ show the alkyne stretching falling at 2206 and 2010 cm^{-1} ,

respectively, at values similar to that of 2208 cm^{-1} observed for the free ligand. These is in line with the lack of significant changes in the $\text{C}\equiv\text{C}$ distance found in structural characterizations of the free linker and the relevant CPs. The solid-state absorption and emission spectra of $(\mathbf{2}\cdot\mathbf{L5}\cdot\text{CHCl}_3)_\infty$ and $(\mathbf{3}\cdot\mathbf{L5})_\infty$ are shown in Figure 76. Both CPs feature a strong absorption in the UV region, similarly to $\mathbf{L5}$, as showed by the diffuse reflectance measurements with maximum at 400 and 350 nm for $(\mathbf{2}\cdot\mathbf{L5}\cdot\text{CHCl}_3)_\infty$ and $(\mathbf{3}\cdot\mathbf{L5})_\infty$, respectively. The absorption spectrum for the free linker is shown as dashed black line in Figure 76 for the sake of comparison. The luminescence emission spectra in the solid state feature slightly broader emission curves if compared with the luminescence properties of the starting material ($\lambda_{\text{max}} = 512\text{ nm}$). Similarly to $\mathbf{L5}$, the spectra for $(\mathbf{2}\cdot\mathbf{L5}\cdot\text{CHCl}_3)_\infty$ and $(\mathbf{3}\cdot\mathbf{L5})_\infty$ feature a maximum centred at 512 and 526 nm, respectively. In addition, we observed the comparison of a more energetic band, but with lower intensity, centred at 408 and 423 nm for $(\mathbf{2}\cdot\mathbf{L5}\cdot\text{CHCl}_3)_\infty$ and $(\mathbf{3}\cdot\mathbf{L5})_\infty$.

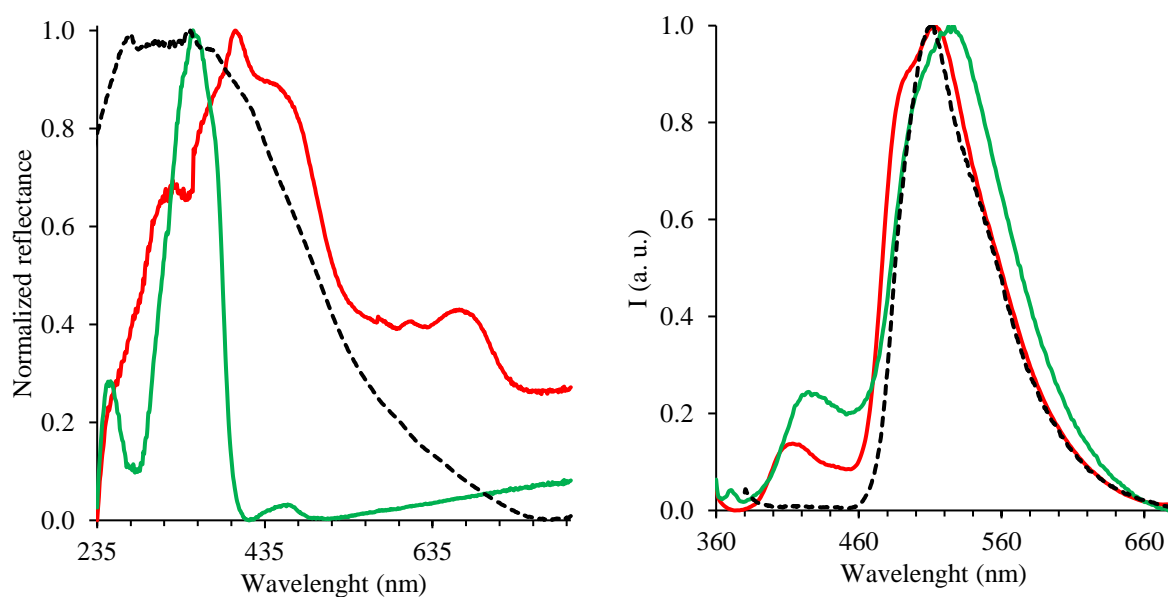
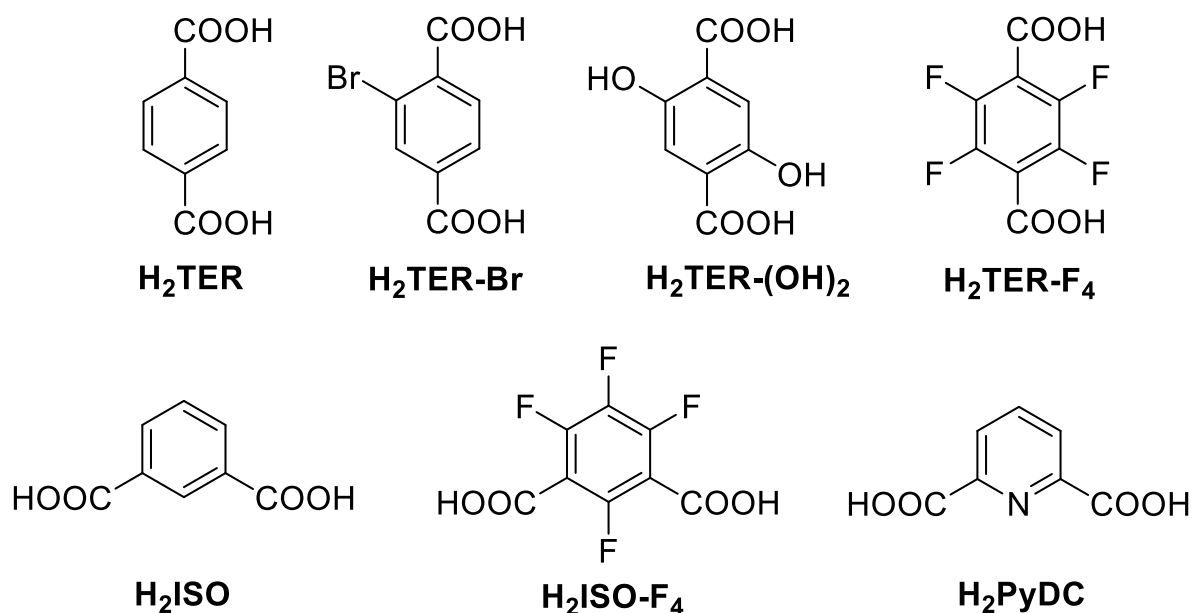


Figure 76 Diffuse reflectance (left) and solid state emission spectra (right) for $(\mathbf{2}\cdot\mathbf{L5}\cdot\text{CHCl}_3)_\infty$ (red), $(\mathbf{3}\cdot\mathbf{L5})_\infty$ (green) and $\mathbf{L5}$ (dashed black) ($\lambda_{\text{ex}} = 350 - 370\text{ nm}$).

3.1.2. Interaction between N-donors and carboxylic acids

In order to investigate the formation of HOFs starting from the synthesized N-donors, we carried out a preliminary study based on the reaction of **L1** and **L2** and **L7** and **L8** with differently substituted benzenedicarboxylic acids. The choice of **L1** and **L2** and which feature *meta*- and *para*-substitution at pyridyl rings aimed to explore different orientations and conformations of the linker, in the attempt of rationalizing the type and number of networks that can be possibly formed. **L7** and **L8** present a very similar conformation but longer lengths. As acidic complementary synthons, we decided to use the commercially available benzenedicarboxylic organic acids summarized in Scheme 19.



Scheme 19 Organic benzenedicarboxylic acids used for the formation of co-crystals. Terephthalic acid (**H₂TER**), 2-bromoterephthalic acid (**H₂TER-Br**), 2,5-dihydroxyterephthalic acid (**H₂TER-(OH)₂**), tetrafluoroterephthalic acid (**H₂TER-F₄**), isophthalic acid (**H₂ISO**), tetrafluoroisophthalic acid (**H₂ISO-F₄**), 2,5-pyridinedicarboxylic acid (**H₂PyDC**).

Before discussing the obtained results, an important point should be pointed out regarding the nature of the products obtained by reacting di-pyridine-based and di-carboxylate-based substrates. When organic bases are reacted with organic acids, if the resulting compounds remain neutral they are referred to as co-crystals.^[208] If the components undergo an intermolecular proton transfer between the complementary acid and basic functional groups, the resulting product is a molecular salt.^[208] Recently, Lemmerer *et al.* reported the difference in pK_a values of the acid and basic functional groups as a criterion to obtain an indication on the nature of the outcoming product.^[376] The criterion is based on the so-called “rule of 3” stating that for ΔpK_a differences (calculated between the pK_a of the protonated base and that of

the acid) around zero or less than zero a co-crystal forms containing the components in their neutral states, for ΔpK_a values greater than three, a molecular salt forms containing the components in their charged form (i.e. a protonated base and a deprotonated acid).^[377] For values between zero and three the resulting product is governed by the variety of intermolecular interactions that can drive to a predominance of one of the two limit cases or allows for a co-existence of both species within the crystal.^[376] In the case of molecules containing two basic and two acid functional groups the exact nature of the final product is complicated by the fact that only one of them can undergo proton transfer, and that molecules protonated either on one or on the other nitrogen can be indiscriminately present in the crystal. A clear discerning of the nature of the product can come only from very high-quality crystals that allow for the detection of the electron density of the relevant protons and then clarify their position either on the basic or on the acidic functional group of the interacting molecules. Unfortunately, the SC-XRD analysis of the crystals here discussed did not allow for an experimental detection of the proton and the refinement performed on freely hydrogen atoms did not properly converge. We then decided to calculate the ΔpK_a differences between the pK_a of the protonated base **HL1**⁺ and **HL2**⁺ and that of the organic benzenedicarboxylic acids, obtained using the SCI-finder Advanced Chemistry Development (ACD/Labs) Software V11.02 (© 1994-2021 ACD/Labs). The calculated pK_a values for the protonated bases and of the benzenedicarboxylic acids are reported in the first column and in the first row of Table 14, respectively. The values in the crossing cells report the corresponding ΔpK_a .

Table 14 Predicted pK_a values for the selected substrates.

Compound	pK_a	H₂TER	H₂TERBr	H₂TER(OH)₂	H₂TERF₄	H₂ISO	H₂ISOF₄	H₂PyDC
pK_a		3.49±0.10	2.44±0.10	2.17±0.10	0.95±0.10	3.53±0.10	1.27±0.10	2.97±0.10
HL1 ⁺	2.07±0.12	-1.42	-0.37	-0.1	1.12	-1.46	0.8	-0.9
HL2 ⁺	1.51±0.10	-1.98	-0.93	-0.66	0.56	-2.02	0.24	-1.46

The pK_a values of 2.07 and 1.51 reported for **HL1**⁺ and **HL2**⁺ are quite lower than that of 5.2 reported for the free pyridinium cation, and this implies ΔpK_a values either negative or very close to zero, that moved us to refine the structures as co-crystals between interacting neutral molecules adding the hydrogen atoms at the carboxylic groups in calculated positions and refining them using the riding model.

3.1.2.1. Interaction between L1 and L2 with carboxylic acids

The N-donors **L1** and **L2** and the benzenedicarboxylic acids were reacted in ethanolic solution in a 1:1 ratio and stirred at room temperature for 24-72 h leading to solid products that were filtered and dried at 60 °C for overnight. The products were analysed by means of elemental analysis and FT-IR spectroscopy. The elemental analyses were in good agreement with the 1:1 ratio expected due to the presence of the same number of binding sites on the donor and the acceptor substrates. The spectroscopic characterizations of the products are reported in the experimental section (§5) and the relevant spectra given as supplementary materials within Appendix 2: FT-IR spectra. It is interesting to note that for all compounds a broad IR absorption band was found in the region 2600-2200 cm⁻¹, often centred at around 2400 cm⁻¹, assigned to the stretching of hydrogen bonded OH fragments, that confirms a co-crystals nature for the obtained products. Although **L1** and **L2** were reacted with all the seven carboxylic acids presented in Scheme 19, only the structurally characterized products will be discussed here (crystal data and refinement parameters in Table 16). The reactions performed starting from **L1** yielded products unsuitable for structural characterization by means of SC-XRD analyses with the only exception of the co-crystal (**L1**·**H₂TER**)_∞ formed from the self-assembly of **L1** and **H₂TER**. The obtained data are here compared with those of the hydrate chloride salt **HL1Cl**·**3H₂O** serendipitously obtained while investigating the reactivity of **L1** towards H₂AuCl₄. The reactions starting from the *para*-substituted analogue **L2**, yielded crystalline 1:1 co-crystals with five of the selected carboxylic acids namely (**L2**·**H₂TER-Br**)_∞, (**L2**·**H₂TER-(OH)₂**)_∞, (**L2**·**H₂ISO**)_∞, (**L2**·**H₂ISO-F₄**)_∞, (**L2**·**H₂PyDC**)_∞. Poor quality crystals were obtained from the reaction of **L2** with **H₂TER**, that allowed to clarify only the 1:1 connectivity, without producing a full structural characterization. It is interesting to note that the reaction between ethanolic solution of **L2** and **H₂TER-F₄**, corresponding to the highest ΔpK_a difference among those examined for **L2**, caused the instantaneous precipitation of a white solid, which we were unable to recrystallize into single crystals.

The reaction of **L1** towards H₂AuCl₄ in acetonitrile serendipitously yielded **HL1Cl**·**3H₂O** that crystallize in a monoclinic lattice within the centrosymmetric space group *I2/a*. The asymmetric unit contains one protonated **HL1**⁺ unit, a chloride anion, and three co-crystallized water molecules (Figure 77). **HL1**⁺ is arranged in the antiperiplanar conformation with a N10–N16 distance of 8.896(3) Å and the pyridyl rings slightly tilted with an angle of 11.26(8) °.

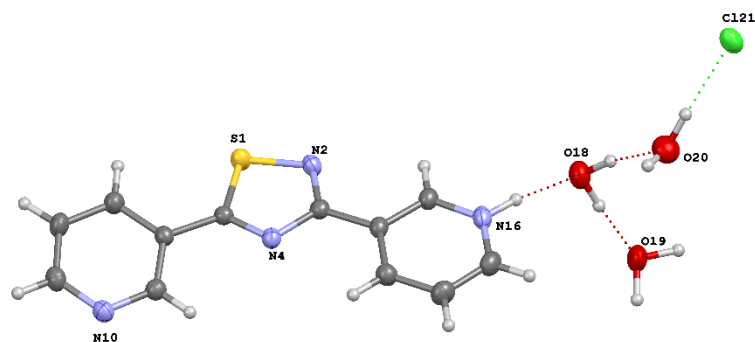


Figure 77 Asymmetric unit in the crystal structure of **HL1Cl·3H₂O**. Thermal ellipsoids are drawn at 50 % probability level.

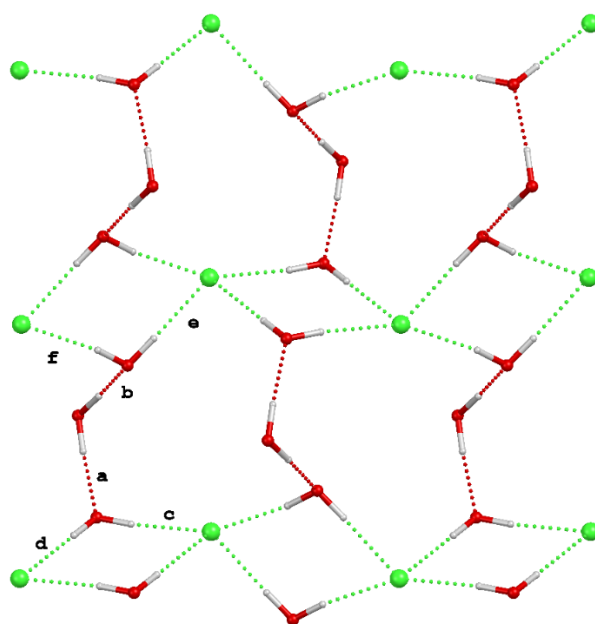


Figure 78 View along the *c* axis of the hydrogen bonded network built upon the interactions between water molecules with chloride anions. Interactions are labelled according to Table 15.

Table 15 Hydrogen bonding in the crystal structure of **HL1Cl·3H₂O**.

Interaction	D	H	A	$d_{D...A}$ (Å)	$d_{H...A}$ (Å)	D-H...A (°)
a	O18	H18A	O19	2.767(3)	1.799(15)	176(3)
b	O18	H18B	O20	2.729(3)	1.77(3)	169(3)
c	O19	H19A	Cl21 ³	3.199(2)	2.237(15)	175(2)
d	O19	H19B	Cl21 ²	3.231(2)	2.26(3)	178(3)
e	O20	H20A	Cl21	3.132(2)	2.17(2)	175(3)
f	O20	H20B	Cl21 ¹	3.202(2)	2.24(2)	170(2)
g	C17	H17	N10	3.247(2)	2.33(2)	162.49(8)
h	N16	H16	O18	2.665(2)	1.72(2)	173.47(9)

Symmetry codes: ¹ 1/2-x,3/2-y,3/2-z; ² 1-x,1/2+y,3/2-z; ³ 1/2+x,2-y,+z.

The co-crystallized water molecules and the chloride anions are involved in the hydrogen bonding network shown in Figure 78 where each chloride anion is surrounded by four water molecules arranged into two main cyclic patterns: concatenated rhombic $R_4^2(8)$ motifs formed by couples of water molecules bridging pairs of chloride anions in extended bidimensional ribbons, and a second more complex $R_7^7(16)$ pattern ensuing from two additional water molecules bridging the above described ribbons (Figure 78). **HL1**⁺ units interact through the abovementioned hydrogen bonded pattern by interactions **g** and **h** (Table 15, Figure 79)

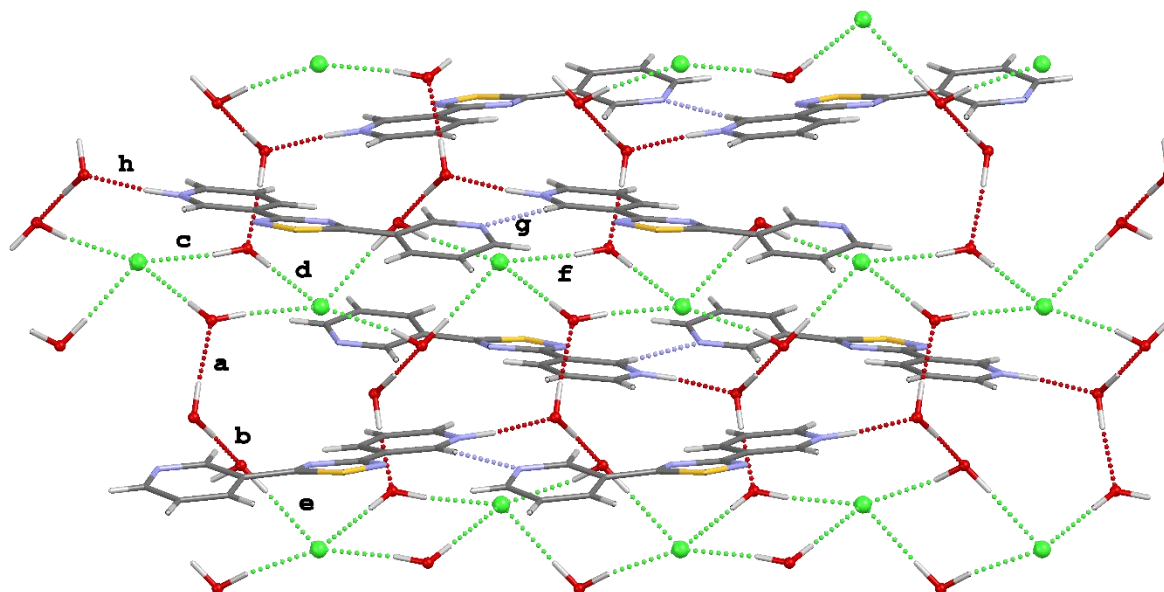


Figure 79 Packing diagram of **HL1Cl·3H₂O** along the *c* axis. Interactions are labelled according to Table 15.

Table 16 Crystal data and refinement parameters for **HL1Cl·3H₂O**, **(L1·H₂TER)_∞**, **(L2·H₂TER-Br)_∞**, **(L2·H₂TER-(OH)₂)_∞**, **(L2·H₂ISO)_∞**, **(L2·H₂ISO-F₄)_∞**, **(L2·H₂PyDC)_∞**.

Compound	HL1Cl·3H ₂ O	(L1·H ₂ TER) _∞	(L2·H ₂ TER-(OH) ₂) _∞	(L2·H ₂ TER-Br) _∞	(L2·H ₂ ISO) _∞	(L2·H ₂ ISO-F ₄) _∞	(L2·H ₂ PyDC) _∞
Formula	C ₁₂ H ₁₅ ClN ₄ SO ₃	C ₂₀ H ₁₄ N ₄ O ₄ S	C ₂₀ H ₁₄ N ₄ O ₆ S	C ₂₀ H ₁₃ BrN ₄ O ₄ S	C ₂₀ H ₁₄ N ₄ O ₄ S	C ₂₀ H ₁₀ F ₄ N ₄ O ₄ S	C ₁₉ H ₁₃ N ₅ O ₄ S
<i>D</i> _{calc.} / g cm ⁻³	1.451	1.516	1.556	1.695	1.516	1.689	1.568
<i>μ</i> /mm ⁻¹	0.405	1.951	0.223	4.309	0.220	0.251	2.032
Formula Weight	330.79	406.41	438.41	485.31	406.41	478.38	407.40
Colour	colourless	colourless	yellow	colourless	colourless	colourless	colourless
Shape	prism	prism	prism	block	prism	prism	needles
Size/mm ³	0.16×0.15×0.10	0.18×0.06×0.06	0.22×0.05×0.05	0.18×0.17×0.05	0.21×0.12×0.03	0.06×0.06×0.03	0.36×0.09×0.04
<i>T</i> /K	173(2)	173(2)	173(2)	100(2)	173(2)	173(2)	173(2)
Crystal System	monoclinic	triclinic	monoclinic	monoclinic	triclinic	orthorhombic	monoclinic
Flack Parameter						-0.07(4)	
Hooft Parameter						-0.06(3)	
Space Group	<i>I</i> 2/ <i>a</i>	<i>P</i> -1	<i>C</i> 2/ <i>c</i>	<i>C</i> 2/ <i>c</i>	<i>P</i> -1	<i>P</i> 2 ₁ 2 ₁ 2 ₁	<i>P</i> 2 ₁ / <i>c</i>
<i>a</i> /Å	13.1842(14)	7.0329(2)	13.756(4)	14.8521(3)	6.95291(13)	6.4480(8)	6.5965(2)
<i>b</i> /Å	9.7907(9)	16.1567(6)	12.644(3)	6.8512(2)	7.25352(17)	14.3873(19)	19.8417(6)
<i>c</i> /Å	23.562(2)	16.5449(5)	10.932(3)	37.6513(8)	19.8242(4)	20.277(3)	13.1943(6)
<i>α</i> /°	90.0000	102.923(3)	90	90	92.6045(18)	90	90
<i>β</i> /°	95.224(9)	98.139(3)	100.220(14)	96.909(2)	92.0422(16)	90	92.362(3)
<i>γ</i> /°	90.0000	98.705(3)	90	90	116.710(2)	90	90
<i>V</i> /Å ³	3028.8(5)	1780.97(10)	1871.2(9)	3803.38(16)	890.42(4)	1881.1(4)	1725.49(11)
<i>Z</i>	8	4	4	8	2	4	4
<i>Z</i> '	1	2	0.5	1	1	1	1
Wavelength/Å	0.71075	1.54184	0.71075	1.54178	0.71075	0.71075	1.54178
Radiation type	MoK _α	CuK _α	MoK _α	CuK _α	MoK _α	MoK _α	CuK _α
<i>θ</i> _{min} /°	1.736	2.787	2.204	4.732	2.061	1.736	4.026
<i>θ</i> _{max} /°	31.856	68.304	25.459	68.242	28.199	25.375	73.360
Measured Refl's.	18544	18676	8145	17245	26500	12009	5640
Indep't Refl's	5001	6341	1733	3481	3861	3417	3326
Refl's I≥2 <i>σ</i> (I)	2787	5517	1257	3321	3418	3219	2330
<i>R</i> _{int}	0.0807	0.0336	0.1002	0.0522	0.0334	0.0296	0.0399
Parameters	218	565	172	412	283	323	284
Restraints	10	28	1	36	125	10	17
Largest Peak	0.40	0.252	0.194	0.606	0.267	0.178	0.248
Deepest Hole	-0.33	-0.292	-0.173	-0.455	-0.264	-0.183	-0.220
GooF	1.014	1.082	1.043	1.138	1.140	1.071	1.044
<i>wR</i> ₂ (all data)	0.1372	0.1130	0.0976	0.2088	0.1149	0.0692	0.1469
<i>wR</i> ₂	0.1104	0.1093	0.0857	0.2077	0.1120	0.0678	0.1264
<i>R</i> ₁ (all data)	0.1412	0.0477	0.0645	0.0854	0.0488	0.0332	0.0780
<i>R</i> ₁	0.0616	0.0415	0.0383	0.0836	0.0425	0.0299	0.0513

The reaction between **L1** and **H₂TER** in ethanol yielded colourless crystals upon slow evaporation of the solvent. SC-XRD analysis revealed the formation of a 1:1 co-crystal corresponding to formula **(L1·H₂TER)_∞** crystallized in the triclinic space group *P*-1 with two crystallographically independent molecules of **L1** and **H₂TER** in the asymmetric unit (Figure 80).

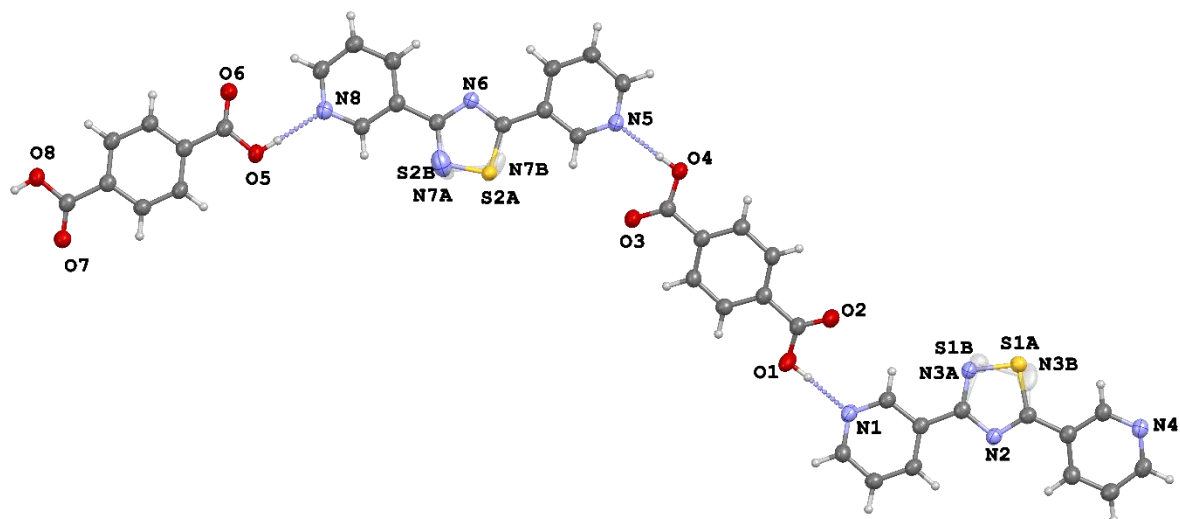


Figure 80 Asymmetric unit and atom numbering scheme for **(L1·H₂TER)_∞**.

The N-donors are arranged along a periplanar conformation with N–N distances of 9.629(2) and 9.641(2) Å, for N1–N4 and N5–N8, respectively. The pyridyl rings are almost coplanar in one case and slightly tilted in the other, with angles of 1.49(6) and 16.26(6) ° for Py3[^]Py4 and Py1[^]Py2, respectively. The angles between different planes in **(L1·H₂TER)_∞** are summarized in Table 17.

Table 17 Angles (°) between different planes in the crystal structure of **(L1·H₂TER)_∞**.

Py1 [^] Py2	16.26(6)	Py1 [^] Ph1	18.93(6)	Py2 ^{1^} Ph2	16.91(6)
Py3 [^] Py4	1.49(6)	Py3 [^] Ph1	17.26(6)	Py4 [^] Ph2	2.28(5)

Py1: N1-C1-C2-C3-C4-C5; Py2: N4-C8-C9-C10-C11-C12; Py3: N5-C21-C22-C23-C24-C25; Py4: N8-C28-C29-C30-C31; Ph1: C14-C15-C16-C17-C18-C19; Ph2: C34-C35-C36-C3-C38-C39. Symmetry code: 1 +x, -2+y, 1+z.

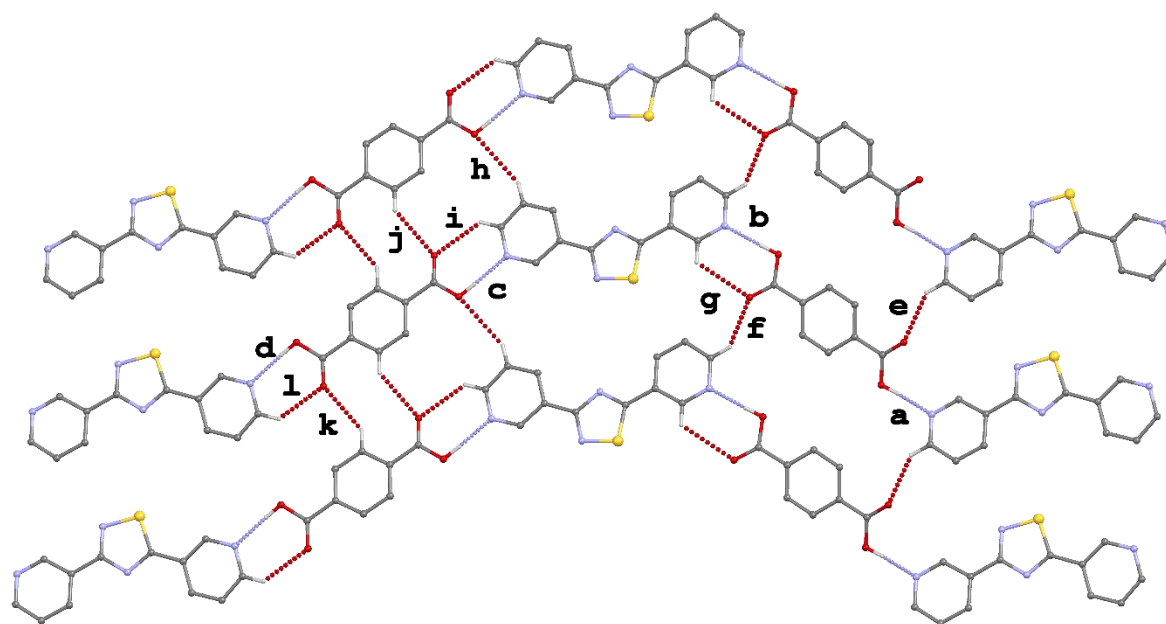
The thiadiazol rings are disordered and were modelled over two positions with partial occupancies 68:32 and 85:15 using RIGU, SIMU and SADI restraints. The dipyridyl derivatives are bridged by **H₂TER** units resulting in undulated polymeric 1D chains held together by strong hydrogen bonds (interactions **a-d** in Table 18, Figure 81).

Table 18 Intermolecular hydrogen bonding found in $(\mathbf{L1}\cdot\mathbf{H2TER})_\infty$

Interaction	D	H	A	$d_{D\cdots A}$ (Å)	$d_{H\cdots A}$ (Å)	D-H \cdots A (°)
a	O1	H1A	N1	2.654(2)	1.815(14)	175.68(11)
b	O4	H4	N5	2.660(2)	1.826(14)	172.06(10)
c	O5	H5A	N8	2.694(2)	1.854(15)	177.73(10)
d	O8	H8	N4 ¹	2.706(2)	1.874(14)	170.11(10)
e	C1 ¹	H1 ¹	O2	3.165(2)	2.377(14)	140.04(11)
f	C21 ²	H21 ²	O3	3.090(2)	2.312(14)	138.67(12)
g	C25	H25	O3	3.334(2)	2.734(13)	121.78(11)
h	C30	H30	O5 ¹	3.655(2)	2.819(12)	147.27(12)
i	C31	H31	O6	3.140(2)	2.453(13)	129.17(12)
j	C38 ¹	H38 ¹	O6	3.329(2)	2.572(14)	136.85(11)
k	C35 ²	H35 ²	O7	3.268(2)	2.494(13)	138.71(11)
l	C11 ²	H11 ²	O7 ¹	3.151(2)	2.443(13)	131.20(12)

Symmetry codes: ¹ +x, -2+y, 1+z; ² 1+x, +y, +z.

Adjacent chains interact through weaker hydrogen bonds (interactions **e-l** in Table 18, Figure 81) forming undulated 2D sheets running parallel to the *a* vector.

**Figure 81** View of the intermolecular hydrogen bonding in $(\mathbf{L1}\cdot\mathbf{H2TER})_\infty$ along the [111] direction. Interactions are labelled according to Table 18. Disorder at thiadiazol ring is not shown for clarity.

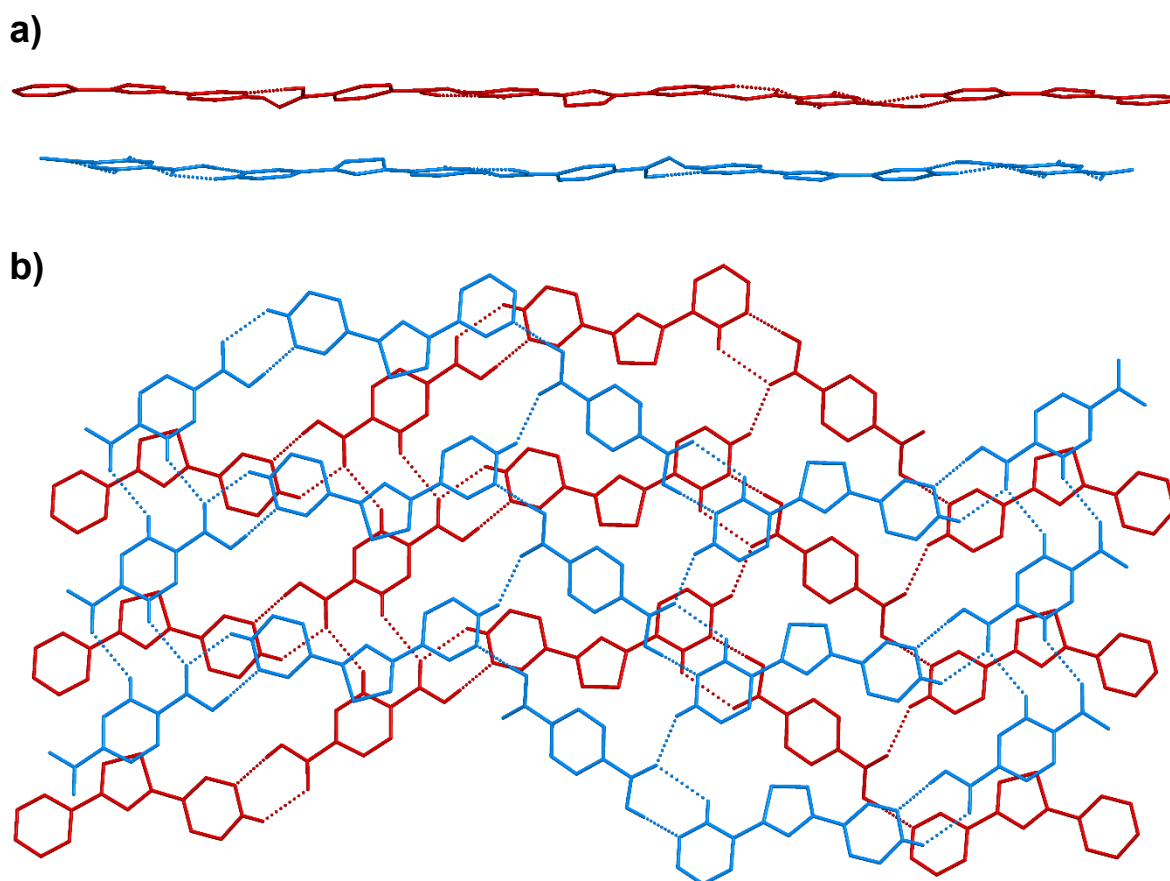


Figure 82 Packing diagrams views of $(\mathbf{L1}\cdot\mathbf{H2TER})_{\infty}$ showing a) hydrogen bonded sheets running parallel to the a axis; b) overlapped sheets along the $[111]$ direction.

The same reaction performed starting from **L2** and **H₂TER** yielded poor quality crystals identified as the 1:1 co-crystal $(\mathbf{L2}\cdot\mathbf{H2TER})_{\infty}$. The connectivity observed strongly resembles what found for the analogue $(\mathbf{L1}\cdot\mathbf{H2TER})_{\infty}$ except for the undulation of the layered structure which is governed by the geometrical differences between **L1** and **L2** producing an almost linear polymeric network.

Recrystallization of the reaction product between **L2** and **H₂TER-Br** in ethanol produced colourless blocks corresponding to 1:1 co-crystals with formula $(\mathbf{L2}\cdot\mathbf{H2TER-Br})_{\infty}$, that crystallizes in the $C2/c$ space group, with one **L2** and one **H₂TER-Br** molecule in the asymmetric unit (Figure 83).

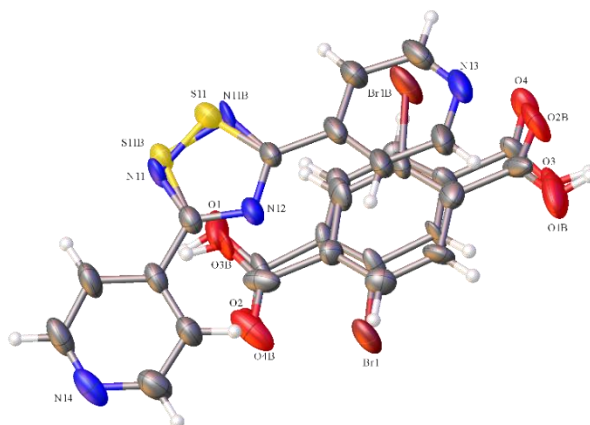


Figure 83 Asymmetric unit and atom labelling scheme for $(\mathbf{L2}\cdot\mathbf{H2TER}\text{-}\mathbf{Br})_{\infty}$. Thermal ellipsoids are drawn at 50 % probability level.

Within the crystal, disorder was found both on the carboxylic building block $\mathbf{H2TER}\text{-}\mathbf{Br}$ and the thiadiazol fragment that were modelled using a number of SADI restraints over two positions with fractional occupancies of 56:44 and 59:41, respectively. The N13–N14 distance is 10.063(2) Å and the angle between pyridyl rings is about 18.23(19) °. The building blocks are connected through $\text{N}\cdots\text{H}\text{-}\text{O}$ H-bonds and are arranged into polymeric chains running perpendicular to the *b* axis (interactions **a** and **b** in Table 19, Figure 84).

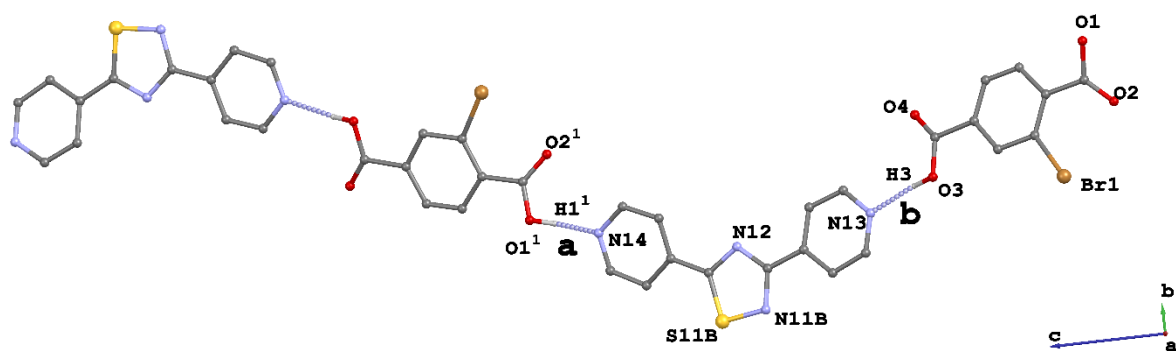


Figure 84 View of the polymeric hydrogen bonded network in $(\mathbf{L2}\cdot\mathbf{H2TER}\text{-}\mathbf{Br})_{\infty}$ along the [100] direction. Interactions are labelled according to Table 19.

Table 19 Intermolecular hydrogen bonding found in $(\mathbf{L2}\cdot\mathbf{H2TER}\text{-}\mathbf{Br})_{\infty}$

Interaction	D	H	A	$d_{\text{D}\cdots\text{A}}$ (Å)	$d_{\text{H}\cdots\text{A}}$ (Å)	D–H \cdots A (°)
a	O1 ¹	H1 ¹	N14	2.59(2)	1.804(5)	154.8(19)
b	O3	H3	N13	2.612(13)	1.798(5)	162.7(9)
c	C15 ²	H15 ²	O4	3.316(14)	2.493(12)	145.0(5)
d	C6 ³	H6 ³	Br1	3.680(12)	2.870(11)	144.0(7)
e	C21 ⁴	H21 ⁴	Br1	3.749(6)	2.983(8)	138.7(4)

Symmetry codes: ¹ $-1/2+x, 3/2-y, 1/2+z$; ² $+x, 1+y, +z$; ³ $+x, -1+y, +z$; ⁴ $1/2+x, 1/2-y, -1/2+z$.

Adjacent chains pack along the *b* axis resulting in 2D-sheets stabilized by weak hydrogen bonds between the double bonded O4 atom and the pyridyl fragment C15-H15 and weak interactions between the Br atom and aromatic protons from both pyridyl and benzene rings of adjacent molecules (interactions **a-e** in Figure 89). Different layers interact by means of intermolecular π - π interactions between pyridyl and phenyl rings as shown in Figure 86.

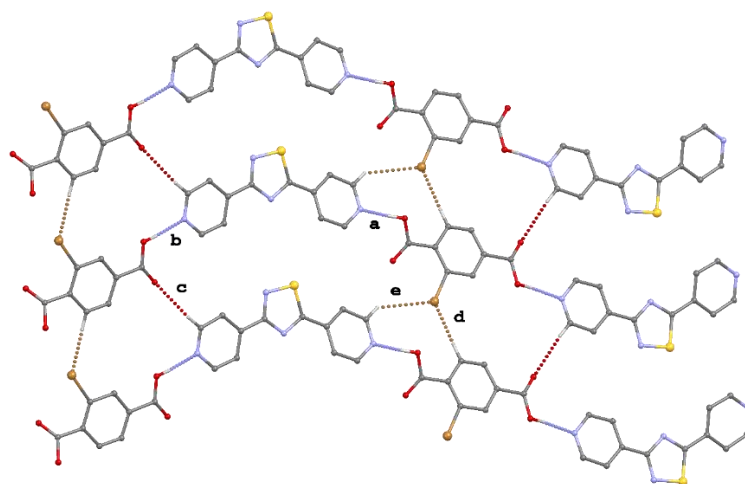


Figure 85 View of intermolecular interactions in the co-crystal $(\text{L2}\cdot\text{H}_2\text{TER}\cdot\text{Br})_\infty$ along the *a* axis according to Table 19.

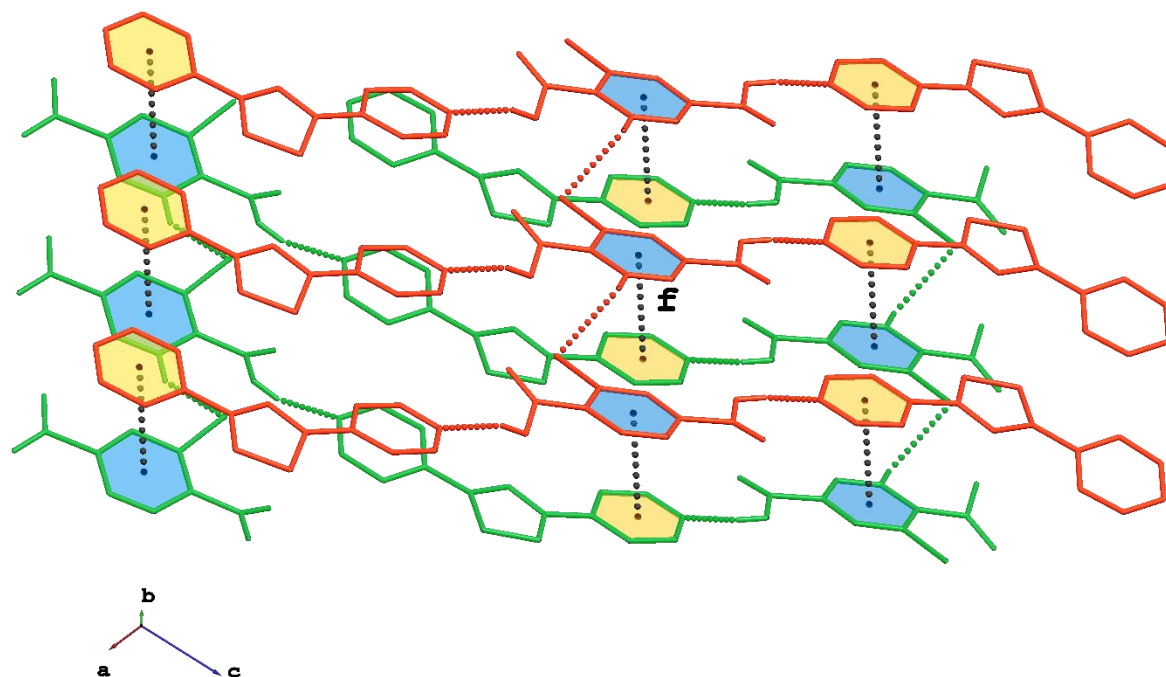


Figure 86 Intermolecular π - π interaction in $(\text{L2}\cdot\text{H}_2\text{TER}\cdot\text{Br})_\infty$: f) Py \cdots Ph (centroid-centroid distance: 3.765(5) Å; $\alpha = 3.5(5)^\circ$).

The reaction between **L2** and **H₂TER-(OH)₂** in ethanol produced the co-crystal **(L₂·H₂TER-(OH)₂)_∞**. The structural characterization on yellow prisms show that the product crystallizes in the monoclinic lattice within the centrosymmetric *C2/c* space group with *Z'* = 0.5 (Figure 87). The thiadiazol ring features positional disorder and the occupancy at S and N atoms was fixed to 0.5.

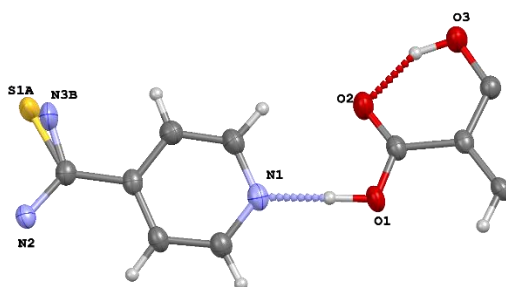


Figure 87 Asymmetric unit and atom labelling scheme for **(L₂·H₂TER-(OH)₂)_∞**. Thermal ellipsoids are drawn at 50 % probability level.

The linker features N1-N1¹ distance of 10.117(4) Å and Py¹Py¹ angle of 17.32(10) ° (¹1 -x, +y, 3/2-z), similarly to those found in the analogous with **H₂TER-Br**. As expected, **L₂** interact with **H₂TER-(OH)₂** via hydrogen bond (interaction **a** in Table 20, Figure 88) generating a polymeric 1D chain running along the *a* axis as shown in Figure 88.

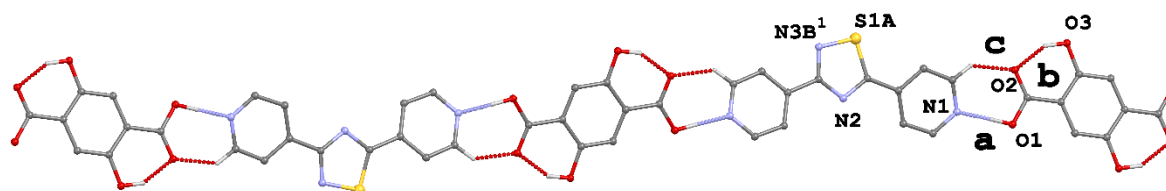


Figure 88 View along the *c* axis of a H-bonded polymeric chain in **(L₂·H₂TER-(OH)₂)_∞**. Symmetry code: ¹1 -x, +y, 3/2-z. Interactions are labelled according to Table 20.

The hydroxyl substituents in **H₂TER-(OH)₂** gave rise to intra- and inter-molecular hydrogen bonding that reinforce the chains and pack them in the *a* axis direction (interactions **b-d** in Table 20, Figure 89) in 2D layers where adjacent chains are slipped of about 9.2 Å.

Table 20 Intra- and intermolecular hydrogen bonding found in **(L₂·H₂TER-(OH)₂)_∞**

Interaction	D	H	A	d _{D...A} (Å)	d _{H...A} (Å)	D-H...A (°)
a	O1	H1A	N1	2.575(2)	1.605(18)	179(3)
b	O3	H3	O2	2.558(2)	1.68(3)	150(3)
c	C1	H1	O2	3.086(2)	2.34(2)	133.0(17)
d	C5 ²	H5 ²	O3 ¹	3.333(3)	2.59(2)	134.5(16)

Symmetry codes: ¹1 -x, +y, 3/2-z; ²-1/2-x, +1/2+y, -3/2-z.

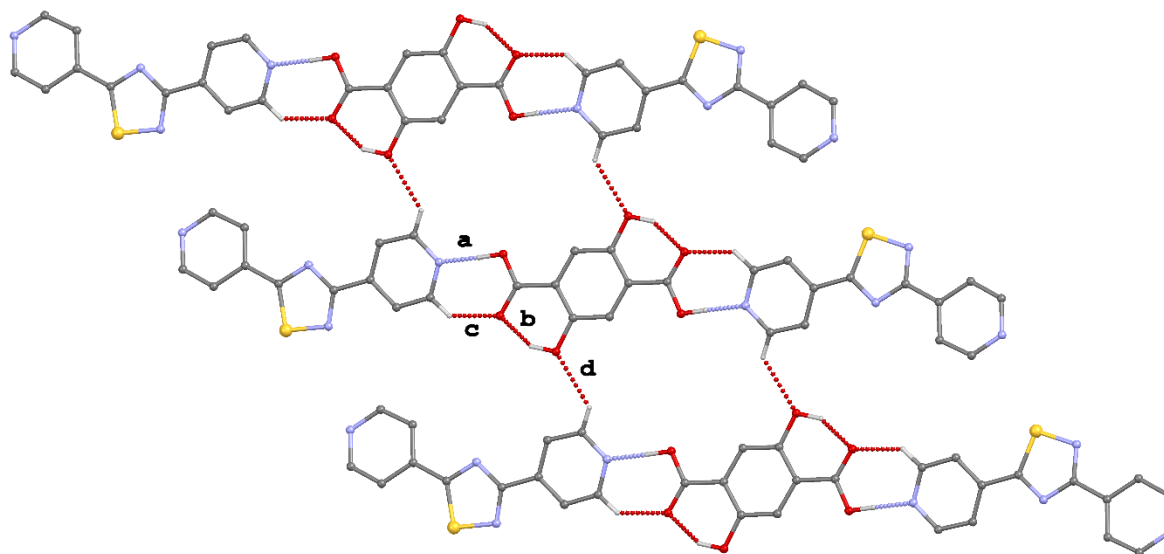


Figure 89 Intra- and intermolecular hydrogen bonding in $(\text{L2}\cdot\text{H}_2\text{TER}-(\text{OH})_2)_\infty$ labelled according to Table 20.

The layers are stabilized by intermolecular π - π stacking between pyridyl and phenyl rings as shown in Figure 90 (interactions **e** and **f**).

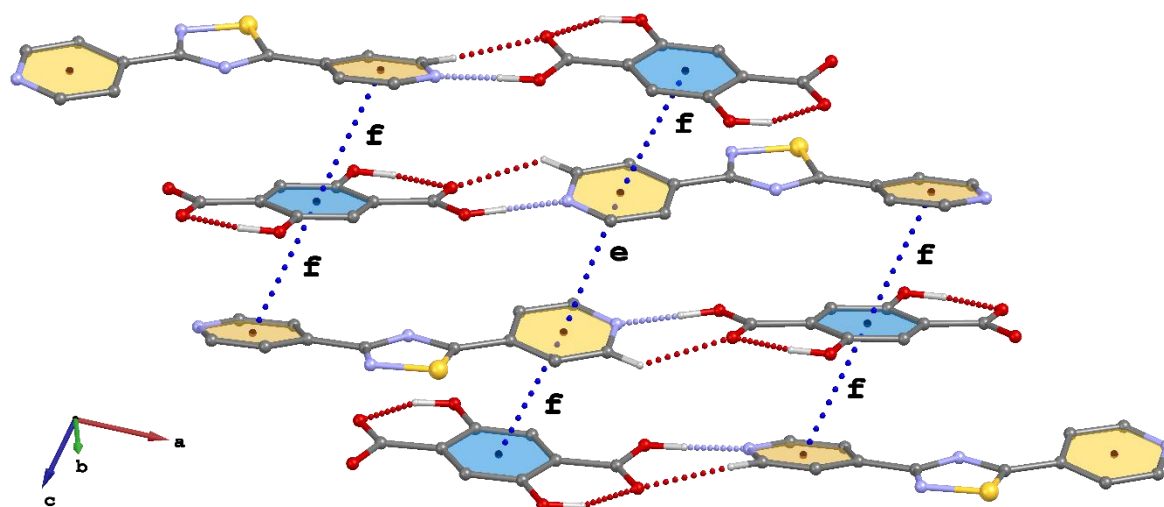


Figure 90 Intermolecular π - π interaction in $(\text{L2}\cdot\text{H}_2\text{TER}-(\text{OH})_2)_\infty$: **e**) $\text{Py}\cdots\text{Py}^1$ (centroid-centroid distance: 3.703(18) Å; $\alpha = 0^\circ$); **f**) $\text{Py}\cdots\text{Ph}^2$ (centroid-centroid distance: 3.652(12) Å; $\alpha = 3.67(8)^\circ$). Symmetry codes: ¹ $\frac{1}{2}-x, \frac{1}{2}-y, 1-z$; ² $1-x, +y, 2-z$.

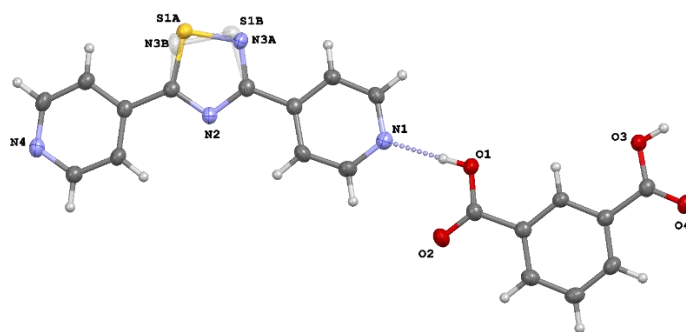
The bond distances and angles of the carboxylic groups in $(\text{L2}\cdot\text{H}_2\text{TER}-(\text{OH})_2)_\infty$ strongly resemble those found in the analogue co-crystal $(\text{L2}\cdot\text{H}_2\text{TER}-\text{Br})_\infty$ as summarized in Table 21.

Table 21 Bond lengths (Å) and angles (°) of the carboxylic groups in $(\mathbf{L2}\cdot\mathbf{H2TER}\cdot(\mathbf{OH})_2)_\infty$ and $(\mathbf{L2}\cdot\mathbf{H2TER}\cdot\mathbf{Br})_\infty$.

$(\mathbf{L2}\cdot\mathbf{H2TER}\cdot\mathbf{Br})_\infty$		$(\mathbf{L2}\cdot\mathbf{H2TER}\cdot(\mathbf{OH})_2)_\infty$	
O1–C7	1.30(2)	O1–C7	1.295(2)
O2–C7	1.220(2)	O2–C7	1.235(2)
O3–C8	1.305(17)	O1–C7–O2	123.56(17)
O4–C8	1.182(17)		
O1B–C7B	1.31(2)		
O2B–C7B	1.208(19)		
O3B–C8B	1.30(2)		
O4B–C8B	1.185(19)		
O1–C7–O2	124.5(13)		
O3–C8–O4	130.0(13)		
O1B–C7B–O2B	121.9(18)		
O3B–C8B–O4B	131.5(19)		

Reaction between **L2** and **H2ISO** in ethanol produced a white solid which was recrystallized in the same solvent yielding the co-crystal $(\mathbf{L2}\cdot\mathbf{H2ISO})_\infty$. The product crystallized in the triclinic space group *P*-1 with one **L2** and one **H2ISO** molecules in the asymmetric unit (Figure 91).

The thiadiazol ring is disordered and the pentatomic ring was modelled over two positions (fractional occupancy 67:33) using RIGU, SIMU and SADI restraints.

**Figure 91** View and atom labelling scheme of the asymmetric unit of $(\mathbf{L2}\cdot\mathbf{H2ISO})_\infty$. Thermal ellipsoids are drawn at 50 % probability level.

The N1–N4 distance is 10.06(19) Å and the pyridyl rings are tilted of about 9.63(6) °. The angles between the carboxylic groups and the phenyl ring in **H2ISO** are 1.30(7) and 4.90(7) °, respectively resulting in an overall almost planar geometry. The building blocks are engaged in strong hydrogen bonds between the pyridyl and the carboxylic acids generating an undulated 1D chain running along the *c* axis as shown in Figure 92 (interactions **a** and **b** in Table 22 and Figure 93). The angles between the phenyl and the pyridyl rings are 12.37(6) and 8.48(6) ° for Ph^{Py}1 and Ph^{Py}2, respectively.

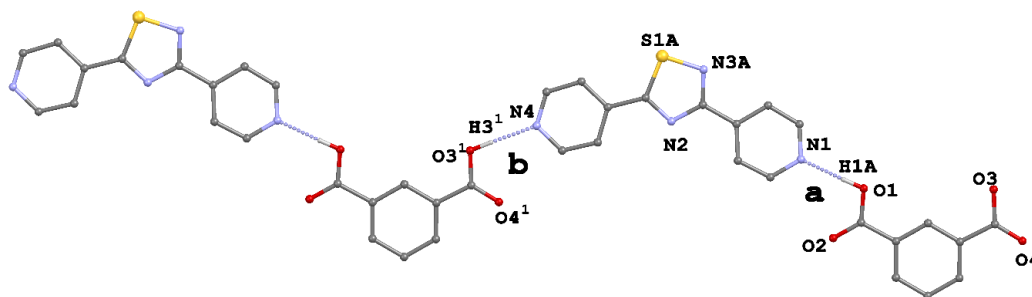


Figure 92 View of the hydrogen bonded undulated 1D chain in the co-crystal $(\mathbf{L2}\cdot\mathbf{H2ISO})_{\infty}$ along the b axis. Ph: C14-C15-16-C17-C18-C19; Py1: N1-C1-C2-C3-C4-C5; Py2: N4-C8-C9-C10-C11-C12. Interactions are labelled according to Table 22.

The crystal packing features undulated chains stacked along the a axis and stabilized by intermolecular hydrogen bonds as described in Table 22 and Figure 93 (interactions **c-e**).

Table 22 Intermolecular hydrogen bonding found in $(\mathbf{L2}\cdot\mathbf{H2ISO})_{\infty}$

Interaction	D	H	A	$d_{D\cdots A}(\text{\AA})$	$d_{H\cdots A}(\text{\AA})$	D-H \cdots A ($^{\circ}$)
a	O1	H1A	N1	2.616(18)	1.776(14)	178.18(9)
b	O3 ¹	H3 ¹	N4	2.683(19)	1.843(14)	178.19(9)
c	C11	H11	O4 ²	3.226(2)	2.339(12)	155.15(11)
d	C5	H5	O2 ³	3.112(2)	2.329(13)	139.32(10)
e	C10	H10	O4 ¹	3.099(2)	2.390(13)	131.09(10)

Symmetry codes: ¹ $+x, +y, -1+z$; ² $1+x, +y, -1+z$; ³ $1+x, +y, +z$.

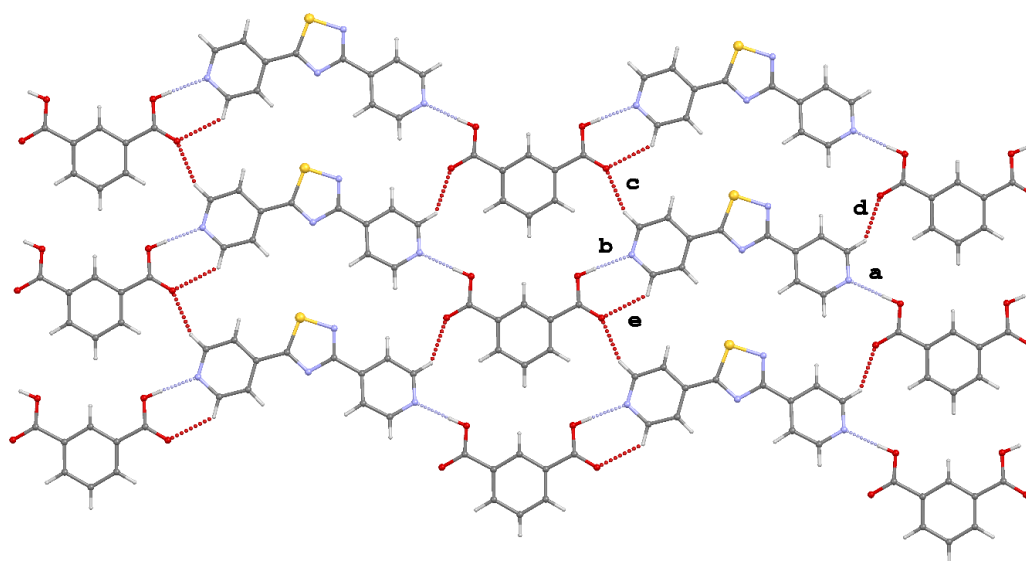


Figure 93 View along the b axis of interacting chains in $(\mathbf{L2}\cdot\mathbf{H2ISO})_{\infty}$. Intermolecular hydrogen bonding labelled according to Table 22. Disorder at thiadiazol ring is not shown for clarity.

The packing diagrams of $(\mathbf{L2}\cdot\mathbf{H2ISO})_\infty$ along the a and b axis are shown in Figure 94. Adjacent sheets are staggered and interact *via* weak π - π interactions between the disordered pentatomic ring and the phenyl of $\mathbf{H2ISO}$ unit (centroid-centroid distance > 3.82 Å).

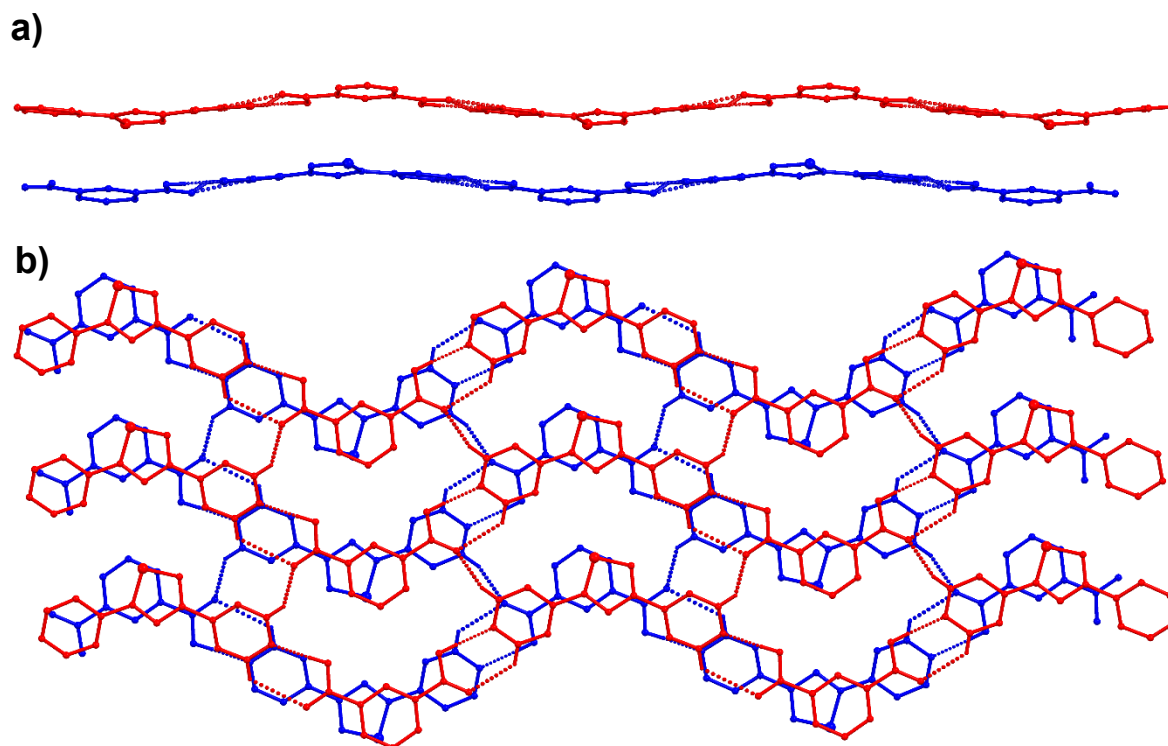


Figure 94 Packing diagrams showing a) hydrogen bonded undulated sheets running parallel to the a axis; b) overlapped sheets along the b axis.

The reaction between $\mathbf{L2}$ and $\mathbf{H2ISO-F4}$ led to the crystalline product $(\mathbf{L2}\cdot\mathbf{H2ISO-F4})_\infty$ which crystallizes in the orthorhombic crystal system within the non-centrosymmetric $P2_12_12_1$ space group. The asymmetric unit consists of one molecule of $\mathbf{L2}$ and $\mathbf{H2ISO-F4}$ as shown in Figure 95. The disorder at the pentatomic thiadiazol ring was modelled over two positions (fractional occupancy 75:25) using RIGU, SIMU and SADI restrains. The distance O1-H1A was restrained using DFIX.

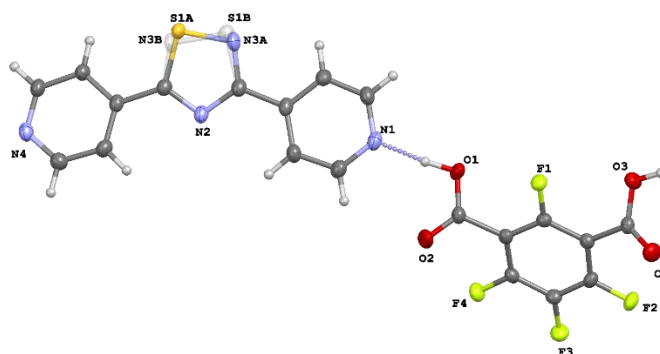


Figure 95 Asymmetric unit and atom labelling scheme for $(\mathbf{L2}\cdot\mathbf{H2ISO-F4})_\infty$.

The N1–N4 distance is 10.173(4) Å and the angle between the two pyridyl rings is about 11.02(9)°. The two building blocks interact *via* strong hydrogen bonds engaged between the N-atoms N1 and N4 and the carboxylic acids of **H₂ISO-F₄** generating polymeric undulated chains, similar to those found for (**L2·H₂ISO**)_∞ (Figure 96).

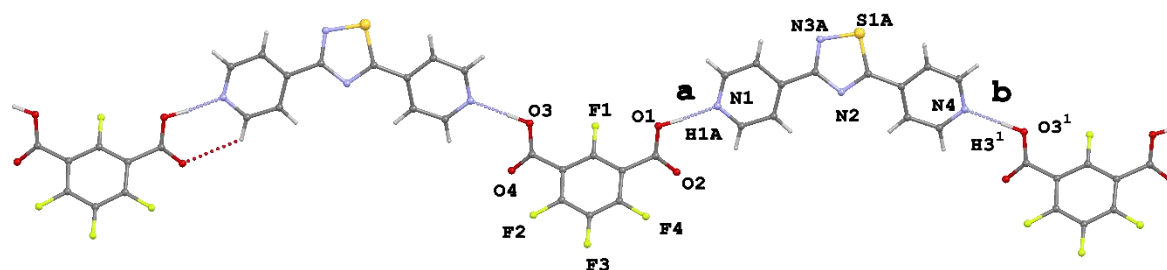


Figure 96 View of the polymeric hydrogen bonded network in the co-crystal (**L2·H₂ISO-F₄**)_∞ along the *c* axis. Interactions are labelled according to Table 23.

In contrast to the planar setting of the carboxylic acids with respect to the phenyl ring in **H₂ISO**, the presence of F atoms in **H₂ISO-F₄** causes a non-planar geometry of the building block, with angles of 49.21(12) and 43.12(10)° between the carboxylic groups and the perfluorinated aryl core. The deviation from planarity in the carboxylic acid is reflected in the overall geometry of the polymeric arrangement in (**L2·H₂ISO-F₄**)_∞ with angles calculated between the phenyl and the pyridyl rings of 44.85(9) and 47.37(9)° for Ph[^]Py1 and Ph[^]Py2, respectively.

Table 23 Intermolecular hydrogen bonding found in (**L2·H₂ISO-F₄**)_∞

Interaction	D	H	A	d _{D...A} (Å)	d _{H...A} (Å)	D-H...A (°)
a	O1	H1A	N1	2.556(3)	1.58(2)	174(3)
b	O3 ¹	H3 ¹	N4	2.614(3)	1.67(4)	163(3)
c	C1	H1	O2 ²	3.250(4)	2.544(3)	131.33(19)
d	C1	H1	F4 ²	3.314(3)	2.504(15)	143.30(17)
e	C10	H10	O4 ³	3.263(4)	2.522(2)	134.91(19)
f	C10	H10	F2 ³	3.136(3)	2.318(15)	143.83(18)

Symmetry codes: ¹ +x, +y, -1+z; ² -1+x, +y, +z; ³ -1+x, +y, -1+z.

The primary packing is governed by strong hydrogen bonds (interactions **a** and **b** in Table 23, Figure 97) which generates polymeric chains running along the *c* axis. The structure is strengthened by secondary hydrogen bonds between aromatic protons of the pyridyl rings and adjacent F and O atoms (interactions **c-f** in Table 23, Figure 97).

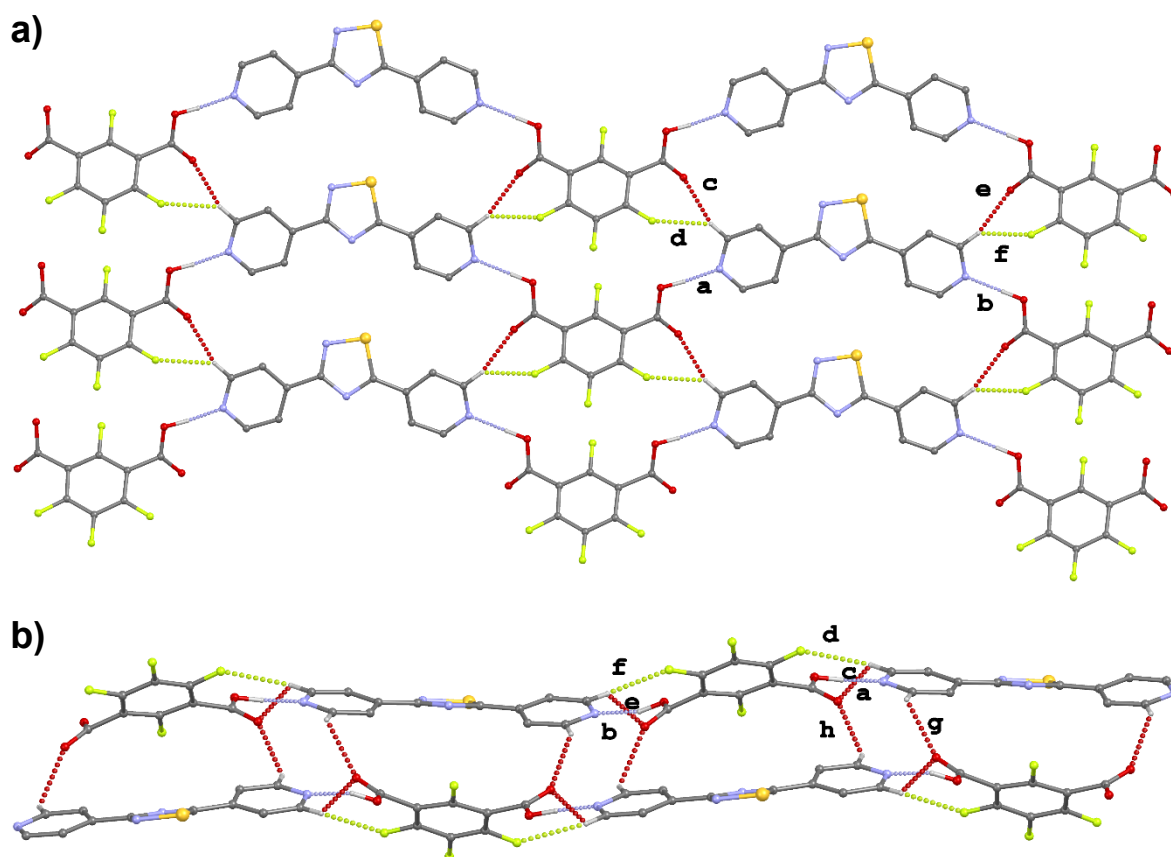


Figure 97 Intermolecular hydrogen bonding in $(\mathbf{L2} \cdot \mathbf{H2ISO-F4})_{\infty}$ labelled according to Table 23. a) shows interactions found in a single sheet along the *b* axis. b) shows additional interactions along the *a* axis **g** and **h** which stabilize adjacent sheets. Disorder at thiadiazol ring is not shown for clarity.

The angled conformation of carboxylic acids in $(\mathbf{L2} \cdot \mathbf{H2ISO-F4})_{\infty}$ is responsible of intermolecular hydrogen bonds between adjacent sheets (interactions **g** and **h**) as shown in Figure 97.

When **L2** was reacted with **H2PyDC** the formation of the 1:1 co-crystal $(\mathbf{L2} \cdot \mathbf{H2PyDC})_{\infty}$ was observed. Single crystals were grown by slow evaporation of an ethanolic solution containing an equimolar amount of the constituent building blocks. XRD analysis demonstrated that the product consists of a monoclinic lattice which was solved in the centrosymmetric $P2_1/c$ space group with $Z = 1$ (Figure 98). The N9–N15 distance is 10.13(3) Å and the angle between the pyridyl rings at **L2** is 7.88(9)°. The angles between the carboxylic groups and the pyridyl ring at **H2PyDC** are 12.83(16) and 11.72(12)°, respectively. Therefore, when the phenyl ring of **H2ISO** is replaced by a pyridyl ring such as in **H2PyDC**, a deviation from planarity is observed. It is worth noting that the extend of variation from **H2ISO** is roughly a quarter to what observed in the case of $(\mathbf{L2} \cdot \mathbf{H2ISO-F4})_{\infty}$ (44.85(9) and 47.37(9)° for Ph[^]Py1 and Ph[^]Py2).

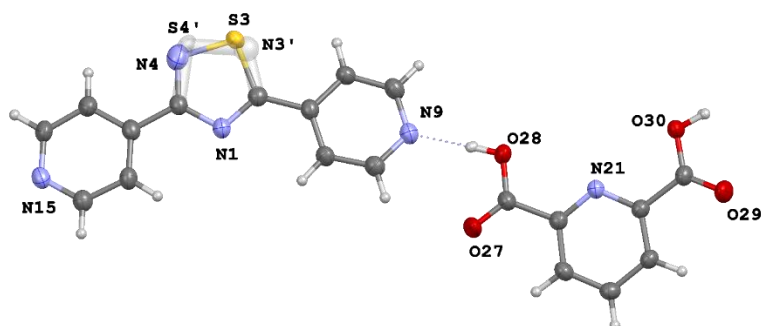


Figure 98 Asymmetric unit and atom numbering scheme for $(\text{L2}\cdot\text{H}_2\text{PyDC})_\infty$. Thermal ellipsoids are drawn at 50 % probability level.

The disorder at the pentatomic ring was refined over two positions with fractional occupancy (59:41). The primary packing consists of a polymeric 1D chain running along the *b* axis held together by strong hydrogen bonds as shown in Figure 99.

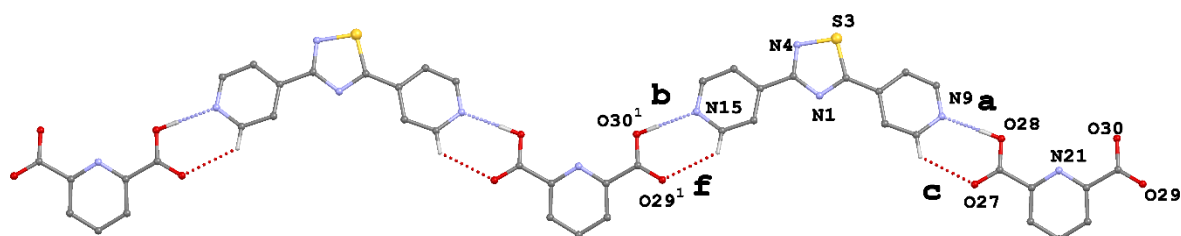


Figure 99 View along the *c* axis of the polymeric chain in $(\text{L2}\cdot\text{H}_2\text{PyDC})_\infty$. Disorder is not shown for clarity. Interactions are labelled according to Table 24.

The intermolecular hydrogen bonds are found similar to what observed in the case of $(\text{L2}\cdot\text{H}_2\text{ISO})_\infty$ and $(\text{L2}\cdot\text{H}_2\text{ISO}\cdot\text{F}_4)_\infty$ and are described as **c-f** in Table 24 and Figure 100. Weaker interactions responsible for the formation of 2D undulated sheets are shown in Figure 100. Due to the angled conformation of carboxylic groups in the crystal structure of $(\text{L2}\cdot\text{H}_2\text{PyDC})_\infty$, adjacent sheets interact with the interaction **g** described in Table 24 and shown in Figure 100.

Table 24 Intermolecular hydrogen bonding found in $(\text{L2}\cdot\text{H}_2\text{PyDC})_\infty$

Interaction	D	H	A	$d_{\text{D}\cdots\text{A}}$ (Å)	$d_{\text{H}\cdots\text{A}}$ (Å)	D-H \cdots A (°)
a	O28	H28A	N9	2.625(7)	1.725(5)	177.81(11)
b	O30 ¹	H30 ¹	N15	2.645(7)	1.750(5)	172.51(4)
c	C8	H8	O27	3.160(7)	2.528(6)	124.10(7)
d	C10	H10	O27 ²	3.088(8)	2.367(7)	132.36(15)
e	C14	H14	O29 ³	3.123(8)	2.410(7)	131.66(15)
f	C16	H16	O29 ³	3.203(7)	2.558(6)	125.34(6)
g	C8 ⁴	H8 ⁴	O29	3.358(12)	2.668(10)	129.92(2)

Symmetry codes: ¹ +*x*, 1+*y*, +*z*; ² 1+*x*, +*y*, +*z*; ³ 1+*x*, 1+*y*, +*z*; ⁴ -*x*, -1/2+*y*, 3/2-*z*.

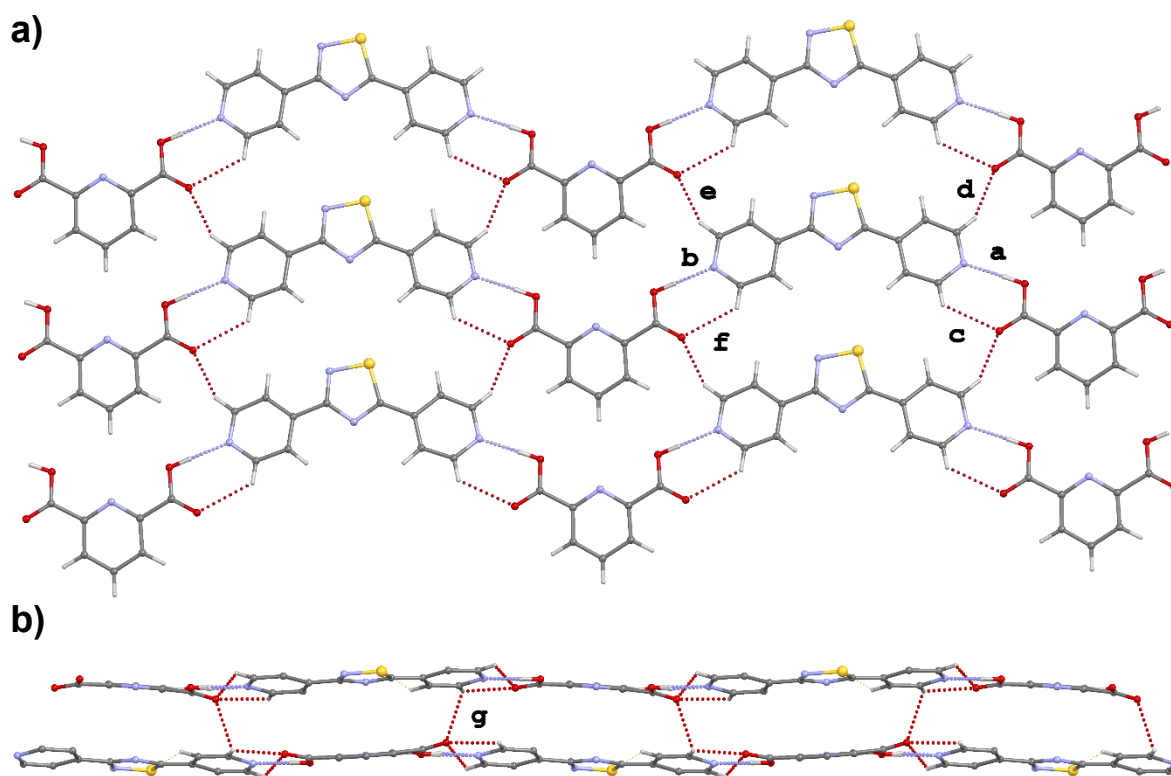


Figure 10 Views of intermolecular interaction in the co-crystal $(\mathbf{L2}\cdot\mathbf{H2PyDC})_{\infty}$ along the c (a) and a (b) axis, labelled according to Table 24.

Table 25 Bond lengths (Å) and angles (°) of the carboxylic groups in $(\mathbf{L2}\cdot\mathbf{H2ISO})_{\infty}$, $(\mathbf{L2}\cdot\mathbf{H2ISO-F4})_{\infty}$ and $(\mathbf{L2}\cdot\mathbf{H2PyDC})_{\infty}$.

$(\mathbf{L2}\cdot\mathbf{H2ISO})_{\infty}$		$(\mathbf{L2}\cdot\mathbf{H2ISO-F4})_{\infty}$		$(\mathbf{L2}\cdot\mathbf{H2PyDC})_{\infty}$	
01-C13	1.311(2)	01-C13	1.283(3)	028-C27	1.306(2)
02-C13	1.211(2)	02-C13	1.204(3)	027-C27	1.207(2)
03-C20	1.320(2)	03-C20	1.306(3)	030-C29	1.309(3)
04-C20	1.214(2)	04-C20	1.212(3)	029-C29	1.217(3)
01-C13-02	123.59(15)	01-C13-02	125.0(3)	027-C27-028	123.9(3)
03-C20-04	123.33(16)	03-C20-04	124.9(3)	029-C29-030	123.8(2)

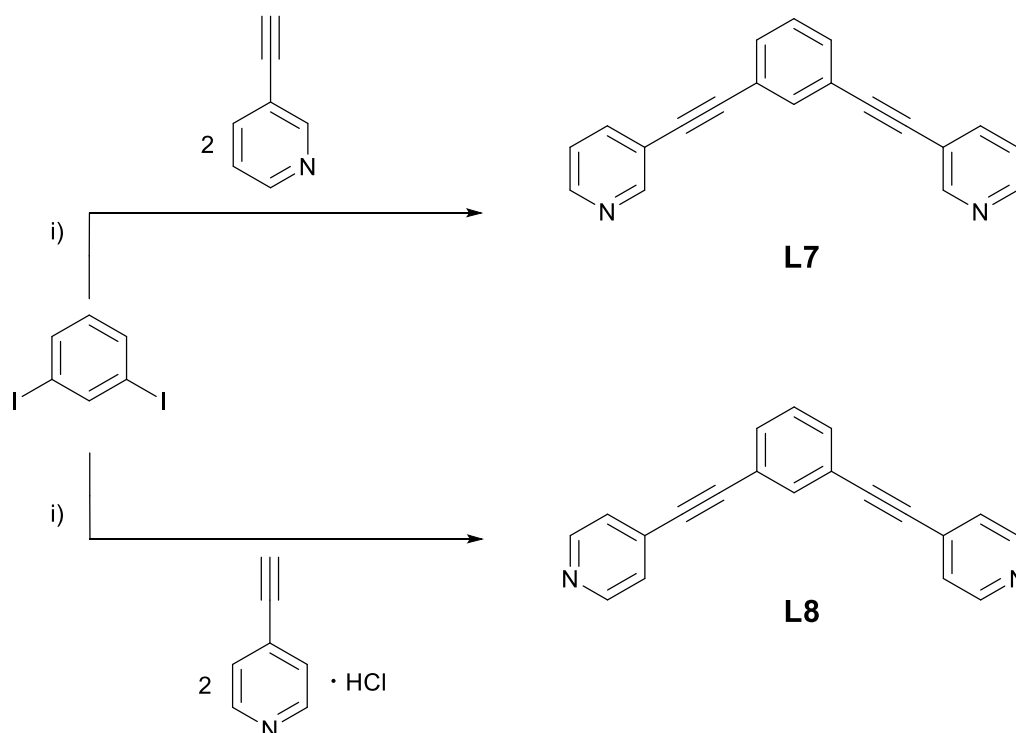
A comparison between the structures obtained by reacting **L1** and **L2** with the selected benzenedicarboxylic acids showed that, both ligands are versatile building blocks for the formation of co-crystals. Differently to what observed for the reaction with metal ions, the *para*-isomer resulted more prone to form crystalline co-crystals built up by strong H-bonding interactions involving the pyridyl nitrogen atoms and the carboxylic groups. The shape of the resulting infinite polymeric chains is mainly governed by the reciprocal position of the carboxylic group in the phenyl ring, also due to the almost linear structure of **L2** spacer. The

presence of electron-withdrawing substituents enhances the acidity of the groups and slightly influence the bond length distances and angles within the COOH substituents as summarized in Table 25. This is consistent with the FT-IR spectra of the products where the C–O stretching mode falls at 1693, 1697 and 1709 cm^{-1} for $(\mathbf{L2}\cdot\mathbf{H2ISO})_{\infty}$, $(\mathbf{L2}\cdot\mathbf{H2PyDC})_{\infty}$ and $(\mathbf{L2}\cdot\mathbf{H2ISO-F4})_{\infty}$ (Figures S90, S95 and S92).

3.1.2.2. Interaction between L7 with H₂TER

Ligands **L7** and **L8** features the same ethynyl-pyridyl branches of **L3-L6** but differ for the presence of the central 1,3-substituted phenyl ring. Their synthesis was carried out by one-step Sonogashira coupling reaction between 3-ethynylpyridine or 4-ethynylpyridine hydrochloride and 1,3-diiodobenzene as shown in Scheme 20 (§5.2.7 and §5.2.8). The N-donors were fully characterized by means of elemental analysis, FT-IR and NMR analysis. The FT-IR spectra of both **L7** and **L8** show a band at 2208 and 2212 cm^{-1} respectively, assigned to the alkyne stretching, similarly to that found for **L3-L6** (Figures S63 and S64). The ¹H and ¹³C{¹H} NMR spectra of both **L7** and **L8** are in agreement with those previously reported and will not be discussed here (Figures

S16, S17, S18, S19).^[378,379] The linkers **L7**^[378,380–386] and **L8**^[387,388] were previously employed as building blocks for the preparation of supramolecular assemblies.



Scheme 20 Sonogashira coupling reactions for the preparation of ligand **L7** and **L8**. i) $\text{Pd}(\text{PPh}_3)_2\text{Cl}_2$, CuI , NHEt_2 , N_2 , reflux, 48 h.

In an attempt to prepare MOFs by means of three-component approaches (§3.2.4) by reacting equimolar amounts of **L7**, zinc(II) nitrate hexahydrate and **H₂TER** under solvothermal conditions in a 2:1 ethanol/chloroform mixture, colorless crystals of the 1:1 co-crystal (**L7**·**H₂TER**)_∞ were obtained, and will be discussed here.

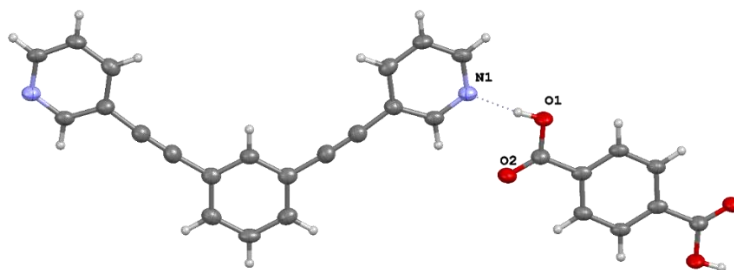


Figure 101 View and atom numbering scheme for (**L7**·**H₂TER**)_∞.

(**L7**·**H₂TER**)_∞ crystallized in a monoclinic lattice and was solved in the centrosymmetric space group $P2_1/m$ (crystal data and structure refinement in Table S142) with half of both **L7** and **H₂TER** in the asymmetric unit (Figure 101). **L7** is arranged in a periplanar conformation with $N\cdots N^1$ ($^1+x, 3/2-y, +z$) distance of 11.321(4) Å, thus halfway to the overall length of **L1** (7.688(5) – 8.912(4) Å) and **L3** (13.228(2) – 14.885(7) Å). **L7** features a slightly tilted skeleton as suggested by the angle between the two pyridyl rings of 17.1(2)°. In addition, the angle between Py-Ph-Py¹ centroids is 68.47(5) ° ($^1+x, 3/2-y, +z$). The length of pyridyl arms strongly resemble that found for the *meta*-substituted spacer **L3** (7.433(5) – 7.492(8) Å) with a value of 7.685(4) Å. **L7** units in (**L7**·**H₂TER**)_∞ are bridged by **H₂TER** units through hydrogen bonding between the carboxylic and the pyridyl groups (interaction **a** in Figure 102) resulting in a undulated polymeric 1D chain running along the *b* vector (Figure 102).

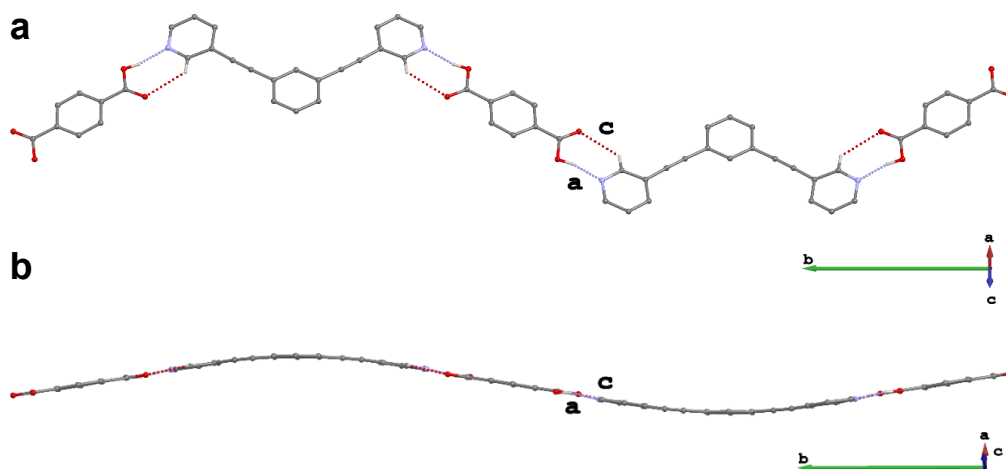


Figure 102 Views of the undulated polymeric 1D chain in (**L7**·**H₂TER**)_∞. Interactions are labelled according to Table 26.

Adjacent chains interact *via* weaker hydrogen bonds between pyridyl protons and the double bonded O atom of the carboxylic functionality (interactions **b** and **c** in Table 26 and Figure 103) generating undulated 2D-sheets.

Table 26 Intermolecular hydrogen bonding found in $(L7 \cdot H_2TER)_\infty$

Interaction	D	H	A	$d_{D \cdots A}(\text{\AA})$	$d_{H \cdots A}(\text{\AA})$	D-H \cdots A ($^\circ$)
a	O1	H1	N1	2.684(5)	1.84(2)	168(6)
b	C10	H10	O1 ¹	3.167(5)	2.417(3)	135.7(3)
c	C11	H11	O2	3.259(6)	2.588(3)	127.9(3)

Symmetry codes: ¹ 1+x,y, -1+z.

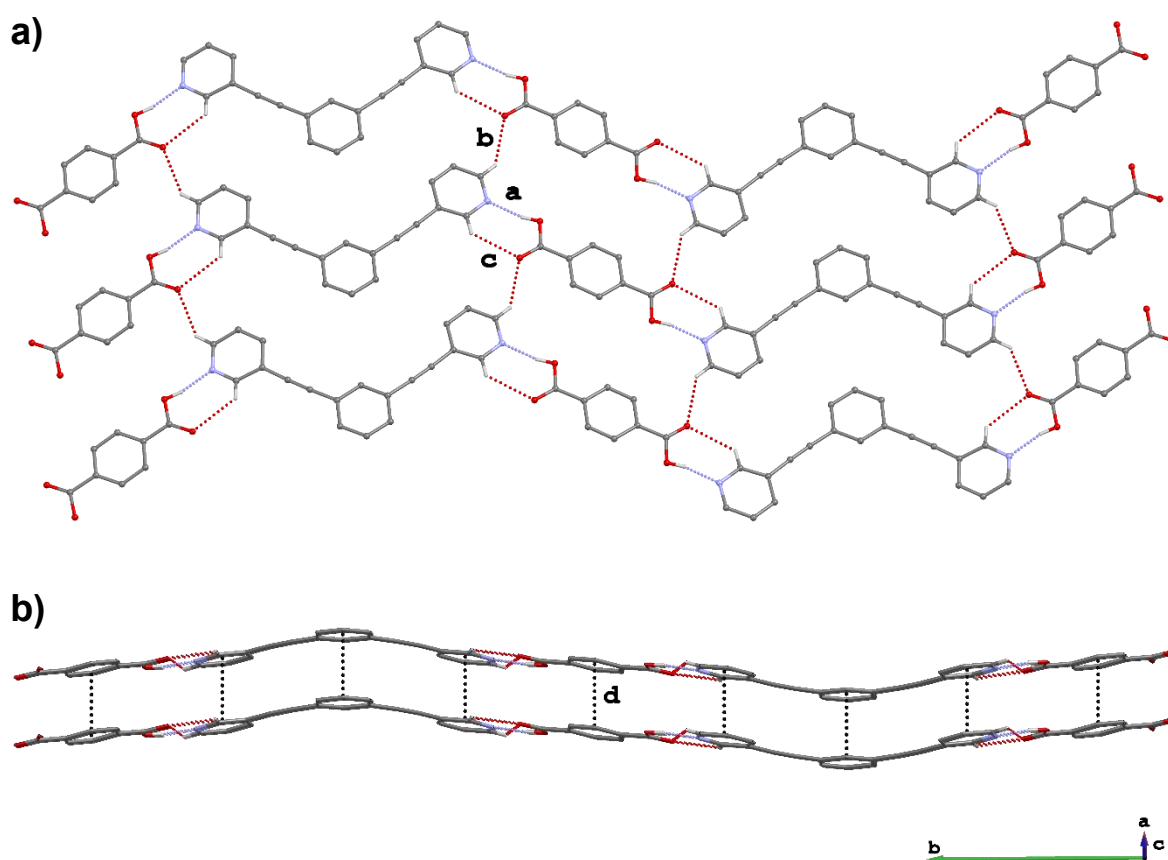


Figure 103 Packing views of $(L7 \cdot H_2TER)_\infty$ showing the intermolecular interactions a) along the [101] direction; b) intermolecular π - π interactions between parallel undulated 2D sheets. Interactions labelled according to Table 26.

The crystal packing is extended by intermolecular π - π stacking between aromatic rings of (interaction **d** in Figure 103 b)) parallel sheets with centroid-centroid distances of 3.795(3) \AA and shift distance of 1.711(8) \AA .

Interestingly, the C–O bond lengths in $(\mathbf{L7}\cdot\mathbf{H}_2\mathbf{TER})_\infty$ are slightly elongated if compared with those found in the crystal structures of $(\mathbf{L1}\cdot\mathbf{H}_2\mathbf{TER})_\infty$, $(\mathbf{L2}\cdot\mathbf{H}_2\mathbf{TER}\text{-}\mathbf{Br})_\infty$ and $(\mathbf{L2}\cdot\mathbf{H}_2\mathbf{TER}\text{-}(\mathbf{OH})_2)_\infty$ which feature terephthalic acid derivatives as building block (Table 27).

Table 27 Bond lengths (Å) and angles (°) of the carboxylic groups in $(\mathbf{L7}\cdot\mathbf{H}_2\mathbf{TER})_\infty$, $(\mathbf{L1}\cdot\mathbf{H}_2\mathbf{TER})_\infty$, $(\mathbf{L2}\cdot\mathbf{H}_2\mathbf{TER}\text{-}\mathbf{Br})_\infty$ and $(\mathbf{L2}\cdot\mathbf{H}_2\mathbf{TER}\text{-}(\mathbf{OH})_2)_\infty$.

$(\mathbf{L7}\cdot\mathbf{H}_2\mathbf{TER})_\infty$		$(\mathbf{L1}\cdot\mathbf{H}_2\mathbf{TER})_\infty$		$(\mathbf{L2}\cdot\mathbf{H}_2\mathbf{TER}\text{-}\mathbf{Br})_\infty$		$(\mathbf{L2}\cdot\mathbf{H}_2\mathbf{TER}\text{-}(\mathbf{OH})_2)_\infty$	
O1–C11	1.341(5)	O1–C13	1.311(2)	O1–C7	1.30(2)	O1–C7	1.295(2)
O2–C11	1.216(5)	O2–C13	1.210(2)	O2–C7	1.220(2)	O2–C7	1.235(2)
		O3–C20	1.206(2)	O3–C8	1.305(17)	O1–C7–O2	123.56(17)
		O4–C20	1.319(2)	O4–C8	1.182(17)		
		O5–C33	1.329(2)	O1B–C7B	1.31(2)		
		O6–C33	1.210(2)	O2B–C7B	1.208(19)		
		O7–C40	1.214(2)	O3B–C8B	1.30(2)		
		O8–C40	1.328(2)	O4B–C8B	1.185(19)		
O1–C11–O2	122.7(4)	O1–C13–O2	123.50(17)	O1–C7–O2	124.5(13)		
		O3–C20–O4	123.76(16)	O3–C8–O4	130.0(13)		
		O5–C33–O6	122.94(16)	O1B–C7B–O2B	121.9(18)		
		O7–C40–O8	123.45(16)	O3B–C8B–O4B	131.5(19)		

3.1.3. Interaction between N-donors and borasiloxanes: COFs

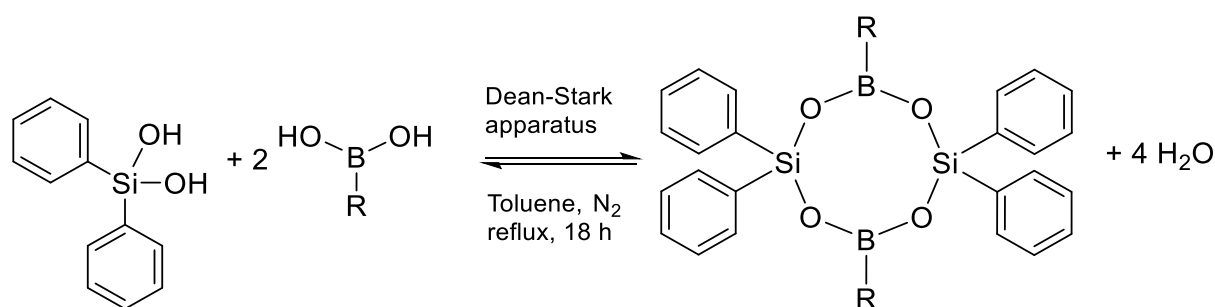
3.1.3.1. Design of cyclic borasiloxanes R1-R3

Covalently assembled crystalline species (including Covalent Organic Frameworks, COFs) are far fewer in number compared to reported structures of MOFs, CPs, and HOFs, due to their highly challenging synthesis.^[389–391] Recently, the formation of N–B bonds have been exploited for the preparation of ‘covalent’ supramolecular scaffolds such as cages, polymers and 2D/3D networks.^[91,99,392–394] We then decided to investigate the construction of supramolecular assemblies through the formation of B–N bonds starting from the eight-member cyclic borasiloxanes 8-diphenyl-2,2,6,6-tetraphenyl-1,3,5,7,2,6,4,8-tetraoxadisiladiborocane (**R1**), 8-bis(4-fluorophenyl)-2,2,6,6-tetraphenyl-1,3,5,7,2,6,4,8-tetraoxadisiladiborocane (**R2**), and 4,8-bis(3,5-difluorophenyl)-2,2,6,6-tetraphenyl-1,3,5,7,2,6,4,8-tetraoxadisiladiborocane (**R3**).

Borasiloxanes are a renowned class of compounds with unique thermal and chemical stabilities, employed for the development of borosilicate materials and with applications as flame retardants,^[395] sensors,^[396] and non-linear optical (NLO) materials.^[397] Cyclic-borasiloxanes and cages have also been reported, such as those used in this work, and represent a promising family of synthons in supramolecular chemistry since the three-coordinated boron atoms can

act as Lewis and react with properly designed amines generating extended network build up by N–B bonds.

Borasiloxanes **R1-R3** (§1.1.3) were prepared by cyclocondensation reactions between diphenylsilanediol and three different boronic acids, namely phenylboronic acid, 4-fluorophenyl boronic acid and 3,5-difluorophenylboronic acid leading to compounds **R1-R3**, respectively (Scheme 21).



R = phenyl, **R1**; 4-fluorophenyl, **R2**; 3,5-difluorophenyl, **R3**

Scheme 21 Formation of eight-membered cyclic borasiloxanes **R1-R3** via cyclocondensation reactions of diphenylsilanediol and boronic acids.

Due to the reversible nature of the involved reactions, the three borasiloxane derivatives were prepared by means of a Dean-Stark apparatus in order to remove the water formed as a product and push the reaction towards the formation of **R1-R3**. The isolation of cyclic eight-membered borasiloxanes as the only products is likely due to thermodynamic reasons. Previous studies attributed their formation as the results of a ring-ring transformation from six-membered cyclic heterosiloxanes.^[398] The products were isolated as white powders and purified by recrystallization from a mixture of dry diethyl ether/dichloromethane. Crystalline materials were then stored in a desiccator equipped with dry silica gel pellets, under nitrogen atmosphere. It is worth evidencing that compound **R1** was previously published (refcode: VUMTIG) and was used as a benchmark for the preparation of novel compounds **R2** and **R3**.^[399]

FT-IR spectra of cyclic borasiloxanes **R2** and **R3** feature strong absorptions due to the synergic contributes of stretching and bending vibrational modes typical of Si–O and B–O which were observed in the regions: 1427-1219, 1198-1119, 750-675, 575-488 cm^{-1} (Figures S70, S71). **R2** and **R3** were characterized by means of multinuclear NMR spectroscopy on the following nuclei: ^1H , ^{11}B , ^{13}C , ^{19}F , ^{29}Si (Figures S41, S42, S43, S44, S45, S46, S47, S48, S49, S50). The ^1H NMR spectra in CDCl_3 of both cyclic borasiloxanes are in good agreement with the proposed structure. The signals resonating between 7.71 – 7.29 ppm in both **R2** and **R3** were assigned to

the aryl rings bonded to the Si atoms. The protons at the boron substituents fall at different values for **R2** and **R3**: protons in the *ortho* and *meta* positions in **R2** resonate at 8.07 – 8.00 and 7.15 – 7.08 ppm; proton in *para* at the boron substituent of **R3** resonate at 6.95 ppm and the signal for protons in the *ortho* position of **R3** falls at 7.52 – 7.42 ppm overlapped to that of the protons in *para* at the silicon substituent. The $^{13}\text{C}\{^1\text{H}\}$ spectra recorded in CDCl_3 show eight signals in the range 165.7 – 115.2 and 163.1 – 107.3 ppm for **R2** and **R3**, respectively. The $^{11}\text{B}\{^1\text{H}\}$ spectra recorded in CDCl_3 show only one signal at 25.55 and 25.49 ppm, for **R2** and **R3**, respectively, in agreement with the values found for boron nuclei with three coordinated environments.^[399] The $^{19}\text{F}\{^1\text{H}\}$ NMR spectra in CDCl_3 for **R2** and **R3** show only a signal at -107.9 and -110.4 ppm, respectively. The $^{29}\text{Si}\{^1\text{H}\}$ spectra in CDCl_3 feature the presence of a singlet resonating at -44.6 and -44.0 ppm for **R2** and **R3**, respectively. The novel cyclic-borasiloxanes **R2** and **R3** were structurally characterized and crystal data and refinement parameters are reported in Table S138. As showed in Figure 104 and Figure 105, **R2** and **R3** feature eight-membered rings composed of two tetrahedral silicon atoms and two trigonal planar boron atoms held together by four alternating oxygens ($\text{B}_2\text{Si}_2\text{O}_4$).

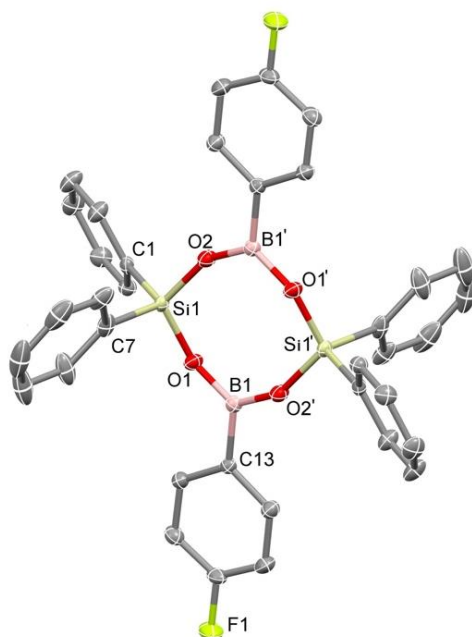


Figure 104 Crystal structure and numbering scheme of **R2**. Ellipsoids are drawn at 30 % probability level.

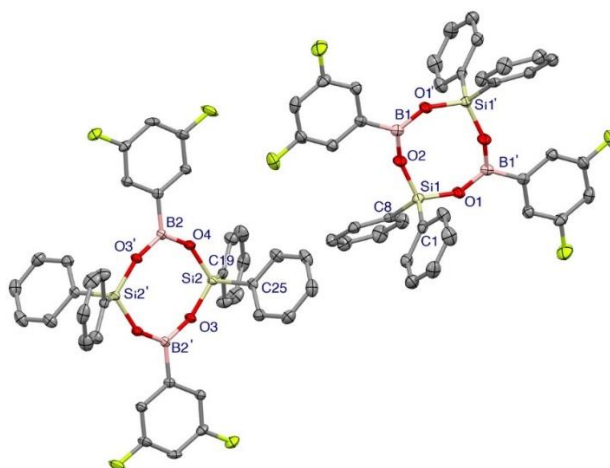


Figure 105 Crystal structure and numbering scheme of **R3**. Ellipsoids are drawn at 30 % probability level.

The $\text{Si}_2\text{B}_2\text{O}_4$ rings in **R2** and **R3** are almost planar and bond lengths and angles at Si and B sites strongly resemble those found in the crystal structure of **R1**.^[399] The bond angles at Si atoms are consistent with its tetrahedral environment ranging between $107.5 - 113.2^\circ$ and $107.2 - 115.3^\circ$ for **R2** and **R3**, respectively. Similarly, the bond angles at B atoms are very close to the ideal value of 120° for the trigonal planar geometry. The main bond lengths and angles for **R2** and **R3** are listed in Table 28 alongside with the values of **R1** for the sake of comparison.

Table 28 Selected bond lengths (Å) and angles ($^\circ$) for **R1-R3**.

	R1		R2		R3
Si1–O1	1.628(3)	Si1–O1	1.625(14)	Si1–O1	1.639(19)
Si1–O2	1.616(4)	Si1–O2	1.618(16)	Si1–O2	1.616(16)
Si1–C1	1.845(5)	Si1–C1	1.849(2)	Si1–C1	1.849(3)
Si1–C7	1.847(5)	Si1–C7	1.856(2)	Si1–C7	1.855(3)
B1–O1	1.347(5)	B1–O1	1.367(3)	B1–O1	1.361(3)
B1–O2	1.345(7)	B1–O2	1.360(3)	B1–O2	1.362(3)
B1–C13	1.554(7)	B1–C13	1.556(3)	B1–C13	1.561(4)
		F1–C16	1.368(2)	F1–C15	1.363(3)
				F2–C17	1.361(3)
O1–Si1–O2	112.04(3)	O1–Si1–O2	113.21(8)	O1–Si1–O2	112.03(10)
O1–Si1–C1	106.8(2)	O1–Si1–C1	107.54(9)	O1–Si1–C1	108.11(12)
O1–Si1–C7	109.54(19)	O1–Si1–C7	108.89(10)	O1–Si1–C7	106.78(11)
O2–Si1–C1	109.1(2)	O2–Si1–C1	108.57(9)	O2–Si1–C1	107.49(12)
O2–Si1–C7	106.7(2)	O2–Si1–C7	107.58(10)	O2–Si1–C7	107.24(12)
C1–Si1–C7	112.62(18)	C1–Si1–C7	111.0(10)	C1–Si1–C7	115.28(12)
O1–B1–O2	121.2(4)	O1–B1–O2	121.70(2)	O1–B1–O2	121.30(3)
O1–B1–C13	119.4(4)	O1–B1–C13	119.10(2)	O1–B1–C13	118.90(3)
O2–B1–C13	119.4(3)	O2–B1–C13	119.20(2)	O2–B1–C13	119.70(19)
B1–O1–Si1	145.2(4)	B1–O1–Si1	143.08(16)	B1–O1–Si1	138.43(19)
B1–O2–Si1	161.0(3)	B1–O2–Si1	151.03(16)	B1–O2–Si1	154.50(2)

Notes: **R1** values are reproduced from refcode VUMTIG; **R3** values are given as mean values calculated on the two crystallographically independent molecules.

Borasiloxane molecules in **R2** pack through hydrogen bond interactions involving the F atom and two distinct protons at the aryl substituents bonded to the Si. A portion of the crystal packing is showed in Figure 106.

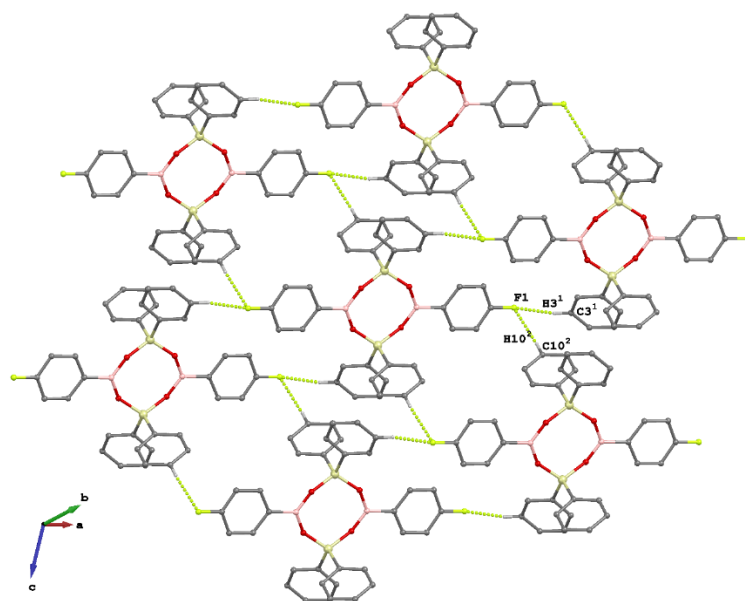


Figure 106 Intermolecular interactions found in **R2**: $C3^1-H3^1 \cdots F1$ ($d_{D \cdots A} = 3.238(3) \text{ \AA}$; $d_{H \cdots A} = 2.5922(2) \text{ \AA}$; $\alpha_{D-H \cdots A} = 125.57(17)^\circ$); $C10^2-H10^2 \cdots F1$ ($d_{D \cdots A} = 3.433(3) \text{ \AA}$; $d_{H \cdots A} = 2.5377(3) \text{ \AA}$; $\alpha_{D-H \cdots A} = 157.0(2)^\circ$). Only H atoms involved in intermolecular interactions are shown for clarity. Symmetry codes: $^1 2-x, 2-y, 1-z$; $^2 1+x, 1+y, 1+z$.

In the crystal packing, **R3** molecules are involved in similar $H \cdots F$ intermolecular hydrogen bonding between adjacent molecules in the $R_2^2(8)$ pattern, according to the Graph Sets analysis (§ 1.1.2), showed in Figure 107 and listed in Table 29.

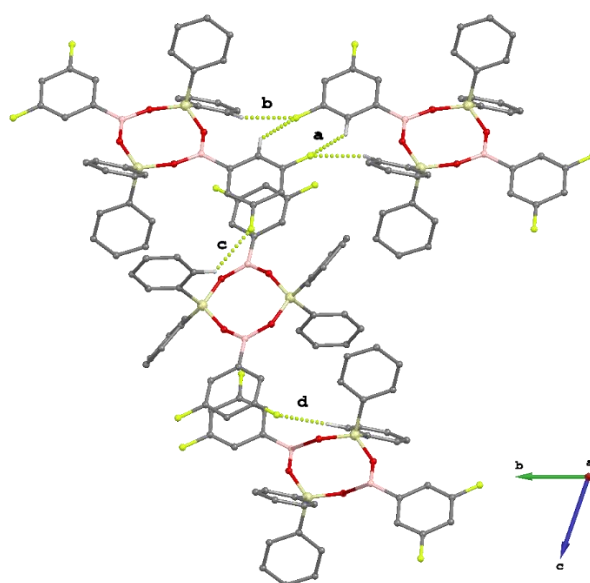


Figure 107 View along the a axis of the intermolecular hydrogen bonds in **R3** showing the cyclic dimeric pattern $R_2^2(8)$ formed between $(C35-F4 \cdots H36-C36)_2$ along with other hydrogen bonds according to Table 29.

Table 29 Intermolecular hydrogen bonding interactions found in **R3**.

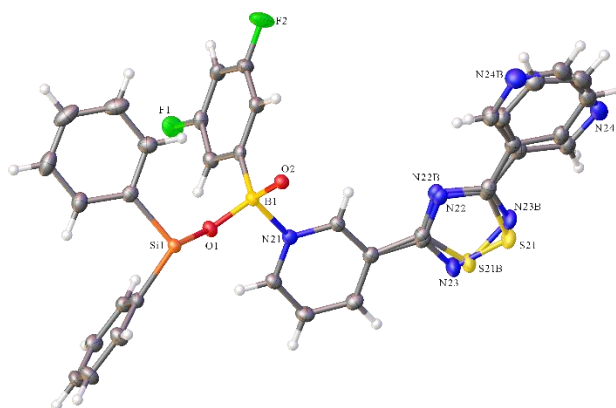
Interaction	D	H	A	$d_{D...A}$ (Å)	$d_{H...A}$ (Å)	D-H...A (°)
a	C36 ³	H36 ³	F4	3.446(4)	2.653(2)	141.27(15)
b	C24 ³	H24 ³	F4	3.504(3)	2.641(18)	151.3(2)
c	C6 ¹	H6 ¹	F3 ³	3.274(4)	2.568(2)	131.33(17)
d	C20 ²	H20 ²	F1 ¹	3.576(4)	2.871(19)	131.83(17)

Symmetry codes: ¹ 1-x,1-y,1-z; ² 2-x,-y,1-z; ³ 1-x,1-y,-z.

Borasiloxane **R2** and **R3** were reacted with ligands **L1-L6** but crystals were obtained only for the *meta*-pyridyl-derivatives, and in particular compounds (**L1**)₂·**R3**, (**L3**·**R2**)_∞, (**L3**·**R3**)_∞, (**L5**·**R2**)_∞ will be here discussed.

3.1.3.2. Interaction between **L1** and the cyclic borasiloxane **R3**

The reaction of **L1** with **R3** in 1:1 mixture of dry dichloromethane/diethyl ether at room temperature yielded colourless crystalline product which was characterized by single crystal XRD as a dimeric adduct with formula (**L1**)₂·**R3** that crystallize in the triclinic *P*-1 space group (crystal data and refinement parameters in Table S139) The asymmetric unit comprises one ligand **L1** and half borasiloxane **R3**; the thiadiazolyl ring and the free pyridyl moiety of **L1** are disordered over two positions with fractional occupancy of 87 and 13% (Figure 108). The planar arrangement of the boron atoms in the borasiloxane ring allows for an attack by the N-donor atoms on both sides of the molecular plane leading to boron geometry change from trigonal planar to tetrahedral.

**Figure 108** Representation of the asymmetric unit of adduct (**L1**)₂·**R3**. Displacement ellipsoids are drawn at 50 % probability level.

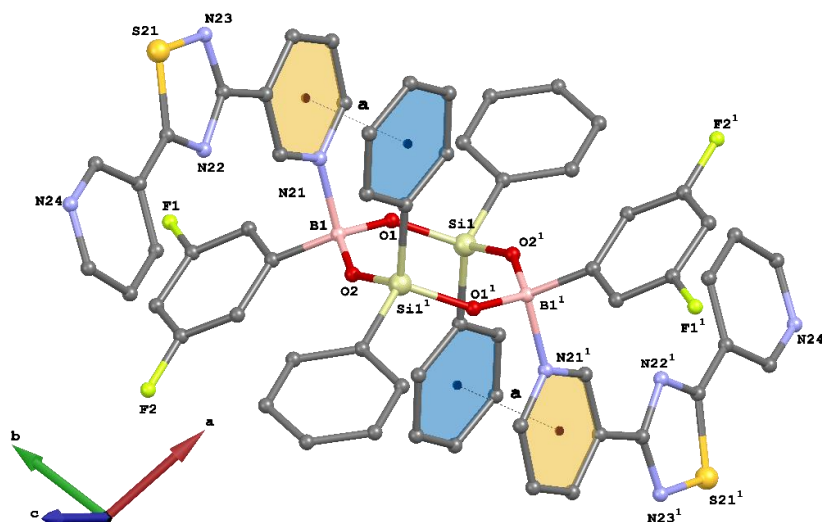


Figure 109 Ball and stick representation of the 2:1 adduct found in $(\mathbf{L1})_2 \cdot \mathbf{R3}$. Disorder and H atoms are not shown for clarity. Symmetry code: $^1 1-x, 1-y, 1-z$.

The bond distances B–O and B–C in $(\mathbf{L1})_2 \cdot \mathbf{R3}$ are slightly elongated if compared with the free $\mathbf{R3}$, as a result of B–N bond formation, and are consistent with literature values for similar fragments and in perfect agreement with the mean values of 1.48(5) and 1.63(3) Å calculated for B–O and B–C bond distances in tetra-coordinated boron derivatives (bond lengths and angles in Table S140 and Table S141). The B–N distance is 1.6881(14) Å, resulting slightly longer than the mean value of 1.54(5) Å calculated on the structures of similar tetracoordinated boron fragments found in the CDS. The geometrical changes in boron environment becomes apparent comparing the bond angles of $\mathbf{R3}$ with those found in the dimeric arrangement $(\mathbf{L1})_2 \cdot \mathbf{R3}$. The internal ring angles in $(\mathbf{L1})_2 \cdot \mathbf{R3}$ are consistent with those observed in the borasiloxane cage-pyridine adduct $[\text{Bu}^t\text{Si}(\text{OPhBO})_3\text{SiBu}^t]$ (refcode ODIYAC) reported a few years ago.^[400] Intramolecular π - π interactions involve the coordinated pyridyl ring and one of the Si aryl substituent (interaction **a** in Figure 109) with centroid-centroid distance of 3.685(10), and an angle between the involved rings of 15.75(6)°. Adjacent dimers pack interacting by means of intermolecular π - π interaction between pyridyl rings of $\mathbf{L1}$ which will not be here discussed due to the disorder affecting the heterocyclic rings.

3.1.3.3. Interaction between $\mathbf{L3}$ and the cyclic borasiloxanes $\mathbf{R2}$ and $\mathbf{R3}$

The reaction of $\mathbf{L3}$ with $\mathbf{R2}$ and $\mathbf{R3}$ in a 1:2 mixture of dry diethyl ether/dichloromethane gave clear yellowish solutions that upon slow evaporation of the solvent mixture, yielded pale yellow and colourless crystals that were analysed by means of XRD showing the formation of the

polymeric helices $(\mathbf{L3}\cdot\mathbf{R2})_\infty$ and $(\mathbf{L3}\cdot\mathbf{R3})_\infty$, that crystallize in the tetragonal $P4_32_12_1$ and $P4_3$ space groups, respectively (crystal data and refinement parameters are listed in Table S139). The asymmetric unit of $(\mathbf{L3}\cdot\mathbf{R2})_\infty$ comprises half of both borasiloxane $\mathbf{R2}$ and ligand $\mathbf{L3}$; whereas two independent borasiloxane $\mathbf{R3}$ and ligand $\mathbf{L3}$ molecules are present in the asymmetric unit of $(\mathbf{L3}\cdot\mathbf{R3})_\infty$ (Figure 110). It is interesting to note that the helices feature the pyridyl rings of the bridging $\mathbf{L3}$ molecules angled by about 65° whilst they are nearly coplanar in the free ligand $\mathbf{L3}$ (12°); this flexibility allows the N atoms from neighbouring $\mathbf{L3}$ bridging ligands to bind the two boron atoms on the same side of the cycloborasiloxane plane (periplanar conformation), generating helices.

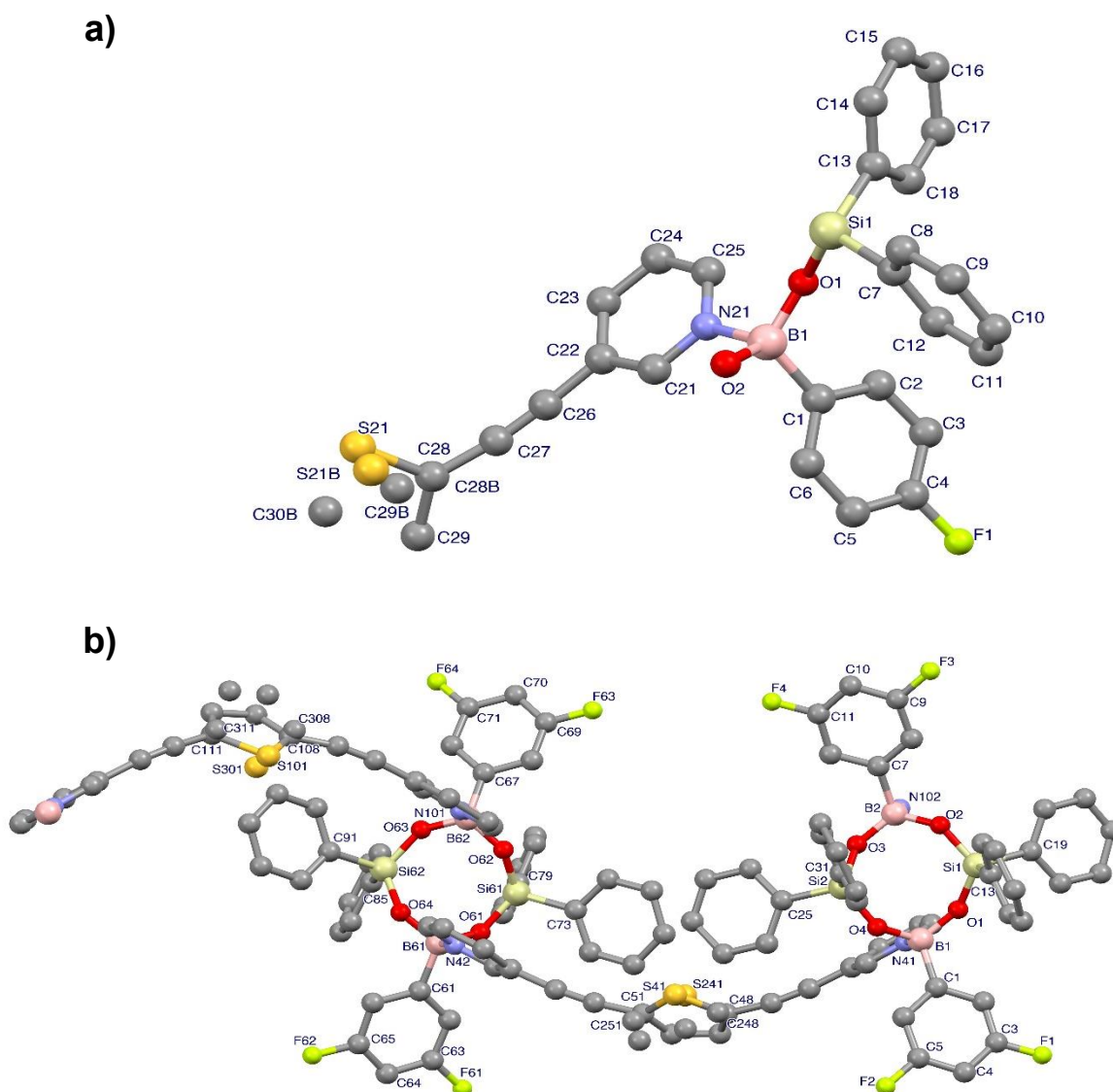


Figure 110 Asymmetric unit and numbering scheme for helices $(\mathbf{L3}\cdot\mathbf{R2})_\infty$ and $(\mathbf{L3}\cdot\mathbf{R3})_\infty$ in a) and b), respectively. Hydrogen atoms are omitted for clarity.

Both polymeric structures consist of left-handed helices running along c axis with pitch values of 23.734 and 23.888 Å for $(\mathbf{L3}\cdot\mathbf{R2})_\infty$ and $(\mathbf{L3}\cdot\mathbf{R3})_\infty$, respectively (Figure 111). The Flack parameter was refined to $-0.06(4)$ and $-0.005(7)$ for $(\mathbf{L3}\cdot\mathbf{R2})_\infty$ and $(\mathbf{L3}\cdot\mathbf{R3})_\infty$, respectively, indicating in both cases the presence of just one enantiomer in the crystal. Thiophene rings are disordered over two positions in both crystal structures. The N–B bond lengths are consistent with literature values for similar fragments.^[400]

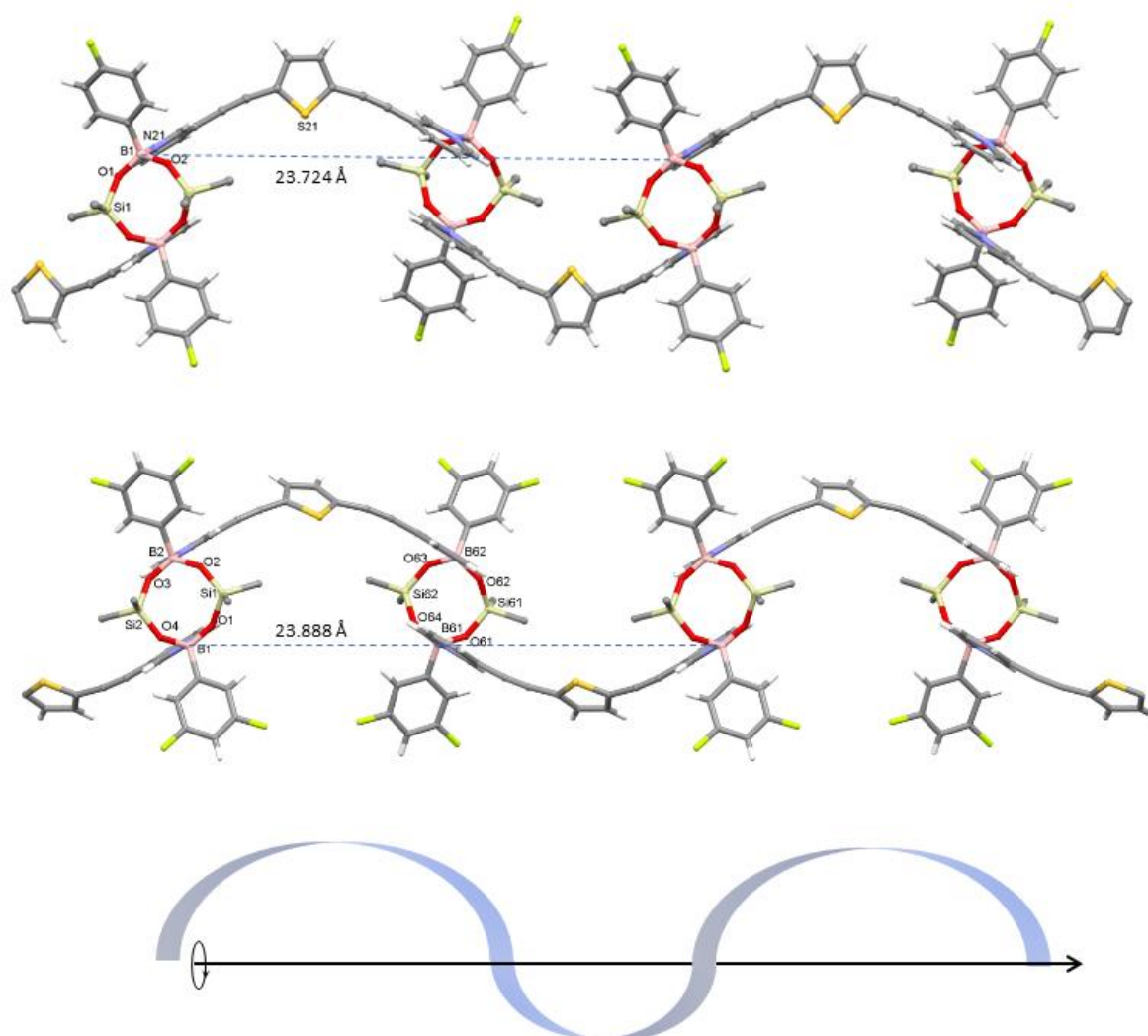


Figure 111 View of the polymeric helices of $(\mathbf{L3}\cdot\mathbf{R2})_\infty$ (top) and $(\mathbf{L3}\cdot\mathbf{R3})_\infty$ (bottom). Phenyl substituents at Si atoms are depicted as single carbon atoms for clarity.

The Si–O and B–O bonds are a little shortened and elongated, respectively, compared to those of $\mathbf{R2}$ and $\mathbf{R3}$ (bond lengths and angles in Table S140 and Table S141). In the crystal, 2D-helices rotated by about 90° around a 4-fold screw axis pack through intermolecular π - π

interactions between almost parallel pyridine and phenyl rings at the silicon atoms, displaying centroid-centroid distances of 3.570 Å for $(\mathbf{L3}\cdot\mathbf{R2})_\infty$, and in the range 3.551-3.602 Å for compound $(\mathbf{L3}\cdot\mathbf{R3})_\infty$. A representation of the packing diagram for $(\mathbf{L3}\cdot\mathbf{R3})_\infty$ is given in Figure 112.

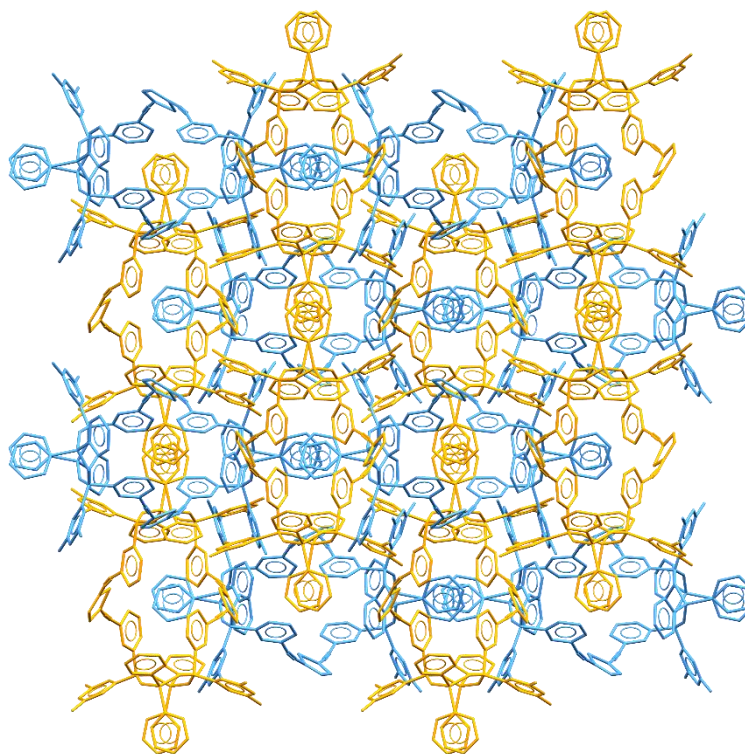


Figure 112 Packing diagram of $(\mathbf{L3}\cdot\mathbf{R3})_\infty$ along c axis showing symmetry related chains in different colours to evidence rotation (yellow: x, y, z , and $-x, -y, \frac{1}{2} + z$; light blue: $y, x, \frac{1}{4} + z$, and $-y, x, \frac{3}{4} + z$). H-atoms and disorder at thiophene rings are omitted for clarity.

FT-IR analysis (Figures S70, S71, S97, S98) revealed notable differences between the spectra of $(\mathbf{L3}\cdot\mathbf{R2})_\infty$ and $(\mathbf{L3}\cdot\mathbf{R3})_\infty$ and those of the constituent building blocks, mainly ascribable to the variation of boron geometry after N–B bond formation. Vibrational frequencies attributed to synergic Si–O and B–O stretching and bending modes show typical $^{10}\text{B}/^{11}\text{B}$ isotopic splitting, and were observed in regions 1198-1144, 750-675, and 575-496 cm^{-1} for both compounds $(\mathbf{L3}\cdot\mathbf{R2})_\infty$ and $(\mathbf{L3}\cdot\mathbf{R3})_\infty$. Alkyne stretching frequencies fall at 2218 and 2212 cm^{-1} for $(\mathbf{L3}\cdot\mathbf{R2})_\infty$ and $(\mathbf{L3}\cdot\mathbf{R3})_\infty$, respectively, slightly shifted to higher frequencies compared with the value of 2202 cm^{-1} observed for compound **L3**.

The photophysical properties were investigated in the solid-state by means of reflectance (Figure S110) and emission spectroscopies (Figure 113). It is worth noticing that photoluminescence emission values measured for helices $(\mathbf{L3}\cdot\mathbf{R2})_\infty$ and $(\mathbf{L3}\cdot\mathbf{R3})_\infty$ show maxima

at 417 and 437 nm. These values are between the λ_{em} of 514 nm recorded for **L3**, and those of 357 and 320 nm of **R2** and **R3**, respectively, suggesting that a charge transfer occurs between the two synthons. A similar trend is also shown by reflectance spectra (Figure S110).

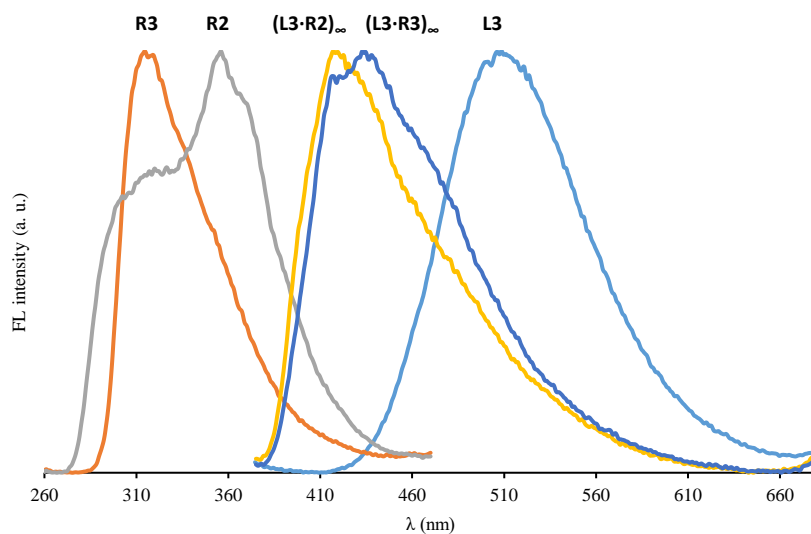


Figure 113 Solid-state photoluminescent spectra for borasiloxanes **R2** and **R3**, ligand **L3**, helices $(\mathbf{L3}\cdot\mathbf{R2})_{\infty}$ and $(\mathbf{L3}\cdot\mathbf{R3})_{\infty}$. Excitation wavelength: 250 nm (**R2**,**R3**); 350 nm (**L3**, $(\mathbf{L3}\cdot\mathbf{R2})_{\infty}$, $(\mathbf{L3}\cdot\mathbf{R3})_{\infty}$)

The change in luminescence properties can be directly ascribed to the formation of the helices and the generation of the B–N bonds.

The NMR spectra of $(\mathbf{L3}\cdot\mathbf{R2})_{\infty}$ and $(\mathbf{L3}\cdot\mathbf{R3})_{\infty}$ recorded in CDCl_3 show peaks at values that can be directly ascribed to those recorded for the relevant precursors. This allowed to suppose that the helices exist only in the solid state and the formation of the N–B bonds is governed by an equilibrium between reagents and product that is consistent with the dynamic nature previously observed for B–N bonds.^[401,402] These observations were confirmed by recording the emission spectra of $(\mathbf{L3}\cdot\mathbf{R2})_{\infty}$ and $(\mathbf{L3}\cdot\mathbf{R3})_{\infty}$ in CDCl_3 solution were two distinct emission peaks were found falling at the same values of those observed for **R2**, **R3** and **L3**.

Therefore, we decided to perform solid-state NMR characterization of $(\mathbf{L3}\cdot\mathbf{R2})_{\infty}$ and $(\mathbf{L3}\cdot\mathbf{R3})_{\infty}$. ^{13}C CP/MAS NMR spectra of $(\mathbf{L3}\cdot\mathbf{R2})_{\infty}$ and $(\mathbf{L3}\cdot\mathbf{R3})_{\infty}$ (Figures S55, S56) show peaks in the region 164.21–86.85 and 164.48–86.82 ppm, respectively. The broad signals centred at 147.74 ppm and 157.12 ppm for $(\mathbf{L3}\cdot\mathbf{R2})_{\infty}$ and $(\mathbf{L3}\cdot\mathbf{R3})_{\infty}$, respectively, can be attributed to the C–B moieties, due to coupling with boron.

PXRD analysis were carried out on $(\mathbf{L3}\cdot\mathbf{R2})_{\infty}$ and $(\mathbf{L3}\cdot\mathbf{R3})_{\infty}$ and the experimental patterns compared with those calculated from the SC-XRD show in both cases a good agreement, thus confirming the purity of the bulk materials (Figure 114).

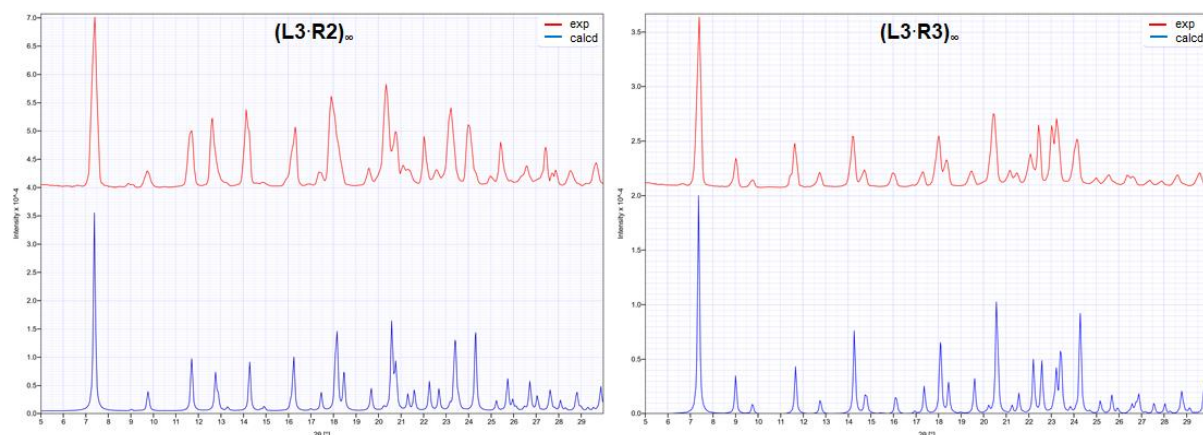


Figure 114 Experimental (red) and calculated (blue) PXRD patterns I vs 2θ for $(\mathbf{L3}\cdot\mathbf{R2})_{\infty}$ and $(\mathbf{L3}\cdot\mathbf{R3})_{\infty}$ in the region $5\text{--}30^\circ$.

Calculations at the density-functional (DFT)^[300] level of theory were carried out to investigate the electronic structure of $(\mathbf{L3}\cdot\mathbf{R2})_{\infty}$ and $(\mathbf{L3}\cdot\mathbf{R3})_{\infty}$ and their relevant precursors **R2**, and **R3** (calculations for **L3** were also performed, and were discussed above in §3.1.1). Borasiloxane rings in **R2** and **R3**, feature positive charges on the B atoms ($Q_B = 1.256$ and $1.259 |e|$ for **R2** and **R3**, respectively), accompanied by a KS-LUMO localized on the empty p orbital on boron atoms (Figure 115) available to react with the Kohn-Sham (KS) HOMO-3 and KS-HOMO-2 of the di-pyridyl ligand **L3** previously discussed and also reported in Figure 115 for clarity.

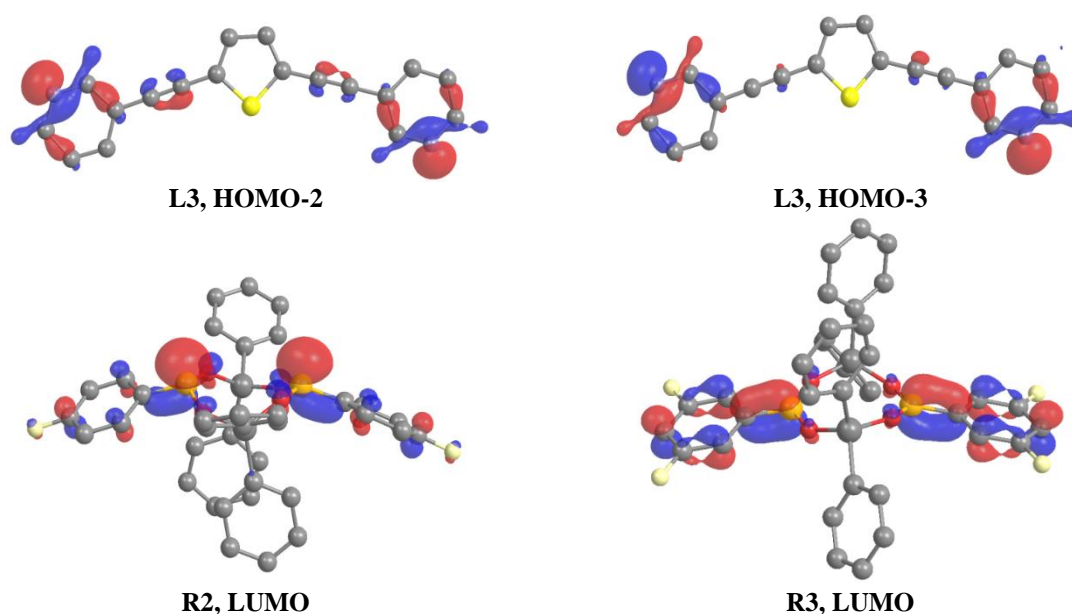
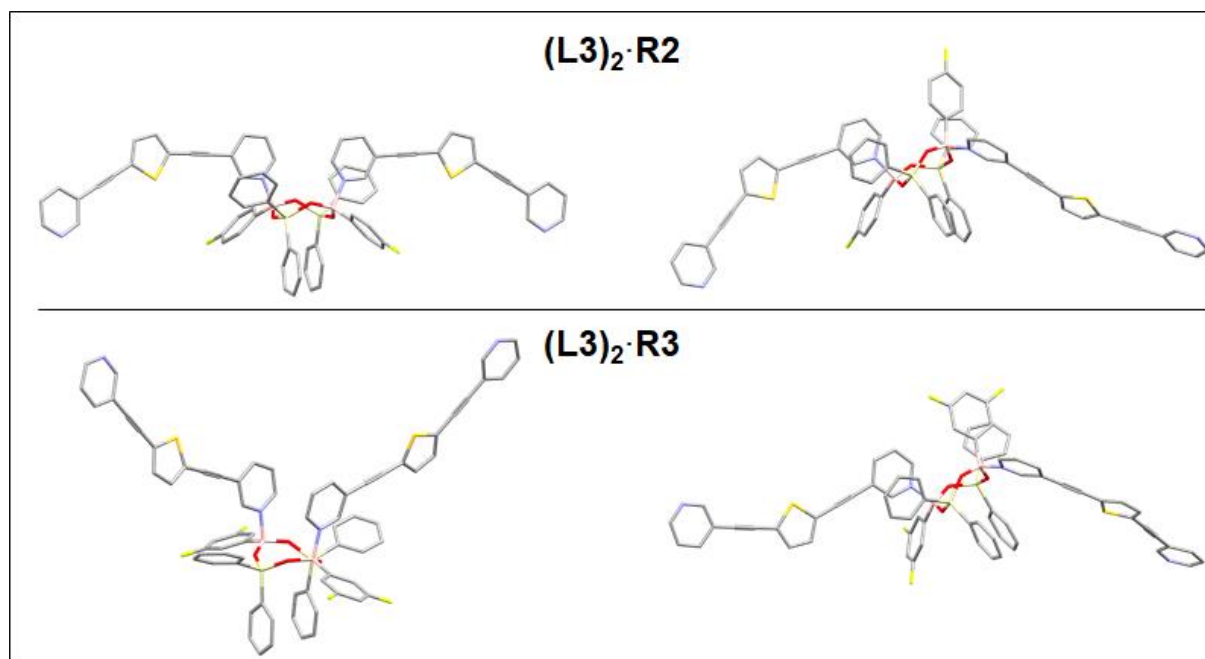


Figure 115 Isosurface drawings of selected frontier Kohn-Sham molecular orbitals calculated for **L3**, **R2**, and **R3** at the optimized geometry. Hydrogen atoms were omitted for clarity. Cutoff value = $0.05 |e|$.

Calculation on the polymeric helices were executed by using the model fragments $(\mathbf{L3})_2\cdot\mathbf{R2}$ and $(\mathbf{L3})_2\cdot\mathbf{R3}$, containing two units of ligand $\mathbf{L3}$ bound to the boron atoms of $\mathbf{R2}$ and $\mathbf{R3}$, respectively (Figure 116)

Figure 116 Optimized geometries for cisoid and transoid adducts of $(\mathbf{L3})_2\cdot\mathbf{R2}$ and $(\mathbf{L3})_2\cdot\mathbf{R3}$.



It is interesting to note that the total electronic energies calculated for the systems $(\mathbf{L3})_2\cdot\mathbf{R2}$ and $(\mathbf{L3})_2\cdot\mathbf{R3}$ arranged in periplanar conformation only slightly differ from those calculated for the antiperiplanar geometry ($\Delta E = 2.76$ and 2.56 kcal mol⁻¹ for $(\mathbf{L3})_2\cdot\mathbf{R2}$ and $(\mathbf{L3})_2\cdot\mathbf{R3}$, respectively). The average NBO charges on B and N atoms calculated for $(\mathbf{L3})_2\cdot\mathbf{R2}$ and $(\mathbf{L3})_2\cdot\mathbf{R3}$ adducts are $Q_B = 1.209, 1.213$ and $Q_N = -0.489, -0.489$ |e|, respectively. Second order perturbation theory analysis supports the formation of N–B bonds, with average donor-acceptor energies of 130.19 and 147.93 kcal mol⁻¹ and Wiberg bond indexes of 0.429 and 0.431 for $(\mathbf{L3})_2\cdot\mathbf{R2}$ and $(\mathbf{L3})_2\cdot\mathbf{R3}$, respectively. These values confirm that the N–B bonds in $(\mathbf{L3})_2\cdot\mathbf{R2}$ and $(\mathbf{L3})_2\cdot\mathbf{R3}$ are mainly covalent in nature, even if strongly polarised. These findings endorse the high potential of cyclic borasiloxanes as suitable building blocks for the construction of supramolecular helicoidal systems assembled through covalent N–B bonds, by reaction with appropriate dipyriddy donors. The use of luminescent compounds $\mathbf{L3}$, $\mathbf{R2}$ and $\mathbf{R3}$ as building blocks allowed investigation of the changes in solid-state luminescence which revealed that the emission energies of helices $(\mathbf{L3})_2\cdot\mathbf{R2}$ and $(\mathbf{L3})_2\cdot\mathbf{R3}$ fall at values intermediate between those of the starting materials, directly ascribed to N–B bond generation. Luminescence variation also allows for the development of supramolecular systems structurally tailored by a rational choice

of differently substituted borasiloxanes and dipyridyl substrates. As previously shown in the case of the coordination polymers formed by dipyridyl derivatives and coordinatively unsaturated Ni^{II} complexes,^[293,298,403] the topology of the spacers can allow to predict the resulting supramolecular architectures. Further studies on these systems are underway in our laboratories in order to rationally predict formation of luminescent helices with tailored emission properties for potential sensing applications.

3.1.3.4. Interaction between *L5* and the cyclic borasiloxane *R3*

The reaction of **L5** with **R2** in a 1:1 mixture of dry diethyl ether/chloroform yielded pale yellow crystals of the polymeric assembly (**L5**·**R2**)_∞ which crystallize in the *P*-1 space group; the crystallographic data and refinement parameters are listed in Table S139.

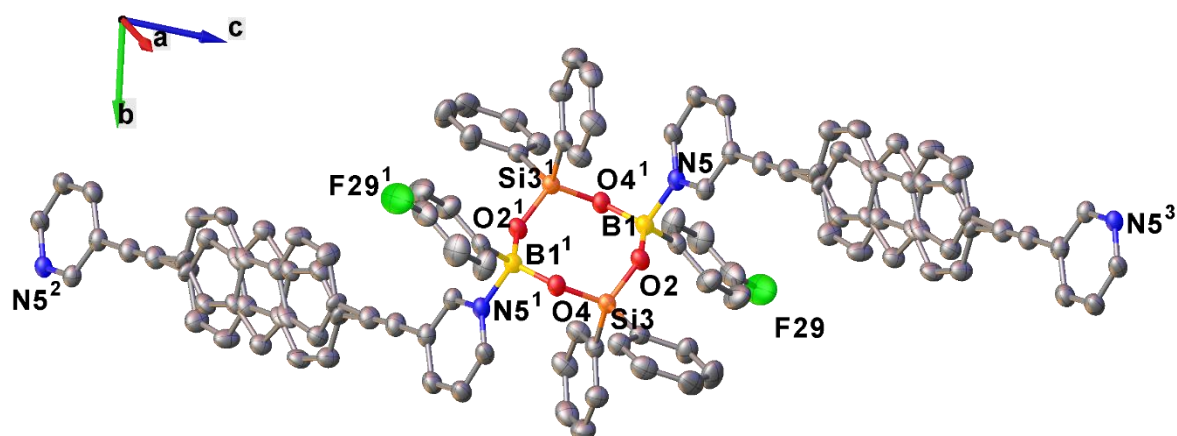


Figure 117 Crystal structure and numbering scheme for polymer (**L5**·**R2**)_∞. H atoms are omitted for clarity. Symmetry codes: ¹ -x, 1-y, -z; ² 2-x, -y, 1-z; ³ -2+x, 1+y, -1+z.

The asymmetric unit of (**L5**·**R2**)_∞ comprises half of both the cyclic borasiloxane **R2** and the dipyridyl derivative **L5**, similarly to what observed for (**L5**·**R2**)_∞. Moreover, **L5** is arranged in an antiperiplanar conformation with the fluorene unit disordered over two positions (refined with fractional occupancy of 50 %) and parallel pyridyl rings.

The bond lengths and angles of (**L5**·**R2**)_∞ strongly resemble those found in the previous cases of both the dimeric adduct (**L1**)₂·**R3** and the chiral helices (**L3**·**R2**)_∞ and (**L3**·**R3**)_∞ (bond lengths and angles in Table S140 and Table S141) with B1–O distances of 1.429(3) and 1.436(3) Å for B1–O2 and B1–O4, respectively, and a B1–N5 distance of 1.704(2) Å. **L5** units bridge borasiloxane rings generating undulated chains as shown in Figure 118.

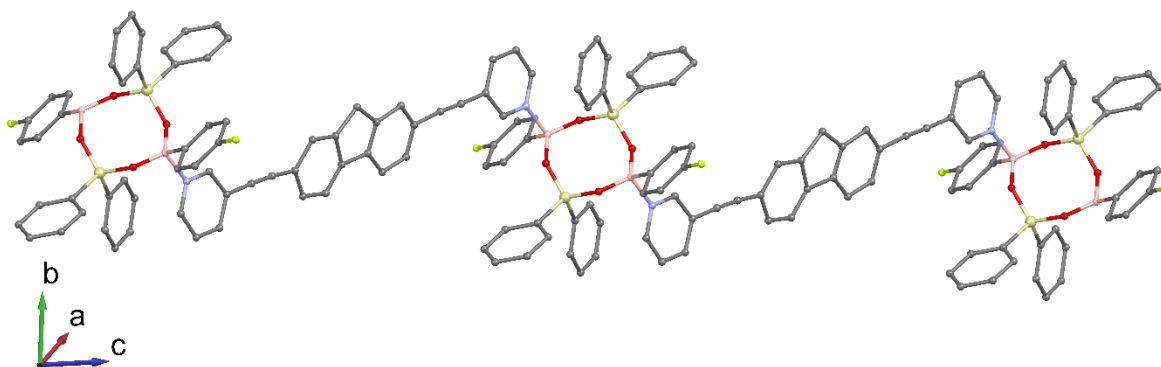


Figure 118 Polymeric 1D chain of $(\mathbf{L5}\cdot\mathbf{R2})_{\infty}$. Disorder and H atoms are not shown for clarity.

The polymeric chains show intramolecular interactions involving the pyridyl ring and the adjacent aryl substituent at the Si, similar to what observed in the case of $(\mathbf{L1})_2\cdot\mathbf{R3}$ (centroid-centroid distance of 3.80 Å, $\alpha = 20.24(7)^\circ$). 1D chains pack slipped of (10.57 Å) and interact via weak π - π interactions involving the disordered fluorene fragment and the pyridyl rings of adjacent $\mathbf{L5}$ molecules (Figure 119).

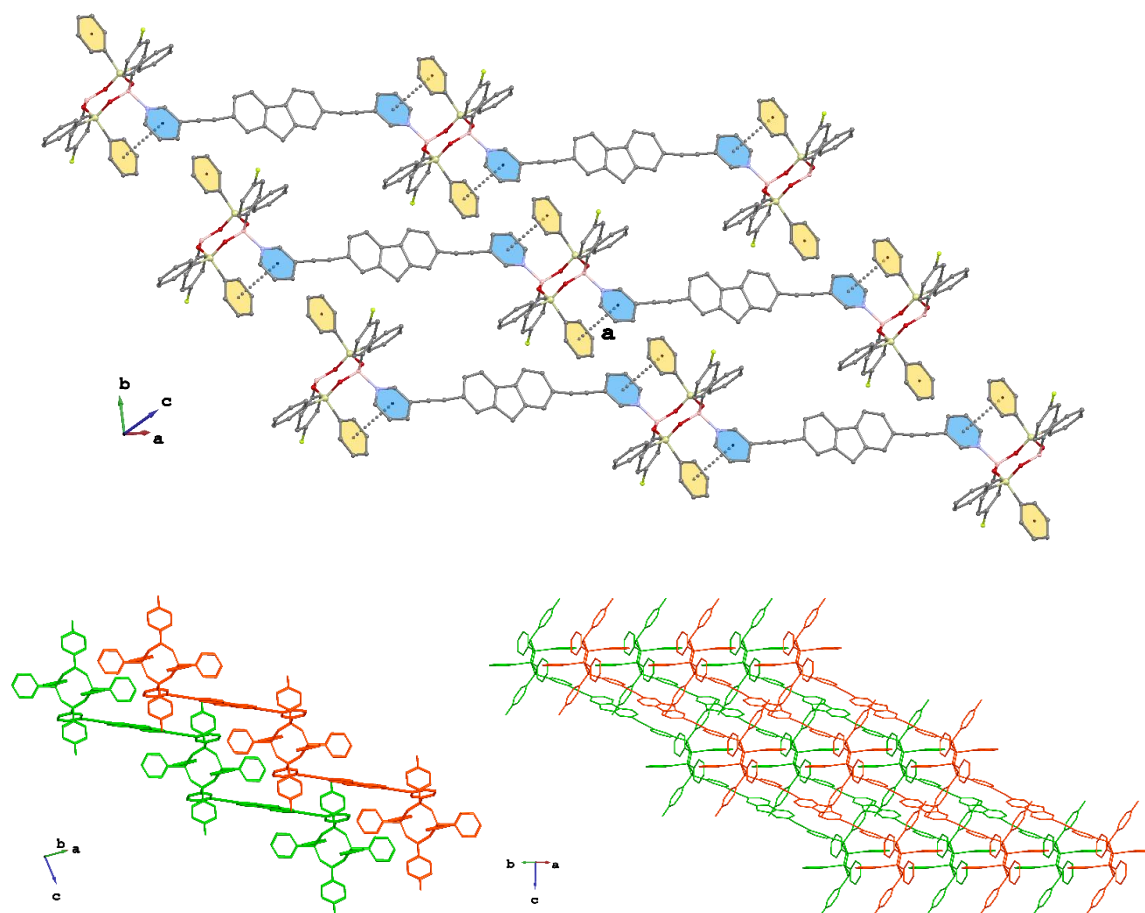


Figure 119 Packing diagrams of $(\mathbf{L5}\cdot\mathbf{R2})_{\infty}$. π - π interactions are shown in the top image. The slipped packing of 1D chain is shown in the bottom figures. H atoms and disorder are omitted for clarity.

3.1.4. Interaction between N-donors and halogens

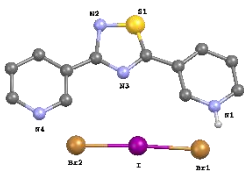
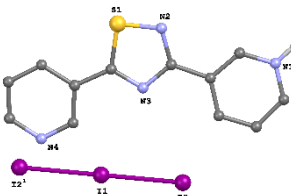
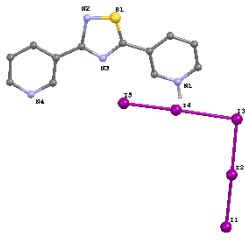
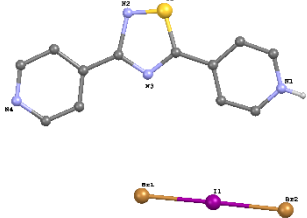
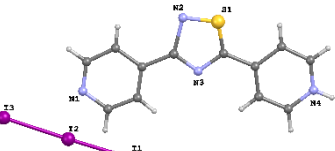
Halogens (X_2 ; $X = I_2, Br_2$), interhalogenic compounds (IX ; $X = Cl, Br$) and perfluoro-halogenated compounds are known to react with substrates containing chalcogen (S, Se, Te) and pnictogen (P, N) atoms forming a wide variety of compounds depending on the nature of the involved reagents and on the experimental condition used such as solvent, temperature, and molar ratio (§1.1.4). Following the historical interests of our research group, pyridyl ligands **L1-L3**, **L11** obtained by functionalization of ligands **L9** (§5) and compounds dipyrind-2-yldiselenide (**L12**), dipyrind-2-ylditelluride (**L13**), and 2-(p-tolyl)selenopheno[2,3-b]pyridine (**L14**) prepared in collaboration with the research group of prof. K. K. Bhasin of the University of Panjab, India and prof. Eder J. Lenardao of the Universidade Federal de Pelotas, Brazil, were reacted with molecular halogens, interhalogens and 1,4-diiodotetrafluorobenzene.

The reactions were carried out in different molar ratios at room temperature using acetonitrile, dichloromethane, chloroform and ethanol as solvents; reactions of molecular bromine and iodine diffusion on solutions of the relevant substrates were also performed. Due to the huge amount of performed reactions and to the difficult often encountered in fully characterize the obtained products, only the results regarding structurally characterized compounds will be here discussed.

3.1.4.1. Interaction between L1 and L2 and halogens

The reaction of **L1** and **L2** with halogens and interhalogens was previously reported by our research group,^[134] and the results obtained are summarized in Table 30.

Table 30 CT adducts and ionic compounds obtained from N-donors **L1** and **L2**.

CT adducts	$L1 \cdot 2I_2$	$L2 \cdot 2I_2$	
Ionic compounds	 <p>(HL1)IBr₂</p>	 <p>(HL1)I₃</p>	 <p>(HL1)I₅</p>
	 <p>(HL2)IBr₂</p>	 <p>(HL2)I₃</p>	

Refcodes: **L1**·2I₂ (WEDHUK); (HL1)I₃ (WEDGUJ); (HL1)I₅ (WEDHAQ), (HL1)IBr₂ (WEDHEU), (HL2)I₃ (WEDHIY); (HL2)IBr₂ (WEDHOE). Note: **L2**·2I₂ was not structurally characterized.

The results showed that donors **L1** and **L2** can give either N-protonation or CT I₂-adducts depending on the solvent polarity. The reaction of **L1** with molecular iodine in CH₂Cl₂ led to the bis-adduct **L1·2I₂** with a N···I bond distance of 2.505 Å, notably shorter compared to those found in adducts between bidentate N-donors and iodine, featuring extended neutral chains ...N—N···I₂···N—N··· with N···I bond distances ranging between 3.085 and 2.92 Å.¹³⁴ The N···I—I interaction is almost linear (179.7 °) with the iodine molecules lying in the pyridyl plane, with a I—I distance of 2.761 Å only slightly elongated with respect to that observed in solid I₂ (2.715 Å).^[404] In the crystal packing, intermolecular long contacts involving iodine molecules form infinite I₂ chains which enfold the adduct molecules in parallel ribbons.¹³⁴ The reaction of **L2** and molecular iodine under the same experimental conditions led to a solid non-crystalline compound that was recognized as the analogous **L2·2I₂** adduct on the base of elemental analysis and FT-Raman characterizations.

When **L1** and **L2** were reacted with I₂ or IBr in ethyl alcohol, the ionic compounds (**HL1**)I₃, (**HL2**)I₃, (**HL1**)IBr₂, (**HL2**)IBr₂, and (**HL1**)I₅ were obtained and characterized by means of single crystal XRD (Table 30). The structures of the ionic compounds show the protonation of the pyridyl nitrogen and the formation of head-to-tail polymeric chains built up through charge-assisted NH⁺···N hydrogen bonding (N···N bond distances in the range 2.662 – 2.770 Å, N—H—N angle in the range 156 – 176 °) featuring a geometry strongly dependent on the position of the pyridyl nitrogens: helices or zig-zag chains of cations (**HL1**)⁺ and undulating chains of cations (**HL2**)⁺. The cationic compounds are counterbalanced by I₃⁻, IBr₂⁻, and I₅⁻ anions. In compound (**HL1**)I₅, the V-shaped I₅⁻ anion units are linked by I···I contacts to form helices with shapes complementary to those formed by the cationic (**HL1**)⁺ units showing a nice example of extended anion network templated by helical cations. Conversely, the I₃⁻ and IBr₂⁻ anions simply fill the spaces left between the helices or chains of cationic units, favored by weak C—H···I/Br contacts.^[134]

In order to extend the study to halogen containing species, **L1** and **L2** were reacted with 1,4-diiidotetrafluorobenzene (**1,4-DITFB**) widely employed in the preparation of supramolecular networks.^[405–409] The 1:1 reaction of **L2** and **1,4-DITFB** in chloroform at room temperature form a clear solution that upon slow evaporation of the solvent mixture afforded colorless crystals, whilst no crystalline product were obtained from the reaction of **L1** and **1,4-DITFB**. XRD analysis of the crystals revealed the formation of the neutral halogen bonded 1D polymer (**L2·1,4-DITFB**)_∞ crystallized in the triclinic space group *P*-1 (structural and refinement data are reported in Table S143).

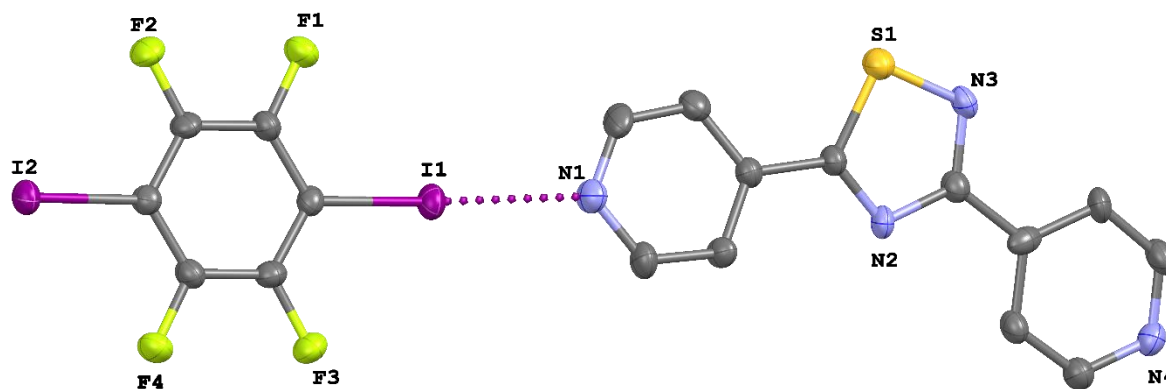


Figure 120 Crystal structure of $(\mathbf{L2}\cdot\mathbf{1,4-DITFB})_{\infty}$. Thermal ellipsoids are drawn at 50 % probability level.

The **1,4-DITFB** molecules interact with **L2** forming neutral adducts with $d_{\text{N}\cdots\text{I}}$ distances of 2.801(5) and 2.951(5) Å and $\text{C-I}\cdots\text{N}$ angles of 177.64(19) and 168.06(19)° for $\text{N1}\cdots\text{I1}$ and $\text{N4}^1\cdots\text{I2}$, respectively ($^1 -2-x, 1+y, 1+z$). Selected bond lengths and angles are reported in Table S144. The values are similar to the average value of 2.9(2) Å found on CSD for the structures of similar systems involving interacting **1,4-DITFB** and pyridyl based donors with $\text{N}\cdots\text{I}$ distances up to the sum of N and I van der Waals radii: 3.53 Å).

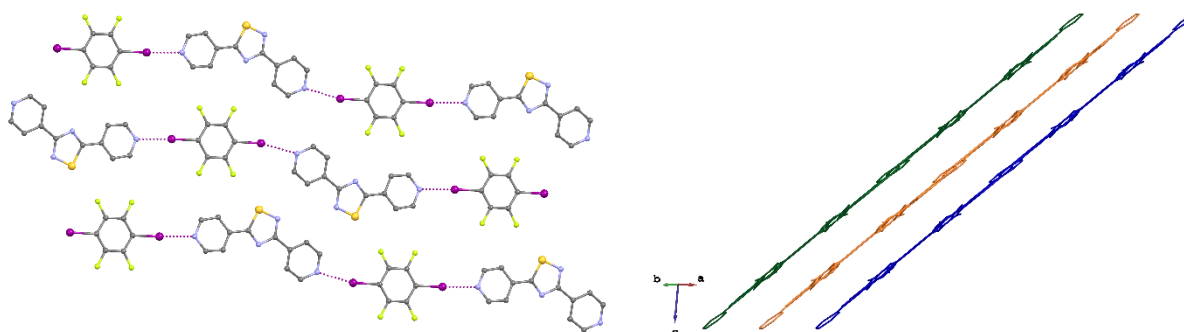
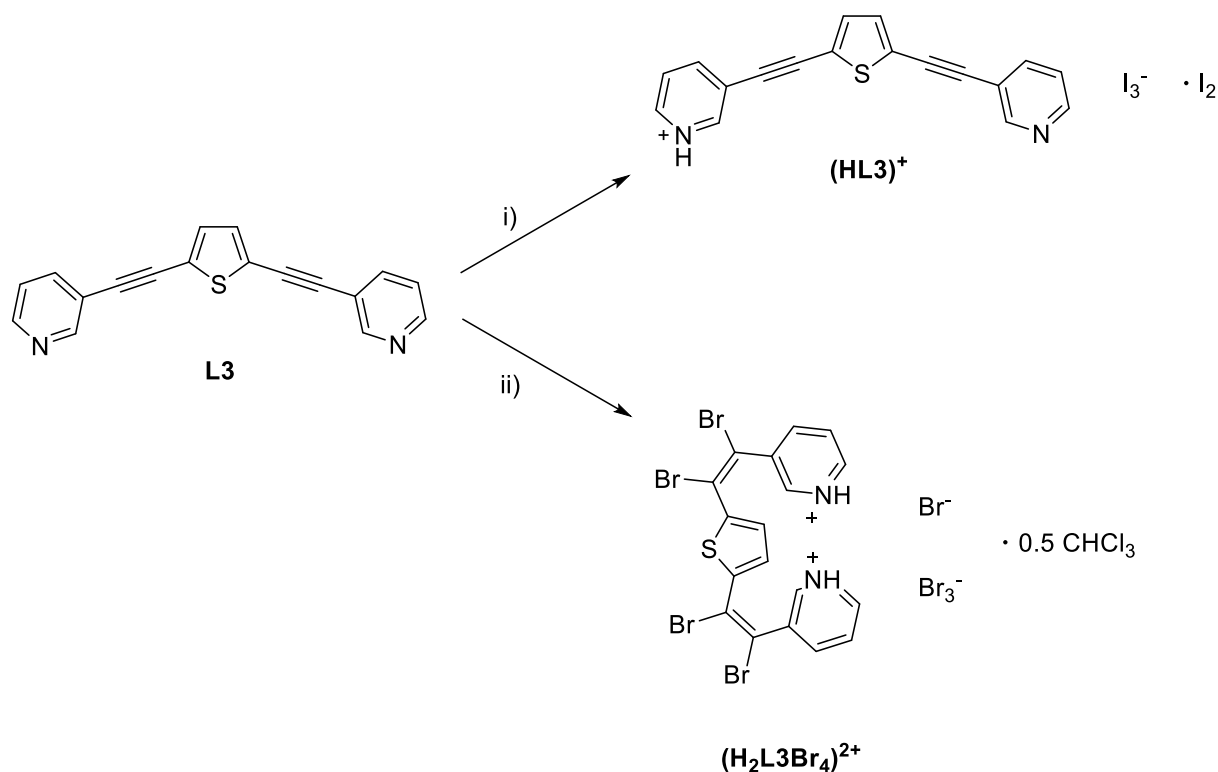


Figure 121 Packing diagrams of $(\mathbf{L2}\cdot\mathbf{1,4-DITFB})_{\infty}$ along [101] direction (left) showing a single layer and [110] direction (right) showing layers in different colours. Halogen bonds are depicted as dashed purple lines. Hydrogen atoms have been omitted for clarity.

The resulting $(\mathbf{L2}\cdot\mathbf{1,4-DITFB})_{\infty}$ 1D chains pack in a layered network (Figure 121). The FT-IR spectrum recorded on $(\mathbf{L2}\cdot\mathbf{1,4-DITFB})_{\infty}$ shows a shift of the C–I stretching frequency from 760 to 748 cm^{-1} passing from the free **1,4-DITFB** to $(\mathbf{L2}\cdot\mathbf{1,4-DITFB})_{\infty}$ adduct, as expected from the literature (Figure S96).^[410]

3.1.4.2. Interaction between L3 and halogens

As described above in more details (§3.1.1.2), ligands **L3** and **L4** present structural features similar to those of ligands **L1** and **L2** with two main differences residing in the nature of the central penta-atomic ring and in the presence of triple carbon-carbon bonds in the pyridyl arms of **L3** and **L4**. The reaction of **L4** with halogens did not afford clearly characterized compounds, whilst different products were obtained in the case of **L3**, depending on the experimental conditions, as summarized in Scheme 22.



Scheme 22 Formation of $(HL3)I_3 \cdot I_2$ and $(H_2L3Br_4)BrBr_3 \cdot 0.5CHCl_3$. i) $L3:I_2$ (1:1) CH_3CN ; ii) $L3:Br_2$ (1:5) $CHCl_3$.

The reaction of **L3** with an equimolar amount of iodine in acetonitrile formed a brown solution. Upon slow evaporation of the solvent, small crystals were obtained that were analyzed by X-Ray diffraction. Unfortunately, the quality of the obtained crystals was not so good to allow a full characterization of the structure, but the connectivity data suggest the formation of the interesting ionic product $(HL3)I_3 \cdot I_2$ that will be here briefly presented.

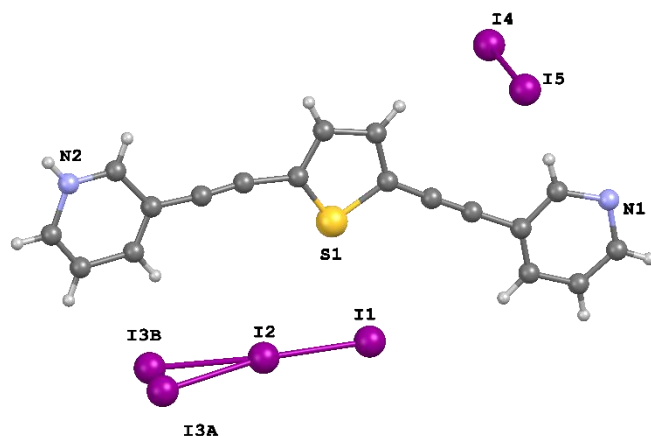


Figure 122 Preliminary crystal structure of $(\text{HL3})\text{I}_3 \cdot \text{I}_2$. Crystal data: $a = 3.5862(12)$; $b = 9.6320(9)$; $c = 32.929 \text{ \AA}$; $\beta = 90.068(12)^\circ$; $V = 2089.0(5) \text{ \AA}^3$; Space group: $P2/c$.

The preliminary structure of $(\text{HL3})\text{I}_3 \cdot \text{I}_2$ was solved in the centrosymmetric space group $P2/c$ which belong to a monoclinic lattice (Figure 122). However, the close proximity to 90° of the β angle could potentially lead to a solution in a higher orthorhombic lattice in future recollection on better quality crystals. The **L3** units undergo protonation at pyridyl fragments and are arranged in positively charged head-to-tail polymeric chains featuring $\text{NH}^+ \cdots \text{N}$ hydrogen bonds with the H atom formally associated to both N atoms with occupancy fixed to 0.5 (Figure 123), similarly to the previously discussed cases of $(\text{HL1})^+$ and $(\text{HL2})^+$ (§3.1.4.1), with the positive charge at $(\text{HL3})^+$ unit counterbalanced by disordered triiodide anion (see salts $(\text{HL1})\text{I}_3$ and $(\text{HL2})\text{I}_3$ in Table 30). The salt $(\text{HL3})\text{I}_3 \cdot \text{I}_2$ features also I_2 molecule co-crystallized into an infinite linear arrangement of I_2 molecules running along the a axis.

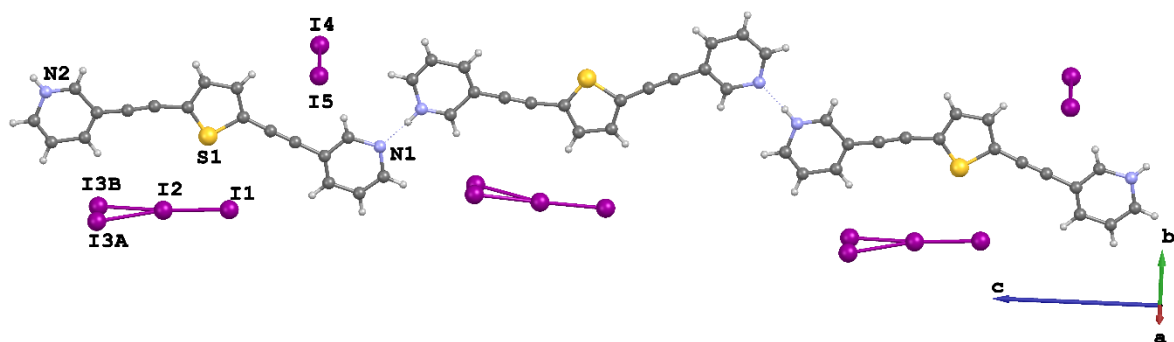


Figure 123 Cationic head-to-tail arrangement of $(\text{HL3})^+$, counterbalanced by disordered triiodide anions.

The reaction of **L3** with a fivefold excess of molecular bromine in chloroform afforded a red solution. After one week at 4°C , dark red crystals were separated from the reaction mixture

and characterized by single crystal X-ray diffraction as $(\text{H}_2\text{L3Br}_4)\text{BrBr}_3 \cdot 0.5\text{CHCl}_3$, accordingly to Scheme 22. The salt crystallizes in the triclinic space group $P-1$ with two independent cations, two tribromide and bromide anions, and one solvent molecule in asymmetric unit (Figure 124). The tribromide fragments are disordered over two positions and were refined with fractional occupancy 91:9 and 99:1 using a number of SADI, SIMU, DELU and RIGU restrains. The co-crystallized chloroform molecule was refined over two positions with fractional occupancy 50:50 using SADI, SIMU and RIGU restrains, and the thermal ellipsoids of the C atoms of the solvent were constrained using EADP. Crystal data and refinement parameters, and selected bond lengths and angles are reported in Table S145 and Table S146, respectively.

The unprecedented cation $(\text{H}_2\text{L3Br}_4)^{2+}$ resulted from the oxidative dibromination of the C–C triple bonds of **L3** with formation of two $E\text{-BrC}=\text{CBr}$ moieties. Both pyridyl rings are protonated at the N atoms, and the positive charges counterbalanced by a bromide and a tribromide anions. The tribromide anions feature almost linear geometries ($173.1(9) \leq \alpha \leq 177.64(9)^\circ$) and result slightly asymmetric with Br–Br distances ranging from 2.4795(7) to 2.6510(6) Å for Br12–Br13 and Br11–Br12, thus elongated of about 9–17 % if compared with the Br–Br distance of solid Br_2 (2.27 Å).

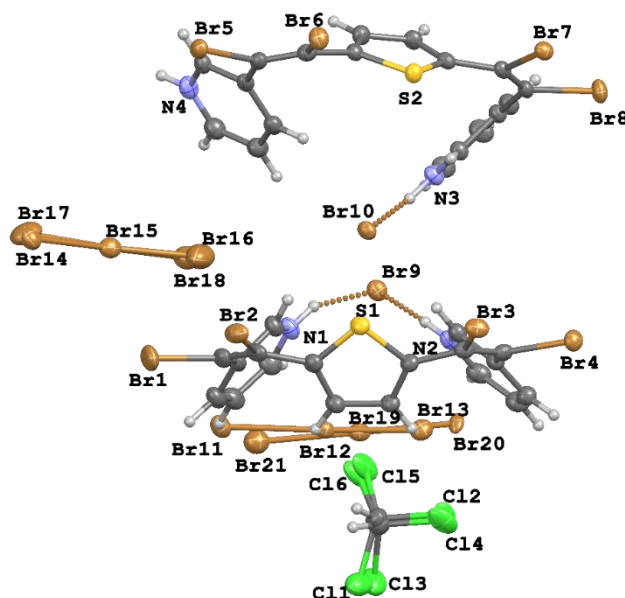


Figure 124 Asymmetric unit and numbering scheme of $(\text{H}_2\text{L3Br}_4)\text{BrBr}_3 \cdot 0.5\text{CHCl}_3$. Thermal ellipsoids are drawn at 50 % probability level.

The cations $[(\text{H}_2\text{L3Br}_4)]^{2+}$ are not planar with angles between the pyridyl and the central thiophene rings of $70.80(19)$ and $72.8(2)^\circ$ for $\text{Py1}^\wedge\text{Tph1}$ and $\text{Py2}^\wedge\text{Tph1}$ and $75.90(19)$ and

82.5(2)° for Py3⁺Tph₂ and Py4⁺Tph₂, respectively (Table 32). Pyridyl rings in the two cations are oriented in a different manner as showed in Figure 125 and Table 32. In the first one Py1 and Py2 are angled of 87.48(14)° and point to the same side with N1 and N2 interacting with the bromide anion Br9⁻ through interactions **a** and **b** described in Table 31 and shown in Figure 125 and Table 32. In addition, N1 interact with the other bromide Br10⁻ through a weaker intermolecular interaction described as **e** in Table 31 and Figure 125.

Table 31 Hydrogen bonds and contacts found within the crystal structure of (H₂L3Br₄)BrBr₃·0.5CHCl₃.

Interaction		d _{D...A} (Å)	d _{H...A} (Å)	D-H...A (°)
a	N1-H1...Br9	3.346(4)	2.618(4)	140.6(3)
b	N2-H2...Br9	3.255(3)	2.440(4)	153.9(2)
c	N3-H3A...Br10	3.248(3)	2.555(4)	136.1(2)
d	N4-H4...Br9 ¹	3.364(4)	2.624(4)	142.4(3)
e	N1-H1...Br10	3.442(4)	2.844(4)	126.6(3)
f	N3-H3A...Br9	3.493(4)	2.874(4)	128.7(2)
		d(Å)		
g	Br10...Br5 ¹	3.617(6)		
h	Br10...Br7 ²	3.521(6)		
i	Br4...Br1 ³	3.324(7)		
j	Br6 ¹ ...Br15	3.394(6)		
k	Br2...Br11 ²	3.492(7)		
l	Br2...Br21 ²	3.34(4)		
m	Br3...Br13 ²	3.559(6)		
n	Br3...Br20 ²	3.39(3)		

Symmetry codes: ¹ 1+x, +y, +z; ² 1-x, 2-y, 1-z; ³ +x, 1+y, +z.

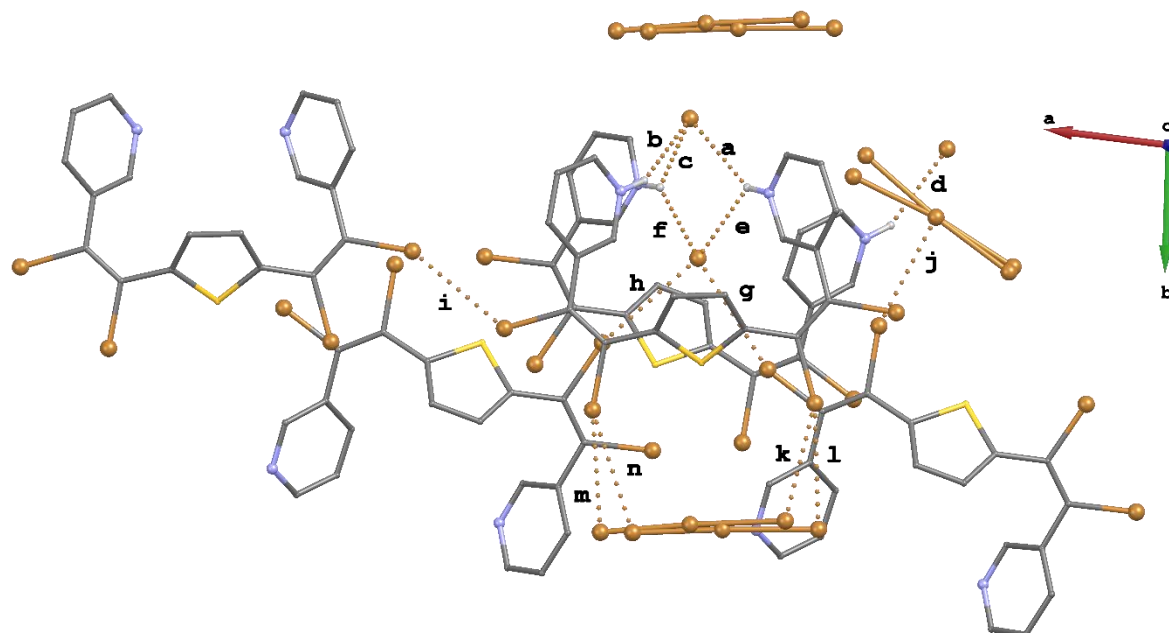
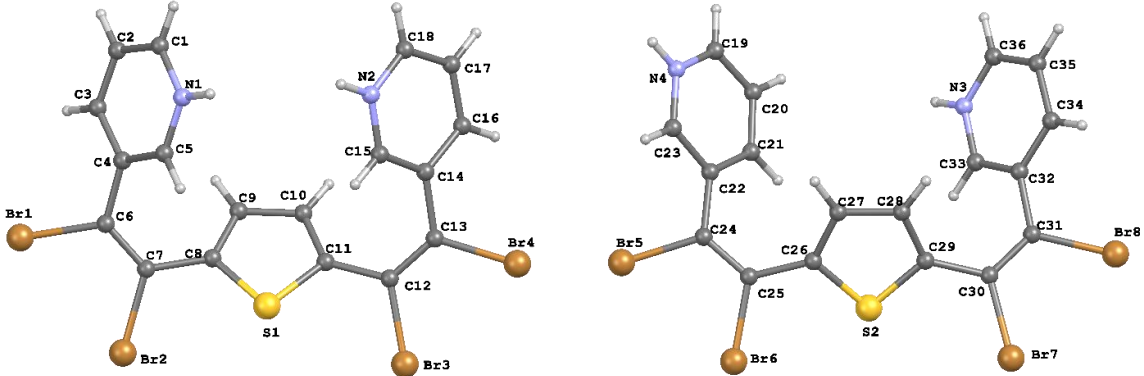


Figure 125 View of intermolecular interactions of (H₂L3Br₄)BrBr₃·0.5CHCl₃ along the *c* axis. Interactions are labelled according to Table 31.

In the other cation Py3 and Py4 are angled of $87.38(14)^\circ$ pointing towards opposite directions due to the interactions with different bromide anions: N3 interacts with Br10⁻ and Br9⁻ through interactions **c** and **f**, respectively (Table 31, Figure 125). In contrast N4 is involved in an intermolecular interaction with the bromide Br9⁻ depicted as **d** in Table 31 and Figure 125. In addition to the interactions described for fragments N-H \cdots Br, a few Br \cdots Br contacts are found involving C-Br \cdots Br⁻ (interactions **g** and **h**), C-Br \cdots Br-C (interaction **i**) and C-Br \cdots Br₃⁻ (interactions **j-n**) as shown in Figure 125 and described in Table 31.

The bond distances and angles found in **(H₂L3Br₄)BrBr₃·0.5CHCl₃** closely resemble those found in the above discussed structure obtained by oxidative bromination of 1,4-bis(pyridin-3-ylethynyl)benzene (OKUYAB, §1.1.4). The resulting cation featured C-Br distances ranging from 1.891(6) to 1.918(6) Å resulting very similar to those observed in both cations **[(H₂L3Br₄)²⁺**. In contrast, the C=C double bond distances in **(H₂L3Br₄)BrBr₃·0.5CHCl₃** are slightly longer if compared to those found in the crystal structure of OKUYAB (1.330(7) and 1.311(7) Å) (Table 32).

Table 32 Selected bond lengths (Å) and angles (°) for the cationic fragments **(H₂L3Br₄)²⁺** in **(H₂L3Br₄)BrBr₃·0.5CHCl₃**.



Br1-C6	1.884(4)	Br5-C24	1.900(4)
Br2-C7	1.897(4)	Br6-C25	1.897(4)
Br3-C12	1.892(4)	Br7-C30	1.900(4)
Br4-C13	1.883(4)	Br8-C31	1.893(4)
S1-C8	1.714(4)	S2-C26	1.728(4)
S1-C11	1.719(4)	S2-C29	1.723(4)
C6-C7	1.335(7)	C24-C25	1.336(6)
C7-C8	1.471(6)	C25-C26	1.463(6)
C11-C12	1.461(6)	C29-C30	1.459(5)
C12-C13	1.340(6)	C30-C31	1.336(6)
Br1-C6-C7-Br2	10.4(5)	Br5-C24-C25-Br6	9.7(5)
Br2-C7-C8-S1	40.9(4)	Br6-C25-C26-S2	151.5(4)
S1-C11-C12-Br3	39.6(4)	S2-C29-C30-Br7	39.9(4)
Br3-C12-C13-Br4	5.0(4)	Br7-C30-C31-Br8	7.5(5)
Py1 [^] Tph1	70.80(19)	Py3 [^] Tph2	75.90(19)
Tph1 [^] Py2	72.8(2)	Tph2 [^] Py4	82.5(2)
Py1 [^] Py2	87.48(14)	Py3 [^] Py4	87.38(14)

Py1: N1-C1-C2-C3-C4-C5; Py2: N2-C14-C15-C16-C17-C18; Tph1: S1-C8-C9-C10-C11; Py3: N3-C33-C34-C35-C36-37; Py4: N4-C19-C20-C21-C22-C23; Tph2: S2-C26-C27-C28-C29.

The crystal packing is decorated by the intermolecular interactions described above and the packing diagrams along the *b* and *c* axis are shown in Figure 126.

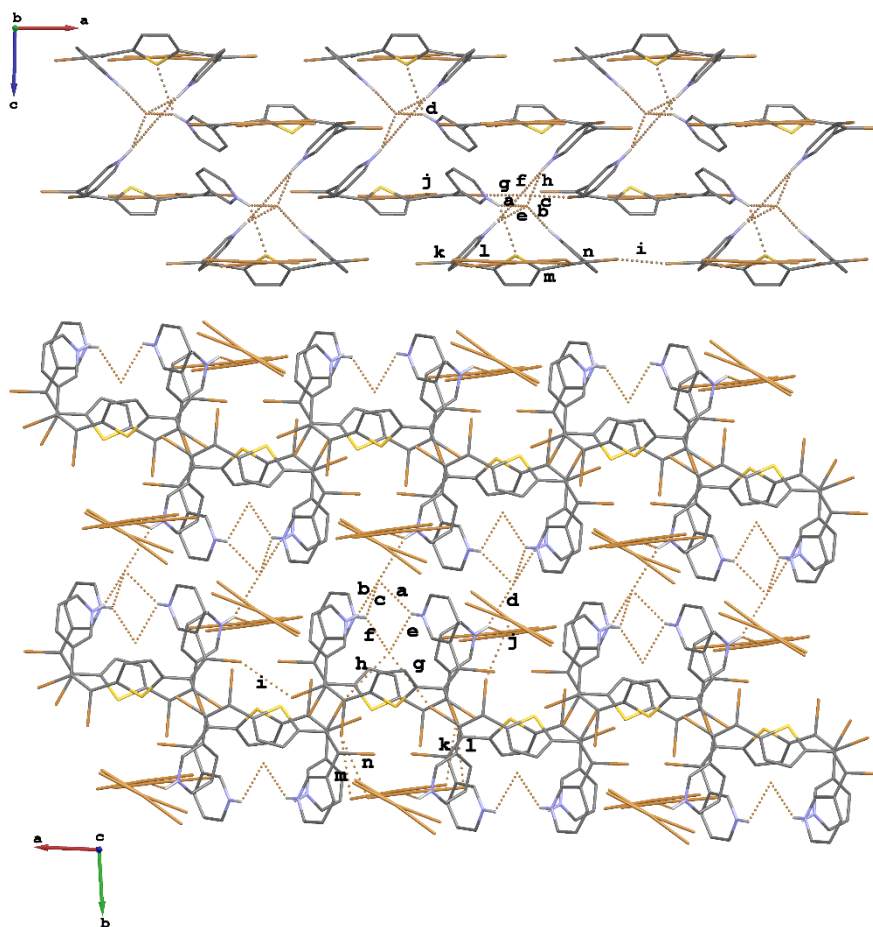
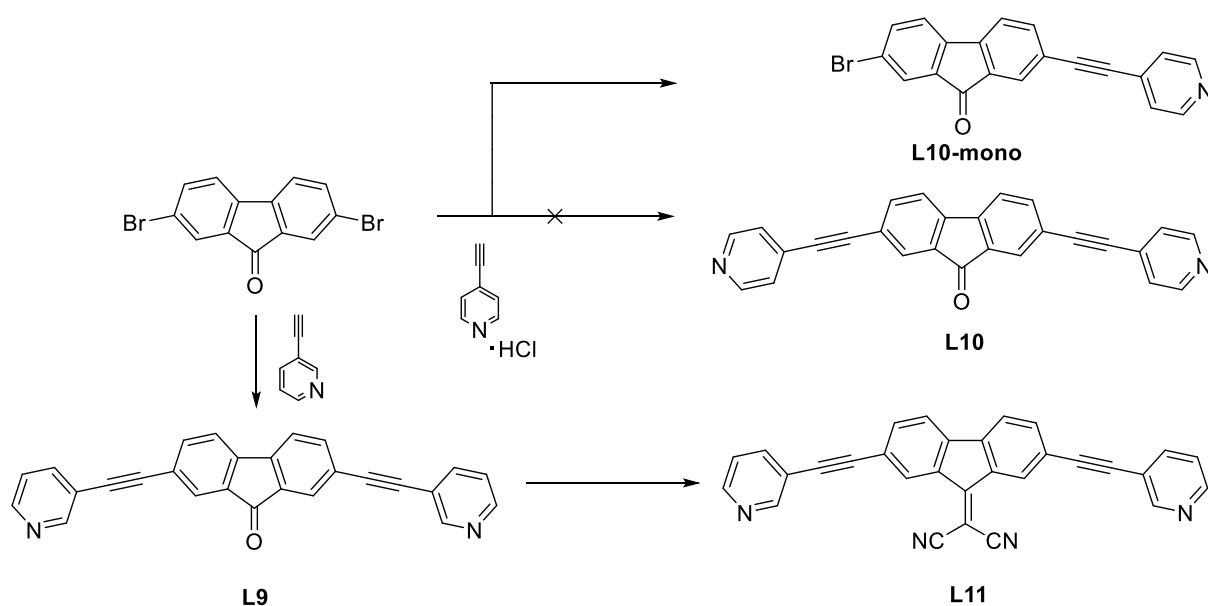


Figure 126 Packing diagrams of $(\text{H}_2\text{L3Br}_4)\text{BrBr}_3 \cdot 0.5\text{CHCl}_3$ along the *b* and *c* axis from top to bottom, respectively.

3.1.4.3. Interaction between L11 and halogens

The crystal engineering of predictable halogen bonded supramolecular assemblies is a topical issue and several papers were recently published aimed to establish a hierarchy of interactions among halogen bond donors and acceptors. Desper and co-workers proposed a hierarchy based on the electrostatic potential surfaces calculated at the DFT level of theory, where pyridyl groups were classified as better XB acceptors if compared with imidazolyl derivatives, due to the higher partial negative electrostatic potential of the pyridyl site.^[212,411–413] Anyway, the order coming out from such considerations not always matches with the existent structural data. For example, DFT calculations on 4-cyanopyridine (4-CNPy) calculated electrostatic potentials of -159 and -145 kJ mol^{-1} for the CN and Py moieties, respectively, suggesting that the nitrile

group should be a better XB acceptor if compared with pyridine group,^[414] but the crystal structures reported in the CSD revealed that the pyridine is a better XB acceptor than CN.^[414] The predictability of the final network in such systems is in fact complicated by the existence of several factors among which the competition between hydrogen and halogen bond. Recently, the reactivity of 4-CNPy towards aliphatic and aromatic halogenated derivatives was investigated, and examples of both supramolecular synthons $X\cdots N_{Py}$ and $X\cdots N_{CN}$ reported.^[406] In order to study the reactivity of a mixed pyridyl/nitrile donor towards “naked” halogens, we designed the organic spacer 2-(2,7-bis(pyridin-3-ylethynyl)fluoren-9-ylidene)malononitrile (**L11**) which features both pyridyl and nitrile functionalities, following the two-step synthesis reported in Scheme 23.



Scheme 23 Synthetic approach for the preparation of **L9**, **L10** and **L11**.

The Sonogashira coupling reaction of 3-ethynylpyridine with 2,7-dibromofluoren-9-one yielded 2,7-bis(pyridin-3-ylethynyl)fluoren-9-one (**L9**) that was then converted into the desired spacer **L11** through the reaction with malononitrile in DMSO (§5.2.10). When a similar approach was used for the preparation of the *para*-substituted analogue **L10**, we were only able to isolate and characterize the mono-substituted derivative **L10mono**. The characterization of **L9** and **L10mono** are provided as supplementary materials in the present thesis (§Appendix 7: Supplementary Information).

The multitopic ligand **L11** was fully characterized by means of elemental analysis, FT-IR, ¹H and ¹³C NMR spectroscopies. Middle infrared spectrum features two absorption bands at 2225 and 2198 cm⁻¹, assigned to the C≡N and C≡C stretching modes (Figure S66). The ¹H NMR

spectrum shows the pyridyl signals centered at 8.80, 8.59, 8.55 and 7.33 ppm and those of the fluorene-9-ylidene fragment at 7.87, 7.71 and 7.60 ppm (Figure S22). The $^{13}\text{C}\{^1\text{H}\}$ spectrum features a signal at 159.9 ppm assigned to the C atom in position 9 in the fluorene-9-ylidene moiety, and three signals resonating at 91.5, 88.6 and 77.9 ppm attributed to the alkyne and nitrile functionalities (Figure S23). Recrystallization from chloroform yielded beautiful purple needle-shaped crystals which were structurally characterized. **L11** crystallizes in the monoclinic space group $P2_1/c$ with one molecule in the asymmetric unit (Figure 127).

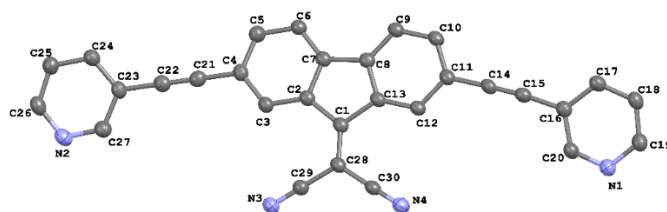


Figure 127 Representation of the asymmetric unit of the crystal structure of **L11** along the a axis. Thermal ellipsoids are drawn at 50 % probability level. Hydrogen atoms have been omitted for clarity reasons.

The main crystal data and structure refinement parameters are listed in Table S147. The ligand adopts a periplanar conformation and is almost planar with a small rotation of the pyridyl rings of about 7 and 8 ° with respect to the plane defined by the fluorene moiety, that confers to **L11** a slightly waved shape. A comparison with the structures of *meta*-substituted ligands **L5** (18.721 Å) and **L9** (19.451 Å) show similar length with intramolecular N...N distance of 18.095(2) Å for **L11**. The central bis(fluorene-9-ylidene)malononitrile features a planar arrangement stabilized by intramolecular hydrogen bonds between fluorenyl protons and nitrile functionalities and are described as interactions **a** and **b** in Table 33 and Figure 128.

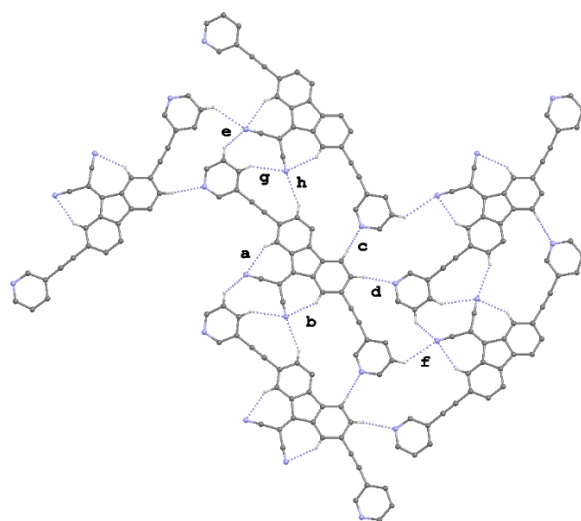


Figure 128 Intra- and inter-molecular hydrogen bonds found in the crystal structure of **L11**, labelled according to Table 33.

L11 molecules pack in undulated sheets perpendicular to the *a* axis stabilized *via* intermolecular hydrogen bonds between the N atoms of pyridyl rings and the aromatic protons of adjacent fluoren-9-ylidene moieties, and N atoms of nitrile groups and pyridyl protons of adjacent **L11** units (interactions **c-h** in Table 33 and Figure 128). The sheets pack along the [101] direction through weak π - π interactions between pyridyl rings (interaction **i**, centroid-centroid distance 3.725(10) Å, $\alpha = 6.31(6)^\circ$) (Figure 129).

Table 33 Intra and intermolecular hydrogen bonding interactions in **L11** and **(L11·I₂)·0.5I₂**.

	L11	<i>d</i> _{D-A} (Å)	<i>d</i> _{H-A} (Å)	D-H...A (°)	(L11·I₂)·0.5I₂	<i>d</i> _{D-A} (Å)	<i>d</i> _{H-A} (Å)	D-H...A (°)
a	C3-H3...N3	3.440(2)	2.617(14)	145.13(10)	C13-H13...N3	3.483(10)	2.69(7)	141.1(4)
b	C12-H12...N4	3.348(2)	2.519(14)	145.88(11)	C20-H20...N4	3.374(10)	2.57(7)	144.7(4)
c	C9-H9...N1 ¹	3.617(2)	2.713(13)	159.16(11)	C17-H17...N2 ⁴	3.516(10)	2.63(8)	160.4(5)
d	C10-H10...N2 ²	3.414(2)	2.483(15)	167.21(12)	C2-H2...N3 ⁴	3.437(12)	2.79(7)	127.5(6)
e	C25-H25...N3 ¹	3.517(2)	2.896(13)	123.70(13)	C3-H3...N3 ⁴	3.482(10)	2.88(7)	123.8(6)
f	C18-H18...N3 ³	3.646(2)	2.910(15)	135.15(11)	C9-H9...N4 ⁴	3.476(10)	2.56(7)	166.8(5)
g	C24-H24...N4 ¹	3.701(2)	2.896(15)	143.18(12)	C27-H27...N4 ⁵	3.339(11)	2.76(7)	121.2(6)
h	C5-H5...N4 ¹	3.767(2)	2.896(14)	152.91(11)				

Symmetry codes: ¹ -1+x, +y, -1+z; ² 1-x, -1/2+y, 1/2-z; ³ 2-x, -1/2+y, 3/2-z; ⁴ 1+x, 1+y, +z; ⁵ -x, -y, 1-z.

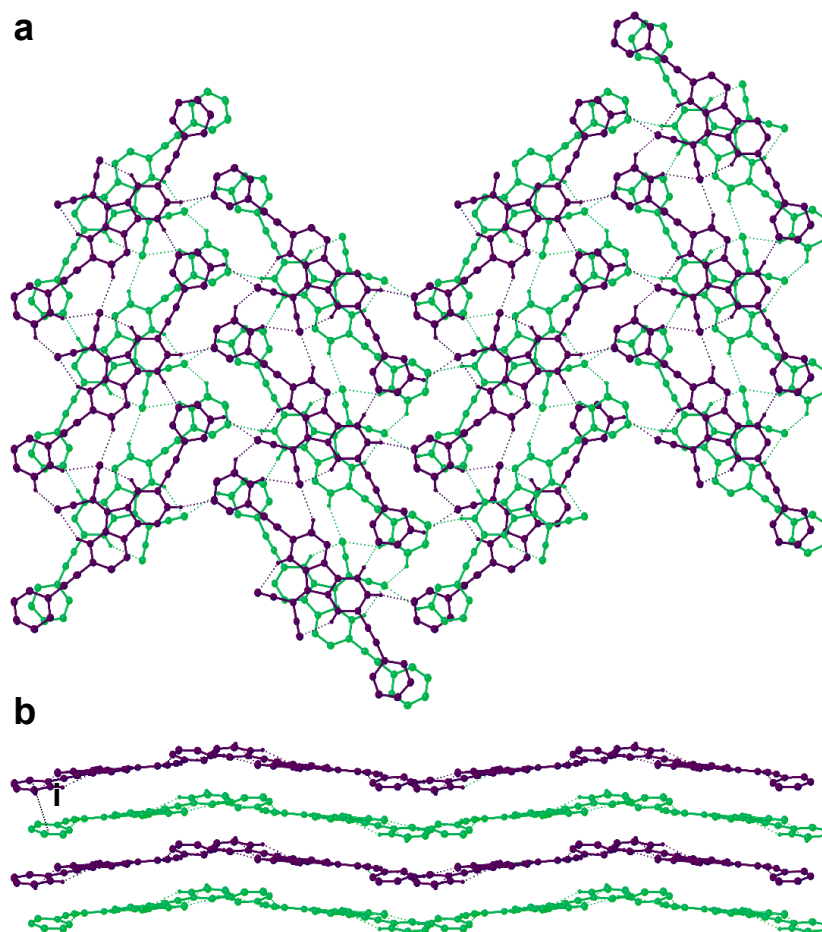


Figure 129 Packing diagrams of **L11** along [100] and [101] directions showing undulated sheets in a) and b), respectively. Adjacent layers are coloured in different colours for the sake of clarity. Hydrogen bonds are represented as dashed lines, interaction **i** is depicted as dashed black line. Non interacting hydrogens have been omitted for clarity.

Ligand **L11** was made to react with I₂, Br₂, IBr and ICl in the same reaction conditions used for **L3**, but the only crystalline product was obtained by vapor diffusion of a hexane solution of I₂ into a solution of **L11** in chloroform. The red block-shaped crystals crystallize in the triclinic space group *P*-1 with one molecule of the CT adduct **L11·I₂** and half of an additional I₂ molecule in the asymmetric unit (Figure 127), corresponding to the formula **(L11·I₂)·0.5I₂**. The main crystal data and structure refinement parameters are listed in Table S147 and Table S148. The ligand in **(L11·I₂)·0.5I₂** adopts a periplanar conformation, similarly to what observed for the free ligand. The pyridyl rings are angled of about 8.4(2) and 16.7(3)° with respect to the plane defined by the fluorenyl moiety, empathizing the waved shape found in **L11** were the same angles were 7 and 8 °, respectively. A comparison with the structure of the **L11** show very similar length with intramolecular N···N distance of 18.025(11) Å. The central bis(fluoren-9-ylidene)malononitrile features a planar arrangement stabilized by intramolecular hydrogen bonds with distances and angles that closely resemble those found for the free linker as summarized in Table 33 (interactions **a** and **b**, Figure 132).

In the adduct **(L11·I₂)** the N1 nitrogen of one pyridyl donor site is involved in the formation of a CT adduct with molecular iodine I1–I2, with a N1···I1 distance of 2.562(7) Å, only 28 % shorter than the sum of the van der Waals radii of the involved atoms, quite longer than that of 2.358 Å found for the similar adduct with 1,4-bis(pyridin-3-ylethynyl)benzene previously reported by our research group.^[132] The N···I–I interaction is almost linear with an angle of 175.09(16) °, in agreement with the linearity observed in similar CT adducts,^[127,132,415] with the iodine molecule lying in the pyridyl plane. The I1–I2 distance of 2.7375(9) Å results only slightly elongated with respect to that observed in solid I₂ (2.715 Å).^[404] and shorter than that of 2.804 Å found in the adduct with 1,4-bis(pyridin-3-ylethynyl)benzene.

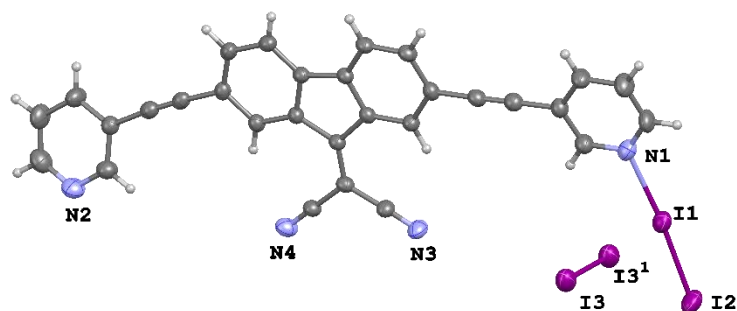


Figure 130 View of the crystal structure of **(L11·I₂)·0.5I₂** along the *a* axis. Thermal ellipsoids are drawn at 30 % probability level. Symmetry code: ¹ -x, 1-y, -z.

The I1–I2 distance is in line with those found for medium-weak CT adducts, accordingly to the data reported in Table 2 (§1.1.4). The weak interaction with N1 allows the I1–I2 molecule to further interact with the additional I3–I3¹ molecule (¹ -x, 1-y, -z) featuring a I–I distance of 2.7053(15) Å. The two diiodine molecules interact with I1⋯I3 distance of 3.4857(9) Å and I2–I1⋯I3 angle of 101.98(3) ° generating the discrete Z-shaped assemblies showed in Figure 131.

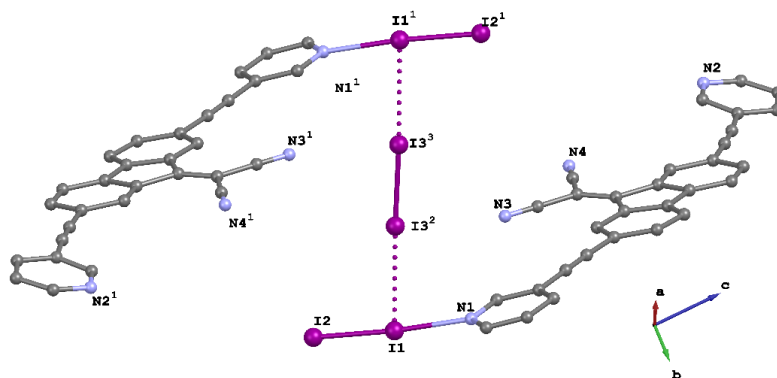


Figure 131 View of the CT adduct (**L11·I₂**)·0.5**I₂** showing the Z-shaped assembly formed by three I₂ molecules. Thermal ellipsoids are drawn at 30 % probability level. Symmetry codes: ¹ 2-x, 1-y, z; ² 1-x, 1-y, -z; ³ 1+x, 1+y, +z.

The involvement of only one of the two pyridyl rings of **L11** in the interaction with I₂ can be explained taking into account the strong competitiveness between hydrogen and halogen bonds. The second pyridyl ring is engaged in a hydrogen bond between N2 and the aromatic proton of an adjacent molecule, described as **c** in Table 33 and shown in Figure 132. The same pyridyl group also interact with the nitrile group of an adjacent molecule through interaction **g** (Table 33, Figure 132). The strong propensity of nitrile to engage hydrogen bonds is corroborated by interactions **f**, **d** and **e** established between the aromatic proton of an adjacent fluorenyl fragment and a halogen bonded pyridine from the same molecule, respectively (Table 33, Figure 132).

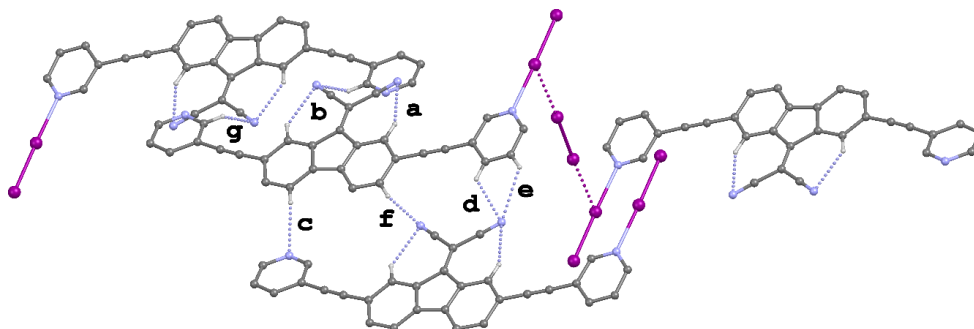


Figure 132 Intra- and inter-molecular hydrogen bonds found in the crystal structure of (**L11·I₂**)·0.5**I₂**, labelled according to Table 33.

Molecules of **L11** in $(\mathbf{L11}\cdot\mathbf{I}_2)\cdot\mathbf{0.5I}_2$ are arranged to form discrete zig-zag dimeric units which can be simplified by the formula $(\mathbf{L11})_2\mathbf{Z}$ (where $\mathbf{Z} = 3\mathbf{I}_2$). The crystal packing features interdigitated dimers which are stabilized by the abovementioned hydrogen bonded network and weak π - π interactions between fluoren-9-ylidene cores as shown in Figure 133 (centroid-centroid distance 3.811(4), $\alpha = 3.2(2)^\circ$).

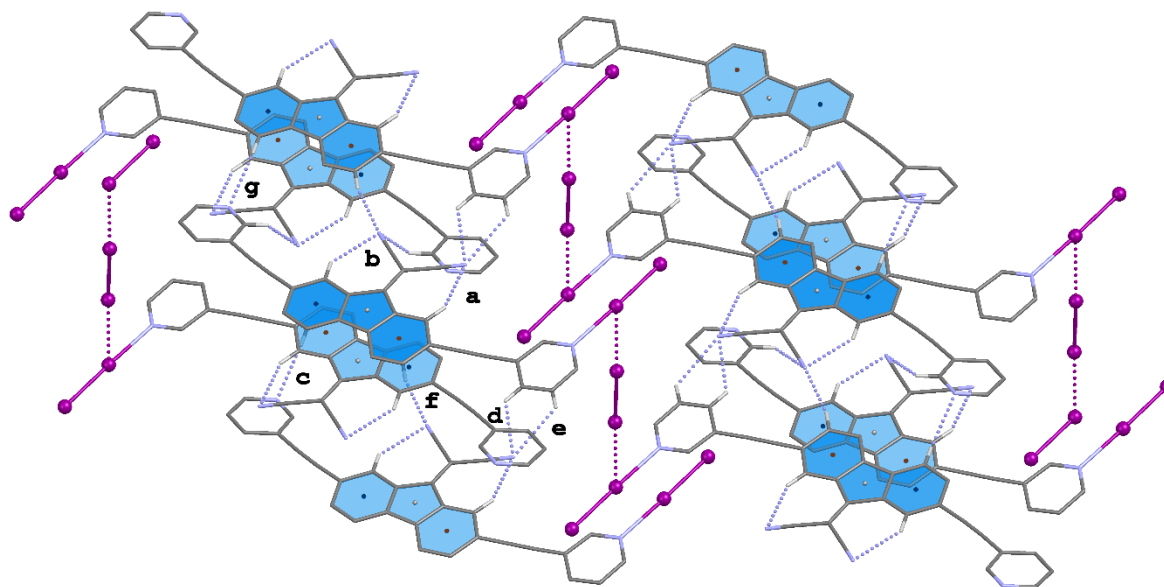


Figure 133 Representation of dimers $(\mathbf{L11})_2\mathbf{Z}$ found in the crystal structure of $(\mathbf{L11}\cdot\mathbf{I}_2)\cdot\mathbf{0.5I}_2$. The crystal packing features multiple hydrogen bonds labelled according to Table 33. Weak π - π interactions occurring between fluoren-9-ylidene cores are coloured in light blue.

Although limited to one example only, a preferential affinity of the halogen towards the pyridyl donor site can be noticed with respect to the nitrile ones.

3.1.4.4. Interaction between L12-L14 and halogens

The study on pyridyl based compounds able to react with halogens was extended to different substrates, namely dipyrilid-2-yldiselenide ($\mathbf{Py}_2\mathbf{Se}_2$, **L12**), dipyrilid-2-ylditelluride ($\mathbf{Py}_2\mathbf{Te}_2$, **L13**), and 2-(p-tolyl)selenopheno[2,3-b]pyridine **L14**, in order to continue the studies of our research group on the analogue dipyrilid-2-yldisulfide ($\mathbf{Py}_2\mathbf{S}_2$, **L12s**).^[135] The reaction of **L12s** with \mathbf{I}_2 in CH_2Cl_2 solution in different molar ratios afforded $(\mathbf{HL12s})\mathbf{I}\cdot\mathbf{2.5I}_2$ as the only compound featuring a $(\mathbf{HPy}_2\mathbf{S}_2)^+$ cation with one protonated pyridine ring, counterbalanced by a rare pseudo-cubic 3D-network featuring $\mathbf{I}\cdot\mathbf{5I}_2$ nodes, arranged into a distorted square pyramidal geometry, and maintaining unaltered the disulfide bond.^[135] The reaction of **L12** with \mathbf{I}_2 under the same experimental conditions (1:3 L/ \mathbf{I}_2 , §5.2.54) yielded a crystalline product identified as

(HL12)I·2.5I₂ by XRD analysis, isostructural with the sulfurated analogous **(HL12s)I·2.5I₂**, structural parameters and data refinement, and selected bond lengths and angles for both compounds are reported in Table S149 and in Table 34. The asymmetric unit of **(HL12)I·2.5I₂** contains one 2-(pyridin-2-ylselaneyl)pyridinium cation **HL12⁺**, one iodide anion and two and a half iodine molecules (Figure 134).

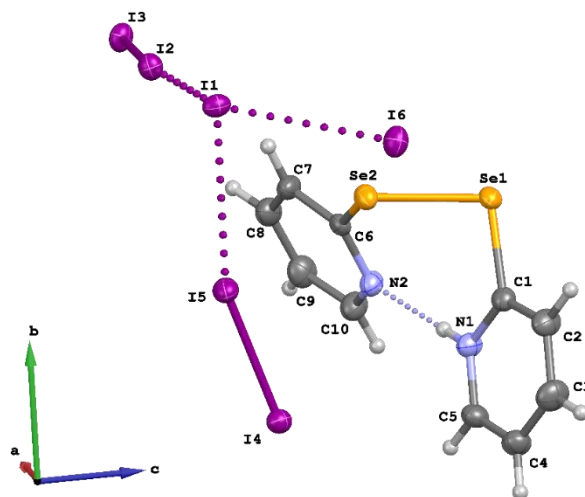


Figure 134 Asymmetric unit of compound **(HL12)I·2.5I₂**. N–H is displaced over the two N atoms with fractional occupancy of 50 %. Only one position is shown for clarity. Displacement ellipsoids are drawn at 50 % probability level.

Table 34 Selected bond lengths (Å) and angles (°) for **(HL12)I·2.5I₂** and **(HL12s)I·2.5I₂**.

	(HL12)I·2.5I₂	(HL12s)I·2.5I₂
E–E	2.3268(5)	2.052(4)
N1–N2	2.726(5)	2.694(14)
C–E–E–C	85.83(17)	87.3(5)
Py [^] Py	10.79(17)	15.3(5)
I1···I2	3.5271(4)	3.4492(11)
I1···I3 ¹	3.1506(6)	3.1505(11)
I1···I4	3.3040(7)	3.2819(11)
I1···I5 ²	3.3425(7)	3.3536(11)
I1···I6	3.4862(4)	3.4750(11)
I2···I3	2.7917(4)	2.7829(11)
I4···I5	2.7666(3)	2.7603(11)
I6···I6 ³	2.7361(5)	2.7376(15)
I1···I2···I3	160.23(5)	163.94(3)
I1···I3 ¹ ···I2 ¹	178.97(2)	177.89(4)
I1···I4···I5	169.38(3)	170.10(4)
I1···I5 ² ···I4 ²	168.55(3)	169.61(4)
I1···I6···I6 ³	172.58(2)	170.71(5)

E = S, Se; Symmetry codes: ¹ 1/2-x, 1/2+y, 1/2-z; ² -1+x, +y, +z; ³ -x, 1-y, 1-z.

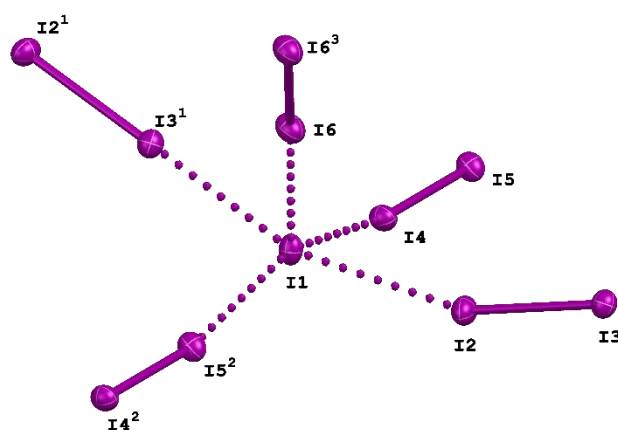


Figure 135 View of $I \cdot 5I_2$ nodes, arranged into a distorted square pyramidal geometry in the crystal structure of $(HL12)I \cdot 2.5I_2$. Symmetry codes: ¹ $1/2-x, 1/2+y, 1/2-z$; ² $-1+x, +y, +z$; ³ $-x, 1-y, 1-z$.

The I–I bond lengths in the diiodine molecules range between 2.7361(5) and 2.7917(3) Å, slightly elongated with respect to the solid-state I–I distance [2.715(6) Å].^[404] The rare $I \cdot 5I_2$ node is shown in Figure 135 and is labelled according to Table 34. The polyiodide 3D-network closely resembles the parallelepiped-like box found for $(HL12_s)I \cdot 2.5I_2$ with two $HL12^+$ cations trapped inside the anionic box as shown in Figure 136.

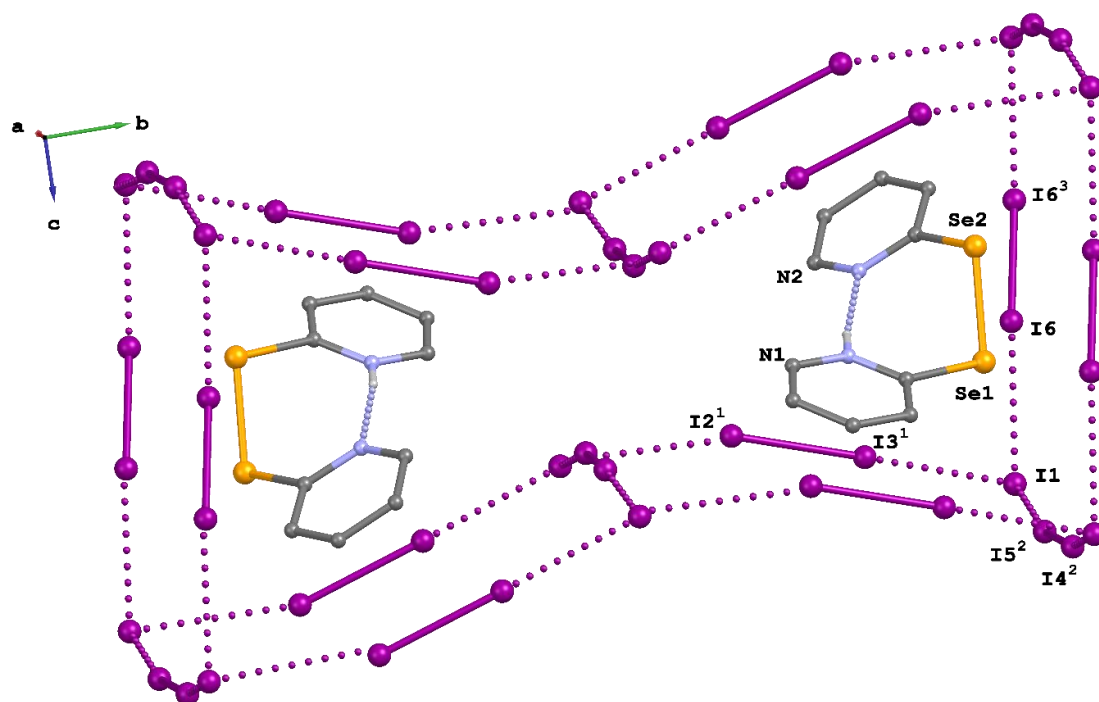


Figure 136 Parallelepiped-like box found in $(HL12)I \cdot 2.5I_2$. Two cations are enclosed in the 3D-polyiodide network. Symmetry codes: ¹ $1/2-x, 1/2+y, 1/2-z$; ² $-1+x, +y, +z$; ³ $-x, 1-y, 1-z$.

Figure 137 reports the overlapping of $(\text{HL12})\text{I}\cdot 2.5\text{I}_2$ and $(\text{HL12s})\text{I}\cdot 2.5\text{I}_2$ networks in different colors in order to evidence the analogies and the small differences mainly due to the different E–E bond length on passing from sulfur to selenium.

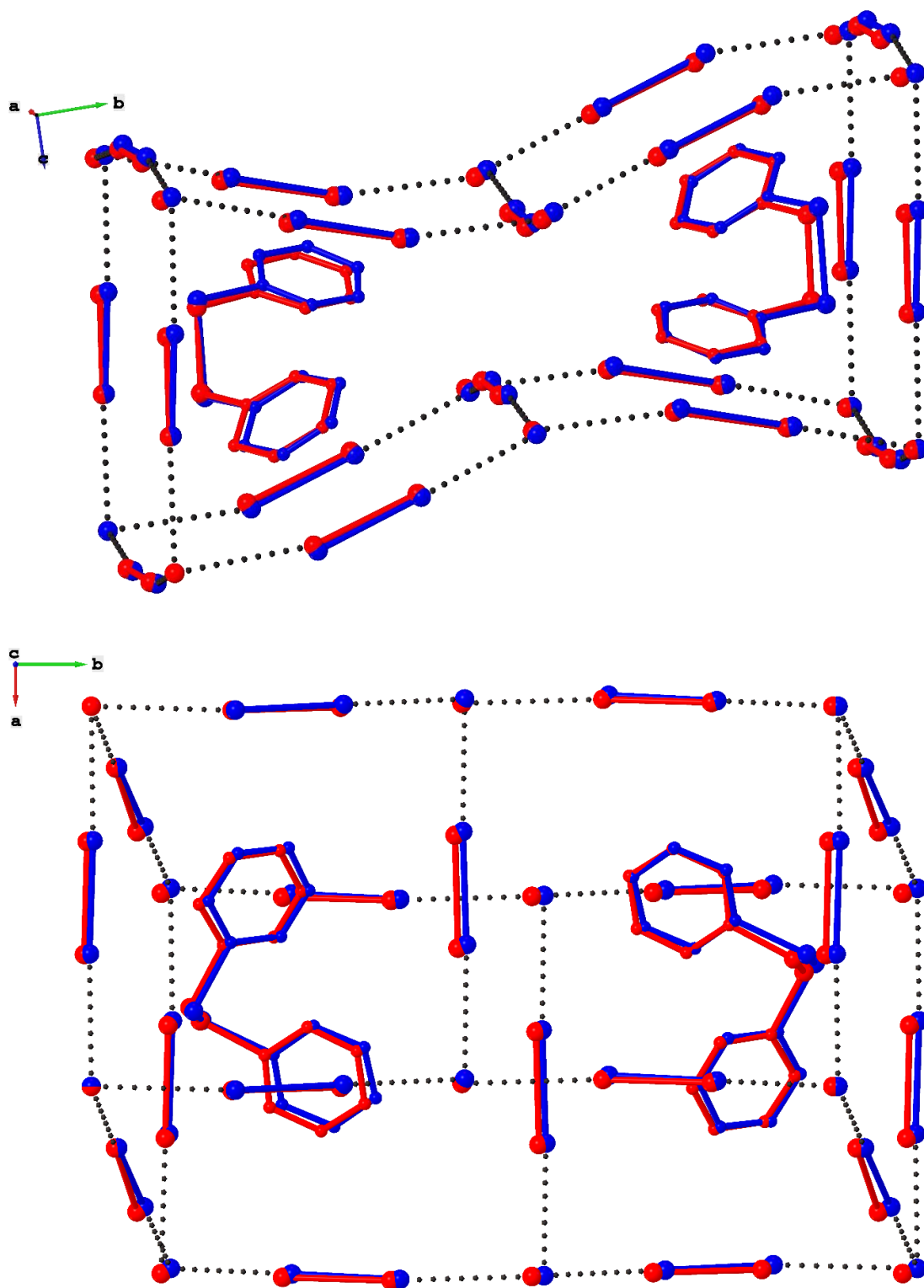
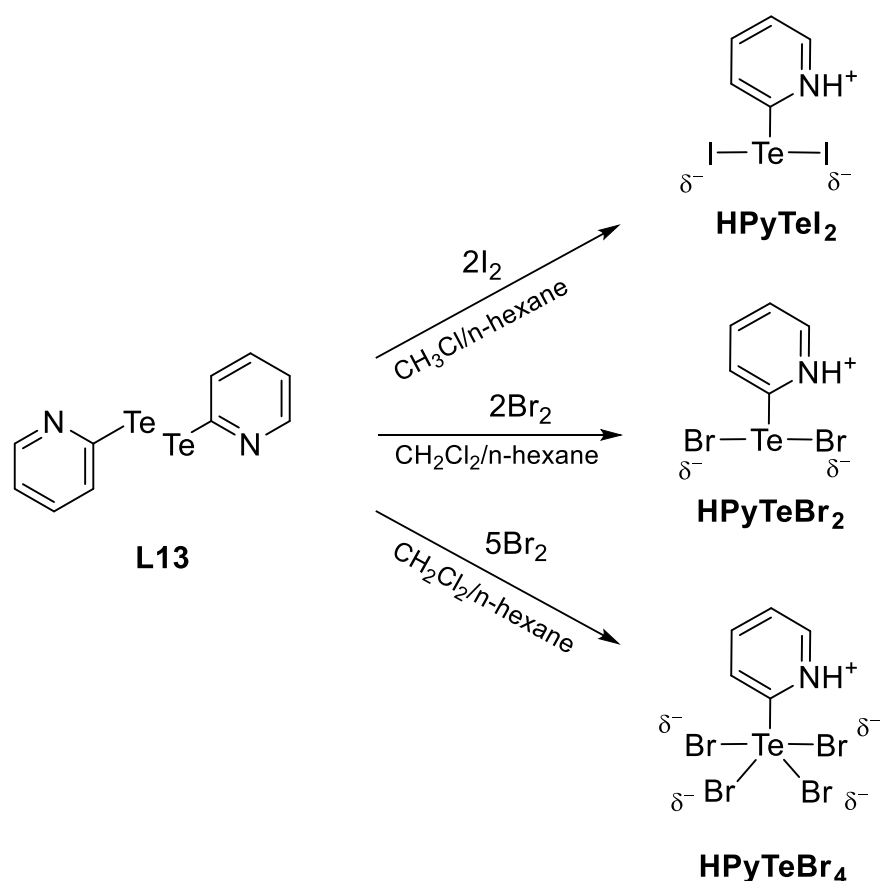


Figure 137 Overlapped crystal structures of compounds $(\text{HL12})\text{I}\cdot 2.5\text{I}_2$ (blue) and $(\text{HL12s})\text{I}\cdot 2.5\text{I}_2$ (red).

Compound **Py₂Te₂** (**L13**) was reacted towards molecular halogens (I₂ and Br₂) and interhalogens (IBr and ICl) using different molar ratios, different solvents (acetonitrile, dichloromethane, chloroform and ethanol) and different crystallization techniques. Although we were unable to obtain crystalline products from the reactions with interhalogens, reactions with molecular iodine and bromine proved successful and several products were isolated and characterized (Scheme 24).



Scheme 24 Hypervalent tellurium compounds prepared from **L13**: **HPyTeI₂**, **HPyTeBr₂**, **HPyTeBr₄**.

All reactions proceeded through Te–Te bond cleavage and formation of insertion compounds featuring a hypervalent tellurium atom bound to a pyridinium ring and two or four halogens: **HPyTeI₂**, **HPyTeBr₂**, and **HPyTeBr₄**.

The reaction of **Py₂Te₂** (**L13**) with iodine in the same experimental conditions (1:2 L/I₂, §5.2.55) used for the analogous **Py₂S₂** and **Py₂Se₂** yielded dark red crystals that analyzed by means of SC-XRD techniques were elucidated as the T-shaped zwitterion **HPyTeI₂** showed in Figure 138. The compound crystallizes in the monoclinic *P2₁/n* space group with only one molecule in the asymmetric unit (crystal data and refinement parameters in Table S150; selected bond lengths and angles in Table S151). The tellurium atom is bound to the pyridyl cation and

to two iodides thus resulting in the hypervalent coordination 10–E–3, according to Martin and Arduengo’s notation, introduced in §1.1.4. The almost linear I2–Te1–I1 moiety features slightly different I–Te bond distances of 2.9886(2) and 2.9070(2) for I1–Te1 and I2–Te1, respectively, and an I–Te–I angle of 176.383(7)°, in line with the values found for analogous systems.^[416] The molecule is not planar with the pyridyl ring angled of 46.48(6)° with respect to the plane defined by the I–Te–I moiety.

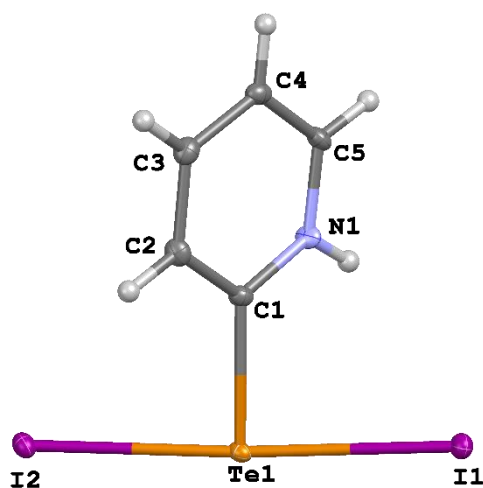
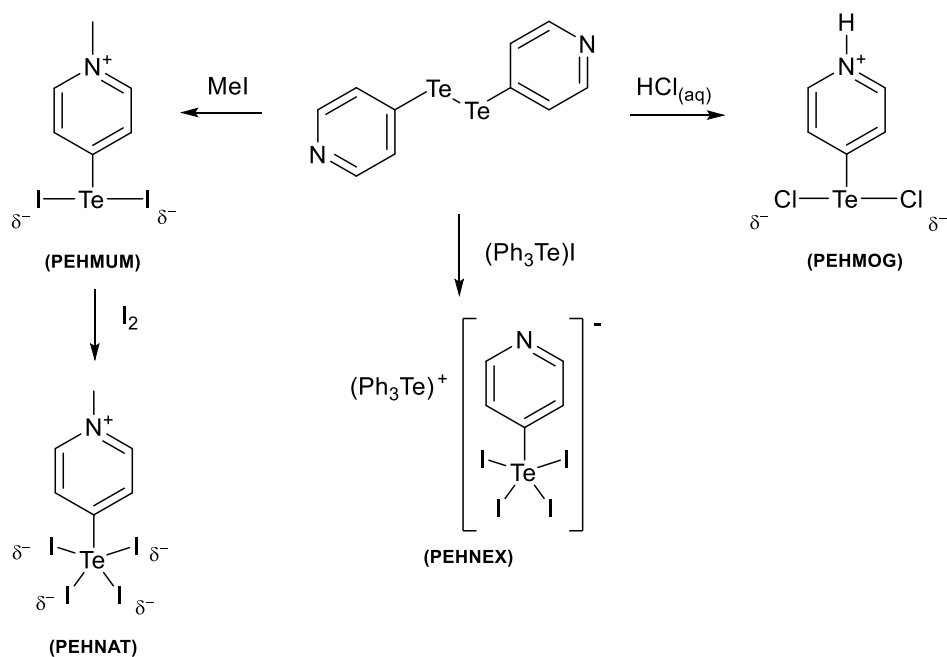


Figure 138 Crystal structure of **HPyTeI₂**. Displacement ellipsoids are drawn at 50 % probability level.

The class of compounds **HPyTeX₂** containing a similar skeleton and different halogens bound to the hypervalent tellurium atom was recently investigated by Khrustalev and co-workers that reported on the formation of **HPyTeCl₂** (refcode: EHALIK) prepared by reacting the same **Py₂Te₂** substrate with sulfuryl chloride in dichloromethane,^[417] and by Lang which illustrated the reactivity of dipyrilid-4-yltelluride towards various substrates, yielding to the formation of several zwitterions (**PEHMOG**, **PEHMUM** and **PEHNAT**), a telluronium-tellurolate salt (**PEHNEX**) (Scheme 25) and a Cobalt (II) CP.^[416] The reported T-shaped adducts feature almost linear fragments X–E–X with Cl–Te–Cl angle of 177.3 ° and I–Te–I angles of 174.7 and 176.1 ° (calculated on the two crystallographically independent molecules), similar to those found in **HPyTeI₂**. A comparison between the T-shaped adducts geometry revealed that the crystal structure of **PEHMOG** features a roughly planar molecule with pyridyl rings angled of 21.4(5)° with respect to the X–E–X plane. The analogous angles measured on both crystallographically independent molecules of **PEHMUM** are 29.0(4)° and 50.7(5), similarly to that found for **HPyTeI₂**.



Scheme 25 Hypervalent tellurium compounds prepared from dipyrid-4-yltelluride. Refcodes are indicated in parenthesis.

The diffusion of a bromine solution in hexane into a dichloromethane solution of **Py₂Te₂ (L13)** yielded red block crystals of compound **HPyTeBr₂** (§5.2.56) and tiny yellow blocks of compound **HPyTeBr₄** (§5.2.57), for 2:1 and 5:1 Br₂:Py₂Te₂ molar ratio, respectively (Scheme 24). The crystals were analyzed by means of SC-XRD and the main crystallographic data and refinement parameters for both compounds are summarized in Table S150.

The tellurium in **HPyTeBr₂** adopts a T-shaped arrangement similar to that observed in the analogous **HPyTeI₂**. Two crystallographic independent molecules are found within the asymmetric unit, differing for the angles between the pyridyl rings and the plane defined by the Br–Te–Br fragment, of 5.8 and 17.1 °, for PyN1 and PyN2, respectively. The bond lengths and angles are very similar for both zwitterions with slightly different Te–Br bond lengths varying from 2.6902(3) to 2.7655(3) Å and almost linear Br–Te–Br fragments with angles of and 178.2 177.5° for Br1–Te1–Br2 and Br3–Te2–Br4, respectively (Table S151). A search in the CDS database showed several structures containing anionic Ph–TeBr_n fragments with n = 2, 3, 4, but only two of them contain a three coordinated T-shaped Tellurium atom, namely the compounds corresponding to the refcodes FALCIH and YEQYID featuring Br–Te–Br fragments with similar bond lengths and angles.^[418,419]

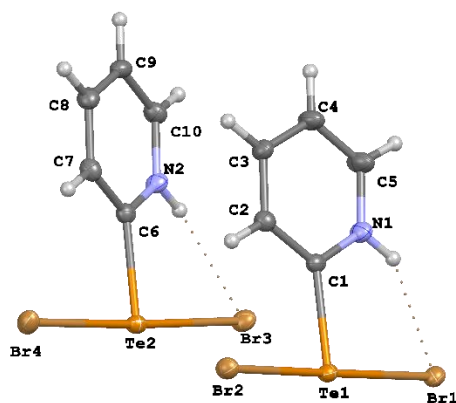


Figure 139 Asymmetric unit with numbering scheme of **HPyTeBr₂** along the [101] direction. Thermal ellipsoids are drawn at 50 % probability level.

The terminal Br atoms of **HPyTeBr₂** are involved in several intermolecular Te \cdots Br and C–H \cdots Br interactions showed in Figure 140 and listed in Table 35; interactions **c–h** involving the protons at the pyridine nitrogen atoms and the bromides, are responsible for the herringbone packing showed in Figure 141.

Table 35 Intra- and inter-molecular interactions found in **HPyTeBr₂**.

Interaction	d_{D-A} (Å)	d_{H-A} (Å)	$\alpha_{D-H\cdots A}$ (°)	
a	Te1 \cdots Br4 ¹	3.559(3)		
b	Te2 \cdots Br2 ¹	3.574(4)		
c	N1–H1 \cdots Br1	3.151(3)	2.397(3)	144.0
d	C2–H2 \cdots Br2	3.360(3)	2.670(3)	130.0
e	N2–H1A \cdots Br3	3.130(2)	2.445(3)	135.1
f	C7–H7 \cdots Br4	3.365(3)	2.683(3)	129.2
g	C5–H5 \cdots Br3 ²	3.568(3)	2.774(3)	141.6
h	C3–H3 \cdots Br4 ³	3.605(3)	2.867(3)	135.3

Symmetry codes: ¹ 1-x, 1-y, 1-z; ² 1-x, -1/2 + y, 1/2-z; ³ 2-x, 1-y, 1-z.

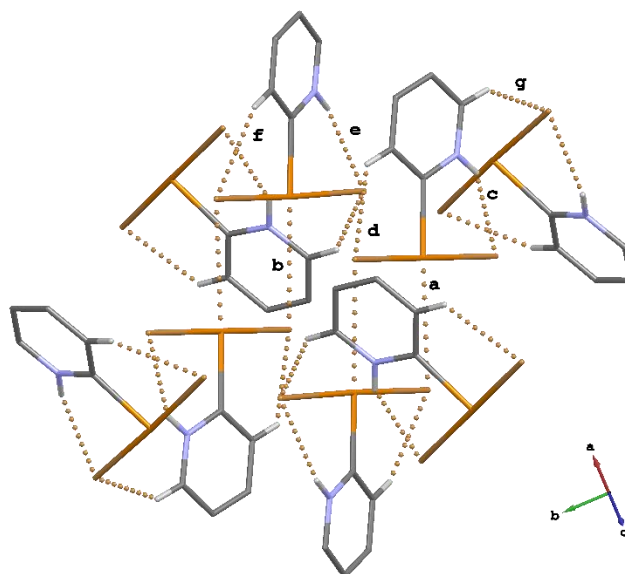


Figure 140 View of intra- and inter-molecular interactions in **HPyTeBr₂** along the [101] direction. Interactions are labelled according to Table 35.

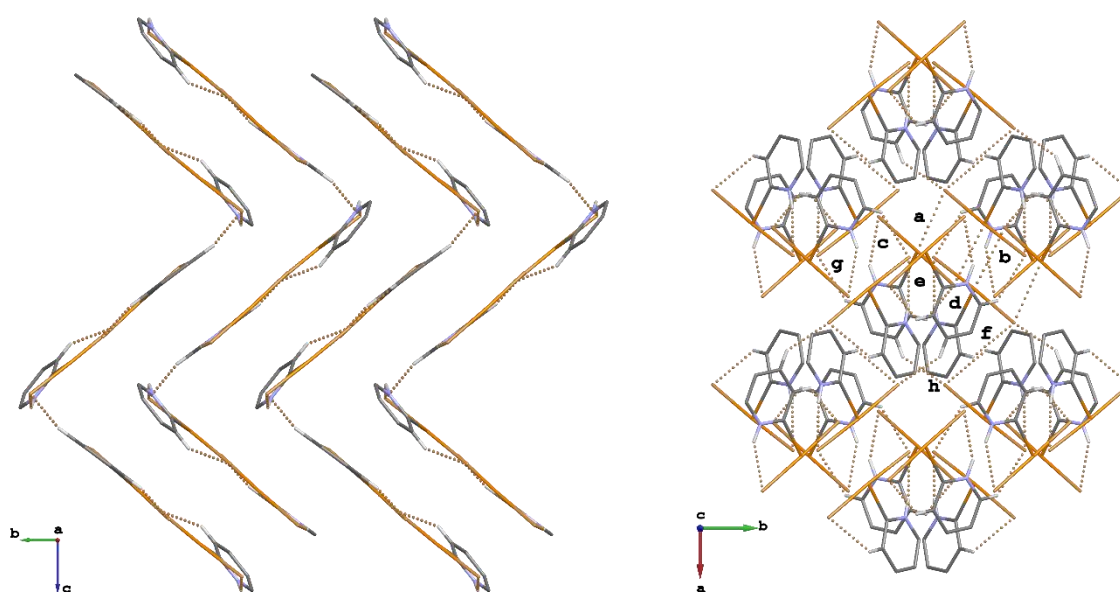


Figure 141 Packing diagrams showing the herringbone arrangement of **HPyTeBr₂** molecules along the *a* and *c* axis. Interactions are labelled according to Table 35.

The product **HPyTeBr₄** obtained using an excess of bromine adopts a square pyramidal geometry with a central hypervalent tellurium coordinated by an axial pyridinium cation and four bromine atoms in the equatorial plane (Figure 142).

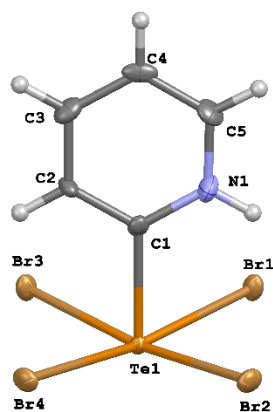


Figure 142 Molecular view of **HPyTeBr₄** along the *b* axis. Thermal ellipsoids are drawn at 50 % probability level.

Selected bond lengths and angles are reported in Table S151. The Te–Br bond lengths range from 2.6600(10) to 2.6793(10) Å, resulting slightly shorter than those found in **HPyTeBr₂**. The Te–C bond distance is slightly elongated with a value of 2.171(9) Å with respect to the value of 2.140(3) and 2.141(3) Å observed in **HPyTeBr₂**.

A search in the CDS database showed several structures containing Ph–TeBr₄ anions with similar square pyramidal penta-coordinated tellurium atoms with tellurium-bromine bond lengths and angles similar to those found in **HPyTeBr₄**.^[420–424] The terminal Br atoms of **HPyTeBr₄** are involved in several intermolecular Te⋯Br and C–H⋯Br interactions showed in Figure 143, along with a packing view.

Table 36 Intramolecular interactions found in **HPyTeBr₄**.

Interaction	d_{D-A} (Å)	d_{H-A} (Å)	$\alpha_{D-H\cdots A}$ (°)
a	Te1⋯Br4 ¹	3.7658(11)	
b	Te1⋯Br2 ¹	3.7542(11)	
c	N1–H1⋯Br1 ²	3.538(8)	2.896(9) 132.9(6)
d	C2–H2⋯Br3 ³	3.561(9)	2.884(9) 130.6(5)

Symmetry codes: ¹ +*x*, ½–*y*, –½+*z*; ² 1–*x*, 1–*y*, 1–*z*; ³ –*x*, 1–*y*, 1–*z*.

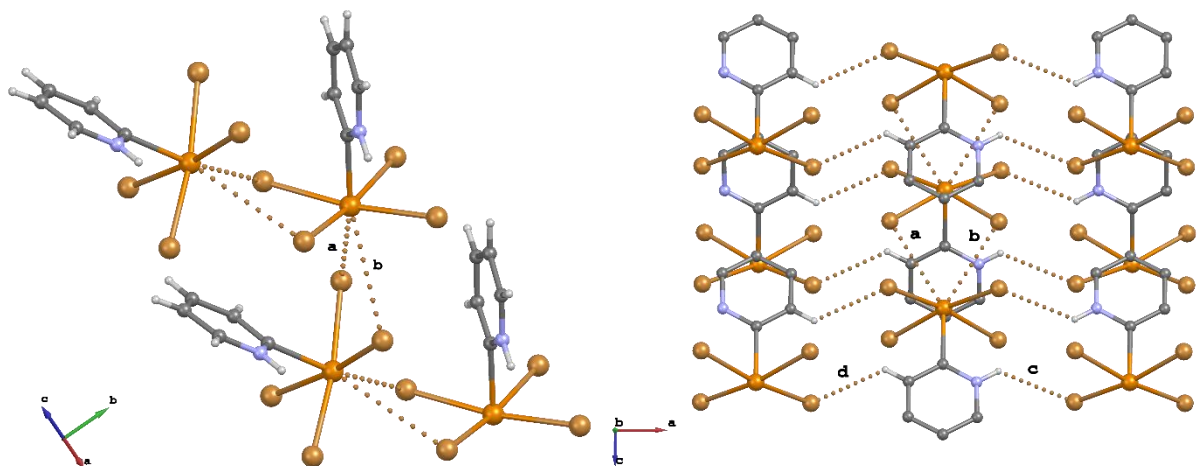


Figure 144 Views of the intermolecular interactions found in **HPyTeBr₄**, labelled according to Table 36, along the [101] and [010] directions from left to right.

The reaction of 2-(p-tolyl)selenopheno[2,3-b]pyridine (**L14**), with molecular halogens (I₂, Br₂) and interhalogens (ICl, IBr) was performed in different solvents and in different stoichiometric X:L ratios, ranging from 0.5:1 to 5:1, but only the reaction with ICl yielded crystalline products upon slow evaporation of the solvent. Crystals of two different morphologies were found in the glass vial, which were structurally characterized by XRD analysis. Colorless lath-shaped crystals revealed to be a dihydrate chloride salt of the ligand **HL14Cl·2H₂O** (Figure 145) whilst the dark red block crystals were solved as compound **[(HL14)I₂Cl]₃·0.5I₂** containing the same **HL14⁺** pyridinium cation, a I₂Cl⁻ counterion and fraction of an additional iodine molecule (Figure 147). Crystal data and refinement parameters for both compounds are reported in Table S152, and selected bond lengths and angles in Table S153.

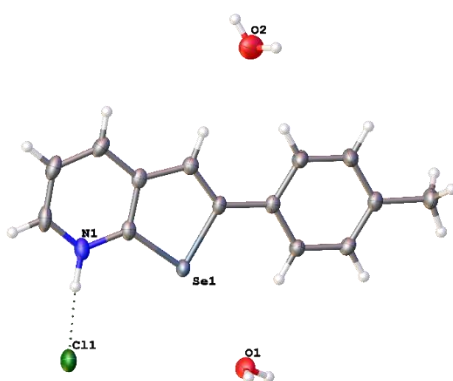


Figure 145 Crystal structure and atom numbering scheme for **HL14Cl·2H₂O**. Thermal ellipsoids are drawn at 50 % probability level.

The **HL14**⁺ cations are planar and present similar structural features in both compounds. The asymmetric unit of **[(HL14)L₂Cl]₃·0.5I₂** contains three independent cations with similar values for the angles calculated between the aryl and the heterocycle selenopheno[2,3-b]pyridine, with values of 5.31(9), 2.91(9), and 1.71(9)°, respectively. Similarly, the analogous angle in the crystal structure of **HL14Cl·2H₂O** has the value of 1.38(7)°. The positive charge is counterbalanced either by chloride anions or complex I₂Cl⁻ anions that interact with the protonated nitrogen of the pyridinium cations through Cl⁻⋯H as showed in Figure 145 and Figure 146 and reported in Table 37.

Table 37 Hydrogen bonding interactions found in **[(HL14)L₂Cl]₃·0.5I₂**. Calculated distances (Å) and angles (°) are summarized below.

	HL14Cl·2H₂O		[(HL14)L₂Cl]₃·0.5I₂	
	N1–H1⋯Cl1	N1–H1⋯Cl1	N2 ¹ –H2 ¹ ⋯Cl2	N3 ² –H3 ² ⋯Cl3
<i>d</i> _{D-A}	3.022(2)	3.054(3)	3.066(3)	3.076(3)
<i>d</i> _{H-A}	2.011(19)	2.389(8)	2.254(8)	2.258(8)
<i>α</i> _{D-H⋯A}	174(3)	153.97(18)	153.30(18)	154.62(18)

Symmetry codes: ¹ 1-x, 1-y, 1-z; ² +x, 1+y, +z.

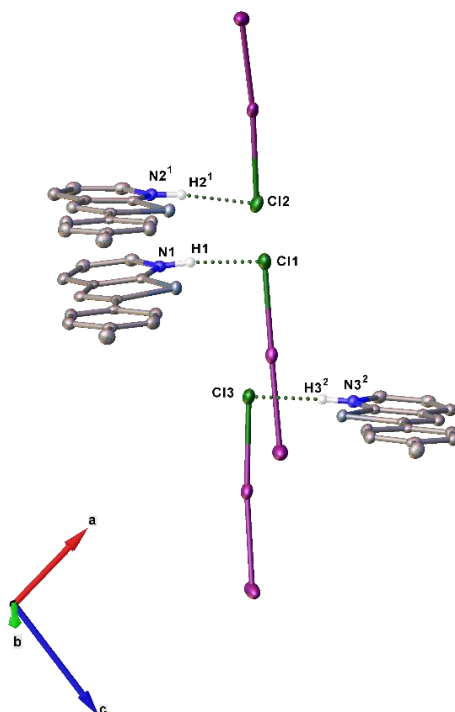


Figure 146 Hydrogen bonding interactions found in **[(HL14)L₂Cl]₃·0.5I₂**. Thermal ellipsoids are drawn at 50 % probability level. Only interacting hydrogens are shown for clarity.

The I_2Cl^- fragments are disordered over two positions and were modelled with fractional occupancy of 75/25, 55/45, 60/40 for I2A/I2B, I4A/I4B and I6A/I6B, respectively. Moreover, a half occupied I_2 molecule is found within the asymmetric unit yielding the overall formula $[(HL14)I_2Cl]_3 \cdot 0.5I_2$ (Figure 147).

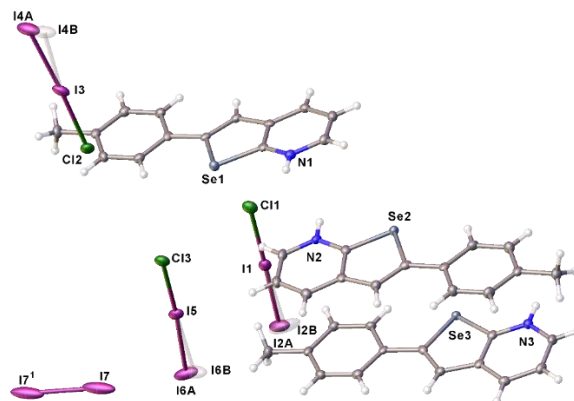


Figure 147 View along the a axis and numbering scheme of the asymmetric unit of $[(HL14)I_2Cl]_3 \cdot 0.5I_2$. Thermal ellipsoids are drawn at 50 % probability level. Symmetry code: ¹ 2-x, 2-y, 2-z.

The polyhalide fragments exhibit an almost linear geometry, with the terminal I atoms disordered over two positions. The interaction between four I_2Cl^- and one I_2 molecule generate the unique H-shaped polyhalide network with formula $I_{10}Cl_4^{4-}$ shown in Figure 148. It is worth noting that the $Cl_2-I_3-I_4^-$ anion is not involved in the formation of the polyhalide network, all distances with neighbor atoms being higher than the sum of the relative van der Waals radii.

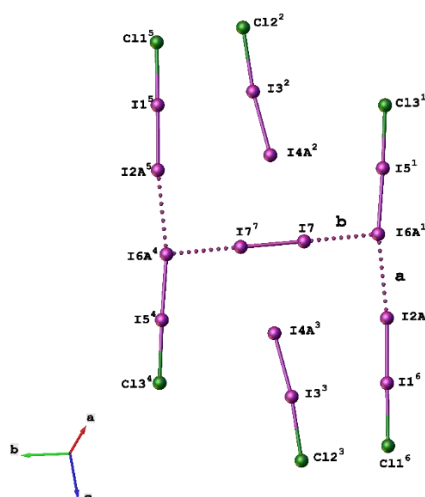


Figure 148 Unique H-shaped polyhalide $I_{10}Cl_4^{4-}$ network formed in $[(HL14)I_2Cl]_3 \cdot 0.5I_2$. I...I interactions are depicted as **a** and **b** ($I6A^1-I2A^6$: 3.641(6) Å; $I6A^1-I7$: 3.289(12) Å; $I6B^1-I2B^6$: 3.685(8) Å; $I6B^1-I7$: 3.585(11) Å). Disorder is not shown for clarity reasons. Symmetry codes: ¹ 1+x,+y,+z; ² 2-x,2-y,1-z; ³ +x,+y,1+z; ⁴ 1-x,2-y,2-z; ⁵ 1+x,1+y,+z; ⁶ 1-x,1-y,2-z; ⁷ 2-x,2-y,2-z.

In the crystal packing, **(HL14)⁺** cations are slightly slipped and stack *via* intermolecular π - π interactions between parallel pyridyl and *p*-tolyl of adjacent molecules as shown Figure 149 (centroid-centroid distance 3.58(3) Å).

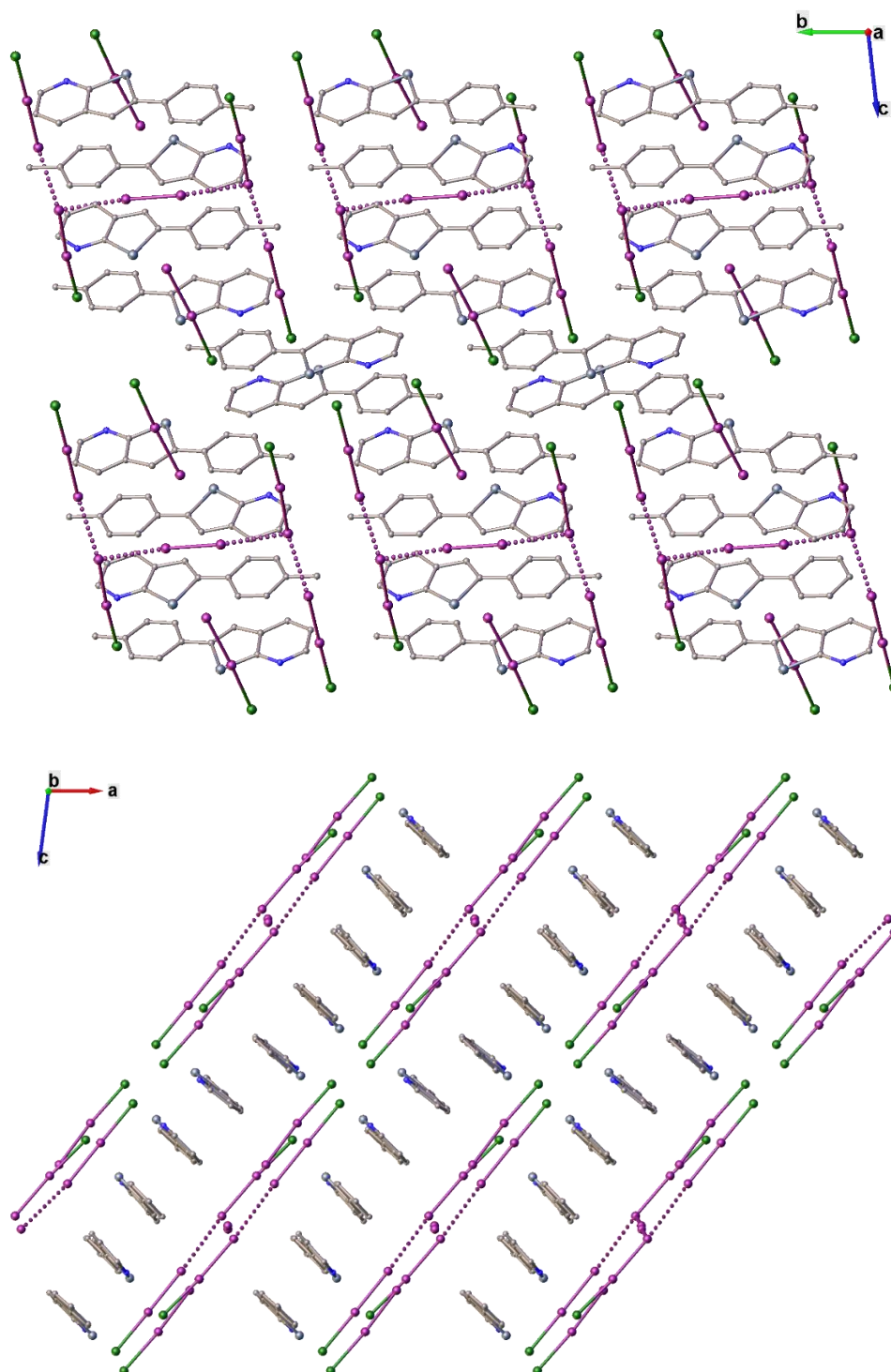
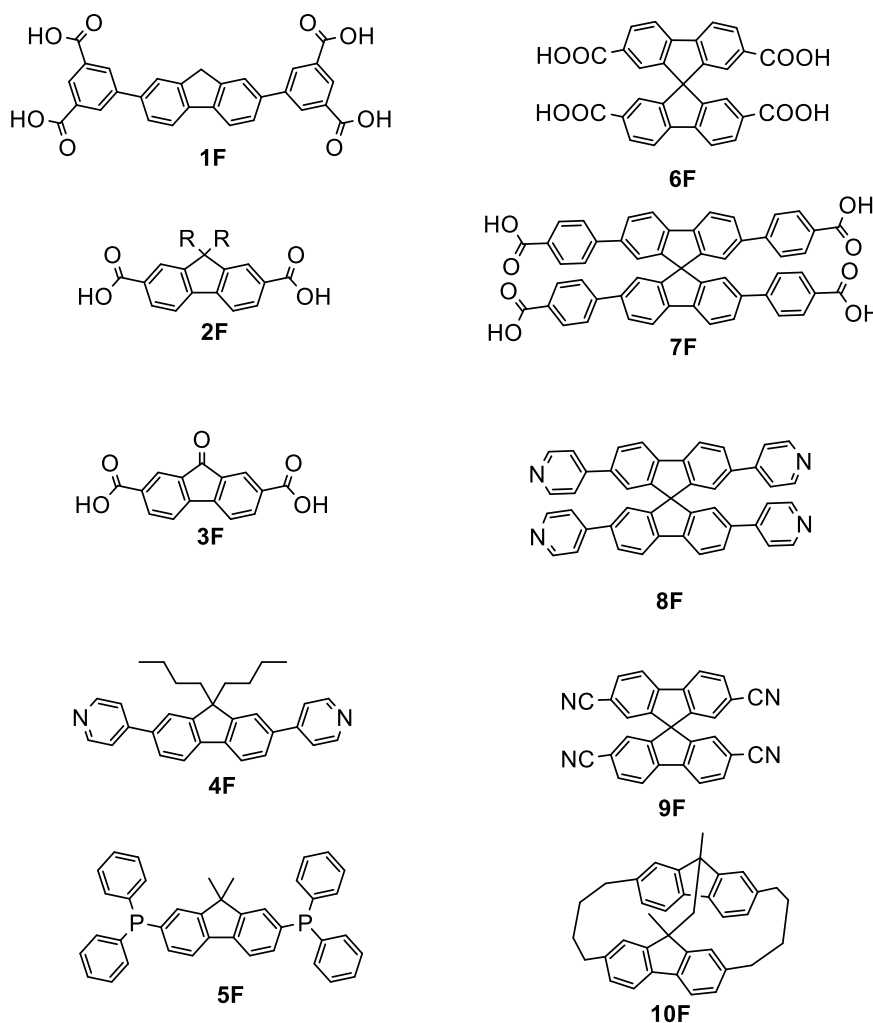


Figure 149 Balls and sticks representation of the crystal packing along the *a* (top) and *b* (bottom) axis. Hydrogen atoms and disordered fragments have been omitted for clarity.

3.2. Charged carboxylate-based building blocks: bifluorene derivatives

Fluorene derivatives have been extensively studied in the last years for their versatility in material science related applications. The chemistry of poly-fluorenes, a renowned class of electroactive and photoactive materials is of particular interest for the generation of light emitting diodes, featuring tunable electronic properties and blue-light emission.^[425–430] Moreover, oligo- and poly-fluorenes have been employed as a model for understanding the excimer formation and hole stabilization in π -stacked assemblies, which play a key role in biological systems such as DNA, as well as in the preparation of functional polymeric materials.^[431–435] Supramolecular assemblies originated by fluorene derivatives have led to significant examples of MOFs featuring remarkable properties as separating agents^[436–438], sensors^[439–441] and electrophosphorescence materials.^[442] Some selected examples of significant fluorene-based building blocks reported in the literature are reported in Scheme 26.

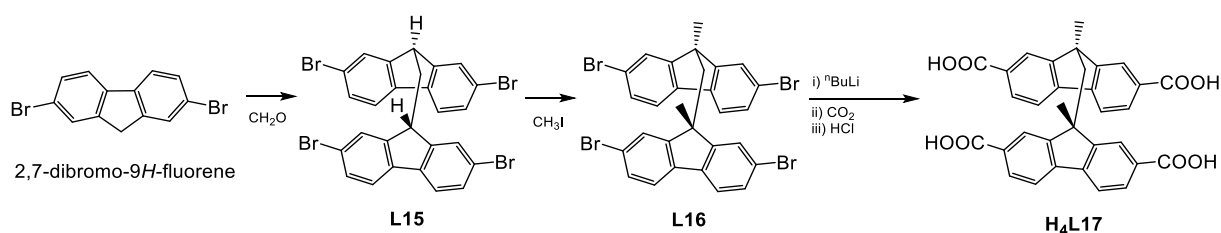


Scheme 26 Selected fluorene-based building blocks from literature. Compounds numbers are listed below with the relevant reference reported as superscripts. **1F**,^[437] **2F** where: R = H,^[439] R = Me, Et,^[443] R = Pr,^[444] **3F**,^[441] **4F**,^[440] **5F**,^[442] **6F**,^[445] **7F**,^[438] **8F-9F**,^[446] **10F**.^[431]

Compounds **1F-5F** are characterized by the presence of a single fluorene unit, **6F-9F** feature a spirobifluorene core that allowed to develop more sophisticated supramolecular networks,^[438,445,446] and **10F** is an example of the new family of co-facial bifluorenes recently reported by Reid and co-workers.^[431] In their study, a few rigid torsionomers of co-facial bifluorenes were designed, featuring a variable extent of overlap between the two chromophore units, demonstrating that a perfect overlay of the fluorene units is responsible of excimer formation. In contrast, the hole delocalization was established to be less geometrically restrictive and was observed also in twisted and sterically hindered torsionomers. This new class of bifluorenes, which allows different conformations of the ligands characterized by different fluorescence responses was never used for the construction of supramolecular networks. We then decided to prepare the novel building block 9,9'-methylenebis(9H-fluorene-2,7-dicarboxylic acid) (**H₄L17**), featuring four carboxylic groups in order to study its reactivity as supramolecular building block in the formation of networks built up by different interactions. We therein report the synthesis and the characterization of the new ligand **H₄L17**, and related precursors **L15** and **L16**, and the results obtained by reaction of **H₄L17** with metal ions (§3.2.2), bipyridine bases (§3.2.3), and with both metal ions and bipyridyl based spacers for the formation of three-component networks (§3.2.4).

3.2.1. Bifluorene derivatives **L15**, **L16** and **H₄L17**

The tetracarboxylic linker 9,9'-methylenebis(9H-fluorene-2,7-dicarboxylic acid) (**H₄L17**) was realized by the three-step synthetic approach reported in Scheme 27.



Scheme 27 Three-step synthetic approach for **H₄L17**.

The 2,7-dibromo-9H-fluorene was reacted with paraformaldehyde to generate the ligand **L15** in excellent yield (§5.2.11). The protons in position 9 of the co-facial bifluorene skeleton thus prepared were methylated by using methyl iodide (§5.2.12) obtaining **L16** that was isolated and purified by chromatography tools. Full experimental procedures and characterization of both **L15** and **L16** are provided in the experimental section and as supplementary material. The tetrabrominated derivative **L16** was also characterized by means of SC-XRD. The main crystal

data and refinement parameters are given in Table S154. The colorless block crystals obtained by recrystallization of **L16** in acetone crystallize in the monoclinic space group $P2_1/c$ with a single molecule present in the asymmetric unit featuring the two fluorene units rotated of about 25° . It is worth mentioning that the fluorene moieties are not parallel, but slightly opened of an angle of about 14° , with intra-molecular distance of 3.63 \AA , resembling the shape of a butterfly with almost closed wings (Figure 150).

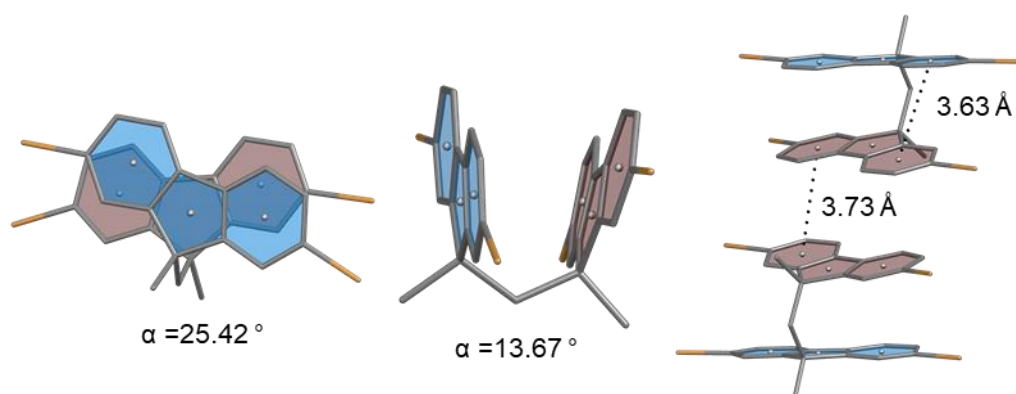


Figure 150 Crystal structure of **L16**. Torsional angles, intra- and intermolecular π - π interactions are represented.

Pairs of **L16** molecules interacting through π - π interactions with centroid distance of 3.73 \AA and an angle of 7° between the rings (Figure 150) pack in the herringbone pattern (§1.1.1) shown in Figure 151.

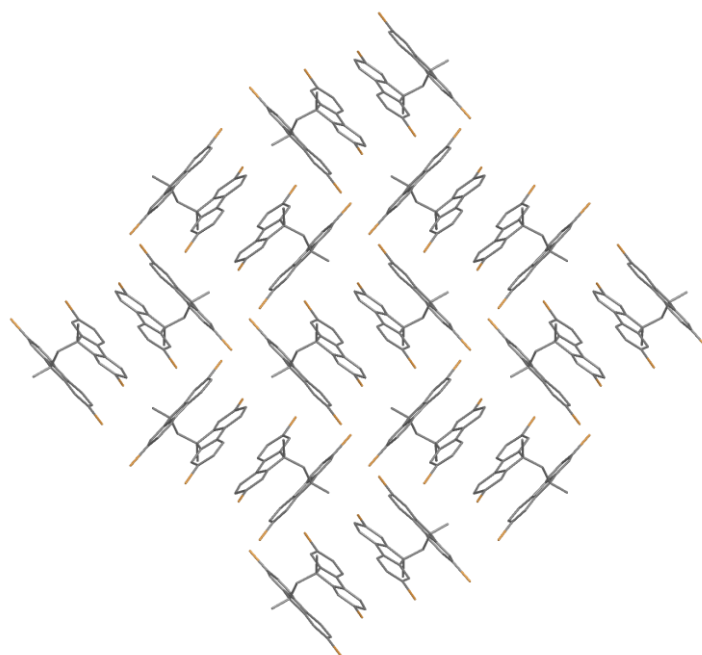


Figure 151 Packing diagram of **L16** along the a axis. Displacement ellipsoids are drawn at 50% probability level. Hydrogen atoms have been omitted for clarity.

The tetrabrominated derivative **L16** was then reacted with *n*-BuLi at $-78\text{ }^{\circ}\text{C}$, and the carboxylation achieved by CO_2 bubbling into the reaction mixture. The pure tetracarboxylic acid **H4L17** was isolated upon acidic workup (§5.2.13). It is important to note that the optimization of the synthesis was not trivial since a mixture of partially carboxylated derivatives **H4L17**, **H3L17Br** and **H2L17Br2** in Figure 152, was obtained in the initial attempts as elucidated by TOF ES MS– characterization. The pure tetracarboxylic acid **H4L17** was obtained when a discrete excess of *n*-BuLi was used (1.5 eq. for each site). The comparison between the mass spectra obtained for the mixture of partially substituted ligand (a) and its pure form (b) is showed in Figure 152.

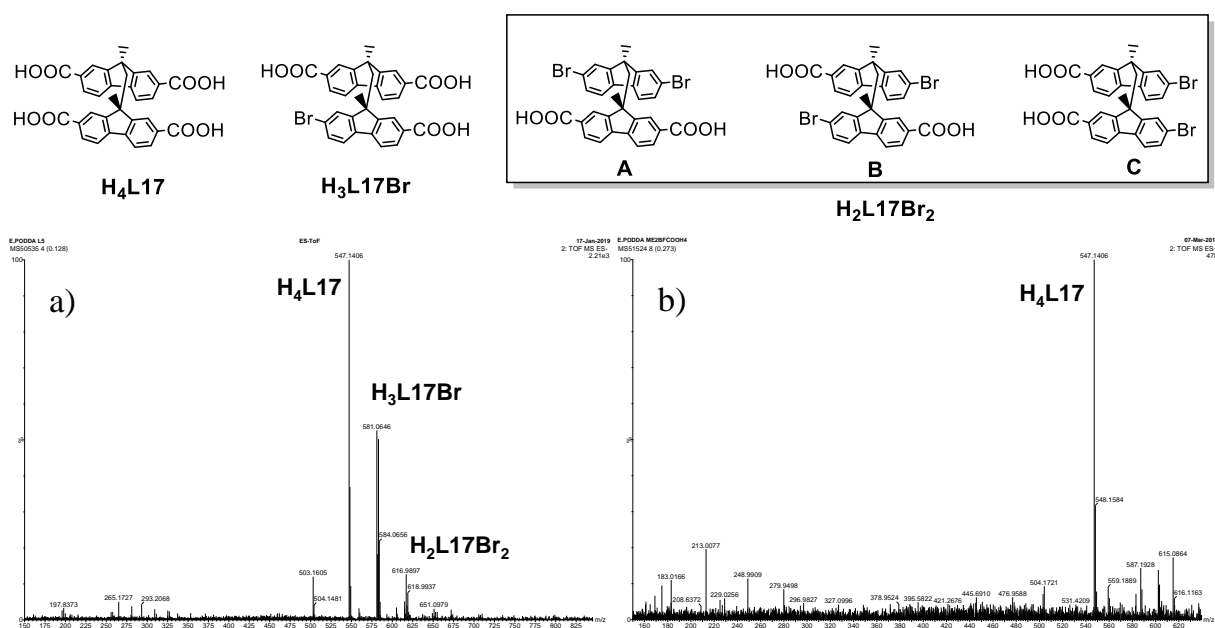


Figure 152 Mass spectra of the (a) mixture of tetra- (**H4L17**), tri- (**H3L17Br**) and di-substituted (**H2L17Br2**) derivatives and (b) of the fully carboxylated **H4L17**.

The FT-IR spectrum of **H4L17** features broad absorption bands at about 2900 and 2600 cm^{-1} , assigned to the OH stretching modes (Figure S69), strong absorption at 1689 cm^{-1} falling in the C=O region, and medium-strong bands in the region $1300\text{--}1260\text{ cm}^{-1}$ assigned to C–O stretching modes. ^1H NMR analysis of **H4L17** in DMSO-d_6 exhibited a broad signal centered at 12.59 ppm for the protons of the carboxylic acids, two groups of signals in the aromatic region of the spectrum from 7.59 to 7.24 ppm, assigned to the aromatic protons of the fluorene units, and a signal of the methylene bridge at 3.31 ppm, partially overlapped with the water residue present in the deuterated solvent. The singlet resonating at 1.33 ppm is consistent with the presence of methyl substituent in position 9 (Figure S32). The ^{13}C NMR analysis in the same solvent (Figure S33) shows the signals of the carboxylic groups at 166.9 ppm, that of methyl groups at 49.2

ppm, and the signals of the methylene bridge at 28.6 ppm as supported by 2D-NMR analysis according to ^1H - ^{13}C HMQC sequence (Figure S35). The results coming from the ^1H - ^1H COSY experiment are reported in Figure S34 for the sake of completeness.

The absorption and emission properties of **H4L17** were analyzed in solution and in the solid-state and the corresponding spectra are showed in Figure 153. The UV-vis characterization in DMSO revealed three main absorption bands in the UV region with maxima at 294, 303 and 327 nm. The photoluminescence emission spectrum in the same solvent features a strong emission centered at 439 nm, for $\lambda_{ex} = 303$ nm. Similarly, the diffuse reflectance analysis performed in the solid sample displayed a broad absorption in the UV region with a pattern similar to that observed in solution, and the solid-state emission spectrum features a maximum at 492 nm for $\lambda_{ex} = 350$ nm (Figure 153). It is interesting to note that the solid state emission spectrum of the mono-fluorene derivative 9,9'-dimethylfluorene-2,7-dicarboxylic acid (compound **2F** in Scheme 26) exhibited a maximum emission wavelength at 410 nm in the solid state,^[443] emphasizing the influence of the co-facial fashion of **H4L17** in the resulting photoluminescence properties.

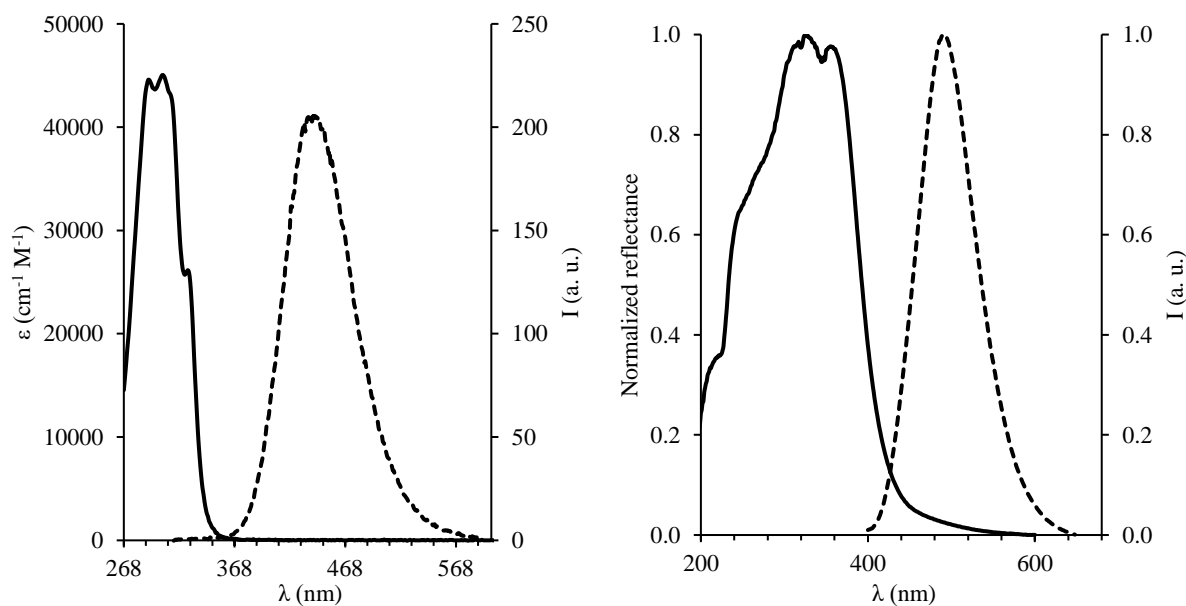


Figure 153 Absorption (solid line) and emission (dashed line) spectra for **H4L17** measured in DMSO (left) ($[\text{H}_4\text{L17}] = 10^{-5}$ M, $\lambda_{ex} = 303$ nm) and in the solid state (right) ($\lambda_{ex} = 350$ nm).

After several attempts, single crystals of **H4L17** were finally grown by carefully layering a solution of the ligand in DMF onto water. After one week, XRD quality crystals were isolated at the interface and structurally characterized.

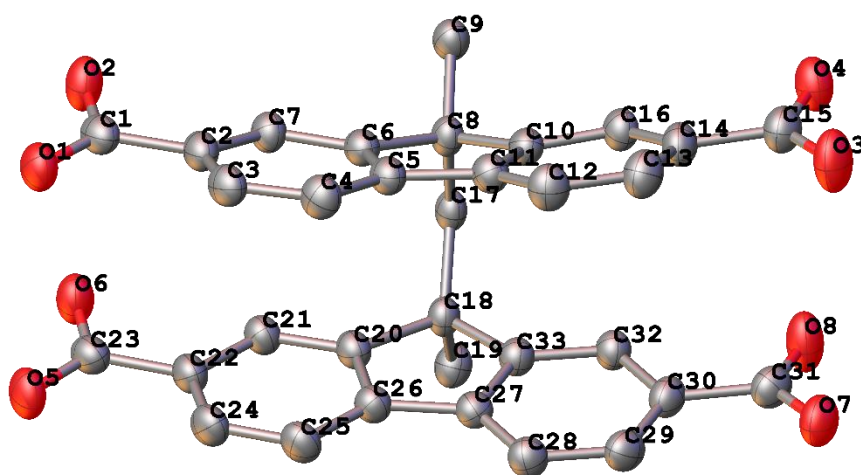


Figure 154 Crystal structure of **H₄L17**. Thermal ellipsoids are drawn at 50 % probability level. Hydrogen atoms have been omitted for clarity.

The tetracarboxylic donor crystallizes in the triclinic space group *P*-1 with the asymmetric unit comprising a single **H₄L17** molecule (*Z'* = 1) (Figure 154). The main crystallographic data and refinement parameters for **H₄L17** are given in Table S154. The angle calculated between the planes built on fluorene units is about 20 °, wider than that of 14° observed in **L16**, with a resulting “spread wings” butterfly shape. On the contrary, the angle of just 5 ° found between fluorene units in **H₄L17** is smaller than that of 25 ° found in **L16**, allowing for intramolecular π - π interaction between the fluorene units with centroid-centroid distances of 3.47 and 3.66 Å (interactions **a** and **b** in Figure 155). As expected, **H₄L17** molecules are involved in strong hydrogen bonds (interactions **c-f** in Figure 155 and Table S154) among the four carboxylic acids present in each molecule that link adjacent molecules in slightly undulated 1D chains along the *c* axis (Figure 155).

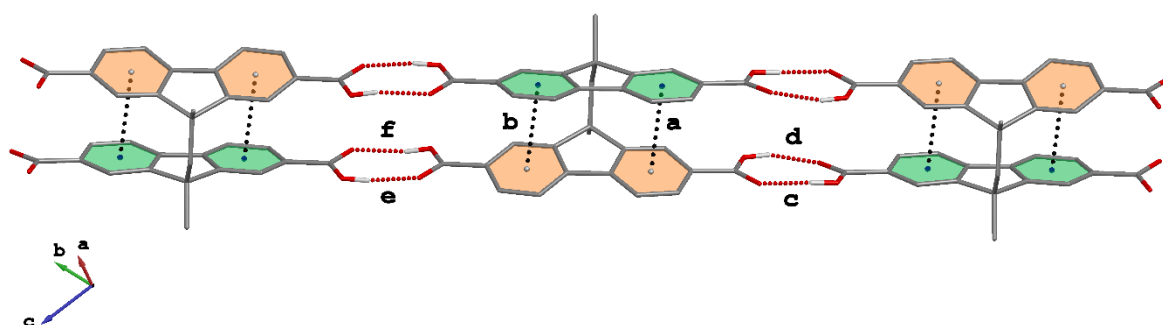


Figure 155 View of the mono-dimensional hydrogen bonded chain in the crystal structure of **H₄L17**. H-bonds are depicted in dashed red lines and are labelled accordingly to Table 38.

The crystal packing features staggered 1D chains interacting by means of multiple interlayer interactions generating a layered structure as showed in Figure 156 and Figure 157.

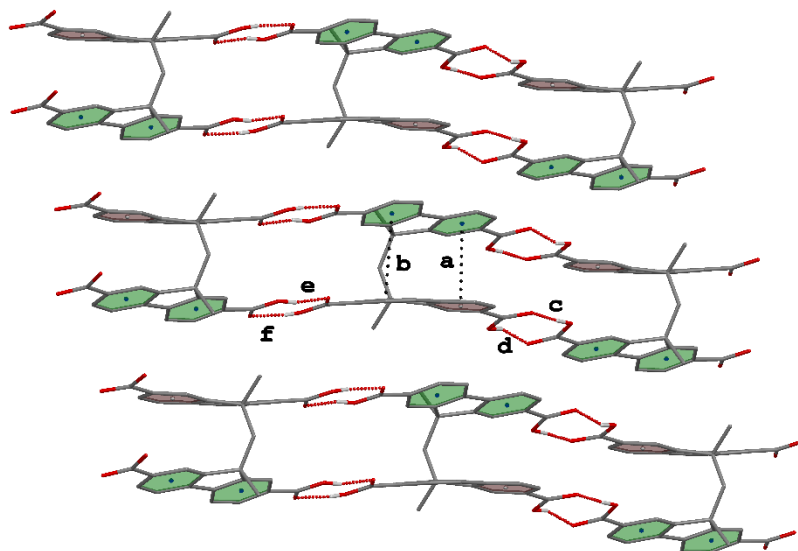


Figure 156 View of the layered structure in the crystal structure of **H₄L17** along the *c* axis. Intramolecular π - π interactions and hydrogen bonds are depicted in dashed lines and labelled according to Table 38.

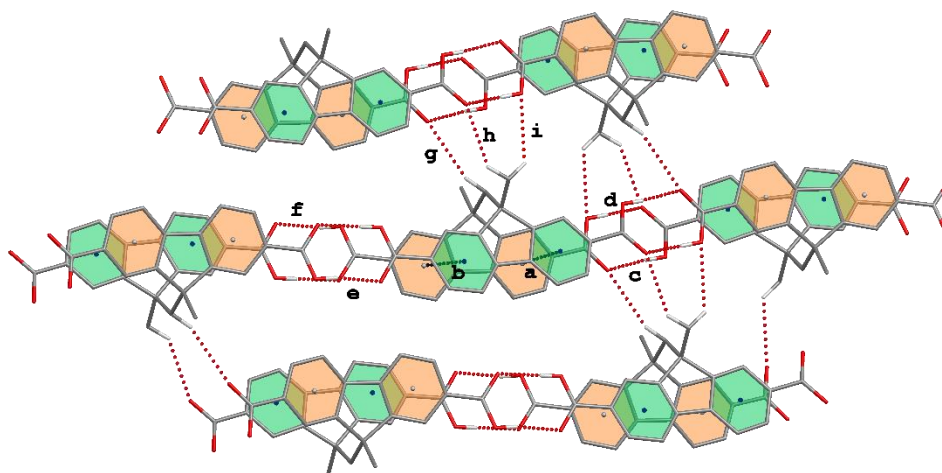


Figure 157 Interlayer hydrogen bonding network found in **H₄L17**. H-bonds are depicted in dashed red lines and are labelled accordingly to Table 38. Aryl protons are not shown for clarity reasons.

In addition, an intricate hydrogen bonding network decorates the crystal packing and held together adjacent layers *via* weak hydrogen bonds. The supramolecular interactions of the crystal packing are summarized in Table 38.

Table 38 Hydrogen bonding network in the crystal structure of **H₄L17**.

#		d_{D...A} (Å)	d_{H...A} (Å)	α_{D-H...A} (°)
c	O6 ¹ -H6 ¹ ...O1	2.641(3)	1.79(6)	175(5)
d	O2-H2...O5 ²	2.604(3)	1.82(2)	160.3(2)
e	O8 ² -H8 ² ...O3	2.589(3)	1.75(5)	170(6)
f	O4-H4...O7 ²	2.664(3)	1.84(6)	171(6)
g	C17-H17B...O1 ³	3.595(2)	2.750(18)	146.1(3)
h	C19-H19A...O5 ³	3.478(2)	2.687(14)	140.1(3)
i	C19-H19B...O2 ⁴	3.450(2)	2.766(15)	128.8(3)

Symmetry codes: ¹ 1-x, -y, -z; ² 1-x, 2-y, 1-z; ³ +x, 1+y, +z; ⁴ 1-x, 1-y, -z.

3.2.2. Interaction between **H₄L17** and metal ions

The reactions of **H₄L17** and several metal ions were performed under solvothermal conditions, but, up till now, only the compounds obtained starting from cadmium and copper nitrate were fully isolated and will be reported here.

3.2.2.1. [(Cd₂L17·3H₂O)·3H₂O]_∞ and [(Cd₂L17·6H₂O)·2H₂O]_∞

Cd(NO₃)₂·4H₂O and **H₄L17** were reacted in a 2:1 molar ratio in a mixture of DMA/H₂O (2:1 v/v) at 120 °C for 24 h and then slowly cooled at a rate of about 10 °C/h, up to room temperature. When the obtained colorless crystals were observed with the microscope under a polarized light, two different morphologies were identified and characterized by SC-XRD as a 3D-MOF and a CP of formula [(Cd₂L17·3H₂O)·3H₂O]_∞ and [(Cd₂L17·6H₂O)·2H₂O]_∞, respectively. The main crystallographic data and refinement parameters of the two compounds are listed in Table 40 for the sake of comparison.

The compound corresponding to formula [(Cd₂L17·3H₂O)·3H₂O]_∞ crystallizes in the orthorhombic non-centrosymmetric space group *Cmc*2₁. The asymmetric unit comprises four halves of crystallographically independent Cd^{II} ions, a fully deprotonated **L17⁴⁻** ligand and five water molecules, four of which are lying on special positions (Figure 158).

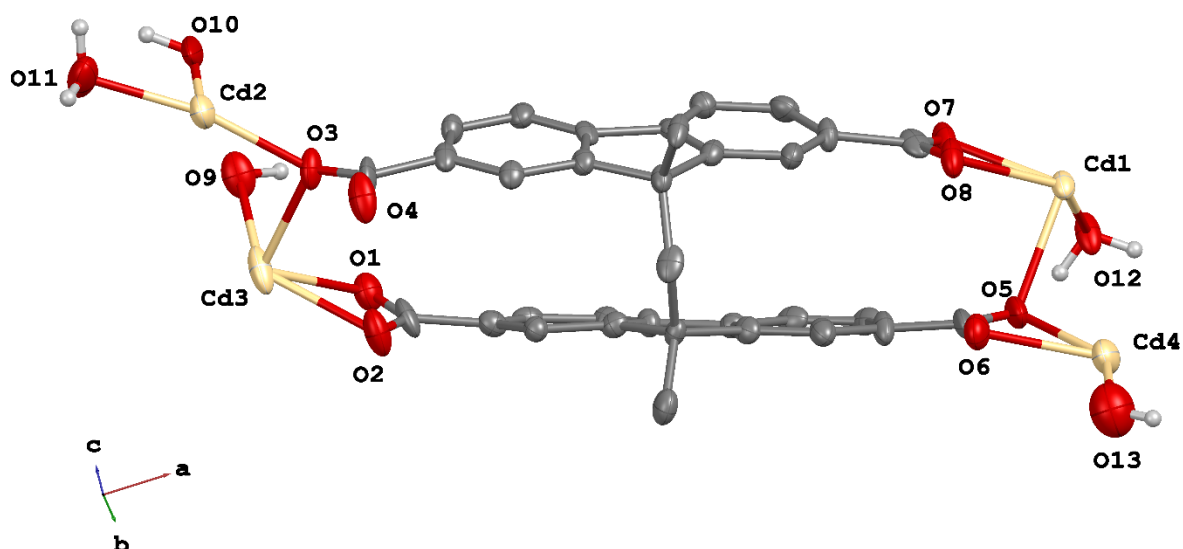


Figure 158 Asymmetric unit of the crystal structure of MOF $[(\text{Cd}_2\text{L17}\cdot 3\text{H}_2\text{O})\cdot 3\text{H}_2\text{O}]_\infty$.

Moreover, three disordered water molecules are present in the asymmetric unit and were subjected to SQUEEZE routine. A solvent mask was calculated, and 250 electrons were found in a volume of 1220 \AA^3 /per unit cell. This is consistent with the presence of 24 H_2O molecules per unit cell.

The four independent Cd^{II} ions feature different coordination geometries: the $\text{Cd}2^4$ is hexa-coordinated into a distorted octahedral geometry by two monocoordinated oxygen from two different L17^{4-} anions ($\text{O}3^1$ and $\text{O}3^4$ in Figure 159), a μ_2 - H_2O ($\text{O}12$) molecule that lies between $\text{Cd}1$ and $\text{Cd}2^4$, and three H_2O molecules ($\text{O}10^4$, $\text{O}11^4$, $\text{O}11^1$) that are strongly engaged in H-bonds with the carboxylic units coordinated to $\text{Cd}1$ and $\text{Cd}3$ (interactions **b**, **c** and **d** in Figure 159 and Table 39). $\text{Cd}1$, $\text{Cd}3$ and $\text{Cd}4$ are hepta-coordinated and adopt a capped trigonal prismatic geometry constructed by four oxygens from two chelating carboxylates ($\text{O}7^{\wedge}\text{O}8$ and $\text{O}7^5\wedge\text{O}8^5$, $\text{O}1^2\wedge\text{O}2^2$ and $\text{O}1^6\wedge\text{O}2^6$, $\text{O}5\wedge\text{O}6$ and $\text{O}5^5\wedge\text{O}6^5$, for $\text{Cd}1$, $\text{Cd}3^2$ and $\text{Cd}4$, respectively), two oxygens ($\text{O}5$ and $\text{O}5^5$) arranged into a μ_2 - η^2 - η^1 coordination mode for $\text{Cd}1$ and $\text{Cd}4$ and μ_2 - η^2 coordination mode for $\text{Cd}3^2$ ($\text{O}3^2$, $\text{O}3^6$), and a capping H_2O molecule ($\text{O}9^2$). The latter water molecule is involved in hydrogen bonding with $\text{O}5$ and $\text{O}5^5$ (interaction **a** in Figure 159 and Table 39). The three different coordination modes adopted by L17^{4-} are outlined in Scheme 28.

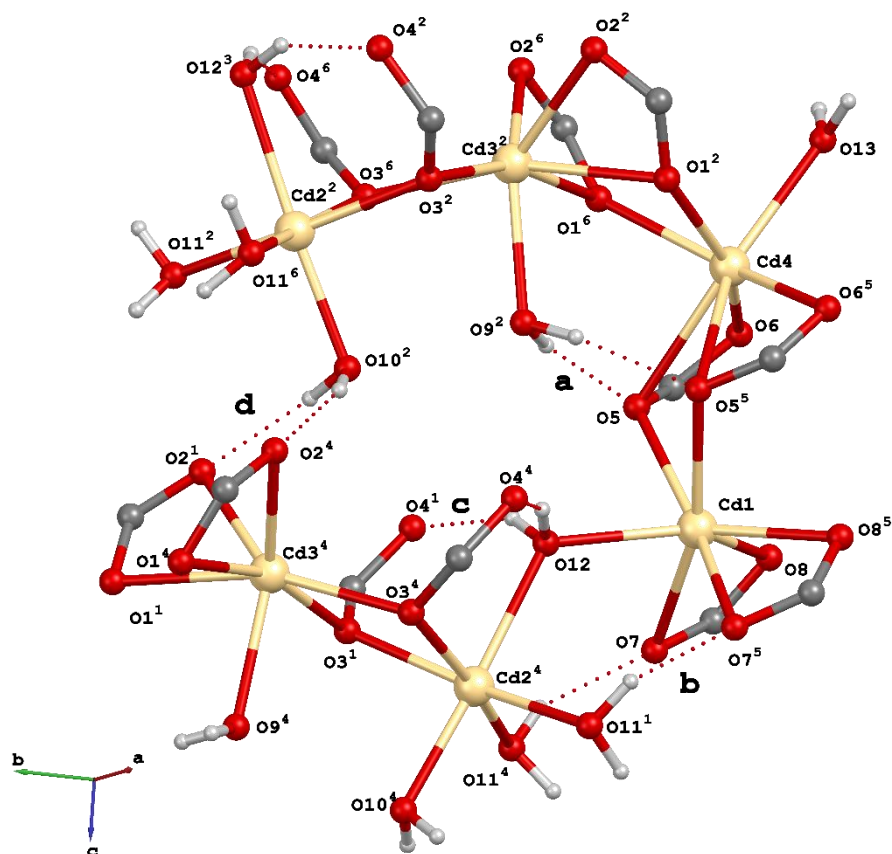
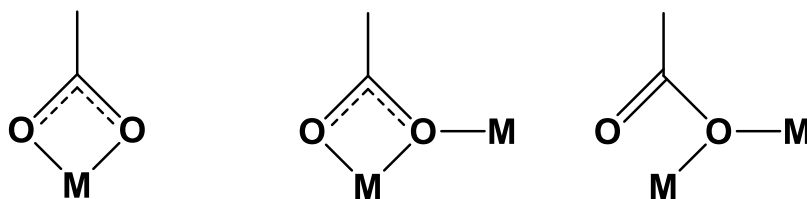


Figure 159 Balls and sticks representation of the Cd-SBU found in MOF $[(\text{Cd}_2\text{L17}\cdot 3\text{H}_2\text{O})\cdot 3\text{H}_2\text{O}]_\infty$. Only carboxylate functionalities are shown for clarity reasons. Interactions are labelled according to Table 39 along with the relevant symmetry codes.

Table 39 Intermolecular hydrogen bonds found in the crystal structure of $[(\text{Cd}_2\text{L17}\cdot 3\text{H}_2\text{O})\cdot 3\text{H}_2\text{O}]_\infty$.

#	$\text{d}_{\text{D}\cdots\text{A}}$ (Å)	$\text{d}_{\text{H}\cdots\text{A}}$ (Å)	$\alpha_{\text{D-H}\cdots\text{A}}$ (°)	
a	$\text{O9}^2\text{-H9}^6\cdots\text{O5}$	2.825(19)	1.96(12)	155.4(8)
b	$\text{O11}^1\text{-H11A}^1\cdots\text{O7}^5$	2.69(3)	1.92(14)	145.0(3)
c	$\text{O12-H12B}^5\cdots\text{O4}^1$	2.672(13)	1.91(11)	148.9(13)
d	$\text{O10}^2\text{-H10}^2\cdots\text{O2}^1$	2.75(2)	1.94(5)	157(13)

Symmetry codes according to Figure 159: ¹ $3/2-x, 1/2+y, +z$; ² $1/2+x, 3/2-y, 1/2+z$; ³ $+x, 2-y, -1/2+z$; ⁴ $1/2+x, 1/2+y, +z$; ⁵ $2-x, +y, +z$; ⁶ $3/2-x, 3/2-y, -1+z$.



Scheme 28 Different coordination modes of **L17⁴⁺** in $[(\text{Cd}_2\text{L17}\cdot 3\text{H}_2\text{O})\cdot 3\text{H}_2\text{O}]_\infty$: chelating (η^2), chelating/bridging ($\mu_2\text{-}\eta^2\text{-}\eta^1$), bridging ($\mu_2\text{-}\eta^2$).

The overall coordination generates the extended MOF $[(\text{Cd}_2\text{L17}\cdot 3\text{H}_2\text{O})\cdot 3\text{H}_2\text{O}]_\infty$ reported in Figure 160 with unusual secondary building unit (SBU) formed by hexanuclear cadmium arrangements bridged by six **L17⁴⁺** ligands and linked by a bridging water molecule (O12³ in Figure 159).

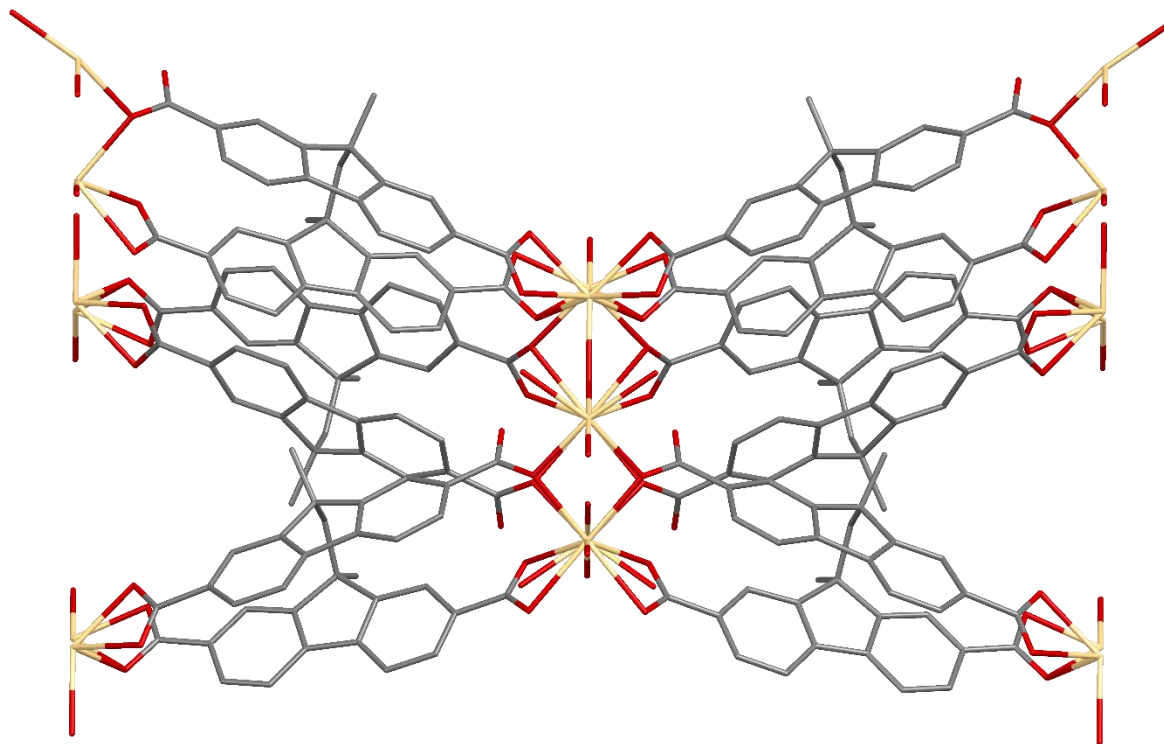


Figure 160 View of the crystal structure of $[(\text{Cd}_2\text{L17}\cdot 3\text{H}_2\text{O})\cdot 3\text{H}_2\text{O}]_\infty$ along the *c* axis. Hydrogen atoms have been omitted for clarity. Thermal ellipsoids are drawn at 50 % probability level.

The ligand adopts in this case a closed wings butterfly shape arrangement with almost parallel fluorene moieties (plane to plane angle = 7°); the fluorene units are rotated of about 22° more than found in **H4L17** (5° rotation angle) and similar to the scenario observed in **L16**. The intramolecular $\pi\text{-}\pi$ interactions range from 3.237 and 3.618 Å. In addition, two intermolecular $\pi\text{-}\pi$ edge to face interactions are present, with carbon to centroid distances of 4.02 and 4.36-4.41 Å for the T-shaped and the Y-shaped (§1.1.1), respectively (Figure 161).

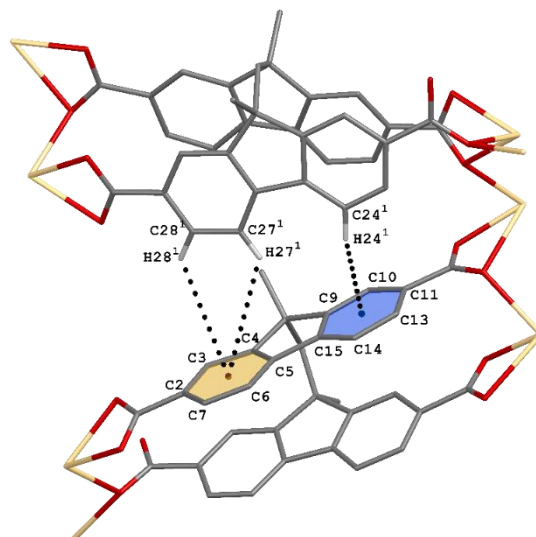


Figure 161 View of intermolecular π - π edge to face interactions in $[(\text{Cd}_2\text{L17}\cdot 3\text{H}_2\text{O})\cdot 3\text{H}_2\text{O}]_\infty$ along the [110] direction. T-shaped: $d_{\text{C24}^1\text{...centroid}} = 4.02 \text{ \AA}$, $d_{\text{H24}^1\text{...centroid}} = 3.18 \text{ \AA}$; Y-shaped: $d_{\text{C27}^1\text{...centroid}} = 4.41 \text{ \AA}$, $d_{\text{H27}^1\text{...centroid}} = 3.78 \text{ \AA}$; $d_{\text{C28}^1\text{...centroid}} = 4.36 \text{ \AA}$, $d_{\text{H28}^1\text{...centroid}} = 3.66 \text{ \AA}$. Symmetry code: $^1 3/2-x, 3/2-y, -1/2+z$.

The main bond lengths (\AA) and angles ($^\circ$) found in the crystal structure of $[(\text{Cd}_2\text{L17}\cdot 3\text{H}_2\text{O})\cdot 3\text{H}_2\text{O}]_\infty$ are listed in Table S155.

The crystal packing features ellipsoidal nanochannels along the c axis with openings of about $10.8 \times 8.8 \text{ \AA}$ (Figure 162). This space of solvent-accessible voids covers the 17.5 % of the unit cell volume and is occupied by the disordered water molecules which have been masked out as discussed above.

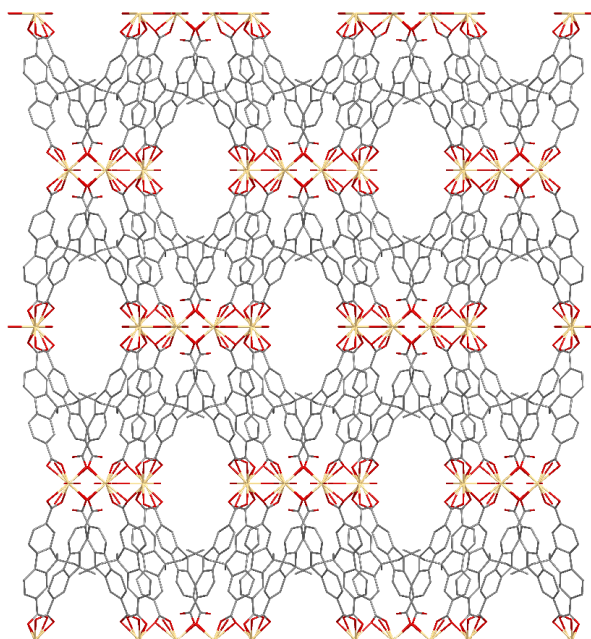


Figure 162 Packing diagram of $[(\text{Cd}_2\text{L17}\cdot 3\text{H}_2\text{O})\cdot 3\text{H}_2\text{O}]_\infty$ along the c axis. Hydrogen atoms have been omitted for clarity reasons.

The supramolecular network $[(\text{Cd}_2\text{L17}\cdot 6\text{H}_2\text{O})\cdot 2\text{H}_2\text{O}]_\infty$ crystallizes in the triclinic space group $P-1$ with a single L17^{4-} unit, two Cd^{II} ions, 6 coordinated water molecules, and two co-crystallized water molecules in the asymmetric unit (Figure 163). Both crystallographic independent Cd^{II} ions feature $\text{CN} = 7$ and adopt a pentagonal bipyramidal coordination geometry. The five equatorial positions are occupied by two chelating carboxylates and one water molecule. The axial positions are then filled by two more water molecules that complete the coordination sphere around the metals.

Table 40 Crystal data and structure refinement parameters for $[(\text{Cd}_2\text{L17}\cdot 3\text{H}_2\text{O})\cdot 3\text{H}_2\text{O}]_\infty$ and $[(\text{Cd}_2\text{L17}\cdot 6\text{H}_2\text{O})\cdot 2\text{H}_2\text{O}]_\infty$.

	$[(\text{Cd}_2\text{L17}\cdot 3\text{H}_2\text{O})\cdot 3\text{H}_2\text{O}]_\infty$	$[(\text{Cd}_2\text{L17}\cdot 6\text{H}_2\text{O})\cdot 2\text{H}_2\text{O}]_\infty$
Formula	$\text{C}_{33}\text{H}_{26}\text{Cd}_2\text{O}_{11}\cdot 3\text{H}_2\text{O}$	$\text{C}_{33}\text{H}_{36}\text{Cd}_2\text{O}_{16}$
$D_{\text{calc.}} / \text{g cm}^{-3}$	1.649	1.808
μ / mm^{-1}	10.775	1.345
Formula Weight	823.34	913.42
Colour	colourless	colourless
Shape	needle	plate
Size/ mm^3	$0.06 \times 0.01 \times 0.01$	$0.08 \times 0.07 \times 0.03$
T / K	100(2)	100(2)
Crystal System	orthorhombic	triclinic
Flack Parameter	-0.005(12)	-
Hooft Parameter	-0.002(6)	-
Space Group	$Cmc2_1$	$P-1$
$a / \text{\AA}$	27.4335(7)	7.7940(3)
$b / \text{\AA}$	18.9368(6)	14.7078(6)
$c / \text{\AA}$	12.7660(5)	15.9272(6)
$\alpha / ^\circ$	90	67.884(4)
$\beta / ^\circ$	90	86.175(3)
$\gamma / ^\circ$	90	82.860(3)
$V / \text{\AA}^3$	6632.0(4)	1677.93(12)
Z	8	2
Z'	1	1
Wavelength/ \AA	1.54184	0.71075
Radiation type	$\text{Cu K}\alpha$	$\text{MoK}\alpha$
$\theta_{\text{min}} / ^\circ$	2.835	2.390
$\theta_{\text{max}} / ^\circ$	68.243	27.484
Measured Refl's.	29109	38564
Indep't Refl's	6102	7689
Refl's $I \geq 2 \sigma(I)$	4540	6284
R_{int}	0.0790	0.0504
Parameters	437	476
Restraints	8	1
Largest Peak	1.004	2.452
Deepest Hole	-0.937	-0.959
Goof	1.043	1.031
wR_2 (all data)	0.1819	0.1070
wR_2	0.1672	0.1012
R_1 (all data)	0.0888	0.0585
R_1	0.0649	0.0437

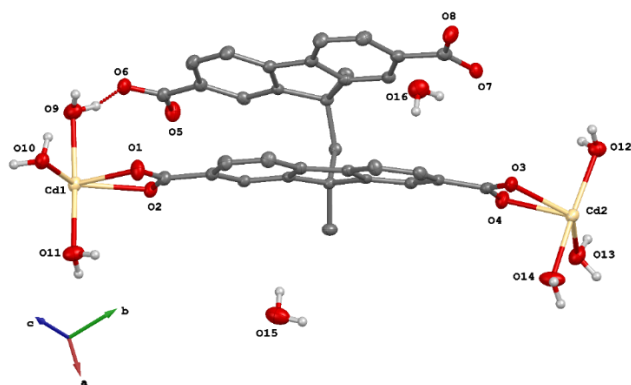


Figure 163 Numbering scheme in the asymmetric unit of $[(\text{Cd}_2\text{L17}\cdot 6\text{H}_2\text{O})\cdot 2\text{H}_2\text{O}]_\infty$. Displacement ellipsoids are drawn at 50 % probability level.

The two cadmium ions show different coordination environments: the equatorial positions at Cd1 are occupied by two chelating carboxylates ($\text{O1}^1\text{O2}$ and $\text{O5}^2\text{O6}^2$) from two different L17^{4-} anions and a water molecule (O10) (Figure 164). The axial position at the same metal ion are fulfilled by two water molecules (O9 and O11) one of which bridges a symmetry generated metal node by hydrogen bonding (interaction **a** in Figure 164) to a carboxylate group belonging to the second L17^{4-} fluorene unit ($\text{O5}^1\text{O6}^1$). A similar scenario is observed for Cd2 with two carboxylate ($\text{O3}^1\text{O4}$ and $\text{O7}^1\text{O8}^1$) and a water molecule (O13) lying at its equatorial positions and two additional water molecules (O12 and O14) arranged at the axial positions (Figure 164). Two Cd2 environments are linked by hydrogen bonds engaged between O12 and the adjacent carboxylate $\text{O3}^1\text{O4}^1$ (interaction **b** in Figure 164), similarly to what observed for the Cd1 SBU.

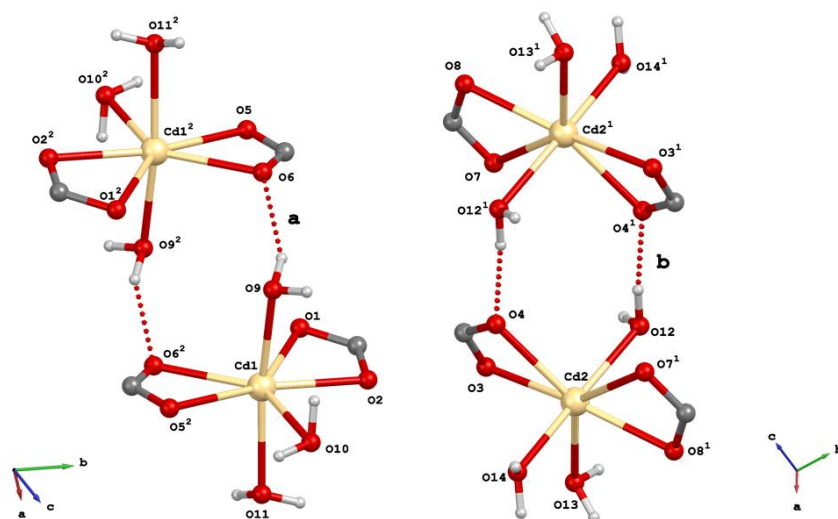


Figure 164 Perspective views of the SBUs present in $[(\text{Cd}_2\text{L17}\cdot 6\text{H}_2\text{O})\cdot 2\text{H}_2\text{O}]_\infty$. Interactions are described in Table 41. Symmetry codes: ¹ 1-x, 2-y, -z; ² -x, -y, 1-z.

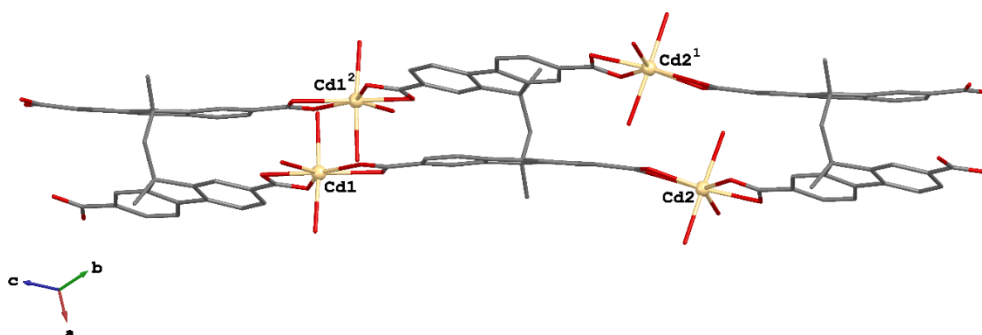
Table 41 Intermolecular interactions found in $[(\text{Cd}_2\text{L17}\cdot 6\text{H}_2\text{O})\cdot 2\text{H}_2\text{O}]_\infty$.

#	$d_{\text{D}\cdots\text{A}}$ (Å)	$d_{\text{H}\cdots\text{A}}$ (Å)	$\alpha_{\text{D-H}\cdots\text{A}}$ (°)	
a	09–H9A \cdots 06	2.759(4)	1.97(3)	152.2(2)
b	012–H12A \cdots 04 ¹	2.693(4)	1.85(3)	174.2(2)
c	015–H15A \cdots 03	2.741(5)	1.98(3)	148.2(3)
d	012–H12B \cdots 010	2.783(4)	2.06(3)	142.6(2)
e	010–H10A \cdots 015	2.800(5)	2.00(4)	153.4(2)
f	010–H10B \cdots 08 ²	2.739(4)	2.04(3)	137.3(2)
g	016 ¹ –H16E ¹ \cdots 012	2.970(5)	2.15(3)	162.8(3)
h	014–H14A \cdots 015 ³	2.687(5)	1.85(4)	165.6(3)
i	014–H14B \cdots 07 ³	2.710(5)	1.88(3)	165.3(3)
j	011–H11A \cdots 016 ⁴	2.841(5)	2.03(4)	157.7(2)
k	011–H11B \cdots 01 ⁵	2.679(4)	1.85(3)	165.6(2)
l	016 ⁴ –H16D ⁴ \cdots 02	2.775(5)	1.94(3)	166.4(3)
m	09–H9B \cdots 08 ⁶	3.032(5)	2.31(3)	142.3(2)

Symmetry codes: ¹ 1-x, 2-y, -z; ² -x, 2-y, -z; ³ 1+x, +y, +z; ⁴ 1-x, 1-y, 1-z; ⁵ 1-x, -y, 1-z; ⁶ -x, 1-y, 1-z.

The fluorene units in $[(\text{Cd}_2\text{L17}\cdot 6\text{H}_2\text{O})\cdot 2\text{H}_2\text{O}]_\infty$, as already observed in $[(\text{Cd}_2\text{L17}\cdot 3\text{H}_2\text{O})\cdot 3\text{H}_2\text{O}]_\infty$, differ from the free ligand **H4L17** and are rotated of about 26°, with an angle of 19° between the main planes which confers to the ligand a spread wings fashion. This conformation affects the intramolecular π - π interactions between the fluorene moieties which show centroid-centroid distances (3.56 and 3.62 Å) slightly longer than those found with **H4L17**. The main bond lengths and angles found in the crystal structure of $[(\text{Cd}_2\text{L17}\cdot 6\text{H}_2\text{O})\cdot 3\text{H}_2\text{O}]_\infty$ are listed in Table S156.

The twisted **L17**⁴⁻ anions bridge the cadmium ions into undulated polymeric ribbons as shown in Figure 165.

**Figure 165** Polymeric network of $[(\text{Cd}_2\text{L17}\cdot 6\text{H}_2\text{O})\cdot 2\text{H}_2\text{O}]_\infty$ along the [111] direction. Hydrogen atoms and co-crystallized water molecules have been omitted for clarity. Symmetry codes: ¹ -x, 2-y, -z; ² -x, -y, 1-z.

The ribbons pack through strong H-bonding interactions involving the carboxylate oxygen atoms, the coordinated water molecules and the co-crystallized ones (Table 41, Figure 166).

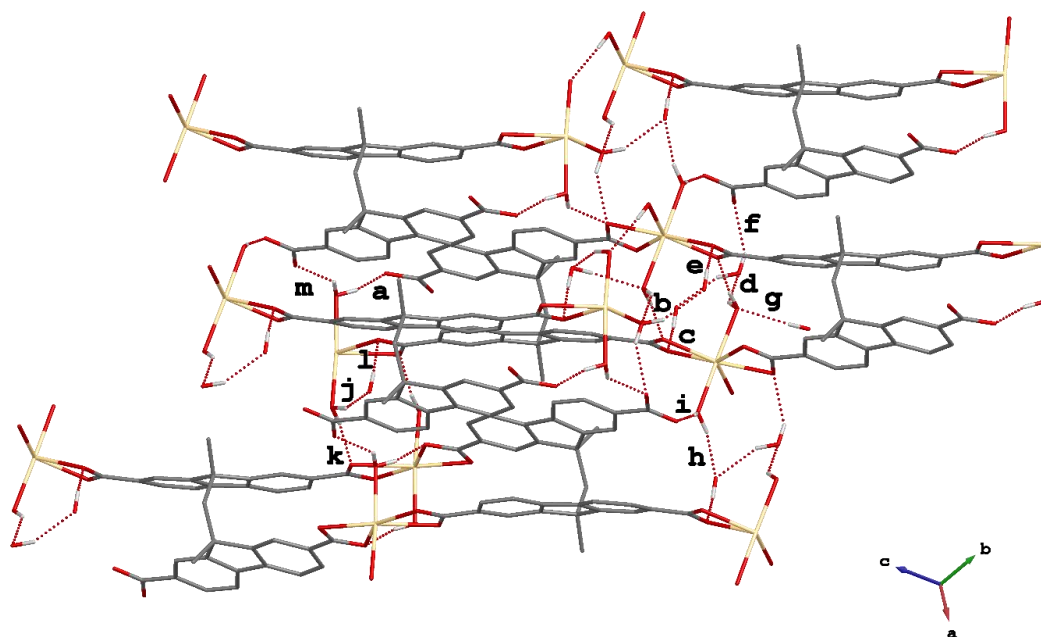


Figure 166 Intermolecular hydrogen bonding in the crystal structure of $[(\text{Cd}_2\text{L17}\cdot 6\text{H}_2\text{O})\cdot 2\text{H}_2\text{O}]_\infty$. Interactions are labelled according to Table 41. Only interacting H atoms are shown for clarity.

It is interesting to note that there are not intermolecular π - π interactions because of the interlayer distance imparted by the coordinated water molecules.

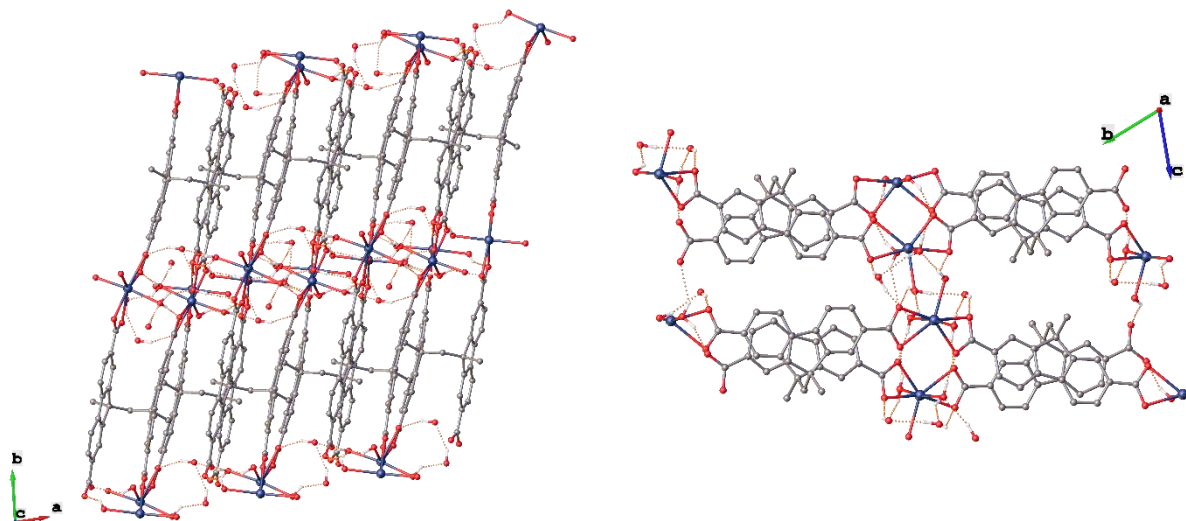


Figure 167 Packing diagrams of $[(\text{Cd}_2\text{L17}\cdot 6\text{H}_2\text{O})\cdot 2\text{H}_2\text{O}]_\infty$ along the c and a axis. Only interacting H atoms are depicted for clarity.

An extensive synthetic effort on the synthesis optimization did not led to the isolation of only one product from the solvothermal approach. A comparison between the experimental PXRD

analysis on the as-synthesized sample with the simulated patterns from the SC-XRD data of MOF $[(\text{Cd}_2\text{L17}\cdot 3\text{H}_2\text{O})\cdot 3\text{H}_2\text{O}]_\infty$ and of the CP $[(\text{Cd}_2\text{L17}\cdot 6\text{H}_2\text{O})\cdot 2\text{H}_2\text{O}]_\infty$ revealed that both phases are present in the sample. Preliminary attempts of activating the material removing the solvent from the cavities by heating were unsuccessful. Unfortunately, the supramolecular assemblies collapsed losing their crystallinity as judged by PXRD analysis. Moreover, we tried to exchange the water present in the cavities by suspending the as-synthesized sample into different solvents for 24 h (DCM, *n*-hexane, acetonitrile and toluene), but all the attempts led to loss of crystallinity of the starting material as showed by the PXRD patterns in Figure 168.

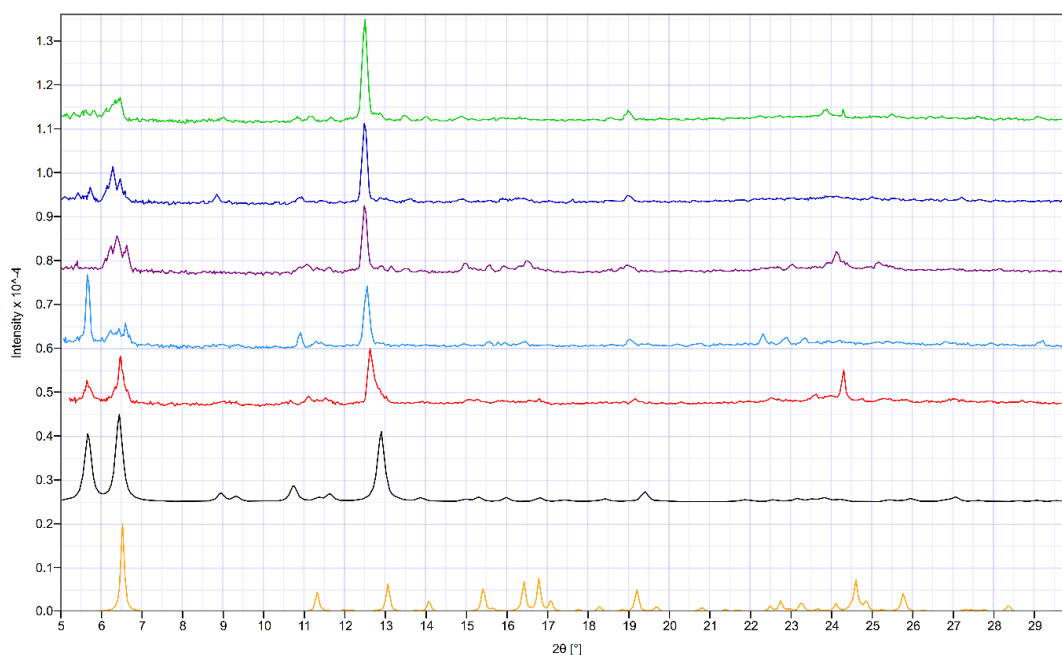


Figure 168 Experimental and simulated PXRD patterns of solvent exchange attempts on as-synthesized material. From the bottom to the top: simulated pattern from SC-XRD data of $[(\text{Cd}_2\text{L17}\cdot 6\text{H}_2\text{O})\cdot 2\text{H}_2\text{O}]_\infty$ (orange) and $[(\text{Cd}_2\text{L17}\cdot 3\text{H}_2\text{O})\cdot 3\text{H}_2\text{O}]_\infty$ (black); experimental pattern from as-synthesized sample (red); experimental patterns after 24 soaking in DCM (light blue), *n*-hexane (purple), acetonitrile (blue) and toluene (green).

Differential Scanning Calorimetry (DSC) analysis of the supramolecular assemblies corroborates an irreversible degradation of the product during the heating process.

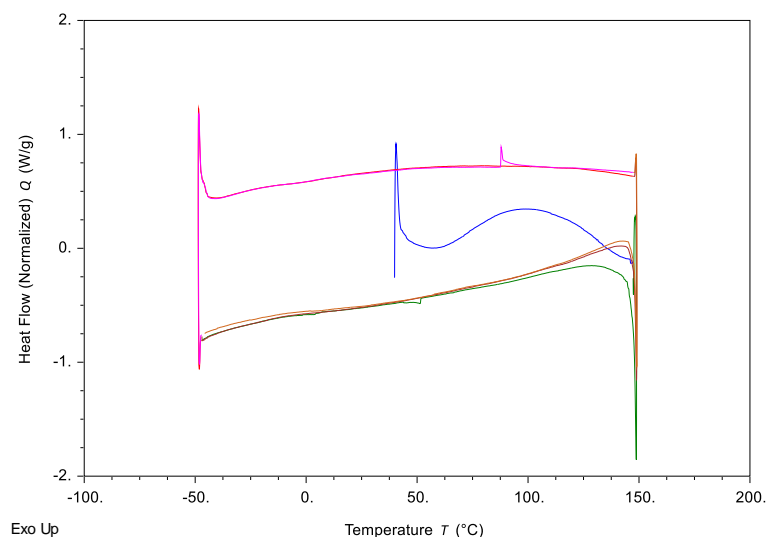


Figure 169 DSC analysis on the as-synthesised sample ramping the temperature from RT to 150 °C (blue) and two more consecutive cooling-heating cycles in the range (-50 to 150 °C).

The photophysical properties of the as-synthesized material were studied in the solid-state and are summarized in Figure 170 along with that of the free ligand **H4L17**. The emission spectrum of the product features an emission centered at 433 nm, thus remarkably blue-shifted if compared with the bifluorene **H4L17**. The emission changes can be tentatively attributed to the coordination of carboxylate groups and to the different conformation adopted by the fluorene moieties in the free and complexed **H4L17** molecules.

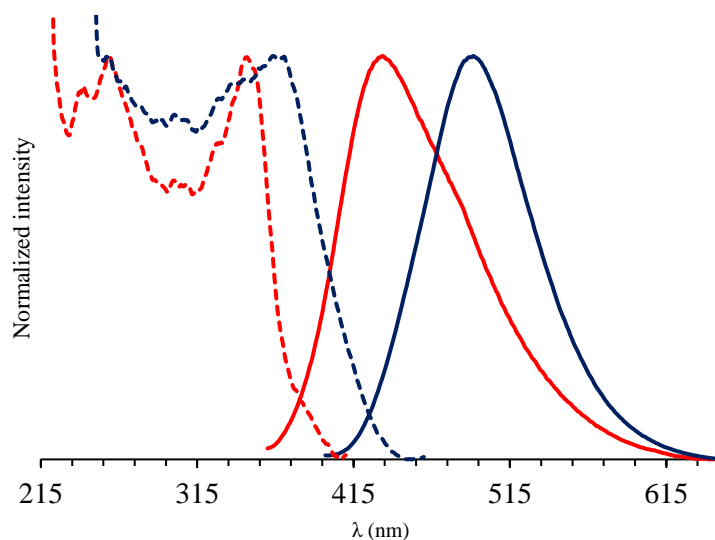


Figure 170 Photoluminescence excitation (dashed line) and emission (solid line) for **H4L17** (blue) and the as-synthesized material (red) in the solid state. Emission spectra were recorded with $\lambda_{\text{ex}} = 350$ and 370 nm for **H4L17** and the polymeric product, respectively.

3.2.2.2. $[(\text{Cu}_2\text{L17})\cdot 3\text{DMF}]_\infty$

The reaction of **H4L17** with $\text{Cu}(\text{NO}_3)_2\cdot 2.5\text{H}_2\text{O}$ in 1:2 molar ratio in different experimental conditions ranging from layering to solvothermal techniques in a mixture $\text{H}_2\text{O}:\text{DMF}$, yielded blue crystalline products corresponding to the same formulation $[(\text{Cu}_2\text{L17})\cdot 3\text{DMF}]_\infty$, as confirmed by the same unit cell parameters (Table 42). Unfortunately, the crystals were very poor in quality and a satisfactory structure refinement could not be obtained for $[(\text{Cu}_2\text{L17})\cdot 3\text{DMF}]_\infty$ due to the following two main reasons. First, the co-facial bifluorene is disordered over two positions featuring the whole molecule rotated of 180° on the two-fold axis passing between the centroids of the pentatomic rings with the consequence that the methylene bridge and the methyl substituents in **H4L17** are present on both extremities with undetermined fractional occupancy. Second, the metal node provided evidence of positional disorder as well, simulating the existence of a $\text{Cu}\cdots\text{Cu}$ interaction at a hypothetical interatomic distance between Cu^{II} ions of 1.65 \AA that is not realistic. The presence of incommensurate disordered DMF molecules in the crystal further obstacle the refinement. However, the connectivity of the supramolecular system is clear and somehow similar to that found for $[(\text{Cd}_2\text{L17}\cdot 6\text{H}_2\text{O})\cdot 2\text{H}_2\text{O}]_\infty$, with L17^{4-} anions coordinated to the copper ions in infinite ribbons which propagate along the c axis. The packing of the ribbons results in quasi-hexagonal nanochannels enclosed in a pillared scaffold. A perspective view of the connectivity found in $[(\text{Cu}_2\text{L17})\cdot 3\text{DMF}]_\infty$, is shown in Figure 171.

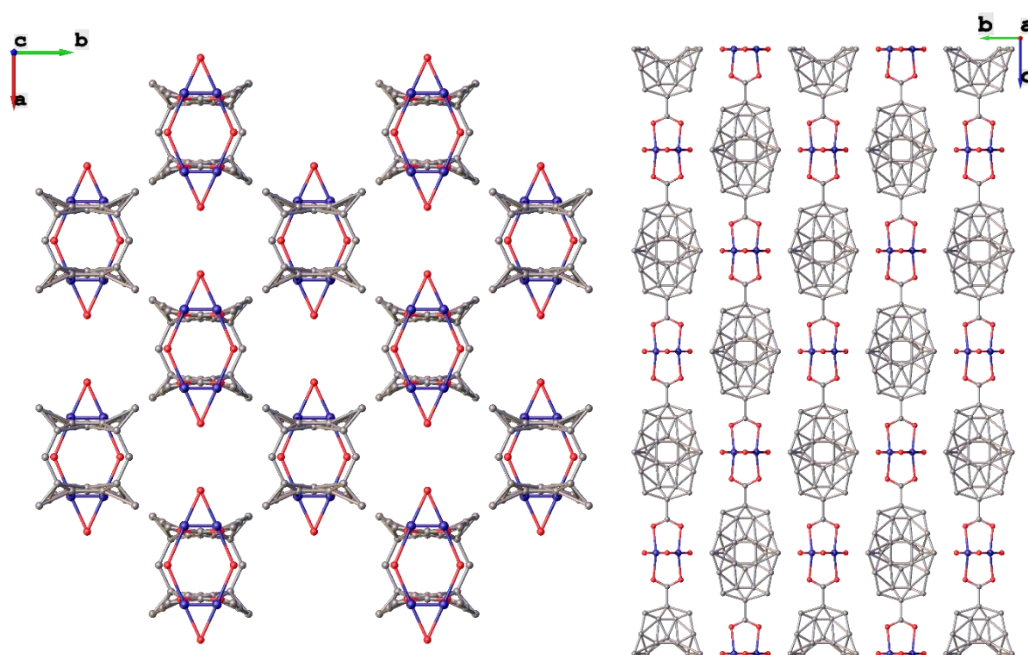


Figure 171 Perspective view of the connectivity of MOF $[(\text{Cu}_2\text{L17})\cdot 3\text{DMF}]_\infty$ along c and a axis. Disordered moieties are shown in both diagrams.

Table 42 Unit cell parameters for [(Cu₂L17)·3DMF]_∞.

Crystal System	orthorhombic		
Space Group	<i>Immm</i>		
<i>a</i> /Å	10.9897(16)	<i>α</i> /°	90
<i>b</i> /Å	11.522(2)	<i>β</i> /°	90
<i>c</i> /Å	14.8995(11)	<i>γ</i> /°	90
<i>V</i> /Å ³	1886.6(5)		
<i>Z</i>	2	<i>Z'</i>	0.125

Several attempts to get a better refinement were made, including collection of the crystal data on MoK α and CuK α sources at 100 K, and by means of synchrotron radiation at lower temperature (70 K) in order to minimize Brownian motions in the system. (The synchrotron facility employed was the Diamond Light Source, UK, equipped with a zirconium edge ($\lambda = 0.6889$ Å)). Unfortunately, no one of the attempts got better results.

3.2.3. Interaction between H₄L17 and pyridyl derivatives

The study of the reactivity of H₄L17 with pyridyl derivatives is still in a preliminary phase and only the co-crystallization of the bifluorene-tetracarboxylic ligand with the commercial 1,2-di(pyridin-4-yl)ethane (Py₂Et) in a 1:2 molar ratio was attempted by layering an ethanolic solution of Py₂Et onto a solution of H₄L17 in a mixture of DMF/H₂O (1:1 v/v). Single crystals of the co-crystals (H₄L17·Py₂Et)_∞ were grown and their crystal structure elucidated by means of SC-XRD analysis; the main crystallographic data and refinement parameters are listed in Table S157. Even though a 1:2 stoichiometric ratio L17:Py₂Et was experimentally used, the obtained compound (H₄L17·Py₂Et)_∞ consists of an infinite network formed by H₄L17 and Py₂Et in equimolar amounts. The asymmetric unit contains one fully protonated H₄L17 ligand, a Py₂Et spacer, and one co-crystallized water molecule (O9) as shown in Figure 172.

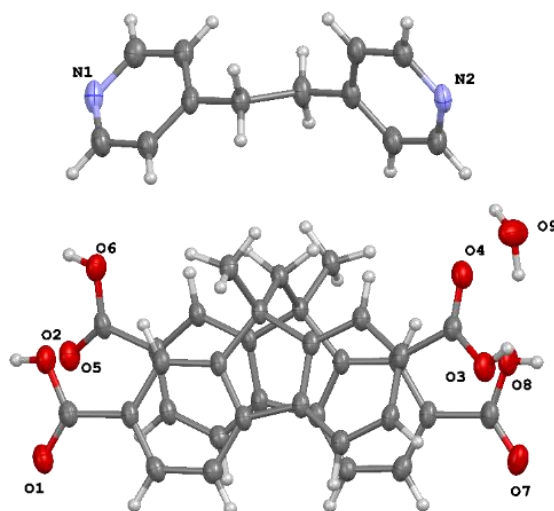


Figure 172 Numbering scheme in the asymmetric unit of (H₄L17·Py₂Et)_∞. Thermal ellipsoids are drawn at 50 % probability level.

The geometrical features of the co-facial bifluorene evidenced a semi-spread wings arrangement, with an angle between the two planes described by fluorene of about 16°, slightly smaller than that of 19° found in the spread wings configuration of $[(\text{Cd}_2\text{L17}\cdot 6\text{H}_2\text{O})\cdot 2\text{H}_2\text{O}]_\infty$. The fluorene moieties are rotated of about 23°, closely resembling what observed in $[(\text{Cd}_2\text{L17}\cdot 6\text{H}_2\text{O})\cdot 2\text{H}_2\text{O}]_\infty$, and showing similar intramolecular π - π interactions with centroid-centroid distances of 3.64, and 3.66 Å, measured between the six-membered rings of fluorene moieties (interactions **g** and **h**, Figure 173).

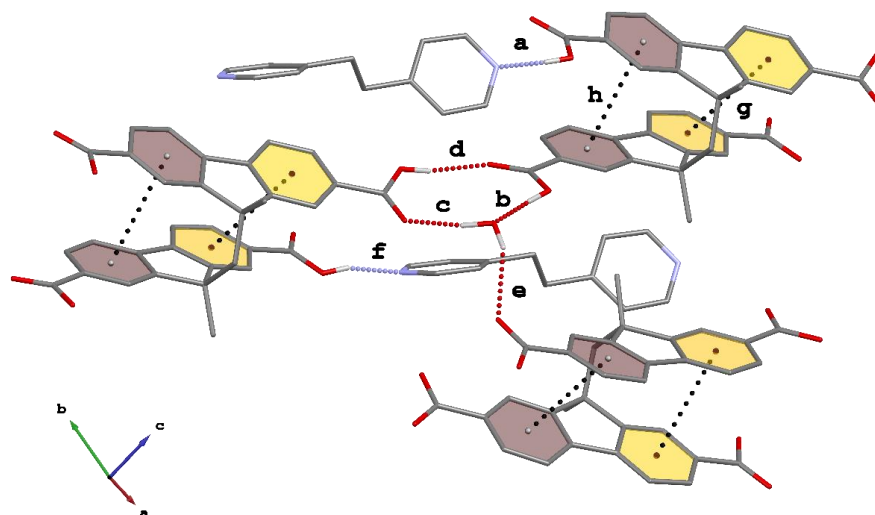


Figure 173 Intra- and inter-molecular interactions in the crystal structure of $(\text{H}_4\text{L17}\cdot\text{Py}_2\text{Et})_\infty$. Only interacting hydrogen atoms are shown for clarity. Interactions are labelled according to Table 43.

As expected, N-donor molecules interact with carboxylic acids through strong hydrogen bonds as described in Table 43 and shown in Figure 173 (interactions **a** and **f**). The remaining carboxylic functionalities at bifluorene units are involved in hydrogen bonds with the co-crystallized water molecule generating a hydrogen bonded pattern formed by interactions **b**, **c** and **d**, that can be ascribed as $R_3^3(10)$ according to the graph set notation (§1.1.2).

Table 43 Summary of the hydrogen bonding interactions in $(\text{H}_4\text{L17}\cdot\text{Py}_2\text{Et})_\infty$.

#		$d_{\text{D}\cdots\text{A}}(\text{Å})$	$d_{\text{H}\cdots\text{A}}(\text{Å})$	$\alpha_{\text{D-H}\cdots\text{A}}(\text{°})$
a	$\text{O}2^2\text{-H}2^2\cdots\text{N}2$	2.544(2)	1.70(16)	175.8(2)
b	$\text{O}6^2\text{-H}6^2\cdots\text{O}9$	2.612(3)	1.78(2)	173.2(2)
c	$\text{O}9\text{-H}9\text{A}\cdots\text{O}4^1$	2.788(3)	1.81(5)	171(5)
d	$\text{O}3^1\text{-H}3^1\cdots\text{O}5^2$	2.727(2)	1.92(2)	160.4(2)
e	$\text{O}9\text{-H}9\text{B}\cdots\text{O}2^4$	3.052(5)	2.21(3)	144.6(4)
f	$\text{O}8^1\text{-H}8^1\cdots\text{N}1^3$	2.609(2)	1.79(2)	163.9(2)

Symmetry codes: ¹ +x, 3/2-y, -1/2+z; ² 1+x, 3/2-y, 1/2+z; ³ 1+x, +y, +z, ⁴ 1-x, +y, +z.

These hydrogen bondings generate the infinite staircase network shown in Figure 174, where **H4L17** molecules are linked at opposite sides and **Py2Et** molecules result enclosed between two staircases. Adjacent layers are staggered and connected through hydrogen bonds between O9–H9B...O2 (interaction **e** in Table 43 and Figure 173).

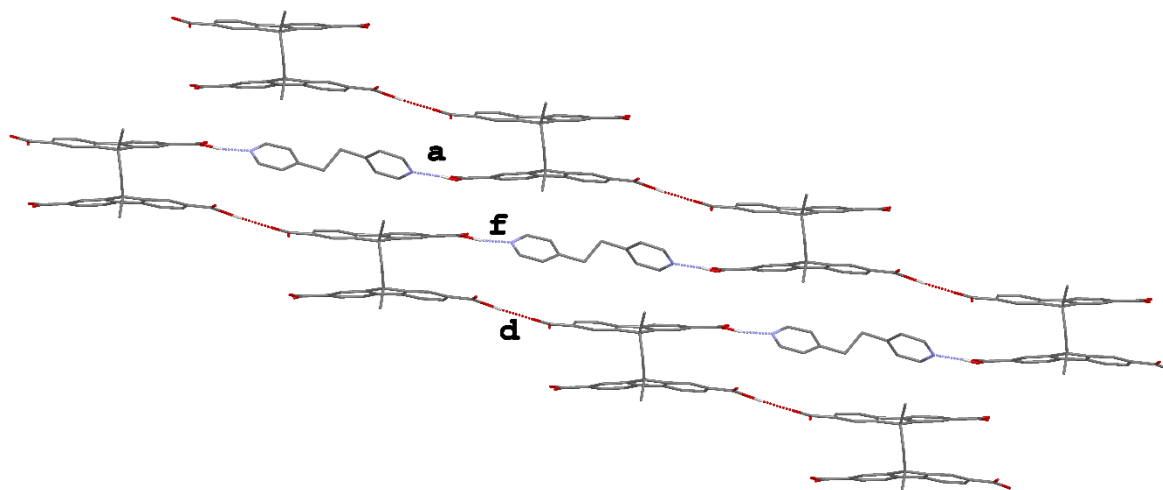


Figure 174 View of the hydrogen-bonded staircase packing in $(\mathbf{H4L17}\cdot\mathbf{Py2Et})_{\infty}$ along the b axis. Only interactions **a**, **d** and **f** are shown for clarity.

The packing diagrams of $(\mathbf{H4L17}\cdot\mathbf{Py2Et})_{\infty}$ along the a and c axis are shown in Figure 175.

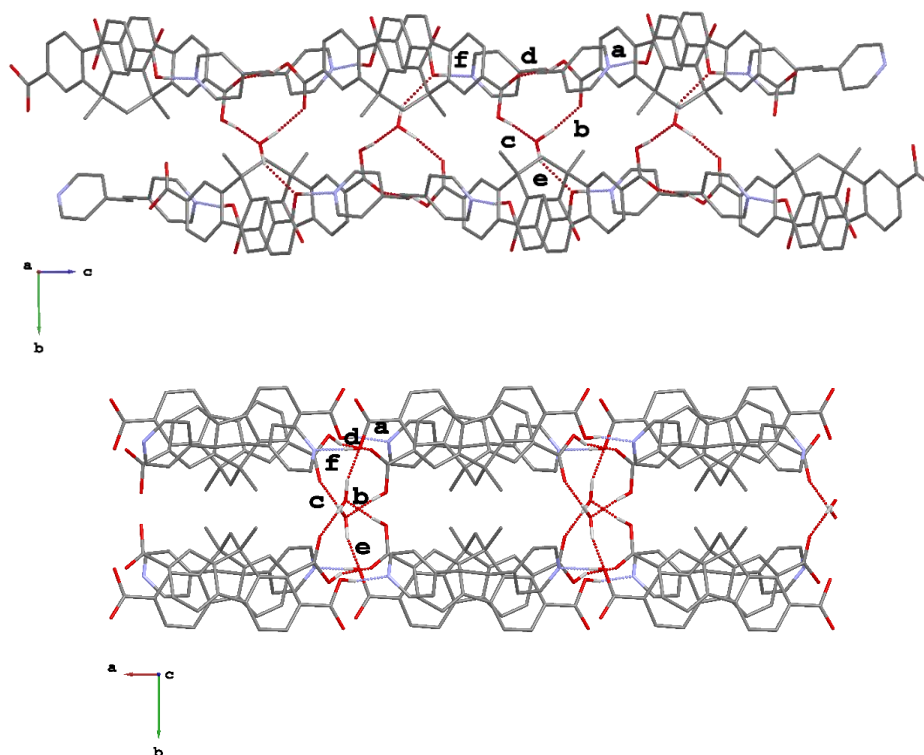


Figure 175 Packing diagrams of $(\mathbf{H4L17}\cdot\mathbf{Py2Et})_{\infty}$ along the a (top) and c (bottom) axis. Interactions are labelled according to Table 43.

3.2.4. Three components supramolecular architectures: *H*₄**L17**, metal ions and pyridyl derivatives

The reactivity of the new and versatile ligand **H**₄**L17** was tested in a three-components approach in order to explore the resulting supramolecular assemblies. Due to the lack of time only the reactions of **H**₄**L17** and **L3** with several metal ions were investigated, and among them only the fully characterized products obtained with cobalt and zinc salts will be here reported.

3.2.4.1. [(Co₂L₃L17·H₂O)·2DMF]_∞

The one-pot reaction of CoCl₂·6H₂O, **L3** and **H**₄**L17** (2:2:1 molar ratios) in a mixture of DMF/H₂O (1:1 v/v) at 80° C for 18 h provided, upon slow cooling, orange crystals.

Single crystal XRD showed that the compound corresponds to the coordination polymer of formula [(Co₂L₃L17·H₂O)·2DMF]_∞. Crystal data and refinement parameters are reported in Table S158, and selected bond lengths and angles in Table S159 and Table S160. The asymmetric unit features one fully deprotonated **L17**⁴⁻ unit, two crystallographically independent Co(II) ions, two **L3** molecules and two coordinated water molecules located on special positions with occupancy 0.5 (Figure 176).

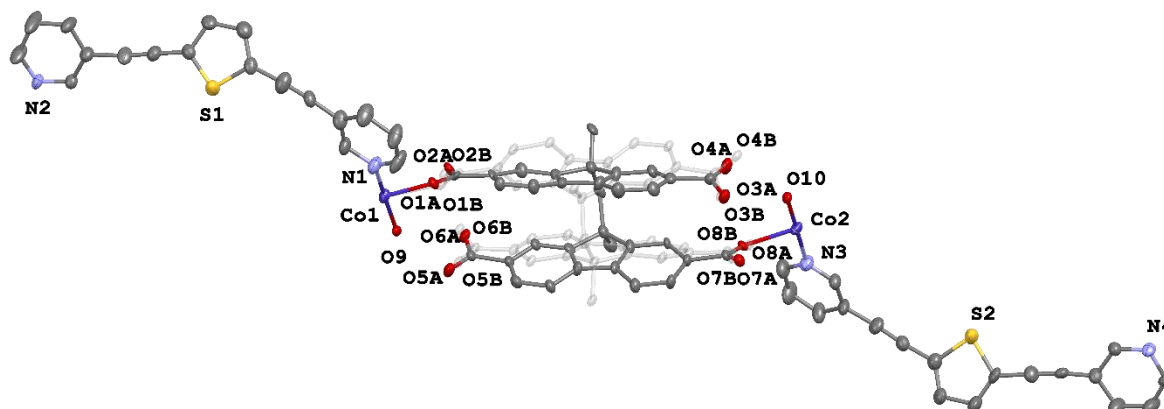


Figure 176 Perspective view along the [101] direction and atom labelling scheme of the asymmetric unit of [(Co₂L₃L17·H₂O)·2DMF]_∞. Thermal ellipsoids are drawn at 50 % probability level. The disordered units of **L17**⁴⁻ are showed in dark and light grey.

Similarly to what found for [(Cu₂L17)·3DMF]_∞, the bifluorene derivative **L17**⁴⁻ is disordered over two positions with fractional occupancy of 80:20. The crystal structure was refined considering the twinned nature of the sample (inversion twin) and the disorder at **L17**⁴⁻ core handled by using a number of RIGU, SIMU, FLAT and SADI restrains. The thermal ellipsoids at the disordered fragment were constrained using EADP. In addition, a solvent mask was calculated for the disordered solvent molecules and 300 electrons were found in a volume of

1630 Å³/unit cell. This is consistent with the presence of eight DMF molecules/unit cell, meaning that two DMF molecules are present in the asymmetric unit, leading to the overall formula [(Co₂L₃L₁₇·H₂O)·2DMF]_∞. The conformation of L₁₇⁴⁻ will not be discussed due to the high number of restrains required in the refinement. The cobalt ions are arranged in binuclear SBUs where each metal ion is hexacoordinated by two μ₂-η¹:η¹ bridging carboxylate units (O1A/B[^]O2A/B and O7A/B[^]O9A/B) for Co1 and Co2, respectively, a bridging water molecule (O9 and O10), an oxygen from a monodentate carboxylate unit (O6A/B and O3A/B) for Co1 and Co2 and two pyridyl rings from bridging L₃ units, (Py_{N1}, Py_{N4} and Py_{N2}, Py_{N3}) for Co1 and Co2, respectively, as shown in Figure 177.

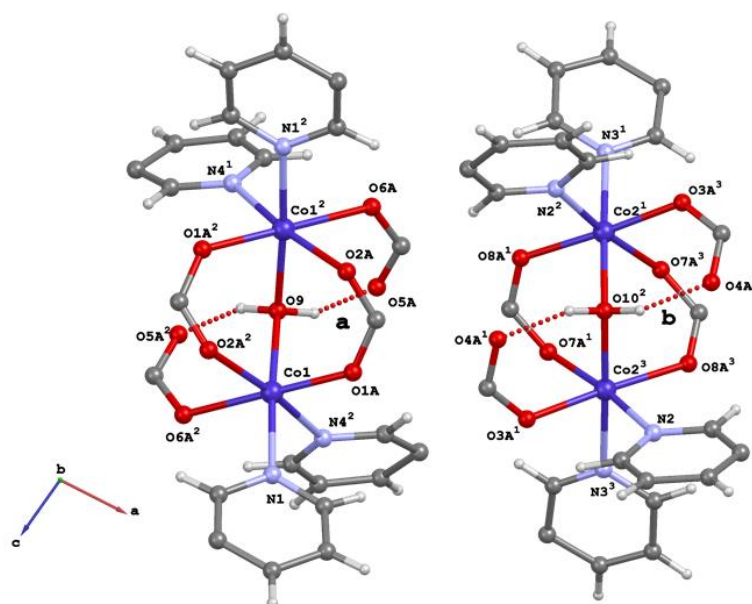


Figure 177 Schematic representation of the SBUs found in [(Co₂L₃L₁₇·H₂O)·2DMF]_∞. Only the major component (A) of L₁₇⁴⁻ unit is shown for clarity. Interactions are labelled according to Table 44.

The two carboxylates coordinating metal ions in a monodentate mode strongly interact with the coordinated water molecule by the **a** and **b** strong hydrogen bonds described in Table 44 and shown in Figure 177.

Table 44 Intermolecular hydrogen bonds in [(Co₂L₃L₁₇·H₂O)·2DMF]_∞.

#		$d_{D...A}$ (Å)	$d_{H...A}$ (Å)	$\alpha_{D-H...A}$ (°)
a	O9–H9B [^] ···O5A	2.501(9)	1.59(8)	153.9(4)
a'	O9–H9B [^] ···O5B	2.64(3)	1.81(3)	142(2)
b	O10 ²⁻ –H10A ²⁻ ···O4A ³	2.612(8)	1.74(7)	147.4(4)
b'	O10 ²⁻ –H10A ²⁻ ···O4B ³	2.50(3)	1.56(3)	161(2)

Symmetry codes: ¹ -1+x, +y, 1+z; ² -1-x, +y, 2-z; ³ -x, +y, 1-z. Note: interactions **a'** and **b'** are calculated on the minor component of the disordered L₁₇⁴⁻ anion and are not shown in Figure 177.

The Co–O distances are slightly different ranging from 1.79 to 2.24 Å for Co1–O2B¹ and Co1–O1B, respectively. A search in the CSD revealed that the same SBU was already reported. A few studies were focused on the studies of supramolecular systems based on different N-donors such as pyridine,^[447–449] 1,10-phenanthroline,^[450–452] 2,2'-bipy,^[453] and quinoline.^[448] A comparison of the geometrical features of the SBUs in [(Co₂L₃L17·H₂O)·2DMF]_∞ with those reported in the literature show very similar values with N–Co–N angles of 92.8(3) and 92.0(3) for N2¹–Co2–N3 and N1–Co1–N4², respectively in line with the mean value of 90(2) ° found for similar SBUs in which the N-donors are pyridyl rings. L₃ spacers are not planar with the pyridyl rings angled of 26.8 and 31.4 °, for Py_{N1}^Py_{N2} and Py_{N3}^Py_{N4}, respectively and adopt a periplanar conformation (Table 45). These geometrical parameters closely resemble those found in the paddle-wheel arrangement found in complex [CuL₃(NO₃)₂·CH₃CN]₂·2CH₃CN (§3.1.1). The pyridyl rings coordinated to the same Co ion are angled of 73.1 and 102.0 °, for Co1 and Co2, respectively, with values consistent to those found in similar fragments (see refcodes: KAFCAW, XEJYIW, YOLZEF).

Table 45 Selected bond lengths (Å) and angles (°) for [(Co₂L₃L17·H₂O)·2DMF]_∞.

	Length/Å		Angle/°		Angle/°
Co1–O1A	1.943(7)	O1A–Co1–O2A ¹	103.3(4)	O8A–Co2–N3	89.0(5)
Co1–O1B	2.24(4)	O1A–Co1–O9	89.4(3)	O8B–Co2–O10	93.1(19)
Co1–O2A ¹	2.132(7)	O1A–Co1–N1	89.0(4)	O8B–Co2–N3	87(2)
Co1–O2B ¹	1.79(4)	O1A–Co1–N4 ²	87.7(4)	O10–Co2–O3B ²	85.3(10)
Co1–O6A ¹	2.233(7)	O1B–Co1–N4 ²	88.0(13)	O10–Co2–O7A ²	92.2(3)
Co1–O6B ¹	1.93(4)	O2A ¹ –Co1–O6A ¹	81.6(4)	O10–Co2–O7B ²	89.5(12)
Co1–O9	2.158(4)	O2A ¹ –Co1–O9	93.2(3)	O10–Co2–O8A	90.6(4)
Co1–N1	2.097(8)	O2B ¹ –Co1–O1B	102.2(18)	O10–Co2–N2 ¹	90.6(3)
Co1–N4 ²	2.281(7)	O2B ¹ –Co1–O9	94.1(15)	O10–Co2–N3	176.6(3)
Co2–O3A ²	2.037(10)	O2B ¹ –Co1–N1	90.6(15)	N2 ¹ –Co2–O3B ²	96.5(13)
Co2–O3B ²	2.19(4)	O6A ¹ –Co1–N4 ²	87.2(3)	N2 ¹ –Co2–O7A ²	173.9(4)
Co2–O7A ²	2.148(12)	O6B ¹ –Co1–O9	94.6(10)	N2 ¹ –Co2–O7B ²	168.6(14)
Co2–O7B ²	2.31(5)	O6B ¹ –Co1–N1	86.4(10)	N2 ¹ –Co2–O8A	89.9(4)
Co2–O8A	2.155(8)	O6B ¹ –Co1–N4 ²	84.5(13)	N2 ¹ –Co2–N3	92.8(3)
Co2–O8B	1.92(5)	O9–Co1–O1B	83.8(13)	N3–Co2–O3B ²	94.7(10)
Co2–O10	2.077(4)	O9–Co1–O6A ¹	87.0(2)	N3–Co2–O7B ²	87.2(12)
Co2–N1 ¹	2.086(7)	O9–Co1–N4 ²	83.5(2)	Co1–O9–Co1 ¹	109.5(3)
Co2–N3	2.177(7)	N1–Co1–O1B	94.7(13)	Co2–O10–Co2 ²	115.6(3)
		N1–Co1–O2A ¹	91.5(3)	Py _{N1} ^Py _{N2}	26.8(4)
		N1–Co1–O6A ¹	94.2(3)	Py _{N3} ^Py _{N4}	31.4(4)
		N1–Co1–O9	175.2(2)		
		N1–Co1–N4 ²	92.0(3)		
		O3A ² –Co2–O7A ²	84.6(4)		
		O3A ² –Co2–O10	92.9(3)		
		O3A ² –Co2–N2 ¹	89.9(4)		
		O3A ² –Co2–N3	87.5(3)		
		O7A ² –Co2–O8A	95.4(5)		
		O7A ² –Co2–N3	84.4(4)		

Symmetry codes: ¹-x,+y,1-z; ²1-x,+y,-z.

The overall structure of $[(\text{Co}_2\text{L}_3\text{L}17\cdot\text{H}_2\text{O})\cdot 2\text{DMF}]_\infty$ is showed in Figure 178, and is formed of undulated ribbons running along the c axis direction and aligned along a .

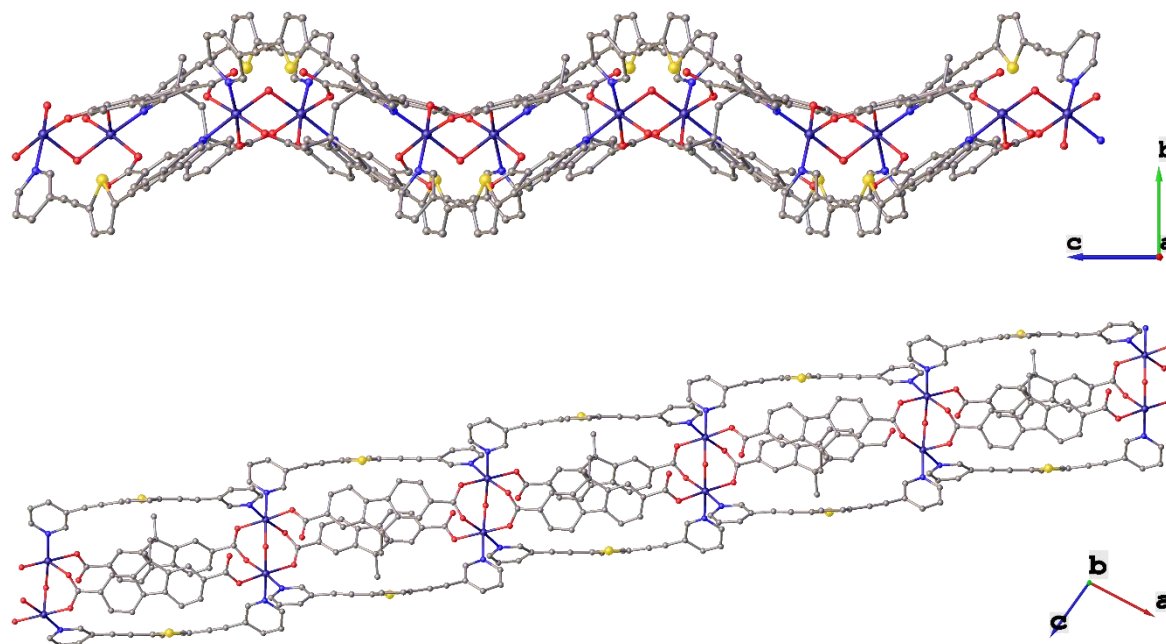


Figure 178 Views of the polymeric arrangement of $[(\text{Co}_2\text{L}_3\text{L}17\cdot\text{H}_2\text{O})\cdot 2\text{DMF}]_\infty$ along the a and b axis, respectively. Disorder at $\text{L}17^+$ units and hydrogen atoms are omitted for clarity.

Solvent accessible channels are present in the spaces between adjacent chains, as clearly visible in Figure 179.

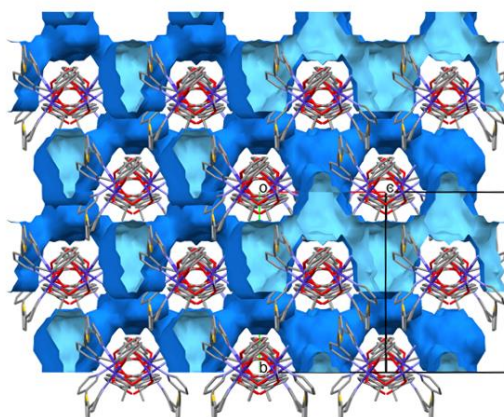


Figure 179 Packing diagram of $[(\text{Co}_2\text{L}_3\text{L}17\cdot\text{H}_2\text{O})\cdot 2\text{DMF}]_\infty$. Solvent accessible channels are represented in light blue.

Table 46 Geometrical features including angles, dihedral angles (°) and distances (Å) of **L3** molecules in the crystal structures of $[(\text{Co}_2\text{L}_3\text{L17}\cdot\text{H}_2\text{O})\cdot 2\text{DMF}]_\infty$, $[\text{CuL}_3(\text{NO}_3)_2\cdot\text{CH}_3\text{CN}]_2\cdot 2\text{CH}_3\text{CN}$ and $[(\text{Zn}_2\text{L}_3\text{L17}\cdot 3\text{H}_2\text{O}\cdot\text{DMF})\cdot 3.5\text{DMF}]_\infty$ (§3.2.4.2). Centroids are identified by numbers (1-3). Atoms have been renumbered for clarity reasons accordingly to the molecular structure presented in Table 10.

	$[(\text{Co}_2\text{L}_3\text{L17}\cdot\text{H}_2\text{O})\cdot 2\text{DMF}]_\infty$	$[\text{CuL}_3(\text{NO}_3)_2\cdot\text{CH}_3\text{CN}]_2\cdot 2\text{CH}_3\text{CN}$	$[(\text{Zn}_2\text{L}_3\text{L17}\cdot 3\text{H}_2\text{O}\cdot\text{DMF})\cdot 3.5\text{DMF}]_\infty$
1-2-3	147.71 150.16	146.17	152.47
Py1-Tph1	8.7 8.0	18.79	56.97
Py1-Py2	16.6 12.6	11.90	24.28
Tph1-Py2	12.4 17.0	29.72	15.06
C5-C6-C7	175.1 173.9	178.68	174.8
C8-C7-C6	176.0 175.5	178.16	176.0
C7-C8-S1	122.8 117.2	120.60	121.6
C12-C11-S1	123.1 118.9	119.89	121.4
C14-C13-C12	171.3 173.2	176.36	177.8
C11-C12-C13	177.1 176.9	177.04	176.4
C4-C5-C8-C9	54.5 54.3	19.16	52.9
C10-C11-C14-C15	29.1 22.9	31.02	78.7
d _{N1-N2}	13.437 13.648	13.228	13.743

3.2.4.2. $[(\text{Zn}_2\text{L}_3\text{L17}\cdot 3\text{H}_2\text{O}\cdot\text{DMF})\cdot 3.5\text{DMF}]_\infty$

Solvothermal reaction of **L3**, **H4L17** and $\text{Zn}(\text{NO}_3)_2\cdot 6\text{H}_2\text{O}$ (1:1:2 molar ratio) in a mixture of DMF/H₂O (1:1 v/v) at 80 °C for 48 h, yielded tiny light-yellow crystals which were structurally characterized as the product $[(\text{Zn}_2\text{L}_3\text{L17}\cdot 3\text{H}_2\text{O}\cdot\text{DMF})\cdot 3.5\text{DMF}]_\infty$ which crystallizes in the triclinic *P*-1 space group. All the screened crystals were found to be non-merohedral twins and weakly diffracting and therefore analyzed by means of synchrotron radiation (the synchrotron

facility employed was the Diamond Light Source, UK, equipped with a zirconium edge ($\lambda = 0.6889 \text{ \AA}$). Crystal data and refinement parameters are reported in Table S158, and selected bond lengths and angles in Table S161. The asymmetric unit features one fully deprotonated **L17**⁴⁻ unit, two crystallographically independent Zn(II) ions and one **L3** molecule (Figure 180).

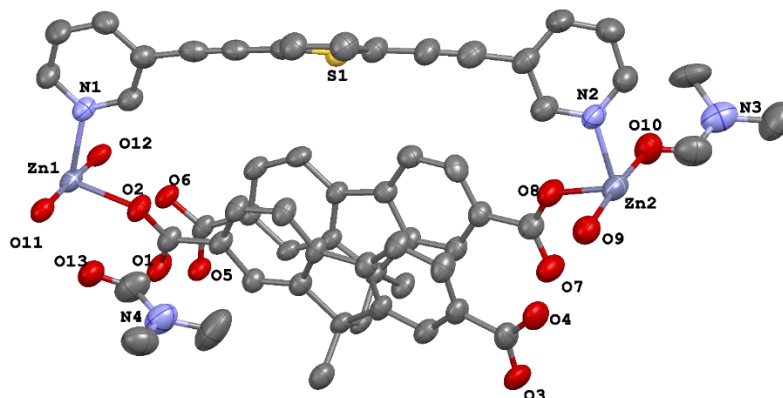


Figure 180 Asymmetric unit of $[(\text{Zn}_2\text{L3L17}\cdot 3\text{H}_2\text{O}\cdot \text{DMF})\cdot 3.5\text{DMF}]_\infty$. Thermal ellipsoids are drawn at 50 % probability level. H atoms have been omitted for clarity.

The **L17**⁴⁻ is arranged in a spread wings conformation with the fluorene units angled of 17.6° and an angle between planes of 15.2° . The zinc ions are hexacoordinated and share the same equatorial coordination: one chelating carboxylate ($\text{O5}^1\wedge\text{O6}^1$ and $\text{O3}^2\wedge\text{O4}^2$), an oxygen from a monodentate carboxylate unit (O2 and O8) and one pyridyl nitrogen from bridging **L3** units (N1 and N2), for Zn1 and Zn2 , respectively, as shown in Figure 181.

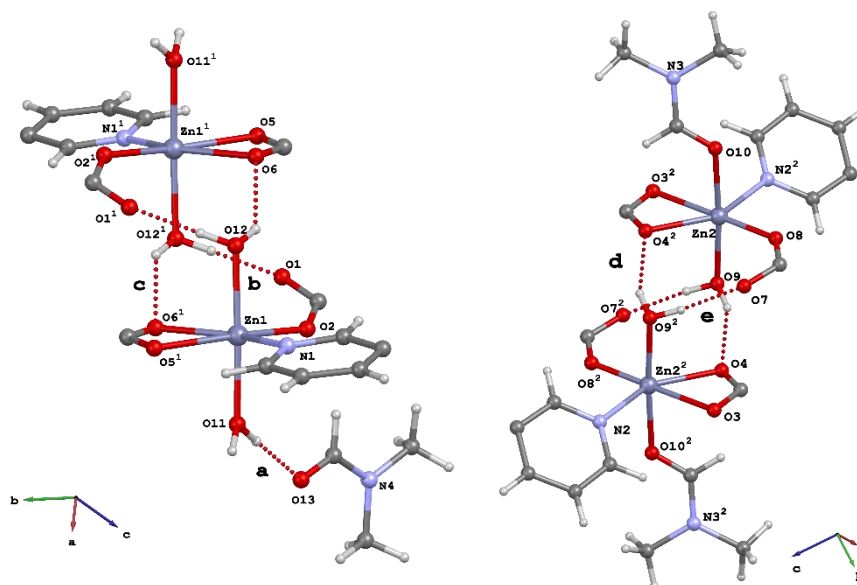


Figure 181 Representation of the SBUs found in $[(\text{Zn}_2\text{L3L17}\cdot 3\text{H}_2\text{O}\cdot \text{DMF})\cdot 3.5\text{DMF}]_\infty$. Zn1-SBU (left) and Zn2-SBU (right). Interactions are labelled according to Table 47.

Table 47 Intermolecular interactions found in the SBUs of $[(\text{Zn}_2\text{L3L17}\cdot 3\text{H}_2\text{O}\cdot \text{DMF})\cdot 3.5\text{DMF}]_\infty$.

#		$d_{\text{D}\cdots\text{A}}(\text{\AA})$	$d_{\text{H}\cdots\text{A}}(\text{\AA})$	$\alpha_{\text{D-H}\cdots\text{A}}(^{\circ})$
a	O11–H11A \cdots O13	2.680(4)	1.81(3)	173.6(2)
b	O12 ¹ –H12A ¹ \cdots O1	2.620(4)	1.77(3)	163.3(2)
c	O12 ¹ –H12A ¹ \cdots O6 ¹	2.757(4)	2.03(3)	140.4(2)
d	O9 ² –H9A ² \cdots O4 ²	2.880(5)	1.88(3)	153.8(2)
e	O9 ² –H9B ² \cdots O7	2.781(5)	1.91(3)	172.1(3)
f	O11–H11B \cdots O5 ³	2.720(4)	1.86(3)	171.8(2)

Symmetry codes: ¹ 1-x, 2-y, 1-z; ² -x, 1-y, 2-z; ³ 1+x, +y, +z.

The axial positions of Zn1 and Zn2 instead, display a different scenario. Zn1 is coordinated by two water molecules (O11 and O12), one of which is involved in a strong hydrogen bond with a co-crystallized DMF molecule (**a** in Figure 181 and Table 47).

On the contrary, Zn2 is surrounded by a water molecule (O9) and a coordinating DMF fragment (O10). Coordinated water molecules at both metal ions are involved in strong hydrogen bonds with O atoms of adjacent carboxylates and are described as interactions **b-e** in Table 47 and shown in Figure 181, resulting in pseudo dinuclear SBUs (Zn1-SBU and Zn2-SBU). It is worth noting that in addition to the abovementioned co-crystallized DMF molecule, a region of disordered solvent molecules was subjected to SQUEEZE routine revealing the presence of 2.5 additional DMF molecules /unit cell.

The overall structure of $[(\text{Zn}_2\text{L3L17}\cdot 3\text{H}_2\text{O}\cdot \text{DMF})\cdot 3.5\text{DMF}]_\infty$ is showed in Figure 182 and consists of undulated ribbons formed by bridging **L17**⁴⁻ units.

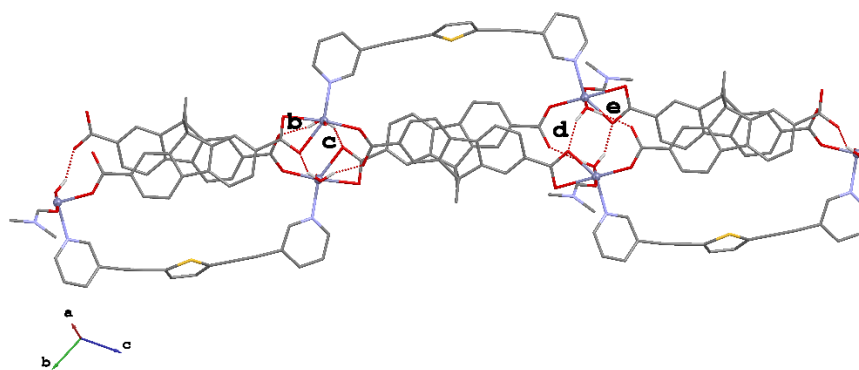


Figure 182 Perspective view of the polymeric network in $[(\text{Zn}_2\text{L3L17}\cdot 3\text{H}_2\text{O}\cdot \text{DMF})\cdot 3.5\text{DMF}]_\infty$. Only H-atoms involved in the interactions (labelled according to Table 47) are depicted; co-crystallized DMF molecules are not shown for clarity.

The primary skeleton in the supramolecular network closely resembles what described in the case of $[(\text{Co}_2\text{L3L17}\cdot \text{H}_2\text{O})\cdot 2\text{DMF}]_\infty$ except for the presence of only one bridging **L3** spacer,

alternatively up-side and down-side arranged along the propagation direction. **L3** is not planar with the pyridyl rings angled of 24.3° and arranged in a periplanar conformation (Table 46). It is worth noting that **L3** features a similar convergent periplanar configuration in both $[(\text{Co}_2\text{L3}_2\text{L17}\cdot\text{H}_2\text{O})\cdot 2\text{DMF}]_\infty$ and $[(\text{Zn}_2\text{L3L17}\cdot 3\text{H}_2\text{O}\cdot\text{DMF})\cdot 3.5\text{DMF}]_\infty$, even if dihedral angles reported in the same table evidence a highly distorted arrangement for **L3**.

The infinite $[(\text{Zn}_2\text{L3L17}\cdot 3\text{H}_2\text{O}\cdot\text{DMF})\cdot 3.5\text{DMF}]_\infty$ ribbons pack along *a* axis *via* hydrogen bonding described as interaction **f** in Table 47 and shown in Figure 183.

Notably, the Zn₂-SBUs of adjacent double chains are not directly interacting because of the longer distance imparted by bulkier DMF molecules coordinated to Zn₂ at its axial positions (Figure 183).

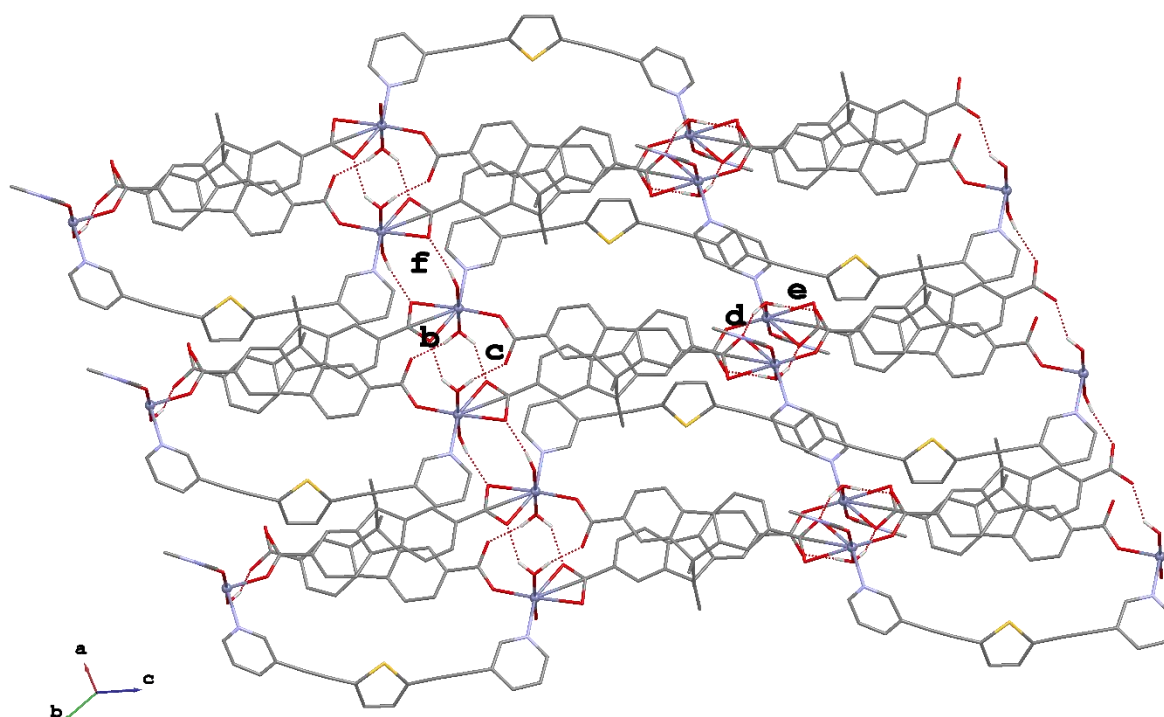


Figure 183 Packing diagram of $[(\text{Zn}_2\text{L3L17}\cdot 3\text{H}_2\text{O}\cdot\text{DMF})\cdot 3.5\text{DMF}]_\infty$ along the [111] direction. Interactions are labelled according to Table 47.

The polymeric network is then extended to a 3D-MOF with potential voids running along the *b* axis as shown in Figure 184.

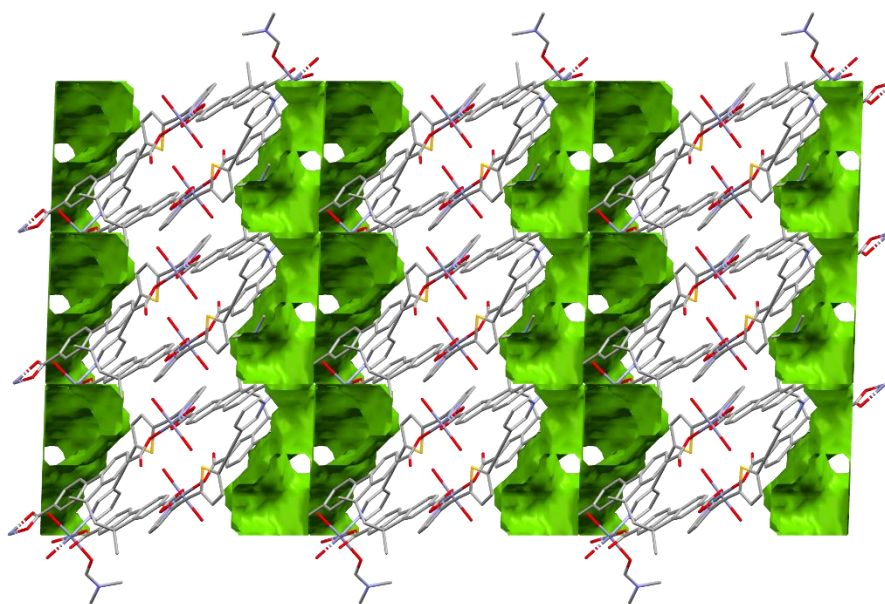


Figure 184 Packing diagram of $[(\text{Zn}_2\text{L3L17}\cdot 3\text{H}_2\text{O}\cdot \text{DMF})\cdot 3.5\text{DMF}]_\infty$ showing solvent accessible voids along the b axis.

4. Conclusions

The ligands **L1-L11** were synthesized, characterized and tested as building blocks for the design of novel supramolecular networks based on different supramolecular interactions and the results are summarized in Table 48.

Table 48 Summary of the supramolecular networks obtained from ligand **L1-L11**.

L1	L2	L3	L4	L5	L7	L11
[AgL1(OTf)((CH ₃) ₂ CO) _{0.5}] _∞	(1·L2) _∞	[AgL3(OTf)((CH ₃) ₂ CO) _{2.5}] _∞	[Co(L4) ₂ Cl ₂] _∞	(2·L5·CHCl ₃) _∞	(L7·H ₂ TER) _∞	(L11·I ₂)·0.5I ₂
[ZnL1(NO ₃) ₂ ·CH ₃ CN] ₂	(L2·H ₂ TER·Br) _∞	[CuL3(NO ₃) ₂ ·CH ₃ CN] ₂ ·2CH ₃ CN		(3·L5) _∞		
(1·L1) ₂	(L2·H ₂ TER·(OH) ₂) _∞	[CdL3(NO ₃) ₂ (H ₂ O) ₂ ·1.5H ₂ O] _∞		(L5·R2) _∞		
(ZnL1Cl ₂) _∞	(L2·H ₂ ISO) _∞	[(Co ₂ L3 ₂ L17·H ₂ O)·2DMF] _∞				
(L1·H ₂ TER) _∞	(L2·H ₂ ISO·F ₄) _∞	[(Zn ₂ L3L17·3H ₂ O·DMF)·3.5DMF] _∞				
(L1) ₂ ·R3	(L2·H ₂ PyDC) _∞	(L3·R2) _∞				
	(L2·1,4-DITFB) _∞	(L3·R3) _∞ ,				
		(HL3) ₃ ·I ₂				
		(H ₂ L3Br ₄)BrBr ₃ ·0.5 CHCl ₃				

Cells are coloured according to the nature of the complementary building blocks.

- metal ions
- metal complexes
- carboxylic acids
- borasiloxanes
- halogenated species

Ligands **L1** and **L2** were prepared according to a synthetic method previously established by the research group and their reactivity, partially explored in previously reported works, extended to novel systems allowing for a better rationalization of the resulting networks. The reactions with metal ions were conducted by using both metal salts and the coordinatively unsaturated cadmium dithiophosphato complex **1** (§3.1.1.1). The obtained results showed that ligand **L1** easily yield crystalline compounds probably due to its versatile nature deriving from the existence of different possible conformers coming from the different reciprocal orientation of the 3-pyridyl substituents with respect to the central thiadiazole ring. The different arrangements (showed in Scheme 14) were calculated to have almost the same energy and the final conformation is driven by other factors such as the coordination geometry of the metal ion, the counterion and the experimental conditions used in the self-assembly process. The periplanar conformation where N-atoms point at the same side can lead either to polymeric motifs, as in the case of the CP [AgL1(OTf)((CH₃)₂CO)_{0.5}]_∞ or to dimeric constructs as in the

case of $[\text{ZnL1}(\text{NO}_3)_2 \cdot \text{CH}_3\text{CN}]_2$ and $(\mathbf{1} \cdot \mathbf{L1})_2$, depending on the coordination geometry around the metal ion and on the different features of the counter ion (steric hindrance, coordinating nature, etc.). When ligand **L1** adopts an antiperiplanar conformation, where N-atoms point at opposite side, polymeric constructs are formed as in the CP $(\text{ZnL1Cl}_2)_\infty$.

Ligand **L2** featuring 4-pyridyl substituents only allows for almost linear conformations which only differ for the rotation of the pyridine rings around the single C–C bond, and undulated polymeric constructs as that found in $(\mathbf{1} \cdot \mathbf{L2})_\infty$ are formed.

The linear arrangement of **L2** resulted favoured in the formation of co-crystals, and the reactions of **L2** with benzenedicarboxylic acids yielded several crystalline products, whilst the same reactions conducted starting from **L1** yielded good crystals only for compound $(\mathbf{L1} \cdot \text{H}_2\text{TER})_\infty$ (§3.1.2.1). The obtained co-crystals $(\mathbf{L1} \cdot \text{H}_2\text{TER})_\infty$, $(\mathbf{L2} \cdot \text{H}_2\text{TER-Br})_\infty$, $(\mathbf{L2} \cdot \text{H}_2\text{TER-(OH)}_2)_\infty$, $(\mathbf{L2} \cdot \text{H}_2\text{ISO})_\infty$, $(\mathbf{L2} \cdot \text{H}_2\text{ISO-F}_4)_\infty$, $(\mathbf{L2} \cdot \text{H}_2\text{PyDC})_\infty$ share the same mono-dimensional main motif consisting in undulated polymeric chains built up by strong H-bonds engaged between the pyridine rings and the protonated carboxylate groups. Extended 3D networks resulted in all the discussed cases by the packing of the chains. In addition, another co-crystal $(\mathbf{L7} \cdot \text{H}_2\text{TER})_\infty$ was serendipitously obtained while investigating the reactivity of **L7** towards metal ions with the presence of complementary building block **H₂TER**.

Ligands **L1** and **L2** confirmed their versatile nature also in the reactions with molecular halogens and interhalogens, and with 1,4-di-iodo-tetrafluoro-benzene (§3.1.4.1), confirming the high predictability of the products ensuing from **L2**. The existence of different conformations for **L1** resulted in an excessively disordered coordination when the reaction with borasiloxanes was performed (§3.1.3.2), and further studies will be necessary to better investigate the reactions of **L1** and **L2** with boron-based acceptors.

The reactivity with metal ions of **L3** and **L4**, which feature the same shape of **L1** and **L2**, but longer lengths, confirmed the above evidenced tendency to form crystalline networks of the spacer with the *meta*-substituted pyridyl substituents. In fact, the CP $[\text{Co}(\mathbf{L4})_2\text{Cl}_2]_\infty$ was the only crystalline product isolated for **L4**, whilst both polymeric and dimeric motifs were obtained for **L3**. Similarly to what observed for **L1**, periplanar conformation of **L3** yielded both the infinite $[\text{AgL3}(\text{OTf})((\text{CH}_3)_2\text{CO})_{2.5}]_\infty$ and the dimeric $[\text{CuL3}(\text{NO}_3)_2 \cdot \text{CH}_3\text{CN}]_2 \cdot 2\text{CH}_3\text{CN}$ assemblies, whilst an infinite motif was observed in the case of $[\text{CdL3}(\text{NO}_3)_2(\text{H}_2\text{O})_2 \cdot 1.5\text{H}_2\text{O}]_\infty$, which contains **L3** in an antiperiplanar conformation.

The reactivity of **L3** and **L4** with carboxylic acids for the formation of co-crystals was not investigated yet, and further studies will be necessary in order to understand if the *para*-

substituted **L4** will show the same high tendency to form crystalline compounds displayed by **L2**.

The products obtained by reacting **L3** with molecular bromine was different from that obtained starting from shorter analogous **L1**, since the presence of two triple carbon bonds yielded to oxidative addition of bromine to **L3** ensuing in the final product $(\mathbf{H}_2\mathbf{L3Br}_4)\mathbf{BrBr}_3 \cdot 0.5 \mathbf{CHCl}_3$ (§3.1.4.2). When the same linker was reacted with molecular iodine a salt with formula $(\mathbf{HL3})\mathbf{I}_3 \cdot \mathbf{I}_2$ was obtained (§3.1.4.2).

The reaction of **L3** with borasiloxanes **R2** and **R3** yielded two unprecedented examples of chiral helices $(\mathbf{L3} \cdot \mathbf{R2})_\infty$ and $(\mathbf{L3} \cdot \mathbf{R3})_\infty$, built up through coordinative N–B bonds (§3.1.3.3).

When the central thiophene was substituted with the longer and rigid 9H-fluorene unit (**L5** and **L6**) no crystalline products were isolated from reactions with metal salts, but two coordination polymers were obtained, namely $(\mathbf{2} \cdot \mathbf{L5} \cdot \mathbf{CHCl}_3)_\infty$ and $(\mathbf{3} \cdot \mathbf{L5})_\infty$, with the coordinatively unsaturated dithiophosphonato cadmium complexes **2** and **3** featuring helicoidal shapes ensuing from the *cis*-coordination of the pyridine at the cadmium ion (§3.1.1.3). The reaction of **L5** and the borasiloxanes **R2** and **R3** was also performed and the polymer $(\mathbf{L5} \cdot \mathbf{R2})_\infty$ obtained differing from the analogous $(\mathbf{L3} \cdot \mathbf{R2})_\infty$ and $(\mathbf{L3} \cdot \mathbf{R3})_\infty$ for the lack of chirality probably due to the more rigid nature imparted by the 9H-fluorene unit (§3.1.3.4). Additional studies will be necessary to further explore the reactivity of these fluorene containing ligands.

The reaction of **L11** with molecular iodine yielded a 1:1 CT adduct $(\mathbf{L11} \cdot \mathbf{I}_2) \cdot 0.5 \mathbf{I}_2$ which is arranged into a discrete Z-shaped construct with formula $(\mathbf{L11})_2\mathbf{Z}$ (where $\mathbf{Z} = 3\mathbf{I}_2$).

The ligands **L12-L14** were reacted with halogens and interhalogens (§3.1.4.4) and the obtained products are summarized in Table 49.

Table 49 Products obtained from the reactions between **L12-L14** and halogens/interhalogens.

L12	L13	L14
$(\mathbf{HL12})\mathbf{I} \cdot 2.5 \mathbf{I}_2$	\mathbf{HPyTeI}_2	$[(\mathbf{HL14})\mathbf{I}_2\mathbf{Cl}]_3 \cdot 0.5 \mathbf{I}_2$
	$\mathbf{HPyTeBr}_2$	
	$\mathbf{HPyTeBr}_4$	

The reaction of **L12** towards molecular iodine yielded a very interesting product $(\mathbf{HL12})\mathbf{I} \cdot 2.5 \mathbf{I}_2$, where two units of the protonated ligand $(\mathbf{HL12})^+$ are enclosed in a rare anionic pseudo-cubic

polyiodide cage. The product is isostructural with **(HL12s)I·2.5I₂**, previously reported by our research group, in which the analogous sulfurated ligand was used as precursor.

When the seleniated ligand **L12** was replaced by its tellurated analogous **L13**, a different scenario was observed. Three zwitterions with formula **HPyTeI₂**, **HPyTeBr₂**, and **HPyTeBr₄** were obtained from the reaction between molecular iodine or bromine in variable molar ratio, respectively. It is interesting to note that these products are originated from the Te–Te bond cleavage of the precursor **L13**, in contrast to what observed in **(HL12)I·2.5I₂** where the Se–Se bond remained unaffected.

The reaction between **L14** and the interhalogen ICl yielded to the salt **[(HL14)I₂Cl]₃·0.5I₂**. The protonated **(HL14)⁺** fragment is charge-balanced by an unusual I₂Cl⁻ anion which is further arranged into a unique discrete H-shaped polyhalide I₁₀Cl₄⁴⁻.

The development of ligand **H₄L17** based on a co-facial bifluorene core gave rise to very interesting MOFs both by interaction with metal salts (§3.2.2) and concomitant interactions with metal salts and **L3** that proved to be perfect in shape to complementary interact with **H₄L17** (§3.2.4). In particular, MOFs **[(Cd₂L17·3H₂O)·3H₂O]_∞**, **[(Co₂L3L17·H₂O)·2DMF]_∞**, **[(Zn₂L3L17·3H₂O·DMF)·3.5DMF]_∞** showed interesting voids occupied by solvent molecules. MOF **[(Cd₂L17·3H₂O)·3H₂O]_∞** was found to crystallize together with a CP with formula **[(Cd₂L17·6H₂O)·2H₂O]_∞**. Unfortunately, we were not able to fully optimize the experimental condition to obtain the porous material as the only product. Preliminary studies on the luminescence properties on the as-synthesized product evidenced variations of the emission wavelength passing from the free ligand to the metal networks (§3.2.2.1). Preliminary attempts of removing the solvent to activate the MOF failed and the collapse of the network was experimented.

Spectrophotometric studies were also performed on the synthesized ligands which showed interesting luminescence emission properties in both solution and in the solid state. In particular, ligands **L3-L6**, **L9**, **H₄L14** feature solid state emission with maximum centred between 483 and 553 nm. Some of the prepared supramolecular assemblies have retained the emission provided by the linkers unchanged or slightly modified, as in the case of **[AgL3(OTf)((CH₃)₂CO)_{2.5}]_∞**, **[CdL3(NO₃)₂(H₂O)₂·1.5H₂O]_∞**, **(L3·R2)_∞**, **(L3·R3)_∞**, **(2·L5·CHCl₃)_∞**, **(3·L5)_∞** and in the mixed system **[(Cd₂L17·3H₂O)·3H₂O]_∞/[(Cd₂L17·6H₂O)·2H₂O]_∞**. Additional studies are required to further explore these properties and to investigate potential applications of these materials as sensors.

4.1. Outlook and future perspectives

The presented results give an outline of the main features of the investigated ligands and create a frame of substrates that can be used as building blocks for the design of extended frameworks by reaction with different complementary Lewis acids and basis. Some of the ligands, such as **L1** and **L2**, were deeply investigated and the networks ensuing from their reactions can be essentially predicted. Further investigations are in doing course in our lab for the other ligands in order to better understand and rationalize their features and promising skills, properties and applications.

5. Experimental

5.1. Methods and materials

All chemicals, reagents and solvents were purchased from Sigma Aldrich, TCI, Fluorochem or VWR Chemicals and used as received without any further purification if not otherwise stated. Diethylamine was distilled over LiAlH_4 and degassed prior to use. All the synthesis and the majority of the experimental procedures were performed at the University of Cagliari and at the Imperial College London. Ligands **L12** and **L13** were prepared in collaboration with the research group of prof. K. K. Bhasin of the University of Panjab, India and were synthesized according to the literature.^[454,455] Ligand **L14** was kindly supplied by the group of prof. Eder J. Lenardao of the Universidade Federal de Pelotas, Brazil. Reactions between **L14** and halogens/interhalogens were performed at the University of Cagliari.

Melting point measurements were carried in capillaries, using FALC melting point device mod. C. (up to 300 °C). Elemental analyses were performed with either a EA1108 CHNS-O Fisons instrument or a Perkin Elmer analyzer. FT-Infrared spectra were recorded on a Thermo Nicolet 5700 spectrometer on KBr pellets. Mass spectra were recorded on Waters LCT Premier (ES-ToF)/Acquity i-Class by the Mass Spectrometry Service at the Department of Chemistry of Imperial College London, UK.

NMR analysis were recorded both at the University of Cagliari, at the Imperial College London and at CeSAR (Centro Servizi di Ateneo per la Ricerca) in Cagliari. ^1H NMR measurements were carried out at 25 °C either through a Bruker Avance 300 MHz or a Bruker Avance III HD 400 MHz spectrometer or Bruker Avance III HD 600 MHz spectrometer. $^{13}\text{C}\{^1\text{H}\}$, $^{11}\text{B}\{^1\text{H}\}$, $^{19}\text{F}\{^1\text{H}\}$, $^{29}\text{Si}\{^1\text{H}\}$ ^1H - ^1H COSY, ^{29}Si - ^1H HMBC NMR spectra were recorded on Bruker AVANCE III HD 400 MHz spectrometer in CDCl_3 or DMSO-d_6 as solvent. ^{13}C CPMAS solid-state NMR spectra were recorded on a Bruker Avance III HD 600 MHz (14.1 T) spectrometer at a frequency of 150.9 MHz, using a 2.5 mm probe-head with 15.5 kHz spinning frequency. The chemical shifts (δ) are reported in ppm and referenced against the solvent residue or by means of external standard such as: $\text{BF}_3 \cdot \text{Et}_2\text{O}$, CFCl_3 and $\text{Si}(\text{CH}_3)_4$ for ^{11}B , ^{19}F and ^{29}Si nuclei respectively.

UV-Vis measurements in solution were recorded in the range 190-1100 nm using quartz cuvettes with a path length of 1 cm by means of either a Thermo evolution 300 dual-beam spectrophotometer or an Agilent Cary 5000 UV-vis-NIR dual-beam spectrophotometer.

Diffuse reflectance measurements were carried out on an Agilent Cary 5000 UV–vis–NIR dual-beam spectrophotometer equipped with a diffuse reflectance accessory. Spectra were corrected for the change in the detector (PMT and InGaAs) at 800 nm.

Photoluminescence excitation and emission spectra in solution and in the solid-state were collected either on a Varian Cary Eclipse spectrofluorometer or a Perkin Elmer LS55 fluorescence spectrometer.

DSC measurements were performed using a TA instrument Discovery™ DSC in combination with liquid nitrogen cooling, a four-axis robotic device and TRIOS software. Samples of a few milligrams were sealed in a TZero® aluminium pan with a high-volume capacity (40 μ L), and the heat flow was measured compared to an empty reference pan as a function of temperature. DSC Tzero® calibration is done using sapphires disks and melting points of indium ($T_m = 429.5$ K and $\Delta H_{fus} = -28.13$ J/g) supplied by TA trios instruments. The sample was cooled and heated between -50°C and 150°C and runs were set at a rate of heating of $20^\circ\text{C}/\text{min}$.

X-ray diffraction analysis

Single-crystal X-ray diffraction analysis were carried out either at the National Crystallography Service (UK), Southampton, at the Imperial College London or University of St. Andrews, UK. SC-XRD data of **L3**, **(L2·H₂TER-Br) $_{\infty}$** , **(L7·H₂TER) $_{\infty}$** , **(L1) $_2$ ·R3**, **(L3·R3) $_{\infty}$** , **(H₂L3Br₄)BrBr₃·0.5 CHCl₃**, **L9**, **L10mono**, **L11**, **HL14Cl·2H₂O**, **H₄L17**, **[(Cd₂L17·3H₂O)·3H₂O] $_{\infty}$** , **(H₄L17·Py₂Et) $_{\infty}$** and **[(Co₂L₃₂L17·H₂O)·2DMF] $_{\infty}$** were collected on a Rigaku 007HF diffractometer, equipped with Varimax confocal mirrors, an AFC11 goniometer, a HyPix 6000 detector and an Oxford Cryosystems low temperature device, operating at 100K.

SC-XRD data of **[AgL3(OTf)((CH₃)₂CO)_{2.5}] $_{\infty}$** , **[CdL3(NO₃)₂(H₂O)₂·1.5H₂O] $_{\infty}$** , **[CuL3(NO₃)₂·CH₃CN]₂·2CH₃CN**, **(Co(L4)₂Cl₂) $_{\infty}$** , **(2·L5·CHCl₃) $_{\infty}$** , **(3·L5) $_{\infty}$** , **(L3·R2) $_{\infty}$** , **(HL3)₃·I₂**, **HPyTeI₂**, **HPyTeBr₂**, **HPyTeBr₄**, **[(HL14)I₂Cl]₃·0.5I₂**, **L16** and **[(Cd₂L17·6H₂O)·2H₂O] $_{\infty}$** were collected on a Rigaku FRE+ diffractometer, equipped with HF Varimax confocal mirrors, an AFC12 goniometer and a HyPix 6000 detector and an Oxford Cryosystems low temperature device, operating at 100K.

SC-XRD data of **(L11·I₂)·0.5I₂** were collected on a Bruker D8 Venture diffractometer equipped with a Photon II detector, operating at 273 K.

SC-XRD data of $[\text{AgL1}(\text{OTf})\cdot((\text{CH}_3)_2\text{CO})_{0.5}]_\infty$, $\text{HL1Cl}\cdot 3\text{H}_2\text{O}$, $(\text{L2}\cdot\text{H}_2\text{TER}\cdot(\text{OH})_2)_\infty$ and $(\text{L2}\cdot\text{1,4-DITFB})_\infty$ were collected on a Rigaku SCX mini diffractometer operating at 173 K.

SC-XRD data of $[\text{ZnL1}(\text{NO}_3)_2\cdot\text{CH}_3\text{CN}]_2$ and $(\text{HL12})\text{I}\cdot 2.5\text{I}_2$, were collected at 125 K on a Rigaku Saturn724+ diffractometer using graphite monochromated Mo-K α radiation.

SC-XRD data of $(\text{ZnL1Cl}_2)_\infty$, $(\text{L1}\cdot\text{H}_2\text{TER})_\infty$ and $(\text{L2}\cdot\text{H}_2\text{ISO})_\infty$ were collected at 173 K on a Rigaku XtaLAB P200 diffractometer using graphite monochromated Mo-K α radiation.

SC-XRD data of $(\text{L2}\cdot\text{H}_2\text{ISO}\cdot\text{F}_4)_\infty$ were collected on a Rigaku Pilatus 200K diffractometer operating at 173 K.

SC-XRD data of $(\text{L2}\cdot\text{H}_2\text{PyDC})_\infty$ and $(\text{L5}\cdot\text{R2})_\infty$ were collected on an Agilent Xcalibur PX Ultra A diffractometer operating at 173 K.

SC-XRD data of **L5**, **R2** and **R3** were collected on an Oxford Diffraction Xcalibur 3E (Mo K α radiation, 0.71075 Å) operating at 173 K.

SC-XRD data of $[(\text{Zn}_2\text{L3L17}\cdot 3\text{H}_2\text{O}\cdot\text{DMF})\cdot 3.5\text{DMF}]_\infty$ and $[(\text{Cu}_2\text{L17})\cdot 3\text{DMF}]_\infty$ were collected at Diamond Light Source (DLS) using synchrotron radiation equipped with a zirconium edge ($\lambda = 0.6889$ Å) and operating at 100 and 70 K, respectively.

SC-XRD data of $(\text{1}\cdot\text{L1})_\infty$, $(\text{1}\cdot\text{L2})_2$, **3** were collected at 120 K by means of combined phi and omega scans on a Bruker-Nonius Kappa CCD area detector, situated at the window of a FR591 rotating anode (graphite Mo-K α).

Datasets were processed using CrysAlis Pro^[456] or APEX3^[457]. The structures were solved with the ShelXT^[458] structure solution program using the Intrinsic Phasing solution method and by using Olex2^[459] as the graphical interface. The models were refined with version 2018/3 of ShelXL^[460] using Least Squares minimisation. All hydrogen atoms were added in calculated positions and refined in riding positions relative to the parent atom.

Powder X-ray Diffraction analysis were performed on a Rigaku Miniflex 600 equipped with CuK α radiation with a scan step of 0.02 ° and a scan speed of 0.03 °/min in the range from 5 to 30 ° in continuous mode. Experimental patterns were then compared with calculated patterns from single crystal X-ray diffraction analysis by means of CrystalDiffract version 6.8.2.

Theoretical calculations

Theoretical calculations were performed at the density functional theory (DFT)^[461] level with the Gaussian 16 (Rev. B.01)^[462] suite of programs on a IBM x3755 server with four 12-core processors and 64 Gb of RAM (OS: SUSE Linux Enterprise Server 11 SP3). The mPW1PW

functional^[463] was adopted, in combination with the full-electron split valence basis sets (BSs) including polarization functions (def2-SVP),^{[464],[465]} obtained from Basis Set Exchange and Basis Set EMSL Library.^[466]

Geometry optimizations were performed starting from structural data. Fine numerical integration grids (*Integral=ultrafine* keyword) were used, and the nature of the minima of each optimized structure was verified by harmonic frequency calculations (*freq=raman* keyword). PES scans were performed on **L3** by imposing the rotation of the pyridine rings (between 0 and 180 °, steps of 10 °) and optimizing the resulting geometry at each rotational step (*opt=modredundant* keyword). A natural population analysis was carried out at the optimized geometries using the natural bonding orbital (NBO) partitioning scheme.^[301] The programs GaussView 6.0.16,^[467] Molden 5.9,^[468] and Chemissian 4.53^[469] were used to investigate the optimized structures and the shapes of Kohn–Sham molecular orbitals.

5.2. Synthesis

5.2.1. Preparation of 3,5-di(pyridin-3-yl)-1,2,4-thiadiazole (L1)

Thionicotinamide (2.01 g; 1.46×10^{-2} mol) was dissolved in warm EtOH (25 mL) and added to a solution of iodine (7.27 g; 2.86×10^{-2} mol) in EtOH (55 mL). The mixture was then heated to reflux for overnight. After cooling in ice bath, the brown precipitate was filtered from the solution, suspended in H₂O, basified to pH = 12 with NaOH 1M, and a saturated solution of Na₂S₂O₃ in H₂O was added dropwise until complete discoloration of the solid was observed. The white solid was filtered off and recrystallized from acetone to give the pure product as an off-white solid. (0.98 g; 4.08 mmol; 56 %) M.p. = 130 °C dec. (TOF MS ES+) for (M+H)⁺ C₁₂H₉N₄S⁺ (m/z): calcd 241.0548; found 241.0551. Elemental analysis calcd (%) for C₁₂H₈N₄S: C 59.98, H 3.36, N 23.32, S 13.34. Found: C 60.18, H 3.29, N 23.16, S 13.25. FT-IR (KBr, 4000–400 cm⁻¹): 3062w, 3037w, 1589m, 1576m, 1497w, 1479s, 1456w, 1429w, 1408s, 1400s, 1338s, 1298m, 1259w, 1236w, 1188w, 1128m, 1092w, 1047w, 1024m, 989m, 901m, 823w, 812m, 727s, 698vs, 656w, 617mw, 494w cm⁻¹. ¹H NMR (400 MHz, CDCl₃) δ 9.61 (dd, *J* = 2.2, 0.9 Hz, 1H), 9.27 (dd, *J* = 2.3, 0.9 Hz, 1H), 8.80 (dd, *J* = 4.9, 1.7 Hz, 1H), 8.74 (dd, *J* = 4.9, 1.7 Hz, 1H), 8.65 (ddd, *J* = 8.0, 2.2, 1.7 Hz, 1H), 8.37 (ddd, *J* = 8.0, 2.3, 1.7 Hz, 1H), 7.51 (ddd, *J* = 8.0, 4.9, 0.9 Hz, 1H), 7.46 (ddd, *J* = 7.9, 4.9, 0.9 Hz, 1H) ppm. ¹³C{¹H} NMR (101 MHz, CDCl₃) δ 185.76, 171.80, 153.04, 151.42, 149.88, 148.70, 135.76, 134.73, 128.59, 126.83, 124.31, 123.81 ppm.

5.2.2. Preparation of 3,5-di(pyridin-4-yl)-1,2,4-thiadiazole (L2)

Thioisonicotinamide (1.98 g; 1.43×10^{-2} mol) was dissolved in warm EtOH (25 mL) and added to a solution of iodine (7.28 g; 2.87×10^{-2} mol) in EtOH (55 mL). The mixture was then heated to reflux for overnight. After cooling in ice bath, the brown precipitate was filtered from the solution, suspended in H₂O, basified to pH = 12 with NaOH 1M, and a saturated solution of Na₂S₂O₃ in H₂O was added dropwise until complete discoloration of the solid was observed. The white solid was filtered off and recrystallized from acetone to give the pure product as colorless needles. (1.15 g; 4.79 mmol; 67 %) M.p. = 177 °C. (TOF MS ES+) for (M+H)⁺ C₁₂H₉N₄S⁺ (m/z): calcd 241.0548; found 241.0554. Elemental analysis calcd (%) for C₁₂H₈N₄S: C 59.98, H 3.36, N 23.32, S 13.34. Found: C 60.31, H 3.10, N 23.01, S 13.42. FT-IR (KBr, 4000–400 cm⁻¹): 3032w, 1601m, 1556w, 1504w, 1466vs, 1408vs, 1385w, 1344s, 1327mw, 1292m, 1252mw, 1219mw, 1128mw, 1066mw, 1007mw, 989mw, 910w, 835m, 823vs, 744m, 733s, 712vs, 677m, 636s, 619w, 503m, 474mw cm⁻¹. ¹H NMR (400 MHz, CDCl₃) δ 8.87 – 8.84 (m, 2H), 8.83 – 8.80 (m, 2H), 8.26 – 8.19 (m, 2H), 7.91 – 7.88 (m, 2H) ppm. ¹³C{¹H} NMR (101 MHz, CDCl₃) δ 186.84, 172.38, 151.44, 150.92, 139.15, 136.94, 122.25, 121.12 ppm.

5.2.3. Preparation of 2,5-bis(pyridin-3-ylethynyl)thiophene (L3)

3-ethynylpyridine (0.518 g; 5.02 mmol), 2,5-diiodothiophene (0.841 g; 2.50 mmol), copper iodide (0.025 g; 0.13 mmol) and Pd(PPh₃)₂Cl₂ (0.089 g; 0.13 mmol) were placed in a three-necked 50 mL round bottom flask which was evacuated and backfilled with nitrogen three times. Freshly distilled and degassed diethylamine (25 mL) was added *via* canula and the mixture was heated to reflux and left for 48 h under nitrogen atmosphere. A NH₄Cl saturated solution (100 mL) was added to the mixture and extracted with ethyl acetate (3x 25 mL). The organic phase was dried over MgSO₄, filtered and concentrated to give the product as a red solid. The crude product was purified by silica gel column chromatography (CH₂Cl₂/EtOAc 2:1) to give the pure product as a pale-yellow solid. (501 mg; 1.75 mmol; 70 %) M. p. = 99 °C. (TOF MS ES+) for (M+H)⁺ C₁₈H₁₁N₂S⁺ (m/z): calcd 287.0643; found 287.0651. Elemental analysis calcd (%) for C₁₈H₁₀N₂S: C 75.50, H 3.52, N 9.78, S 11.20. Found: C 75.23, H 3.14, N 9.95, S 11.07. FT-IR (KBr, 4000–400 cm⁻¹): 3082w, 3049w, 2197w νC≡C, 1581mw, 1560m, 1520mw, 1473m, 1406s, 1188m, 1117m, 1095mw, 1020s, 810vs, 798vs, 704vs, 640mw, 538mw cm⁻¹. ¹H NMR (400 MHz, DMSO-d₆) δ 8.78 (dd, *J* = 2.2, 0.9 Hz, 2H, Py), 8.62 (dd, *J* = 4.9, 1.7 Hz, 2H, Py), 8.06 – 7.98 (m, 2H, Py), 7.51 – 7.47 (m, 4H, Py/thiophene) ppm. ¹³C{¹H} NMR (101 MHz, DMSO-d₆) δ 151.55, 149.51, 138.60, 133.85, 123.69, 123.47, 118.57, 91.30, 84.70 ppm.

5.2.4. Preparation of 2,5-bis(pyridin-4-ylethynyl)thiophene (L4)

4-ethynylpyridine hydrochloride (0.838 g; 6.0 mmol), 2,5-diiodothiophene (1.003 g; 3.0 mmol), copper iodide (57 mg; 0.3 mmol) and Pd(PPh₃)₂Cl₂ (0.210 g; 0.3 mmol) were placed in a three-necked 100 mL round bottom flask which was evacuated and backfilled with nitrogen three times. Freshly distilled and degassed diethylamine (50 mL) was added *via* canula and the mixture was heated to reflux and left for overnight under nitrogen atmosphere. An aqueous NH₄Cl saturated solution (100 mL) was added to the mixture and extracted with ethyl acetate (3x 30 mL). The organic phase was dried over MgSO₄, filtered and concentrated to give the product as a red solid. The crude product was purified by silica gel column chromatography (CH₂Cl₂/EtOAc 2:1) to give the pure product as a pale-yellow solid. (270 mg; 0.94 mmol; 31 %) M.p. = 141 °C dec. Elemental analysis calcd (%) for C₁₈H₁₀N₂S: C 75.50, H 3.52, N 9.78, S 11.20. Found: C 75.88, H 3.04, N 9.65, S 11.39. FT-IR (KBr, 4000- 400 cm⁻¹): 3039w, 3037w, 2962w, 2206m, 1591s, 1537m, 1483m, 1417m, 1261m, 1201mw, 1088m, 1030m, 987w, 810s, 798s, 721w, 694w, 613ms, 530m, 471mw cm⁻¹. ¹H NMR (600 MHz, DMSO-d₆) δ 8.65 (dd, *J* = 4.4, 1.6 Hz, 4H), 7.58 – 7.52 (m, 6H) ppm. ¹³C{¹H} NMR (151 MHz, DMSO-d₆) δ 150.01, 134.60, 129.19, 125.07, 123.54, 91.90, 85.74 ppm.

5.2.5. Preparation of 2,7-bis(pyridin-3-ylethynyl)-9H-fluorene (L5)

3-ethynylpyridine (517 mg; 5.01 mmol), 2,7-dibromofluorene (806 mg; 2.49 mmol), copper iodide (24 mg; 0.13 mmol) and Pd(PPh₃)₂Cl₂ (90 mg; 0.13 mmol) were placed in a three-necked 50 mL round bottom flask which was evacuated and backfilled with nitrogen three times. Dry toluene (20 mL) and freshly distilled and degassed diethylamine (10 mL) were added *via* canula and the mixture was heated to reflux and left for 48 h under nitrogen atmosphere. After cooling at room temperature, the precipitate was filtered off and the solution treated with NH₄Cl saturated solution (50 mL) and extracted with ethyl acetate (3x 25 mL). The organic phase was dried over MgSO₄, filtered and concentrated. The two isolated solids were combined and purified by silica gel column chromatography using a gradient DCM/EtOAc as eluent. (Light yellow solid; 238 mg; 6.46 × 10⁻⁴ mol; 26 %) M. p. = 107 °C. (TOF MS ES+) for (M+H)⁺ C₂₇H₁₇N₂⁺ (m/z): calcd 369.1362; found 369.1402. Elemental analysis calcd (%) for C₂₇H₁₆N₂: C 88.02, H 4.38, N 7.60. Found: C 87.79, H 4.12, N 7.31. FT-IR (KBr, 4000–400 cm⁻¹): 3049w, 2208m νC≡C, 1581mw, 1562m, 1481s, 1410s, 1329m, 1292mw, 1277mw, 1227w, 1192m, 1174m, 1124mw, 1099mw, 1022s, 1005m, 937mw, 862m, 827vs, 808s, 708vs, 627mw, 555mw, 490mw, 422w, 420w, 403mw cm⁻¹. ¹H NMR (400 MHz, DMSO-d₆) δ 8.79 (m, 2H, Py), 8.60 (dd, *J* = 4.9, 1.6 Hz, 2H, Py), 8.05 (d, *J* = 7.8 Hz, 2H, fluorene), 8.01 (dt, *J* = 8.0, 1.6

Hz, 2H, Py), 7.85 (m, 2H, fluorene), 7.66 (dd, $J = 7.8, 1.4$ Hz, 2H, fluorene), 7.49 (dd, $J = 8.0, 4.9$ Hz, 2H, Py), 4.03 (s, 2H, CH₂) ppm. ¹³C{¹H} NMR (101 MHz, DMSO-d₆) δ 151.59, 148.96, 143.96, 141.15, 138.48, 130.58, 128.29, 123.66, 120.98, 120.35, 119.50, 93.01, 86.56, 36.21 ppm.

5.2.6. Preparation of 2,7-bis(pyridin-4-ylethynyl)-9H-fluorene (L6)

4-ethynylpyridine hydrochloride (0.5953 g; 4.26 mmol), 2,7-diiodofluorene (0.8911 g; 2.13 mmol), copper iodide (0.0205 g; 0.11 mmol) and Pd(PPh₃)₂Cl₂ (0.0771 g; 0.11 mmol) were dried under vacuum and freshly distilled and degassed diethylamine (25 mL) was added under N₂ atmosphere. The mixture was heated to reflux and stirred under inert atmosphere for 48 h. A NH₄Cl saturated solution (100 mL) was added to the mixture and extracted with ethyl acetate (3 x 25 mL). The organic phase was dried over MgSO₄, filtered and concentrated to give the product as a brown solid. The crude product was purified by column chromatography using Al₂O₃ as stationary phase and a gradient of CH₂Cl₂/EtOAc. (Light yellow solid; 44.2 mg; 1.2×10^{-4} mol; 5.6 %) M. p. = 146 °C dec. Elemental analysis calcd (%) for C₂₇H₁₆N₂: C 88.02, H 4.38, N 7.60. Found: C 87.54, H 3.81, N 7.12. FT-IR (KBr, 4000–400 cm⁻¹): 3037w, 2920w, 2848w, 2210ms, 1585vs, 1535m, 1491m, 1404ms, 1294w, 1261w, 1213w, 1080w, 987mw, 939w, 868w, 823vs, 688mw, 542m cm⁻¹. ¹H NMR (500 MHz, CDCl₃) δ 8.62 (d, $J = 5.1$ Hz, 4H), 7.80 (d, $J = 7.9$ Hz, 2H), 7.76 (d, $J = 7.6$ Hz, 2H), 7.61 (d, $J = 7.8$ Hz, 2H), 7.42 (d, $J = 5.9$ Hz, 4H), 3.96 (s, 2H) ppm.

5.2.7. Preparation of 1,3-bis(pyridin-3-ylethynyl)benzene (L7)

3-ethynylpyridine (0.526 g; 5.1 mmol), 1,3-diiodobenzene (0.826 g; 2.5 mmol), copper iodide (0.024 g; 0.13 mmol) and Pd(PPh₃)₂Cl₂ (0.089 g; 0.13 mmol) were dried under vacuum and freshly distilled and degassed diethylamine (25 mL) was added under N₂ atmosphere. The mixture was heated to reflux and stirred under inert atmosphere for 48 h. A NH₄Cl saturated solution (100 mL) was added to the mixture and extracted with ethyl acetate (3x 25 mL). The organic phase was dried over MgSO₄, filtered and concentrated to give the product as a light brown solid. The crude product was purified by silica gel column chromatography (CH₂Cl₂/EtOAc 2:1) to give the pure product as off-white crystals. (0.5501 g; Y = 78 %) M. p. = 61 °C. Elemental analysis calcd (%) for C₂₀H₁₂N₂: C 85.69, H 4.31, N 9.99. Found: C 85.34, H 4.12, N 10.15. FT-IR (KBr, 4000–400 cm⁻¹): 3041w, 2208w, 1595w, 1576m, 1560m, 1481s, 1412vs, 1325w, 1284w, 1259w, 1236w, 1186mw, 1119mw, 1095mw, 1038w, 1022s, 957w, 916w, 910m, 887w, 810s, 796s, 746w, 704vs, 683s, 627m, 540w, 526w, 469w, 436mw cm⁻¹. ¹H NMR (600 MHz, DMSO-d₆) δ 8.78 (d, $J = 1.5$ Hz, 2H), 8.61 (dd, $J = 4.8, 1.6$ Hz, 2H), 7.99

(dt, $J = 7.9, 1.9$ Hz, 2H), 7.80 (t, $J = 1.5$ Hz, 1H), 7.65 (dd, $J = 7.7, 1.6$ Hz, 2H), 7.52 (t, $J = 7.8$ Hz, 1H), 7.47 (ddd, $J = 7.9, 4.9, 0.6$ Hz, 2H) ppm. $^{13}\text{C}\{^1\text{H}\}$ NMR (151 MHz, DMSO- d_6) δ 151.70, 149.23, 138.63, 134.18, 131.98, 129.49, 123.63, 122.43, 119.08, 91.10, 87.02 ppm.

5.2.8. Preparation of 1,3-bis(pyridin-4-ylethynyl)benzene (L8)

4-ethynylpyridine hydrochloride (278 mg; 2.0 mmol), 1,3-diiodobenzene (330 mg; 1.0 mmol), copper iodide (19.0 mg; 0.10 mmol) and Pd(PPh₃)₂Cl₂ (70 mg; 0.10 mmol) were dried under vacuum and freshly distilled and degased diethylamine (25 mL) was added under N₂ atmosphere. The mixture was heated to reflux and stirred under inert atmosphere for 24 h. After cooling the reaction mixture at room temperature an NH₄Cl saturated solution (100 mL) was added, then the solid filtered under reduced pressure. The crude product was purified by column chromatography using Al₂O₃ as stationary phase and DCM as eluent. (0.150 g; Y = 53 %). M. p. = 66 °C. Elemental analysis calcd (%) for C₂₀H₁₂N₂: C 85.69, H 4.31, N 9.99. Found: C 85.31, H 4.17, N 10.22. FT-IR (KBr, 4000–400 cm⁻¹): 3055w, 3024w, 2212mw, 1595vs, 1531m, 1491m, 1412ms, 1385w, 1221m, 987m, 937mw, 924mw, 887m, 820s, 806s, 737mw, 687ms, 550m, 546ms, 525ms, 499m, 467m cm⁻¹. ^1H NMR (600 MHz, DMSO- d_6) δ 8.65 (dd, $J = 4.5, 1.5$ Hz, 4H), 7.86 (t, $J = 1.5$ Hz, 1H), 7.70 (dd, $J = 7.8, 1.6$ Hz, 2H), 7.58 – 7.51 (m, 5H) ppm. $^{13}\text{C}\{^1\text{H}\}$ NMR (151 MHz, DMSO- d_6) δ 150.03, 134.65, 132.64, 129.81, 129.66, 125.41, 122.03, 92.17, 87.56 ppm.

5.2.9. Preparation of 2,7-bis(pyridin-3-ylethynyl)fluoren-9-one (L9)

3-ethynylpyridine (517 mg; 5.0 mmol), 2,7-dibromo-9-fluorenone (845 mg; 2.5 mmol), copper iodide (24 mg; 0.13 mmol) and Pd(PPh₃)₂Cl₂ (90 mg; 0.13 mmol) were dried under vacuum for 20 min and freshly distilled and degased diethylamine (25 mL) was added under N₂ atmosphere. The yellow mixture was heated to 55 °C and stirred under inert atmosphere for 24 h. The mixture slowly turned red in 30 min and the day after an intense yellow color was observed. A NH₄Cl saturated solution (100 mL) was added and the precipitate separated by suction filtration. The crude yellow product was recrystallized from DCM/EtOAc mixture to give the title compound as light orange crystals (230 mg; 0.60 mmol; Y = 24 %) M. p. = 249 °C. Elemental analysis calcd (%) for C₂₇H₁₄N₂O: C 84.80, H 3.69, N 7.33. Found: C 84.20, H 3.45, N 7.21. FT-IR (KBr, 4000–400 cm⁻¹): 3053w, 3035w, 3003w, 2206w $\nu\text{C}\equiv\text{C}$, 1959w, 1928w, 1896w, 1863w, 1807w, 1782w, 1716s, 1614ms, 1604ms, 1581mw, 1556m, 1479vs, 1464ms, 1427m, 1400ms, 1385w, 1315m, 1245m, 1209w, 1194m, 1186m, 1115m, 1020m, 1014m, 982mw, 949w, 922w, 902mw, 831m, 833ms, 802ms, 783s, 735w, 702s, 650m, 623m, 578w, 540m, 515mw, 473w, 428w, 405mw cm⁻¹. ^1H NMR (600 MHz, CDCl₃) δ 8.78 (d, $J = 1.4$ Hz, 2H),

8.58 (dd, $J = 4.9, 1.6$ Hz, 2H), 7.86 – 7.82 (m, 4H), 7.70 (dd, $J = 7.7, 1.4$ Hz, 2H), 7.57 (d, $J = 7.7$ Hz, 2H), 7.33 (dd, $J = 7.7, 4.9$ Hz, 2H) ppm. $^{13}\text{C}\{^1\text{H}\}$ NMR (151 MHz, CDCl_3) δ 192.02, 152.23, 148.87, 143.75, 138.87, 138.15, 134.66, 127.72, 124.03, 123.35, 120.95, 120.22, 91.94, 88.07 ppm.

5.2.10. Preparation of 2-(2,7-bis(pyridin-3-ylethynyl)fluoren-9-ylidene)malononitrile (L11)

Compound **L11** was synthesized according to a slightly modified synthetic procedure reported elsewhere.^[470] **L9** (38.2 mg; 0.10 mmol) and malononitrile (7.2 mg; 0.11 mmol) were reacted in DMSO (0.5 mL) at 110 °C for 5 h. The mixture was cooled at room temperature and the dark solid filtered on a Gooch funnel. The solid was then washed thoroughly with acetonitrile and dried under vacuum. Purple needle-shaped crystals suitable for XRD analysis were grown by slow evaporation of a chloroform solution of the product (28.1 mg; Y = 65 %) M. p. = 301 °C. Elemental analysis calcd (%) for $\text{C}_{30}\text{H}_{14}\text{N}_4$: C 83.71, H 3.28, N 13.02. Found: C 83.27, H 2.79, N 13.88. FT-IR (KBr, 4000–400 cm^{-1}): 3055w, 3028w, 2987w, 2225m $\nu(\text{C}\equiv\text{N})$, 2198w $\nu(\text{C}\equiv\text{C})$, 1963w, 1930w, 1894w, 1861w, 1604w, 1562s, 1481s, 1465ms, 1427m, 1408ms, 1385w, 1321w, 1261w, 1238w, 1222w, 1190mw, 1176mw, 1118m, 1095mw, 1024ms, 987w, 949w, 922w, 899ms, 872ms, 845ms, 802s, 756ms, 700s, 638w, 615w, 597m, 551w, 530w, 513w, 486w, 438w, 405mw cm^{-1} . ^1H NMR (600 MHz, CDCl_3) δ 8.80 (s, 2H, Py), 8.59 (s, 2H, Py), 8.55 (s, 2H, Py), 7.87 (d, $J = 6.6$ Hz, 2H, fl), 7.71 (d, $J = 6.9$ Hz, 2H, fl), 7.60 (d, $J = 7.1$ Hz, 2H, fl), 7.33 (s, 2H, Py) ppm. $^{13}\text{C}\{^1\text{H}\}$ NMR (151 MHz, CDCl_3) δ 159.92, 152.32, 149.06, 141.58, 138.99, 138.12, 134.74, 129.87, 124.32, 123.35, 121.25, 119.96, 112.96, 91.53, 88.65, 77.93 ppm.

5.2.11. Preparation of bis(2,7-dibromo-9H-fluoren-9-yl)methane (L15)

Compound **L15** was synthesized following a previously reported procedure.^[431] 2,7-dibromofluorene (972 mg; 3.0 mmol) was dissolved in dry DMF (15 mL) and the resulting solution cooled at 0 °C. Potassium *tert*-butoxide (34 mg; 0.3 mmol) was added in one portion under N_2 atmosphere and the mixture turned into dark red. After stirring vigorously for 15 min, paraformaldehyde (45 mg; 1.5 mmol) was added and the mixture stirred at room temperature for 2 hours. Water (30 mL) was then added to quench the reaction resulting in the formation of a white precipitate which was isolated by centrifugation, washed with 5% HCl solution, water and dried under vacuum at 40° C for overnight. (White powder 910 mg; 1.38 mmol; 92 %) M. p. = 275 °C. Elemental analysis calcd (%) for $\text{C}_{27}\text{H}_{16}\text{Br}_4$: C 49.13, H 2.44. Found: C 49.25, H 2.37. FT-IR (KBr, 4000–400 cm^{-1}): 2920w, 2850w, 1898w, 1728w, 1674w, 1568w, 1572mw,

1456s, 1414ms, 1398m, 1346w, 1271m, 1155m, 1061s, 1005m, 901mw, 870mw, 854mw, 820vs, 812vs, 725mw, 667m, 447m, 434m cm^{-1} . ^1H NMR (400 MHz, CDCl_3) δ 7.56 – 7.47 (m, 12H), 4.15 (t, $J = 6.7$ Hz, 2H, CH), 2.44 (t, $J = 6.7$ Hz, 2H, CH_2) ppm. $^{13}\text{C}\{^1\text{H}\}$ NMR (101 MHz, CDCl_3) δ 148.40, 139.10, 131.04, 130.53, 128.44, 121.50, 45.69, 44.66 ppm.

5.2.12. Preparation of bis(2,7-dibromo-9-methylfluoren-9-yl)methane (L16)

Compound **L16** was synthesized following a previously reported procedure.^[431] **L15** (1.98 g; 3.0 mmol) was dissolved in dry THF (20 mL) and the solution cooled to 0 °C before KO^tBu (1.00 g; 9.0 mmol) was added under nitrogen atmosphere resulting in the colour change of the reaction which turned into dark red. After stirring for 1 h at the same temperature, iodomethane (0.8 mL; 12.9 mmol) was added dropwise and the mixture slowly became violet and was stirred for overnight. The reaction was quenched by adding 5 % HCl (30 mL) and the mixture turned into yellow. The two layers were separated by extraction with DCM (3 x 30 mL), the organic phase dried over MgSO_4 and concentrated. The crude light brown solid was purified by silica gel column chromatography with DCM/Hexane (1:9) mixture as eluent and the title compound isolated as a white solid. (1.74 g; 2.5 mmol; 84 %) M. p. = 237 °C. Elemental analysis calcd (%) for $\text{C}_{29}\text{H}_{20}\text{Br}_4$: C 50.62, H 2.93. Found: C 50.43, H 2.54. FT-IR (KBr, 4000–400 cm^{-1}): 2956w, 2918w, 1595w, 1450s, 1396ms, 1259s, 1061s, 1003m, 872m, 802vs, 733ms, 665m, 440s cm^{-1} . ^1H NMR (400 MHz, CDCl_3) δ 7.18 (dd, $J = 8.1, 1.8$ Hz, 4H), 7.03 (d, $J = 1.8$ Hz, 4H), 6.92 (d, $J = 8.1$ Hz, 4H), 2.94 (s, 2H, CH_2), 1.29 (s, 6H, CH_3) ppm. $^{13}\text{C}\{^1\text{H}\}$ NMR (101 MHz, CDCl_3) δ 151.22, 137.69, 130.46, 127.12, 121.04, 120.44, 49.93, 48.90, 29.07 ppm.

5.2.13. Preparation of 9,9'-methylenebis(9-methylfluorene-2,7-dicarboxylic acid) (H4L17)

In a 100 mL round bottom two-necked flask 40 mL of dry THF were cooled at -78 °C and then 2.4 mL of n-BuLi (2.5 M in hexane) were added under N_2 atmosphere. After stirring for 15 min at the same temperature, a solution of **L16** (1.00 g; 1.45 mmol) in dry THF (20 mL) was added dropwise to the first solution and stirred for 1.5 h. CO_2 was then bubbled for 3 h into the reaction mixture which turns from pink to violet. The reaction mixture was then kept under N_2 atmosphere for overnight and the temperature slowly raised to room temperature. HCl 1 M (30 mL) was added to quench the reaction, resulting in the precipitation of the product, which was collected by filtration, washed with water, ethyl acetate and dried under vacuum. (560 mg; 1.02 mmol; 70 %) M. p. > 350 °C. Elemental analysis calcd (%) for $\text{C}_{33}\text{H}_{24}\text{O}_8$: C 72.26, H 4.41. Found: C 72.09, H 4.29. (TOF MS ES-) for $(\text{M}-\text{H})^- \text{C}_{33}\text{H}_{23}\text{O}_8^-$ (m/z): calcd 547.1393; found 547.1406. FT-IR (KBr, 4000–400 cm^{-1}): 3437w, 2964br, 2594br, 1689vs, 1608s, 1585s, 1491w,

1469m, 1450ms, 1413s, 1302vs, 1259vs, 1115m, 1007w, 918m, 905m, 835m, 762s, 663m, 580w, 515m, 509m, 428m cm^{-1} . ^1H NMR (400 MHz, DMSO- d_6) δ 12.60 (br, 4H, OH), 7.61 – 7.47 (m, 8H), 7.30 – 7.19 (m, 4H), 3.31 (s, CH_2), 1.33 (s, 6H, CH_3) ppm. $^{13}\text{C}\{^1\text{H}\}$ NMR (101 MHz, DMSO- d_6) δ 167.00, 150.52, 141.91, 129.44, 127.75, 124.67, 119.67, 49.26, 40.19, 28.61 ppm.

5.2.14. Preparation of $\text{C}_{36}\text{H}_{30}\text{B}_2\text{O}_4\text{Si}_2$ (R1).

Diphenylsilanediol (1.032 g; 4.77×10^{-3} mol), phenylboronic acid (0.585 g; 4.80×10^{-3} mol) were dissolved in dry toluene (50 mL) in a 100 mL round-bottom flask equipped with a Dean-Stark apparatus and the mixture heated to reflux for overnight under nitrogen atmosphere. The aqueous phase was discarded, and the solvent removed under reduced pressure to give a white solid which was purified by recrystallization from a 3:1 diethyl ether/petroleum ether mixture. Colourless crystals were collected by filtration and stored under nitrogen atmosphere (1.32 g; 2.18 mmol; 92 %). M.p. = 142-144 °C. Elemental analysis calcd (%) for $\text{C}_{36}\text{H}_{30}\text{B}_2\text{O}_4\text{Si}_2$: C 71.54, H 5.00. Found: C 71.33, H 4.89. ^1H -NMR (400 MHz, CDCl_3) δ 8.12 – 8.06 (m, 4H, *o*- $\text{C}_6\text{H}_5\text{B}$), 7.76 – 7.70 (m, 8H, *o*- $\text{C}_6\text{H}_5\text{Si}$), 7.57 – 7.51 (m, 2H, *p*- $\text{C}_6\text{H}_5\text{B}$), 7.49 – 7.38 (m, 8H, *m*- $\text{C}_6\text{H}_5\text{B}$; *p*- $\text{C}_6\text{H}_5\text{Si}$), 7.36 – 7.29 (m, 8H, *m*- $\text{C}_6\text{H}_5\text{Si}$) ppm. $^{13}\text{C}\{^1\text{H}\}$ NMR (101 MHz, CDCl_3) δ 135.80, 134.28, 133.56, 131.89, 130.75, 128.21, 128.08 ppm. $^{11}\text{B}\{^1\text{H}\}$ NMR (128 MHz, CDCl_3) δ 25.92 ppm. $^{29}\text{Si}\{^1\text{H}\}$ NMR (80 MHz, CDCl_3) δ - 45.01 ppm.

5.2.15. Preparation of $\text{C}_{36}\text{H}_{28}\text{B}_2\text{F}_2\text{O}_4\text{Si}_2$ (R2).

Diphenylsilanediol (1.007 g; 4.66×10^{-3} mol), 4-fluorophenylboronic acid (0.650 g; 4.65×10^{-3} mol) were dissolved in dry toluene (50 mL) in a 100 mL round-bottom flask equipped with a Dean-Stark apparatus and the mixture heated to reflux for overnight under nitrogen atmosphere. The aqueous phase was discarded, and the solvent removed under reduced pressure to give a white powder which was purified by recrystallization from a 2:1 diethyl ether/dichloromethane mixture. White crystals were collected by filtration and stored under nitrogen atmosphere (1.44 g; 2.25 mmol; 97 %). M.p. = 194-198 °C. Elemental analysis calcd (%) for $\text{C}_{36}\text{H}_{28}\text{B}_2\text{F}_2\text{O}_4\text{Si}_2$: C 67.52, H 4.41. Found: C 67.64, H 4.56. FT-IR (KBr, 4000–400 cm^{-1}): 3070mw, 3043mw, 3022w, 3010w, 1961w, 1915w, 1892w, 1826w, 1788w, 1705w, 1666w, 1601s, 1591s, 1487m, 1485m, 1416s, 1402s, 1360vs, 1354vs, 1306vs, 1240ms, 1219s, 1149 vs, 1119 vs, 1093ms, 1014ms, 995m, 835s, 806ms, 742ms, 721ms, 719s, 698vs, 656w, 640m, 627mw, 611w, 540m, 519ms, 496s, 434m, 407w cm^{-1} . ^1H NMR (400 MHz, CDCl_3) δ 8.07 – 8.00 (m, 4H, *o*- $\text{FC}_6\text{H}_4\text{B}$), 7.71 – 7.66 (m, 8H, *o*- $\text{C}_6\text{H}_5\text{Si}$), 7.45 – 7.38 (m, 4H, *p*- $\text{C}_6\text{H}_5\text{Si}$), 7.36 – 7.29 (m, 8H, *m*- $\text{C}_6\text{H}_5\text{Si}$), 7.15 – 7.08 (m, 4H, *m*- $\text{FC}_6\text{H}_4\text{B}$) ppm. $^{13}\text{C}\{^1\text{H}\}$ NMR (101 MHz, CDCl_3) δ 165.67 (d, $^1J_{\text{C-F}}$ =

251 Hz), 138.07, 137.99, 134.20, 133.29, 130.88, 128.28, 115.21 (d, $^3J_{\text{H-F}} = 20$ Hz) ppm. $^{11}\text{B}\{^1\text{H}\}$ NMR (128 MHz, CDCl_3) δ 25.55 ppm. $^{19}\text{F}\{^1\text{H}\}$ NMR (377 MHz, CDCl_3) δ -107.93 ppm. $^{29}\text{Si}\{^1\text{H}\}$ NMR (80 MHz, CDCl_3) δ -44.62 ppm.

5.2.16. Preparation of $\text{C}_{36}\text{H}_{26}\text{B}_2\text{F}_4\text{O}_4\text{Si}_2$ (R3)

Diphenylsilanediol (1.371 g; 6.33×10^{-3} mol), 3,5-difluorophenylboronic acid (1.002 g; 6.33×10^{-3} mol) were dissolved in dry toluene (50 mL) in a 100 mL round-bottom flask equipped with a Dean-Stark apparatus and the mixture heated to reflux for overnight under nitrogen atmosphere. The aqueous phase was discarded, and the solvent removed under reduced pressure to give a white powder which was purified by recrystallization from a 2:1 diethyl ether/dichloromethane mixture. White crystals were collected by filtration and stored under nitrogen atmosphere (1.55 g; 2.29 mmol; 72 %). M.p. = 149 °C. Elemental analysis calcd (%) for $\text{C}_{36}\text{H}_{26}\text{B}_2\text{F}_4\text{O}_4\text{Si}_2$: C 63.93, H 3.87. Found: C 64.01, H 3.94. FT-IR (KBr, 4000–400 cm^{-1}): 3072w, 3053w, 3028w, 3005w, 2962w, 1618, 1585ms, 1427vs, 1385s, 1321vs, 1257vs, 1186w, 1119vs, 1018m, 982s, 874m, 852m, 823m, 802m, 739m, 721s, 696vs, 596w, 580ms, 517s, 488ms, 405m cm^{-1} . ^1H NMR (400 MHz, CDCl_3) δ 7.69 – 7.64 (m, 8H, *o*- $\text{C}_6\text{H}_5\text{Si}$), 7.52 – 7.42 (m, 8H, *p*- $\text{C}_6\text{H}_5\text{Si}$, *o*- $\text{F}_2\text{C}_6\text{H}_3\text{B}$), 7.40 – 7.33 (m, 8H, *m*- $\text{C}_6\text{H}_5\text{Si}$), 6.95 (tt, $^3J_{\text{H-F}} = 8.9$ Hz, $^4J_{\text{H-H}} = 2.4$ Hz, 2H, *p*- $\text{F}_2\text{C}_6\text{H}_3\text{B}$) ppm. $^{13}\text{C}\{^1\text{H}\}$ NMR (101 MHz, CDCl_3) δ 163.11 (dd, $^1J_{\text{C-F}} J = 249.8$, $^3J_{\text{C-F}} 11.0$ Hz), 134.48, 134.13, 132.49, 131.20, 128.45, 118.02 – 117.21 (m), 107.29 (t, $^2J_{\text{C-F}} = 25.0$ Hz) ppm. $^{11}\text{B}\{^1\text{H}\}$ NMR (128 MHz, CDCl_3) δ 25.49 ppm. $^{19}\text{F}\{^1\text{H}\}$ NMR (377 MHz, CDCl_3) δ -110.40 ppm. $^{29}\text{Si}\text{-}^1\text{H}$ HMBC NMR (80 MHz, CDCl_3) δ -43.99 ppm.

5.2.17. Preparation of 1

A mixture of $\text{Cd}(\text{NO}_3)_2 \cdot 4\text{H}_2\text{O}$ (1.542 g, 5.0 mmol) and P_2S_5 (1.114 g, 5.0 mmol) in methanol (50 mL) was refluxed for 1 h, and the solvent was then removed under-reduced pressure to give a yellow solid, that was washed with hexane. The crude product was re-crystallized from methanol and isolated as a pale-yellow solid. (1.777 g, 4.2 mmol, Y = 83%) M.p. = 143–145 °C. Elemental analysis calcd (%) for $\text{C}_4\text{H}_{12}\text{O}_4\text{P}_2\text{S}_4\text{Cd}$: C 11.21; H 2.58; S 30.72; found C 11.26; H 2.83; S 30.05. FT-IR (KBr, 4000–400 cm^{-1}): 3504mw, 2998w, 2947mw, 2837w, 1775w, 1594w, 1561mw, 1499w, 1435m, 1385w, 1307w, 1257mw, 1173s, 1016s, 800s, 765s, 659s, 541s cm^{-1} .

5.2.18. Preparation of 2

Lawesson's reagent (404 mg; 1.0 mmol) and $\text{Cd}(\text{NO}_3)_2 \cdot 4\text{H}_2\text{O}$ (30.8 mg; 1.0 mmol) were dissolved in methanol (20 mL) and the reaction mixture heated to reflux for 2 h. The precipitate was filtered and purified by recrystallization from dichloromethane/methanol 4:1 mixture to

give the pure product as colourless crystals (439 mg; 0.38 mmol, Y = 85 % based on C₃₂H₄₀Cd₂O₈P₄S₈) M.p. = 151 °C. Elemental analysis calcd (%) for C₃₂H₄₀Cd₂O₈P₄S₈: C = 33.20, H = 3.48, S = 22.15. Found: C = 33.18, H = 3.57, S = 22.06. FT-IR (KBr, 4000–400 cm⁻¹): 2964w, 2931w, 2834w, 1600s, 1566m, 1500ms, 1456m, 1439m, 1406m, 1385m, 1307ms, 1296ms, 1265s, 1178s, 1112s, 1003vs, 999vs, 827m, 800m, 775s, 717w, 673w, 656s, 640s, 623m, 542s, 470w, 403w cm⁻¹. ¹H NMR (600 MHz, DMSO-d₆) δ 7.94 – 7.82 (m, 8H), 7.01 (dd, ⁴J_{P-H} = 2.8 Hz, ³J_{H-H} = 8.8 Hz, 8H) 3.80 (s, 12H, Ar-OMe), 3.69 (d, ²J_{P-H} = 15.2 Hz, 12H, P-OMe) ppm. ¹³C{¹H} NMR (151 MHz, DMSO-d₆) δ 161.18, 161.16, 131.63, 131.54, 113.28, 113.18, 55.34, 51.04, 51.00 ppm.

5.2.19. Preparation of 3

Lawesson's Reagent (404 mg; 1.0 mmol) and Cd(NO₃)₂·4H₂O (30,8 mg; 1.0 mmol) were placed in a 50 mL round-bottom flask and ethanol (20 mL) added in one portion. The mixture was heated to reflux for 2 hours and the progressive precipitation of a white solid was observed. The mixture was cooled to room temperature and the precipitate filtered on a Gooch funnel. The white powder was then washed with hot ethanol and dried under vacuum. Colourless crystals suitable for X-ray diffraction analysis were grown by slow evaporation from a chloroform solution of the product. (272 mg; 0.22 mmol; 45 %) M. p. = 150 °C. Elemental analysis calcd (%) for C₃₆H₄₈Cd₂O₈P₄S₈: C 35.62, H 3.99, S 21.13. Found: C 35.21, H 3.54, S 20.97. FT-IR (KBr, 4000–400 cm⁻¹): 2972w, 2933w, 2893w, 2837w, 1593s, 1568m, 1500s, 1456mw, 1437mw, 1408w, 1388mw, 1300m, 1296m, 1257s, 1182ms, 1155w, 1115s, 1024s, 949ms, 829m, 802m, 775m, 715w, 654m, 650ms, 623ms, 538s, 443w cm⁻¹. ¹H NMR (600 MHz, DMSO-d₆) δ 7.88 (dd, ³J_{P-H} = 13.8 Hz, ³J_{H-H} = 8.8 Hz, 8H), 7.00 (³J_{H-H} = 8.8 Hz, ⁴J_{P-H} = 2.6 Hz, 8H), 4.13 (dq, ³J_{P-H} = 9.6 Hz, ³J_{H-H} = 7.1 Hz, 8H), 3.80 (s, 12H, Ar-OMe), 1.24 (t, ³J_{H-H} = 7.1 Hz, 12H) ppm. ¹³C{¹H} NMR (151 MHz, DMSO-d₆) δ 161.12, 131.57, 131.48, 113.25, 113.15, 60.33, 55.33, 16.11, 16.05 ppm.

5.2.20. Preparation of [AgL1(OTf)·((CH₃)₂CO)_{0.5}]_∞

[AgL1(OTf)·((CH₃)₂CO)_{0.5}]_∞ was prepared adapting a general method for the preparation of silver(I) supramolecular assemblies reported in the literature.^[383] **L1** (48.0 mg; 0.2 mmol) was dissolved in acetone (3 mL). A solution of AgOTf (54.1 mg; 0.2 mmol) in acetone (3 mL) was added dropwise and the mixture stirred for 30' under light exclusion. The white solid was isolated by filtration, dried and stored in a dark glass vial. (82.3 mg; 7.8·10⁻⁵ mol; 78 % based on: C₂₉H₂₂Ag₂F₆N₈O₇S₄) Suitable crystals for X-ray diffraction analysis were grown by slow evaporation of an acetone solution of the product in the dark. M. p. = 258 °C dec. Elemental

analysis calcd (%) for $C_{29}H_{22}Ag_2F_6N_8O_7S_4$: C 33.09, H 2.11, N 10.65, S 12.18. Found: C 32.74, H 1.81, N 10.36, S 12.32. FT-IR (KBr, 4000–400 cm^{-1}): 3039w, 1591m, 1576w, 1497w, 1479ms, 1456w, 1402ms, 1340ms, 1298vs, 1261vs, 1232s, 1171s, 1128m, 1045vs, 1028m, 989mw, 903w, 814m, 764w, 727ms, 698s, 640s, 579w, 517w, 417w cm^{-1} .

5.2.21. Preparation of $[ZnL1(NO_3)_2 \cdot CH_3CN]_2$

A 25 mL Ace pressure tube was charged with **L1** (12.0 mg; $5.0 \cdot 10^{-5}$ mol) and $Zn(NO_3)_2 \cdot 6H_2O$ (14.9 mg; $5.0 \cdot 10^{-5}$ mmol). 15 mL of acetonitrile were added, and the reaction heated to 120 °C for 1 h. The mixture was then left to slowly cool at room temperature. After 48 h colourless crystals were formed, separated by filtration and air dried (11.4 mg; $2.4 \cdot 10^{-5}$ mol; 48 %). M. p. = 257 °C. Elemental analysis calcd (%) for $C_{14}H_{11}N_7O_6SZn$: C 35.72, H 2.36, N 20.83, S 6.81. Found: C 35.48, H 1.91, N 20.62, S 7.04. FT-IR (KBr, 4000–400 cm^{-1}): 3116 br, 2426vw, 1655m, 1608ms, 1377vs, 1199m, 1140m, 1101w, 1055m, 1036ms, 1003ms, 949w, 913w, 821ms, 731ms, 698s, 648m cm^{-1} .

5.2.22. Preparation of $(ZnL1Cl_2)_\infty$

A 25 mL Ace pressure tube was charged with **L1** (12.0 mg; $5.0 \cdot 10^{-5}$ mol) and $ZnCl_2$ (6.8 mg; $5.0 \cdot 10^{-5}$ mmol). 15 mL of a mixture acetonitrile/chloroform (2:1) were added, and the reaction heated to 120 °C for 1 h. The mixture was then left to slowly cool at room temperature. After 48 h colourless crystals were formed, separated by filtration and air dried (15.8 mg; $4.2 \cdot 10^{-5}$ mol; 84 %). M. p. = 240 °C dec. Elemental analysis calcd (%) for $C_{12}H_8Cl_2N_4SZn$: C 38.28, H 2.14, N 14.88, S 8.51. Found: C 38.05, H 1.97, N 15.16, S 8.34. FT-IR (KBr, 4000–400 cm^{-1}): 3070mw, 2171w, 1606s, 1500s, 1464m, 1458vs, 1433s, 1406s, 1336ms, 1296s, 1240mw, 1194m, 1138m, 1122ms, 1097m, 1055s, 1034m, 1003s, 914m, 829s, 731s, 696vs, 650m, 509w, 467w, 409w cm^{-1} .

5.2.23. Preparation of $(1 \cdot L1)_2$

L1 (12.0 mg; $5.0 \cdot 10^{-5}$ mol) and **1** (21.3 mg; $5.0 \cdot 10^{-5}$ mol) were suspended in a 1:1 mixture of methanol/chloroform (30mL) and reacted at 130 °C. After complete dissolution of solids, the mixture was slowly cooled to room temperature and colourless crystals were isolated by filtration. The product was then washed with fresh methanol and dried under vacuum (11.1 mg; $1.7 \cdot 10^{-5}$ mol; Y = 33%). M. p. = 170 °C. Elemental analysis calcd (%) for $C_{16}H_{20}CdN_4O_4P_2S_5$: C 28.81, H 3.02, N 8.4, S 24.03 found: C 29.29, H 2.83, N 8.32, S 24.72. FT-IR (KBr, 4000–400 cm^{-1}): 2940 w, 2836 w, 2361 w, 1638 mw, 1599 m, 1584 mw, 1502 w, 1468 mw, 1425 mw, 1406 m, 1338 mw, 1304 w, 1238 w, 1193 m, 1173 m, 1136 m, 1125 m, 1012 s, 814 m, 779 ms, 730 m, 696 m, 664 s, 637 ms, 588 w, 517 m, 503 m cm^{-1} .

5.2.24. Preparation of $(\mathbf{1}\cdot\mathbf{L2})_{\infty}$

L2 (12.0 mg; $5.0 \cdot 10^{-5}$ mol) and **1** (21.3 mg; $5.0 \cdot 10^{-5}$ mol) were suspended in a 1:1 mixture of methanol/chloroform (30 mL) and reacted at 120°C. After complete dissolution of solids, the mixture was slowly cooled to room temperature and colourless crystals were isolated by filtration. The product was then washed with fresh methanol and dried under vacuum (17.7 mg; $2.6 \cdot 10^{-5}$ mol; Y = 53%). M.p. = 174–177 °C. Elemental analysis calcd. (%) for $\text{C}_{16}\text{H}_{20}\text{CdN}_4\text{O}_4\text{P}_2\text{S}_5$: C 28.81, H 3.02, N 8.40, S 24.03. Found: C 27.28, H 2.65, N 7.75, S 23.86. FT-IR (KBr, 4000–400 cm^{-1}): 2940w, 2836w, 2361w, 1609m, 1560mw, 1508w, 1468ms, 1415ms, 1338m, 1293w, 1248w, 1228m, 1213m, 1176m, 1132m, 1065m, 1047s, 1016s, 912s, 850m, 840m, 744m, 733m, 709mw, 671 w, 660w, 644w, 553m, 524mw, 442m cm^{-1} .

5.2.25. Preparation of $[\text{AgL3}(\text{OTf})((\text{CH}_3)_2\text{CO})_{2.5}]_{\infty}$

L3 (13.7 mg; $4.8 \cdot 10^{-5}$ mol) was dissolved in acetone (2 mL) and added dropwise to a second solution of silver(I) triflate (12.4 mg; $4.8 \cdot 10^{-5}$ mol) in 2 mL of the same solvent. The mixture was stirred for 1 h at room temperature under light exclusion. The white solid was separated by centrifugation, air dried and stored in a dark glass vial (16.7 mg; $1.36 \cdot 10^{-5}$ mol; 56 % based on $2(\text{C}_{18}\text{H}_{10}\text{AgN}_2\text{S})(\text{SO}_3\text{CF}_3) \cdot 2.5 \text{C}_3\text{H}_6\text{O}$). Suitable crystals for X-ray diffraction analysis were grown by layering a dichloromethane solution of **L3** in the bottom of a test tube. An interlayer of methanol was carefully prepared on the surface. Then, an acetone solution containing an equimolar amount of silver(I) triflate was layered on the top and the test tube stored in the dark for one week. Colorless prisms were formed on the walls of the test tube, isolated and structurally characterized. M. p. = 179 °C dec. Elemental analysis calcd. (%) for $\text{C}_{45.5}\text{H}_{35}\text{Ag}_2\text{N}_4\text{S}_4\text{O}_{8.5}\text{F}_6$: C 44.37, H 2.86, N 4.55, S 10.41. Found: C 43.81, H 2.47, N 4.71, S 10.08. FT-IR (KBr, 4000–400 cm^{-1}): 3074w, 2210m $\nu\text{C}\equiv\text{C}$, 1716w, 1574w, 1570mw, 1483w, 1475m, 1417m, 1279vs, 1250vs, 1176s, 1163vs, 1126m, 1049s, 1024vs, 804s, 758w, 698s, 656ms, 638vs, 573w, 517m, 469w cm^{-1} .

5.2.26. Preparation of $[\text{CdL3}(\text{NO}_3)_2(\text{H}_2\text{O})_2 \cdot 1.5\text{H}_2\text{O}]_{\infty}$

L5 (11.4 mg; $4.0 \cdot 10^{-5}$ mol) was dissolved in 2 mL of acetonitrile. An aqueous solution of $\text{Cd}(\text{NO}_3)_2 \cdot 4\text{H}_2\text{O}$ (12.3 mg; $4.0 \cdot 10^{-5}$ mol) was prepared by dissolving the metal salt in 0.5 mL of H_2O . The metal solution was added dropwise to the solution of the ligand while stirring. The resulting yellowish solution was filtered, and the solvent allowed to slowly evaporate. The crystalline product was isolated after 24 h, washed with hexane and air dried (5.4 mg; $9.7 \cdot 10^{-6}$ mol; 24 % based on $\text{C}_{18}\text{H}_{13}\text{CdN}_4\text{O}_8\text{S}$). M. p. = 160 °C dec. Elemental analysis calcd. (%) for $\text{C}_{18}\text{H}_{13}\text{CdN}_4\text{O}_8\text{S}$: C 38.76, H 2.35, N 10.04, S 5.75. Found: C 38.21, H 1.78, N 9.38, S 5.47.

FT-IR (KBr, 4000–400 cm^{-1}): 3236br, 3097w, 3066w, 2424w, 2393w, 2210m $\nu\text{C}\equiv\text{C}$, 1763w, 1618m, 1572mw, 1448ms, 1387vs, 1311s, 1196m, 1122m, 1051m, 1028m, 825s, 820m, 694s, 652w, 542w, 469w cm^{-1} .

5.2.27. Preparation of $[\text{CuL3}(\text{NO}_3)_2\cdot\text{CH}_3\text{CN}]_2\cdot 2\text{CH}_3\text{CN}$

L5 (11.4 mg; $4.0 \cdot 10^{-5}$ mol) was dissolved in 2 mL of acetonitrile. An aqueous solution of $\text{Cu}(\text{NO}_3)_2\cdot 2.5\text{H}_2\text{O}$ (9.3 mg; $4.0 \cdot 10^{-5}$ mol) was prepared by dissolving the metal salt in 0.5 mL of H_2O . The metal salt solution was added dropwise to the solution of the ligand while stirring. The resulting greenish solution was filtered, and the solvent allowed to slowly evaporate. The green crystalline product was isolated after 24 h, washed with hexane and air dried (10.3 mg; $1.7 \cdot 10^{-5}$ mol; 43 % based on $\text{C}_{24}\text{H}_{19}\text{CuN}_7\text{O}_6\text{S}$). M. p. = 187 °C dec. Elemental analysis calcd. (%) for $\text{C}_{24}\text{H}_{19}\text{CuN}_7\text{O}_6\text{S}$: C 48.28, H 3.21, N 16.42, S 5.37. Found: C 47.94, H 2.96, N 16.57, S 5.31. FT-IR (KBr, 4000–400 cm^{-1}): 3392br, 3068w, 2426vw, 2210m $\nu\text{C}\equiv\text{C}$, 1637mw, 1599mw, 1574mw, 1477m, 1385vs, 1319m, 1198w, 1194mw, 1126w, 1103w, 1059w, 1024w, 810m, 692m, 660w cm^{-1} .

5.2.28. Preparation of $[\text{Co}(\text{L4})_2\text{Cl}_2]_\infty$

A methanolic solution of **L4** (4 mL, $5.0 \cdot 10^{-3}$ M) was layered onto an aqueous CoCl_2 (4 mL, $2.5 \cdot 10^{-3}$ M) solution. Orange crystals formed on the walls of the test tube after 48 h, isolated and structurally characterized.

5.2.29. Preparation of $(2\cdot\text{L5}\cdot\text{CHCl}_3)_\infty$

2 (58.0 mg; 0.05 mmol) was dissolved in methanol (5 mL) and a solution of **L5** (36.9 mg; 0.1 mmol) in chloroform (5 mL) was added dropwise while stirring. The mixture was stirred at room temperature for few minutes and the solvent allowed to slow evaporate for overnight. Light-yellow crystals suitable for X-ray diffraction analysis were isolated and air dried. (80.4 mg; 0.075 mmol, Y = 75 % based on $\text{C}_{43}\text{H}_{36}\text{CdN}_2\text{O}_4\text{P}_2\text{S}_4 \cdot \text{CHCl}_3$) M.p. = 156 °C. Elemental analysis calcd (%) for $\text{C}_{43}\text{H}_{36}\text{CdN}_2\text{O}_4\text{P}_2\text{S}_4 \cdot \text{CHCl}_3$: C = 49.56, H = 3.50, N = 2.63, S = 12.02. Found: C = 49.21, H = 3.37, N = 2.48, S = 11.83. FT-IR (KBr, 4000–400 cm^{-1}): 2939w, 2207w $\nu\text{C}\equiv\text{C}$, 1593ms, 1570mw, 1499ms, 1483m, 1410m, 1291m, 1254s, 1178m, 1114s, 1015s, 833ms, 800m, 772m, 754s, 698m, 666ms, 641ms, 623m, 542m cm^{-1} .

5.2.30. Preparation of $(3\cdot\text{L5})_\infty$

3 (18.2 mg; $1.5 \cdot 10^{-5}$ mol) and **L5** (11.0 mg; $3.0 \cdot 10^{-5}$ mol) were suspended in a mixture chloroform/ethanol 2:1 (10 mL) and stirred at room temperature for few minutes. The resulting light-yellow solution was filtered on a 0.45 μm PTFE septum and the solvent allowed to slow

evaporate. Light-yellow crystals suitable for X-ray diffraction analysis were collected and air dried. (17.3 mg; $1.8 \cdot 10^{-5}$ mol, Y = 59 % based on $C_{45}H_{40}CdN_2O_4P_2S_4$) M.p. = 161 °C. Elemental analysis calcd (%) for $C_{45}H_{40}CdN_2O_4P_2S_4$: C = 49.56, H = 3.50, N = 2.63, S = 12.02. Found: C = 49.21, H = 3.37, N = 2.48, S = 11.83. FT-IR (KBr, 4000–400 cm^{-1}): 3057w, 2926w, 2835w, 2210ms $\nu C\equiv C$, 1595s, 1568m, 1498s, 1470m, 1464m, 1404mw, 1385mw, 1294ms, 1254vs, 1178ms, 1113vs, 1028ms, 910mw, 822ms, 800ms, 731w, 694w, 636mw, 623m, 577m, 542ms, 472mw, 405w cm^{-1} .

5.2.31. General method for the preparation of co-crystals with L1, L2 and benzenedicarboxylic acids.

L1/L2 (0.1 mmol) and benzenedicarboxylic acid (0.1 mmol) were dissolved/suspended in EtOH (10-20 mL) at 50 °C and the mixture stirred for 24-48 h at the same temperature. Water (10 mL) was then added resulting in the instantaneous precipitation of a white powder. The white solid was isolated by filtration and recrystallized from hot ethanol. In the following paragraphs are directly reported the amount of co-crystals obtained, the yield and their characterization.

5.2.32. Preparation of L1·H₂TER

38.1 mg, $9.4 \cdot 10^{-5}$ mol; 94 %. M. p. = 284 °C. Elemental analysis calcd (%) for $C_{20}H_{14}N_4O_4S$: C 59.11, H 3.47, N 13.79, S 7.89. Found: C 58.98, H 3.12, N 13.58, S 8.12. FT-IR (KBr, 4000–400 cm^{-1}): 2792w, 2457br, 1871br, 1701vs, 1599m, 1502mw, 1473mw, 1406ms, 1406ms, 1327m, 1273vs, 1194m, 1126m, 1113m, 1101m, 1086m, 1041m, 1012m, 906m, 879w, 816m, 769m, 729ms, 696m, 640m, 482m cm^{-1} .

5.2.33. Preparation of (L1·H₂TER-Br)_∞

21.6 mg, $4.5 \cdot 10^{-5}$ mol; 44 %. M. p. = 224 °C. Elemental analysis calcd (%) for $C_{20}H_{13}BrN_4O_4S$: C 49.50, H 2.70, N 11.54, S 6.61. Found: C 49.17, H 2.54, N 11.22, S 6.32. FT-IR (KBr, 4000–400 cm^{-1}): 3066w, 2430br, 1894br, 1701vs, 1601m, 1552mw, 1470m, 1402s, 1298vs, 1248vs, 1190s, 1120s, 995s, 997vs, 908mw, 816mw, 771ms, 729m, 696ms, 642m, 498w, 461w cm^{-1} .

5.2.34. Preparation of (L1·H₂TER-(OH)₂)_∞

23.2 mg, $5.3 \cdot 10^{-5}$ mol; 53 %. M. p. = 265 °C. Elemental analysis calcd (%) for $C_{20}H_{14}N_4O_6S$: C 54.79, H 3.22, N 12.78, S 7.31. Found: C 54.38, H 3.06, N 12.54, S 6.88. FT-IR (KBr, 4000–400 cm^{-1}): 3068w, 2407br, 1905br, 1666m, 1605m, 1504ms, 1471m, 1396ms, 1336s, 1300w, 1221vs, 1192vs, 1140s, 1049vs, 997s, 856m, 822m, 766vs, 731ms, 698ms, 648mw, 604w, 523m, 461ms, 438m cm^{-1} .

5.2.35. Preparation of (L1·H₂TER-F₄)_∞

35.8 mg, $7.5 \cdot 10^{-5}$ mol; 75 %. M. p. = 218 °C. Elemental analysis calcd (%) for $C_{20}H_{10}F_4N_4O_6S$: C 50.22, H 2.11, N 11.71, S 6.70. Found: C 50.34, H 2.52, N 11.47, S 6.49. FT-IR (KBr, 4000–400 cm^{-1}): 3072w, 2484br, 1718m, 1630m, 1473s, 1385m, 1340m, 1188w, 1120w, 991s, 814w, 729m, 698m, 617w, 467w cm^{-1} .

5.2.36. Preparation of $L1 \cdot H_2ISO$

35.2 mg, $8.7 \cdot 10^{-5}$ mol; 86 %. M. p. = 243 °C. Elemental analysis calcd (%) for $C_{20}H_{14}N_4O_4S$: C 59.11, H 3.47, N 13.79, S 7.89. Found: C 59.13, H 3.54, N 14.01, S 8.03. FT-IR (KBr, 4000–400 cm^{-1}): 2773w, 2436br, 1873br, 1695vs, 1601s, 1498mw, 1473m, 1417s, 1329s, 1286vs, 1257vs, 1194m, 1147m, 1132m, 1115m, 1090m, 1068mw, 1045ms, 995w, 939w, 906s, 818ms, 773w, 737s, 729s, 698ms, 648m, 434m, 548w, 488m cm^{-1} .

5.2.37. Preparation of $(L1 \cdot H_2ISO \cdot F_4)_\infty$

41.2 mg, $8.6 \cdot 10^{-5}$ mol; 87 %. M. p. = 169 °C. Elemental analysis calcd (%) for $C_{20}H_{10}F_4N_4O_6S$: C 50.22, H 2.11, N 11.71, S 6.70. Found: C 49.88, H 1.65, N 11.32, S 6.18. FT-IR (KBr, 4000–400 cm^{-1}): 3078w, 2409br, 1722vs, 1633ms, 1603m, 1491vs, 1412m, 1392m, 1340m, 1292ms, 1192m, 1101s, 1049ms, 958s, 818m, 731ms, 694ms, 640w, 455mw cm^{-1} .

5.2.38. Preparation of $(L1 \cdot H_2PyDC)_\infty$

18.6 mg, $4.6 \cdot 10^{-5}$ mol; 46 %. M. p. = 192 °C. Elemental analysis calcd (%) for $C_{19}H_{13}N_5O_4S$: C 56.02, H 3.22, N 17.19, S 7.87. Found: C 55.85, H 2.97, N 16.84, S 7.43. FT-IR (KBr, 4000–400 cm^{-1}): 3061w, 2771br, 2470br, 1865br, 1724s, 1599m, 1581m, 1473mw, 1470m, 1421ms, 1404m, 1329ms, 1290ms, 1248ms, 1163m, 1117m, 1045m, 993mw, 906m, 816m, 729m, 692s, 636m, 499w, 453w cm^{-1} .

5.2.39. Preparation of $(L2 \cdot H_2TER)_\infty$

32.5 mg, $8.0 \cdot 10^{-5}$ mol; 80 %. M. p. = 278 °C dec. Elemental analysis calcd (%) for $C_{20}H_{14}N_4O_4S$: C 59.11, H 3.47, N 13.79, S 7.89. Found: C 59.24, H 3.68, N 14.06, S 7.52. FT-IR (KBr, 4000–400 cm^{-1}): 3053w, 2924w, 2789w, 2411br, 1890br, 1701s, 1610m, 1417m, 1410s, 1277vs, 1207m, 1126mw, 1053w, 1057m, 1011m, 999m, 847mw, 827m, 746mw, 733s, 712mw, 688mw, 644mw, 486mw cm^{-1} .

5.2.40. Preparation of $(L2 \cdot H_2TER \cdot Br)_\infty$

23.4 mg, $4.8 \cdot 10^{-5}$ mol; 48 %. M. p. = 230 °C. Elemental analysis calcd (%) for $C_{20}H_{13}BrN_4O_4S$: C 49.50, H 2.70, N 11.54, S 6.61. Found: C 49.69, H 3.02, N 11.31, S 6.09. FT-IR (KBr, 4000–400 cm^{-1}): 3076w, 2773br, 2403br, 1882br, 1709vs, 1610vs, 1552m, 1466ms, 1412s, 1309m, 1290vs, 1252vs, 1124m, 1039ms, 1020s, 825m, 756s, 710ms, 646s, 498m cm^{-1} .

5.2.41. Preparation of $(L2 \cdot H_2TER \cdot (OH)_2)_\infty$

27.9 mg, $6.4 \cdot 10^{-5}$ mol; 64 %. M. p. = 271 °C. Elemental analysis calcd (%) for $C_{20}H_{14}N_4O_6S$: C 54.79, H 3.22, N 12.78, S 7.31. Found: C 54.91, H 2.98, N 12.44, S 7.17. FT-IR (KBr, 4000–400 cm^{-1}): 3080w, 2407br, 1672m, 1614ms, 1483ms, 1468s, 1414s, 1338vs, 1244ms, 1223vs, 1198s, 1041m, 1030ms, 918mw, 854s, 827ms, 808ms, 746vs, 706m, 648m, 606w, 523mw, 459m cm^{-1} .

5.2.42. Preparation of $(L2 \cdot H_2TER \cdot F4)_\infty$

33.7 mg, $7.0 \cdot 10^{-5}$ mol; 70 %. M. p. = 227 °C. Elemental analysis calcd (%) for $C_{20}H_{10}F_4N_4O_6S$: C 50.22, H 2.11, N 11.71, S 6.70. Found: C 50.05, H 1.84, N 11.61, S 6.98. FT-IR (KBr, 4000–400 cm^{-1}): 3082w, 2386br, 1713ms, 1610m, 1470vs, 1414m, 1336ms, 1225m, 1140m, 1028ms, 997s, 839mw, 837m, 752w, 717m, 650mw, 580w, 525w, 465m cm^{-1} .

5.2.43. Preparation of $(L2 \cdot H_2ISO)_\infty$

36.1 mg, $8.9 \cdot 10^{-5}$ mol; 89 %. M. p. = 258 °C. Elemental analysis calcd (%) for $C_{20}H_{14}N_4O_4S$: C 59.11, H 3.47, N 13.79, S 7.89. Found: C 59.18, H 3.59, N 13.68, S 7.95. FT-IR (KBr, 4000–400 cm^{-1}): 3053w, 2804w, 2424br, 1913br, 1693vs, 1610s, 1464m, 1410s, 1319vs, 1290vs, 1244ms, 1144ms, 1012s, 1014s, 825m, 733s, 644ms, 550w cm^{-1} .

5.2.44. Preparation of $(L2 \cdot H_2ISO \cdot F4)_\infty$

39.5 mg, $8.3 \cdot 10^{-5}$ mol; 83 %. M. p. = 184 °C. Elemental analysis calcd (%) for $C_{20}H_{10}F_4N_4O_6S$: C 50.22, H 2.11, N 11.71, S 6.70. Found: C 49.74, H 2.38, N 11.46, S 7.05. FT-IR (KBr, 4000–400 cm^{-1}): 3103w, 2420br, 1927br, 1707s, 1612ms, 1485vs, 1416ms, 1300m, 1290ms, 1223m, 1095s, 1034m, 953s, 843m, 748m, 710m, 646m, 451m cm^{-1} .

5.2.45. Preparation of $(L2 \cdot H_2PyDC)_\infty$

24.3 mg, $6.0 \cdot 10^{-5}$ mol; 60 %. M. p. = 219 °C. Elemental analysis calcd (%) for $C_{19}H_{13}N_5O_4S$: C 56.02, H 3.22, N 17.19, S 7.87. Found: C 56.37, H 2.81, N 17.04, S 7.64. FT-IR (KBr, 4000–400 cm^{-1}): 3057w, 2438br, 1930br, 1695vs, 1610s, 1466s, 1416vs, 1340vs, 1290s, 1242ms, 1157s, 1080ms, 993s, 841m, 822ms, 748m, 698m, 644s, 571w, 507w cm^{-1} .

5.2.46. Preparation of $(L1)_2 \cdot R3$

Ligand **L1** (4.8 mg; 20 μ mol) and compound **R3** (13.5 mg; 20 μ mol) were dissolved in 3 mL of a dry dichloromethane/diethyl ether (1:2) mixture and the resulting solution sonicated for 10 min. The solvents were left to slowly evaporate for overnight. Colourless crystals suitable for X-ray diffraction were collected and structurally characterized.

5.2.47. Preparation of (L3·R2)_∞

Ligand **L3** (11.4 mg; 40 μmol) and compound **R2** (25.6 mg; 40 μmol) were dissolved in 3 mL of a dry dichloromethane/diethyl ether (1:2) mixture upon sonication for 10 min. The yellowish clear solution was left to crystallize overnight at room temperature. Colorless crystals suitable for X-ray diffraction were collected by suction filtration and washed with diethyl ether (yield: 32.0 mg; 3.45 mmol; 86 %). M. p. = 160 °C. Elemental analysis calculated (%) for C₅₄H₃₈B₂F₂N₂O₄SSi₂: C, 69.98; H, 4.13; N, 3.02; S, 3.46. Found: C, 70.01; H, 4.17; N, 2.95; S, 3.38. FT-IR (KBr, 4000–400 cm⁻¹): 3089w, 3051w, 3047w, 3024w, 2220mw, 1587m, 1497m, 1477m, 1429m, 1414m, 1387w, 1329w, 1309w, 1273w, 1188-1178vs (ν_{asSi-O} + ν_{symB-O}), 1120-1111vs (ν_{symSi-O} + ν_{asB-O}), 1097s, 1063s, 1016m, 937w, 899w, 877w, 866w, 835m, 816m, 802m, 750ms, 735s, 706s, 677s, 648m, 634w, 563m, 561ms, 534mw, 496ms, 498ms, 428mw cm⁻¹. ¹³C CP/MAS NMR (151 MHz) δ 164.21, 162.76, 147.74, 145.69, 140.12, 139.38, 134.25, 131.12, 129.22, 127.08, 125.45, 121.74, 114.41, 89.75, 86.85 ppm.

5.2.48. Preparation of (L3·R3)_∞

Ligand **L3** (11.5 mg; 40 μmol) and compound **R3** (27.1 mg; 40 μmol) were dissolved in 3 mL of a dry dichloromethane/diethyl ether (1:2) mixture upon sonication for 10 min. The yellowish clear solution was left to crystallize for overnight at room temperature. Colorless crystals suitable for X-ray diffraction were collected by suction filtration and washed with diethyl ether (yield: 33.5 mg; 3.48 mmol; 87 %) M. p. = 175 °C. Elemental analysis calculated (%) for C₅₄H₃₆B₂F₄N₂O₄SSi₂: C, 67.37; H, 3.77; N, 2.91; S, 3.33. Found: C, 67.41; H, 3.80; N, 2.81; S, 3.28. FT-IR (KBr, 4000–400 cm⁻¹): 3120w, 3089w, 3066w, 3047w, 2212mw, 1612m, 1579ms, 1522w, 1477m, 1416s, 1414s, 1340m, 1325m, 1284vs, 1188s, 1144-1105vs (ν_{asSi-O} + ν_{symB-O}), 1065s, 976s, 962m, 912w, 839mw, 829m, 806m, 719vs, 706s, 652m, 598m, 553ms, 521m, 498s, 417m cm⁻¹. ¹³C CP/MAS NMR (151 MHz) δ 164.48, 162.96, 157.12, 145.86, 140.18, 139.45, 138.03, 134.44, 133.35, 129.50, 128.00, 126.87, 125.18, 121.61, 115.50, 102.05, 90.46, 86.82 ppm.

5.2.49. Preparation of (L5·R2)_∞

Ligand **L5** (14.7 mg; 40 μmol) and compound **R2** (25.6 mg; 40 μmol) were dissolved in 3 mL of a dry chloroform/diethyl ether (1:1) mixture and the resulting solution sonication for 10 min. The solvents were left to slowly evaporate for overnight. Pale yellow crystals suitable for X-ray diffraction were collected and structurally characterized.

5.2.50. Preparation of (L2·1,4-DITFB)_∞

L2 (12.0 mg; $5.0 \cdot 10^{-5}$ mol) and 1,4-DITFB (20.0 mg; $5.0 \cdot 10^{-5}$ mol) were dissolved in chloroform (5 mL) and the mixture stirred at room temperature for 20 min. The mixture was filtered and the solvent left to slowly evaporate. Suitable crystals for X-ray diffraction analysis were isolated and structurally characterized. (10.8 mg; $1.7 \cdot 10^{-5}$ mol; 34 %) Elemental analysis calcd (%) for C₁₈H₈F₄I₂N₄S: C 33.67, H 1.26, N 8.73. Found: C 31.88, H 0.66, N 8.21. FT-IR (KBr, 4000–400 cm⁻¹): 1599m, 1458vs, 1410s, 1335m, 1290m, 1207m, 1124m, 1063m, 995m, 939s, 825ms, 748m, 733ms, 712ms, 677m, 636ms, 505m, 474w, 422w cm⁻¹.

5.2.51. Preparation of (HL3)I₃·I₂

A solution of I₂ in acetonitrile (20 μL, 0.25 M) was slowly added to a solution of **L3** in the same solvent (4 mL, $1.25 \cdot 10^{-3}$ M) and the mixture stirred at room temperature for few minutes. Brown crystals were grown in one week upon slow evaporation of the solvent and structurally characterized by means of SC-XRD analysis.

5.2.52. Preparation of (H₂L3Br₄)BrBr₃·0.5 CHCl₃

A solution of Br₂ in chloroform (100 μL, 0.25 M) was slowly added to a solution of **L3** in the same solvent (4 mL, $1.25 \cdot 10^{-3}$ M). The red solution was stored at 4 °C for one week. Dark red crystals were separated from the reaction mixture and structurally characterized.

5.2.53. Preparation of (L11·I₂)·0.5 I₂

A solution of **L11** in chloroform (4 mL, $1.25 \cdot 10^{-3}$ M) in a 8 mL glass vial was carefully placed in a diffusion chamber containing a solution of I₂ (8 mL, $1.25 \cdot 10^{-3}$ M) in *n*-hexane. Red block-shaped crystals were isolated from the walls of the vial in 48 h and structurally characterized.

5.2.54. Preparation of (HL12)I · 2.5 I₂.

600 μL of a molecular diiodine solution (0.25 M in CH₃CN) were added dropwise to a solution of **L12** (15.7 mg; $5.0 \cdot 10^{-5}$ mol in 4 mL of CH₃CN) while stirring. The resulting solution was stirred at room temperature for 20 min, filtered through a 0.45 μm PTFE filter and the solvent left to slowly evaporate. Brown crystals were isolated, gently washed with petroleum ether and air dried. (20.4 mg; $1.9 \cdot 10^{-5}$ mol; 38 %) M. p. = 78 °C; Elemental analysis calcd (%) for (C₁₀H₉N₂Se₂)I₃ · 1.5 I₂: C 11.16, H 0.84, N 2.60. Found: C 11.58, H 0.32, N 2.37. FT-Raman (600–50 cm⁻¹, 50 mW, 100 scans): 230(0.2), 178(1.8), 165(10.0), 153(8.0), 111(1.5) cm⁻¹ (relative intensities, strongest = 10). FT-IR (KBr, 4000–400 cm⁻¹): 3122w, 3070w, 3030w, 1637w, 1610ms, 1583s, 1544mw, 1473m, 1450ms, 1439s, 1425s, 1406ms, 1385m, 1315mw, 1277mw, 1246mw, 1155mw, 1107w, 1064w, 1047mw, 1010s, 964w, 762vs, 696mw, 636ms, 470ms cm⁻¹.

5.2.55. Preparation of *HPyTeI₂*.

200 μL of a molecular diiodine solution (0.25 M in *n*-hexane) were added dropwise to a solution of **L13** (10.3 mg; $2.5 \cdot 10^{-5}$ mol in 4 mL of CHCl_3) while stirring. The resulting solution was stirred at room temperature for 30 min, filtered through a 0.45 μm PTFE filter and poured inside a screw cap glass vial. The clear solution was stored at 4°C for three days. Brown crystals were isolated from the walls of the vials, gently washed with petroleum ether and air dried. (12.7 mg; $2.8 \cdot 10^{-5}$ mol; 55 %) M. p. = 180-182 °C; Elemental analysis calcd (%) for $\text{C}_5\text{H}_5\text{NTeI}_2$: C 13.04, H 1.09, N 3.04. Found: C 12.89, H 0.97, N 2.83. FT-IR (KBr, 4000–400 cm^{-1}): 3182mw, 3120mw, 3064ms, 3035mw, 2997w, 2924w, 2875w, 1597ms, 1577vs, 1514s, 1431ms, 1385w, 1367m, 1282w, 1253m, 1230mw, 1153mw, 1093mw, 1068w, 1034m, 1005mw, 974w, 899mw, 827mw, 746s, 702w, 617mw, 453m cm^{-1} .

5.2.56. Preparation of *HPyTeBr₂*.

L13 (10.3 mg; $2.5 \cdot 10^{-5}$ mol) was dissolved in 4 mL of CH_2Cl_2 . The vial was then transferred in a diffusion chamber containing a bromine solution in hexane ($1.25 \cdot 10^{-2}$ M, 4 mL) and kept at room temperature for 48 h. The product was obtained as red block crystals suitable for X-ray diffraction analysis. The crystals were carefully transferred on a Petri dish, washed with petroleum ether and air dried. (7.6 mg; $2.1 \cdot 10^{-5}$ mol; 41 %) M. p. = 172 °C; Elemental analysis calcd (%) for $\text{C}_5\text{H}_5\text{NTeBr}_2$: C 16.39, H 1.38, N 3.82. Found: C 16.33, H 1.24, N 3.69. FT-Raman (600–50 cm^{-1} , 50 mW, 100 scans): 249(1.9), 168(10.0), 157(6.8), 114(2.3), 101(2.4), 89(2.5) cm^{-1} (relative intensities, strongest = 10). FT-IR (KBr, 4000–400 cm^{-1}): 2991br, 2777s, 2435mw, 1627mw, 1599m, 1579s, 1504m, 1468ms, 1435ms, 1361w, 1298w, 1244br, 1157w, 1020m, 983w, 885w, 856w, 748m, 723m, 459mw cm^{-1} .

5.2.57. Preparation of *HPyTeBr₄*.

L13 (10.3 mg; $2.5 \cdot 10^{-5}$ mol) was dissolved in 4 mL of CH_2Cl_2 . The vial was then transferred in a diffusion chamber containing a bromine solution in hexane ($3.0 \cdot 10^{-2}$ M, 4 mL) and kept at room temperature for 48 h. The product was obtained as red block crystals suitable for X-ray diffraction analysis. The crystals were carefully transferred on a Petri dish, washed with petroleum ether and air dried. (18.5 mg; $3.5 \cdot 10^{-5}$ mol; 71 %) M. p. = 203 °C dec.; Elemental analysis calcd (%) for $\text{C}_5\text{H}_5\text{NTeBr}_4$: C 11.41, H 0.96, N 2.66. Found: C 11.37, H 0.78, N 2.54. FT-Raman (600–50 cm^{-1} , 50 mW, 100 scans): 251(1.5), 168(10.0), 157(5.1), 116(1.7), 99(1.8), 86(2.0) cm^{-1} (relative intensities, strongest = 10). FT-IR (KBr, 4000–400 cm^{-1}): 3076br, 2777ms, 2424mw, 1628mw, 1599ms, 1577s, 1516s, 1466m, 1435s, 1361m, 1298m, 1232mw, 1465mw, 1080m, 1010m, 1009m, 966w, 885w, 823mw, 725s, 459ms cm^{-1} .

5.2.58. Preparation of $[(HL14)I_2Cl]_3 \cdot 0.5I_2$

A solution of ICl (22 μ L, 0.25 M) in acetonitrile was carefully added to a solution of **L14** (2 mL, $2.75 \cdot 10^{-3}$ M) in the same solvent. Red crystals suitable for X-ray diffraction analysis were isolated upon slow evaporation of some of the solvent.

5.2.59. Preparation of $[(Cd_2L17 \cdot 3H_2O) \cdot 3H_2O]_\infty$ and $[(Cd_2L17 \cdot 6H_2O) \cdot 2H_2O]_\infty$.

A 8 mL glass vial was loaded with 6 mL of a mixture DMA/H₂O (2:1 v/v), a solution of **H4L17** (200 μ L, 0.25 M) in DMA and an aqueous solution of Cd(NO₃)₂·4H₂O (400 μ L, 0.25 M). The mixture was sonicated for few minutes and then heated to 120 °C for 24 h. The mixture was then cooled at room temperature with a cooling rate of 10 °C/h. Two different morphologies of crystals were present at the same time and revealed to be compounds $[(Cd_2L17 \cdot 3H_2O) \cdot 3H_2O]_\infty$ and $[(Cd_2L17 \cdot 6H_2O) \cdot 2H_2O]_\infty$.

5.2.60. Preparation of $(H_4L17 \cdot Py_2Et)_\infty$

An ethanolic solution of **Py₂Et** (400 μ L, $2.50 \cdot 10^{-2}$ M) was carefully layered onto a solution of **H4L17** (4 mL, $1.25 \cdot 10^{-3}$ M) in a mixture of DMF/H₂O (1:1 v/v). Single crystals were isolated in one week and structurally characterized.

5.2.61. Preparation of $[(Co_2L3_2L17 \cdot H_2O) \cdot 2DMF]_\infty$

A 8 mL glass vial was loaded with 6 mL of a mixture DMF/H₂O (1:1 v/v), a solution of **H4L17** (100 μ L, 0.25 M) in DMF, a solution of **L3** (200 μ L, 0.25 M) in DMF and an aqueous solution of CoCl₂·6H₂O (500 μ L, 0.10 M). The mixture was heated to 80 °C for 18 h, then cooled at room temperature with a cooling rate of 10 °C/h. Orange crystals were isolated and structurally characterized.

5.2.62. Preparation of $[(Zn_2L3L17 \cdot 3H_2O \cdot DMF) \cdot 3.5DMF]_\infty$

A 8 mL glass vial was loaded with 6 mL of a mixture DMF/H₂O (1:1 v/v), a solution of **H4L17** (100 μ L, 0.25 M) in DMF, a solution of **L3** (100 μ L, 0.25 M) in DMF and an aqueous solution of Zn(NO₃)₂·6H₂O (250 μ L, 0.10 M). The mixture was heated to 80 °C for 48 h, then cooled at room temperature with a cooling rate of 10 °C/h. Tiny yellow crystals were isolated and structurally characterized.

References

- [1] *IUPAC Compendium of Chemical Terminology*, IUPAC, **2009**.
- [2] J. W. Steed, J. L. Attwood, *Supramolecular Chemistry, 2nd Edition*, Wiley, **2009**.
- [3] P. Chakma, D. Konkolewicz, *Angew. Chemie - Int. Ed.* **2019**, *58*, 9682–9695.
- [4] R. G. Jones, C. K. Ober, P. Hodge, P. Kratochvíl, G. Moad, M. Vert, *Pure Appl. Chem.* **2013**, *85*, 463–492.
- [5] E. Arunan, G. R. Desiraju, R. A. Klein, J. Sadlej, S. Scheiner, I. Alkorta, D. C. Clary, R. H. Crabtree, J. J. Dannenber, P. Hobza, et al., *Pure Appl. Chem.* **2011**, *83*, 1637–1641.
- [6] J. P. M. Antonio, G. D. V. Farias, F. M. F. Santos, R. Oliveira, P. M. S. D. Cal, P. M. P. Gois, in *Non-Covalent Interact. Synth. Des. New Compd.*, John Wiley & Sons, Inc, Hoboken, NJ, **2016**, pp. 23–48.
- [7] G. R. Desiraju, P. Shing Ho, L. Kloo, A. C. Legon, R. Marquardt, P. Metrangolo, P. Politzer, G. Resnati, K. Rissanen, *Pure Appl. Chem.* **2013**, *85*, 1711–1713.
- [8] P. Muller, *Pure Appl. Chem.* **1994**, *66*, 1077–1184.
- [9] W. B. Jennings, B. M. Farrell, J. F. Malone, *Acc. Chem. Res.* **2001**, *34*, 885–894.
- [10] E. C. Lee, D. Kim, P. Jurečka, P. Tarakeshwar, P. Hobza, K. S. Kim, *J. Phys. Chem. A* **2007**, *111*, 3446–3457.
- [11] C. David Sherrill, T. Takatani, E. G. Hohenstein, *J. Phys. Chem. A* **2009**, *113*, 10146–10159.
- [12] S. E. Wheeler, K. N. Houk, *Mol. Phys.* **2009**, *107*, 749–760.
- [13] E. G. Cox, J. A. S. Smith, *Nature* **1954**, *173*, 75.
- [14] J. A. S. S. E. G. Cox, F. R. S., D. W. J. Cruickshank, *Proc. R. Soc. London. Ser. A. Math. Phys. Sci.* **1958**, *247*, 1–21.
- [15] *Proc. R. Soc. London. Ser. A. Math. Phys. Sci.* **1964**, *279*, 98–110.
- [16] G. J. Piermarini, A. D. Mighell, C. E. Weir, S. Block, *Science (80-.)*. **1969**, *165*, 1250–1255.
- [17] C. E. Weir, G. J. Piermasini, S. Block, *J. Chem. Phys.* **1969**, *50*, 2089–2093.
- [18] R. Fourme, D. André, M. Renaud, *Acta Crystallogr. Sect. B Struct. Crystallogr. Cryst. Chem.* **1971**, *27*, 1275–1276.
- [19] M. M. Thiéry, J. M. Léger, *J. Chem. Phys.* **1988**, *89*, 4255–4271.
- [20] F. R. . G. A. Jeffrey, J. R. Ruble, R. K. McMullan, J. A. Pople *, *Proc. R. Soc. London. A. Math. Phys. Sci.* **1987**, *414*, 47–57.
- [21] A. Budzianowski, A. Katrusiak, *Acta Crystallogr. Sect. B Struct. Sci.* **2006**, *62*, 94–101.

- [22] D. E. Fagnani, A. Sotuyo, R. K. Castellano, in *Compr. Supramol. Chem. II*, Elsevier, **2017**, pp. 121–148.
- [23] C. A. Hunter, J. K. M. Sanders, *J. Am. Chem. Soc.* **1990**, *112*, 5525–5534.
- [24] J. H. Williams, *Acc. Chem. Res.* **1993**, *26*, 593–598.
- [25] C. Hansch, A. Leo, R. W. Taft, *Chem. Rev.* **1991**, *91*, 165–195.
- [26] J. I. Seo, I. Kim, Y. S. Lee, *Chem. Phys. Lett.* **2009**, *474*, 101–106.
- [27] S. E. Wheeler, *J. Am. Chem. Soc.* **2011**, *133*, 10262–10274.
- [28] A. L. Ringer, M. O. Sinnokrot, R. P. Lively, C. D. Sherrill, *Chem. - A Eur. J.* **2006**, *12*, 3821–3828.
- [29] R. Podeszwa, R. Bukowski, K. Szalewicz, *J. Phys. Chem. A* **2006**, *110*, 10345–10354.
- [30] K. Szalewicz, *Wiley Interdiscip. Rev. Comput. Mol. Sci.* **2012**, *2*, 254–272.
- [31] K. Patkowski, *Wiley Interdiscip. Rev. Comput. Mol. Sci.* **2019**, DOI 10.1002/wcms.1452.
- [32] R. Podeszwa, K. Szalewicz, *Phys. Chem. Chem. Phys.* **2008**, *10*, 2735–2746.
- [33] C. R. Martinez, B. L. Iverson, *Chem. Sci.* **2012**, *3*, 2191–2201.
- [34] C. D. Sherrill, *Acc. Chem. Res.* **2013**, *46*, 1020–1028.
- [35] E. G. Hohenstein, C. D. Sherrill, *J. Phys. Chem. A* **2009**, *113*, 878–886.
- [36] W. Wang, P. Hobza, *ChemPhysChem* **2008**, *9*, 1003–1009.
- [37] J. Pawliszyn, M. M. Szcześniak, S. Scheiner, *J. Phys. Chem.* **1984**, *88*, 1726–1730.
- [38] A. Ebrahimi, M. Habibi, R. Sadat Neyband, A. Reza Gholipour, *Phys. Chem. Chem. Phys.* **2009**, *11*, 11424–11431.
- [39] D. B. Ninković, G. V. Janjić, S. D. Zarić, *Cryst. Growth Des.* **2012**, *12*, 1060–1063.
- [40] K. Vanommeslaeghe, P. Mignon, S. Loverix, D. Tourwé, P. Geerlings, *J. Chem. Theory Comput.* **2006**, *2*, 1444–1452.
- [41] P. C. Kearney, L. S. Mizoue, R. A. Kumpf, J. E. Forman, A. McCurdy, D. A. Dougherty, *J. Am. Chem. Soc.* **1993**, *115*, 9907–9919.
- [42] L. Yang, J. B. Brazier, T. A. Hubbard, D. M. Rogers, S. L. Cockroft, *Angew. Chemie - Int. Ed.* **2016**, *55*, 912–916.
- [43] L. Yang, C. Adam, G. S. Nichol, S. L. Cockroft, *Nat. Chem.* **2013**, *5*, 1006–1010.
- [44] D. L. Severance, W. L. Jorgensen, *J. Am. Chem. Soc.* **1990**, *112*, 4768–4774.
- [45] H. J. Schneider, *Acc. Chem. Res.* **2015**, *48*, 1815–1822.
- [46] R. Thakuria, N. K. Nath, B. K. Saha, *Cryst. Growth Des.* **2019**, *19*, 523–528.
- [47] S. K. Burley, G. A. Petsko, *Adv. Protein Chem.* **1988**, *39*, 125–189.
- [48] G. B. McGaughey, M. Gagné, A. K. Rappé, *J. Biol. Chem.* **1998**, *273*, 15458–15463.
- [49] R. Scott Lokey, B. L. Iverson, *Nature* **1995**, *375*, 303–305.

- [50] W. R. Zhuang, Y. Wang, P. F. Cui, L. Xing, J. Lee, D. Kim, H. L. Jiang, Y. K. Oh, *J. Control. Release* **2019**, *294*, 311–326.
- [51] S. Xu, T. Liu, Y. Mu, Y.-F. Wang, Z. Chi, C.-C. Lo, S. Liu, Y. Zhang, A. Lien, J. Xu, *Angew. Chemie* **2015**, *127*, 888–892.
- [52] D. Yan, A. Delori, G. O. Lloyd, T. Frišćić, G. M. Day, W. Jones, J. Lu, M. Wei, D. G. Evans, X. Duan, *Angew. Chemie - Int. Ed.* **2011**, *50*, 12483–12486.
- [53] Y. Hong, J. W. Y. Lam, B. Z. Tang, *Chem. Commun.* **2009**, 4332–4353.
- [54] Y. Hong, J. W. Y. Lam, B. Z. Tang, *Chem. Soc. Rev.* **2011**, *40*, 5361–5388.
- [55] H. Li, X. Zhang, Z. Chi, B. Xu, W. Zhou, S. Liu, Y. Zhang, J. Xu, *Org. Lett.* **2011**, *13*, 556–559.
- [56] C. Y. K. Chan, Z. Zhao, J. W. Y. Lam, J. Liu, S. Chen, P. Lu, F. Mahtab, X. Chen, H. H. Y. Sung, H. S. Kwok, et al., *Adv. Funct. Mater.* **2012**, *22*, 378–389.
- [57] J. Zhou, Z. Chang, Y. Jiang, B. He, M. Du, P. Lu, Y. Hong, H. S. Kwok, A. Qin, H. Qiu, et al., *Chem. Commun.* **2013**, *49*, 2491–2493.
- [58] J. Zhang, Q. Zhang, T. T. Vo, D. A. Parrish, J. M. Shreeve, *J. Am. Chem. Soc.* **2015**, *137*, 1697–1704.
- [59] S. Shanmugaraju, P. S. Mukherjee, *Chem. Commun.* **2015**, *51*, 16014–16032.
- [60] M. Bendikov, F. Wudl, D. F. Perepichka, *Chem. Rev.* **2004**, *104*, 4891–4945.
- [61] L. Zang, Y. Che, J. S. Moore, *Acc. Chem. Res.* **2008**, *41*, 1596–1608.
- [62] R. A. Bissell, E. Córdova, A. E. Kaifer, J. F. Stoddart, *Nature* **1994**, *369*, 133–137.
- [63] H. Li, X. Zhang, W. Zu, *J. Appl. Phys.* **2014**, *115*, 054510.
- [64] S. Burattini, B. W. Greenland, D. H. Merino, W. Weng, J. Seppala, H. M. Colquhoun, W. Hayes, M. E. MacKay, I. W. Hamley, S. J. Rowan, *J. Am. Chem. Soc.* **2010**, *132*, 12051–12058.
- [65] S. J. Grabowski, *J. Phys. Org. Chem.* **2004**, *17*, 18–31.
- [66] L. Pauling, *The Nature of the Chemical Bond and the Structure of Molecules and Crystals*, New York, **1939**.
- [67] N. Bjerrum, *Science (80-.)*. **1952**, *115*, 385–390.
- [68] G. Gilli, P. Gilli, *The Nature of the Hydrogen Bond: Outline of a Comprehensive Hydrogen Bond Theory*, Oxford Scholarship Online, **2009**.
- [69] Z.-T. Li, L.-Z. Wu, *Hydrogen Bonded Supramolecular Structures*, Springer, **2015**.
- [70] M. Bailey, C. J. Brown, *Acta Crystallogr.* **1967**, *22*, 387–391.
- [71] B. Omondi, M. A. Fernandes, M. Layh, D. C. Levendis, *Acta Crystallogr. Sect. C Cryst. Struct. Commun.* **2008**, *64*, o137–o138.

- [72] V. Amendola, L. Fabbrizzi, L. Mosca, *Chem. Soc. Rev.* **2010**, *39*, 3889–3915.
- [73] Z. Zhang, P. R. Schreiner, *Chem. Soc. Rev.* **2009**, *38*, 1187–1198.
- [74] Y. Hua, A. H. Flood, *Chem. Soc. Rev.* **2010**, *39*, 1262–1271.
- [75] J. Jański, K. Orzechowski, L. Sobczyk, *Chem. Phys. Lett.* **2020**, *744*, 137218.
- [76] H. Liu, X. Yang, S. Wu, M. Zhang, S. Parkin, S. Cao, T. Li, F. Yu, S. Long, *CrystEngComm* **2020**, *22*, 448–457.
- [77] A. Lemmerer, D. A. Admond, C. Esterhuysen, J. Bernstein, *Cryst. Growth Des.* **2013**, *13*, 3935–3952.
- [78] P. Vishweshwar, A. Nangia, V. M. Lynch, *Cryst. Growth Des.* **2003**, *3*, 783–790.
- [79] T. R. Shattock, K. K. Arora, P. Vishweshwar, M. J. Zaworotko, in *Cryst. Growth Des.*, American Chemical Society, **2008**, pp. 4533–4545.
- [80] K. Lee, K.-J. Kim, J. Ulrich, *Cryst. Res. Technol.* **2016**, *51*, 197–206.
- [81] N. B. Báthori, A. Lemmerer, G. A. Venter, S. A. Bourne, M. R. Caira, *Cryst. Growth Des.* **2011**, *11*, 75–87.
- [82] M. C. Etter, *Acc. Chem. Res.* **1990**, *23*, 120–126.
- [83] M. C. Etter, J. C. MacDonald, J. Bernstein, *Acta Crystallogr. Sect. B* **1990**, *46*, 256–262.
- [84] J. Bernstein, R. E. Davis, L. Shimoni, N. -L Chang, *Angew. Chemie Int. Ed. English* **1995**, *34*, 1555–1573.
- [85] E. Frankland, *Ann. der Chemie und Pharm.* **1862**, *124*, 129–157.
- [86] J. Huang, Y. Li, *Front. Chem.* **2018**, *6*, 341.
- [87] A. Stock, E. Pohland, *Berichte der Dtsch. Chem. Gesellschaft (A B Ser.)* **1926**, *59*, 2215–2223.
- [88] B. Icli, E. Sheepwash, T. Riis-Johannessen, K. Schenk, Y. Filinchuk, R. Scopelliti, K. Severin, *Chem. Sci.* **2011**, *2*, 1719–1721.
- [89] E. Sheepwash, N. Luisier, M. R. Krause, S. Noé, S. Kubik, K. Severin, *Chem. Commun.* **2012**, *48*, 7808–7810.
- [90] E. Sheepwash, V. Krampfl, R. Scopelliti, O. Sereda, A. Neels, K. Severin, *Angew. Chemie Int. Ed.* **2011**, *50*, 3034–3037.
- [91] B. Icli, E. Solari, B. Kilbas, R. Scopelliti, K. Severin, *Chem. - A Eur. J.* **2012**, *18*, 14867–14874.
- [92] F. Cheng, E. M. Bonder, S. Salem, F. Jäkle, *Macromolecules* **2013**, *46*, 2905–2915.
- [93] N. Miyaura, A. Suzuki, *J. Chem. Soc. Chem. Commun.* **1979**, 866–867.
- [94] N. Miyaura, K. Yamada, A. Suzuki, *Tetrahedron Lett.* **1979**, *20*, 3437–3440.
- [95] D. G. Hall, *Boronic Acids: Preparation and Applications in Organic Synthesis, Medicine*

- and Materials (Volume 1 and 2)*, Wiley-VCH, Weinheim, Germany, **2011**.
- [96] C. D. Entwistle, T. B. Marder, *Angew. Chemie Int. Ed.* **2002**, *41*, 2927–2931.
- [97] N. Luisier, K. Bally, R. Scopelliti, F. T. Fadaei, K. Schenk, P. Pattison, E. Solari, K. Severin, *Cryst. Growth Des.* **2016**, *16*, 6600–6604.
- [98] N. Christinat, R. Scopelliti, K. Severin, *Chem. Commun.* **2008**, 3660–3662.
- [99] J. Cruz-Huerta, D. Salazar-Mendoza, J. Hernández-Paredes, I. F. Hernández Ahuactzi, H. Höpfl, *Chem. Commun.* **2012**, *48*, 4241–4243.
- [100] M. Fontani, F. Peters, W. Scherer, W. Wachter, M. Wagner, P. Zanello, *Eur. J. Inorg. Chem.* **1998**, *1998*, 1453–1465.
- [101] J. R. Hunt, C. J. Doonan, J. D. LeVangie, A. P. Côté, O. M. Yaghi, *J. Am. Chem. Soc.* **2008**, *130*, 11872–11873.
- [102] M. A. Beckett, D. E. Hibbs, M. B. Hursthouse, K. M. A. Malik, P. Owen, K. S. Varma, *J. Organomet. Chem.* **2000**, *595*, 241–247.
- [103] W. Liu, M. Pink, D. Lee, *J. Am. Chem. Soc.* **2009**, *131*, 8703–8707.
- [104] M. Gopalakrishnan, T. Viswanathan, E. David, K. Thirumoorthy, N. S. P. Bhuvanesh, N. Palanisami, *New J. Chem.* **2019**, *43*, 10948–10958.
- [105] J. Colin, H. Gaultier de Claubry, *Ann Chim.* **1814**, 74–77.
- [106] P. R. Varadwaj, A. Varadwaj, H. M. Marques, *Inorganics* **2019**, *7*, 40.
- [107] T. Clark, M. Hennemann, J. S. Murray, P. Politzer, *J. Mol. Model.* **2007**, *13*, 291–296.
- [108] L. C. Gilday, S. W. Robinson, T. A. Barendt, M. J. Langton, B. R. Mullaney, P. D. Beer, *Chem. Rev.* **2015**, *115*, 7118–7195.
- [109] J. P. M. Lommerse, A. J. Stone, R. Taylor, F. H. Allen, *J. Am. Chem. Soc.* **1996**, *118*, 3108–3116.
- [110] K. E. Riley, J. S. Murray, P. Politzer, M. C. Concha, P. Hobza, *J. Chem. Theory Comput.* **2009**, *5*, 155–163.
- [111] J.-W. Zou, Y.-J. Jiang, M. Guo, G.-X. Hu, B. Zhang, H.-C. Liu, Q.-S. Yu, *Chem. - A Eur. J.* **2005**, *11*, 740–751.
- [112] Y. X. Lu, J. W. Zou, Y. H. Wang, Y. J. Jiang, Q. Sen Yu, *J. Phys. Chem. A* **2007**, *111*, 10781–10788.
- [113] K. E. Riley, J. S. Murray, J. Fanfrlík, J. Řezáč, R. J. Solá, M. C. Concha, F. M. Ramos, P. Politzer, *J. Mol. Model.* **2013**, *19*, 4651–4659.
- [114] C. Gropp, T. Husch, N. Trapp, M. Reiher, F. Diederich, *J. Am. Chem. Soc.* **2017**, *139*, 12190–12200.
- [115] M. C. Aragoni, M. Arca, F. A. Devillanova, F. Isaia, V. Lippolis, *Cryst. Growth Des.*

- 2012**, *12*, 2769–2779.
- [116] G. C. Pimentel, *J. Chem. Phys.* **1951**, *19*, 446–448.
- [117] R. J. Hach, R. E. Rundle, *J. Am. Chem. Soc.* **1951**, *73*, 4321–4324.
- [118] K. Akiba, Ed. , *Chemistry of Hypervalent Compounds*, Wiley-VCH, New York, **1999**.
- [119] C. W. Perkins, J. C. Martin, A. J. Arduengo, W. Lau, A. Alegría, J. K. Kochi, *J. Am. Chem. Soc.* **1980**, *102*, 7753–7759.
- [120] Z. Rappoport, J. F. Liebman, I. Marek, S. Patai, Eds. , *The Chemistry of Organic Selenium and Tellurium Compounds, Volume 4, Parts 1 and 2 Set | Wiley*, Wiley, **2013**.
- [121] F. Devillanova, W.-W. Du Mont, Eds. , *Handbook of Chalcogen Chemistry: New Perspectives in Sulfur, Selenium and Tellurium Volume 2: Edition 2*, Royal Society Of Chemistry, Cambridge, **2013**.
- [122] A. Mancini, M. C. Aragoni, N. Bricklebank, C. Castellano, F. Demartin, F. Isaia, V. Lippolis, A. Pintus, M. Arca, *Chem. - An Asian J.* **2013**, *8*, 639–647.
- [123] R. Montis, M. Arca, M. C. Aragoni, A. Bauzá, F. Demartin, A. Frontera, F. Isaia, V. Lippolis, *CrystEngComm* **2017**, *19*, 4401–4412.
- [124] E. J. Juárez-Pérez, M. C. Aragoni, M. Arca, A. J. Blake, F. A. Devillanova, A. Garau, F. Isaia, V. Lippolis, R. Núñez, A. Pintus, et al., *Chem. - A Eur. J.* **2011**, *17*, 11497–11514.
- [125] M. C. Aragoni, M. Arca, F. Demartin, F. A. Devillanova, A. Garau, F. Isaia, F. Lelj, V. Lippolis, G. Verani, *Chem. – A Eur. J.* **2001**, *7*, 3122–3133.
- [126] W. T. Pennington, T. W. Hanks, H. D. Arman, in *Struct. Bond.*, Springer Verlag, **2008**, pp. 65–104.
- [127] M. Tuikka, M. Haukka, *Acta Crystallogr. Sect. E Crystallogr. Commun.* **2015**, *71*, o463.
- [128] O. Hassel, H. Hope, N. A. Sørensen, H. Dam, B. Sjöberg, J. Toft, *Acta Chem. Scand.* **1961**, *15*, 407–416.
- [129] T. Dahl, O. Hassel, K. Sky, Å. Nilsson, H. Theorell, R. Blinc, S. Paušak, L. Ehrenberg, J. Dumanović, *Acta Chem. Scand.* **1967**, *21*, 592–593.
- [130] C. Rømming, P. Klæboe, E. E. Tucker, J. Songstad, S. Svensson, *Acta Chem. Scand.* **1972**, *26*, 1555–1560.
- [131] R. Montis, M. Arca, M. C. Aragoni, A. J. Blake, C. Castellano, F. Demartin, F. Isaia, V. Lippolis, A. Pintus, E. J. Lenardão, et al., *New J. Chem.* **2018**, *42*, 10592–10602.
- [132] M. C. Aragoni, M. Arca, S. J. Coles, F. A. Devillanova, M. B. Hursthouse, S. L. Coles, F. Isaia, V. Lippolis, A. Mancini, *CrystEngComm* **2011**, *13*, 6319–6322.
- [133] M. C. Aragoni, M. Arca, F. A. Devillanova, M. B. Hursthouse, S. L. Huth, F. Isaia, V. Lippolis, A. Mancini, H. Ogilvie, *Inorg. Chem. Commun.* **2005**, *8*, 79–82.

- [134] M. C. Aragoni, M. Arca, C. Caltagirone, C. Castellano, F. Demartin, A. Garau, F. Isaia, V. Lippolis, R. Montis, A. Pintus, *CrystEngComm* **2012**, *14*, 5809–5823.
- [135] M. C. Aragoni, M. Arca, F. A. Devillanova, M. B. Hursthouse, S. L. Huth, F. Isaia, V. Lippolis, A. Mancini, *CrystEngComm* **2004**, *6*, 540–542.
- [136] M. C. Aragoni, M. Arca, F. A. Devillanova, M. B. Hursthouse, S. L. Huth, F. Isaia, V. Lippolis, A. Mancini, G. Verani, *Eur. J. Inorg. Chem.* **2008**, *2008*, 3921–3928.
- [137] M. C. Aragoni, M. Arca, S. J. Coles, F. A. Devillanova, M. B. Hursthouse, S. L. Coles, F. Isaia, V. Lippolis, A. Mancini, *CrystEngComm* **2011**, *13*, 6319–6322.
- [138] M. C. Aragoni, M. Arca, F. A. Devillanova, F. Isaia, V. Lippolis, A. Mancini, L. Pala, A. M. Z. Slawin, J. D. Woollins, *Chem. Commun.* **2003**, *3*, 2226–2227.
- [139] K.-F. Tebbe, R. Buchem, *Angew. Chemie Int. Ed. English* **1997**, *36*, 1345–1346.
- [140] M. Wolff, J. Meyer, C. Feldmann, *Angew. Chemie Int. Ed.* **2011**, *50*, 4970–4973.
- [141] A. Vanderkooy, A. K. Gupta, T. Földes, S. Lindblad, A. Orthaber, I. Pápai, M. Erdélyi, *Angew. Chemie - Int. Ed.* **2019**, *58*, 9012–9016.
- [142] J. Barluenga, J. M. González, P. J. Campos, G. Asensio, *Angew. Chemie Int. Ed. English* **1985**, *24*, 319–320.
- [143] M. Rahm, R. Hoffmann, N. W. Ashcroft, *Chem. - A Eur. J.* **2016**, *22*, 14625–14632.
- [144] I. Mayer, *Chem. Phys. Lett.* **1983**, *97*, 270–274.
- [145] N. Biot, D. Bonifazi, *Chem. – A Eur. J.* **2020**, *26*, 2904–2913.
- [146] A. C. B. Lucassen, T. Zubkov, L. J. W. Shimon, M. E. Van Der Boom, *CrystEngComm* **2007**, *9*, 538–540.
- [147] M. J. Bojdys, M. E. Briggs, J. T. A. Jones, D. J. Adams, S. Y. Chong, M. Schmidtman, A. I. Cooper, *J. Am. Chem. Soc.* **2011**, *133*, 16566–16571.
- [148] E. Bosch, C. L. Barnes, *Cryst. Growth Des.* **2002**, *2*, 299–302.
- [149] P. Metrangolo, G. Resnati, *Science (80-.)*. **2008**, *321*, 918–919.
- [150] A. M. S. Riel, R. K. Rowe, E. N. Ho, A. C. C. Carlsson, A. K. Rappé, O. B. Berryman, P. S. Ho, *Acc. Chem. Res.* **2019**, *52*, 2870–2880.
- [151] P. Metrangolo, H. Neukirch, T. Pilati, G. Resnati, *Acc. Chem. Res.* **2005**, *38*, 386–395.
- [152] L. Brammer, *Faraday Discuss.* **2017**, *203*, 485–507.
- [153] P. Metrangolo, F. Meyer, T. Pilati, G. Resnati, G. Terraneo, *Angew. Chemie - Int. Ed.* **2008**, *47*, 6114–6127.
- [154] M. Saccone, L. Catalano, *J. Phys. Chem. B* **2019**, *123*, 9281–9290.
- [155] W. Wang, Y. Zhang, W. J. Jin, *Coord. Chem. Rev.* **2020**, *404*, 213107.
- [156] R. L. Sutar, S. M. Huber, *ACS Catal.* **2019**, *9*, 9622–9639.

- [157] J. Bamberger, F. Ostler, O. G. Mancheño, *ChemCatChem* **2019**, *11*, 5198–5211.
- [158] V. Govindaraj, H. Ungati, S. R. Jakka, S. Bose, G. Mugesh, *Chem. – A Eur. J.* **2019**, *25*, chem.201902243.
- [159] M. A. Ruiz-Preciado, D. J. Kubicki, A. Hofstetter, L. McGovern, M. H. Futscher, A. Ummadisingu, R. Gershoni-Poranne, S. M. Zakeeruddin, B. Ehrler, L. Emsley, et al., *J. Am. Chem. Soc.* **2020**, *142*, 1645–1654.
- [160] R. Wilcken, M. O. Zimmermann, A. Lange, A. C. Joerger, F. M. Boeckler, *J. Med. Chem.* **2013**, *56*, 1363–1388.
- [161] S. Scheiner, *Faraday Discuss.* **2017**, *203*, 213–226.
- [162] T. Lu, J. Zhang, Q. Gou, G. Feng, *Phys. Chem. Chem. Phys.* **2020**, *22*, 8467–8475.
- [163] S. Moaven, M. C. Andrews, T. J. Polaske, B. M. Karl, D. K. Unruh, E. Bosch, N. P. Bowling, A. F. Cozzolino, *Inorg. Chem.* **2019**, *58*, 16227–16235.
- [164] A. C. Legon, *Phys. Chem. Chem. Phys.* **2017**, *19*, 14884–14896.
- [165] S. R. Batten, N. R. Champness, X. M. Chen, J. Garcia-Martinez, S. Kitagawa, L. Öhrström, M. O’Keefe, M. P. Suh, J. Reedijk, *Pure Appl. Chem.* **2013**, *85*, 1715–1724.
- [166] W. L. Leong, J. J. Vittal, *Chem. Rev.* **2011**, *111*, 688–764.
- [167] M. Böhme, A. Jochim, M. Rams, T. Lohmiller, S. Suckert, A. Schnegg, W. Plass, C. Näther, *Inorg. Chem.* **2020**, *59*, 5325–5338.
- [168] C. Musumeci, S. Osella, L. Ferlauto, D. Niedzialek, L. Grisanti, S. Bonacchi, A. Jouaiti, S. Milita, A. Ciesielski, D. Beljonne, et al., *Nanoscale* **2016**, *8*, 2386–2394.
- [169] B. Bhattacharya, A. A. L. Michalchuk, D. Silbernagl, M. Rautenberg, T. Schmid, T. Feiler, K. Reimann, A. Ghalgaoui, H. Sturm, B. Paulus, et al., *Angew. Chemie Int. Ed.* **2020**, *59*, 5557–5561.
- [170] M. Liu, H. S. Quah, S. Wen, J. Wang, P. S. Kumar, G. Eda, J. J. Vittal, W. Ji, *J. Mater. Chem. C* **2017**, *5*, 2936–2941.
- [171] B. Schmaltz, A. Jouaiti, M. W. Hosseini, A. De Cian, *Chem. Commun.* **2001**, 1242–1243.
- [172] D. Hagrman, R. P. Hammond, R. Haushalter, J. Zubieta, *Chem. Mater.* **1998**, *10*, 2091–2100.
- [173] B. Dutta, D. Das, J. Datta, A. Chandra, S. Jana, C. Sinha, P. P. Ray, M. H. Mir, *Inorg. Chem. Front.* **2019**, *6*, 1245–1252.
- [174] E. Yashima, N. Ousaka, D. Taura, K. Shimomura, T. Ikai, K. Maeda, *Chem. Rev.* **2016**, *116*, 13752–13990.
- [175] X. Ma, W. Kong, M. Abudourehman, J. Zhang, X. Xuan, *New J. Chem.* **2019**, *43*, 15023–15029.

- [176] S. R. Batten, B. F. Hoskins, R. Robson, *Chem. – A Eur. J.* **2000**, *6*, 156–161.
- [177] H. Wu, J. Yang, Z. M. Su, S. R. Batten, J. F. Ma, *J. Am. Chem. Soc.* **2011**, *133*, 11406–11409.
- [178] R. Haldar, N. Sikdar, T. K. Maji, *Mater. Today* **2015**, *18*, 97–116.
- [179] H. L. Jiang, T. A. Makal, H. C. Zhou, *Coord. Chem. Rev.* **2013**, *257*, 2232–2249.
- [180] Y. He, Z. Zhang, S. Xiang, F. R. Fronczek, R. Krishna, B. Chen, *Chem. Commun.* **2012**, *48*, 6493–6495.
- [181] Q. Yao, J. Su, O. Cheung, Q. Liu, N. Hedin, X. Zou, *J. Mater. Chem.* **2012**, *22*, 10345–10351.
- [182] J. J. Zhang, L. Wojtas, R. W. Larsen, M. Eddaoudi, M. J. Zaworotko, *J. Am. Chem. Soc.* **2009**, *131*, 17040–17041.
- [183] S. Bureekaew, H. Sato, R. Matsuda, Y. Kubota, R. Hirose, J. Kim, K. Kato, M. Takata, S. Kitagawa, *Angew. Chemie Int. Ed.* **2010**, *49*, 7660–7664.
- [184] S. S. Y. Chui, S. M. F. Lo, J. P. H. Charmant, A. G. Orpen, I. D. Williams, *Science (80-.)*. **1999**, *283*, 1148–1150.
- [185] H. Li, M. Eddaoudi, M. O’Keeffe, O. M. Yaghi, *Nature* **1999**, *402*, 276–279.
- [186] O. M. Yaghi, M. J. Kalmutzki, C. S. Diercks, *Introduction to Reticular Chemistry: Metal-Organic Frameworks and Covalent Organic Frameworks.*, Wiley-VCH, **2019**.
- [187] M. Eddaoudi, J. Kim, N. Rosi, D. Vodak, J. Wachter, M. O’Keeffe, O. M. Yaghi, *Science (80-.)*. **2002**, *295*, 469–472.
- [188] M. O’Keeffe, M. A. Peskov, S. J. Ramsden, O. M. Yaghi, *Acc. Chem. Res.* **2008**, *41*, 1782–1789.
- [189] M. J. Kalmutzki, N. Hanikel, O. M. Yaghi, *Sci. Adv.* **2018**, *4*, eaat9180.
- [190] S. Canossa, A. Gonzalez-Nelson, L. Shupletsov, M. Carmen Martin, M. A. Van der Veen, *Chem. – A Eur. J.* **2020**, *26*, 3564–3570.
- [191] T. E. Webber, S. P. Desai, R. L. Combs, S. Bingham, C. C. Lu, R. L. Penn, *Cryst. Growth Des.* **2020**, acs.cgd.9b01590.
- [192] R. S. Forgan, *Chem. Sci.* **2020**, DOI 10.1039/D0SC01356K.
- [193] G. Wißmann, A. Schaate, S. Lilienthal, I. Bremer, A. M. Schneider, P. Behrens, *Microporous Mesoporous Mater.* **2012**, *152*, 64–70.
- [194] O. V. Gutov, M. G. Hevia, E. C. Escudero-Adán, A. Shafir, *Inorg. Chem.* **2015**, *54*, 8396–8400.
- [195] S.-J. Lee, J. L. Mancuso, K. N. Le, C. D. Malliakas, Y.-S. Bae, C. H. Hendon, T. Islamoglu, O. K. Farha, *ACS Mater. Lett.* **2020**, 499–504.

- [196] A. P. Nelson, O. K. Farha, K. L. Mulfort, J. T. Hupp, *J. Am. Chem. Soc.* **2009**, *131*, 458–460.
- [197] ‘Case: How many MOFs are there in the CSD? - The Cambridge Crystallographic Data Centre (CCDC)’, can be found under <https://www.ccdc.cam.ac.uk/support-and-resources/support/case/?caseid=9833bd2c-27f9-4ff7-8186-71a9b415f012>, **n.d.**
- [198] O. K. Farha, I. Eryazici, N. C. Jeong, B. G. Hauser, C. E. Wilmer, A. A. Sarjeant, R. Q. Snurr, S. T. Nguyen, A. Ö. Yazaydin, J. T. Hupp, *J. Am. Chem. Soc.* **2012**, *134*, 15016–15021.
- [199] H. Furukawa, K. E. Cordova, M. O’Keeffe, O. M. Yaghi, *Science* **2013**, *341*, 1230444.
- [200] Ü. Kökçam-Demir, A. Goldman, L. Esrafilı, M. Gharib, A. Morsali, O. Weingart, C. Janiak, *Chem. Soc. Rev.* **2020**, DOI 10.1039/c9cs00609e.
- [201] M. Ding, R. W. Flaig, H.-L. Jiang, O. M. Yaghi, *Chem. Soc. Rev.* **2019**, *48*, 2783–2828.
- [202] X. Zhao, Y. Wang, D.-S. Li, X. Bu, P. Feng, *Adv. Mater.* **2018**, *30*, 1705189.
- [203] S. Kousik, S. Velmathi, *Chem. – A Eur. J.* **2019**, *25*, 16451–16505.
- [204] H. Q. Yin, X. B. Yin, *Acc. Chem. Res.* **2020**, DOI 10.1021/acs.accounts.9b00575.
- [205] B. Qian, Z. Chang, X. H. Bu, *Top. Curr. Chem.* **2020**, *378*, 1–39.
- [206] Z. Hu, B. J. Deibert, J. Li, *Chem. Soc. Rev.* **2014**, *43*, 5815–5840.
- [207] J. Yang, Y. Yang, *Small* **2020**, *16*, 1906846.
- [208] S. Aitipamula, R. Banerjee, A. K. Bansal, K. Biradha, M. L. Cheney, A. R. Choudhury, G. R. Desiraju, A. G. Dikundwar, R. Dubey, N. Duggirala, et al., *Cryst. Growth Des.* **2012**, *12*, 2147–2152.
- [209] M. Karimi-Jafari, L. Padrela, G. M. Walker, D. M. Croker, *Cryst. Growth Des.* **2018**, *18*, 6370–6387.
- [210] C. B. Aakeröy, A. S. Sinha, *Co-Crystals: Preparation, Characterization and Applications*, Royal Society Of Chemistry, **2018**.
- [211] C. W. Pouton, *Eur. J. Pharm. Sci.* **2006**, *29*, 278–287.
- [212] C. B. Aakeröy, P. D. Chopade, J. Desper, *Cryst. Growth Des.* **2013**, *13*, 4145–4150.
- [213] C. B. Aakeröy, M. Fasulo, N. Schultheiss, J. Desper, C. Moore, *J. Am. Chem. Soc.* **2007**, *129*, 13772–13773.
- [214] B. Sarma, N. K. Nath, B. R. Bhogala, A. Nangia, *Cryst. Growth Des.* **2009**, *9*, 1546–1557.
- [215] S. Tothadi, P. Sanphui, G. R. Desiraju, *Cryst. Growth Des.* **2014**, *14*, 5293–5302.
- [216] D. J. Duchamp, R. E. Marsh, *Acta Crystallogr. Sect. B Struct. Crystallogr. Cryst. Chem.* **1969**, *25*, 5–19.

- [217] C. V. K. Sharma, M. J. Zaworotko, *Chem. Commun.* **1996**, 2655–2656.
- [218] T. R. Shattock, P. Vishweshwar, Z. Wang, M. J. Zaworotko, *Cryst. Growth Des.* **2005**, *5*, 2046–2049.
- [219] C. B. Aakeröy, A. M. Beatty, B. A. Helfrich, *Angew. Chemie Int. Ed.* **2001**, *40*, 3240–3242.
- [220] F. Topić, K. Rissanen, *J. Am. Chem. Soc.* **2016**, *138*, 6610–6616.
- [221] M. Paul, S. Chakraborty, G. R. Desiraju, *J. Am. Chem. Soc.* **2018**, *140*, 2309–2315.
- [222] W. Yang, A. Greenaway, X. Lin, R. Matsuda, A. J. Blake, C. Wilson, W. Lewis, P. Hubberstey, S. Kitagawa, N. R. Champness, et al., *J. Am. Chem. Soc.* **2010**, *132*, 14457–14469.
- [223] R. B. Lin, Y. He, P. Li, H. Wang, W. Zhou, B. Chen, *Chem. Soc. Rev.* **2019**, *48*, 1362–1389.
- [224] Y.-F. Han, Y.-X. Yuan, H.-B. Wang, *Molecules* **2017**, *22*, 266.
- [225] I. Hisaki, C. Xin, K. Takahashi, T. Nakamura, *Angew. Chemie Int. Ed.* **2019**, *58*, 11160–11170.
- [226] P. Li, P. Li, M. R. Ryder, Z. Liu, C. L. Stern, O. K. Farha, J. F. Stoddart, *Angew. Chemie Int. Ed.* **2019**, *58*, 1664–1669.
- [227] L. C. Delmas, P. N. Horton, A. J. P. White, S. J. Coles, P. D. Lickiss, R. P. Davies, *Chem. Commun.* **2017**, *53*, 12524–12527.
- [228] X. Z. Luo, X. J. Jia, J. H. Deng, J. L. Zhong, H. J. Liu, K. J. Wang, D. C. Zhong, *J. Am. Chem. Soc.* **2013**, *135*, 11684–11687.
- [229] M. Morshedi, M. Thomas, A. Tarzia, C. J. Doonan, N. G. White, *Chem. Sci.* **2017**, *8*, 3019–3025.
- [230] J. H. Fournier, T. Maris, J. D. Wuest, W. Guo, E. Galoppini, *J. Am. Chem. Soc.* **2003**, *125*, 1002–1006.
- [231] T. H. Chen, I. Popov, W. Kaveevivitchai, Y. C. Chuang, Y. S. Chen, O. Daugulis, A. J. Jacobson, O. Miljanić, *Nat. Commun.* **2014**, *5*, 1–8.
- [232] K. C. Ranjeesh, R. Illathvalappil, S. D. Veer, J. Peter, V. C. Wakchaure, Goudappagouda, K. V. Raj, S. Kurungot, S. S. Babu, *J. Am. Chem. Soc.* **2019**, *141*, 14950–14954.
- [233] C. Chaumont, P. Mobian, N. Kyritsakas, M. Henry, *CrystEngComm* **2013**, *15*, 6845–6862.
- [234] Z. Sun, Y. Li, L. Chen, X. Jing, Z. Xie, *Cryst. Growth Des.* **2015**, *15*, 542–545.
- [235] P. Li, O. Alduhaish, H. D. Arman, H. Wang, K. Alfooty, B. Chen, *Cryst. Growth Des.*

- 2014**, *14*, 3634–3638.
- [236] A. Pulido, L. Chen, T. Kaczorowski, D. Holden, M. A. Little, S. Y. Chong, B. J. Slater, D. P. McMahon, B. Bonillo, C. J. Stackhouse, et al., *Nature* **2017**, *543*, 657–664.
- [237] H. Wang, B. Li, H. Wu, T. L. Hu, Z. Yao, W. Zhou, S. Xiang, B. Chen, *J. Am. Chem. Soc.* **2015**, *137*, 9963–9970.
- [238] J. Lü, C. Perez-Krap, M. Suyetin, N. H. Alsmail, Y. Yan, S. Yang, W. Lewis, E. Bichoutskaia, C. C. Tang, A. J. Blake, et al., *J. Am. Chem. Soc.* **2014**, *136*, 12828–12831.
- [239] B. Wang, X. L. Lv, J. Lv, L. Ma, R. B. Lin, H. Cui, J. Zhang, Z. Zhang, S. Xiang, B. Chen, *Chem. Commun.* **2019**, *56*, 66–69.
- [240] Q. Yin, P. Zhao, R.-J. Sa, G.-C. Chen, J. Lü, T.-F. Liu, R. Cao, *Angew. Chemie Int. Ed.* **2018**, *57*, 7691–7696.
- [241] H. Wang, Z. Bao, H. Wu, R. B. Lin, W. Zhou, T. L. Hu, B. Li, J. C. G. Zhao, B. Chen, *Chem. Commun.* **2017**, *53*, 11150–11153.
- [242] E. Gomez, M. Gutiérrez, B. Cohen, I. Hisaki, A. Douhal, *J. Mater. Chem. C* **2018**, *6*, 6929–6939.
- [243] I. Hisaki, N. Q. Emilya Affendy, N. Tohnai, *CrystEngComm* **2017**, *19*, 4892–4898.
- [244] A. P. Côté, A. I. Benin, N. W. Ockwig, M. O’Keeffe, A. J. Matzger, O. M. Yaghi, *Science* (80-.). **2005**, *310*, 1166–1170.
- [245] S. L. Zhang, Y. Lu, Y. H. Li, K. Y. Wang, J. H. Chen, Z. Yang, *Org. Lett.* **2017**, *19*, 3986–3989.
- [246] ‘The 2016 Nobel Prize in Chemistry - Press release - NobelPrize.org’, can be found under <https://www.nobelprize.org/prizes/chemistry/2016/press-release/>, **n.d.**
- [247] Y. Jin, C. Yu, R. J. Denman, W. Zhang, *Chem. Soc. Rev.* **2013**, *42*, 6634.
- [248] Y. Liu, K. C.-F. Leung, Eds. , *Dynamic Covalent Chemistry. Principles, Reactions, and Applications*, John Wiley & Sons, **2017**.
- [249] R. C. Boutelle, B. H. Northrop, *J. Org. Chem.* **2011**, *76*, 7994–8002.
- [250] J. L. Segura, M. J. Mancheño, F. Zamora, *Chem. Soc. Rev.* **2016**, *45*, 5635–5671.
- [251] N. E. S. K. Peter C. Vollhardt, *Organic Chemistry; Palgrave Version: Structure and Function*, **2014**.
- [252] M. Matsumoto, R. R. Dasari, W. Ji, C. H. Feriante, T. C. Parker, S. R. Marder, W. R. Dichtel, *J. Am. Chem. Soc.* **2017**, *139*, 4999–5002.
- [253] F. J. Uribe-Romo, J. R. Hunt, H. Furukawa, C. Klöck, M. O’Keeffe, O. M. Yaghi, *J. Am. Chem. Soc.* **2009**, *131*, 4570–4571.
- [254] Y. B. Zhang, J. Su, H. Furukawa, Y. Yun, F. Gándara, A. Duong, X. Zou, O. M. Yaghi,

- J. Am. Chem. Soc.* **2013**, *135*, 16336–16339.
- [255] F. J. Uribe-Romo, C. J. Doonan, H. Furukawa, K. Oisaki, O. M. Yaghi, *J. Am. Chem. Soc.* **2011**, *133*, 11478–11481.
- [256] H. Fan, A. Mundstock, J. Gu, H. Meng, J. Caro, *J. Mater. Chem. A* **2018**, *6*, 16849–16853.
- [257] D. Kaleeswaran, P. Vishnoi, R. Murugavel, *J. Mater. Chem. C* **2015**, *3*, 7159–7171.
- [258] J. Guo, Y. Xu, S. Jin, L. Chen, T. Kaji, Y. Honsho, M. A. Addicoat, J. Kim, A. Saeki, H. Ihee, et al., *Nat. Commun.* **2013**, *4*, 1–8.
- [259] D. A. Pyles, J. W. Crowe, L. A. Baldwin, P. L. McGrier, *ACS Macro Lett.* **2016**, *5*, 1055–1058.
- [260] X. Guan, F. Chen, Q. Fang, S. Qiu, *Chem. Soc. Rev.* **2020**, *49*, 1357–1384.
- [261] H. M. El-Kaderi, J. R. Hunt, J. L. Mendoza-Cortés, A. P. Côté, R. E. Taylor, M. O’Keeffe, O. M. Yaghi, *Science (80-.)*. **2007**, *316*, 268–272.
- [262] G. Lin, H. Ding, D. Yuan, B. Wang, C. Wang, *J. Am. Chem. Soc.* **2016**, *138*, 3302–3305.
- [263] P. Kuhn, M. Antonietti, A. Thomas, *Angew. Chemie Int. Ed.* **2008**, *47*, 3450–3453.
- [264] K. T. Jackson, T. E. Reich, H. M. El-Kaderi, *Chem. Commun.* **2012**, *48*, 8823–8825.
- [265] C. Gervais, J. Maquet, F. Babonneau, C. Duriez, E. Framery, M. Vaultier, P. Florian, D. Massiot, *Chem. Mater.* **2001**, *13*, 1700–1707.
- [266] Q. H. Wang, K. Kalantar-Zadeh, A. Kis, J. N. Coleman, M. S. Strano, *Nat. Nanotechnol.* **2012**, *7*, 699–712.
- [267] T. E. Reich, K. T. Jackson, S. Li, P. Jena, H. M. El-Kaderi, *J. Mater. Chem.* **2011**, *21*, 10629–10632.
- [268] H. Furukawa, O. M. Yaghi, *J. Am. Chem. Soc.* **2009**, *131*, 8875–8883.
- [269] R. Babarao, J. Jiang, *Energy Environ. Sci.* **2008**, *1*, 139–143.
- [270] C. J. Doonan, D. J. Tranchemontagne, T. G. Glover, J. R. Hunt, O. M. Yaghi, *Nat. Chem.* **2010**, *2*, 235–238.
- [271] H. Oh, S. B. Kalidindi, Y. Um, S. Bureekaew, R. Schmid, R. A. Fischer, M. Hirscher, *Angew. Chemie Int. Ed.* **2013**, *52*, 13219–13222.
- [272] H. Ma, H. Ren, S. Meng, Z. Yan, H. Zhao, F. Sun, G. Zhu, *Chem. Commun.* **2013**, *49*, 9773–9775.
- [273] Y. Lan, M. Tong, Q. Yang, C. Zhong, *CrystEngComm* **2017**, *19*, 4920–4926.
- [274] S. Y. Ding, J. Gao, Q. Wang, Y. Zhang, W. G. Song, C. Y. Su, W. Wang, *J. Am. Chem. Soc.* **2011**, *133*, 19816–19822.
- [275] L. Stegbauer, K. Schwinghammer, B. V. Lotsch, *Chem. Sci.* **2014**, *5*, 2789–2793.

- [276] S. Lin, C. S. Diercks, Y. B. Zhang, N. Kornienko, E. M. Nichols, Y. Zhao, A. R. Paris, D. Kim, P. Yang, O. M. Yaghi, et al., *Science* (80-.). **2015**, *349*, 1208–1213.
- [277] P. Pachfule, A. Acharjya, J. Roeser, T. Langenhahn, M. Schwarze, R. Schomäcker, A. Thomas, J. Schmidt, *J. Am. Chem. Soc.* **2018**, *140*, 1423–1427.
- [278] S. Chandra, T. Kundu, S. Kandambeth, R. Babarao, Y. Marathe, S. M. Kunjir, R. Banerjee, *J. Am. Chem. Soc.* **2014**, *136*, 6570–6573.
- [279] X. Ding, J. Guo, X. Feng, Y. Honsho, J. Guo, S. Seki, P. Maitarad, A. Saeki, S. Nagase, D. Jiang, *Angew. Chemie Int. Ed.* **2011**, *50*, 1289–1293.
- [280] G. Das, B. P. Biswal, S. Kandambeth, V. Venkatesh, G. Kaur, M. Addicoat, T. Heine, S. Verma, R. Banerjee, *Chem. Sci.* **2015**, *6*, 3931–3939.
- [281] S. Jhulki, A. M. Evans, X. L. Hao, M. W. Cooper, C. H. Feriante, J. Leisen, H. Li, D. Lam, M. C. Hersam, S. Barlow, et al., *J. Am. Chem. Soc.* **2020**, *142*, 783–791.
- [282] M. C. Scicluna, L. Vella-Zarb, *ACS Appl. Nano Mater.* **2020**, 3097–3115.
- [283] F. Xu, S. Yang, X. Chen, Q. Liu, H. Li, H. Wang, B. Wei, D. Jiang, *Chem. Sci.* **2019**, *10*, 6001–6006.
- [284] R. Shi, L. Liu, Y. Lu, C. Wang, Y. Li, L. Li, Z. Yan, J. Chen, *Nat. Commun.* **2020**, *11*, 1–10.
- [285] B. Xu, S. Li, H. Jiao, J. Yin, Z. Liu, W. Zhong, *J. Mater. Chem. A* **2020**, *8*, 3865–3871.
- [286] L. Ma, S. Wang, X. Feng, B. Wang, *Chinese Chem. Lett.* **2016**, *27*, 1383–1394.
- [287] Z. Wang, S. Zhang, Y. Chen, Z. Zhang, S. Ma, *Chem. Soc. Rev.* **2020**, *49*, 708–735.
- [288] M. C. Aragoni, M. Arca, F. Demartin, F. A. Devillanova, C. Grai, F. Isaia, V. Lippolis, A. Tiripicchio, G. Verani, *J. Chem. Soc. Dalt. Trans.* **2001**, 2671–2677.
- [289] M. C. Aragoni, M. Arca, N. R. Champness, A. V. Chernikov, F. A. Devillanova, F. Isaia, V. Lippolis, N. S. Oxtoby, G. Verani, S. Z. Vatsadze, et al., *Eur. J. Inorg. Chem.* **2004**, 2008–2012.
- [290] C. Huang, Y.-J. Liu, Y.-T. Chen, D.-M. Chen, B.-X. Zhu, *Eur. J. Inorg. Chem.* **2020**, *2020*, 704–710.
- [291] R. Mandal, A. Garai, K. Biradha, *Dalt. Trans.* **2019**, *48*, 17456–17460.
- [292] M. C. Aragoni, M. Arca, V. Cabras, S. J. Coles, G. Ennas, F. Isaia, R. Lai, V. Lippolis, E. Podda, *Supramol. Chem.* **2017**, *29*, 853–864.
- [293] M. C. Aragoni, M. Arca, S. J. Coles, M. Crespo Alonso, S. L. Coles (née Huth), R. P. Davies, M. B. Hursthouse, F. Isaia, R. Lai, V. Lippolis, *CrystEngComm* **2016**, *18*, 5620–5629.
- [294] C. S. Lai, E. R. T. Tiekink, *CrystEngComm* **2004**, *6*, 593–605.

- [295] Y. S. Tan, A. Otero-De-La-Roza, M. M. Jotani, E. R. T. Tiekink, *Cryst. Growth Des.* **2020**, *20*, 3272–3283.
- [296] R. Khajuria, S. Kumar, A. Syed, G. Kour, S. Anthal, V. K. Gupta, R. Kant, S. K. Pandey, *J. Coord. Chem.* **2014**, *67*, 2925–2941.
- [297] ‘CAGLIARI 143 - C26H28Cd1N2O4P2S4 - eCrystals - University of Southampton’, can be found under <http://ecrystals.chem.soton.ac.uk/247/>, **n.d.**
- [298] E. Podda, M. Arca, S. J. Coles, M. Crespo Alonso, F. Isaia, A. Pintus, V. Lippolis, M. C. Aragoni, *Supramol. Chem.* **2020**, 267–275.
- [299] M. C. Aragoni, M. Arca, S. J. Coles, M. Crespo Alonso, S. L. Coles, R. P. Davies, M. B. Hursthouse, F. Isaia, R. Lai, V. Lippolis, *CrystEngComm* **2016**, *18*, 5620–5629.
- [300] W. Koch, M. C. Holthausen, *A Chemist’s Guide to Density Functional Theory*, Wiley-VCH, **2001**.
- [301] A. E. Reed, R. B. Weinstock, F. Weinhold, *J. Chem. Phys.* **1985**, *83*, 735–746.
- [302] D. H. Johnston, D. F. Shriver, *Inorg. Chem.* **1993**, *32*, 1045–1047.
- [303] G. Socrates, *Infrared and Raman Characteristic Group Frequencies. Tables and Charts*, Wiley, **2001**.
- [304] S. Liu, Y. M. Wang, J. Han, *J. Photochem. Photobiol. C Photochem. Rev.* **2017**, *32*, 78–103.
- [305] S. U. Son, B. Y. Kim, C. H. Choi, S. W. Lee, Y. S. Kim, Y. K. Chung, *Chem. Commun.* **2003**, *3*, 2528–2529.
- [306] M. E. Moon, J. Y. Park, K. K. Hwan, K. W. Chi, *Bull. Korean Chem. Soc.* **2007**, *28*, 2099–2102.
- [307] W. Shi, M. Shafaei-Fallah, C. E. Anson, A. Rothenberger, *J. Chem. Soc. Dalt. Trans.* **2006**, 3257–3262.
- [308] P. Kilian, A. M. Z. Slawin, J. D. Woollins, *Eur. J. Inorg. Chem.* **1999**, *1999*, 2327–2333.
- [309] T. B. Rauchfuss, G. A. Zank, *Inorg. Chem.* **1986**, *25*, 1431–1435.
- [310] C. E. Housmekerides, D. L. Ramage, C. M. Kretz, J. T. Shontz, R. S. Pilato, G. L. Geoffrey, A. L. Rheingold, B. S. Haggerty, *Inorg. Chem.* **1992**, *31*, 4453–4468.
- [311] Z. Weng, W. K. Leong, J. J. Vittal, L. Y. Goh, *Organometallics* **2003**, *22*, 1645–1656.
- [312] G. Moula, M. Bose, H. Datta, S. Sarkar, *Polyhedron* **2013**, *52*, 900–908.
- [313] R. F. Semeniuc, T. J. Reamer, J. P. Blitz, K. A. Wheeler, M. D. Smith, *Inorg. Chem.* **2010**, *49*, 2624–2629.
- [314] X.-Y. Wang, Y. Li, Q. Ma, Q.-F. Zhang, *Organometallics* **2010**, *29*, 2752–2760.
- [315] Q. Ma, X. Y. Wang, Q. Chen, W. H. Leung, Q. F. Zhang, *Inorganica Chim. Acta* **2011**,

378, 148–153.

- [316] B. Tong, M. Zhang, Z. Han, Q. Mei, Q. Zhang, *J. Organomet. Chem.* **2013**, 724, 180–185.
- [317] H. L. Liu, H. Y. Mao, C. Xu, H. Y. Zhang, H. W. Hou, Q. A. Wu, Y. Zhu, B. X. Ye, L. J. Yuan, *Polyhedron* **2004**, 23, 1799–1804.
- [318] S. Sewpersad, B. Omondi, W. E. Van Zyl, *Acta Crystallogr. Sect. E Struct. Reports Online* **2012**, 68, m1534–m1534.
- [319] ‘CAGLIARI 167 - C28H33N3Ni1O5P2S4 - eCrystals - University of Southampton’, can be found under <http://ecrystals.chem.soton.ac.uk/229/>, **n.d.**
- [320] ‘CAGLIARI 172 - C21H22Fe0.5N1Ni0.5O2P1S2 - eCrystals - University of Southampton’, can be found under <http://ecrystals.chem.soton.ac.uk/231/>, **n.d.**
- [321] J. P. Fackler, L. D. Thompson, *Inorganica Chim. Acta* **1981**, 48, 45–52.
- [322] G. Sánchez, J. García, D. J. Meseguer, J. L. Serrano, J. Pérez, E. Molins, G. López, *Inorganica Chim. Acta* **2004**, 357, 677–683.
- [323] M. Carla Aragoni, M. Arca, F. Demartin, F. A. Devillanova, F. Isaia, V. Lippolis, G. Verani, *Inorganica Chim. Acta* **2005**, 358, 213–216.
- [324] I. P. Gray, A. M. Z. Slawin, J. D. Woollins, *Dalt. Trans.* **2004**, 2477–2486.
- [325] Y. ÖZCAN, S. IDE, M. KARAKU, H. YILMAZ, *Anal. Sci.* **2002**, 18, 1285–1286.
- [326] W. Shi, R. Kelting, M. Shafaei-Fallah, A. Rothenberger, *J. Organomet. Chem.* **2007**, 692, 2678–2682.
- [327] M. D. Santana, G. García, C. M. Navarro, A. Abel Lozano, J. Pérez, L. García, G. López, *Polyhedron* **2002**, 21, 1935–1942.
- [328] Y. Özcan, S. Ide, M. Karakuş, H. Yilmaz, *Acta Crystallogr. Sect. C Cryst. Struct. Commun.* **2002**, 58, m388–m389.
- [329] E. Alberti, G. A. Ardizzoia, S. Brenna, F. Castelli, S. Galli, A. Maspero, *Polyhedron* **2007**, 26, 958–966.
- [330] M. C. Aragoni, M. Arca, S. L. Coles, F. A. Devillanova, M. B. Hursthouse, F. Isaia, V. Lippolis, *Dalt. Trans.* **2012**, 41, 6611–6613.
- [331] M. C. Aragoni, M. Arca, M. Crespo, F. A. Devillanova, M. B. Hursthouse, S. L. Huth, F. Isaia, V. Lippolis, G. Verani, *CrystEngComm* **2007**, 9, 873–878.
- [332] E. G. Sağlam, E. Bulat, C. T. Zeyrek, H. Dal, T. Hökelek, *J. Mol. Struct.* **2019**, 1178, 112–125.
- [333] M. Arca, A. Cornia, F. A. Devillanova, A. C. Fabretti, F. Isaia, V. Lippolis, G. Verani, *Inorganica Chim. Acta* **1997**, 262, 81–84.

- [334] M. Karakus, P. Lönnecke, E. Hey-Hawkins, *Zeitschrift für Anorg. und Allg. Chemie* **2004**, *630*, 1249–1252.
- [335] T. J. Ajayi, M. N. Pillay, W. E. van Zyl, *Phosphorus, Sulfur Silicon Relat. Elem.* **2017**, *192*, 1205–1211.
- [336] M. C. Aragoni, M. Arca, F. Demartin, F. A. Devillanova, C. Grai, F. Isaia, V. Lippolis, A. Tiripicchio, G. Verani, *J. Chem. Soc. Dalton Trans.* **2001**, 2671–2677.
- [337] M. Karakus, I. Kara, Ö. Çelik, I. Orujalipoor, S. İde, H. Yilmaz, *J. Mol. Struct.* **2018**, *1163*, 128–136.
- [338] A. A. E. Saadat, A., Banaee, A., McArdle, P., Zare, K., Gholivand, K., Valmoozi, *J. Chem. Sci.* **2014**, *126*, 1125–1133.
- [339] M. C. Aragoni, M. Arca, F. Demartin, F. A. Devillanova, C. Graiff, F. Isaia, V. Lippolis, A. Tiripicchio, G. Verani, *Eur. J. Inorg. Chem.* **2000**, *2000*, 2239–2244.
- [340] M. C. Aragoni, M. Arca, F. A. Devillanova, M. B. Hursthouse, S. L. Huth, F. Isaia, V. Lippolis, A. Mancini, S. Soddu, G. Verani, *Dalt. Trans.* **2007**, 2127–2134.
- [341] V. G. Albano, M. C. Aragoni, M. Arca, C. Castellari, F. Demartin, F. A. Devillanova, F. Isaia, V. Lippolis, L. Loddo, G. Verani, *Chem. Commun.* **2002**, *11*, 1170–1171.
- [342] M. C. Aragoni, M. Arca, M. Crespo, F. A. Devillanova, M. B. Hursthouse, S. L. Huth, F. Isaia, V. Lippolis, G. Verani, *Dalt. Trans.* **2009**, 2510–2520.
- [343] W. Shi, M. Shafaei-Fallah, C. E. Anson, A. Rothenberger, *Dalt. Trans.* **2005**, 3909–3912.
- [344] E. G. Sałlam, A. Ebinç, C. T. Zeyrek, H. Ünver, T. Hökelek, *J. Mol. Struct.* **2015**, *1099*, 490–501.
- [345] S. Sewpersad, W. E. Van Zyl, *Acta Crystallogr. Sect. E Struct. Reports Online* **2012**, *68*, m1457–m1457.
- [346] S. Sewpersad, B. Omondi, W. E. Van Zyl, *Acta Crystallogr. Sect. E Struct. Reports Online* **2012**, *68*, m1483–m1483.
- [347] A. Maspero, I. Kani, A. A. Mohamed, M. A. Omary, R. J. Staples, J. P. Fackler, *Inorg. Chem.* **2003**, *42*, 5311–5319.
- [348] W. E. Van Zyl, R. J. Staples, J. P. Fackler, *Inorg. Chem. Commun.* **1998**, *1*, 51–54.
- [349] M. N. Pillay, B. Omondi, R. J. Staples, W. E. Van Zyl, *CrystEngComm* **2013**, *15*, 4417–4421.
- [350] I. Haiduc, G. Mezei, R. Micu-Semeniuc, F. T. Edelmann, A. Fischer, *Zeitschrift für Anorg. und Allg. Chemie* **2006**, *632*, 295–300.
- [351] R. F. Semeniuc, R. R. Baum, J. J. Veach, K. A. Wheeler, P. J. Pellechia, *Inorganica*

- Chim. Acta* **2013**, *400*, 228–238.
- [352] W. E. van Zyl, *Comments Inorg. Chem.* **2010**, *31*, 13–45.
- [353] N. R. M. Crawford, C. Schrodt, A. Rothenberger, W. Shi, R. Ahlrichs, *Chem. - A Eur. J.* **2008**, *14*, 319–324.
- [354] D. Sun, Z. H. Wei, C. F. Yang, N. Zhang, R. Bin Huang, L. S. Zheng, *Inorg. Chem. Commun.* **2010**, *13*, 1191–1194.
- [355] D. Sun, R. Bin Huang, *Acta Crystallogr. Sect. C Cryst. Struct. Commun.* **2011**, *67*, m315–m317.
- [356] H. H. Murray, G. Garzón, R. G. Raptis, A. M. Mazany, L. C. Porter, J. P. Fackler, *Inorg. Chem.* **1988**, *27*, 836–842.
- [357] W. Shi, R. Ahlrichs, C. E. Anson, A. Rothenberger, C. Schrodt, M. Shafaei-Fallah, *Chem. Commun.* **2005**, 5893–5895.
- [358] W. Shi, A. Rothenberger, *Eur. J. Inorg. Chem.* **2005**, *2005*, 2935–2937.
- [359] W. E. Van Zyl, J. M. López-De-Luzuriaga, A. A. Mohamed, R. J. Staples, J. P. Fackler, *Inorg. Chem.* **2002**, *41*, 4579–4589.
- [360] M. N. Pillay, J. H. Liao, C. W. Liu, W. E. Van Zyl, *Inorg. Chem.* **2019**, *58*, 7099–7106.
- [361] ‘CAGLIARI 142 - C₂₉H₃₄Cd₁N₂O₄P₂S₄ - eCrystals - University of Southampton’, can be found under <http://ecrystals.chem.soton.ac.uk/248/>, **n.d.**
- [362] ‘CAGLIARI 154a - C₂₈H₃₂N₂O₄P₂S₄Zn₁ - eCrystals - University of Southampton’, can be found under <http://ecrystals.chem.soton.ac.uk/238/>, **n.d.**
- [363] ‘CAGLIARI 161 - C₂₈H₃₂Cd₁N₂O₄P₂S₄ - eCrystals - University of Southampton’, can be found under <http://ecrystals.chem.soton.ac.uk/235/>, **n.d.**
- [364] A. Banaei, A. Saadat, P. McArdle, M. Mohammad Goli, *Phosphorus, Sulfur Silicon Relat. Elem.* **2018**, *193*, 369–374.
- [365] S. Blaurock, F. T. Edelman, I. Haiduc, G. Mezei, P. Poremba, *Inorganica Chim. Acta* **2008**, *361*, 407–410.
- [366] M. Karakus, H. Yilmaz, E. Bulak, P. Lönnecke, *Appl. Organomet. Chem.* **2005**, *19*, 396–397.
- [367] S. Sewpersad, W. E. Van Zyl, *Acta Crystallogr. Sect. E Struct. Reports Online* **2012**, *68*, m1488–m1489.
- [368] ‘CAGLIARI 144a - C₂₈H₃₂Cd₁N₂O₄P₂S₄ - eCrystals - University of Southampton’, can be found under <http://ecrystals.chem.soton.ac.uk/246/>, **n.d.**
- [369] ‘CAGLIARI 145 - C₂₈H₃₀Cd₁N₂O₄P₂S₄ - eCrystals - University of Southampton’, can be found under <http://ecrystals.chem.soton.ac.uk/245/>, **n.d.**

- [370] M. Karakus, H. Yilmaz, Y. Ozcan, S. Ide, *Appl. Organomet. Chem.* **2004**, *18*, 141–142.
- [371] A. Banaei, A. Saadat, M. Mohammad Goli, P. McArdle, E. Pourbasheer, P. Pargolghasemi, *Heteroat. Chem.* **2016**, *27*, 353–360.
- [372] ‘CAGLIARI 137a - C₃₆H₄₈Hg₂O₈P₄S₈ - eCrystals - University of Southampton’, can be found under <http://ecrystals.chem.soton.ac.uk/250/>, **n.d.**
- [373] ‘CAGLIARI 141 - C₃₆H₄₈Hg₂O₈P₄S₈ - eCrystals - University of Southampton’, can be found under <http://ecrystals.chem.soton.ac.uk/249/>, **n.d.**
- [374] M. C. Aragoni, M. Arca, F. Demartin, F. A. Devillanova, C. Graiff, F. Isaia, V. Lippolis, A. Tiripicchio, G. Verani, *Eur. J. Inorg. Chem.* **2000**, *2000*, 2239–2244.
- [375] W. Shi, M. Shafaei-Fallah, C. E. Anson, A. Rothenberger, *Dalt. Trans.* **2006**, 3257.
- [376] A. Lemmerer, S. Govindraju, M. Johnston, X. Motloun, K. L. Savig, *CrystEngComm* **2015**, *17*, 3591–3595.
- [377] A. J. Cruz-Cabeza, *CrystEngComm* **2012**, *14*, 6362–6365.
- [378] P. Liao, B. W. Langloss, A. M. Johnson, E. R. Knudsen, F. S. Tham, R. R. Julian, R. J. Hooley, *Chem. Commun.* **2010**, *46*, 4932–4934.
- [379] L. Xu, X. Shen, Z. Zhou, T. He, J. Zhang, H. Qiu, M. L. Saha, S. Yin, P. J. Stang, *J. Am. Chem. Soc.* **2018**, *140*, 16920–16924.
- [380] K. J. Kilpin, M. L. Gower, S. G. Telfer, G. B. Jameson, J. D. Crowley, *Inorg. Chem.* **2011**, *50*, 1123–1134.
- [381] D. P. August, G. S. Nichol, P. J. Lusby, *Angew. Chemie Int. Ed.* **2016**, *55*, 15022–15026.
- [382] N. Schultheiss, J. Ellsworth, E. Bosch, C. Barnes, *Eur. J. Inorg. Chem.* **2005**, *2005*, 45–46.
- [383] K. J. Kilpin, M. L. Gower, S. G. Telfer, G. B. Jameson, J. D. Crowley, *Inorg. Chem.* **2011**, *50*, 1123–1134.
- [384] S. Shanmugaraju, A. K. Bar, S. A. Joshi, Y. P. Patil, P. S. Mukherjee, *Organometallics* **2011**, *30*, 1951–1960.
- [385] B. Jiang, J. Zhang, J. Q. Ma, W. Zheng, L. J. Chen, B. Sun, C. Li, B. W. Hu, H. Tan, X. Li, et al., *J. Am. Chem. Soc.* **2016**, *138*, 738–741.
- [386] S. Shanmugaraju, A. K. Bar, H. Jadhav, D. Moon, P. S. Mukherjee, *Dalt. Trans.* **2013**, *42*, 2998–3008.
- [387] A. M. S. Riel, D. A. Decato, O. B. Berryman, *Cryst. Growth Des.* **2016**, *16*, 974–980.
- [388] K. Uehara, T. Oishi, T. Hirose, N. Mizuno, *Inorg. Chem.* **2013**, *52*, 11200–11209.
- [389] H.-L. Qian, C.-X. Yang, X.-P. Yan, *Nat. Commun.* **2016**, *7*, 12104.
- [390] J. Zhang, X. Han, X. Wu, Y. Liu, Y. Cui, *J. Am. Chem. Soc.* **2017**, *139*, 8277–8285.

- [391] X. Han, Q. Xia, J. Huang, Y. Liu, C. Tan, Y. Cui, *J. Am. Chem. Soc.* **2017**, *139*, 8693–8697.
- [392] E. Sheepwash, N. Luisier, M. R. Krause, S. Noé, S. Kubik, K. Severin, *Chem. Commun.* **2012**, *48*, 7808.
- [393] E. Sheepwash, V. Krampfl, R. Scopelliti, O. Sereda, A. Neels, K. Severin, *Angew. Chemie Int. Ed.* **2011**, *50*, 3034–3037.
- [394] N. Luisier, K. Bally, R. Scopelliti, F. T. Fadaei, K. Schenk, P. Pattison, E. Solari, K. Severin, *Cryst. Growth Des.* **2016**, *16*, 6600–6604.
- [395] K. S. Smaran, R. Badam, R. Vedarajan, N. Matsumi, *Front. Energy* **2019**, *13*, 163–171.
- [396] W. Liu, M. Pink, D. Lee, *J. Am. Chem. Soc.* **2009**, *131*, 8703–8707.
- [397] M. Gopalakrishnan, T. Viswanathan, E. David, K. Thirumoorthy, N. S. P. Bhuvanesh, N. Palanisami, *New J. Chem.* **2019**, *43*, 10948–10958.
- [398] D. A. Foucher, A. J. Lough, I. Manners, *Inorg. Chem.* **1992**, *31*, 3034–3043.
- [399] B. J. Brisdon, M. F. Mahon, K. C. Molloy, P. J. Schofield, *J. Organomet. Chem.* **1992**, *436*, 11–22.
- [400] G. Ferguson, S. E. Lawrence, L. A. Neville, B. J. O’Leary, T. R. Spalding, *Polyhedron* **2007**, *26*, 2482–2492.
- [401] K. Song, W. Ye, X. Gao, H. Fang, Y. Zhang, Q. Zhang, X. Li, S. Yang, H. Wei, Y. Ding, *Mater. Horizons* **2021**, DOI 10.1039/d0mh01142h.
- [402] E. N. Keyzer, A. Sava, T. K. Ronson, J. R. Nitschke, A. J. McConnell, *Chem. – A Eur. J.* **2018**, *24*, 12000–12005.
- [403] M. Crespo Alonso, M. Arca, F. Isaia, R. Lai, V. Lippolis, S. K. Callear, M. Caricato, D. Pasini, S. J. Coles, M. C. Aragoni, *CrystEngComm* **2014**, *16*, 8582–8590.
- [404] F. van Bolhuis, P. B. Koster, T. Migchelsen, *Acta Crystallogr.* **1967**, *23*, 90–91.
- [405] M.-P. Zhuo, J.-J. Wu, X.-D. Wang, Y.-C. Tao, Y. Yuan, L.-S. Liao, *Nat. Commun.* **2019**, *10*, DOI 10.1038/s41467-019-11731-7.
- [406] Y. V. Torubaev, I. V. Skabitsky, *CrystEngComm* **2019**, *21*, 7057–7068.
- [407] L. Flores, I. López Duarte, B. Gómez-Lor, E. Gutierrez-Puebla, G. Hennrich, *CrystEngComm* **2020**, *22*, 416–419.
- [408] Y. Huang, X. Zhang, W. Cui, X. Wang, B. Li, Y. Zhang, J. Yang, *New J. Chem.* **2019**, *44*, 614–625.
- [409] X.-H. Ding, Y.-Z. Chang, C.-J. Ou, J.-Y. Lin, L.-H. Xie, W. Huang, *Natl. Sci. Rev.* **2020**, DOI 10.1093/nsr/nwaa170.
- [410] H. Wang, W. J. Jin, *Acta Crystallogr. Sect. B Struct. Sci. Cryst. Eng. Mater.* **2017**, *73*,

210–216.

- [411] C. B. Aakeröy, T. K. Wijethunga, J. Desper, *J. Mol. Struct.* **2014**, *1072*, 20–27.
- [412] C. B. Aakeröy, M. Baldrighi, J. Desper, P. Metrangolo, G. Resnati, *Chem. - A Eur. J.* **2013**, *19*, 16240–16247.
- [413] M. Saccone, V. Dichiarante, A. Forni, A. Goulet-Hanssens, G. Cavallo, J. Vapaavuori, G. Terraneo, C. J. Barrett, G. Resnati, P. Metrangolo, et al., *J. Mater. Chem. C* **2015**, *3*, 759–768.
- [414] C. B. Aakeröy, C. L. Spartz, S. Dembowski, S. Dwyre, J. Desper, *IUCrJ* **2015**, *2*, 498–510.
- [415] L. J. McAllister, P. Carsten, J. P. W. Wong, R. J. Thatcher, A. C. Whitwood, B. Donnio, P. O'brien, P. B. Karadakov, D. W. Bruce, *Chem. Commun.* **2013**, *49*, 3946–3948.
- [416] S. S. Dos Santos, B. N. Cabral, U. Abram, E. S. Lang, *J. Organomet. Chem.* **2013**, *723*, 115–121.
- [417] V. N. Khrustalev, Z. V. Matsulevich, J. M. Lukyanova, R. R. Aysin, A. S. Peregudov, L. A. Leites, A. V. Borisov, *Eur. J. Inorg. Chem.* **2014**, *2014*, 3582–3586.
- [418] E. Faoro, G. Manzoni de Oliveira, E. Schulz Lang, *Zeitschrift für Anorg. und Allg. Chemie* **2006**, *632*, 2049–2052.
- [419] F. D. da Silva, C. A. D. P. Simões, S. S. dos Santos, E. S. Lang, *J. Organomet. Chem.* **2017**, *832*, 66–71.
- [420] S. S. dos Santos, E. Schulz Lang, G. Manzoni de Oliveira, *J. Organomet. Chem.* **2007**, *692*, 3081–3088.
- [421] G. A. Casagrande, C. Raminelli, E. S. Lang, S. D. S. Lemos, *Inorganica Chim. Acta* **2011**, *365*, 492–495.
- [422] Y. V. Torubaev, A. V. Pavlova, A. A. Pasynskii, A. Raghuvanshi, M. M. Shaikh, *Russ. J. Coord. Chem. Khimiya* **2015**, *41*, 638–643.
- [423] C. Peppe, M. D. A. Mello, T. A. Wioppiold, E. S. Lang, *J. Organomet. Chem.* **2012**, *718*, 52–56.
- [424] E. S. Lang, G. Manzoni de Oliveira, R. M. Fernandes, E. M. Vázquez-López, *Inorg. Chem. Commun.* **2003**, *6*, 869–872.
- [425] B. Liu, W.-L. Yu, Y.-H. Lai, W. Huang, *Chem. Mater.* **2001**, *13*, 1984–1991.
- [426] X. Guo, M. Baumgarten, K. Müllen, *Prog. Polym. Sci.* **2013**, *38*, 1832–1908.
- [427] M. Leclerc, *J. Polym. Sci. Part A Polym. Chem.* **2001**, *39*, 2867–2873.
- [428] U. Scherf, E. J. W. List, *Adv. Mater.* **2002**, *14*, 477–487.
- [429] W.-L. Yu, J. Pei, W. Huang, A. J. Heeger, *Adv. Mater.* **2000**, *12*, 828–831.

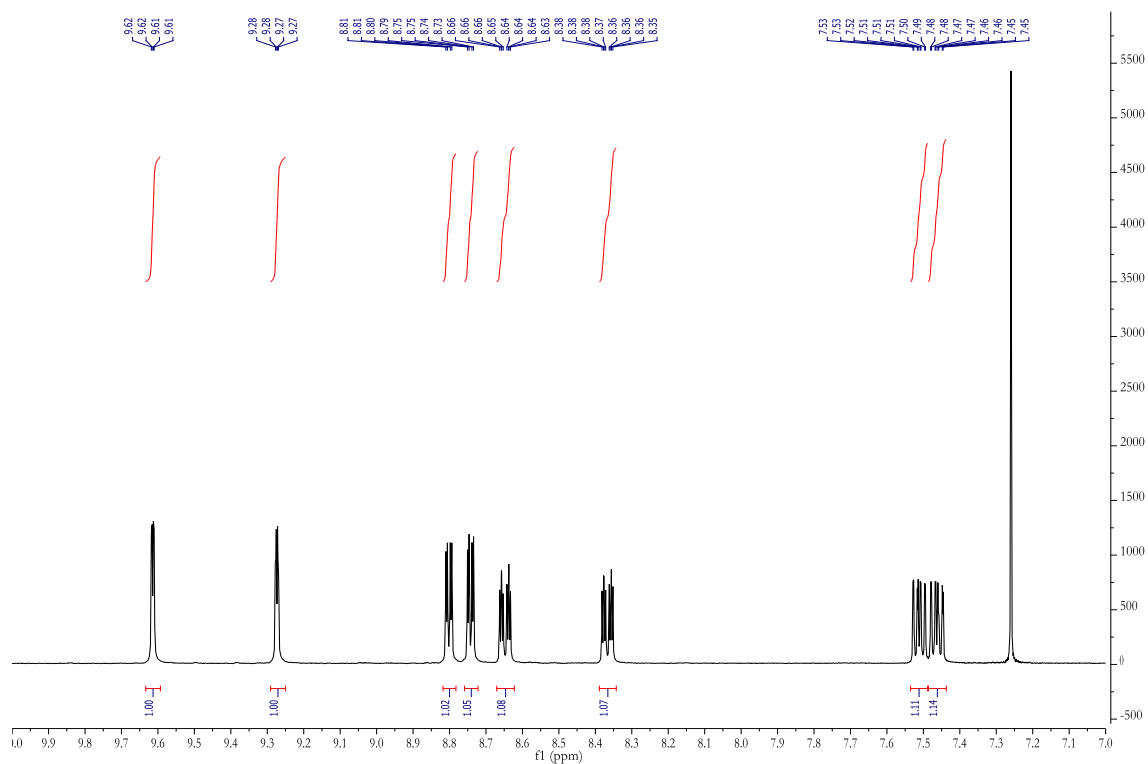
- [430] X. Gong, P. K. Iyer, D. Moses, G. C. Bazan, A. J. Heeger, S. S. Xiao, *Adv. Funct. Mater.* **2003**, *13*, 325–330.
- [431] D. Wang, M. V. Ivanov, D. Kokkin, J. Loman, J.-Z. Cai, S. A. Reid, R. Rathore, *Angew. Chemie Int. Ed.* **2018**, *57*, 8189–8193.
- [432] R. Rathore, S. H. Abdelwahed, I. A. Guzei, *J. Am. Chem. Soc.* **2003**, *125*, 8712–8713.
- [433] D. Kokkin, M. Ivanov, J. Loman, J. Z. Cai, B. Uhler, N. Reilly, R. Rathore, S. A. Reid, *J. Chem. Phys.* **2018**, *149*, DOI 10.1063/1.5044648.
- [434] H. Qi, J. Chang, S. H. Abdelwahed, K. Thakur, R. Rathore, A. J. Bard, *J. Am. Chem. Soc.* **2012**, *134*, 16265–16274.
- [435] B. Uhler, M. V. Ivanov, D. Kokkin, N. Reilly, R. Rathore, S. A. Reid, *J. Phys. Chem. C* **2017**, *121*, 15580–15588.
- [436] X. Duan, R. Lv, Z. Shi, C. Wang, H. Li, J. Ge, Z. Ji, Y. Yang, B. Li, G. Qian, *J. Solid State Chem.* **2019**, *277*, 159–162.
- [437] X. Duan, Q. Zhang, J. Cai, Y. Cui, C. Wu, Y. Yang, G. Qian, *Microporous Mesoporous Mater.* **2014**, *190*, 32–37.
- [438] H. J. Park, J. K. Jang, S.-Y. Kim, J.-W. Ha, D. Moon, I.-N. Kang, Y.-S. Bae, S. Kim, D.-H. Hwang, *Inorg. Chem.* **2017**, *56*, 12098–12101.
- [439] P. Wang, J. Xu, Q. D. Zhuo, Y. S. Ma, H. J. Cheng, X. Y. Tang, R. X. Yuan, *Inorg. Chem. Commun.* **2016**, *67*, 14–16.
- [440] J. P. Ma, Y. Yu, Y. Bin Dong, *Chem. Commun.* **2012**, *48*, 2946–2948.
- [441] Y. Hong, S. Sun, Q. Sun, E.-Q. Gao, M. Ye, *Mater. Chem. Phys.* **2020**, *243*, 122601.
- [442] Z. You, H. Li, L. Zhang, B. Yu, J. Zhang, X. Wu, *J. Phys. Chem. C* **2017**, *121*, 23072–23079.
- [443] S. Su, C. Qin, Z. Guo, H. Guo, S. Song, R. Deng, F. Cao, S. Wang, G. Li, H. Zhang, *CrystEngComm* **2011**, *13*, 2935–2941.
- [444] H. D. Guo, X. M. Guo, S. R. Batten, J. F. Song, S. Y. Song, S. Dang, G. L. Zheng, J. K. Tang, H. J. Zhang, *Cryst. Growth Des.* **2009**, *9*, 1394–1401.
- [445] F. Moreau, N. Audebrand, C. Poriel, *CrystEngComm* **2019**, *22*, 293–303.
- [446] T. Mocanu, L. Pop, N. D. Hădade, S. Shova, L. Sorace, I. Grosu, M. Andruh, *Eur. J. Inorg. Chem.* **2019**, *2019*, 5025–5038.
- [447] A. Karmakar, R. J. Sarma, J. B. Baruah, *Eur. J. Inorg. Chem.* **2007**, *2007*, 643–647.
- [448] J. Hudák, R. Boča, J. Moncol, J. Titiš, *Inorganica Chim. Acta* **2013**, *394*, 401–409.
- [449] R. J. Pakula, A. M. Martinez, E. A. Noten, C. F. Harris, J. F. Berry, *Polyhedron* **2019**, *161*, 93–103.

- [450] F. P. Pruchnik, U. Dawid, A. Kochel, *Polyhedron* **2006**, *25*, 3647–3652.
- [451] C. Sen Liu, J. J. Wang, L. F. Yan, Z. Chang, X. H. Bu, E. C. Sañudo, J. Ribas, *Inorg. Chem.* **2007**, *46*, 6299–6310.
- [452] X. L. Wang, Y. Q. Chen, G. C. Liu, H. Y. Lin, W. Y. Zheng, J. X. Zhang, *J. Organomet. Chem.* **2009**, *694*, 2263–2269.
- [453] C. S. Wu, B. S. Zhang, Y. X. Li, J. P. Qiu, *Zeitschrift für Krist. - New Cryst. Struct.* **2014**, *229*, 303–304.
- [454] C. O. Kienitz, C. Thöne, P. G. Jones, *Inorg. Chem.* **1996**, *35*, 3990–3997.
- [455] K. K. Bhasin, V. Arora, T. M. Klapötke, M.-J. Crawford, *Eur. J. Inorg. Chem.* **2004**, *2004*, 4781–4788.
- [456] ‘CrysAlis Pro | Rigaku Global Website’, can be found under <https://www.rigaku.com/products/crystallography/crysalis>, **n.d.**
- [457] ‘APEX3-PROTEUM3 Software | Bruker’, can be found under <https://www.bruker.com/en/products-and-solutions/diffractometers-and-scattering-systems/single-crystal-x-ray-diffractometers/sc-xrd-software/apex3-proteum3.html>, **n.d.**
- [458] G. M. Sheldrick, *Acta Crystallogr. Sect. A Found. Crystallogr.* **2015**, *71*, 3–8.
- [459] O. V. Dolomanov, L. J. Bourhis, R. J. Gildea, J. A. K. Howard, H. Puschmann, *J. Appl. Crystallogr.* **2009**, *42*, 339–341.
- [460] G. M. Sheldrick, *Acta Crystallogr. Sect. C Struct. Chem.* **2015**, *71*, 3–8.
- [461] W. Koch, M. C. Holthausen, *A Chemist’s Guide to Density Functional Theory*, Wiley-VCH, **2001**.
- [462] M. J. Frisch, G. W. Trucks, H. B. Schlegel, G. E. Scuseria, M. A. Robb, J. R. Cheeseman, G. Scalmani, V. Barone, G. A. Petersson, H. Nakatsuji, et al., *Gaussian 16, Rev. B.01, Wallingford, CT, 2016* **2016**, Wallingfor.
- [463] C. Adamo, V. Barone, *J. Chem. Phys.* **1998**, *108*, 664–675.
- [464] A. Schäfer, H. Horn, R. Ahlrichs, *J. Chem. Phys.* **1992**, *97*, 2571–2577.
- [465] F. Weigend, R. Ahlrichs, *Phys. Chem. Chem. Phys.* **2005**, *7*, 3297–3305.
- [466] K. L. Schuchardt, B. T. Didier, T. Elsethagen, L. Sun, V. Gurumoorthi, J. Chase, J. Li, T. L. Windus, *J. Chem. Inf. Model.* **2007**, *47*, 1045–1052.
- [467] R. D. Dennington, T. A. Keith, J. M. Millam, *Inc., Shawnee Mission KS* **2016**.
- [468] G. Schaftenaar, J. H. Noordik, *J. Comput. Aided. Mol. Des.* **2000**, *14*, 123–134.
- [469] L. V Skripnikov, **2017**.
- [470] W.-Y. Wong, G.-L. Lu, K.-H. Choi, Z. Lin, *European J. Org. Chem.* **2003**, *2003*, 365–

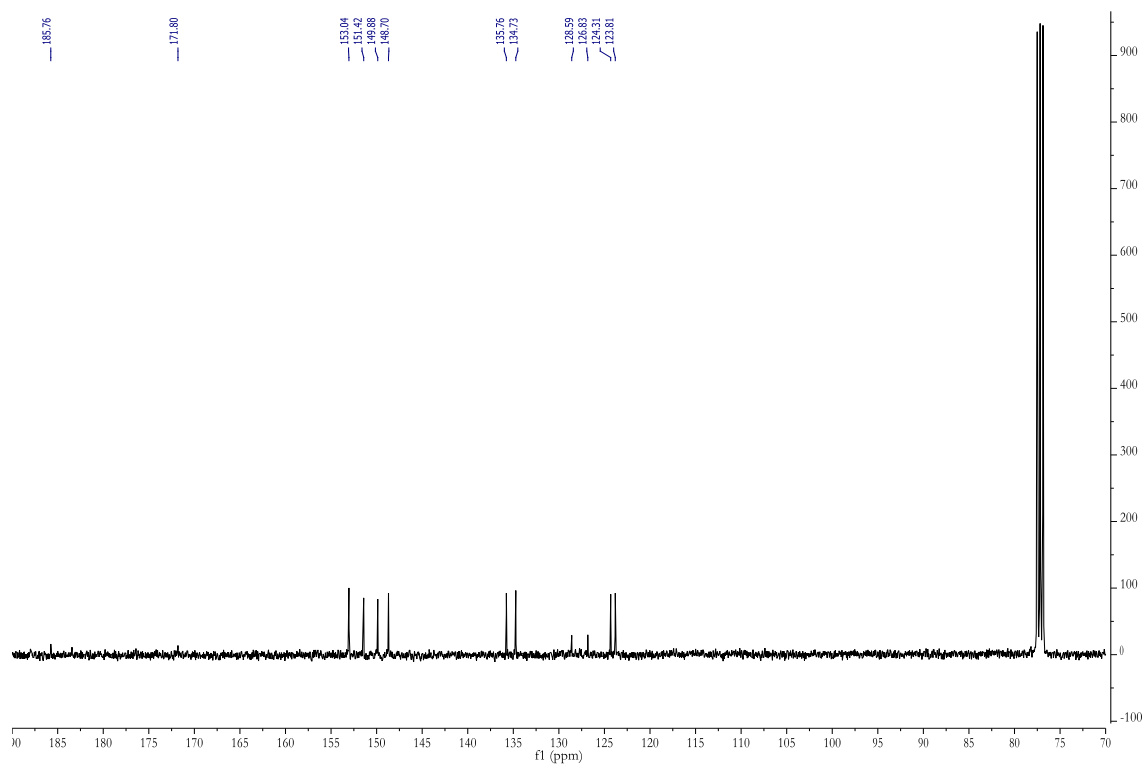
373.

Appendix 1: NMR spectra

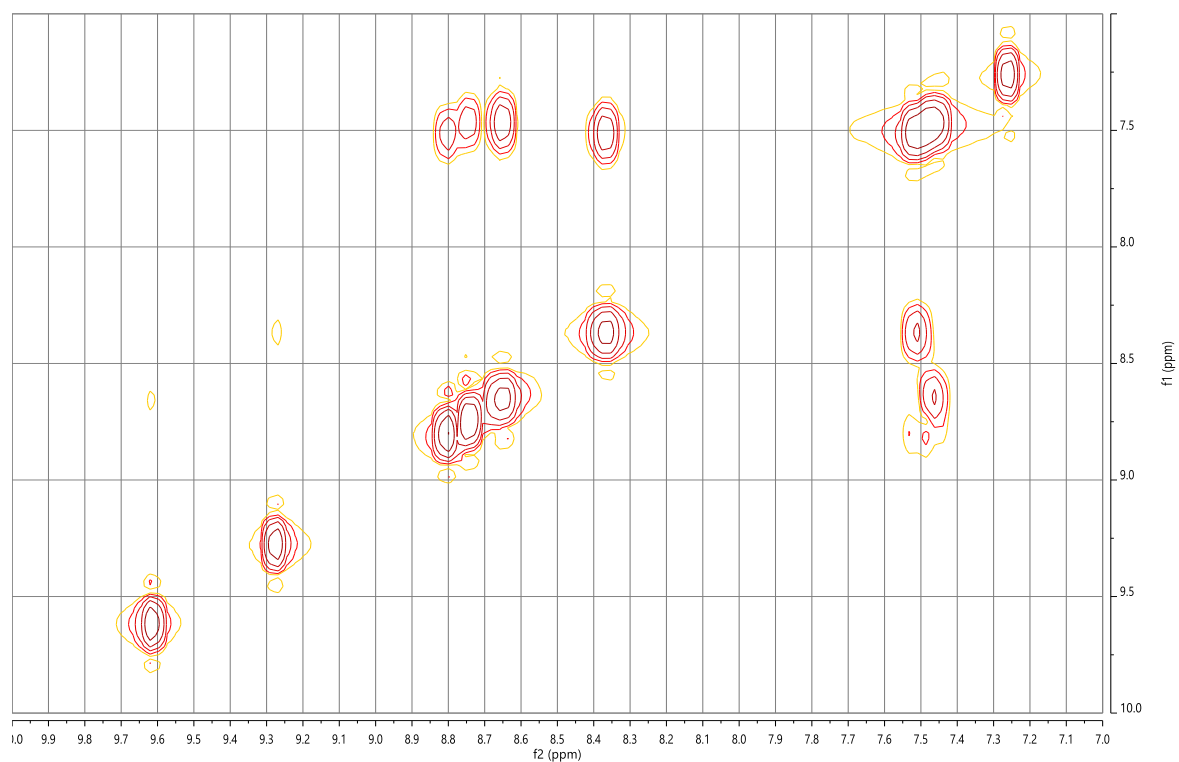
S1 ^1H -NMR (400 MHz, CDCl_3) of L1.



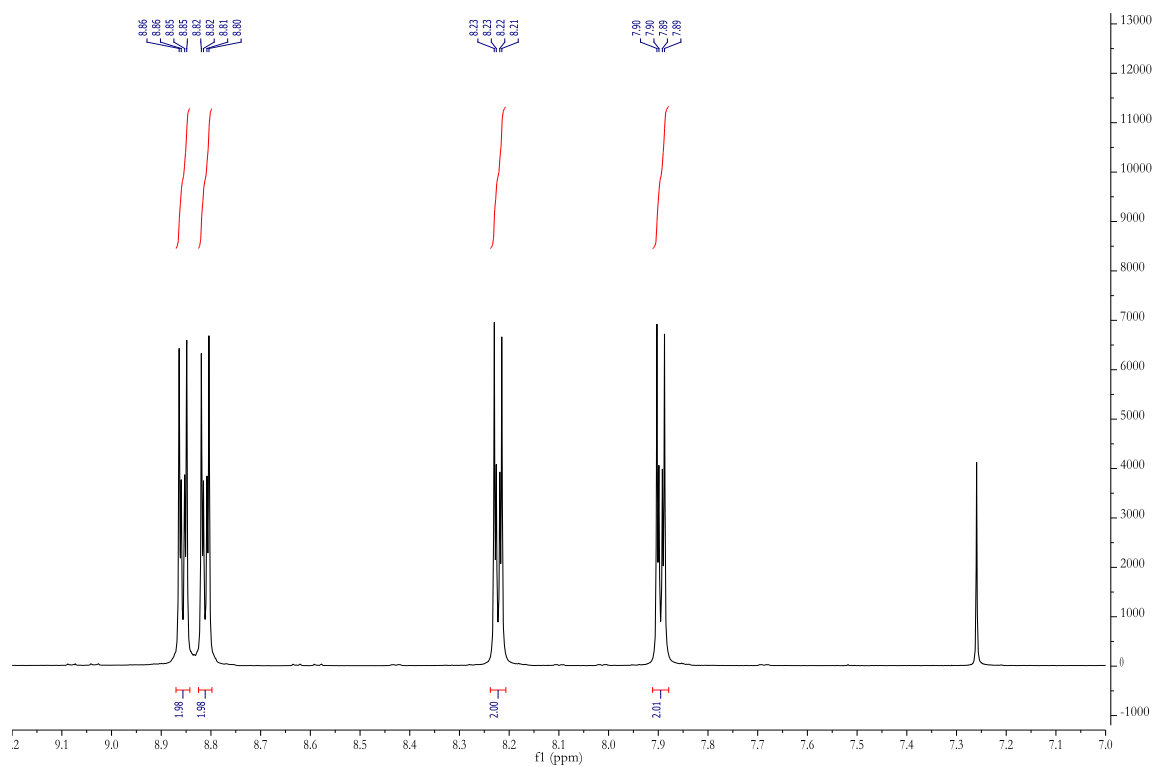
S2 $^{13}\text{C}\{^1\text{H}\}$ NMR (101 MHz, CDCl_3) of L1.



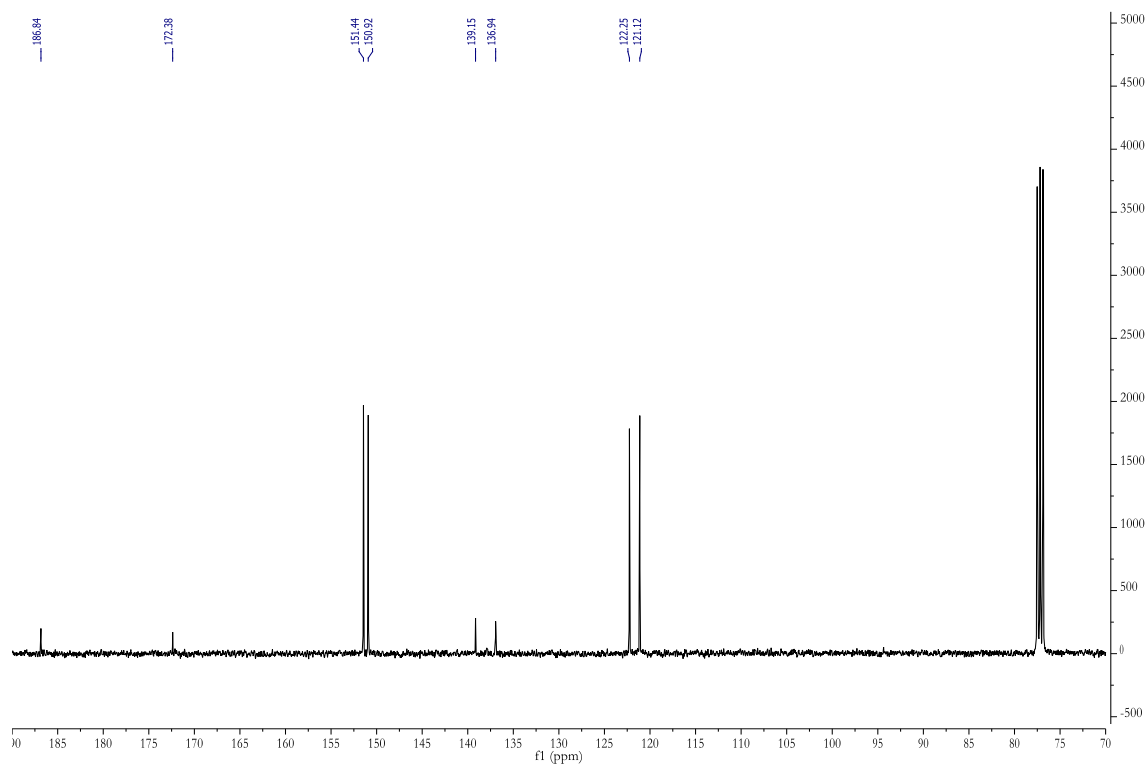
S3 ^1H - ^1H COSY NMR of **L1**.



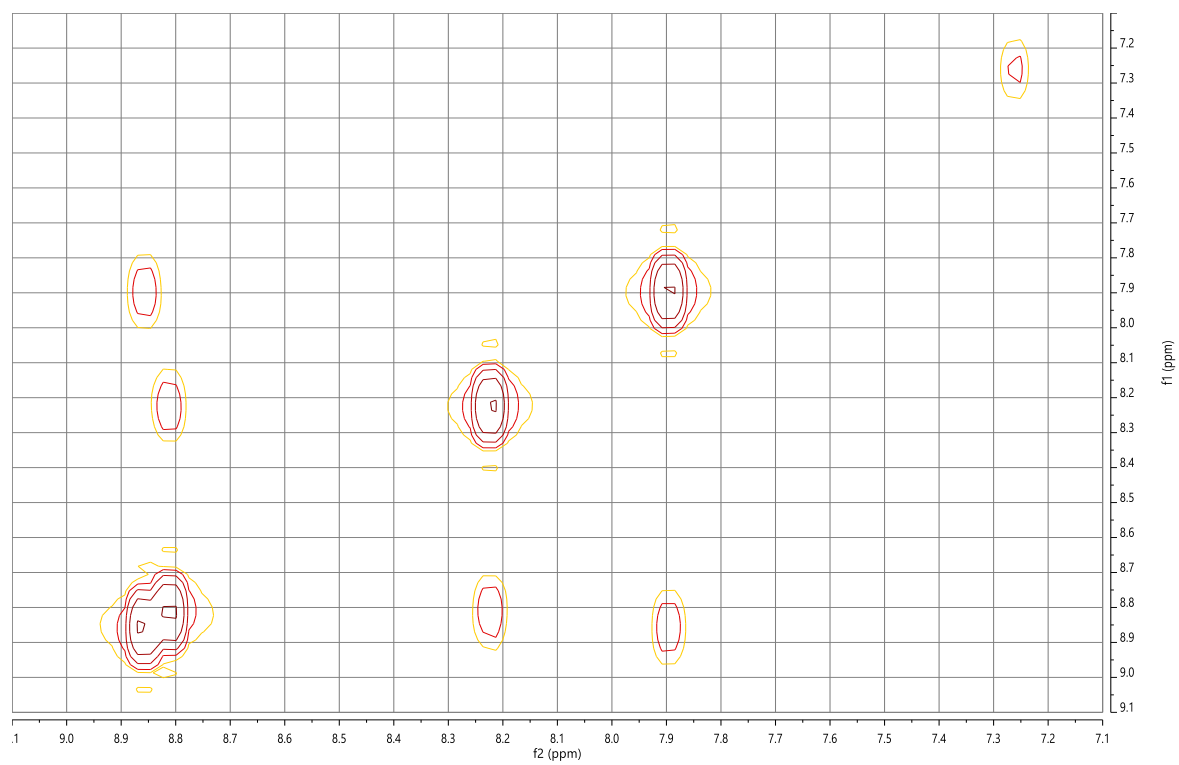
S4 ^1H -NMR (400 MHz, CDCl_3) of **L2**.



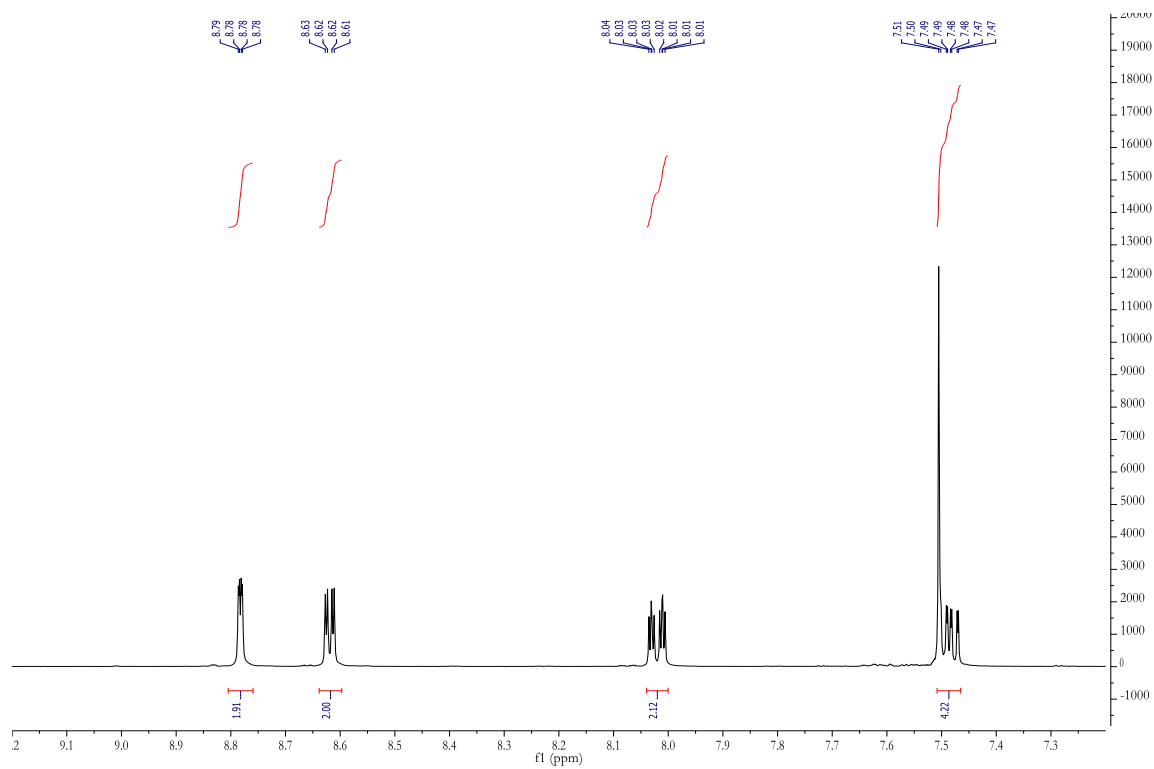
S5 $^{13}\text{C}\{^1\text{H}\}$ NMR (101 MHz, CDCl_3) of **L2**.



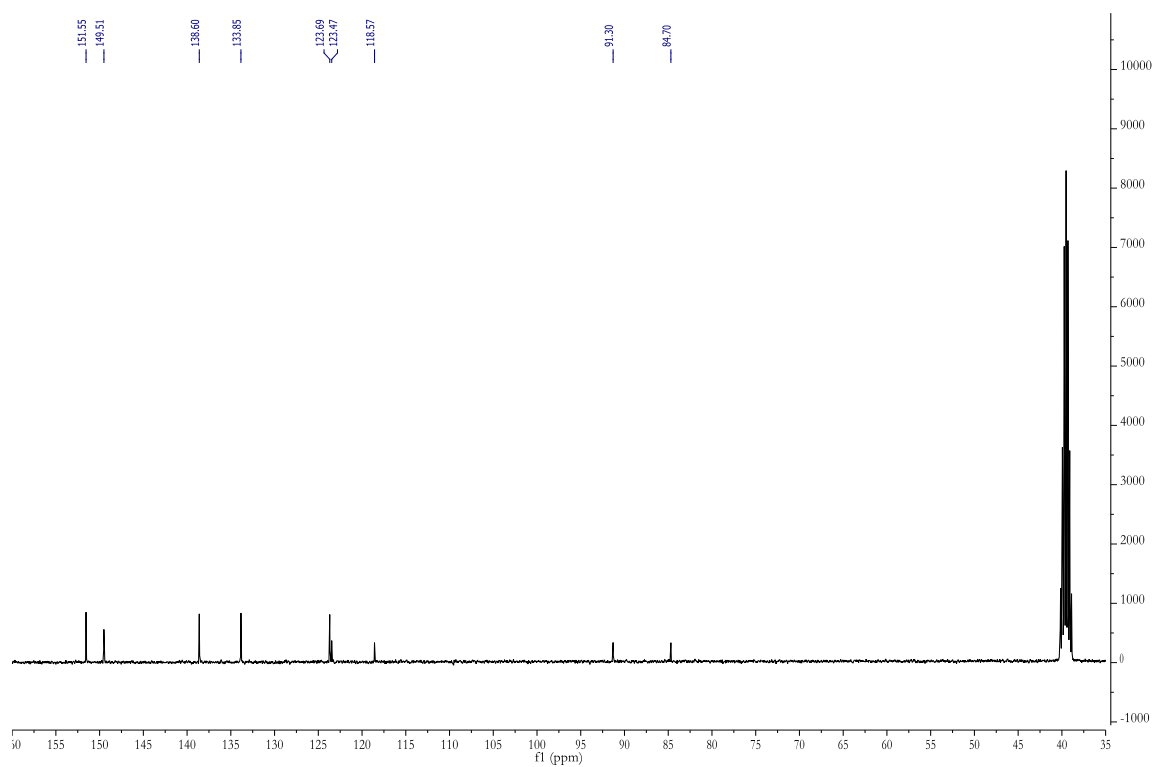
S6 ^1H - ^1H COSY NMR of **L2**.



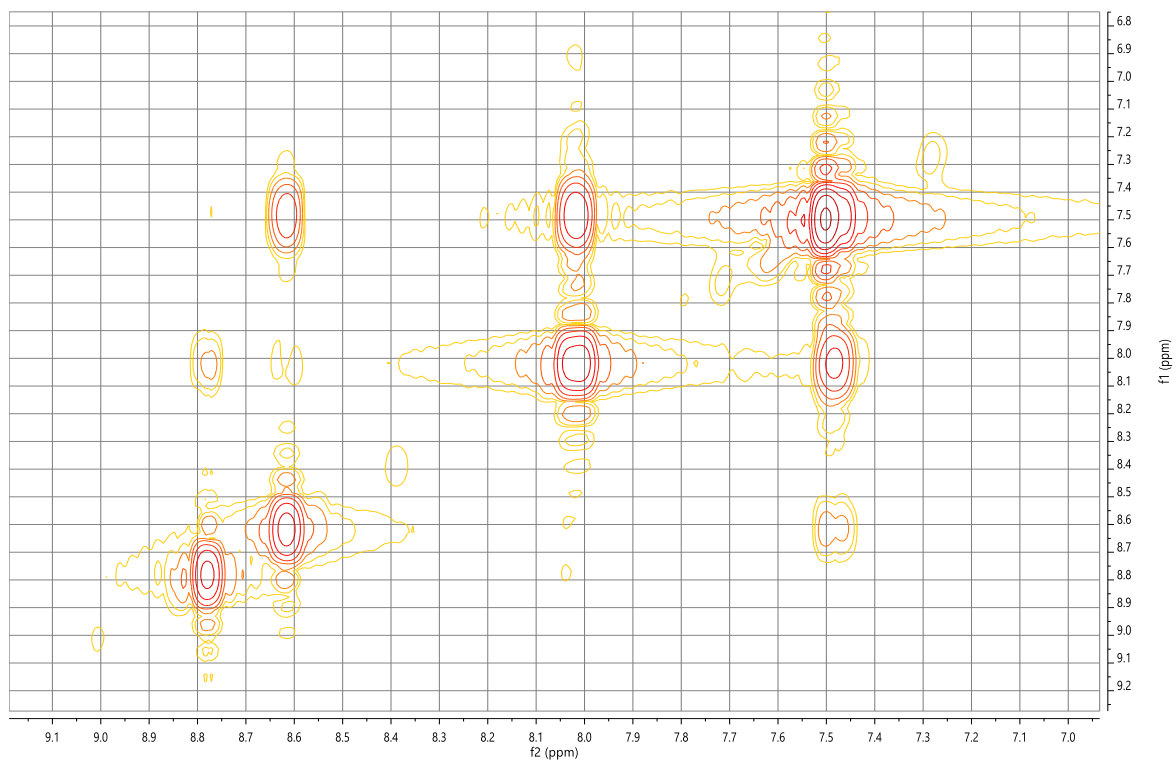
S7 $^1\text{H-NMR}$ (400 MHz, DMSO-d_6) of **L3**.



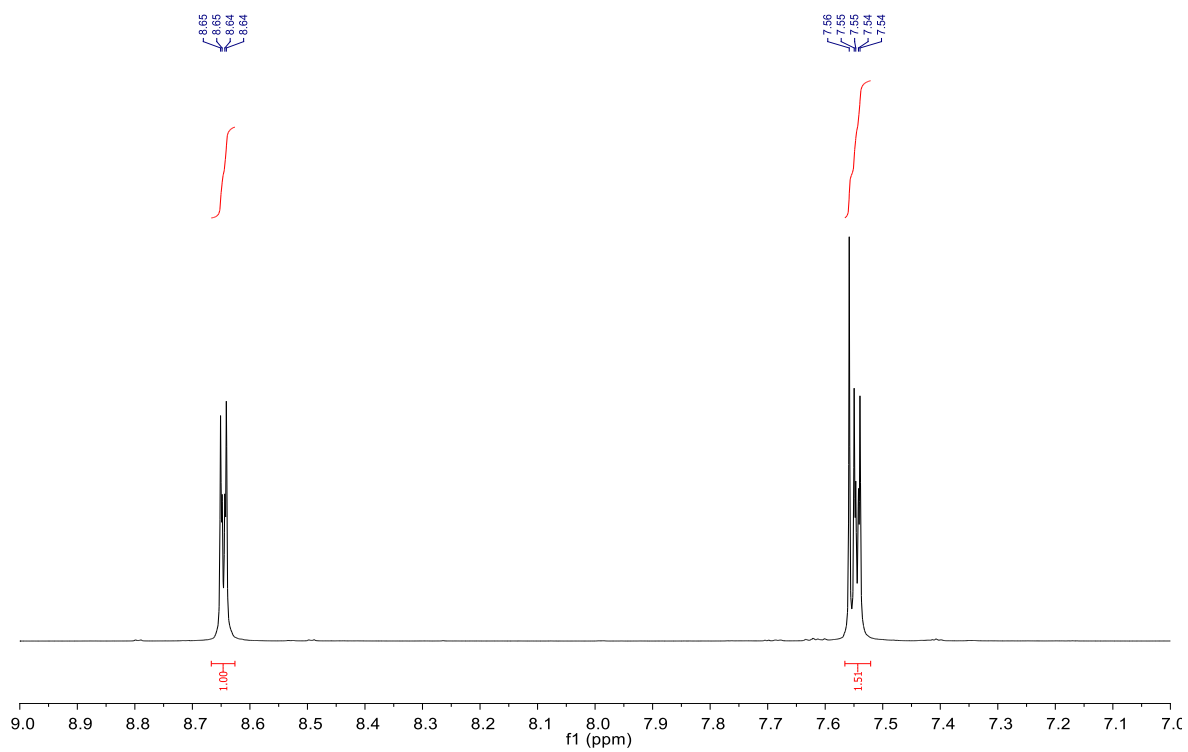
S8 $^{13}\text{C}\{^1\text{H}\}$ NMR (101 MHz, DMSO-d_6) of **L3**.



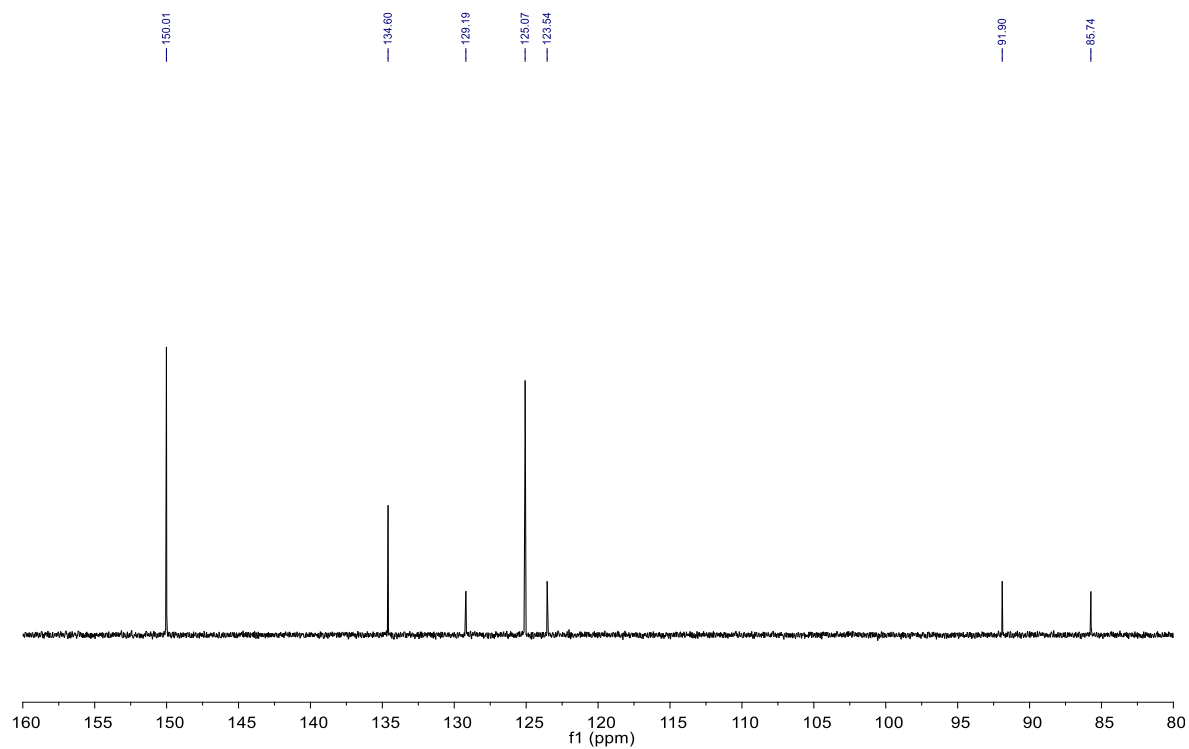
S9 ^1H - ^1H COSY NMR of **L3**.



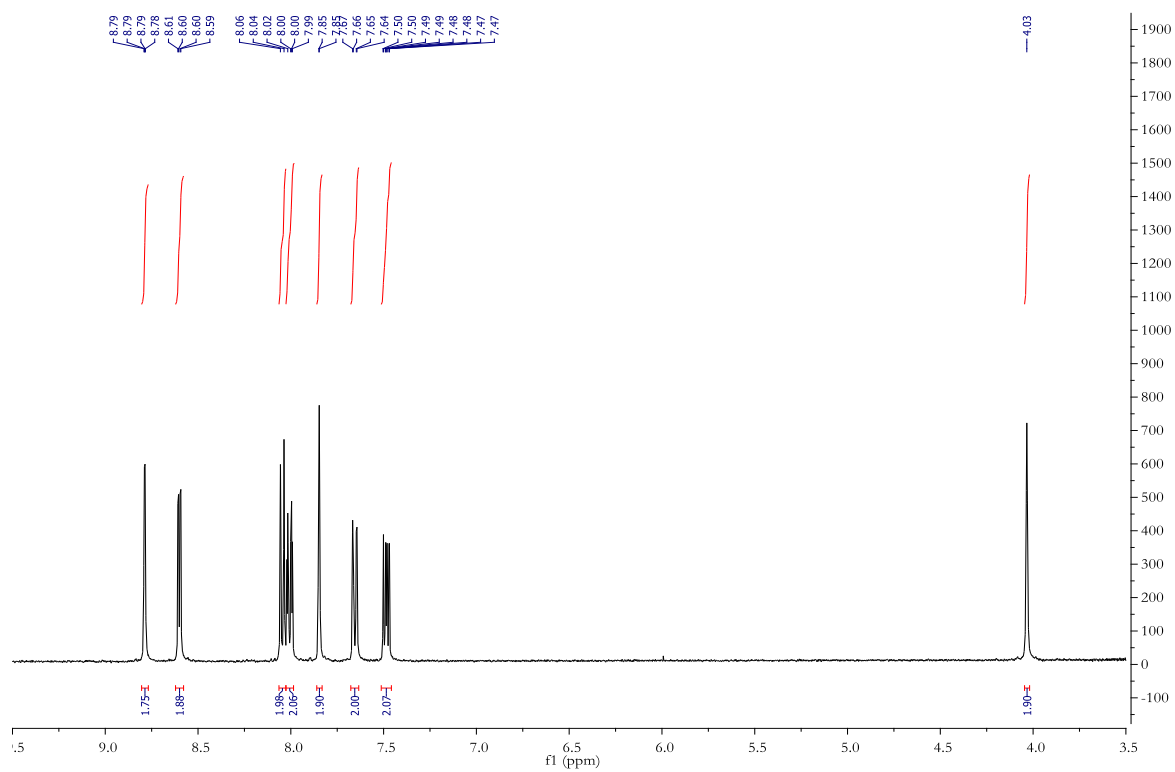
S10 ^1H NMR (600 MHz, DMSO- d_6) of **L4**.



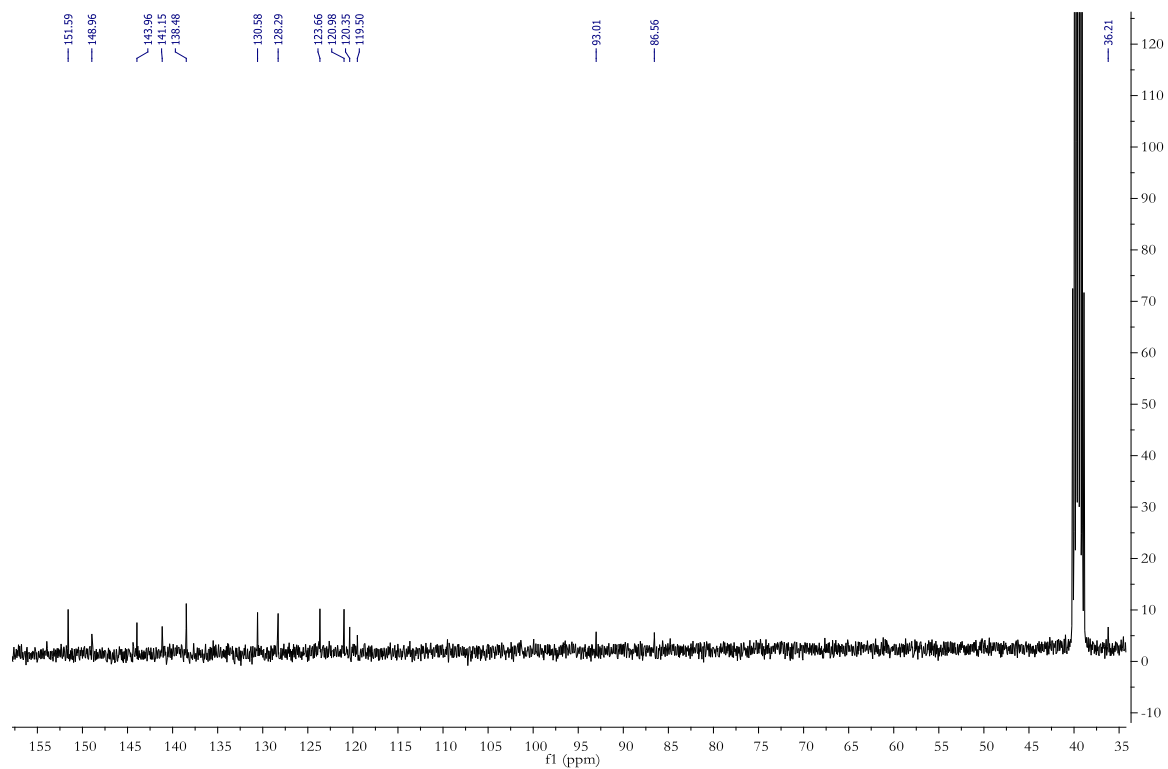
S11 $^{13}\text{C}\{^1\text{H}\}$ NMR (151 MHz, DMSO- d_6) of **L4**.



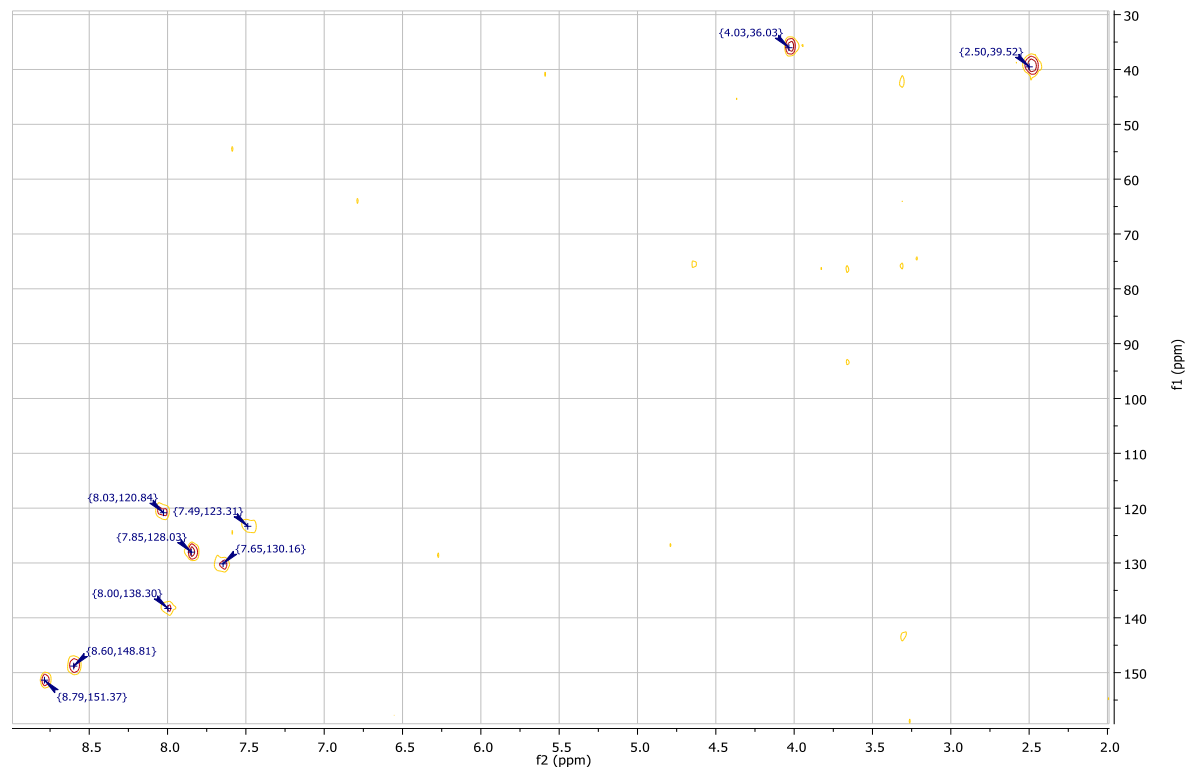
S12 ^1H -NMR (400 MHz, DMSO- d_6) of **L5**.



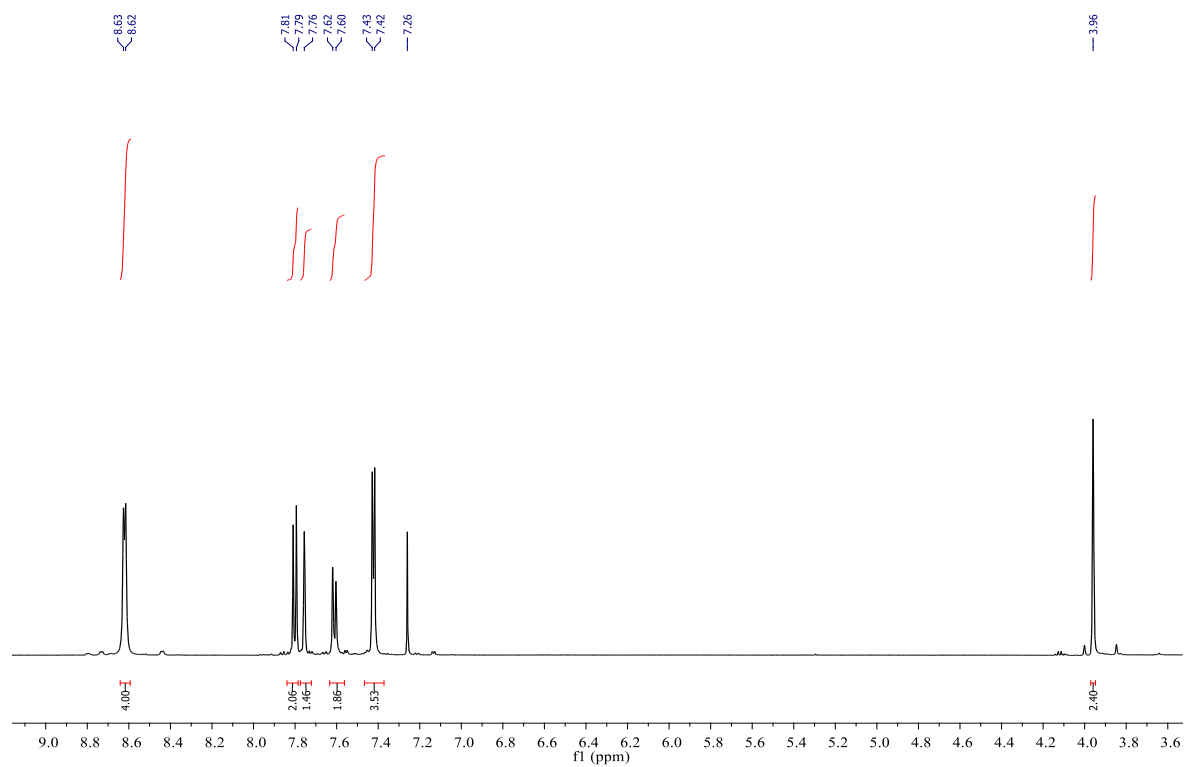
S13 $^{13}\text{C}\{^1\text{H}\}$ NMR (101 MHz, DMSO- d_6) of L5.



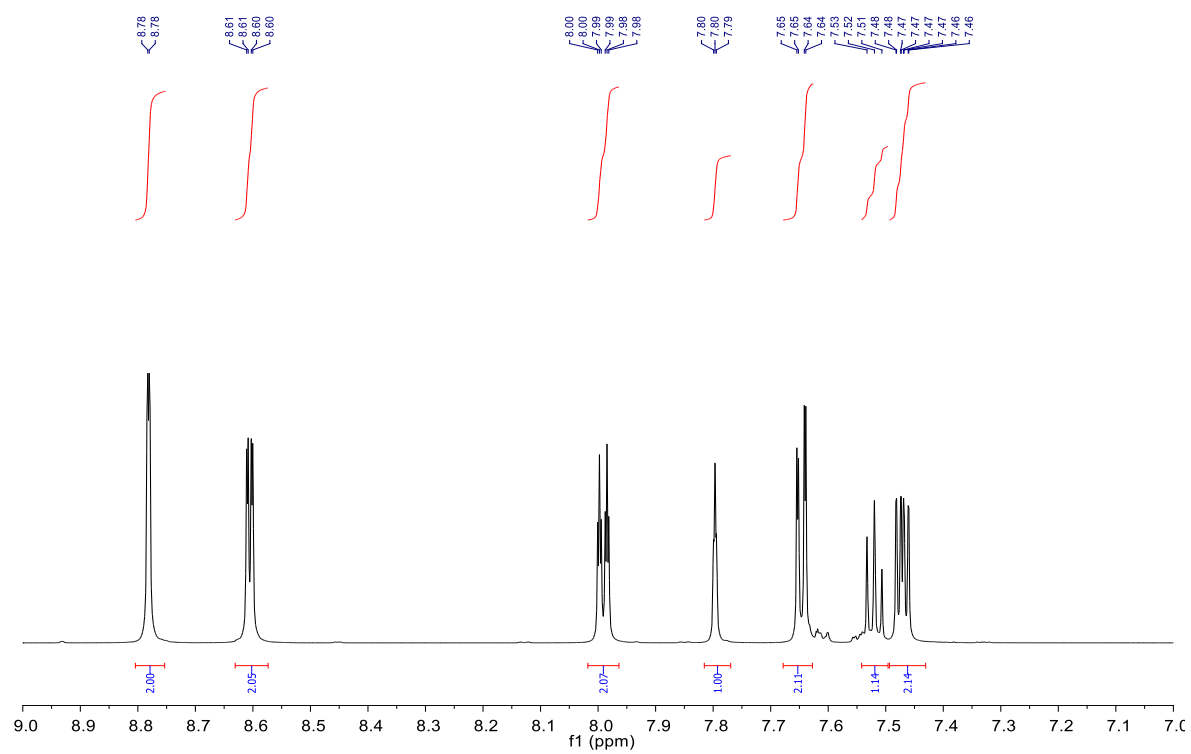
S14 ^1H - ^{13}C HMQC of L5.



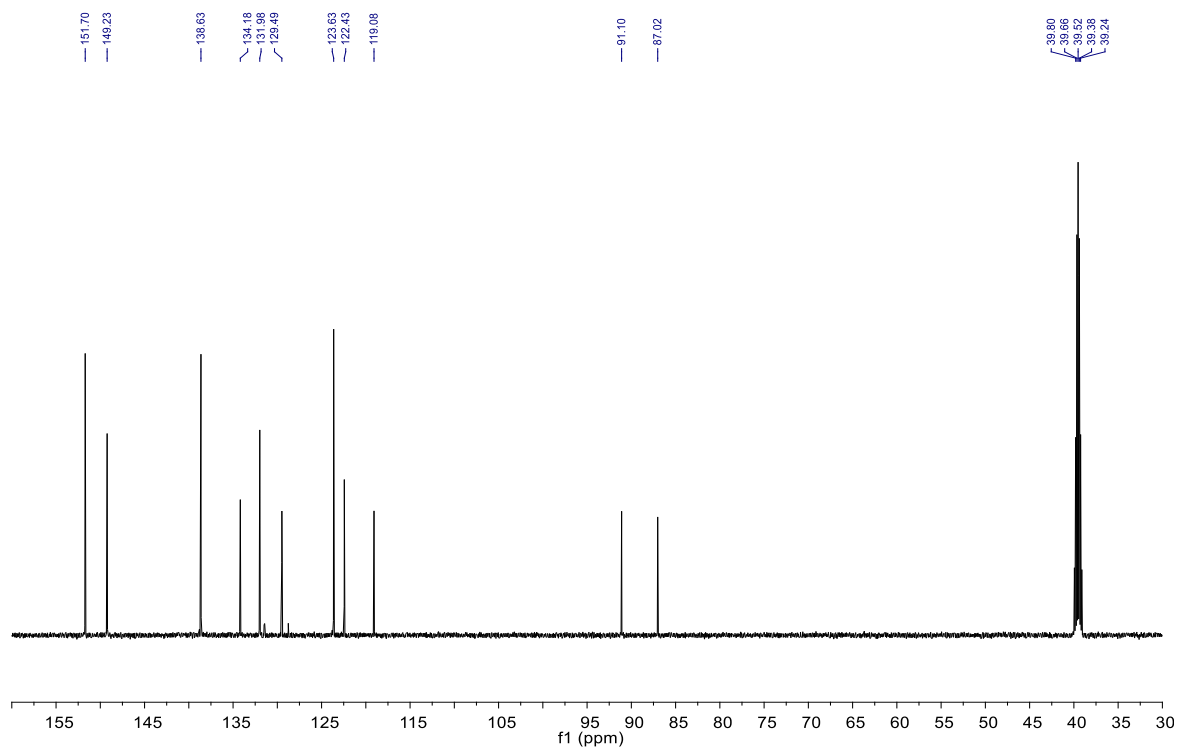
S15 $^1\text{H-NMR}$ (500 MHz, CDCl_3) of **L6**.



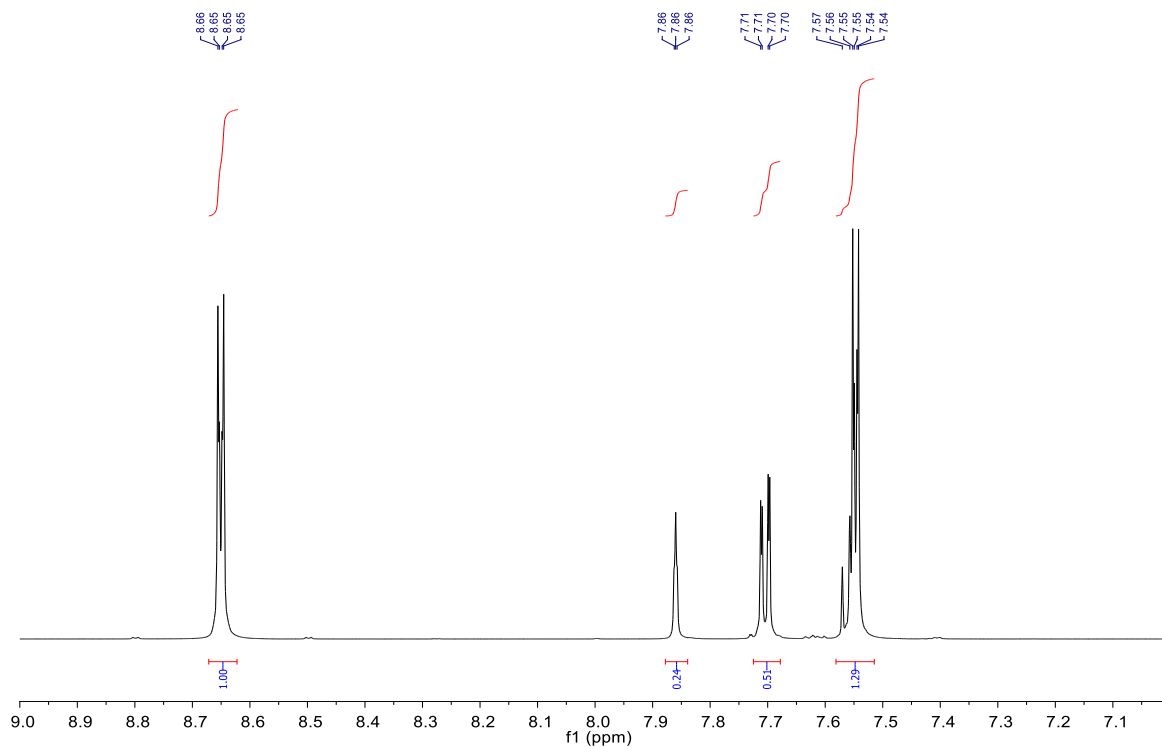
S16 $^1\text{H-NMR}$ (600 MHz, DMSO-d_6) of **L7**.



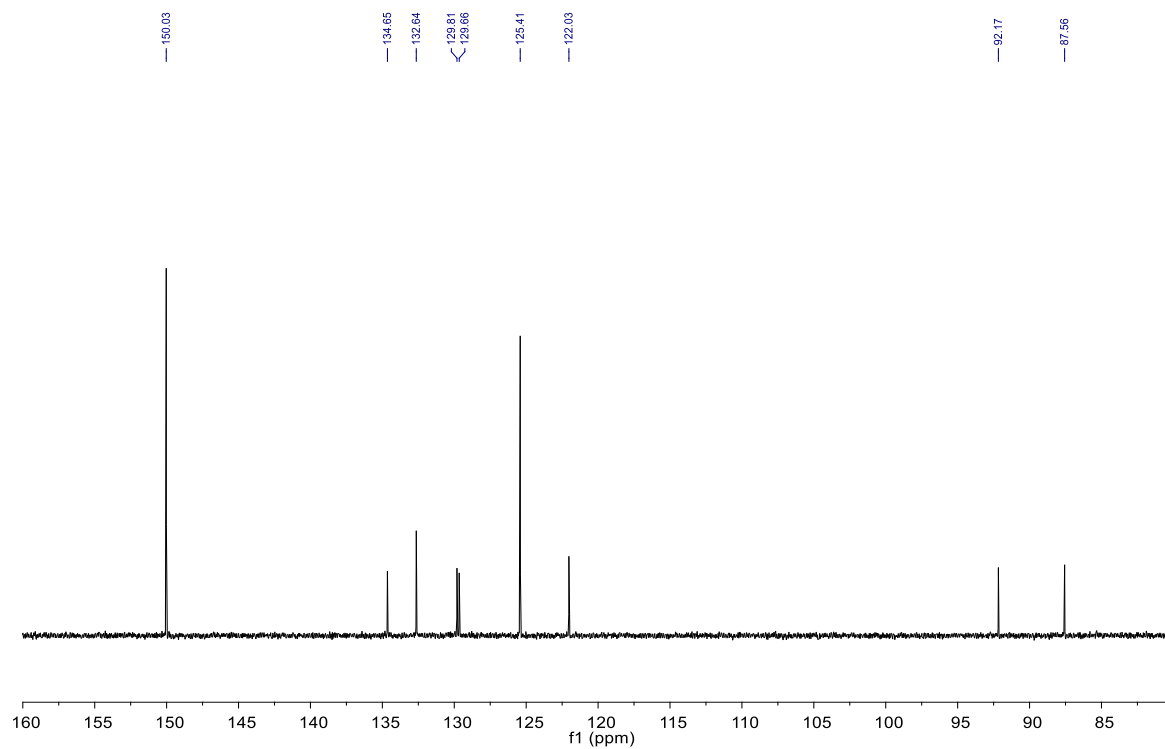
S17 $^{13}\text{C}\{^1\text{H}\}$ NMR (151 MHz, DMSO- d_6) of L7.



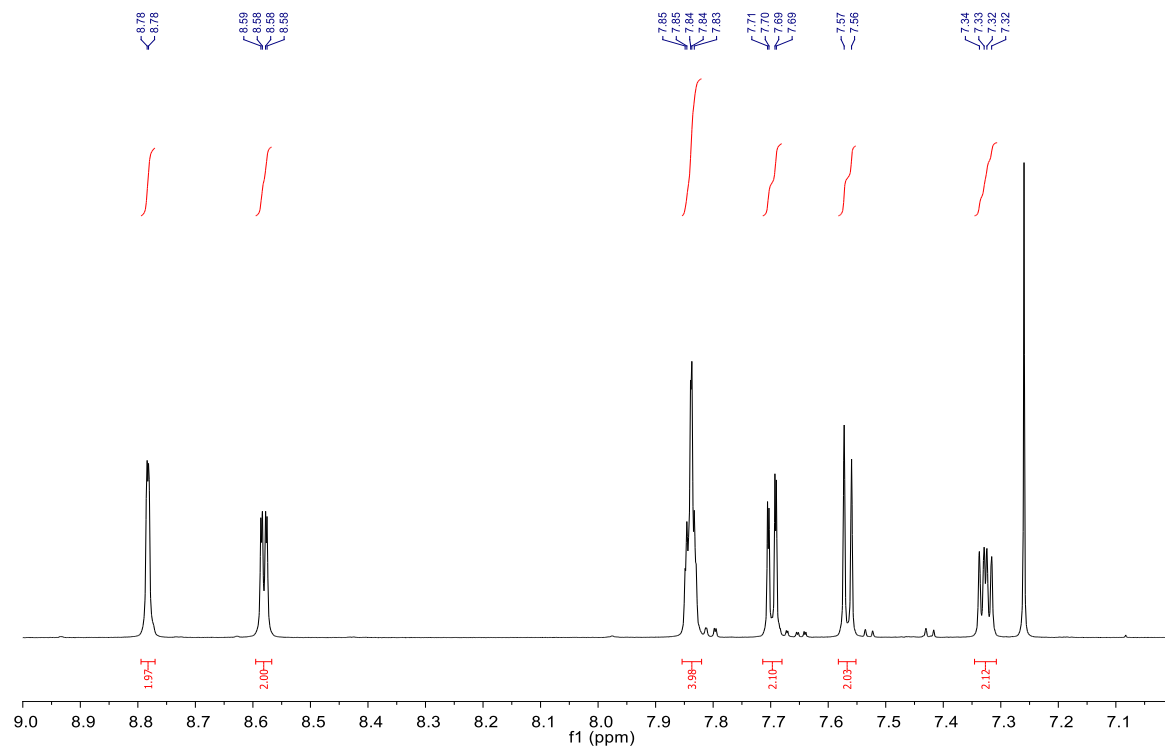
S18 ^1H NMR (600 MHz, DMSO- d_6) of L8.



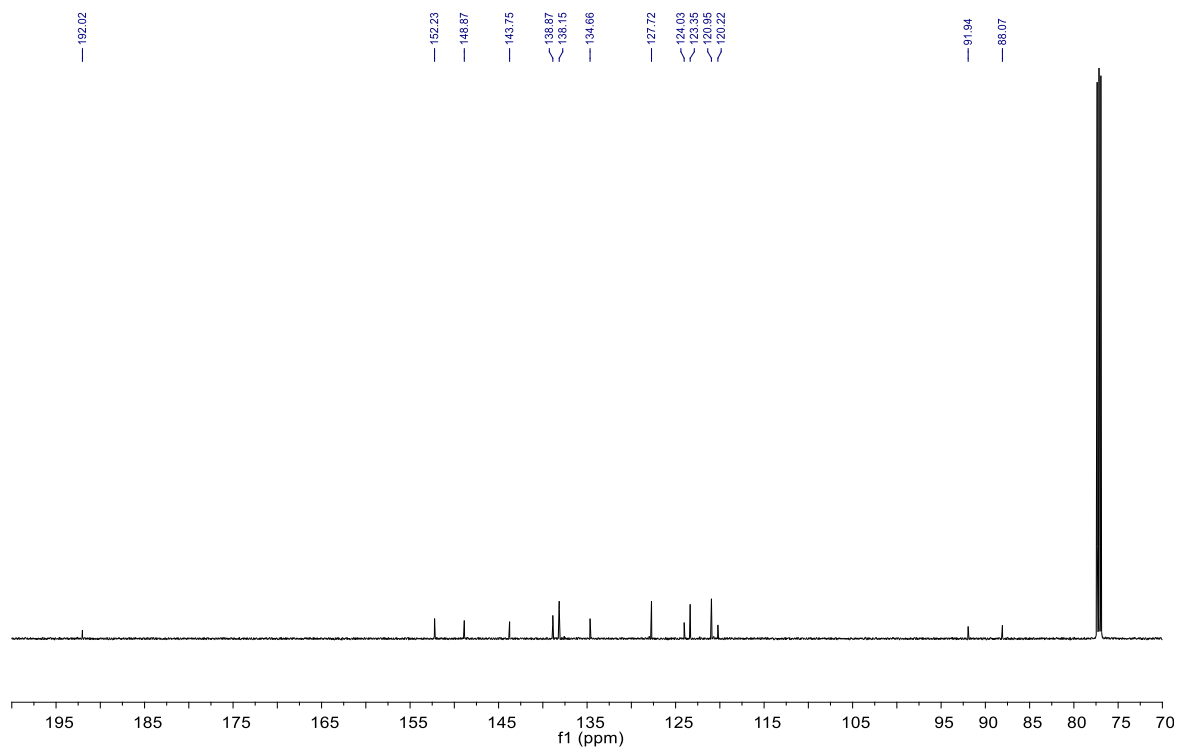
S19 $^{13}\text{C}\{^1\text{H}\}$ NMR (151 MHz, DMSO- d_6) of **L8**.



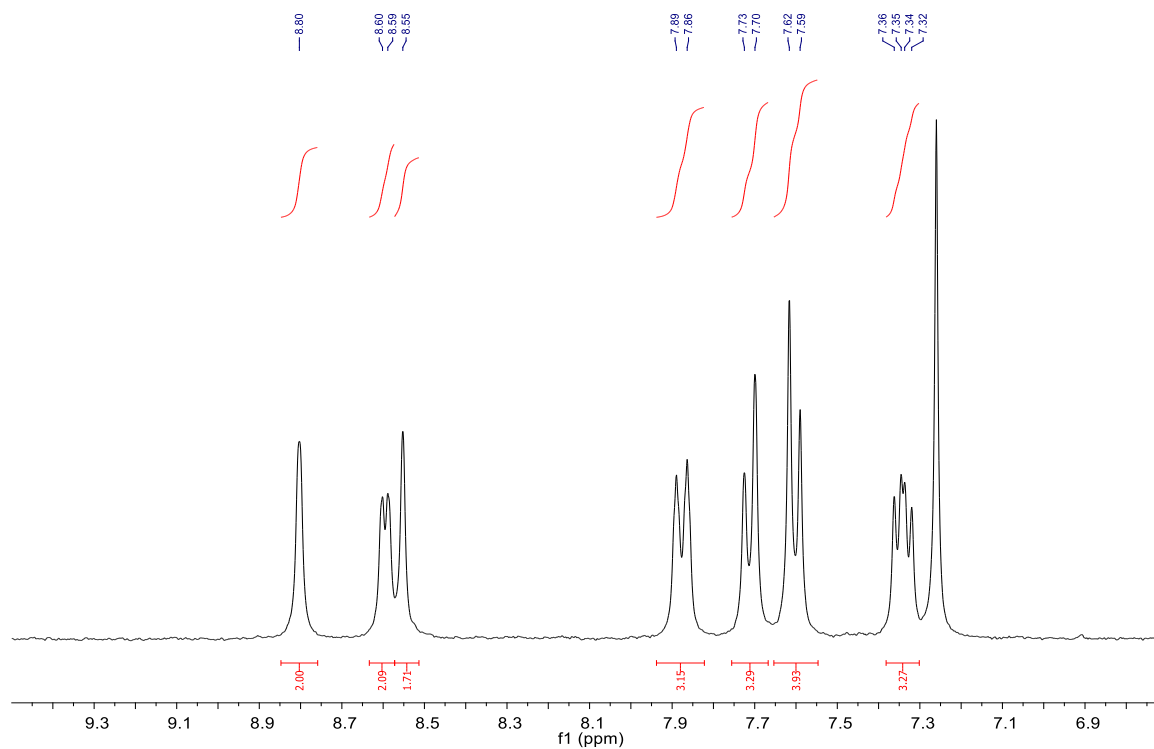
S20 ^1H NMR (600 MHz, CDCl_3) of **L9**.



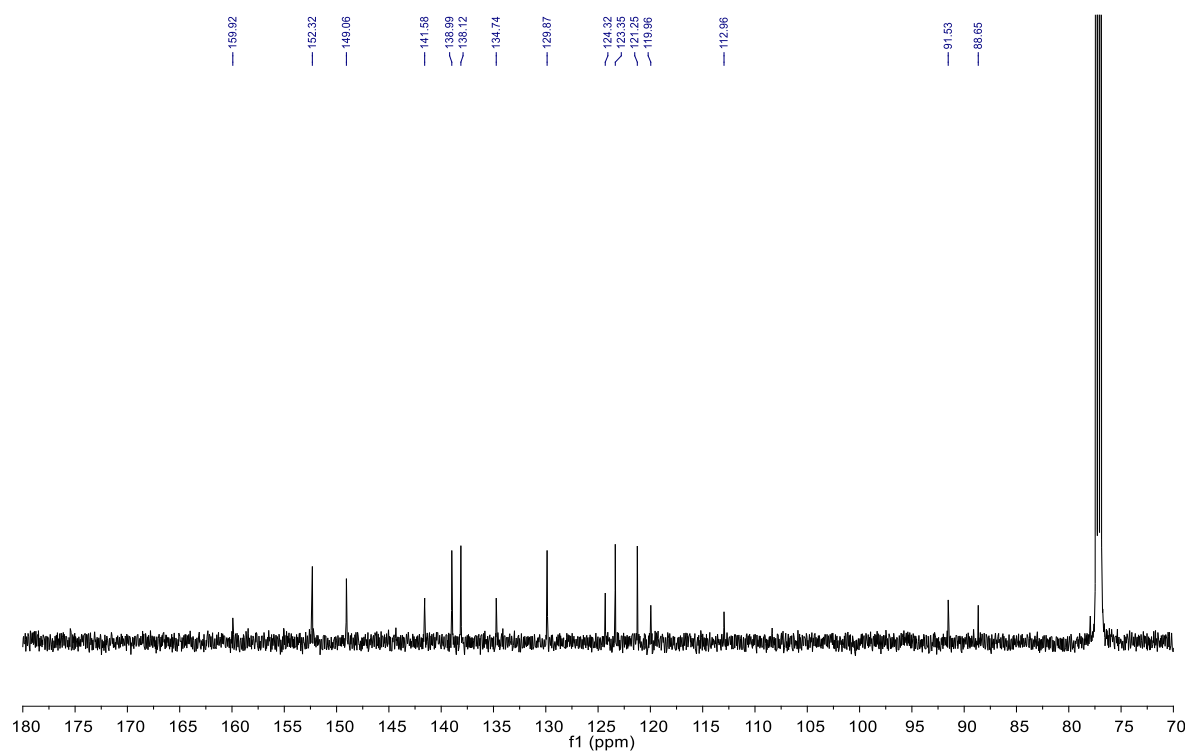
S21 $^{13}\text{C}\{^1\text{H}\}$ NMR (151 MHz, CDCl_3) of **L9**.



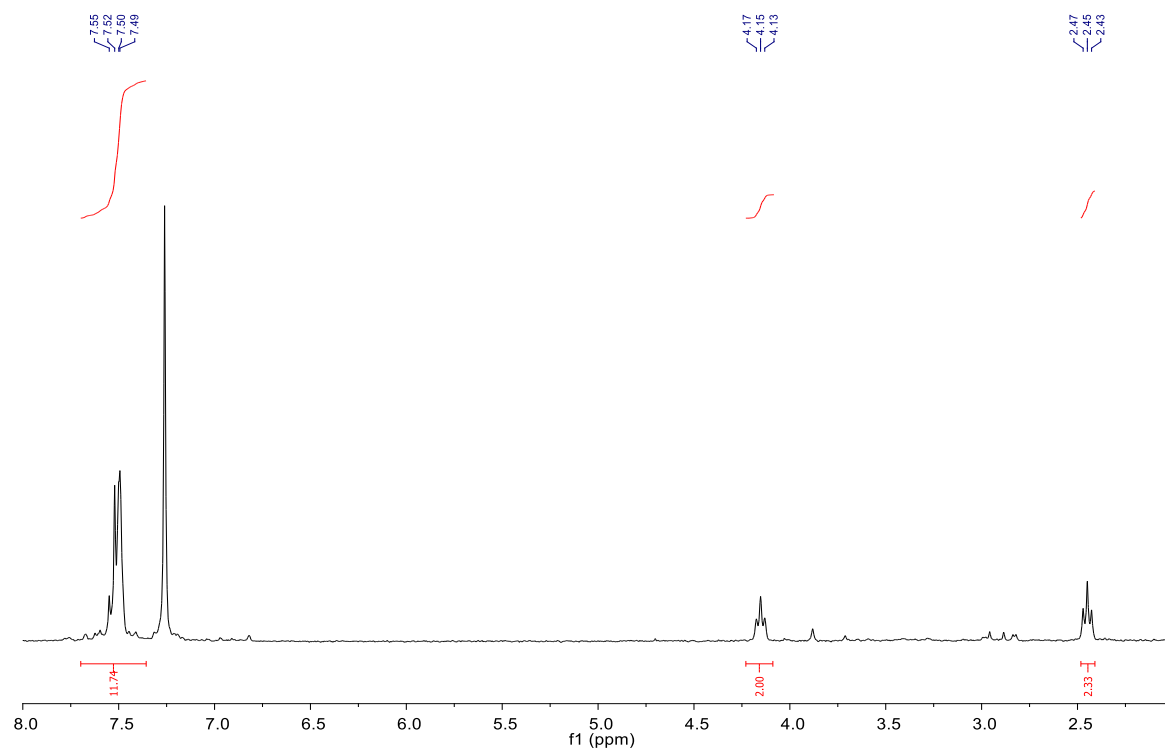
S22 ^1H NMR (300 MHz, CDCl_3) of **L11**.



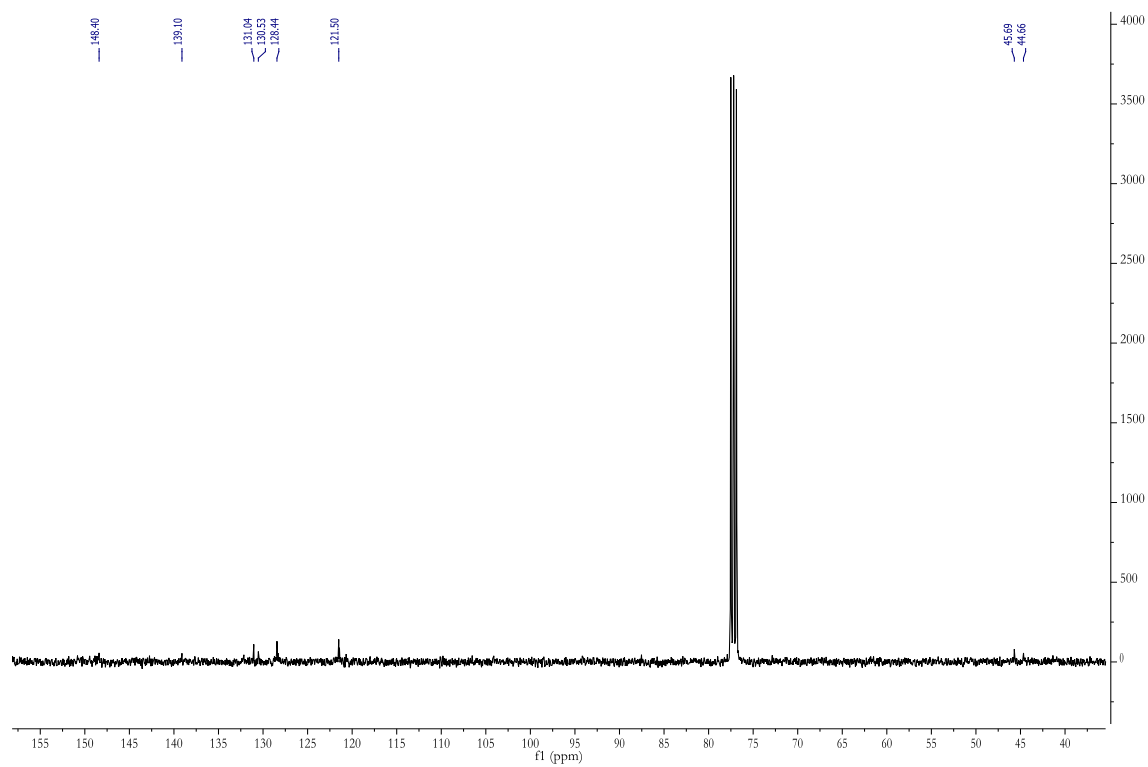
S23 $^{13}\text{C}\{^1\text{H}\}$ NMR (151 MHz, CDCl_3) of **L11**.



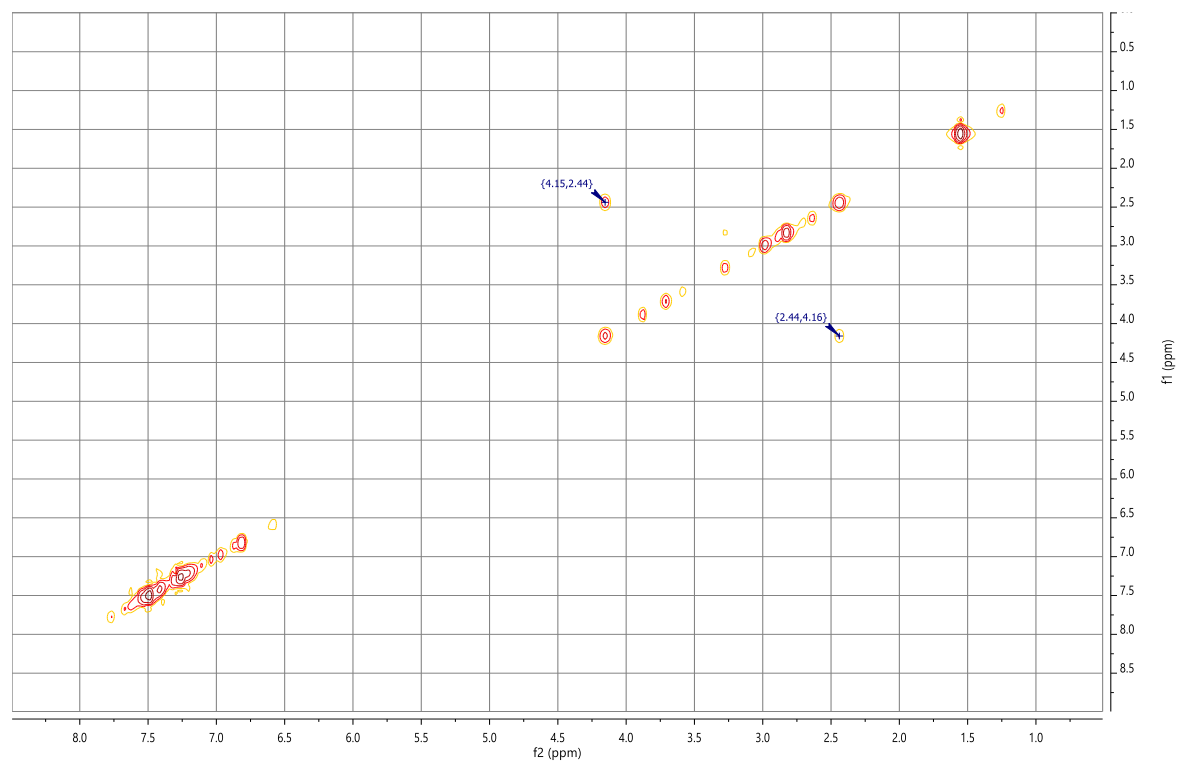
S24 ^1H NMR (300 MHz, CDCl_3) of **L15**.



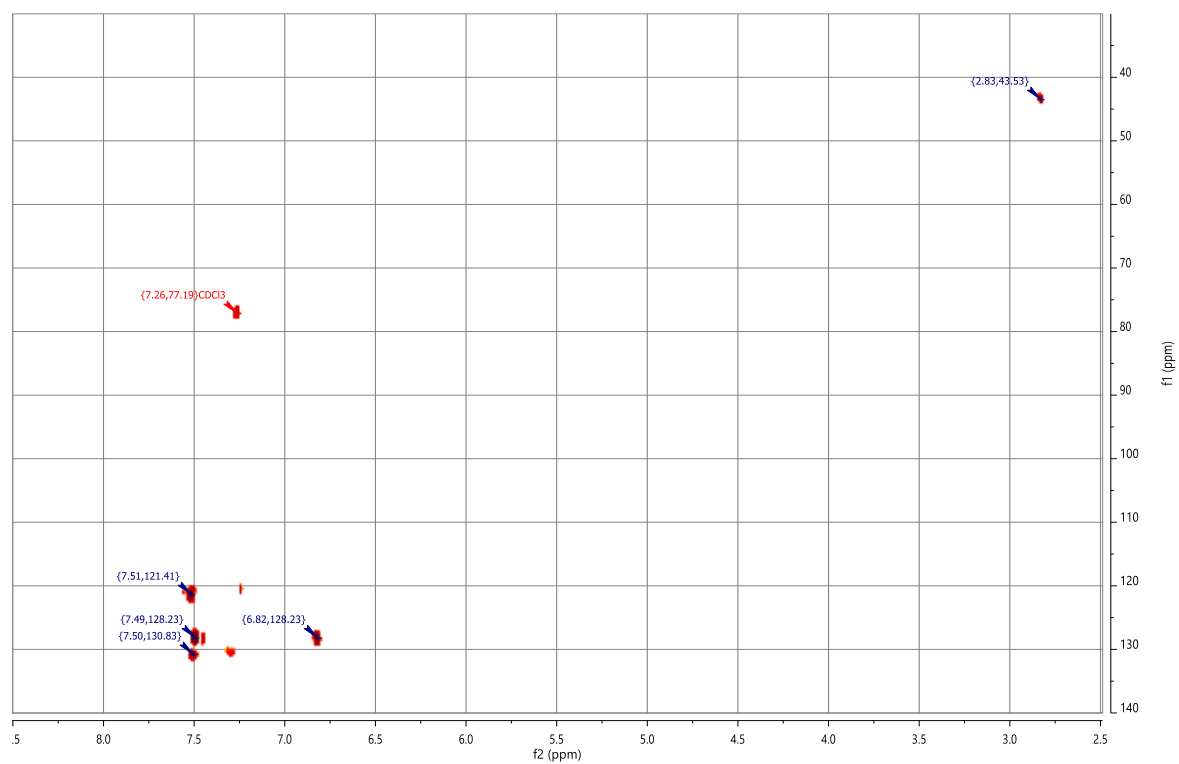
S25 $^{13}\text{C}\{^1\text{H}\}$ NMR (101 MHz, CDCl_3) of L15.



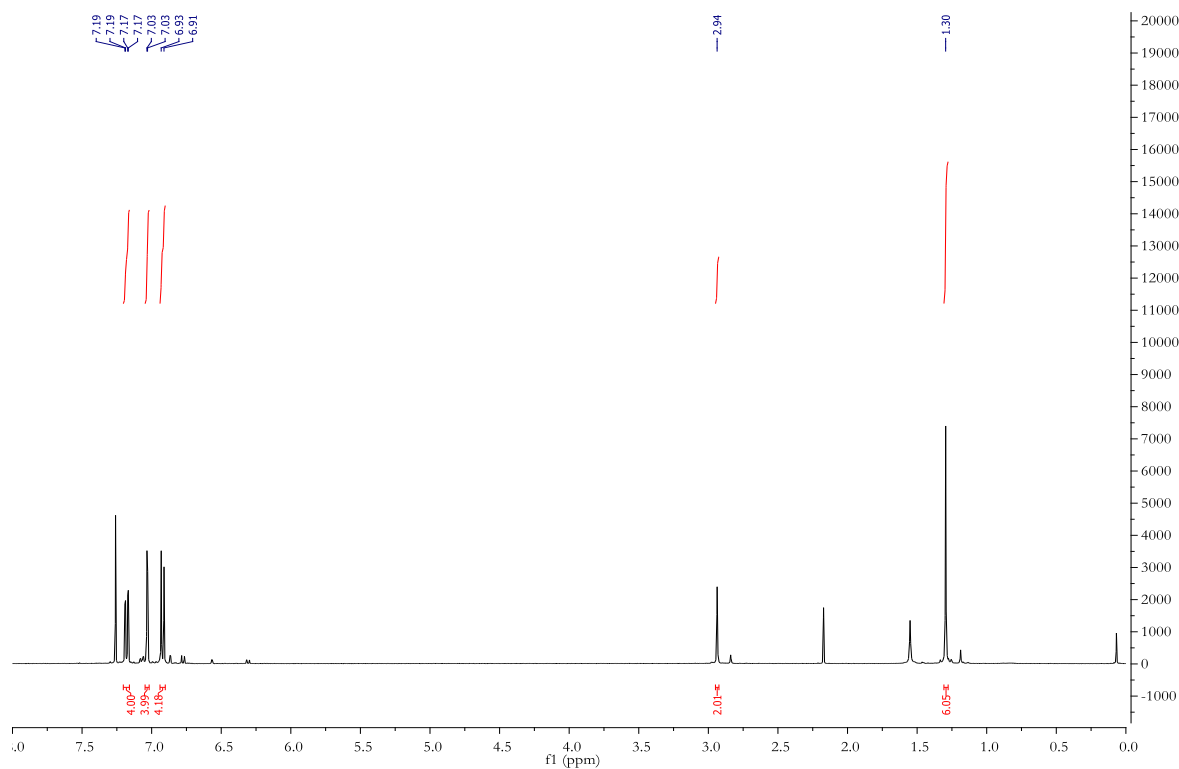
S26 $^1\text{H}\text{-}^1\text{H}$ COSY (CDCl_3) of L15.



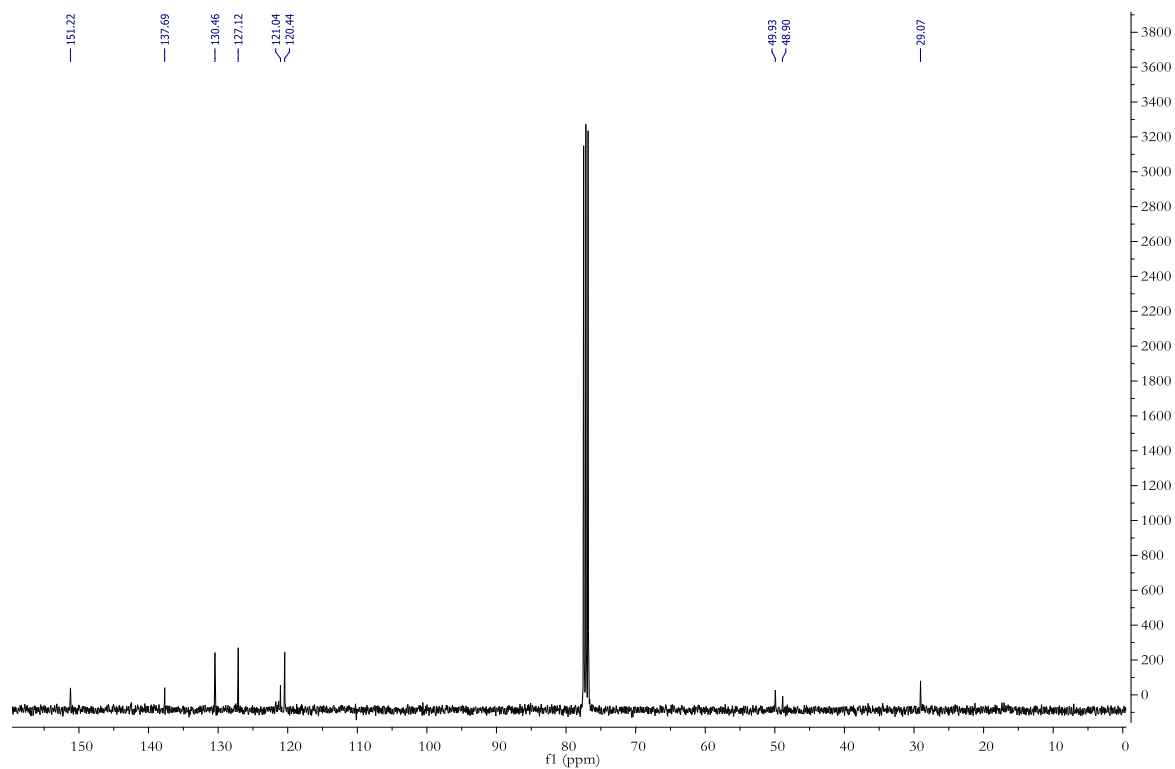
S27 ^1H - ^{13}C HMQC (CDCl_3) of L15.



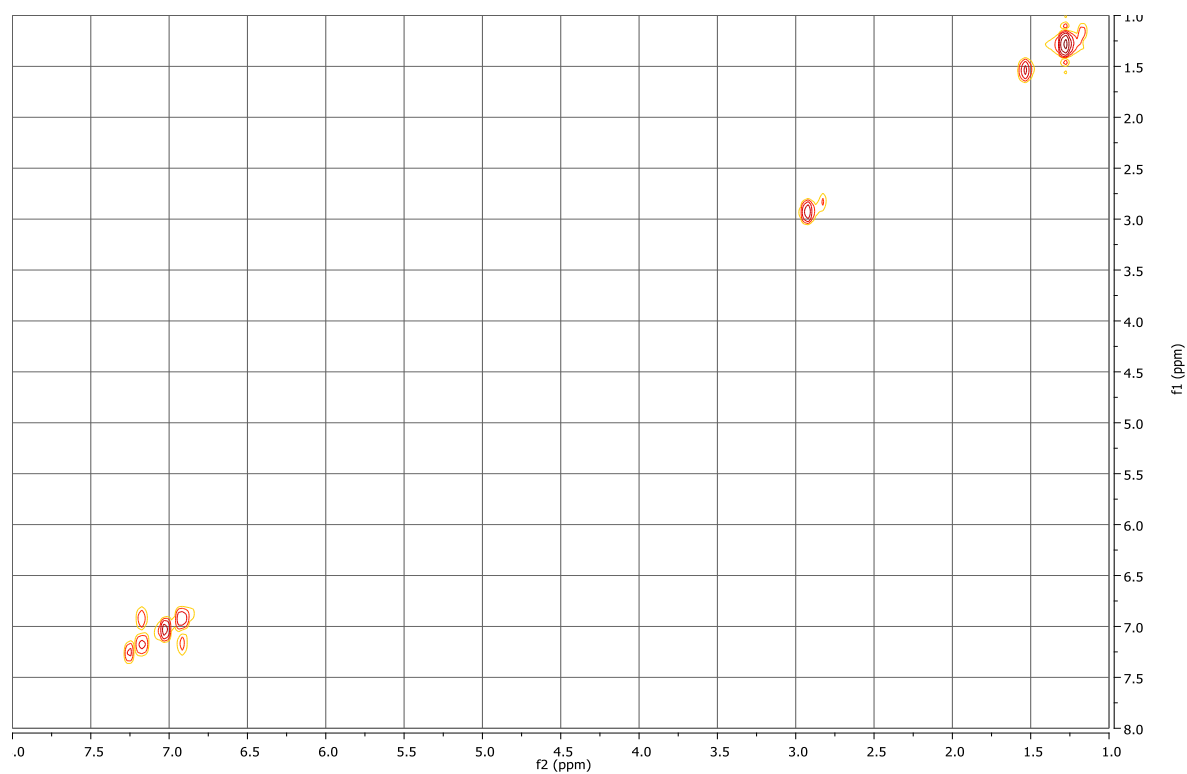
S28 ^1H -NMR (400 MHz, CDCl_3) of L16.



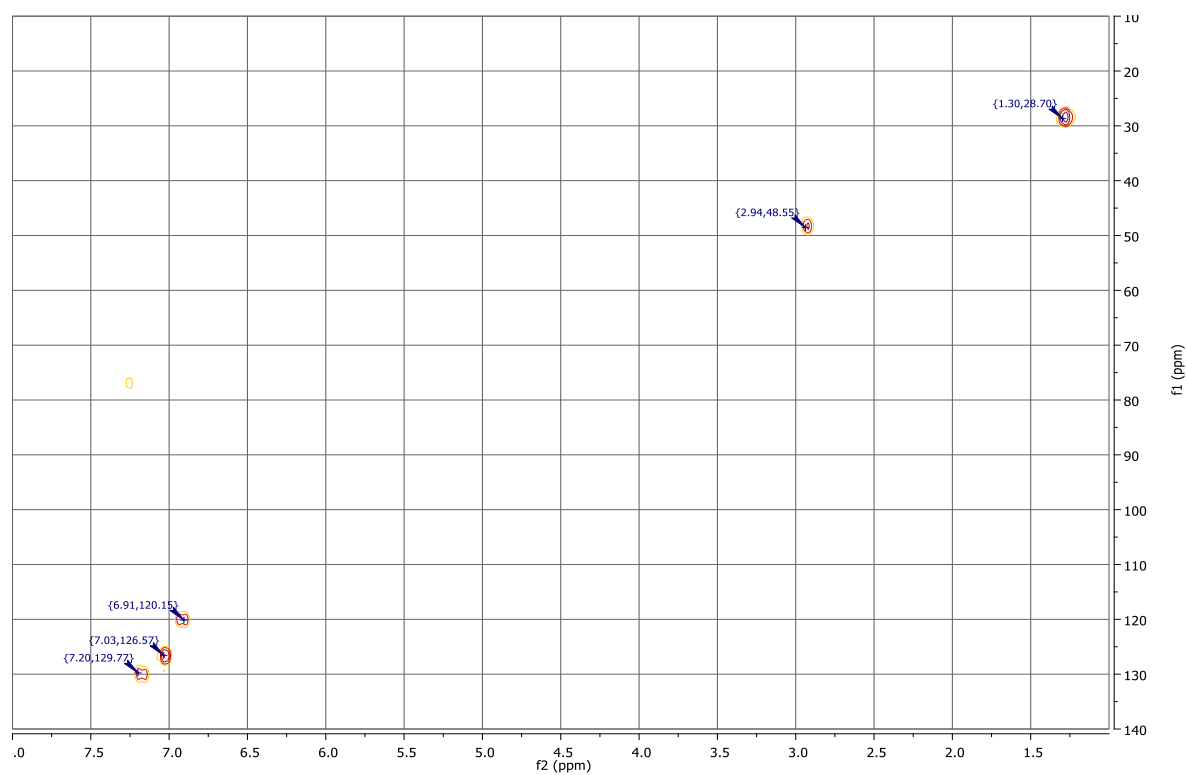
S29 $^{13}\text{C}\{^1\text{H}\}$ NMR (101 MHz, CDCl_3) of **L16**.



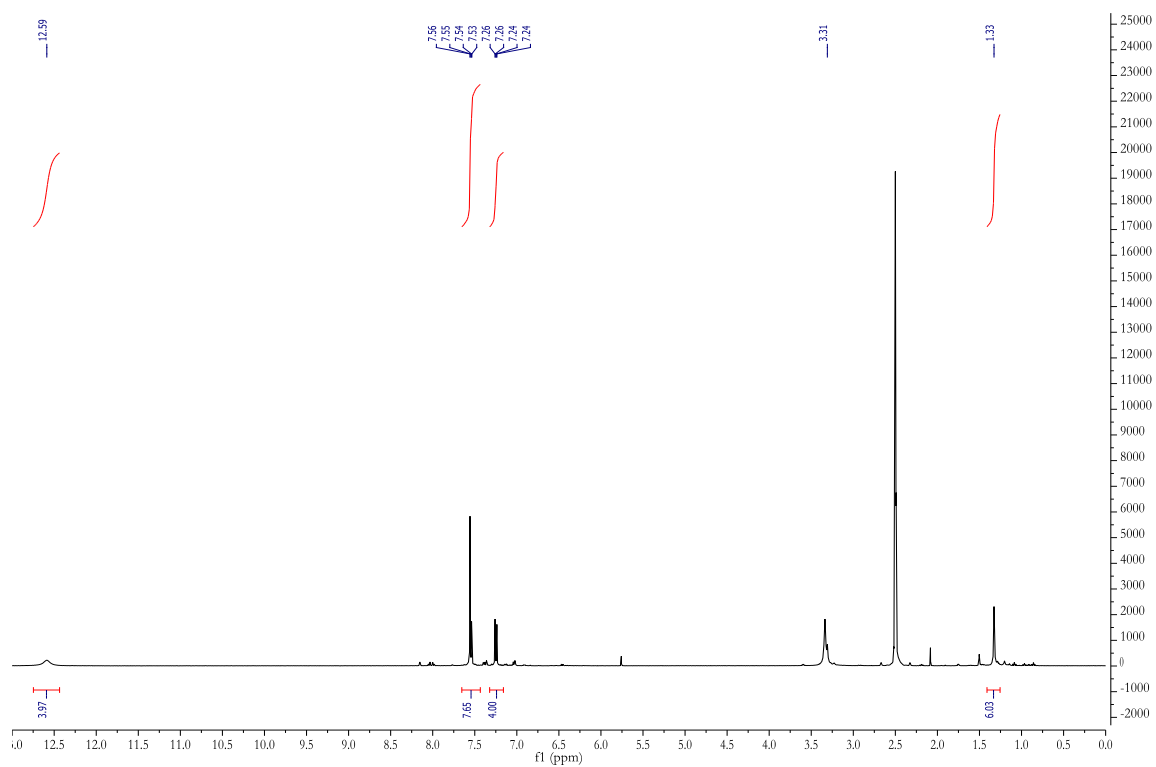
S30 ^1H - ^1H COSY (CDCl_3) of **L16**.



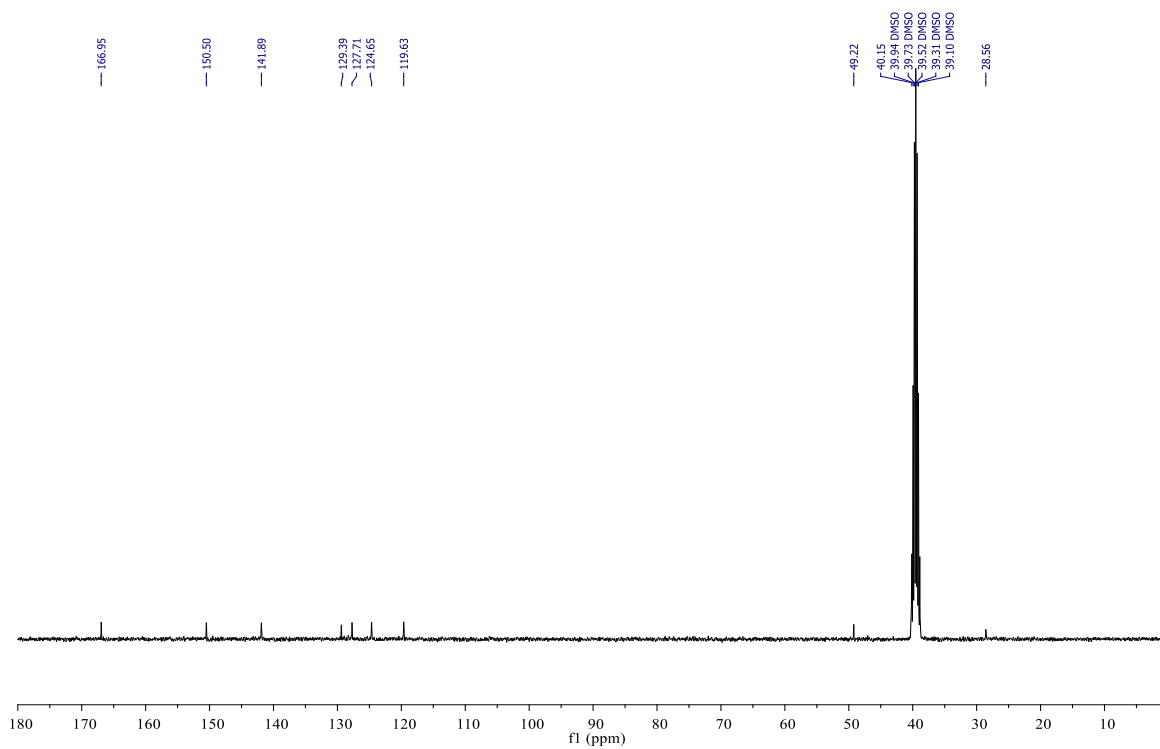
S31 ^1H - ^{13}C HMQC (CDCl_3) of **L16**.



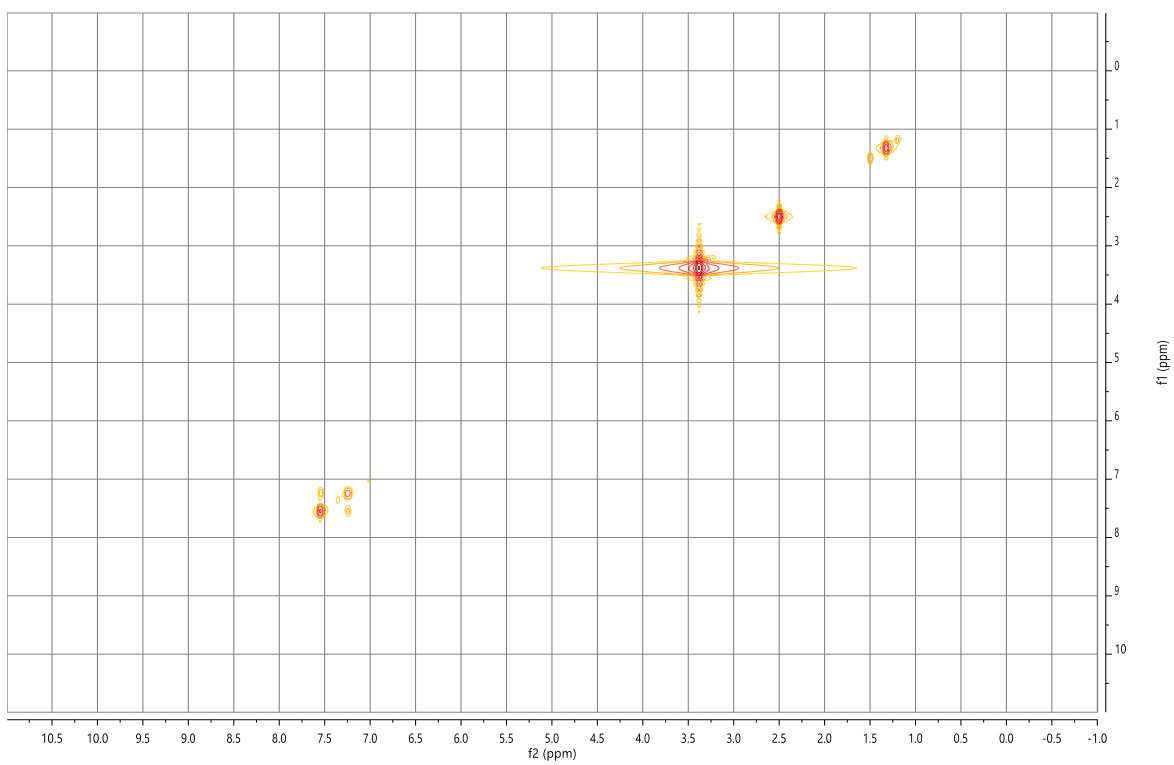
S32 ^1H NMR (400 MHz, DMSO-d_6) of **H4L17**.



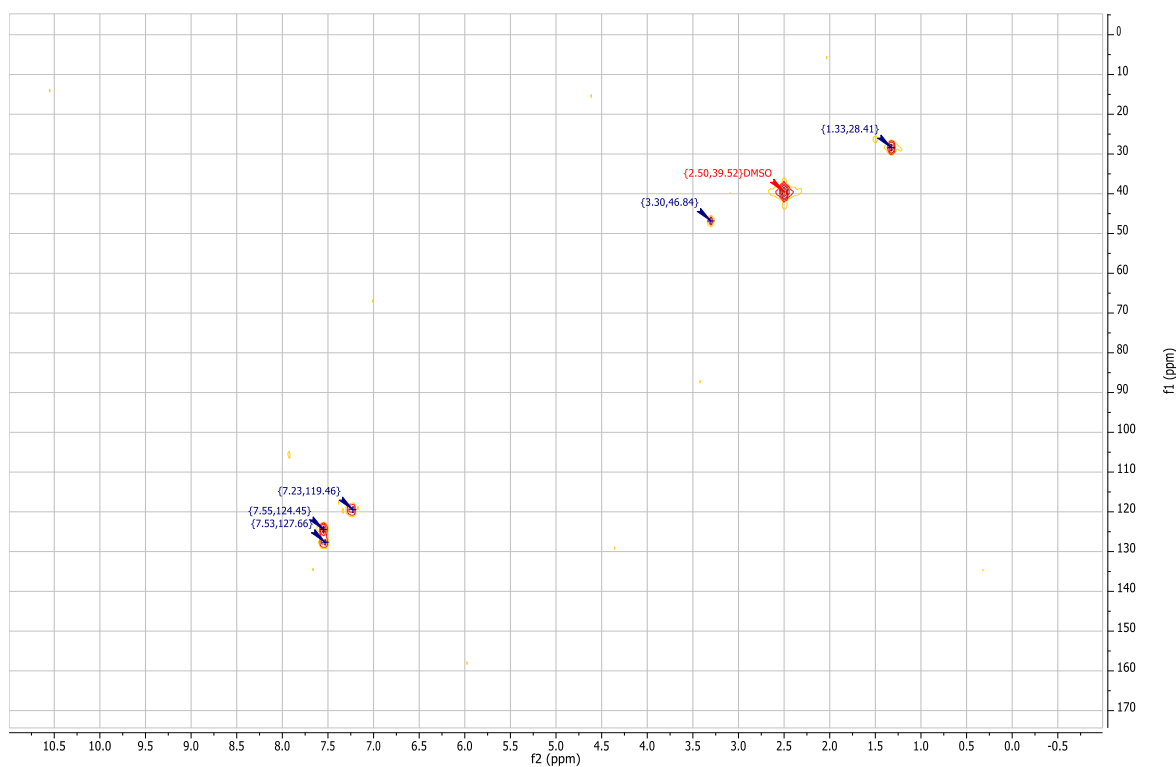
S33 $^{13}\text{C}\{^1\text{H}\}$ NMR (101 MHz, DMSO- d_6) of **H₄L17**.



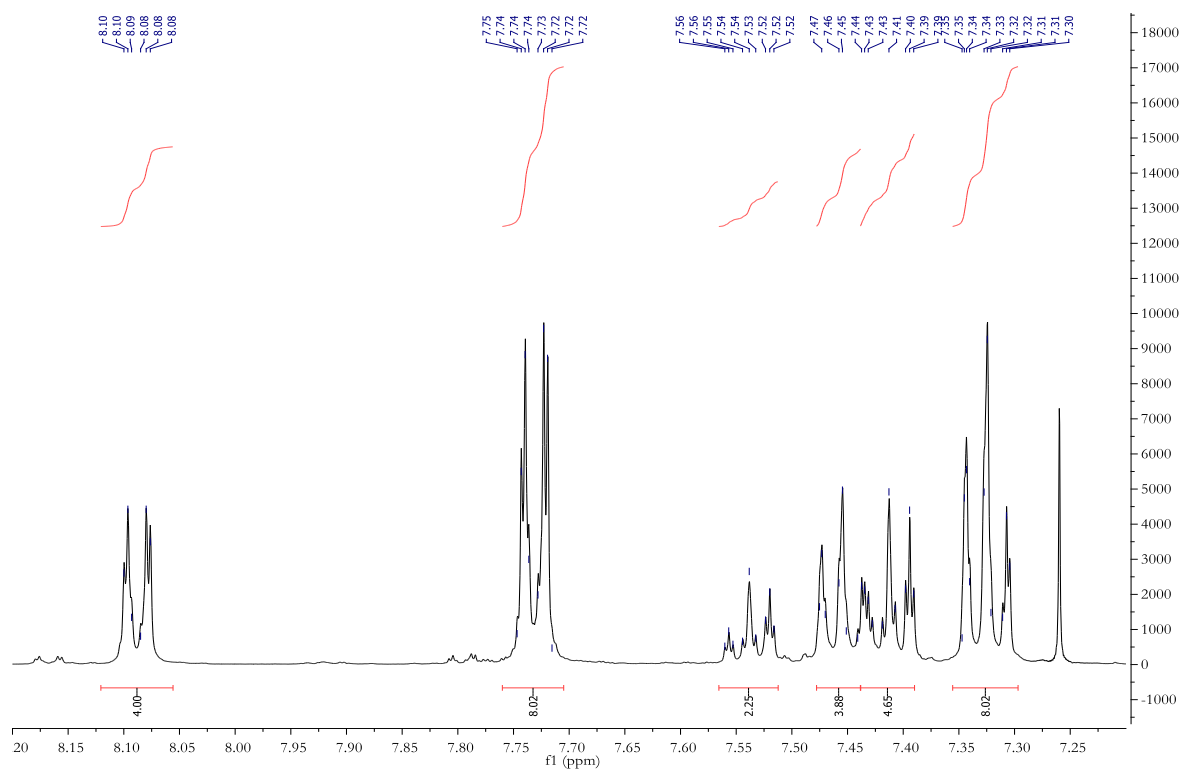
S34 $^1\text{H}\text{-}^1\text{H}$ COSY NMR of **H₄L17**.



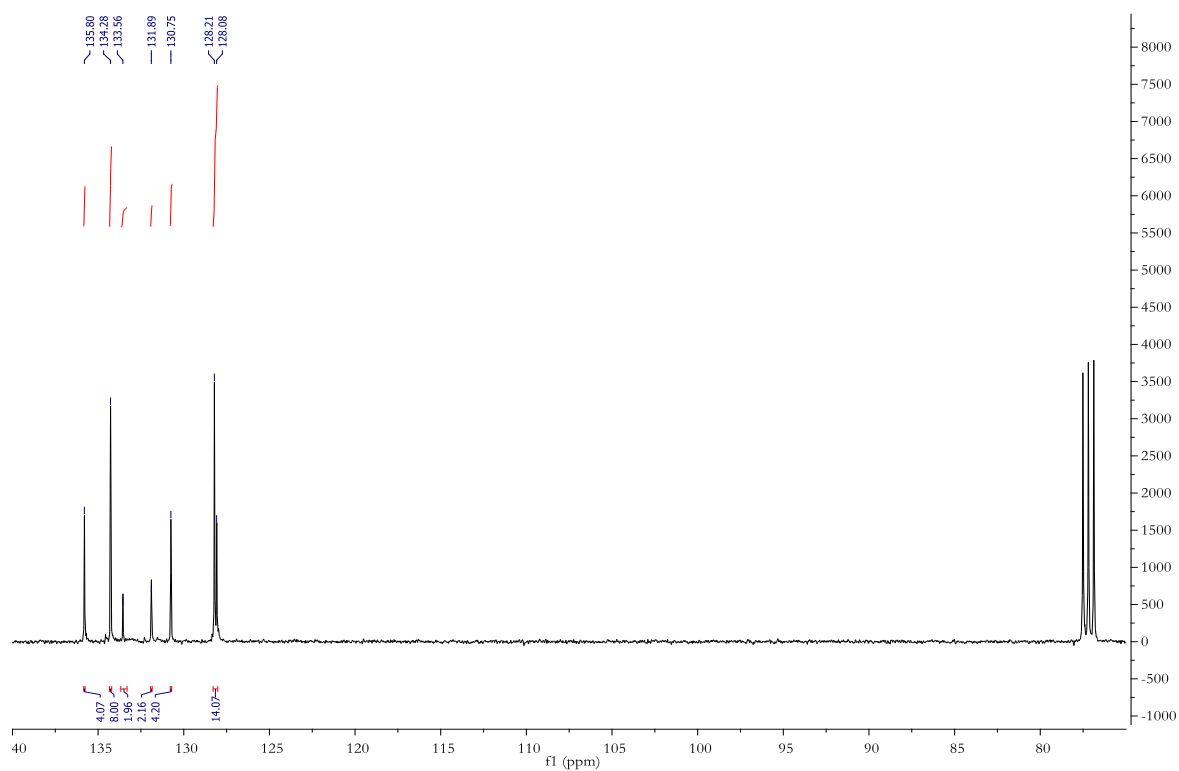
S35 ^1H - ^{13}C HMQC of **H4L17**.



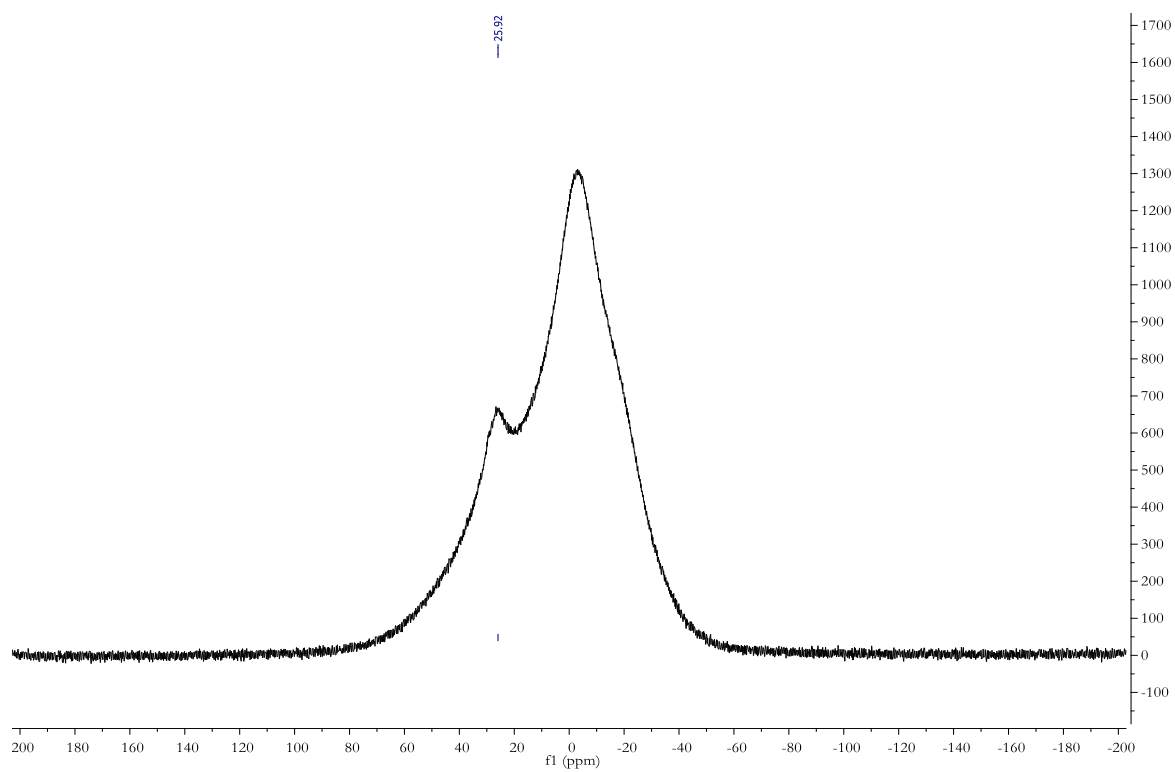
S36 ^1H -NMR (400 MHz, CDCl_3) of **R1**.



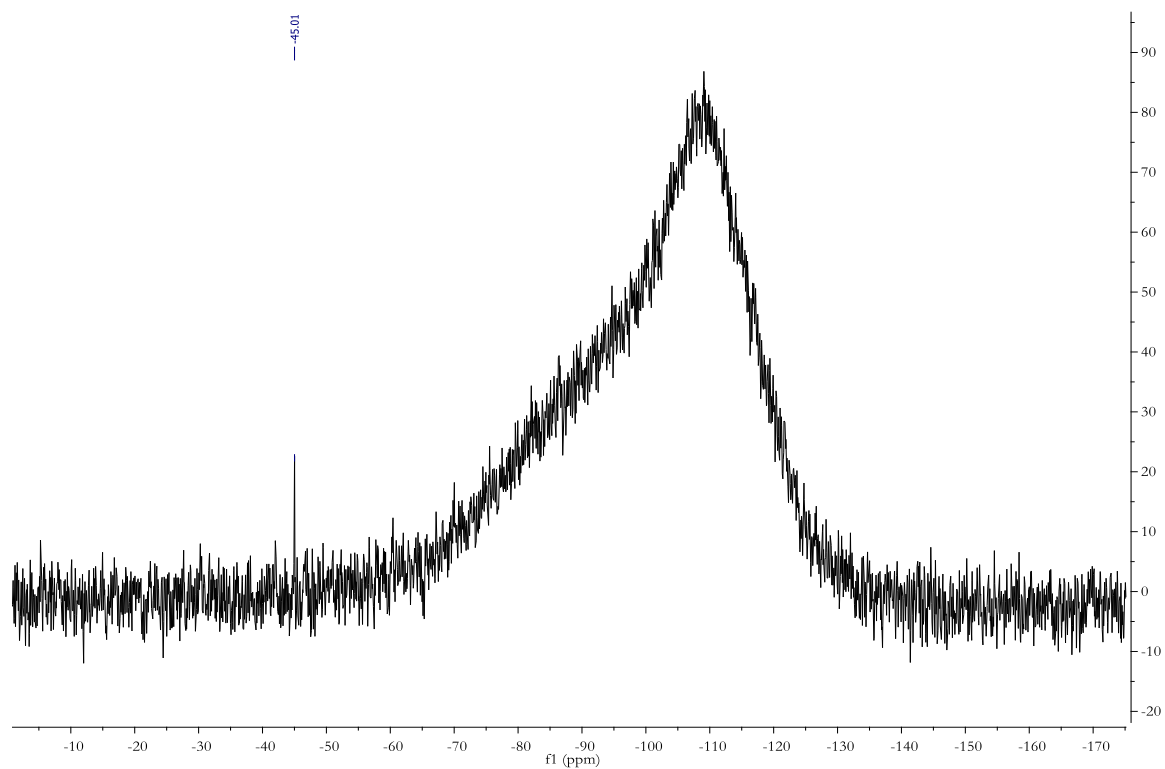
S37 $^{13}\text{C}\{^1\text{H}\}$ NMR (101 MHz, CDCl_3) of **R1**.



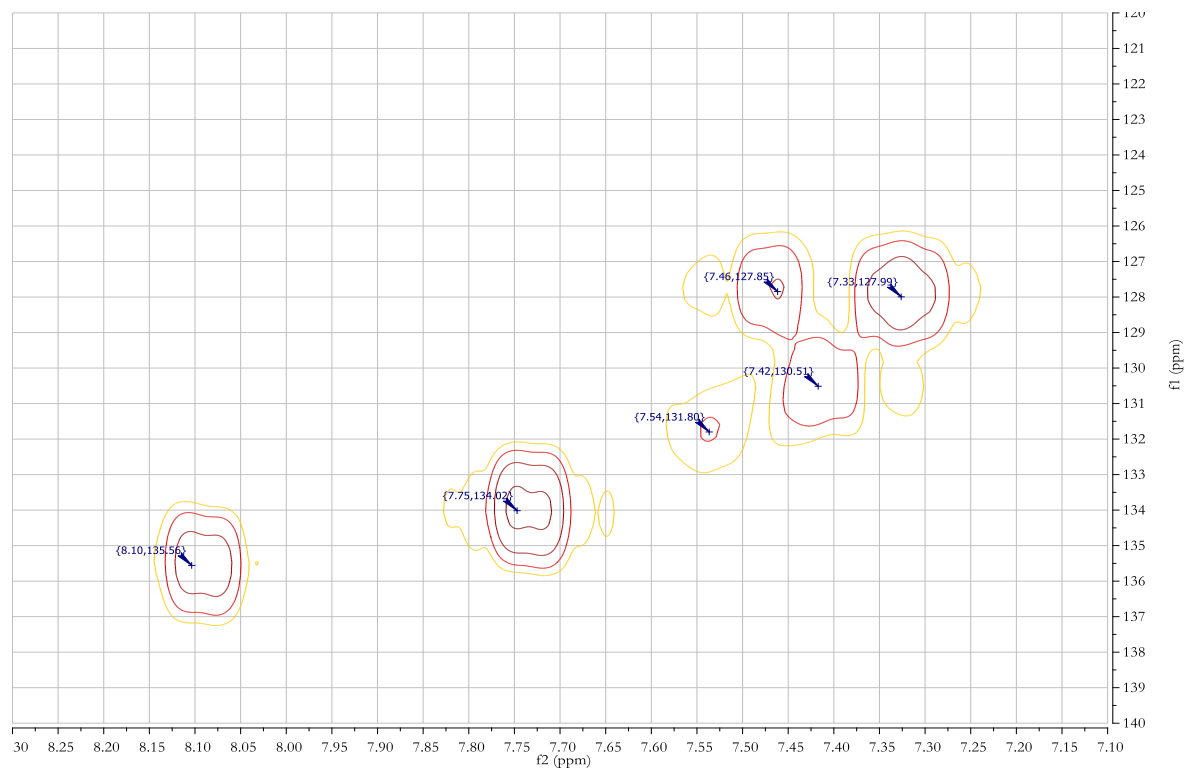
S38 $^{11}\text{B}\{^1\text{H}\}$ NMR (128 MHz, CDCl_3) of **R1**.



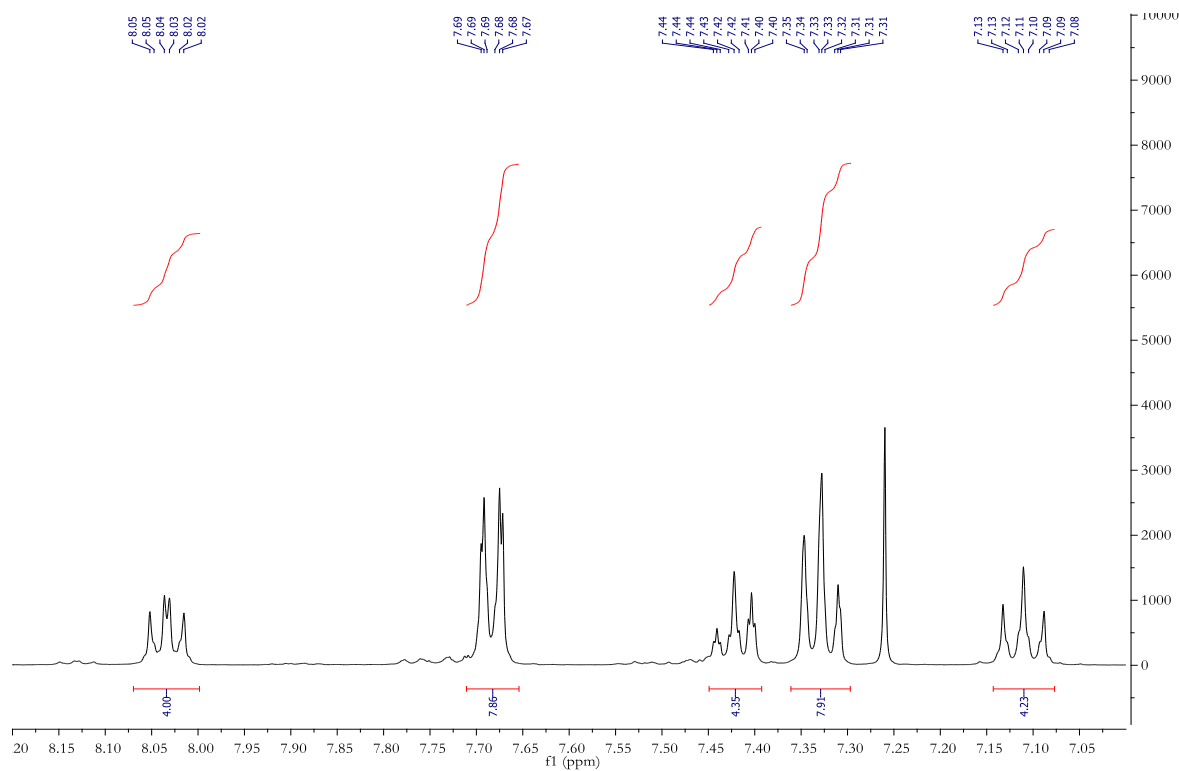
S39 $^{29}\text{Si}\{^1\text{H}\}$ NMR (80 MHz, CDCl_3) of **R1**.



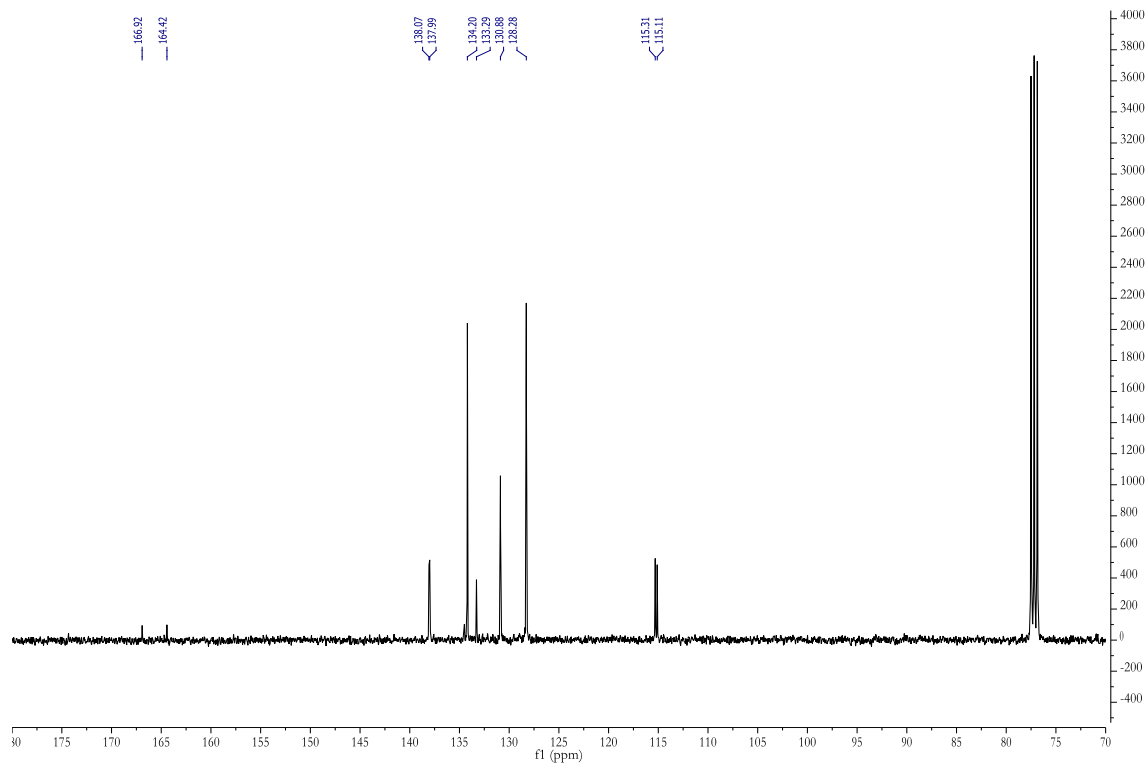
S40 ^1H - ^{13}C HMQC of **R1**.



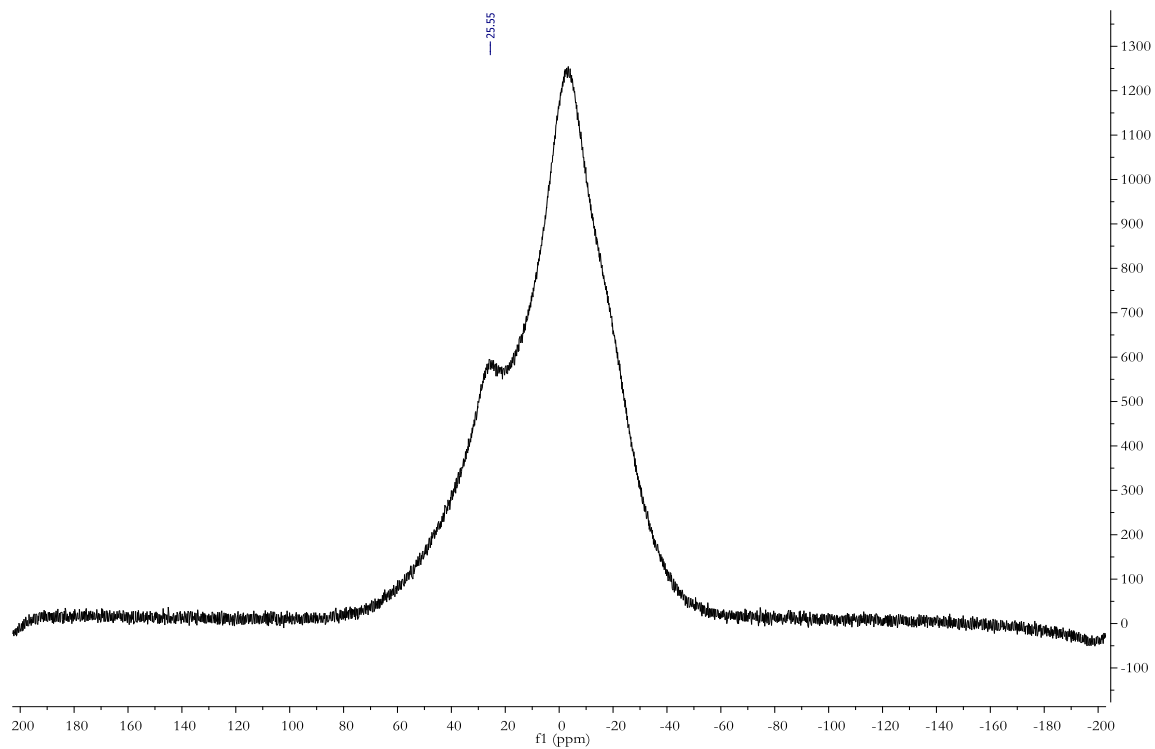
S41 $^1\text{H-NMR}$ (400 MHz, CDCl_3) of **R2**.



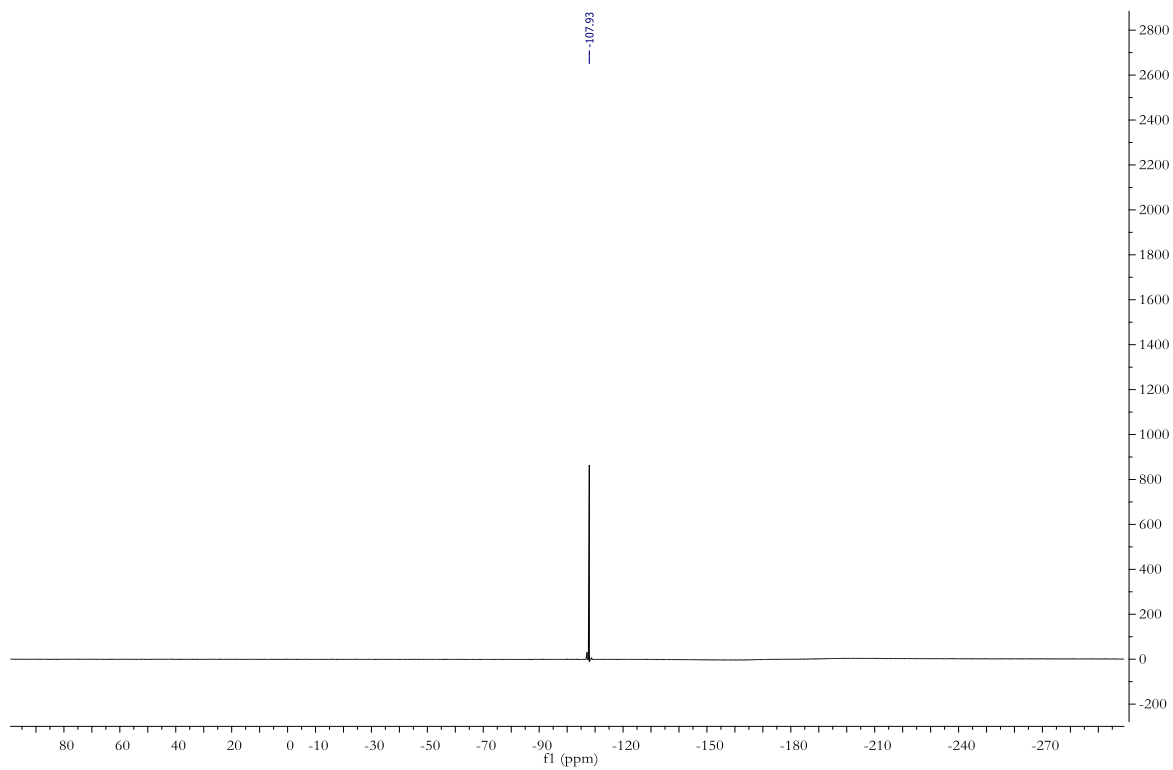
S42 $^{13}\text{C}\{^1\text{H}\}$ NMR (101 MHz, CDCl_3) of **R2**.



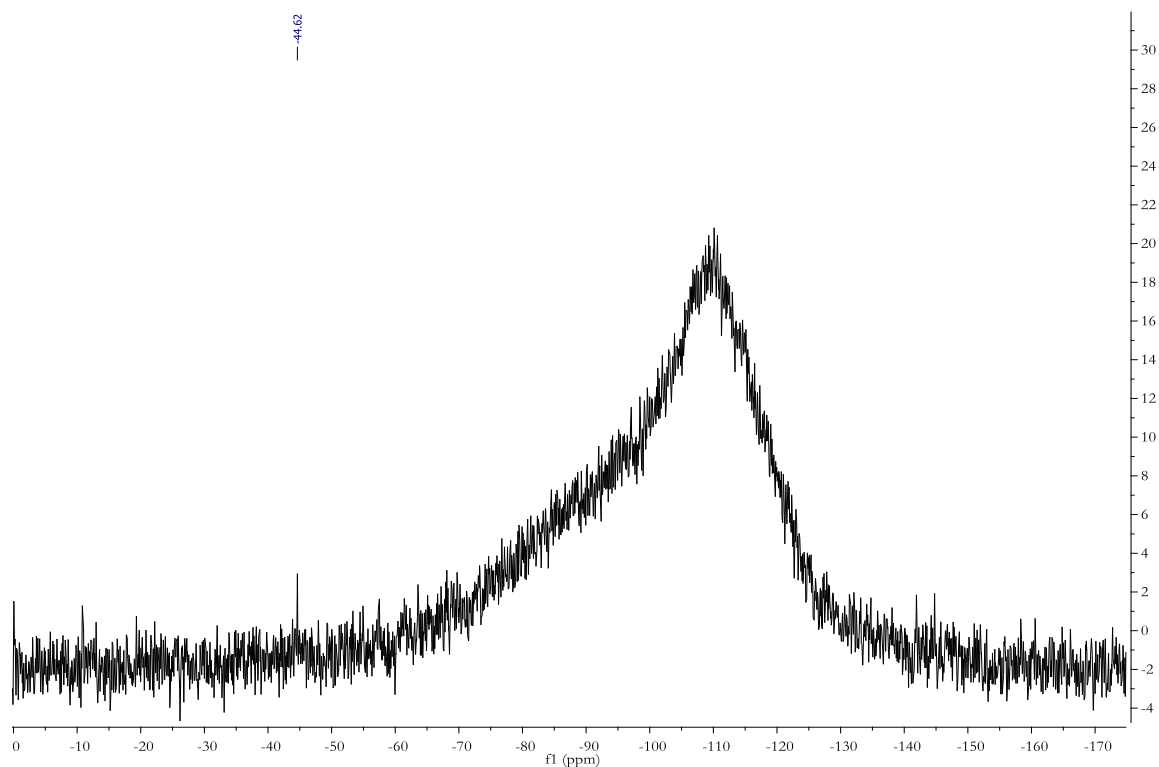
S43 $^{11}\text{B}\{^1\text{H}\}$ NMR (128 MHz, CDCl_3) of **R2**.



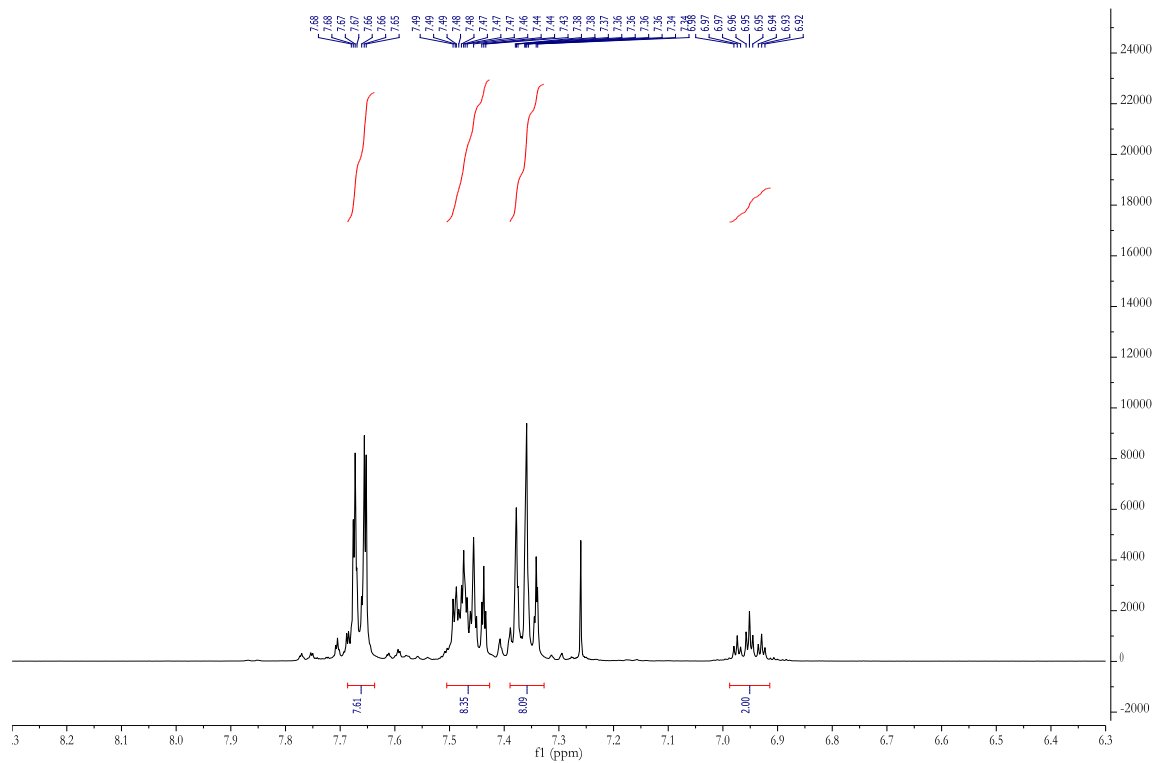
S44 $^{19}\text{F}\{^1\text{H}\}$ NMR (377 MHz, CDCl_3) of **R2**.



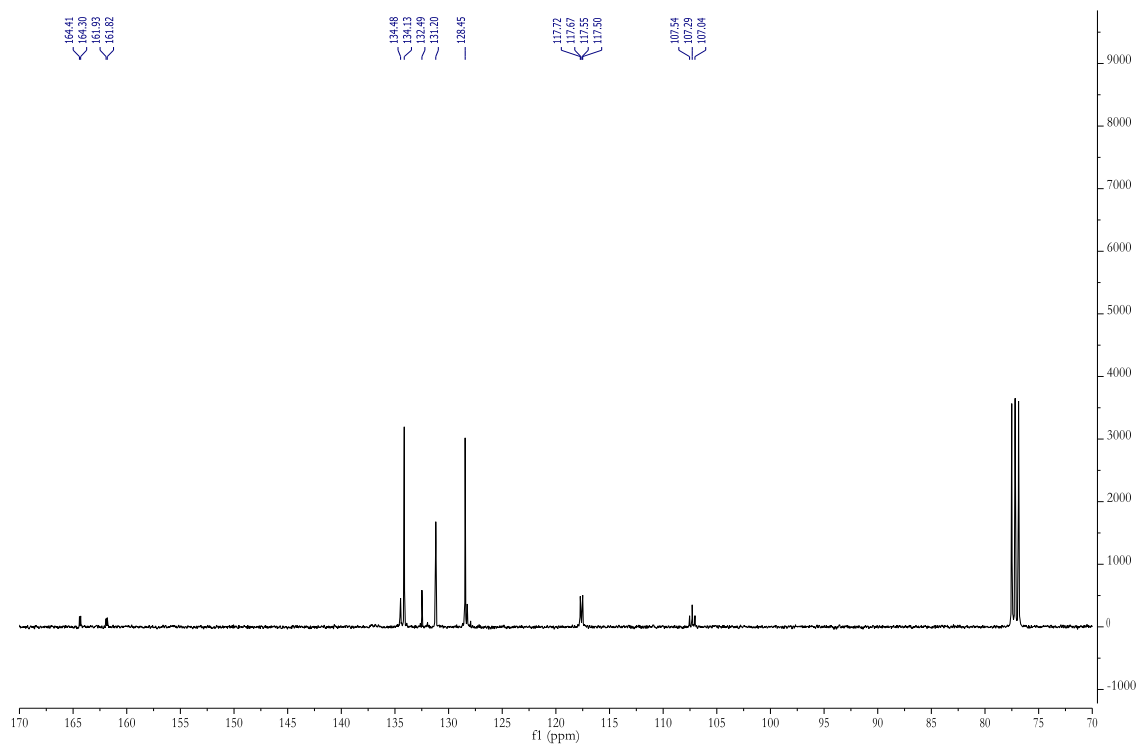
S45 $^{29}\text{Si}\{^1\text{H}\}$ NMR (80 MHz, CDCl_3) of **R2**.



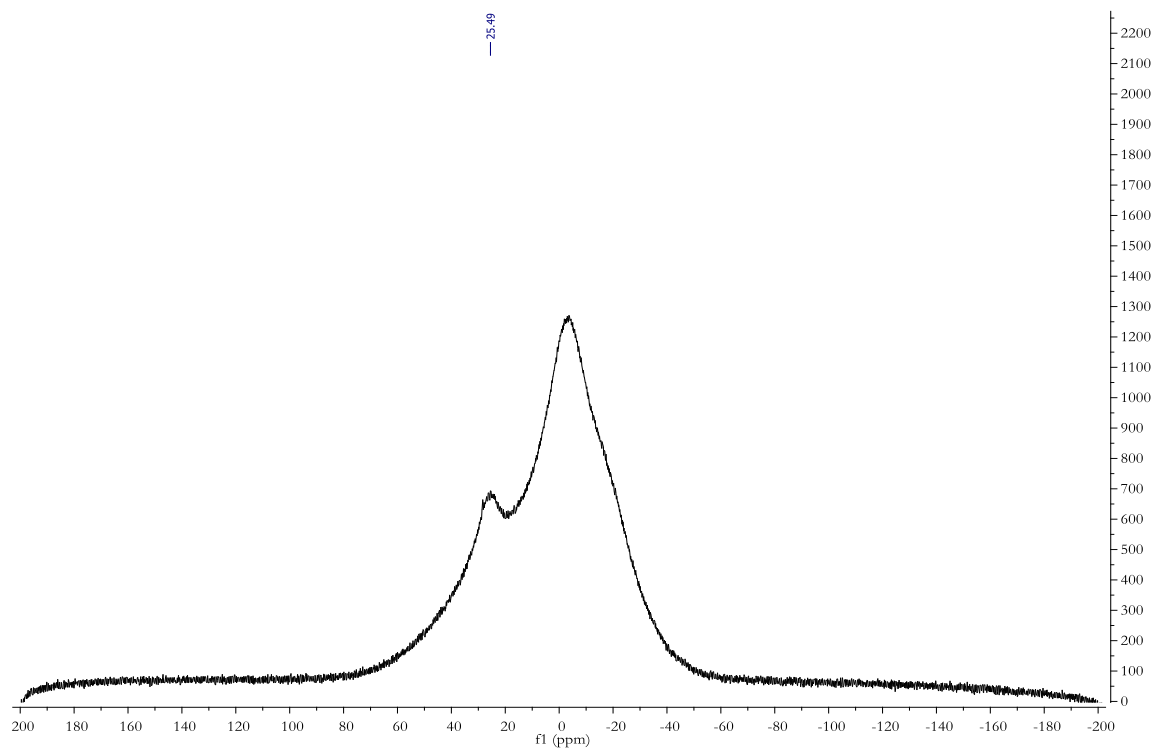
S46 ^1H -NMR (400 MHz, CDCl_3) of **R3**.



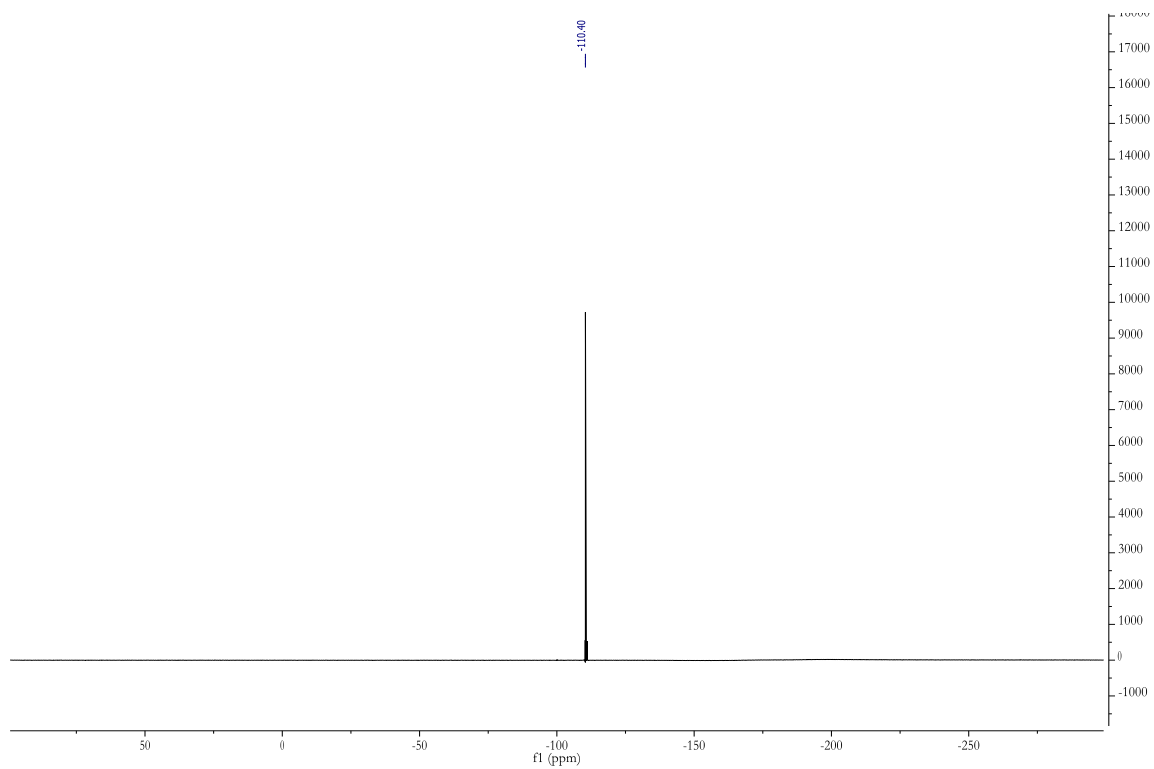
S47 $^{13}\text{C}\{^1\text{H}\}$ NMR (101 MHz, CDCl_3) of **R3**.



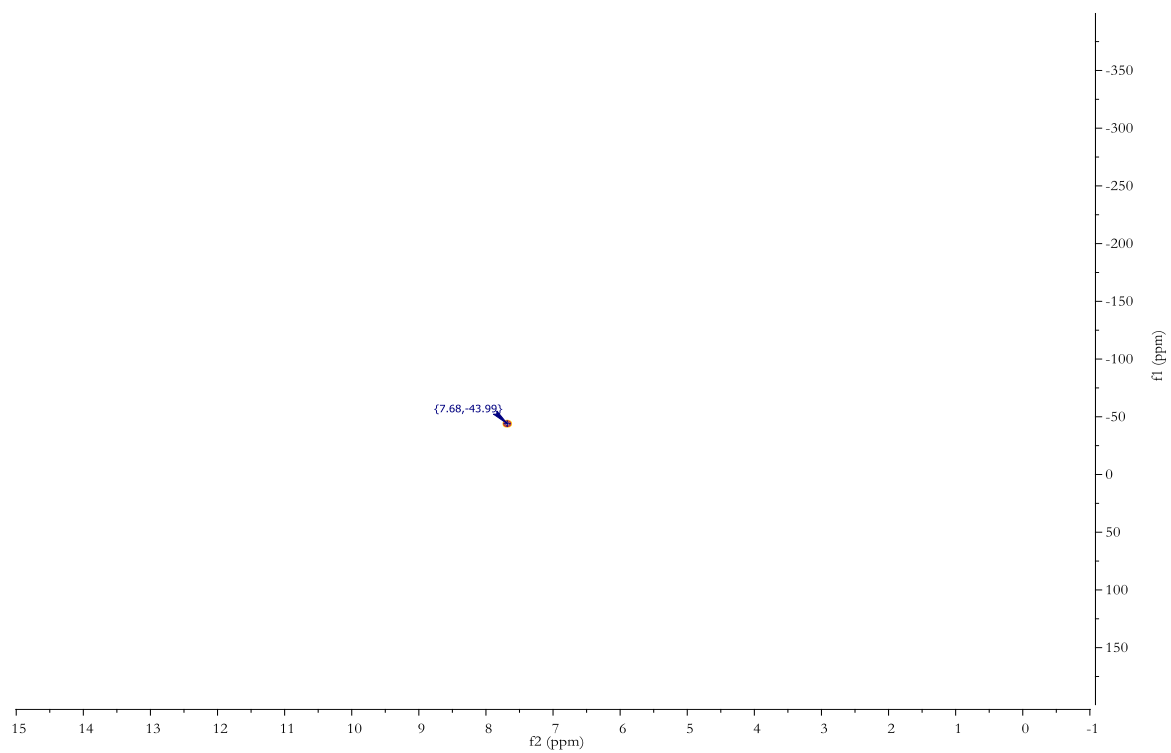
S48 $^{11}\text{B}\{^1\text{H}\}$ NMR (128 MHz, CDCl_3) of **R3**.



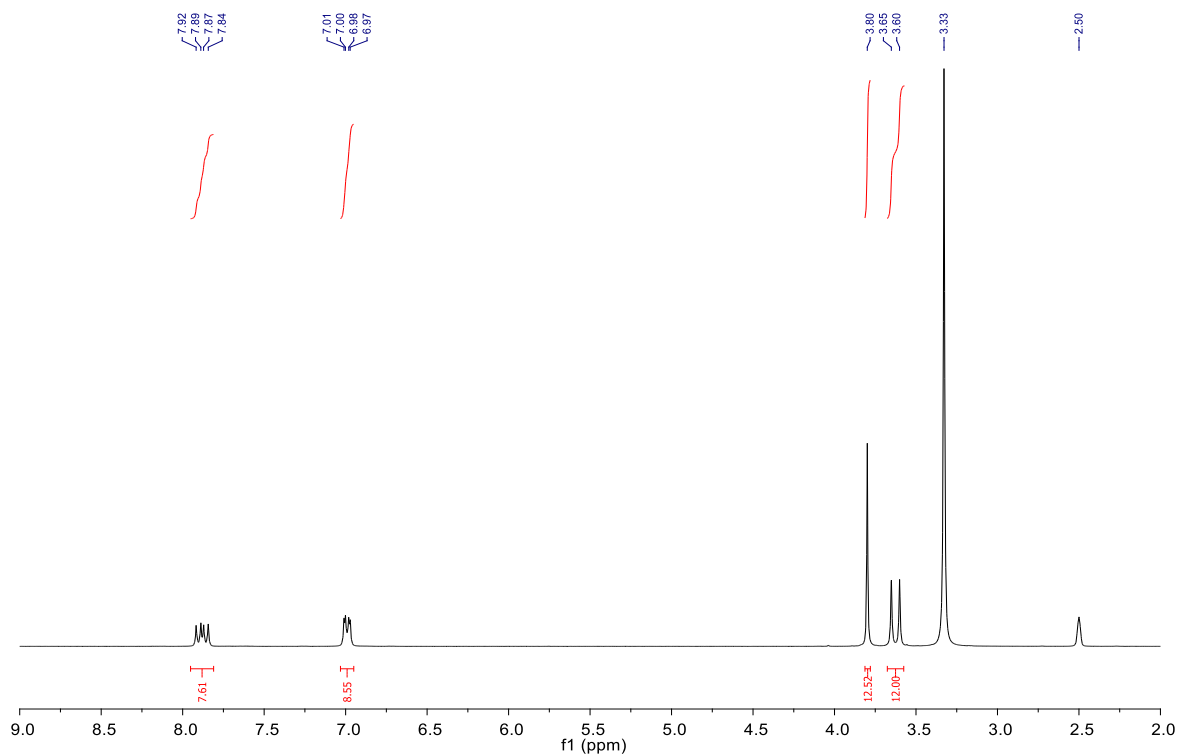
S49 $^{19}\text{F}\{^1\text{H}\}$ NMR (377 MHz, CDCl_3) of **R3**.



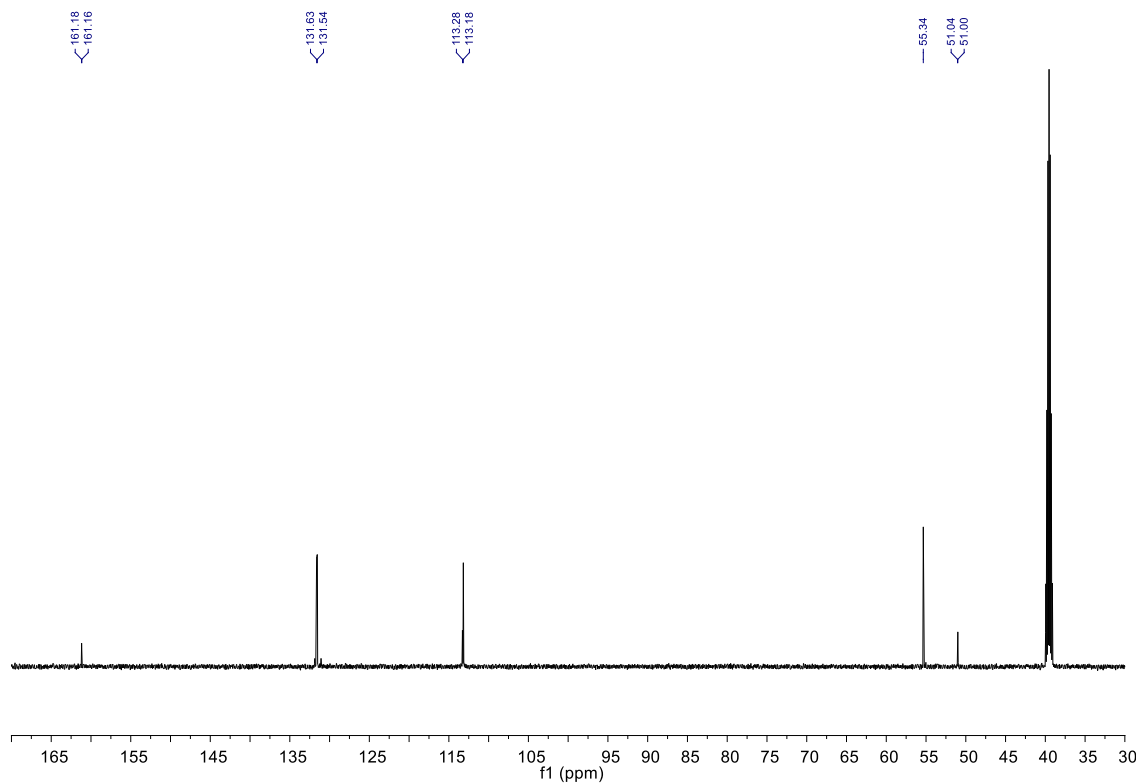
S50 $^{29}\text{Si}\text{-}^1\text{H}$ HMBC of **R3**.



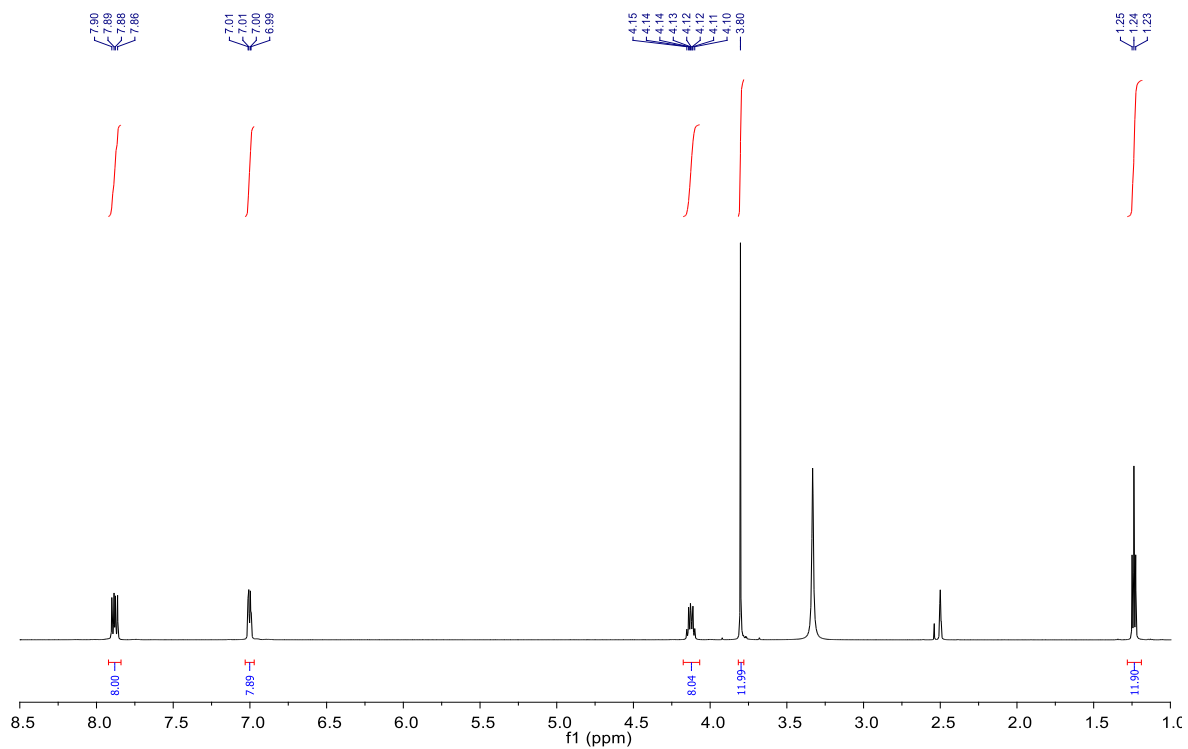
S51 ^1H NMR (300 MHz, DMSO- d_6) of **2**.



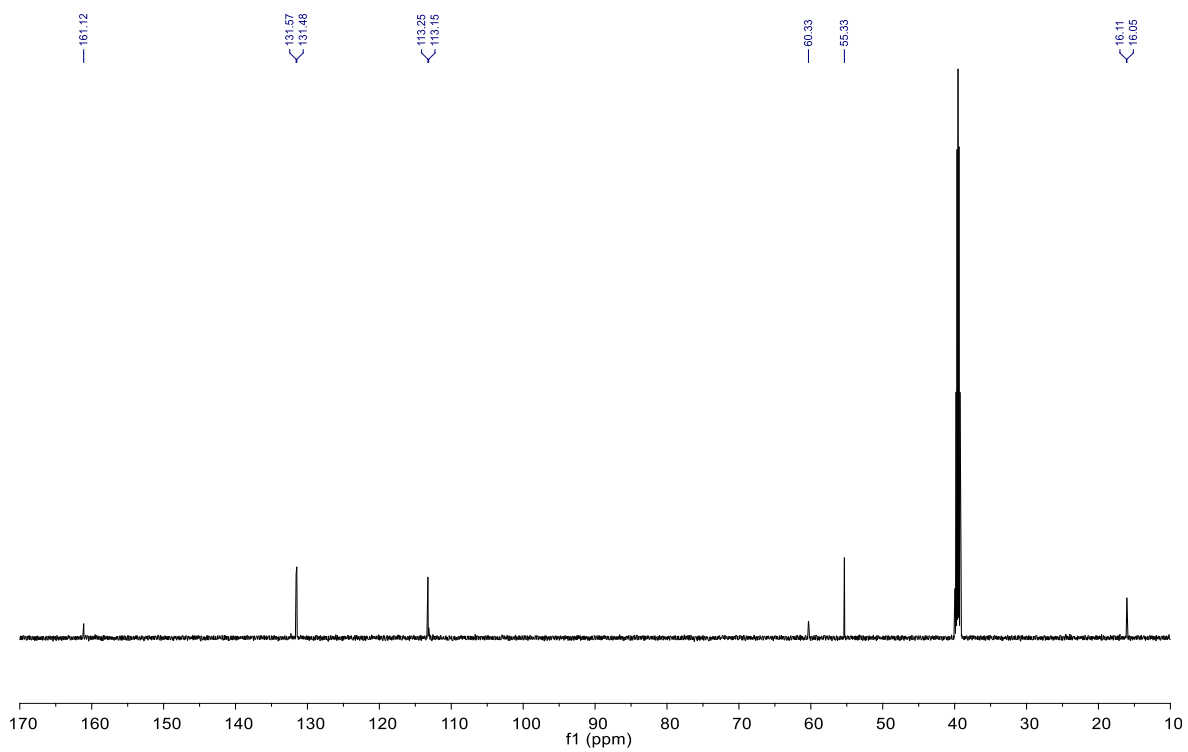
S52 $^{13}\text{C}\{^1\text{H}\}$ NMR (151 MHz, DMSO- d_6) of **2**.



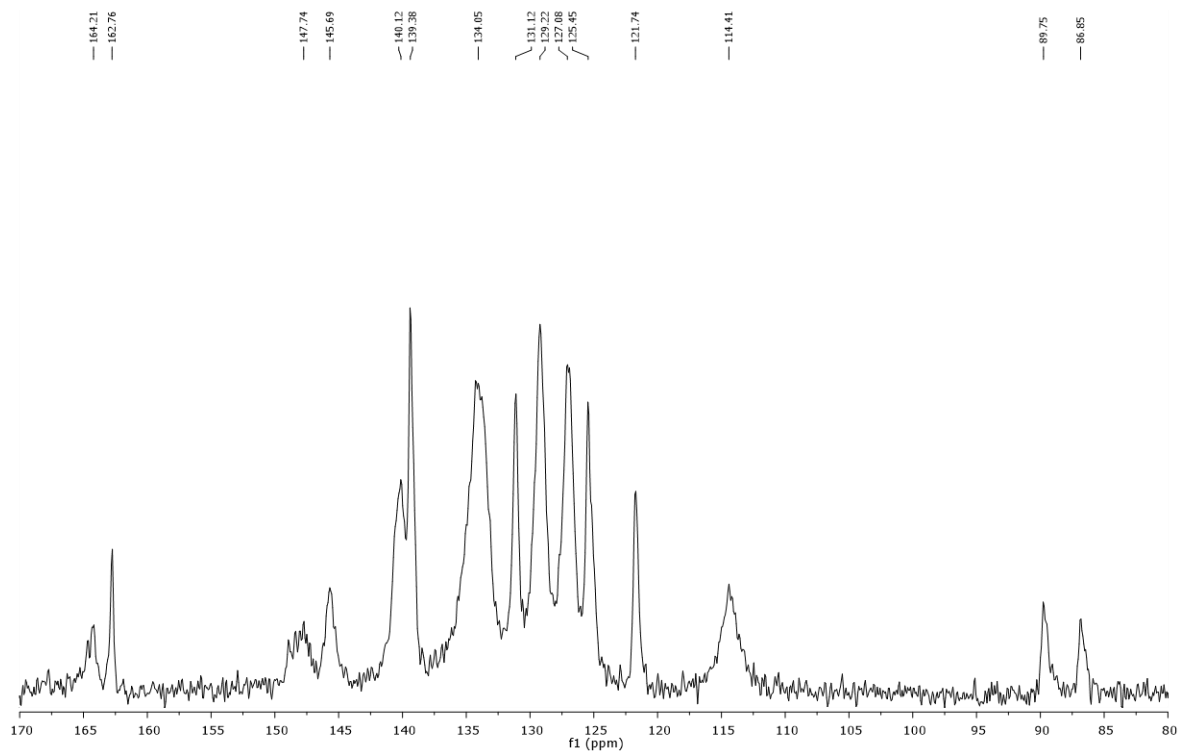
S53 ^1H NMR (300 MHz, DMSO- d_6) of **3**.



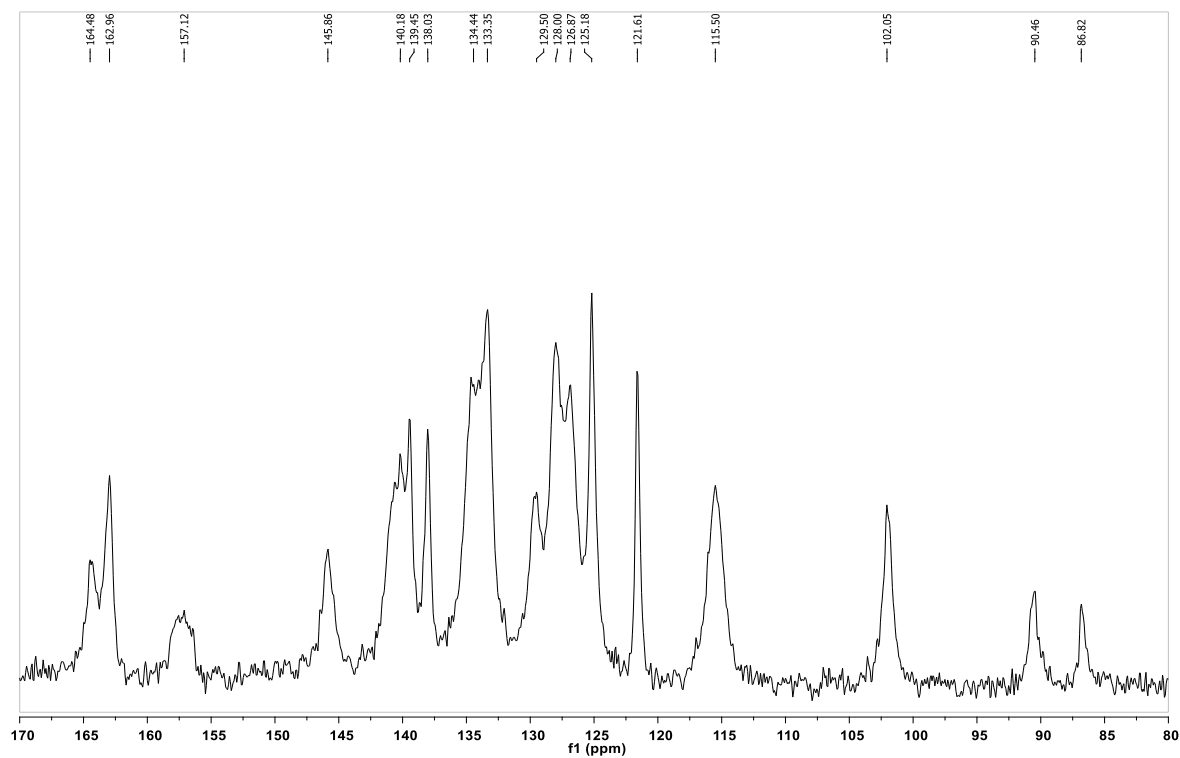
S54 $^{13}\text{C}\{^1\text{H}\}$ NMR (151 MHz, DMSO- d_6) of **3**.



S55 ^{13}C CP/MAS NMR spectrum of (L3-R2) $_{\infty}$.

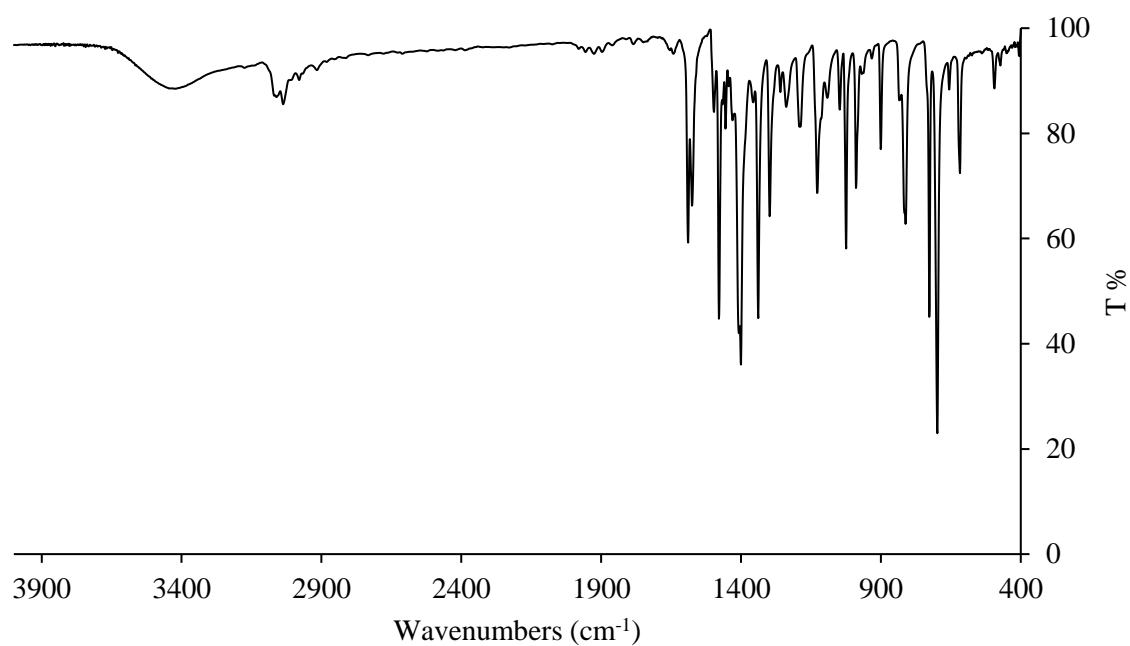


S56 ^{13}C CP/MAS NMR spectrum of (L3-R3) $_{\infty}$.

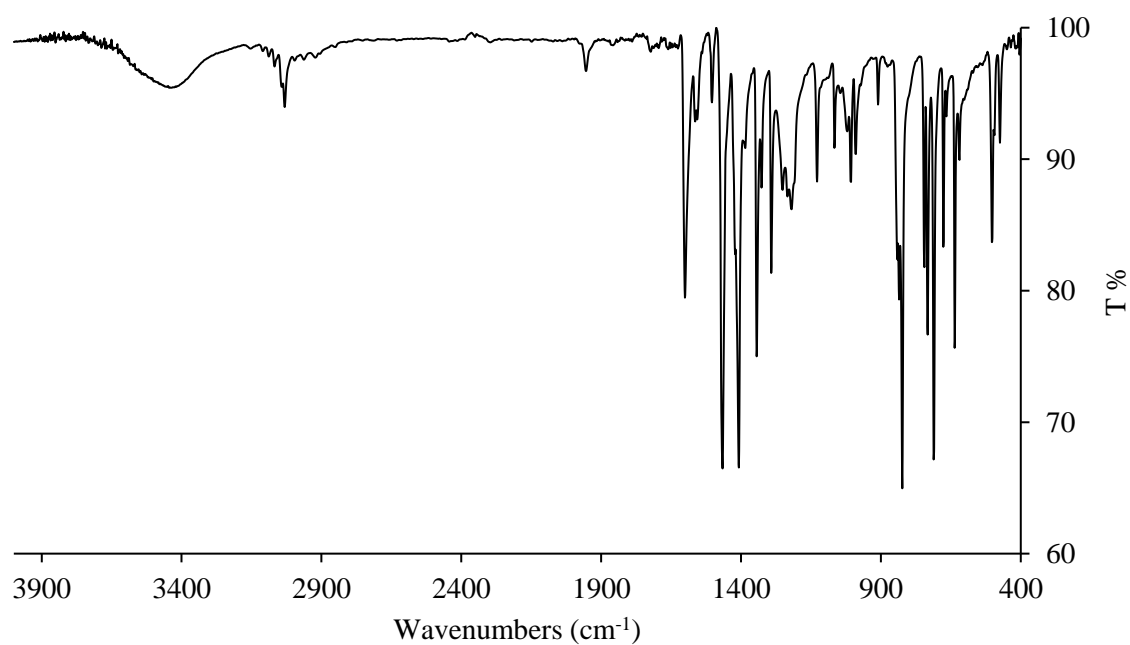


Appendix 2: FT-IR spectra

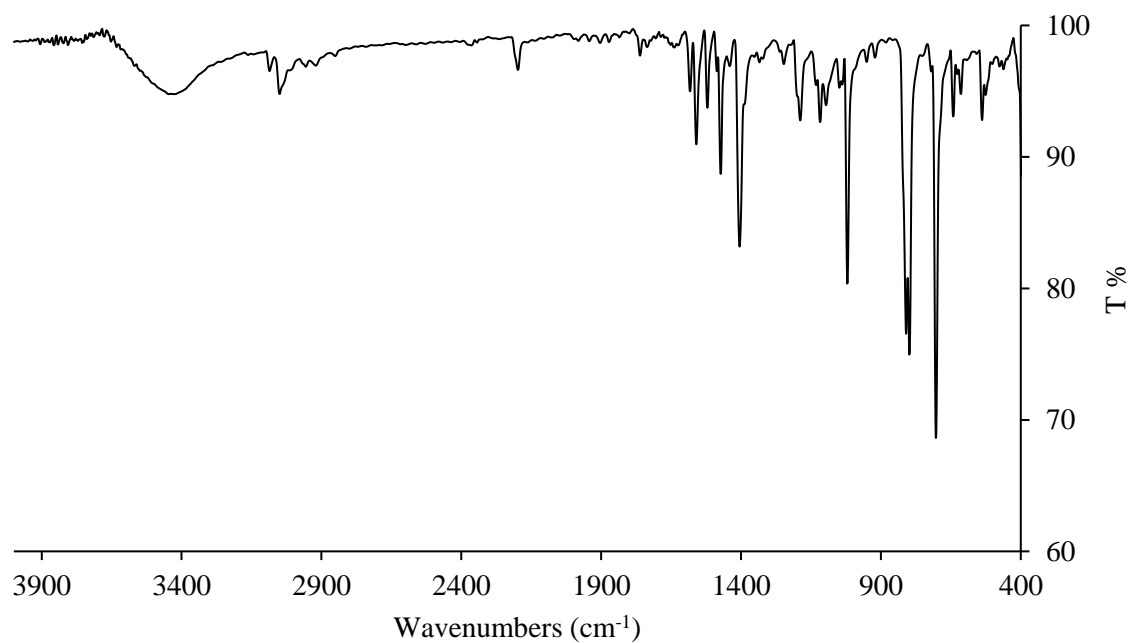
S57 FT-IR spectrum of L1.



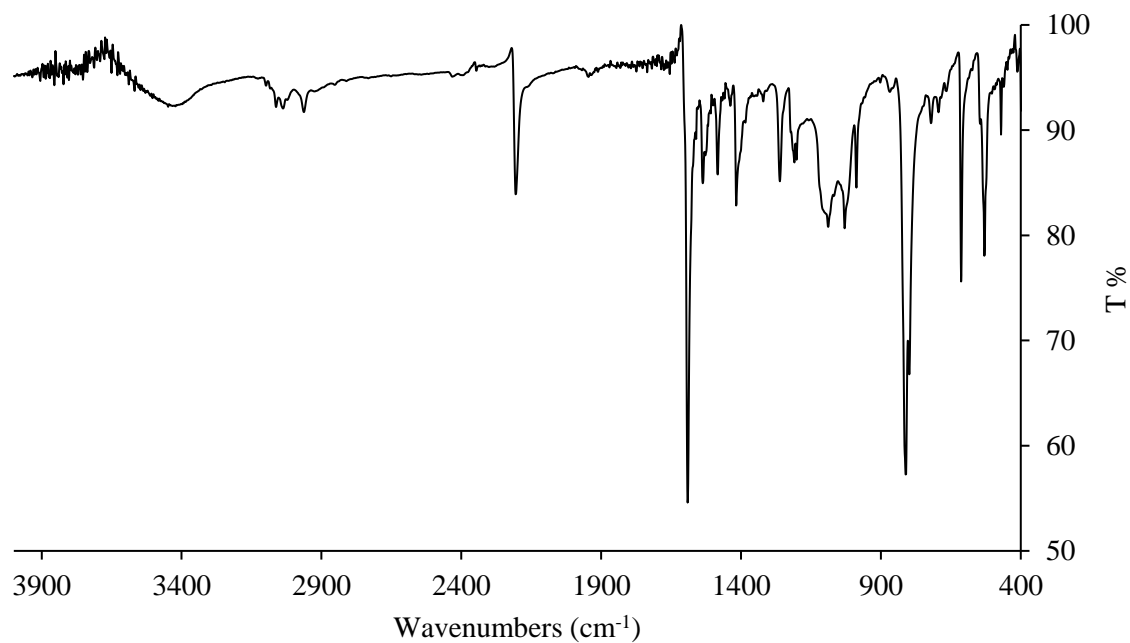
S58 FT-IR spectrum of L2.



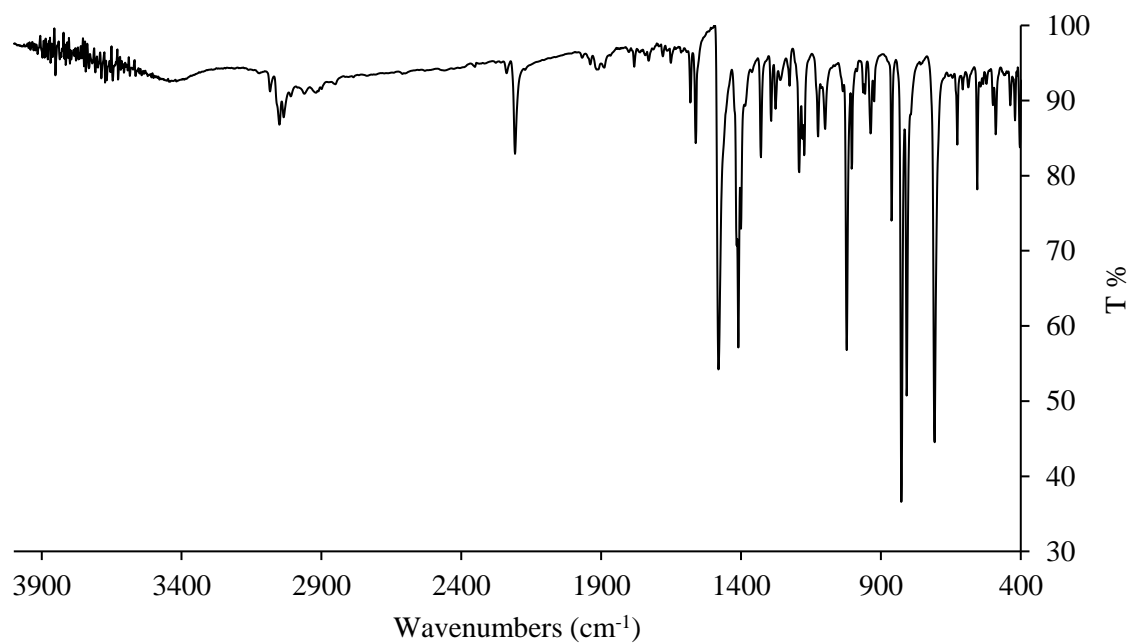
S59 FT-IR spectrum of L3.



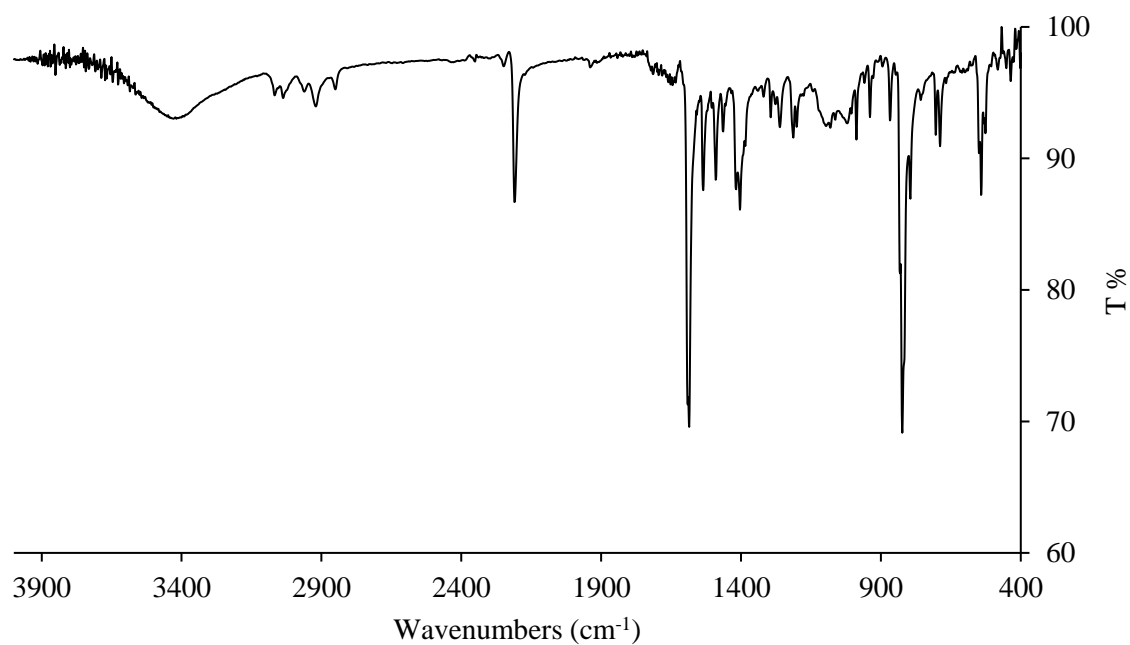
S60 FT-IR spectrum of L4.



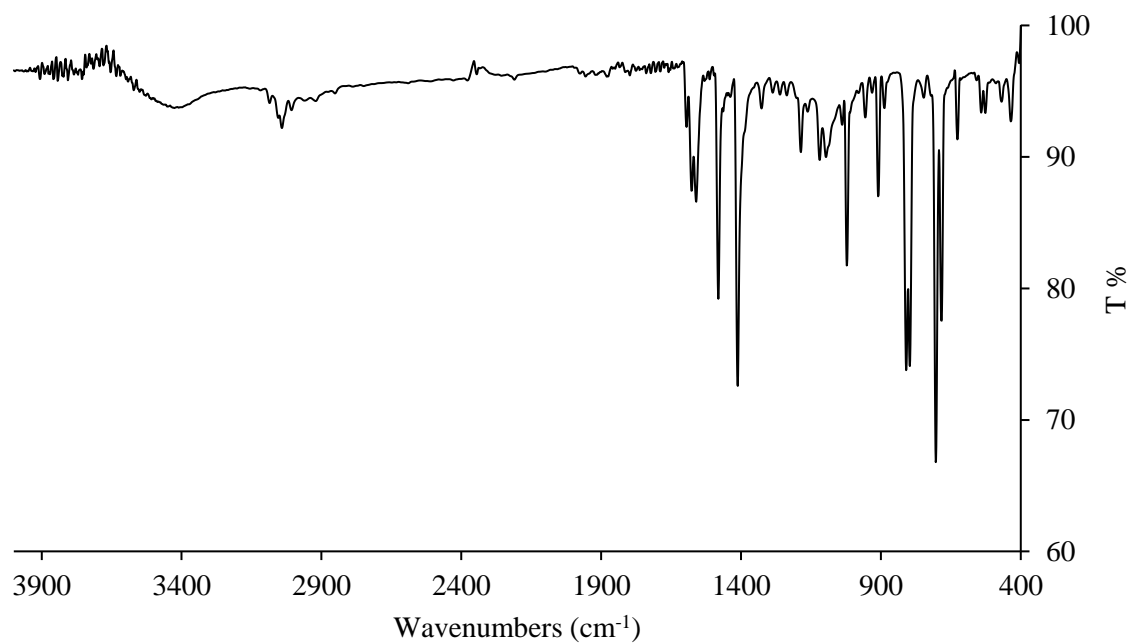
S61 FT-IR spectrum of **L5**.



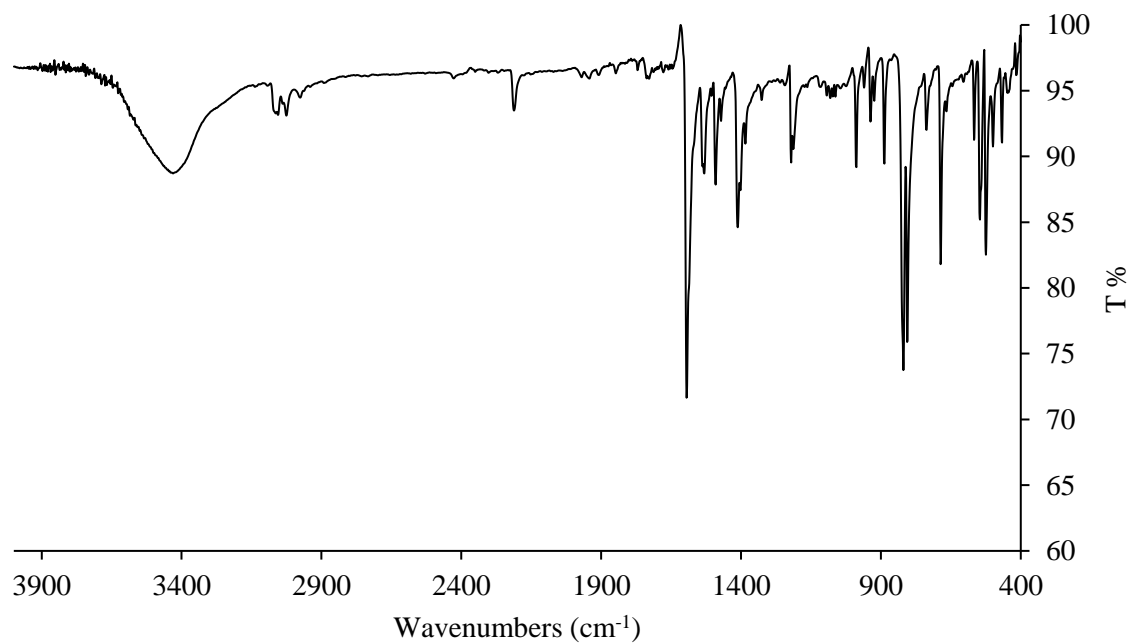
S62 FT-IR spectrum of **L6**



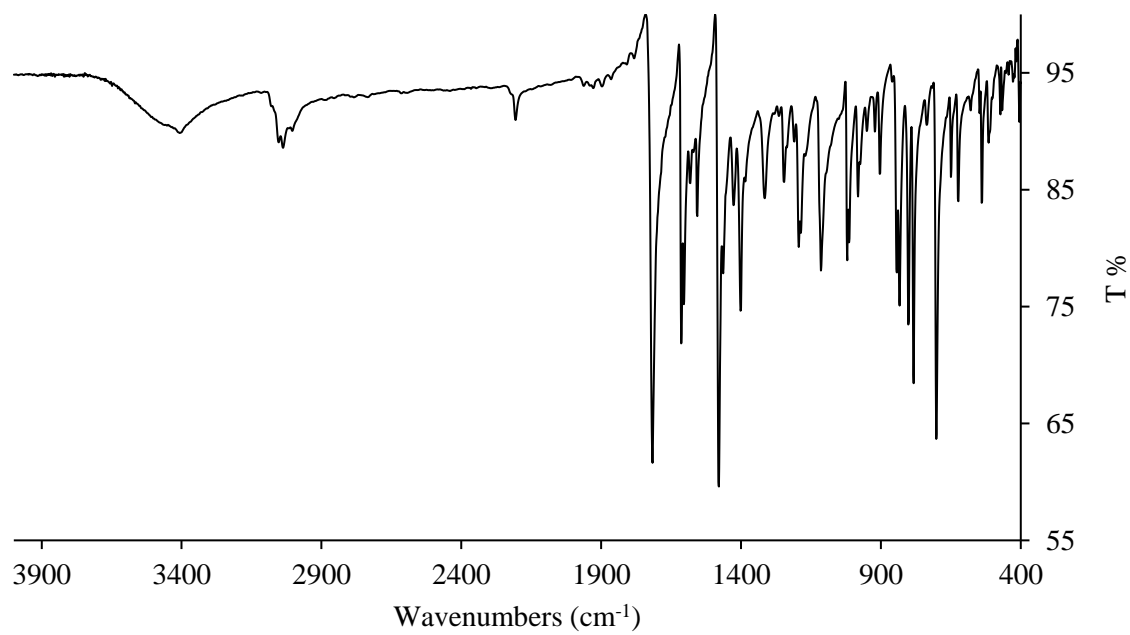
S63 FT-IR spectrum of L7.



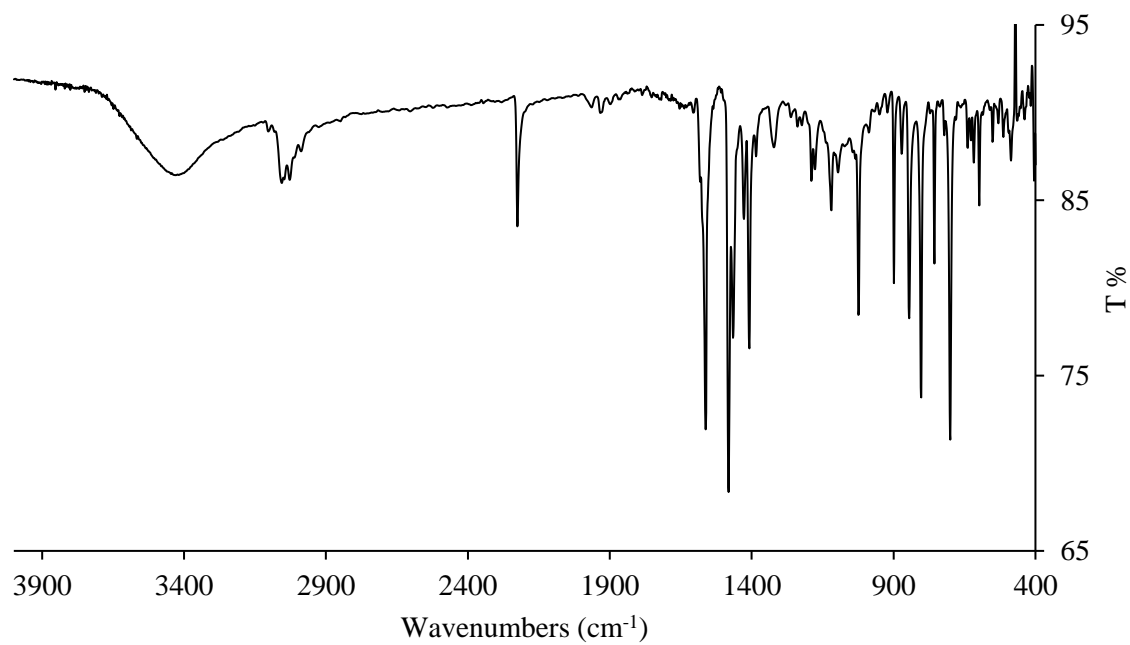
S64 FT-IR spectrum of L8.



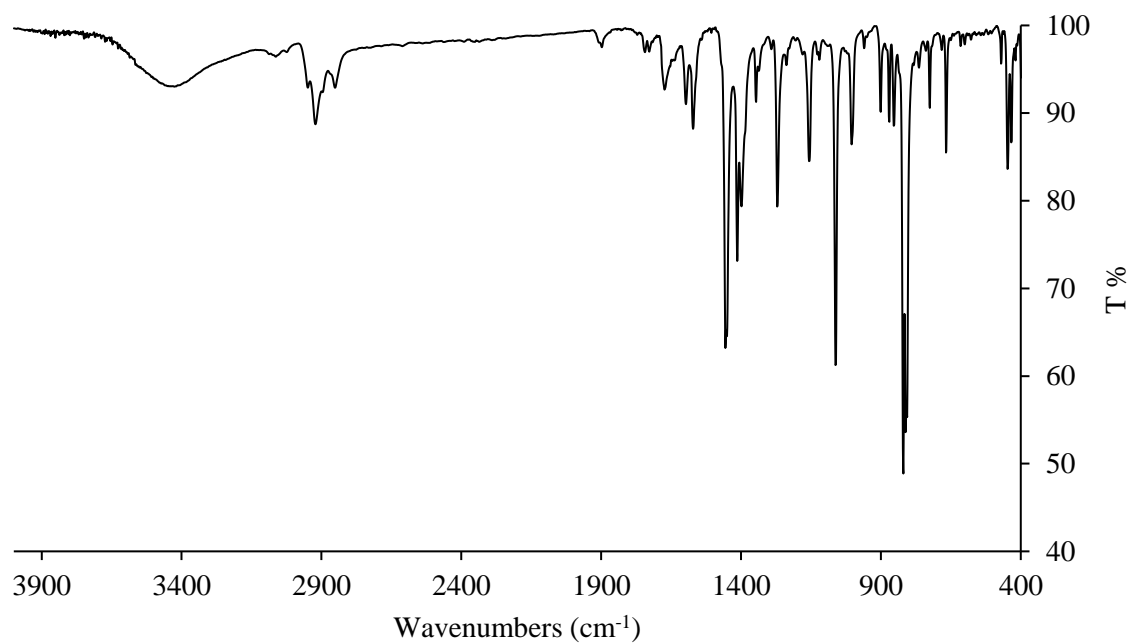
S65 FT-IR spectrum of L9.



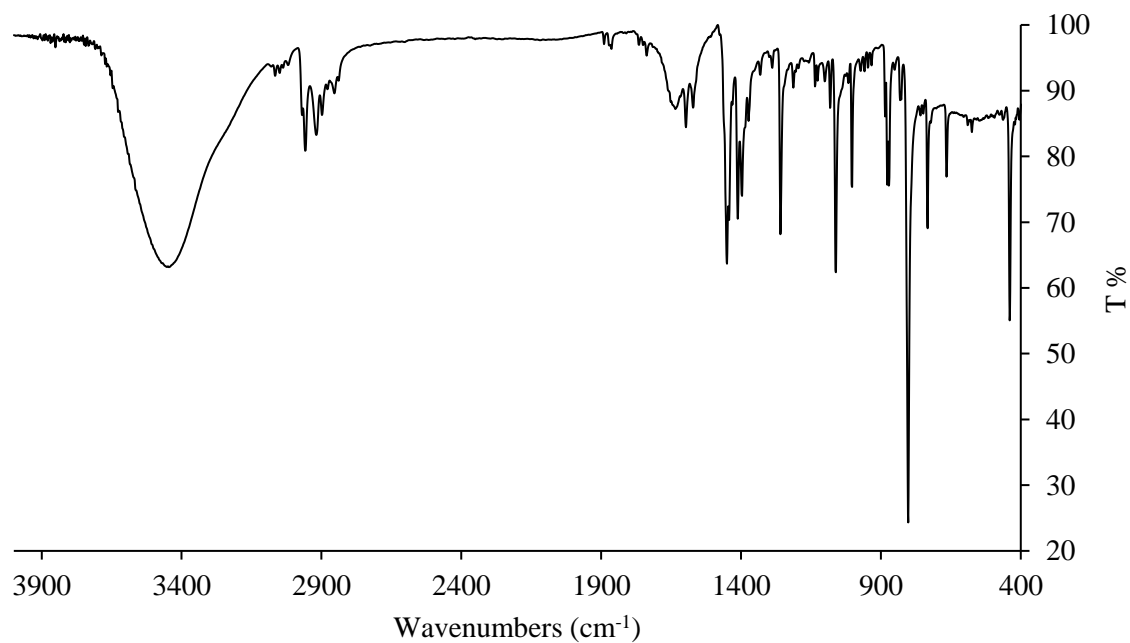
S66 FT-IR spectrum of L11.



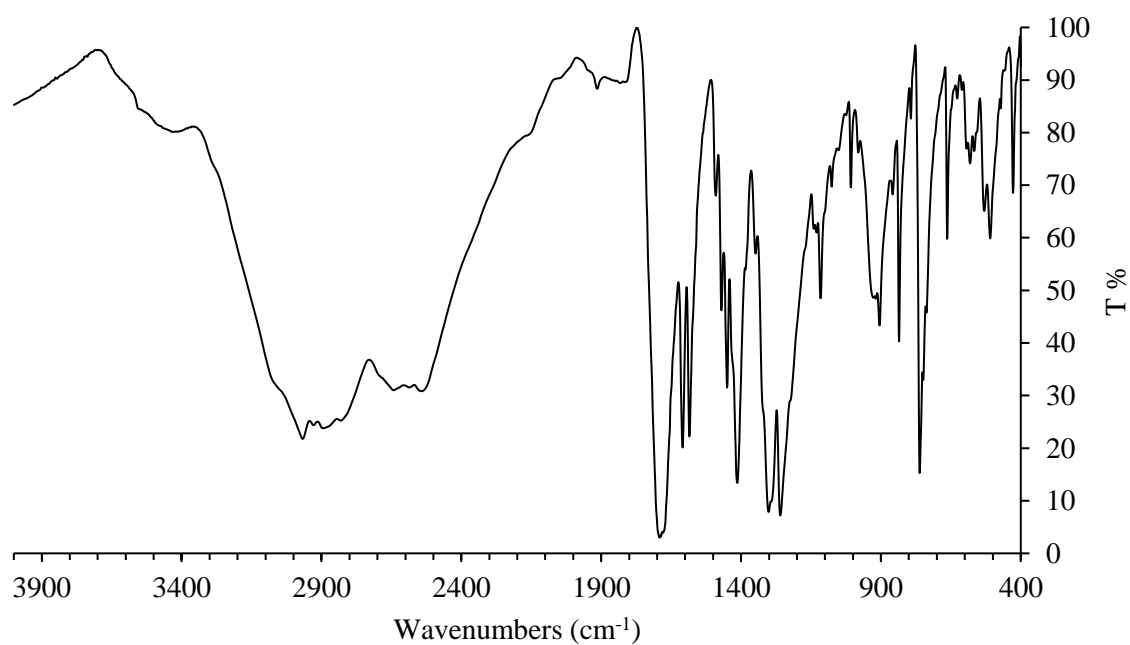
S67 FT-IR spectrum of L15.



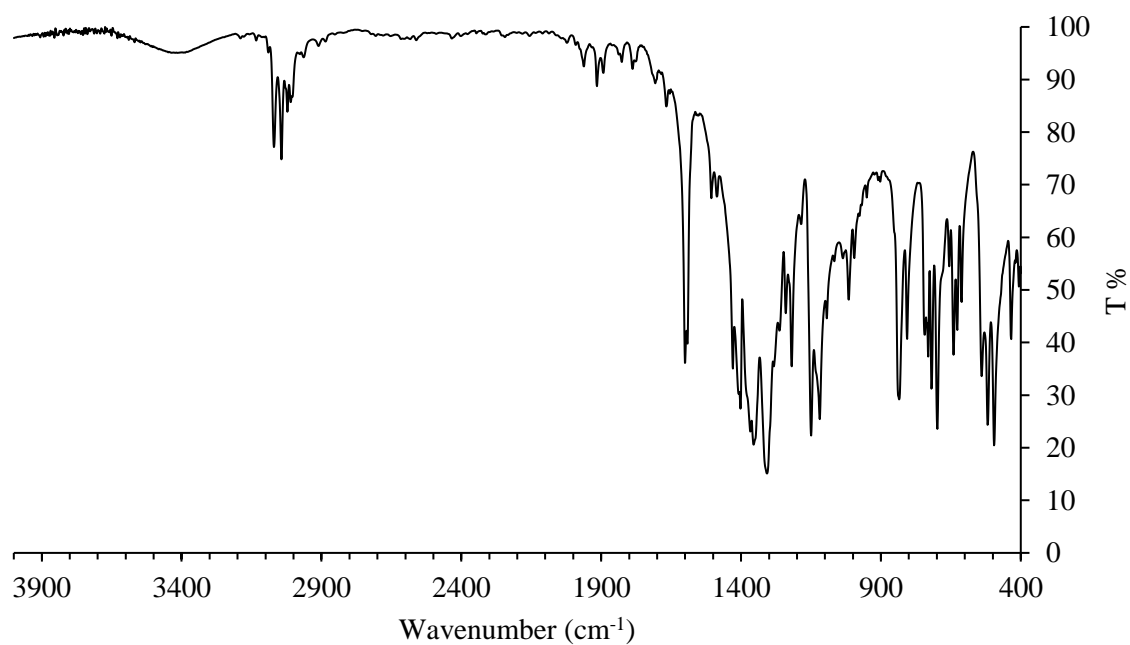
S68 FT-IR spectrum of L16.



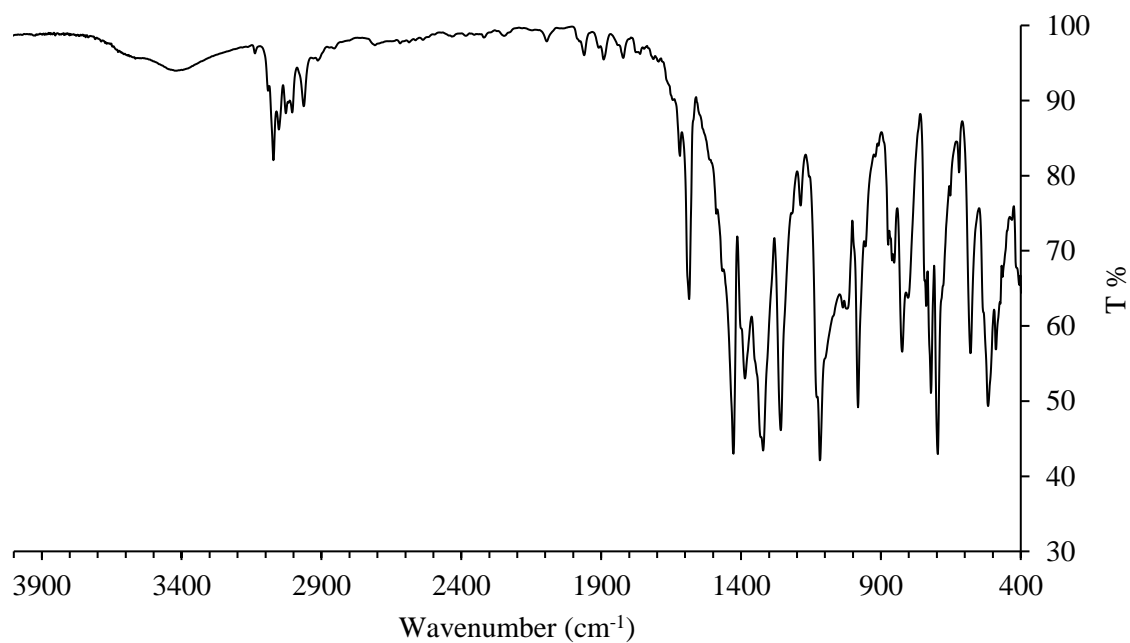
S69 FT-IR spectrum of **H4L17**.



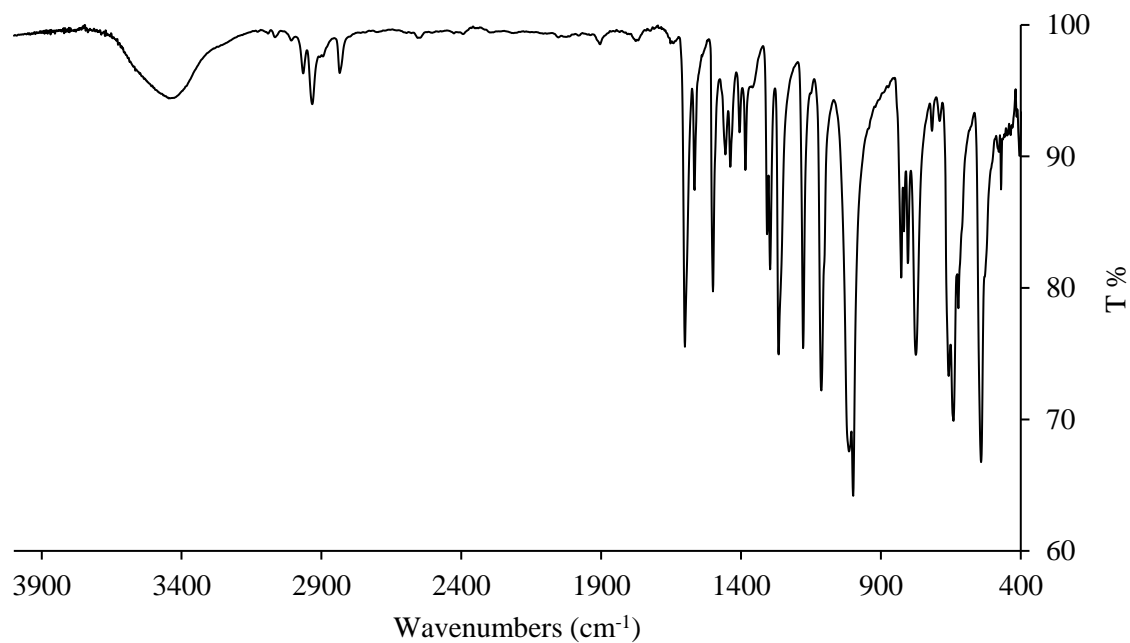
S70 FT-IR spectrum of **R2**.



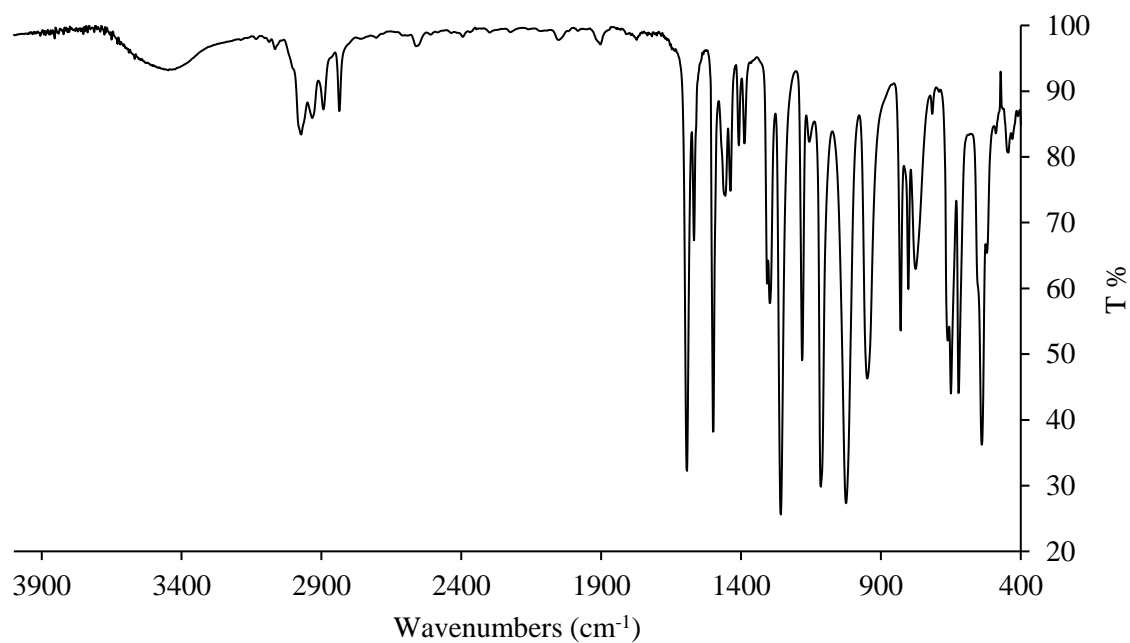
S71 FT-IR spectrum of **R3**.



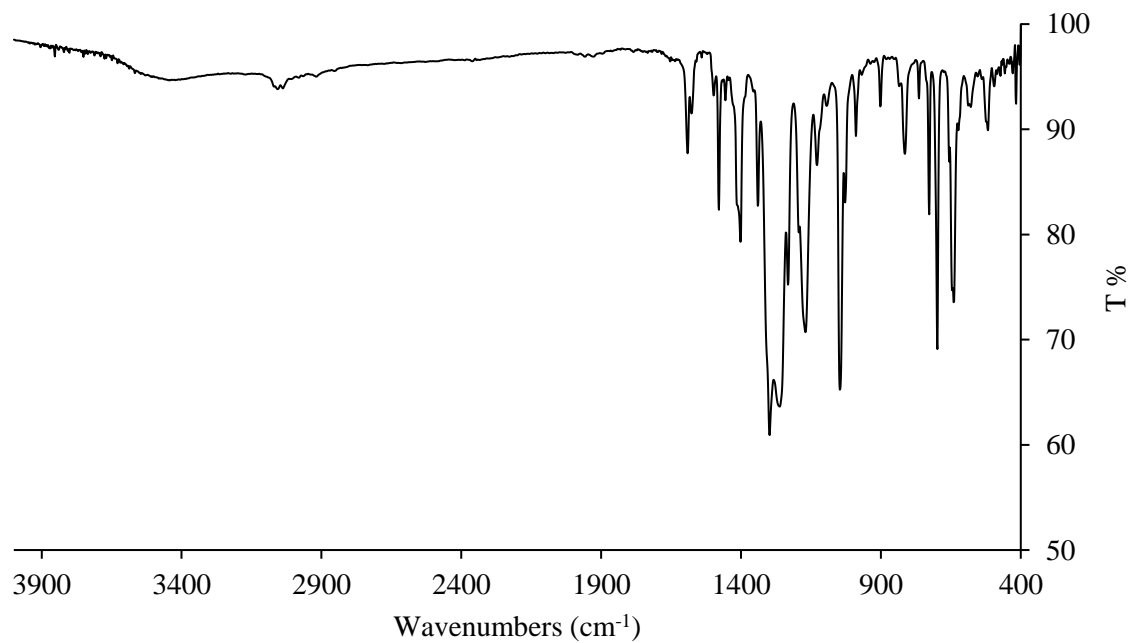
S72 FT-IR spectrum of **2**.



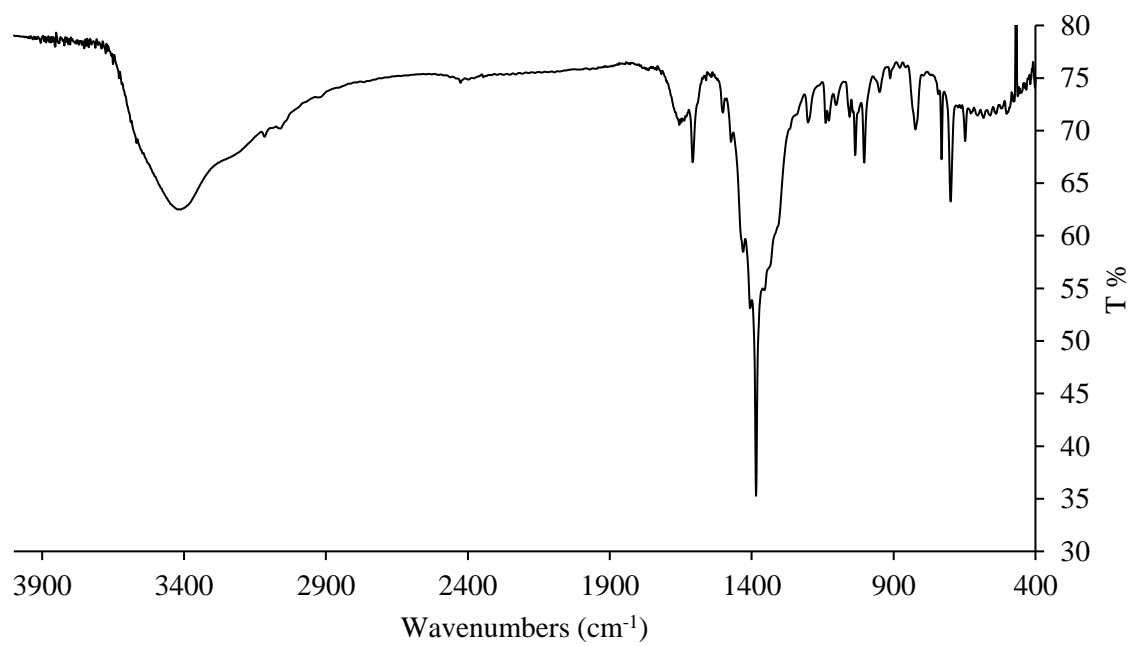
S73 FT-IR spectrum of **3**.



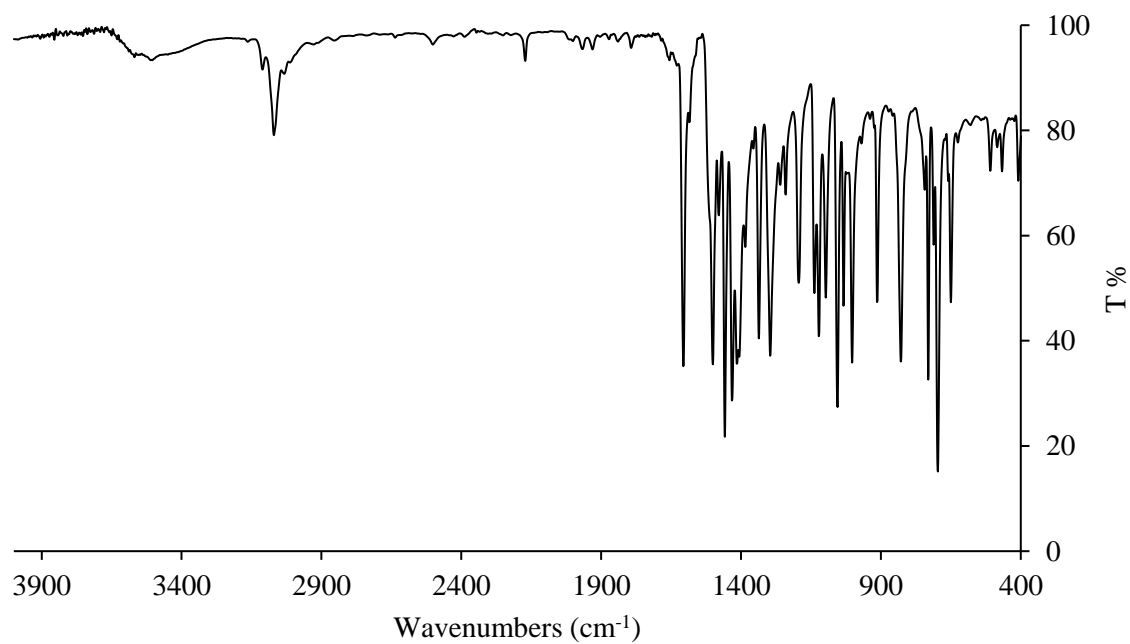
S74 FT-IR spectrum of $[\text{AgL1}(\text{OTf})\cdot((\text{CH}_3)_2\text{CO})_{0.5}]_\infty$.



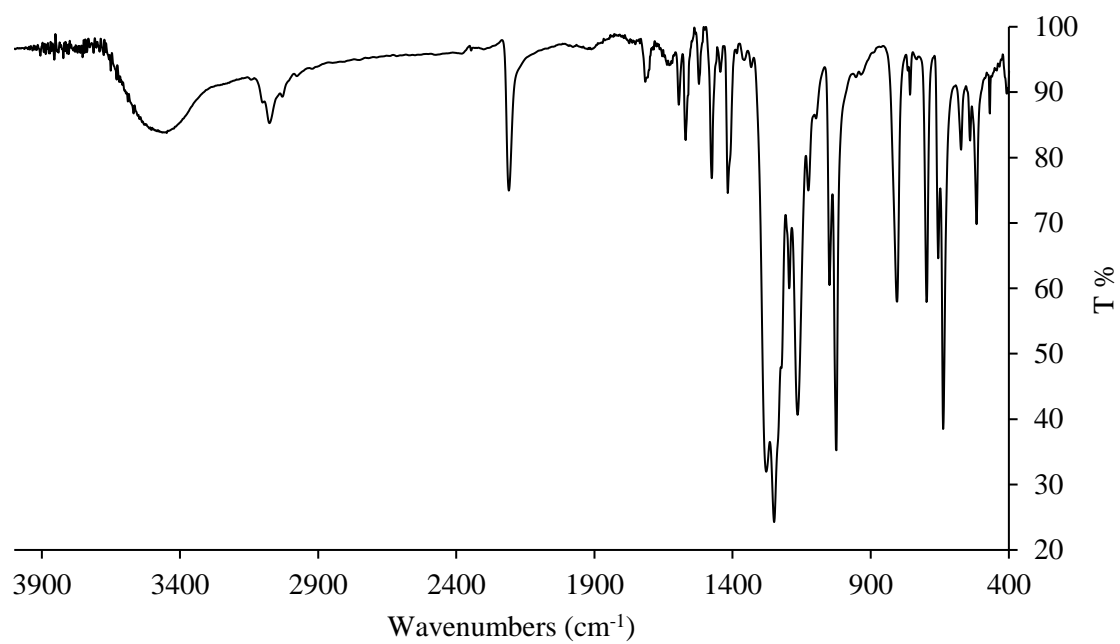
S75 FT-IR spectrum of $[\text{ZnL1}(\text{NO}_3)_2 \cdot \text{CH}_3\text{CN}]_2$.



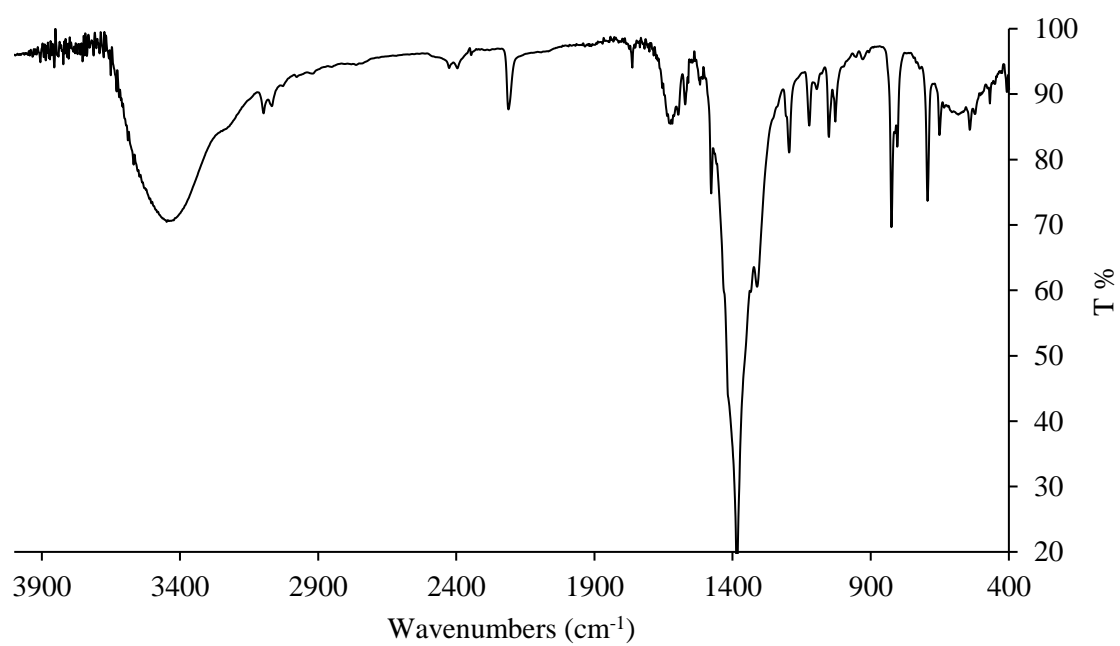
S76 FT-IR spectrum of $(\text{ZnL1Cl}_2)_\infty$.



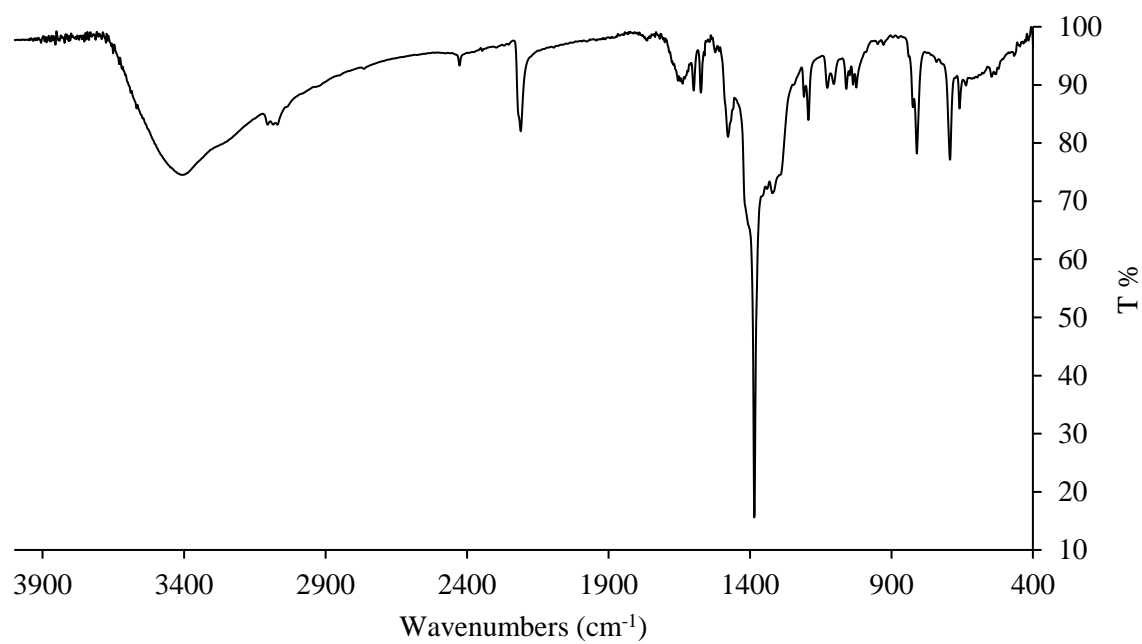
S77 FT-IR spectrum of $[\text{AgL3}(\text{OTf})((\text{CH}_3)_2\text{CO})_{2.5}]_x$.



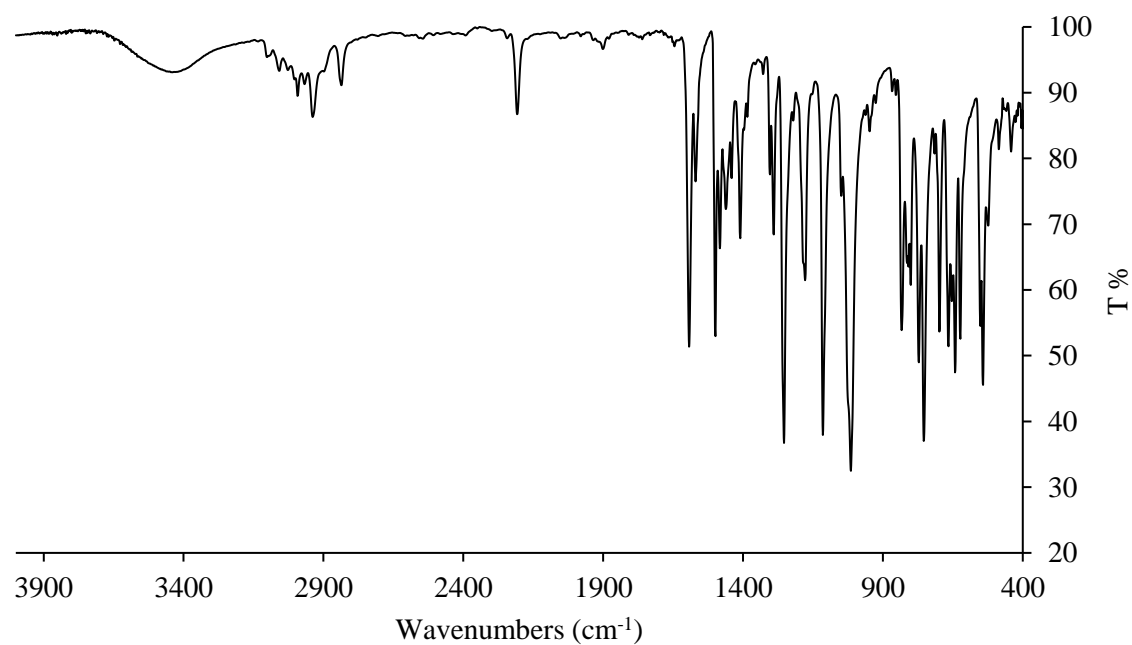
S78 FT-IR spectrum of $[\text{CdL3}(\text{NO}_3)_2(\text{H}_2\text{O})_2 \cdot 1.5\text{H}_2\text{O}]_\infty$.



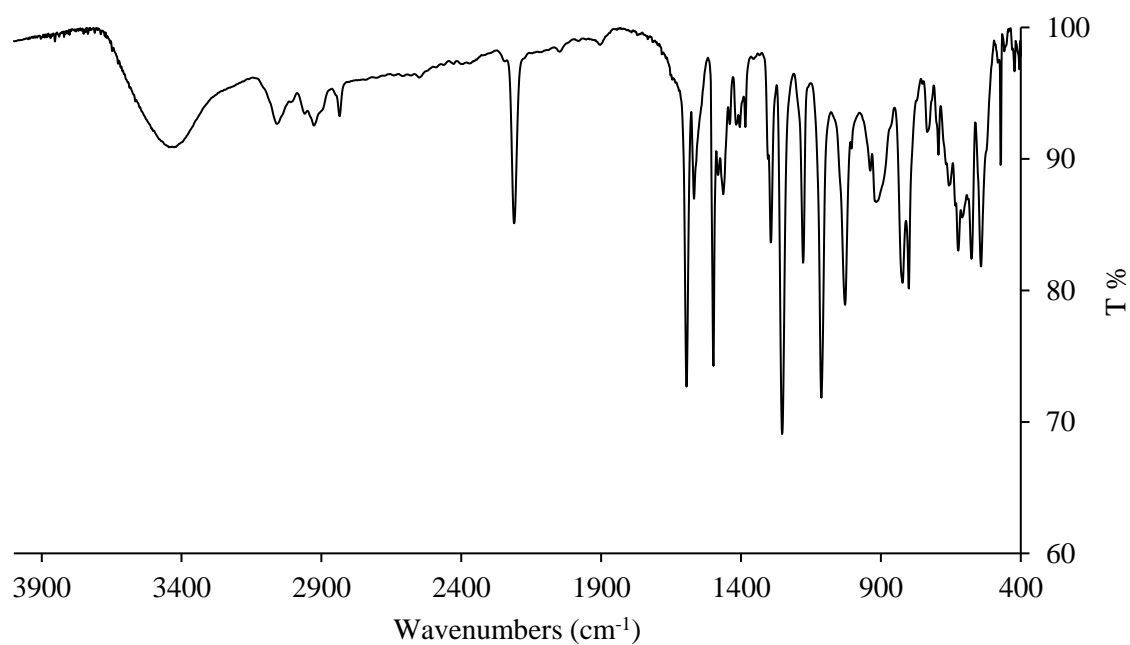
S79 FT-IR spectrum of $[\text{CuL3}(\text{NO}_3)_2 \cdot \text{CH}_3\text{CN}]_2 \cdot 2\text{CH}_3\text{CN}$



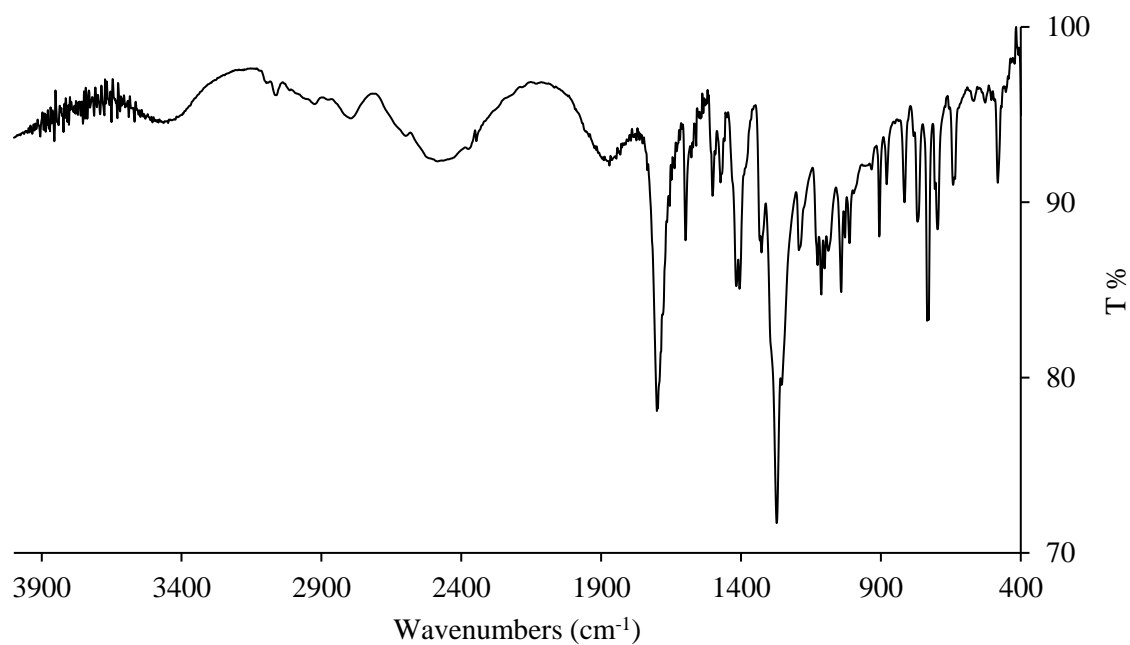
S80 FT-IR spectrum of $[2 \cdot \text{L5} \cdot (\text{CHCl}_3)]_\infty$.



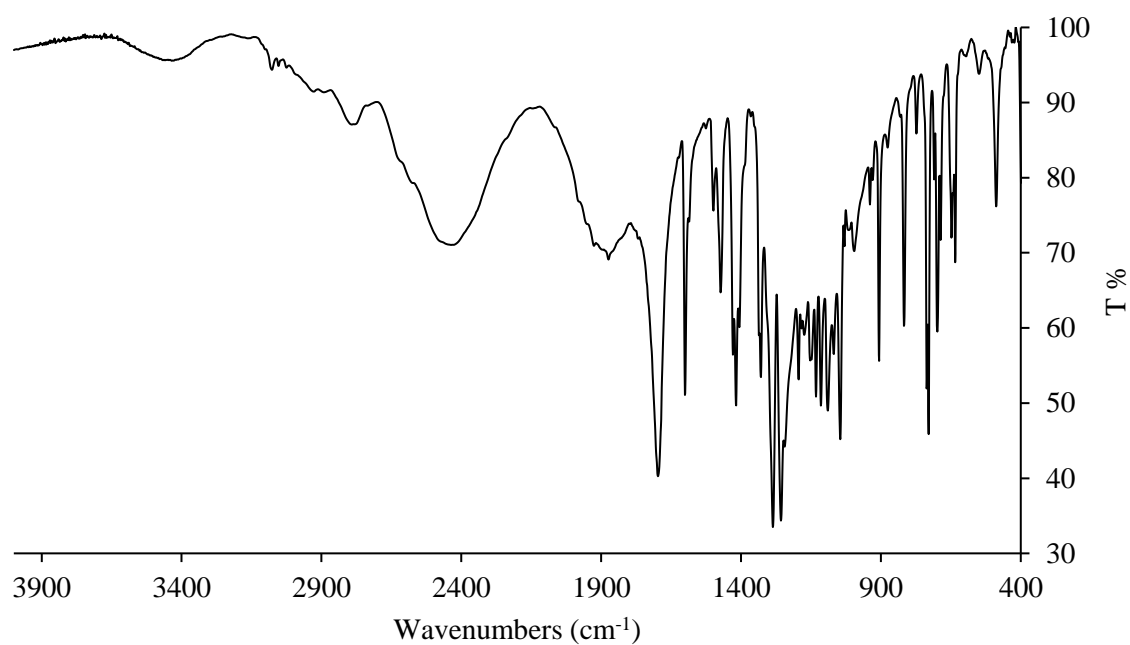
S81 FT-IR spectrum of **[3·L5]_∞**.



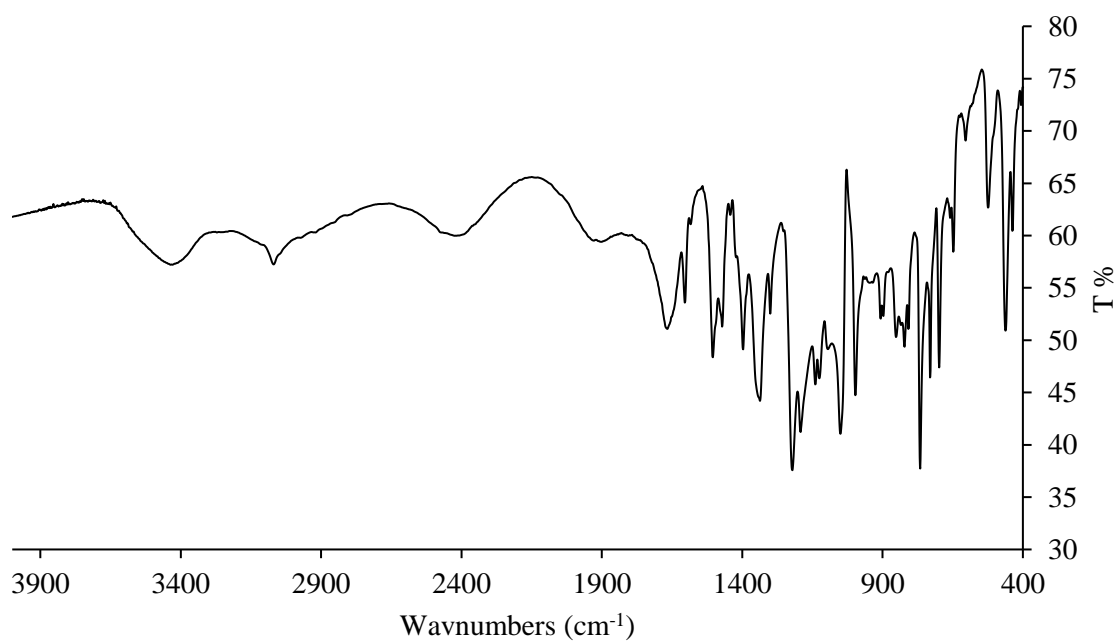
S82 FT-IR spectrum of **L1·H₂TER**.



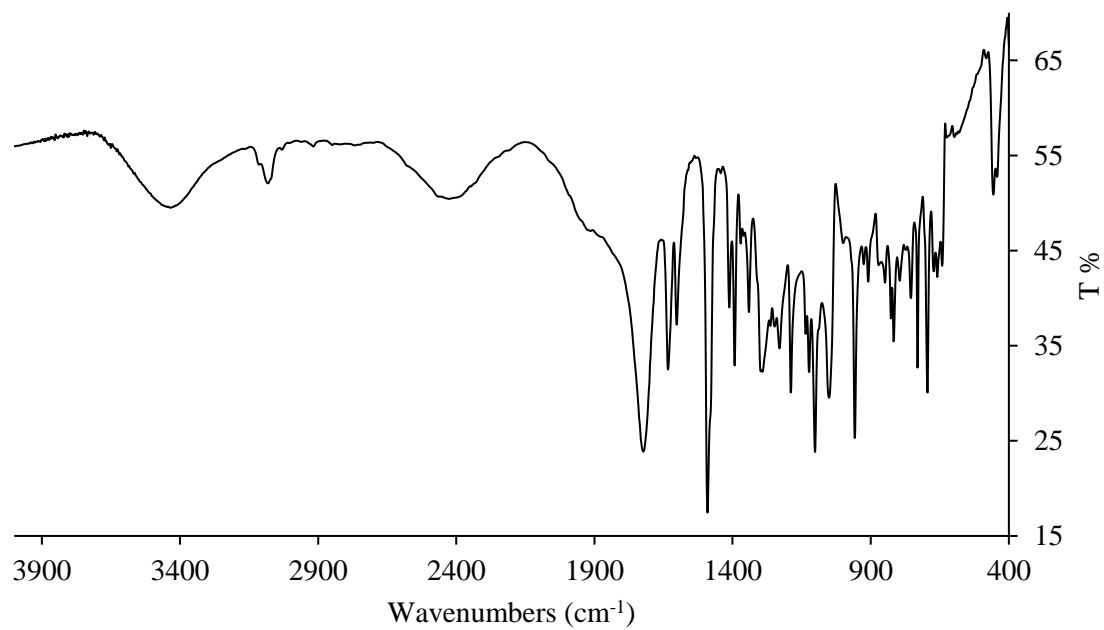
S83 FT-IR spectrum of **L1·H₂ISO**



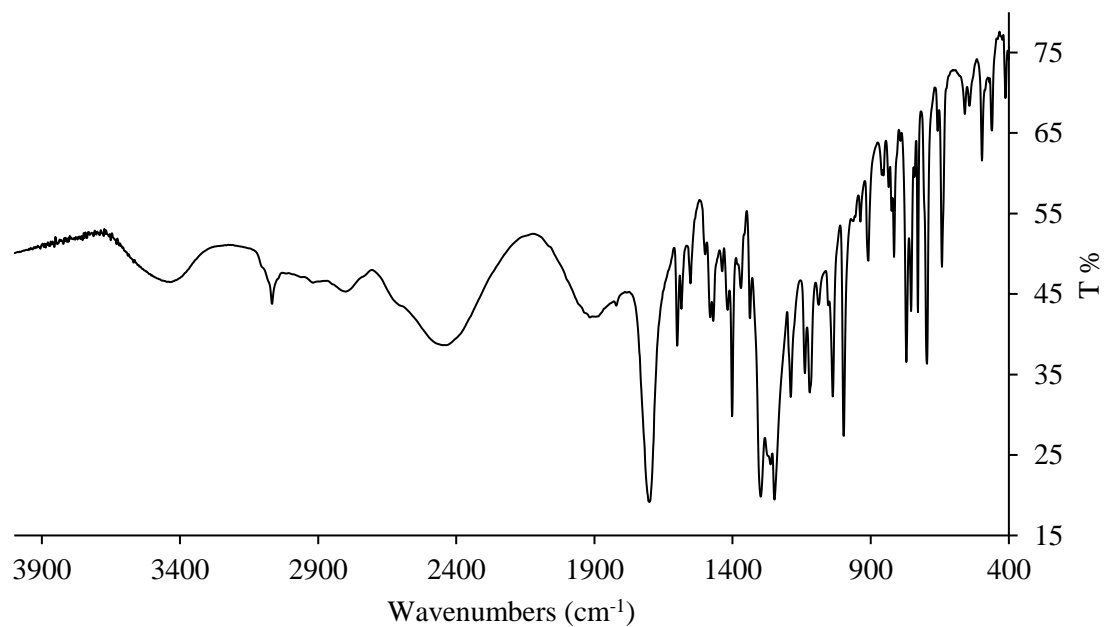
S84 FT-IR spectrum of **(L1·H₂TER-(OH)₂)_∞**



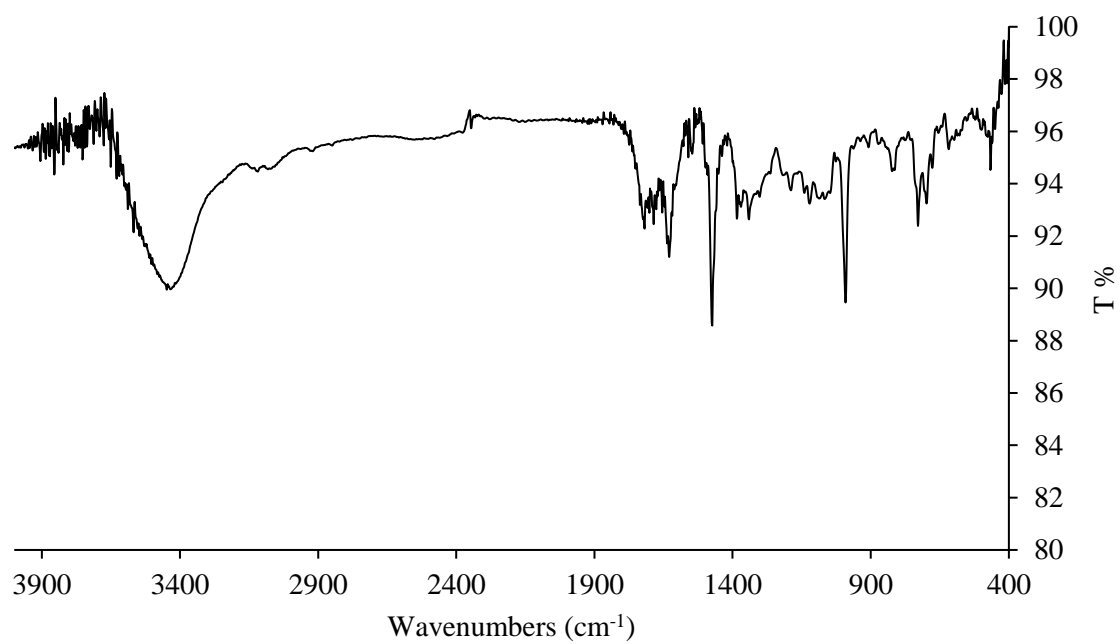
S85 FT-IR spectrum of **L1·H₂ISOF₄**.



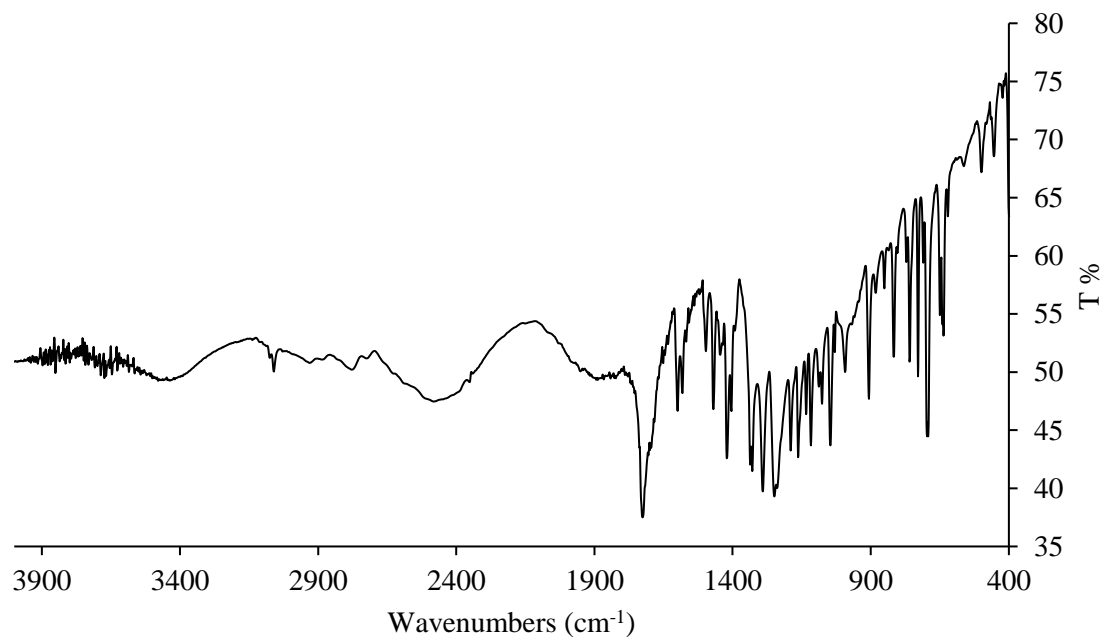
S86 FT-IR spectrum of **L1·H₂TER-Br**



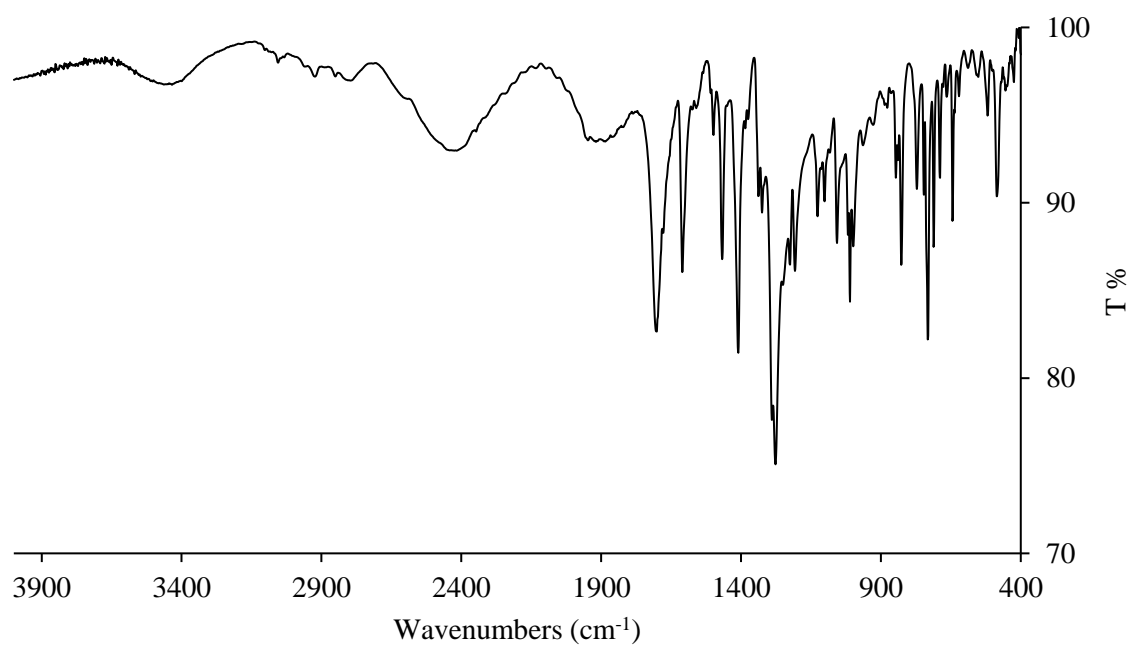
S87 FT-IR spectrum of **L1·H₂TER-F₄**



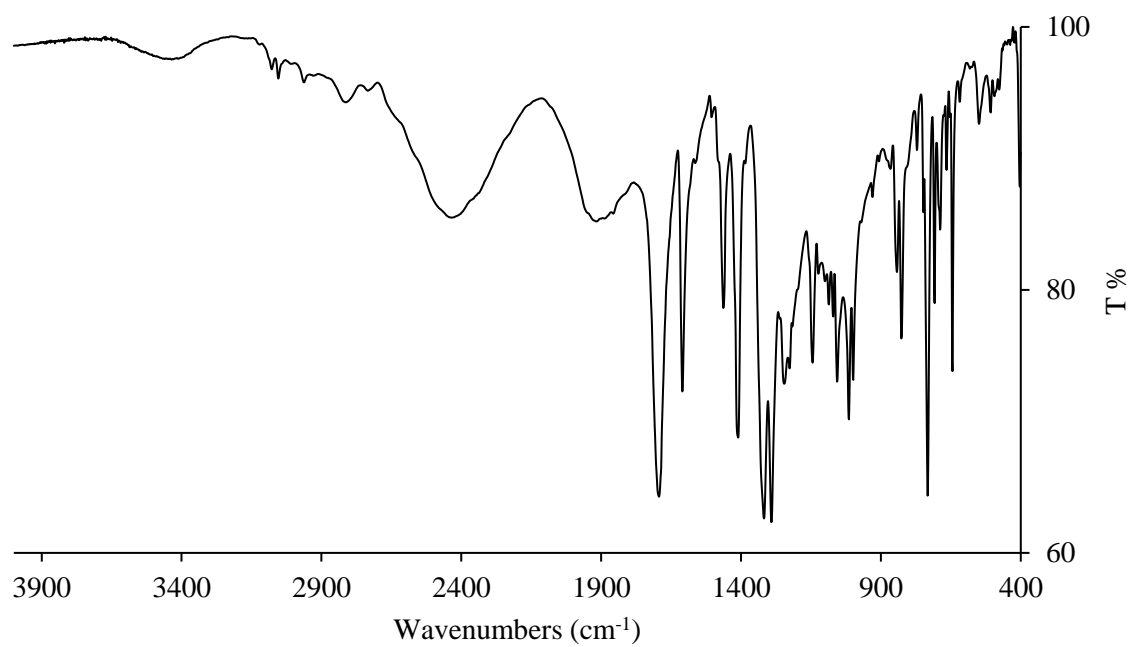
S88 FT-IR spectrum of **L1·H₂PyDC**



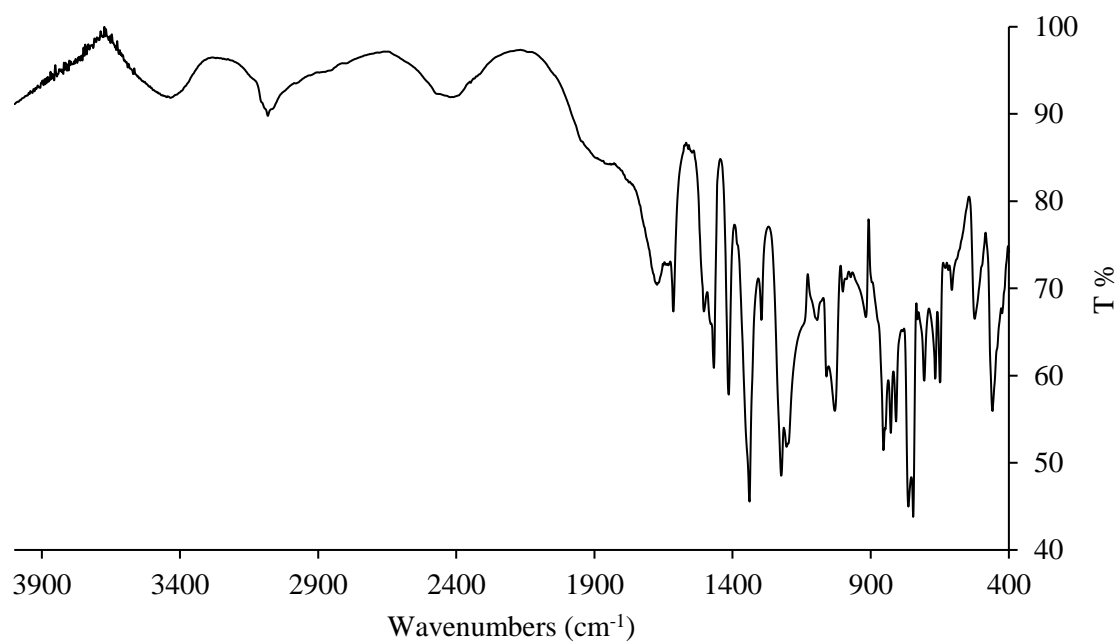
S89 FT-IR spectrum of **L2·H₂TER**



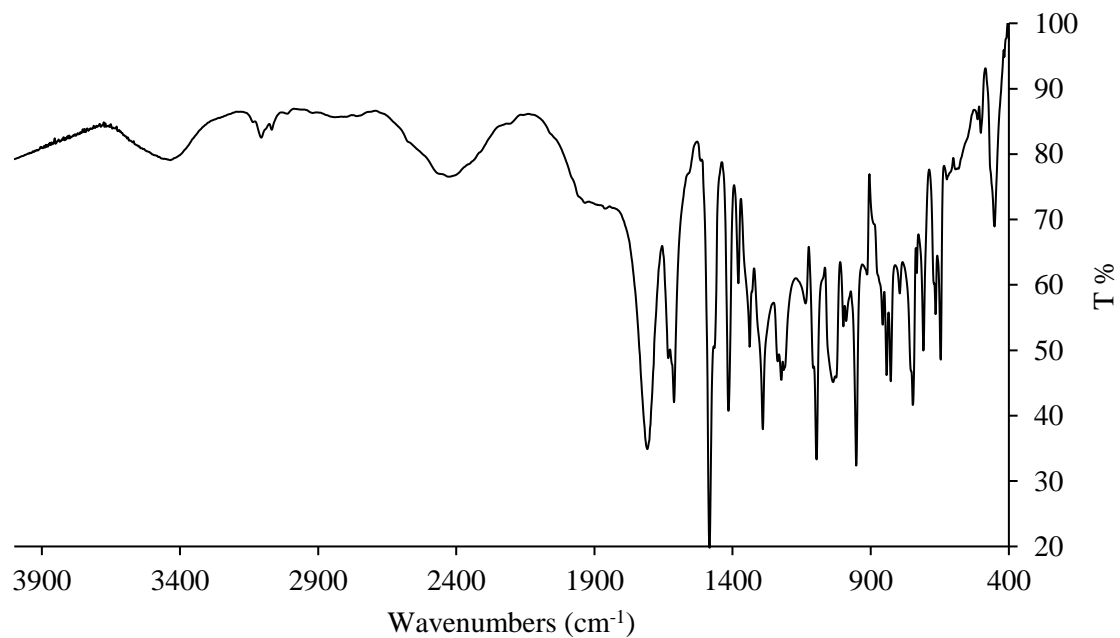
S90 FT-IR spectrum of **L2·H₂ISO**



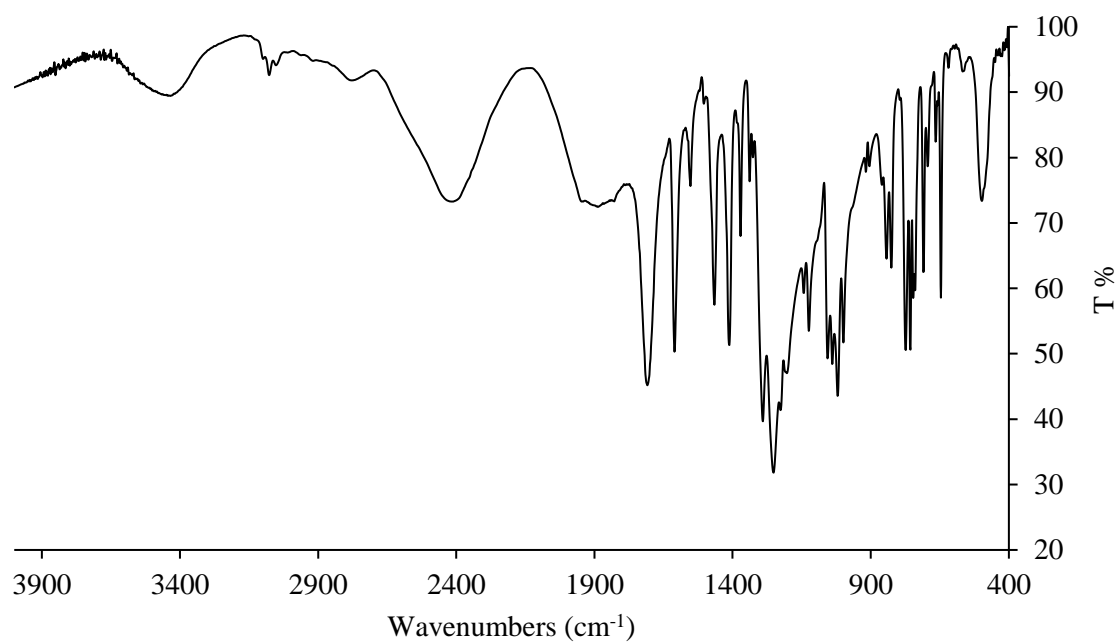
S91 FT-IR spectrum of $(L2 \cdot H_2TER-(OH)_2)_\infty$



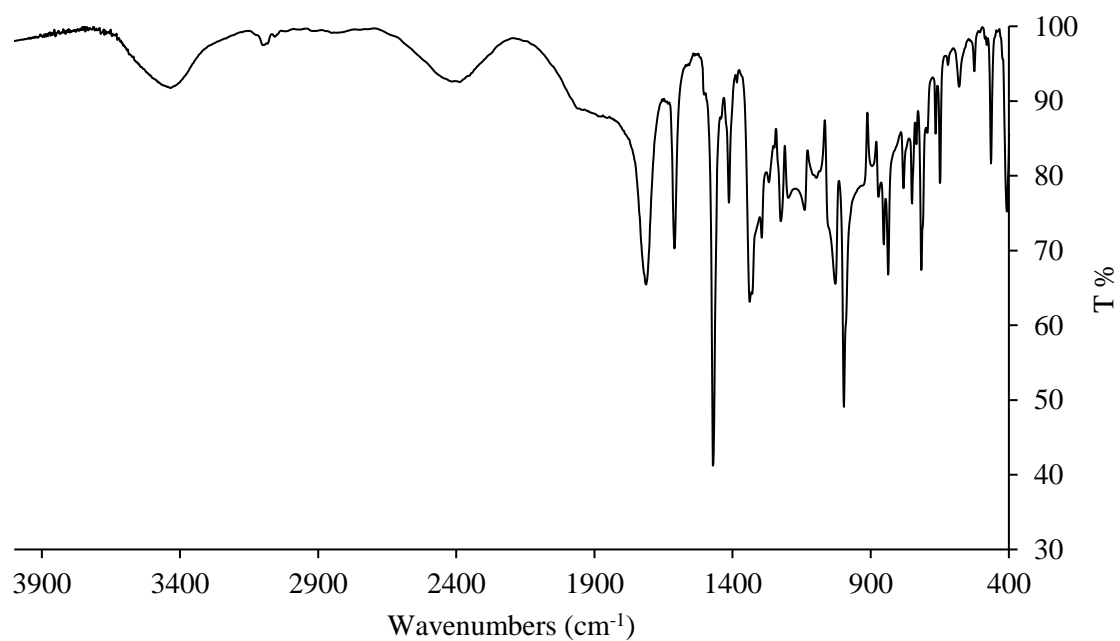
S92 FT-IR spectrum of $L2 \cdot H_2ISOF_4$



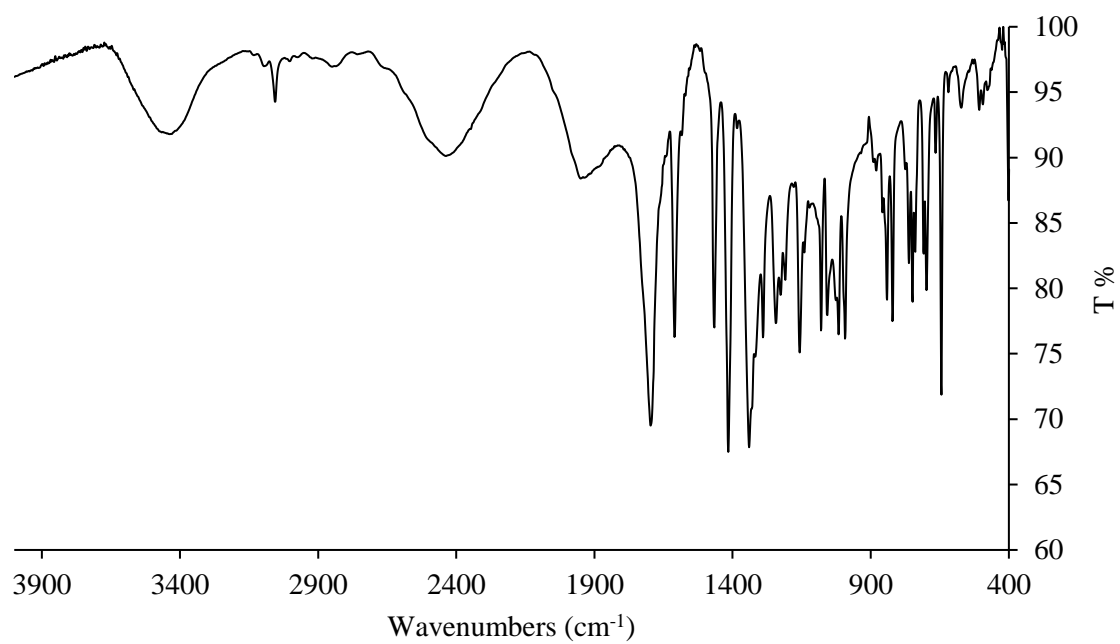
S93 FT-IR spectrum of **L2·H₂TER-Br**



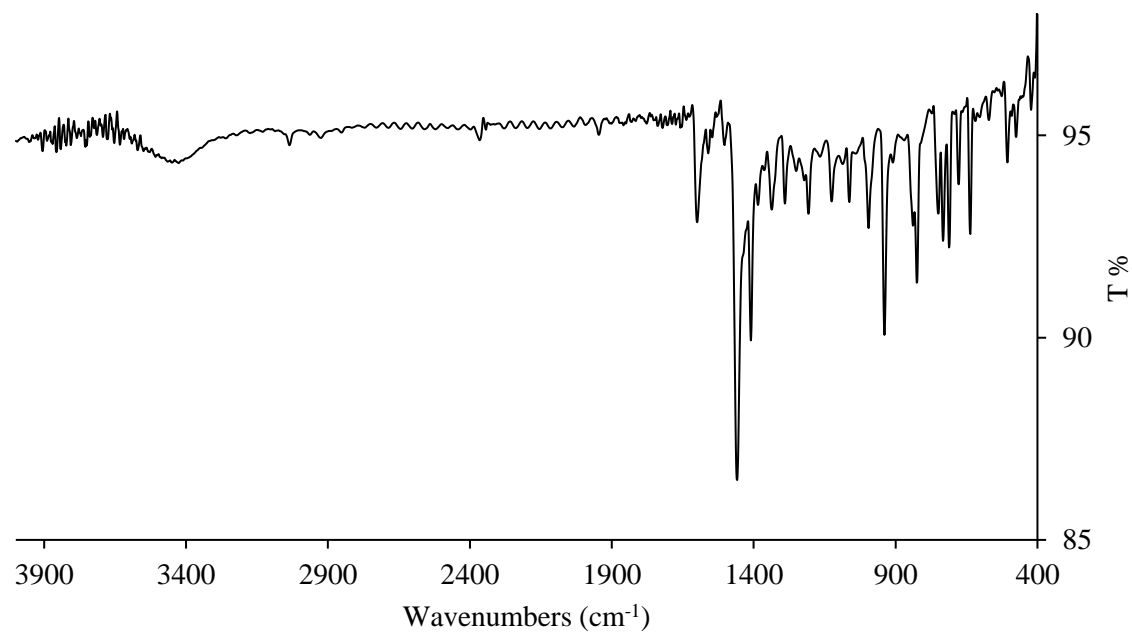
S94 FT-IR spectrum of **L2·H₂TER-F₄**



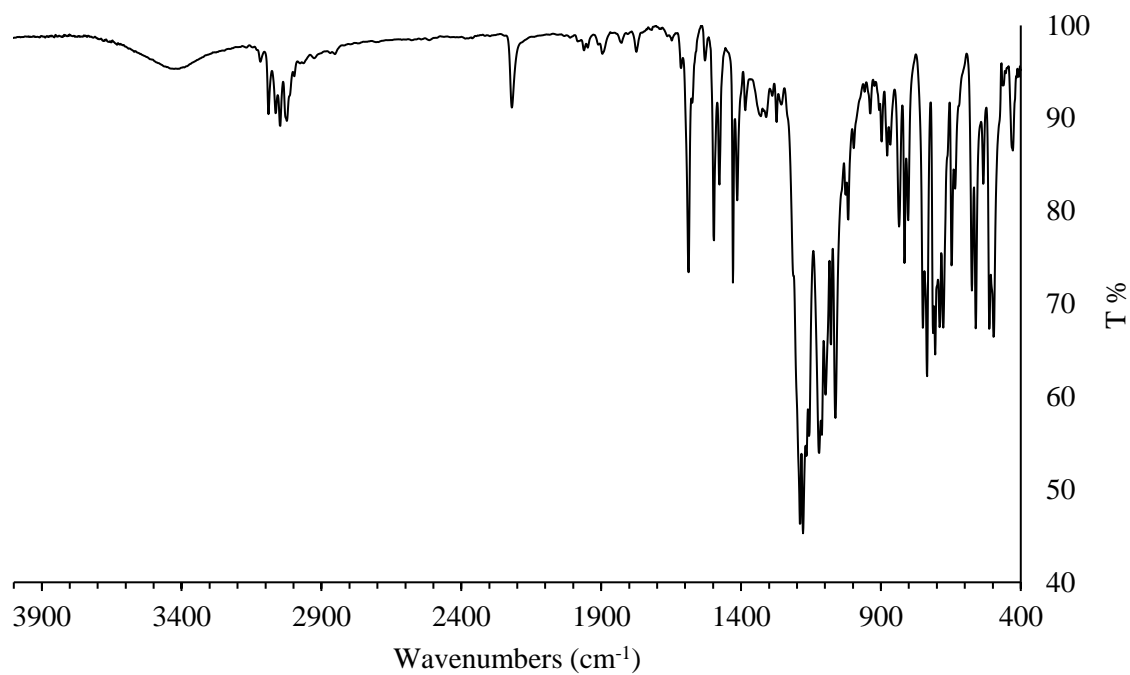
S95 FT-IR spectrum of **L2·H₂PyDC**



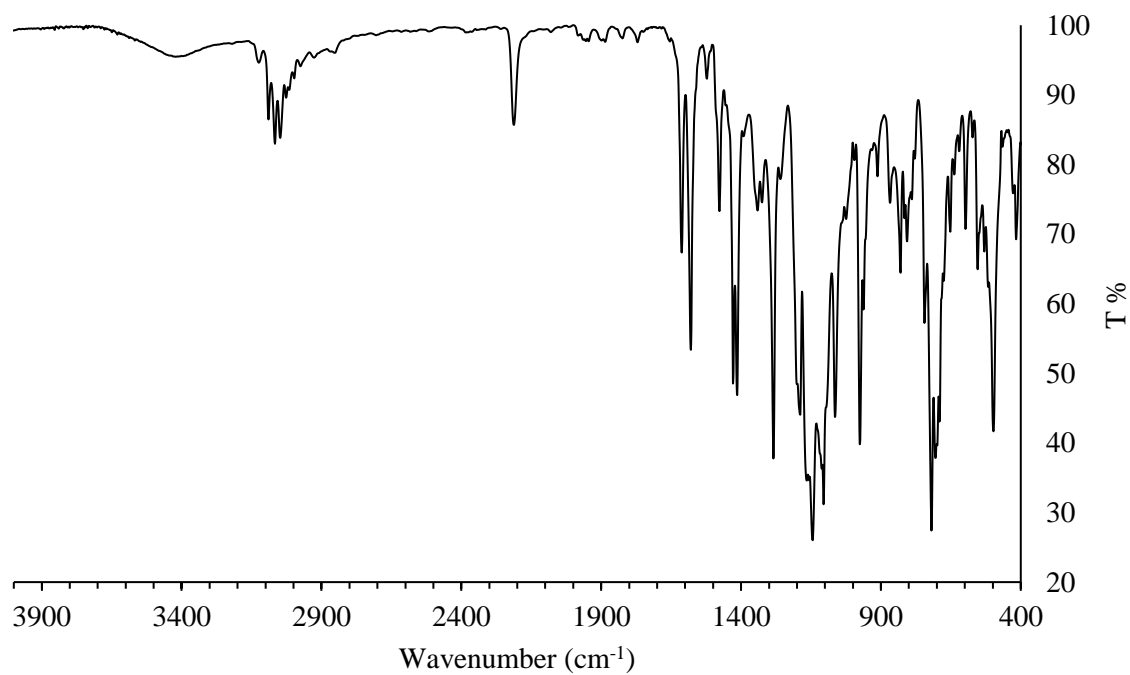
S96 FT-IR spectrum of **L2·1,4-DITFB**.



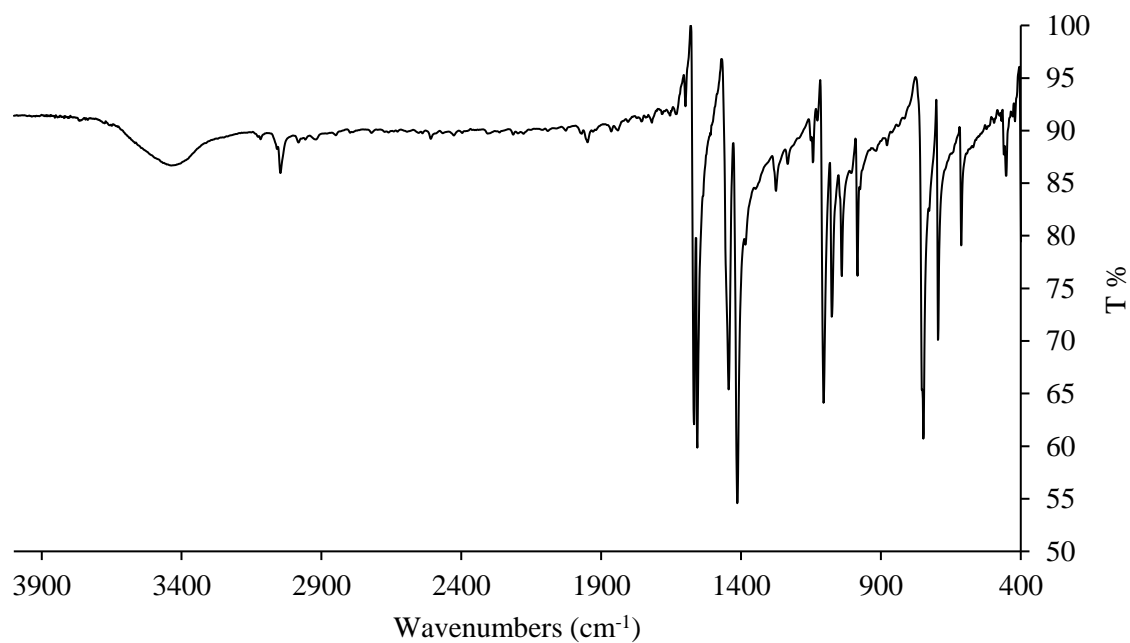
S97 FT-IR spectrum of (L3·R2)_∞.



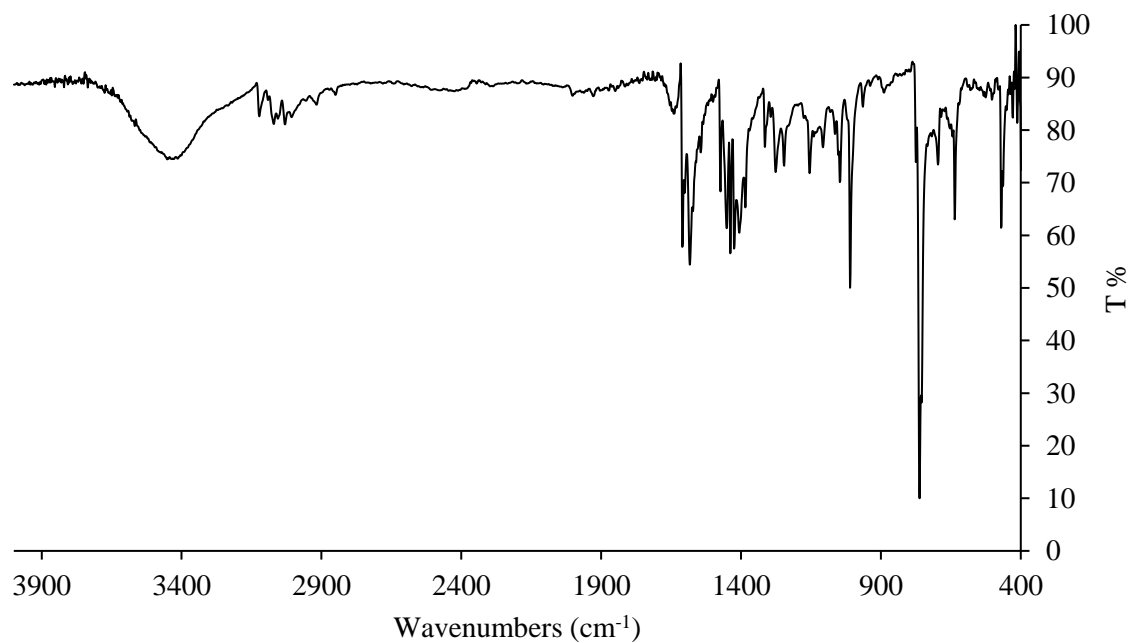
S98 FT-IR spectrum of (L3·R3)_∞.



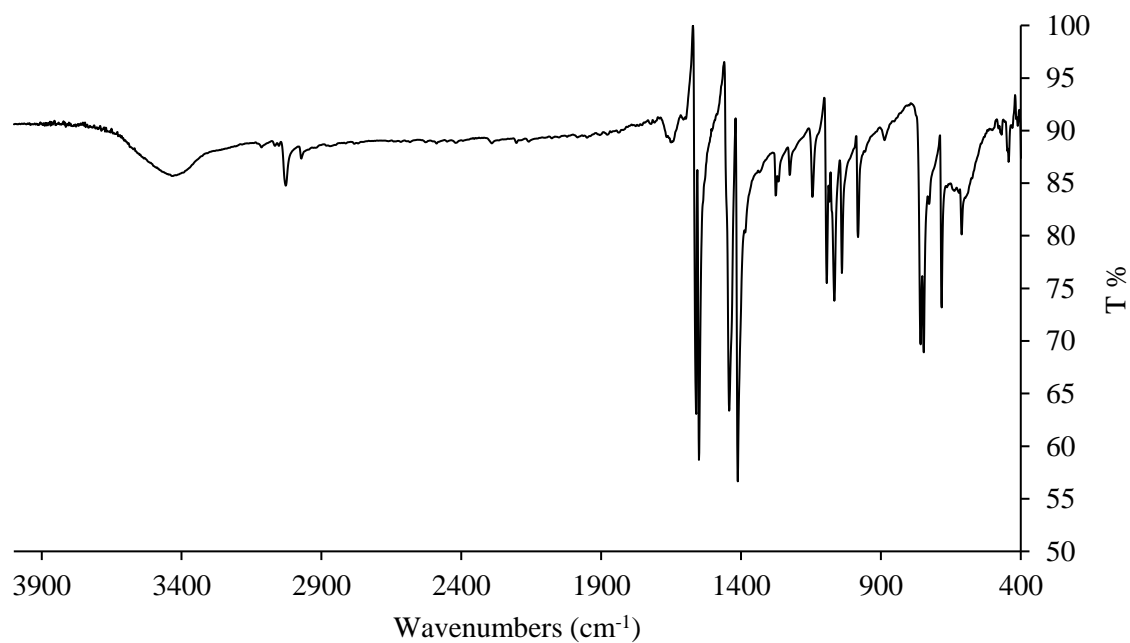
S99 FT-IR spectrum of **L12**



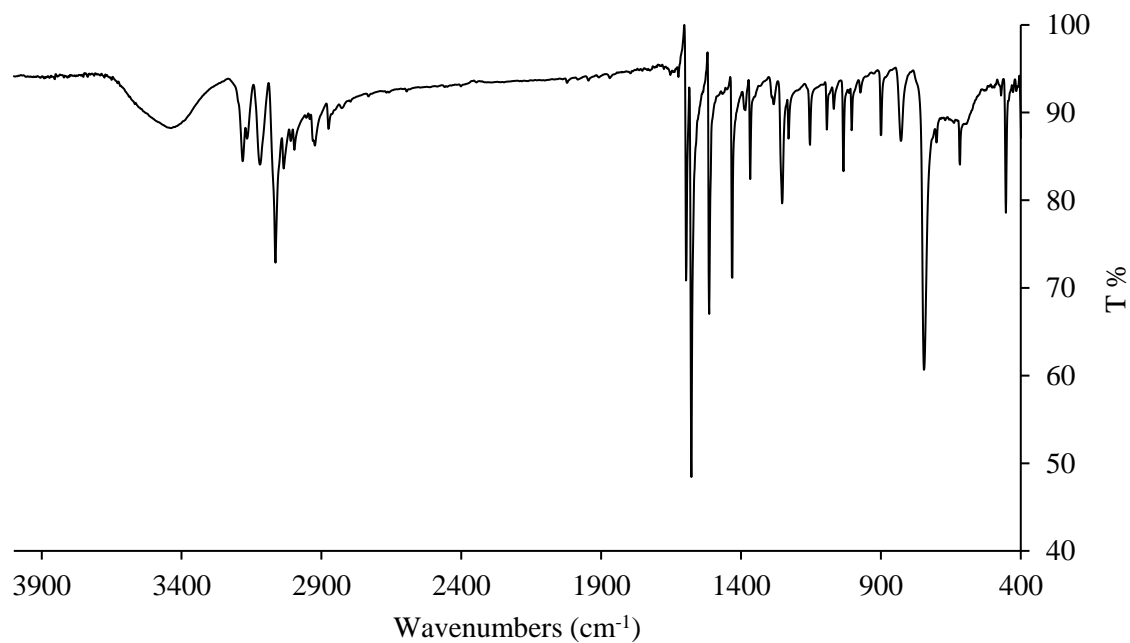
S100 FT-IR spectrum of **(HL12)I · 2.5 I₂**.



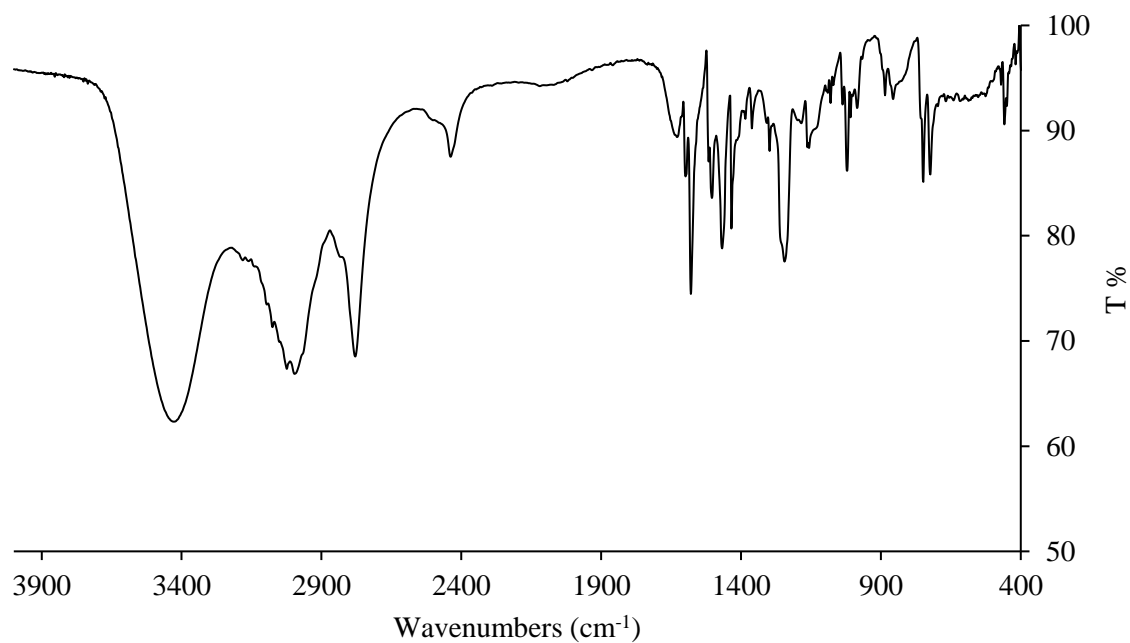
S101 FT-IR spectrum of **L13**



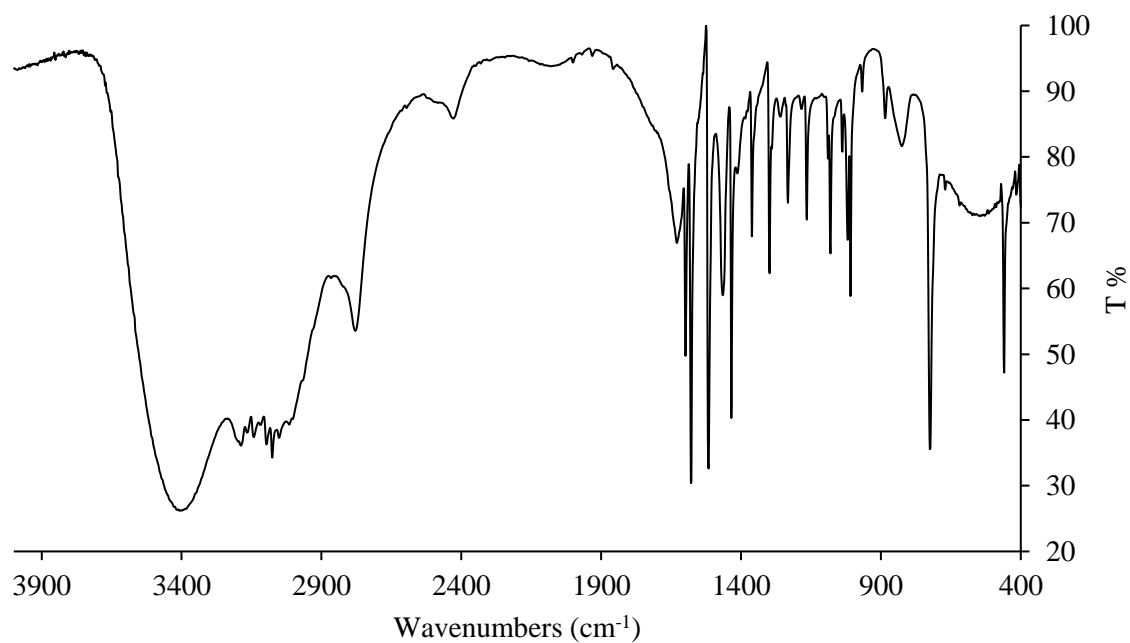
S102 FT-IR spectrum of **HPyTeI₂**.



S103 FT-IR spectrum of **HPyTeBr₂**

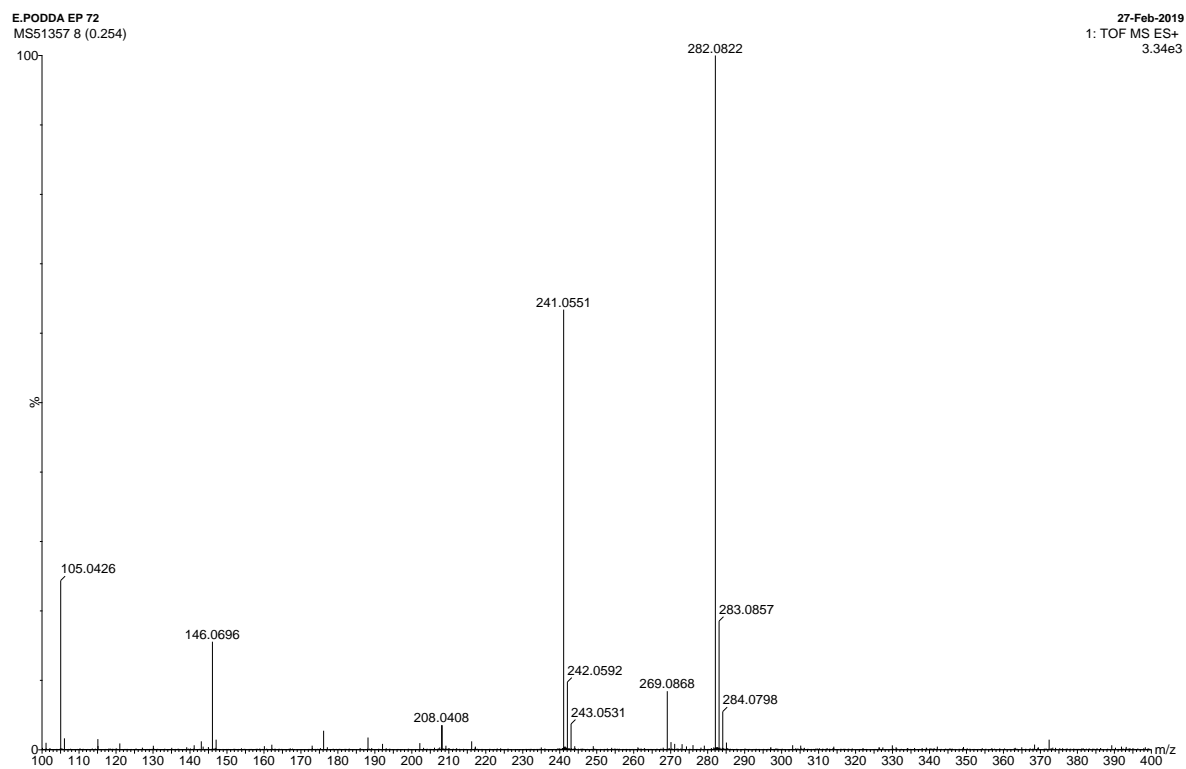


S104 FT-IR spectrum of **HPyTeBr₄**

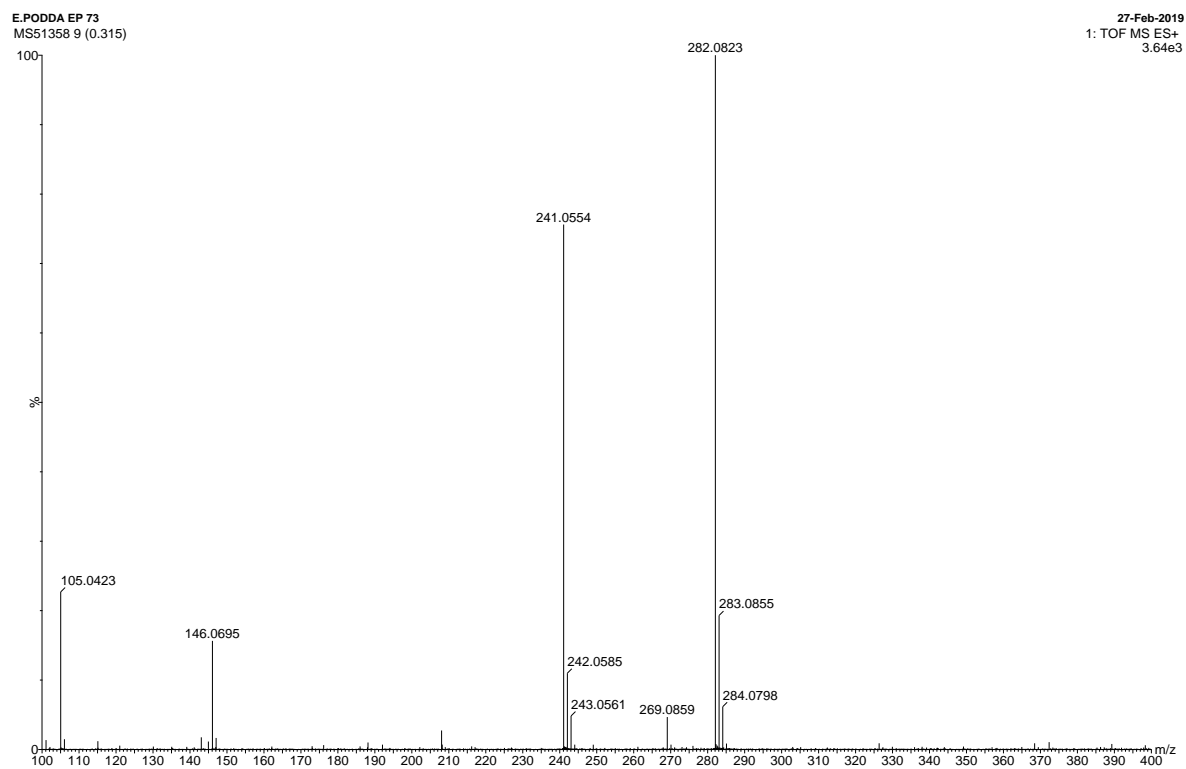


Appendix 3: Mass spectra

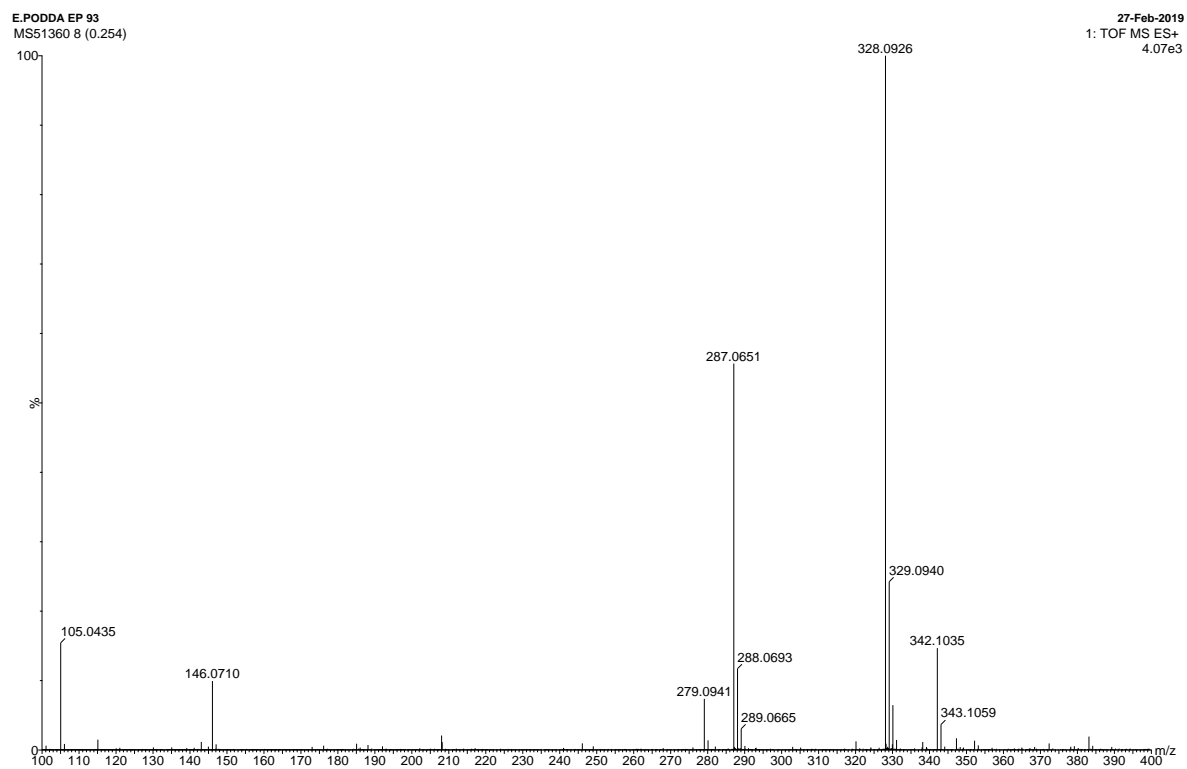
S105 TOF MS ES+ of L1.



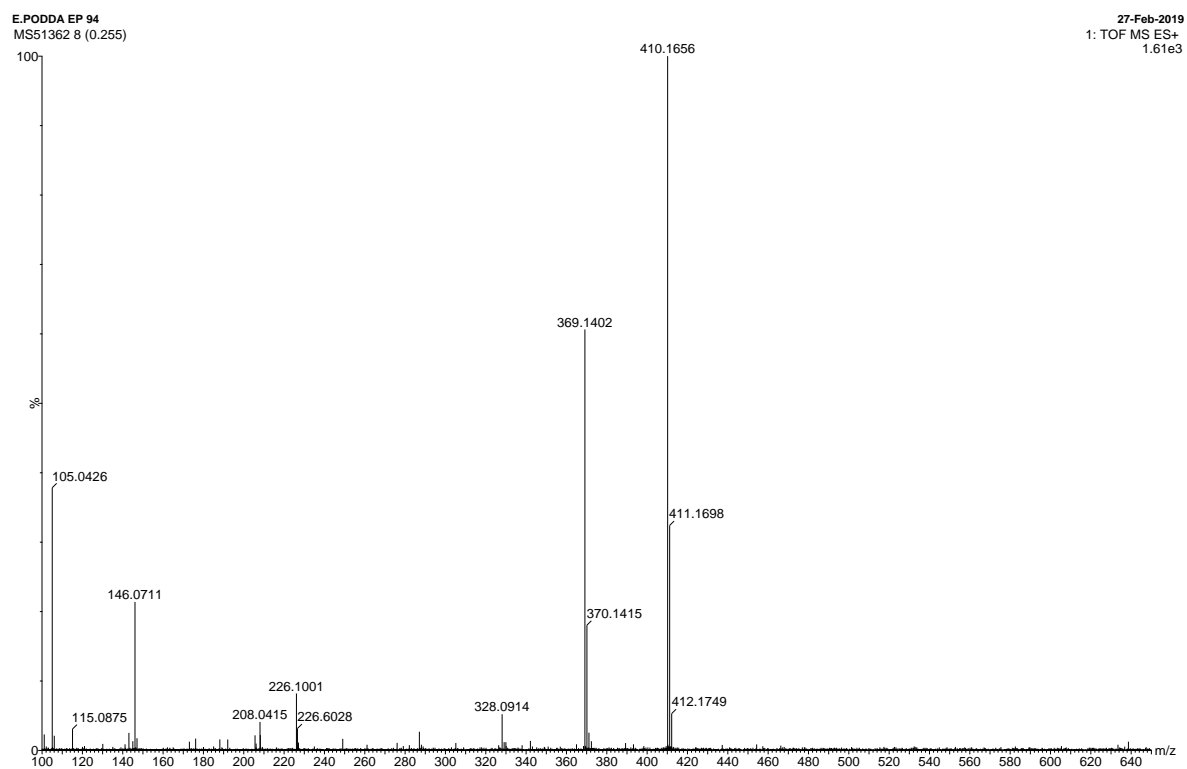
S106 TOF MS ES+ of L2.



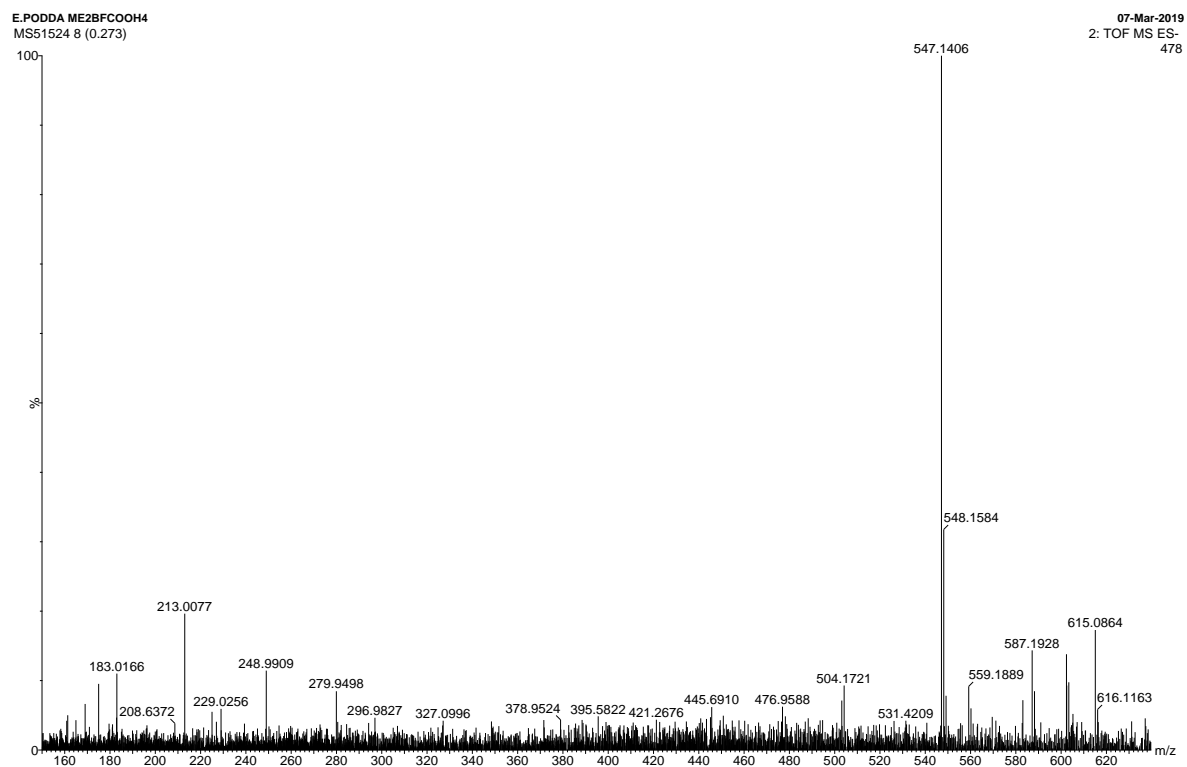
S107 TOF MS ES+ of L3.



S108 TOF MS ES+ of L5.

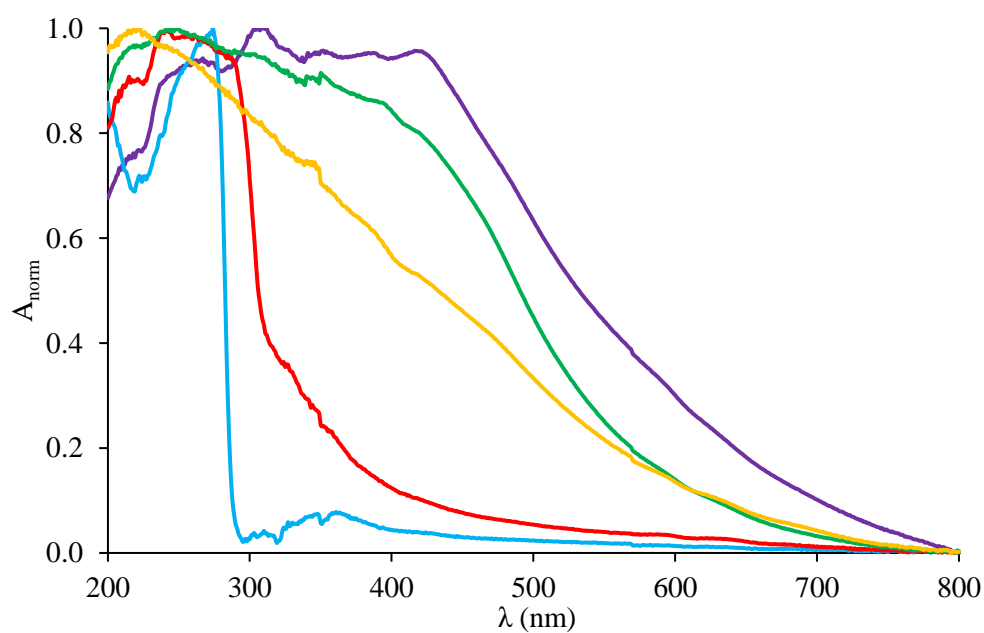


S109 TOF MS ES- of H₄L17.



Appendix 4: Diffuse reflectance spectra

S110 Diffuse reflectance spectra for: **L3**(purple), **R2**(light blue), **R3**(red), **(L3·R2)_∞** (green), **(L3·R2)_∞** (yellow).



Appendix 5: Computational data

S111 Optimised geometry calculated for the antiperiplanar conformation of **L3** at DFT level in the gas phase (total charge = 0, spin multiplicity = 1) in orthogonal Cartesian coordinate format.

Atom number	Z	X	Y	Z
1	6	-1.247285	0.899615	0.000117
2	16	0.009916	-0.298037	0.000057
3	6	1.250487	0.916839	0.000123
4	6	0.695833	2.188207	0.000177
5	6	-0.710506	2.178594	0.000163
6	6	2.609270	0.554879	0.000088
7	6	3.784379	0.227938	0.000043
8	6	5.151256	-0.157869	-0.000017
9	6	5.517310	-1.520372	-0.000144
10	7	6.771856	-1.942566	-0.000207
11	6	7.744324	-1.033369	-0.000153
12	6	7.504217	0.340946	-0.000034
13	6	6.190322	0.788243	0.000039
14	6	-2.601094	0.519513	0.000080
15	6	-3.771459	0.176047	0.000041
16	6	-5.138147	-0.210412	-0.000006
17	6	-5.527304	-1.560756	0.000357
18	6	-6.880797	-1.868133	0.000282
19	6	-7.805397	-0.823396	-0.000140
20	7	-7.453562	0.460599	-0.000493
21	6	-6.163782	0.758207	-0.000434
22	1	4.734058	-2.284683	-0.000196
23	1	5.955920	1.853445	0.000143
24	1	8.335986	1.046499	0.000003
25	1	8.770242	-1.415123	-0.000210
26	1	-8.879232	-1.035802	-0.000202
27	1	-7.219475	-2.904915	0.000548
28	1	-4.769549	-2.345259	0.000696
29	1	-5.897007	1.819565	-0.000732
30	1	1.306596	3.089337	0.000243
31	1	-1.334012	3.070958	0.000198

S112 Optimised geometry calculated for the periplanar conformation of **L3** at DFT level in the gas phase (total charge = 0, spin multiplicity = 1) in orthogonal Cartesian coordinate format.

Atom number	Z	X	Y	Z
1	6	-1.249048	0.000000	-0.880380
2	16	0.000000	0.000000	0.325963
3	6	1.249048	0.000000	-0.880380
4	6	0.703215	0.000000	-2.155481
5	6	-0.703215	0.000000	-2.155481
6	6	2.605390	0.000000	-0.509480
7	6	3.778105	0.000000	-0.174075
8	6	5.147460	0.000000	0.202822
9	6	6.166343	0.000000	-0.772945
10	7	7.458151	0.000000	-0.484295
11	6	7.818995	0.000000	0.797186
12	6	6.901718	0.000000	1.848349
13	6	5.546119	0.000000	1.550387
14	6	-2.605390	0.000000	-0.509480
15	6	-3.778105	0.000000	-0.174075
16	6	-5.147460	0.000000	0.202822
17	6	-5.546119	0.000000	1.550387
18	6	-6.901718	0.000000	1.848349
19	6	-7.818995	0.000000	0.797186
20	7	-7.458151	0.000000	-0.484295
21	6	-6.166343	0.000000	-0.772945
22	1	5.892190	0.000000	-1.832408
23	1	4.793876	0.000000	2.340166
24	1	7.247643	0.000000	2.882739
25	1	8.894295	0.000000	1.002058
26	1	-8.894295	0.000000	1.002058
27	1	-7.247643	0.000000	2.882739
28	1	-4.793876	0.000000	2.340166
29	1	-5.892190	0.000000	-1.832408
30	1	1.320399	0.000000	-3.052227
31	1	-1.320399	0.000000	-3.052227

S113 Optimised geometry calculated for **R2** at DFT level in the gas phase (total charge = 0, spin multiplicity = 1) in orthogonal Cartesian coordinate format.

Atom number	Z	X	Y	Z
1	6	4.404310	-1.744994	-0.555328
2	6	3.484137	-0.763448	-0.957028
3	6	3.691112	-0.120821	-2.187206
4	6	4.776389	-0.455374	-2.995304
5	6	5.675899	-1.437490	-2.583486
6	6	5.489905	-2.082188	-1.361098
7	14	2.014057	-0.354027	0.115257
8	6	2.433864	-0.267882	1.932144
9	6	3.443954	0.601062	2.378110
10	6	3.763214	0.694309	3.730489
11	6	3.078329	-0.085414	4.662740
12	6	2.076375	-0.955971	4.238574
13	6	1.758052	-1.045637	2.884015
14	8	1.465074	1.122049	-0.421085
15	5	0.389143	1.961758	-0.399651
16	6	0.598849	3.470372	-0.766113
17	6	-0.484907	4.361785	-0.819289
18	6	-0.310590	5.703184	-1.144729
19	6	0.973483	6.159257	-1.420410
20	6	2.076375	5.313609	-1.380304
21	6	1.877124	3.975959	-1.053745
22	9	1.152258	7.442189	-1.732252
23	8	-0.856029	1.524970	-0.064197
24	14	-2.014057	0.354027	0.115257
25	8	-1.465074	-1.122049	-0.421085
26	5	-0.389143	-1.961758	-0.399651
27	6	-0.598849	-3.470372	-0.766113
28	6	0.484907	-4.361785	-0.819289
29	6	0.310590	-5.703184	-1.144729
30	6	-0.973483	-6.159257	-1.420410
31	6	-2.076375	-5.313609	-1.380304
32	6	-1.877124	-3.975959	-1.053745
33	9	-1.152258	-7.442189	-1.732252
34	6	-2.433864	0.267882	1.932144
35	6	-3.443954	-0.601062	2.378110
36	6	-3.763214	-0.694309	3.730489
37	6	-3.078329	0.085414	4.662740
38	6	-2.076375	0.955971	4.238574
39	6	-1.758052	1.045637	2.884015
40	6	-3.484137	0.763448	-0.957028
41	6	-3.691112	0.120821	-2.187206
42	6	-4.776389	0.455374	-2.995304
43	6	-5.675899	1.437490	-2.583486
44	6	-5.489905	2.082188	-1.361098
45	6	-4.404310	1.744994	-0.555328

46	8	0.856029	-1.524970	-0.064197
47	1	-1.488511	3.990515	-0.603667
48	1	-1.146893	6.401411	-1.190303
49	1	3.065429	5.714422	-1.604310
50	1	2.734104	3.300513	-1.019703
51	1	-3.992860	-1.215132	1.659436
52	1	-4.549894	-1.375873	4.059477
53	1	-3.328734	0.014595	5.723058
54	1	-1.538399	1.568024	4.964786
55	1	-0.972340	1.732068	2.562782
56	1	-2.994565	-0.654188	-2.513912
57	1	-4.922178	-0.053992	-3.949785
58	1	-6.527020	1.698984	-3.215239
59	1	-6.196017	2.847368	-1.033093
60	1	-4.277182	2.250893	0.405476
61	1	1.488511	-3.990515	-0.603667
62	1	1.146893	-6.401411	-1.190303
63	1	-3.065429	-5.714422	-1.604310
64	1	-2.734104	-3.300513	-1.019703
65	1	3.992860	1.215132	1.659436
66	1	4.549894	1.375873	4.059477
67	1	3.328734	-0.014595	5.723058
68	1	1.538399	-1.568024	4.964786
69	1	0.972340	-1.732068	2.562782
70	1	2.994565	0.654188	-2.513912
71	1	4.922178	0.053992	-3.949785
72	1	6.527020	-1.698984	-3.215239
73	1	6.196017	-2.847368	-1.033093
74	1	4.277182	-2.250893	0.405476

S114 Optimised geometry calculated for **R3** at DFT level in the gas phase (total charge = 0, spin multiplicity = 1) in orthogonal Cartesian coordinate format.

Atom number	Z	X	Y	Z
1	6	3.155545	1.876551	-2.174595
2	6	2.645691	2.368018	-0.963164
3	6	2.932341	3.696288	-0.608737
4	6	3.694333	4.511332	-1.442941
5	6	4.188060	4.007546	-2.645871
6	6	3.919632	2.689175	-3.010376
7	14	1.590200	1.309116	0.148272
8	6	2.023213	1.469365	1.955552
9	6	1.056488	1.776380	2.924637
10	6	1.399967	1.873218	4.272429
11	6	2.718604	1.665069	4.672129
12	6	3.694333	1.362182	3.722345
13	6	3.348486	1.267781	2.376617
14	8	-0.000574	1.750474	-0.014256
15	5	-1.299896	1.514026	-0.330624
16	6	-2.236835	2.733716	-0.667689
17	6	-3.598170	2.530738	-0.935152
18	6	-4.409094	3.618062	-1.228573
19	6	-3.915245	4.916717	-1.267989
20	6	-2.563362	5.099228	-1.001257
21	6	-1.721478	4.036891	-0.703216
22	9	-5.702527	3.421661	-1.481416
23	9	-2.070446	6.336469	-1.034822
24	8	1.826417	-0.258973	-0.361789
25	5	1.299896	-1.514026	-0.330624
26	6	2.236835	-2.733716	-0.667689
27	6	1.721478	-4.036891	-0.703216
28	6	2.563362	-5.099228	-1.001257
29	6	3.915245	-4.916717	-1.267989
30	6	4.409094	-3.618062	-1.228573
31	6	3.598170	-2.530738	-0.935152
32	9	2.070446	-6.336469	-1.034822
33	9	5.702527	-3.421661	-1.481416
34	8	0.000574	-1.750474	-0.014256
35	14	-1.590200	-1.309116	0.148272
36	6	-2.023213	-1.469365	1.955552
37	6	-1.056488	-1.776380	2.924637
38	6	-1.399967	-1.873218	4.272429
39	6	-2.718604	-1.665069	4.672129
40	6	-3.694333	-1.362182	3.722345
41	6	-3.348486	-1.267781	2.376617
42	8	-1.826417	0.258973	-0.361789
43	6	-2.645691	-2.368018	-0.963164
44	6	-2.932341	-3.696288	-0.608737
45	6	-3.694333	-4.511332	-1.442941
46	6	-4.188060	-4.007546	-2.645871
47	6	-3.919632	-2.689175	-3.010376
48	6	-3.155545	-1.876551	-2.174595
49	1	0.667181	-4.229175	-0.504824
50	1	4.563731	-5.760464	-1.500003
51	1	4.030168	-1.530218	-0.916301
52	1	-4.030168	1.530218	-0.916301
53	1	-4.563731	5.760464	-1.500003

54	1	-0.667181	4.229175	-0.504824
55	1	-2.561026	-4.101661	0.336259
56	1	-3.906999	-5.541841	-1.152686
57	1	-4.787164	-4.644263	-3.299674
58	1	-4.309003	-2.291206	-3.949318
59	1	-2.954263	-0.843344	-2.465128
60	1	-0.020927	-1.945155	2.623264
61	1	-0.634147	-2.112478	5.012439
62	1	-2.988807	-1.741582	5.727136
63	1	-4.728635	-1.201533	4.032065
64	1	-4.125658	-1.035946	1.643700
65	1	0.020927	1.945155	2.623264
66	1	0.634147	2.112478	5.012439
67	1	2.988807	1.741582	5.727136
68	1	4.728635	1.201533	4.032065
69	1	4.125658	1.035946	1.643700
70	1	2.561026	4.101661	0.336259
71	1	3.906999	5.541841	-1.152686
72	1	4.787164	4.644263	-3.299674
73	1	4.309003	2.291206	-3.949318
74	1	2.954263	0.843344	-2.465128

S115 Optimised geometry calculated for the antiperiplanar geometry of **L3₂•R2** at DFT level in the gas phase (total charge = 0, spin multiplicity = 1) in orthogonal Cartesian coordinate format.

Atom number	Z	X	Y	Z	Atom number	Z	X	Y	Z
1	6	-14.637321	-6.336178	-0.190191	69	6	-2.362106	-0.004357	2.292013
2	7	-13.364340	-6.368798	-0.578286	70	6	-3.373357	-0.963194	2.110459
3	6	-12.621666	-5.289841	-0.387898	71	6	-4.527279	-0.954701	2.891362
4	6	-13.104704	-4.104392	0.205125	72	6	-4.692082	0.015212	3.880742
5	6	-14.450554	-4.086983	0.608841	73	6	-3.698365	0.970723	4.083617
6	6	-15.225284	-5.220648	0.406831	74	6	-2.547106	0.958358	3.294827
7	6	-12.253733	-2.980927	0.381360	75	8	0.064979	1.273437	1.674820
8	6	-11.519164	-2.018910	0.530920	76	6	0.081645	-1.657282	1.422969
9	6	-10.660152	-0.918032	0.697258	77	6	0.424642	-2.460504	0.325167
10	16	-9.008717	-0.997006	0.169688	78	6	1.105816	-3.665367	0.500940
11	6	-8.699394	0.625487	0.704238	79	6	1.455812	-4.090123	1.781438
12	6	-9.837227	1.188236	1.263530	80	6	1.117164	-3.309117	2.886768
13	6	-10.942119	0.318789	1.259362	81	6	0.433962	-2.108091	2.705598
14	6	-7.425960	1.199873	0.548381	82	6	1.308035	3.477698	1.533739
15	6	-6.312747	1.676748	0.410176	83	6	2.324394	4.311945	1.041736
16	6	-5.015406	2.231253	0.253482	84	6	2.376931	5.672209	1.338157
17	6	-4.021224	1.524404	-0.435864	85	6	1.389675	6.217149	2.149460
18	7	-2.792120	2.010662	-0.601845	86	6	0.361966	5.436742	2.661095
19	6	-2.464437	3.207219	-0.104239	87	6	0.334592	4.077123	2.345984
20	6	-3.389171	3.978576	0.589523	88	9	1.428050	7.521350	2.441907
21	6	-4.675217	3.493612	0.772546	89	1	-2.241300	2.245544	-3.808620
22	5	-1.602033	1.029059	-1.362814	90	1	-3.335570	1.292345	-5.841649
23	6	-2.309558	0.408422	-2.676128	91	1	-3.601715	-2.529285	-3.922134
24	6	-2.548156	1.196513	-3.813020	92	1	-2.508570	-1.578593	-1.875510
25	6	-3.152478	0.680327	-4.957327	93	1	2.566036	-0.733839	-1.107400
26	6	-3.524776	-0.658698	-4.968239	94	1	3.413570	-2.556494	-2.554004
27	6	-3.304827	-1.480784	-3.872119	95	1	3.021447	-2.481066	-5.012721
28	6	-2.699315	-0.936581	-2.738523	96	1	1.784191	-0.564184	-6.007963
29	9	-4.104633	-1.165565	-6.061736	97	1	0.963627	1.265963	-4.569729
30	8	-0.558915	1.971756	-1.650869	98	1	3.786516	2.762621	-2.461982
31	14	1.083397	1.821034	-1.659898	99	1	4.674988	4.892002	-3.343961
32	8	1.672504	1.534504	-0.138000	100	1	3.140394	6.803537	-3.778101
33	5	1.265643	1.891892	1.188393	101	1	0.705784	6.560473	-3.327260
34	7	2.505698	1.209458	2.146898	102	1	-0.185786	4.423754	-2.437683
35	6	2.338831	1.162424	3.473620	103	1	-4.217436	0.546354	-0.874928
36	6	3.320870	0.646853	4.305908	104	1	-5.423442	4.073725	1.313193
37	6	4.499958	0.167464	3.748026	105	1	-3.088809	4.949381	0.982646
38	6	4.669721	0.214916	2.354782	106	1	-1.435722	3.520468	-0.278060
39	6	3.623141	0.756311	1.590092	107	1	-9.851603	2.202448	1.658881
40	6	5.841127	-0.264349	1.712796	108	1	-11.926413	0.569348	1.650922
41	6	6.833414	-0.674597	1.135369	109	1	5.289862	-0.245357	4.376008
42	6	7.974904	-1.147703	0.466037	110	1	1.390125	1.549348	3.844692
43	16	9.357876	-1.715688	1.348169	111	1	3.158574	0.621175	5.383065
44	6	10.216188	-2.074701	-0.116729	112	1	3.665267	0.826679	0.503734
45	6	9.449139	-1.762349	-1.230146	113	1	0.152202	-2.132402	-0.679786

46	6	8.186066	-1.239894	-0.902053	114	1	1.361982	-4.275919	-0.367430
47	6	11.515958	-2.609415	-0.072821	115	1	1.987172	-5.033943	1.920327
48	6	12.643204	-3.072270	-0.023017	116	1	1.379760	-3.643036	3.892879
49	6	13.956038	-3.610679	0.039459	117	1	0.159366	-1.516828	3.583856
50	6	14.573420	-3.865593	1.281973	118	1	-3.256975	-1.734368	1.344150
51	7	15.792848	-4.365278	1.405238	119	1	-5.302413	-1.706469	2.729597
52	6	16.476363	-4.643475	0.297213	120	1	-5.595359	0.023088	4.494014
53	6	15.969530	-4.433908	-0.985683	121	1	-3.820105	1.728903	4.860334
54	6	14.691347	-3.910117	-1.119992	122	1	-1.772234	1.710204	3.456828
55	6	1.709484	0.406809	-2.726590	123	1	3.094996	3.894002	0.390302
56	6	2.404414	-0.684571	-2.185604	124	1	-0.395499	5.900109	3.295286
57	6	2.876789	-1.715433	-2.998340	125	1	-0.476596	3.457957	2.734687
58	6	2.656493	-1.674139	-4.373827	126	1	3.162851	6.317371	0.943812
59	6	1.964317	-0.599332	-4.931720	127	1	14.029557	-3.644251	2.205482
60	6	1.500818	0.429805	-4.115189	128	1	14.254809	-3.729687	-2.103072
61	6	1.732208	3.441648	-2.361140	129	1	16.569683	-4.678365	-1.862948
62	6	3.100635	3.596589	-2.635817	130	1	17.481336	-5.055283	0.433669
63	6	3.607149	4.793834	-3.137480	131	1	7.434818	-0.935151	-1.628937
64	6	2.747338	5.864571	-3.382979	132	1	9.808707	-1.914784	-2.246183
65	6	1.383897	5.727696	-3.129552	133	1	-16.273545	-5.243605	0.707183
66	6	0.884742	4.526861	-2.625532	134	1	-11.578405	-5.338516	-0.714759
67	8	-1.278678	0.027089	-0.389364	135	1	-14.868225	-3.192090	1.071781
68	14	-0.831302	-0.031052	1.193227	136	1	-15.223792	-7.244344	-0.361981

S116 Optimised geometry calculated for the periplanar geometry of **L3₂·R2** at DFT level in the gas phase (total charge = 0, spin multiplicity = 1) in orthogonal Cartesian coordinate format.

Atom number	Z	X	Y	Z	Atom number	Z	X	Y	Z
1	6	-16.090341	-0.864056	-1.215801	69	6	6.579555	-0.875562	2.766975
2	6	-16.202967	-0.771409	0.171801	70	6	7.969484	-0.673242	2.811041
3	6	-15.056607	-0.540932	0.919327	71	16	8.873453	-0.426452	1.349162
4	6	-13.826996	-0.409629	0.251950	72	6	10.361334	-0.266189	2.227708
5	6	-13.837372	-0.522046	-1.154253	73	6	10.148554	-0.402871	3.592082
6	7	-14.933411	-0.741996	-1.862855	74	6	8.800941	-0.631936	3.920542
7	6	-12.614642	-0.172989	0.953090	75	6	11.571474	-0.031347	1.551211
8	6	-11.571452	0.030363	1.551205	76	6	12.614647	0.172412	0.953205
9	6	-10.361305	0.264711	2.227860	77	6	13.826985	0.409539	0.252202
10	6	-10.148498	0.400320	3.592336	78	6	15.056606	0.540409	0.919646
11	6	-8.800883	0.629156	3.920949	79	6	16.202951	0.771397	0.172255
12	6	-7.969449	0.671367	2.811466	80	6	16.090301	0.864967	-1.215283
13	16	-8.873445	0.425713	1.349409	81	7	14.933360	0.743331	-1.862399
14	6	-6.579525	0.873746	2.767533	82	6	13.837336	0.522898	-1.153926
15	6	-5.373617	1.040724	2.705502	83	6	1.439786	1.920221	-2.628660
16	6	-3.969214	1.229518	2.631999	84	6	1.524018	1.028959	-3.708664
17	6	-3.325496	1.294745	1.388200	85	6	1.530892	1.493487	-5.023974
18	7	-2.010066	1.465812	1.280078	86	6	1.452701	2.860786	-5.281347
19	6	-1.249092	1.583889	2.370912	87	6	1.367982	3.762486	-4.220320
20	6	-1.802894	1.538227	3.645493	88	6	1.364425	3.294176	-2.908667
21	6	-3.171585	1.360018	3.783608	89	1	0.882119	-4.279799	0.152536
22	5	-1.324096	1.540010	-0.310279	90	1	1.974801	-6.277935	-0.867384
23	6	-2.022053	2.837309	-0.979023	91	1	4.392462	-3.723405	-3.314381
24	6	-1.662141	4.139014	-0.597747	92	1	3.303372	-1.711106	-2.292969
25	6	-2.257903	5.266978	-1.157919	93	1	-1.576535	0.046135	-3.514143
26	6	-3.238057	5.090317	-2.127243	94	1	-1.593703	-0.778912	-5.850899
27	6	-3.626376	3.824271	-2.541772	95	1	-1.457017	-3.222261	-6.312437
28	6	-3.013888	2.712803	-1.961591	96	1	-1.303994	-4.831749	-4.419874
29	9	-3.816632	6.165397	-2.672929	97	1	-1.299915	-4.013645	-2.092353
30	8	0.073213	1.692391	-0.027461	98	1	-4.412984	-1.146668	-1.024517
31	14	1.448129	1.302823	-0.859184	99	1	-6.267720	-2.187507	0.233289
32	6	2.844599	2.115981	0.112399	100	1	-5.786737	-3.782595	2.081067
33	6	4.184180	1.835032	-0.205048	101	1	-3.428461	-4.327776	2.660432
34	6	5.234435	2.423403	0.496932	102	1	-1.566136	-3.273455	1.405853
35	6	4.965438	3.317216	1.533777	103	1	3.880132	-1.213948	0.453198
36	6	3.644720	3.619409	1.858958	104	1	3.637001	-1.323877	4.767993
37	6	2.598699	3.023108	1.153622	105	1	1.159441	-1.647906	4.517601
38	8	1.722655	-0.321401	-0.934289	106	1	0.184572	-1.714888	2.174622
39	5	1.324110	-1.539771	-0.311270	107	1	8.427352	-0.766039	4.934242
40	6	2.022037	-2.836651	-0.980852	108	1	10.958049	-0.336366	4.316762
41	6	1.661986	-4.138593	-0.600520	109	1	-0.882384	4.279756	0.155511
42	6	2.257744	-5.266213	-1.161389	110	1	-1.975068	6.278517	-0.863182
43	6	3.238037	-5.088955	-2.130461	111	1	-4.392243	3.725502	-3.312242
44	6	3.626490	-3.822650	-2.544077	112	1	-3.303157	1.712572	-2.292052
45	6	3.013998	-2.711541	-1.963216	113	1	1.577588	-0.043844	-3.514095

46	9	3.816614	-6.163700	-2.676806	114	1	1.594765	0.782631	-5.850349
47	8	-0.073203	-1.692290	-0.028541	115	1	1.456945	3.226190	-6.310426
48	14	-1.448132	-1.302246	-0.860018	116	1	1.302790	4.834451	-4.416909
49	8	-1.722603	0.322035	-0.934081	117	1	1.298703	4.014932	-2.089889
50	6	-1.439840	-1.918535	-2.629878	118	1	4.412987	1.147312	-1.023791
51	6	-1.523447	-1.026576	-3.709354	119	1	6.267731	2.187387	0.234625
52	6	-1.530321	-1.490302	-5.024946	120	1	5.786771	3.781306	2.083418
53	6	-1.452765	-2.857483	-5.283136	121	1	3.428497	4.326132	2.663142
54	6	-1.368679	-3.759871	-4.222643	122	1	1.566162	3.272617	1.407902
55	6	-1.365116	-3.292359	-2.910707	123	1	15.097199	0.459863	2.006593
56	6	-2.844589	-2.116028	0.111068	124	1	17.174824	0.878264	0.655555
57	6	-4.184173	-1.834887	-0.206194	125	1	16.977245	1.046626	-1.830521
58	6	-5.234422	-2.423696	0.495429	126	1	12.897584	0.426055	-1.706263
59	6	-4.965411	-3.318153	1.531714	127	1	-1.159391	1.644790	4.518667
60	6	-3.644690	-3.620545	1.856696	128	1	-3.636955	1.320657	4.768844
61	6	-2.598675	-3.023800	1.151727	129	1	-0.184528	1.713381	2.175720
62	7	2.010095	-1.466647	1.279133	130	1	-3.880113	1.213730	0.453977
63	6	3.325524	-1.295623	1.387368	131	1	-10.957974	0.333227	4.316983
64	6	3.969245	-1.231253	2.631210	132	1	-8.427277	0.762461	4.934749
65	6	3.171628	-1.362573	3.782731	133	1	-17.174833	-0.878578	0.655048
66	6	1.802939	-1.540719	3.644500	134	1	-15.097182	-0.461120	2.006329
67	6	1.249134	-1.585503	2.369890	135	1	-16.977296	-1.045302	-1.831145
68	6	5.373647	-1.042495	2.704838	136	1	-12.897631	-0.424834	-1.706543

S117 Optimised geometry calculated for the antiperiplanar geometry of **L3₂•R3** at DFT level in the gas phase (total charge = 0, spin multiplicity = 1) in orthogonal Cartesian coordinate format.

Atom number	Z	X	Y	Z	Atom number	Z	X	Y	Z
1	6	14.695711	4.487683	0.519257	69	6	0.527481	-0.433773	-3.998460
2	6	15.133384	3.728860	-0.566712	70	7	-2.353642	-0.163418	1.493588
3	6	14.253540	2.825134	-1.145688	71	6	-3.531539	0.326743	1.108967
4	6	12.956707	2.708152	-0.617399	72	6	-4.717149	-0.411091	1.220938
5	6	12.628199	3.528116	0.482572	73	6	-4.627819	-1.711909	1.749612
6	7	13.470919	4.388691	1.031279	74	6	-3.391447	-2.202586	2.141464
7	6	12.004651	1.804368	-1.159728	75	6	-2.268022	-1.395813	2.004623
8	6	11.183881	1.029860	-1.622038	76	6	-5.953173	0.152643	0.809389
9	6	10.227512	0.141333	-2.144770	77	6	-7.009973	0.647483	0.457223
10	6	10.359682	-0.737277	-3.211091	78	6	-8.230477	1.212220	0.048446
11	6	9.193065	-1.479971	-3.461058	79	16	-9.698401	0.286334	0.091234
12	6	8.157786	-1.176732	-2.588450	80	6	-10.625609	1.619371	-0.521860
13	16	8.641116	0.041554	-1.450129	81	6	-9.816716	2.724609	-0.743522
14	6	6.863282	-1.722006	-2.548967	82	6	-8.467263	2.495368	-0.422353
15	6	5.735697	-2.183352	-2.500913	83	6	-12.010292	1.493071	-0.731754
16	6	4.421452	-2.715074	-2.442940	84	6	-13.210709	1.371950	-0.910135
17	6	3.530601	-2.290016	-1.443241	85	6	-14.608414	1.226421	-1.116451
18	7	2.291541	-2.762781	-1.360066	86	6	-15.401302	2.281024	-1.600026
19	6	1.844906	-3.668948	-2.238322	87	6	-16.761332	2.069373	-1.778216
20	6	2.656746	-4.144793	-3.256302	88	6	-17.290402	0.815708	-1.470070
21	6	3.957589	-3.668168	-3.364597	89	7	-16.553245	-0.193462	-1.011290
22	5	1.241879	-2.244613	-0.135026	90	6	-15.255723	0.003922	-0.839698
23	6	1.039656	-3.544477	0.828346	91	1	2.268711	-4.882917	-3.957608
24	6	-0.227318	-4.123175	0.977185	92	1	-1.079720	-3.732702	0.421379
25	6	-0.411734	-5.187719	1.849960	93	1	0.475689	-6.572902	3.261508
26	6	0.631503	-5.737401	2.580910	94	1	3.109865	-3.671085	1.504402
27	6	1.888098	-5.164880	2.410769	95	1	3.799060	-1.548929	-0.690824
28	6	2.103516	-4.088158	1.561987	96	1	4.619905	-4.022814	-4.154678
29	9	-1.642168	-5.697469	2.004446	97	1	0.814597	-3.995221	-2.098541
30	9	2.912584	-5.672981	3.097343	98	1	-1.093550	1.801021	3.813612
31	8	1.952346	-1.156220	0.463214	99	1	-2.049913	5.895605	2.907319
32	14	1.667793	-0.191931	1.783824	100	1	-1.466735	3.082780	-0.302209
33	6	2.659791	1.373983	1.489300	101	1	4.329732	-1.052443	2.782519
34	6	3.278182	1.642487	0.259369	102	1	5.113316	-2.173421	4.838622
35	6	4.020420	2.807050	0.063638	103	1	3.496087	-2.764559	6.635332
36	6	4.153981	3.730003	1.099279	104	1	1.085330	-2.215093	6.358597
37	6	3.545266	3.482938	2.329604	105	1	0.295996	-1.096305	4.290386
38	6	2.810378	2.314943	2.520840	106	1	3.167524	0.931462	-0.561354
39	8	0.051302	0.074192	1.990955	107	1	4.494370	2.994909	-0.902167
40	5	-0.932018	0.744299	1.194457	108	1	4.732912	4.643522	0.948690
41	6	-1.259312	2.253008	1.690948	109	1	3.645368	4.203307	3.143858
42	6	-1.298235	2.561265	3.058367	110	1	2.346632	2.133553	3.493779
43	6	-1.580632	3.855711	3.470676	111	1	0.887347	2.058166	-1.717083
44	6	-1.832964	4.883669	2.568810	112	1	2.209080	3.030382	-3.577657
45	6	-1.787350	4.563990	1.218422	113	1	2.463552	1.778855	-5.714630

46	6	-1.508641	3.278388	0.769982	114	1	1.373020	-0.442186	-5.984620
47	9	-1.613261	4.136173	4.776444	115	1	0.040605	-1.403096	-4.138776
48	9	-2.021435	5.531991	0.327395	116	1	-2.843222	1.062667	-2.584631
49	6	2.245880	-1.009887	3.373144	117	1	-5.119525	0.500363	-3.362860
50	6	3.604233	-1.314335	3.557815	118	1	-5.939087	-1.845836	-3.244583
51	6	4.053089	-1.942425	4.717303	119	1	-4.456178	-3.629707	-2.341994
52	6	3.147165	-2.272419	5.725344	120	1	-2.173077	-3.063477	-1.550771
53	6	1.796954	-1.966203	5.568619	121	1	-3.526796	1.339189	0.705532
54	6	1.354196	-1.340228	4.403466	122	1	-5.528468	-2.319040	1.843734
55	8	0.026419	-1.910644	-0.819588	123	1	-3.281201	-3.211119	2.539645
56	14	-0.622393	-0.494308	-1.378631	124	1	-1.265828	-1.714274	2.288038
57	6	-2.338754	-0.960827	-1.997996	125	1	-18.359431	0.619927	-1.600637
58	6	-3.190134	0.027767	-2.520100	126	1	-17.407719	2.864632	-2.151470
59	6	-4.473698	-0.284060	-2.963315	127	1	-14.944653	3.244968	-1.827766
60	6	-4.933465	-1.599750	-2.897848	128	1	-14.668892	-0.838873	-0.461579
61	6	-4.103105	-2.597371	-2.390965	129	1	-7.673934	3.234107	-0.523113
62	6	-2.819468	-2.277447	-1.946414	130	1	-10.208312	3.664928	-1.127415
63	8	-0.741801	0.672857	-0.223537	131	1	16.147763	3.847000	-0.949584
64	6	0.380553	0.251197	-2.781100	132	1	14.552257	2.211121	-1.996186
65	6	0.995674	1.505411	-2.652276	133	1	15.367572	5.208388	0.996109
66	6	1.740227	2.051612	-3.698212	134	1	11.626912	3.462992	0.919351
67	6	1.882614	1.351321	-4.894804	135	1	11.282431	-0.825763	-3.781636
68	6	1.273016	0.105431	-5.045029	136	1	9.091091	-2.221396	-4.251674

S118 Optimised geometry calculated for the periplanar geometry of **L3₂·R3** at DFT level in the gas phase (total charge = 0, spin multiplicity = 1) in orthogonal Cartesian coordinate format.

Atom number	Z	X	Y	Z	Atom number	Z	X	Y	Z
1	6	-7.801876	4.273439	-0.000535	69	6	-1.689586	-5.602043	2.048928
2	16	-6.247935	4.501739	-0.738414	70	7	0.841582	-0.550690	1.961988
3	6	-5.832943	2.831039	-0.512857	71	6	-0.156016	0.228917	2.392637
4	6	-6.864186	2.141008	0.107488	72	6	-0.001120	1.603887	2.508394
5	6	-7.973702	2.954596	0.395895	73	6	1.212621	2.180132	2.159523
6	6	-4.589135	2.329857	-0.932160	74	6	2.254905	1.360145	1.692307
7	6	-3.510607	1.889335	-1.291236	75	6	2.012160	-0.021011	1.617468
8	6	-2.255564	1.361483	-1.690421	76	6	3.509156	1.889432	1.292514
9	6	-2.011338	-0.019438	-1.615989	77	6	4.587038	2.331089	0.932895
10	7	-0.839959	-0.547674	-1.960007	78	6	5.830141	2.833544	0.513018
11	6	0.157071	0.233217	-2.389678	79	16	6.243942	4.504423	0.739408
12	6	0.000727	1.608055	-2.504957	80	6	7.797579	4.277848	0.000353
13	6	-1.213883	2.182806	-2.156642	81	6	7.970109	2.959445	-0.397240
14	5	-0.624360	-2.269678	-1.934924	82	6	6.861424	2.144779	-0.108660
15	6	-1.054788	-2.716040	-3.437352	83	6	8.692050	5.354873	-0.130533
16	6	-0.111977	-2.764536	-4.472721	84	6	9.459324	6.296625	-0.239231
17	6	-0.502082	-3.119213	-5.757525	85	6	10.348875	7.396867	-0.363772
18	6	-1.817635	-3.436195	-6.071763	86	6	9.981393	8.677673	0.099275
19	6	-2.741638	-3.387007	-5.035246	87	7	10.764685	9.740896	0.011312
20	6	-2.384754	-3.035803	-3.739875	88	6	11.965913	9.596163	-0.544036
21	9	0.412961	-3.162068	-6.729720	89	6	12.437908	8.379211	-1.036976
22	9	-4.014024	-3.691084	-5.302964	90	6	11.620115	7.261524	-0.947140
23	6	-8.697214	5.349719	0.130559	91	1	8.998586	8.819119	0.559427
24	6	-9.465256	6.290819	0.239473	92	1	11.947758	6.290044	-1.319211
25	6	-10.355847	7.390195	0.364304	93	1	13.430828	8.312341	-1.483229
26	6	-11.626814	7.253584	0.947962	94	1	12.588897	10.494342	-0.601471
27	6	-12.445662	8.370479	1.038067	95	1	-1.086606	-0.287131	2.625370
28	6	-11.974954	9.587918	0.545107	96	1	-0.831722	2.212906	2.864335
29	7	-10.773987	9.733848	-0.010498	97	1	1.365755	3.256945	2.237024
30	6	-9.989694	8.671389	-0.098726	98	1	2.769081	-0.719383	1.259532
31	8	0.774338	-2.402843	-1.687901	99	1	3.158261	-3.029627	2.967085
32	14	1.805115	-3.130239	-0.626637	100	1	2.116770	-3.720347	7.082693
33	6	1.759233	-4.993789	-0.788540	101	1	-0.935542	-2.551792	4.288177
34	6	1.860457	-5.823590	0.337989	102	1	0.939808	-2.544171	-4.286985
35	6	1.899438	-7.210503	0.205016	103	1	-2.110229	-3.716151	-7.082500
36	6	1.836655	-7.792049	-1.059923	104	1	-3.153262	-3.030005	-2.966514
37	6	1.728370	-6.983558	-2.191011	105	1	4.420464	-3.090240	0.802254
38	6	1.690352	-5.597674	-2.054221	106	1	6.695093	-2.342037	0.206270
39	8	1.540178	-2.721432	0.945731	107	1	7.134955	-1.325719	-2.026713
40	5	0.627918	-2.273112	1.936227	108	1	5.264434	-1.046490	-3.644790
41	6	1.059274	-2.719604	3.438326	109	1	2.983281	-1.797216	-3.046359
42	6	2.389827	-3.037257	3.740510	110	1	1.898883	-5.378201	1.334322
43	6	2.747428	-3.388703	5.035612	111	1	1.971852	-7.839884	1.093860
44	6	1.823598	-3.440199	6.072175	112	1	1.866872	-8.878541	-1.164968
45	6	0.507468	-3.125305	5.758261	113	1	1.671662	-7.434971	-3.183629

46	6	0.116632	-2.770441	4.473729	114	1	1.598908	-4.978219	-2.949632
47	9	4.020367	-3.690763	5.303027	115	1	-1.899240	-5.375515	-1.339089
48	9	-0.407416	-3.170410	6.730510	116	1	-1.975216	-7.837547	-1.103545
49	6	3.520971	-2.487134	-1.072415	117	1	-1.870527	-8.880897	1.153144
50	6	4.591204	-2.630116	-0.174121	118	1	-1.672642	-7.441641	3.174621
51	6	5.878631	-2.211233	-0.506991	119	1	-1.596988	-4.984489	2.945535
52	6	6.124599	-1.639733	-1.755660	120	1	-4.417327	-3.086992	-0.802298
53	6	5.077419	-1.486950	-2.663287	121	1	-6.691462	-2.338653	-0.204812
54	6	3.792700	-1.908058	-2.321337	122	1	-7.130626	-1.326103	2.030073
55	8	-0.770666	-2.408042	1.689803	123	1	-5.259926	-1.051109	3.648603
56	14	-1.801999	-3.131565	0.626508	124	1	-2.979265	-1.802210	3.048768
57	6	-3.517369	-2.487911	1.073463	125	1	-2.767684	-0.718789	-1.258765
58	6	-4.587720	-2.628569	0.174943	126	1	-1.368161	3.259478	-2.233825
59	6	-5.874897	-2.209574	0.508652	127	1	0.830889	2.218152	-2.860077
60	6	-6.120489	-1.640259	1.758387	128	1	1.088380	-0.281736	-2.621958
61	6	-5.073191	-1.489821	2.666267	129	1	-12.598790	10.485494	0.602739
62	6	-3.788739	-1.911072	2.323499	130	1	-13.438408	8.302621	1.484558
63	8	-1.536291	-2.719585	-0.944840	131	1	-11.953435	6.281767	1.320053
64	6	-1.758299	-4.995518	0.784507	132	1	-9.007117	8.813817	-0.559074
65	6	-1.861006	-5.822921	-0.343649	133	1	8.880925	2.613217	-0.882492
66	6	-1.901635	-7.210054	-0.213459	134	1	6.790402	1.083666	-0.343059
67	6	-1.839025	-7.794234	1.050275	135	1	-6.792531	1.079771	0.341104
68	6	-1.729243	-6.988155	2.182940	136	1	-8.884573	2.607302	0.880279

Appendix 6: Crystal data and refinement parameters

Table S119: Crystal data and refinement parameters for $[\text{AgL1}(\text{OTf})\cdot((\text{CH}_3)_2\text{CO})_{0.5}]_\infty$.

$[\text{AgL1}(\text{OTf})\cdot((\text{CH}_3)_2\text{CO})_{0.5}]_\infty$	
Formula	$\text{C}_{14.5}\text{H}_{11}\text{AgF}_3\text{N}_4\text{O}_{3.5}\text{S}_2$
$D_{\text{calc.}} / \text{g cm}^{-3}$	1.952
μ / mm^{-1}	1.417
Formula Weight	526.269
Colour	colorless
Shape	prism
Size/ mm^3	0.30×0.25×0.24
T / K	173
Crystal System	monoclinic
Space Group	$C2/c$
$a / \text{Å}$	13.1248(8)
$b / \text{Å}$	18.4783(9)
$c / \text{Å}$	15.9209(10)
$\alpha / ^\circ$	90
$\beta / ^\circ$	111.957(7)
$\gamma / ^\circ$	90
$V / \text{Å}^3$	3581.1(4)
Z	8
Z'	1
Wavelength/ Å	0.71075
Radiation type	Mo K_α
$\theta_{\text{min}} / ^\circ$	2.00
$\theta_{\text{max}} / ^\circ$	31.79
Measured Refl's.	21667
Indep't Refl's	5794
Refl's $I \geq 2 \sigma(I)$	4492
R_{int}	0.0269
Parameters	273
Restraints	39
Largest Peak	1.0056
Deepest Hole	-1.1964
GooF	1.0072
wR_2 (all data)	0.1386
wR_2	0.1274
R_1 (all data)	0.0679
R_1	0.0492

Table S120: Selected bond lengths (Å) and angles (°) for [AgL1(OTf)·(CH₃)₂CO]_{0.5}∞.

Ag1–N1	2.156(3)
Ag1–N4 ¹	2.165(3)
S2–O2	1.398(4)
S2–O3	1.426(3)
S2–O1	1.435(3)
S2–C13	1.806(5)
F2–C13	1.334(6)
F3–C13	1.310(7)
F1–C13	1.309(9)
O4–C15	1.067(10)
C15–C14	1.622(11)
C15–C14 ²	1.622(11)
N4 ¹ –Ag1–N1	169.73(10)
F2–C13–S2	111.4(4)
F3–C13–S2	110.4(4)
F3–C13–F2	107.1(5)
F1–C13–S2	111.5(5)
F1–C13–F2	106.4(5)
F1–C13–F3	109.9(7)
C14–C15–O4	147.5(4)
C14 ³ –C15–O4	147.5(4)
C14 ³ –C15–C14	65.0(9)
Py [^] Py	142.7(6)

Symmetry codes: ¹-1/2+x,3/2-y,-1/2+z; ²1/2+x,3/2-y,1/2+z; ³2-x,y,3/2-z.

Table S121: Crystal data and refinement parameters for $[\text{ZnL1}(\text{NO}_3)_2 \cdot \text{CH}_3\text{CN}]_2$.

	$[\text{ZnL1}(\text{NO}_3)_2 \cdot \text{CH}_3\text{CN}]_2$
Formula	$\text{C}_{14}\text{H}_{11}\text{N}_7\text{O}_6\text{SZn}$
$D_{\text{calc.}}/\text{g cm}^{-3}$	1.736
μ/mm^{-1}	1.530
Formula Weight	470.73
Colour	colorless
Shape	prism
Size/ mm^3	$0.27 \times 0.24 \times 0.06$
T/K	125
Crystal System	triclinic
Space Group	$P-1$
$a/\text{\AA}$	9.0679(10)
$b/\text{\AA}$	9.0849(8)
$c/\text{\AA}$	12.1511(11)
$\alpha/^\circ$	68.838(8)
$\beta/^\circ$	78.214(9)
$\gamma/^\circ$	76.820(8)
$V/\text{\AA}^3$	900.69(16)
Z	2
Z'	1
Wavelength/ \AA	0.71075
Radiation type	$\text{MoK}\alpha$
$\theta_{\text{min}}/^\circ$	2.328
$\theta_{\text{max}}/^\circ$	28.767
Measured Refl's.	11912
Indep't Refl's	4021
Refl's $I \geq 2 \sigma(I)$	3635
R_{int}	0.0404
Parameters	282
Restraints	18
Largest Peak	0.405
Deepest Hole	-0.417
Goof	1.099
wR_2 (all data)	0.1068
wR_2	0.1037
R_1 (all data)	0.0484
R_1	0.0432

Table S122: Selected bond lengths (Å) and angles (°) for [ZnL1(NO₃)₂·CH₃CN]₂.

Zn1-O1	2.171(2)
Zn1-O2	2.423(3)
Zn1-O4	2.250(2)
Zn1-O5	2.278(2)
Zn1-N1	2.108(2)
Zn1-N4 ¹	2.118(2)
Zn1-N6	2.202(2)
O1-N5	1.260(3)
O2-N5	1.247(3)
O3-N5	1.222(3)
O4-N7	1.264(3)
O5-N7	1.250(3)
O6-N7	1.223(3)
O1-Zn1-O2	54.79(8)
O1-Zn1-O4	133.08(8)
O1-Zn1-O5	170.10(8)
O1-Zn1-N6	86.32(9)
O4-Zn1-O2	78.68(8)
O4-Zn1-O5	56.33(8)
O5-Zn1-O2	134.91(8)
N1-Zn1-O1	88.71(9)
N1-Zn1-O2	94.29(9)
N1-Zn1-O4	89.13(8)
N1-Zn1-O5	88.38(8)
N1-Zn1-N4 ¹	173.28(9)
N1-Zn1-N6	91.35(9)
N4 ¹ -Zn1-O1	97.82(9)
N4 ¹ -Zn1-O2	90.80(9)
N4 ¹ -Zn1-O4	87.57(9)
N4 ¹ -Zn1-O5	84.92(8)
N4 ¹ -Zn1-N6	87.50(9)
N6-Zn1-O2	140.46(9)
N6-Zn1-O4	140.59(9)
N6-Zn1-O5	84.29(8)
Py^Py	1.65(9)

Symmetry code: ¹1-x,1-y,1-z.

Table S123: Crystal data and refinement parameters for **(ZnL1Cl₂)_∞**.

(ZnL1Cl₂)_∞	
Formula	C ₁₂ H ₈ Cl ₂ N ₄ SZn
<i>D</i> _{calc.} / g cm ⁻³	1.723
<i>μ</i> /mm ⁻¹	2.196
Formula Weight	376.55
Colour	colourless
Shape	prism
Size/mm ³	0.06×0.03×0.03
<i>T</i> /K	173
Crystal System	monoclinic
Space Group	<i>P</i> 2 ₁ / <i>n</i>
<i>a</i> /Å	7.1587(3)
<i>b</i> /Å	12.2614(5)
<i>c</i> /Å	16.8290(7)
<i>α</i> /°	90
<i>β</i> /°	100.685(4)
<i>γ</i> /°	90
<i>V</i> /Å ³	1451.56(11)
<i>Z</i>	4
<i>Z</i> '	1
Wavelength/Å	0.71075
Radiation type	MoK _α
<i>θ</i> _{min} /°	2.068
<i>θ</i> _{max} /°	28.251
Measured Refl's.	19361
Indep't Refl's	3127
Refl's I≥2 <i>σ</i> (I)	2618
<i>R</i> _{int}	0.0280
Parameters	200
Restraints	12
Largest Peak	1.980
Deepest Hole	-0.646
Goof	1.066
<i>wR</i> ₂ (all data)	0.1299
<i>wR</i> ₂	0.1250
<i>R</i> ₁ (all data)	0.0579
<i>R</i> ₁	0.0478

Table S124 Selected bond lengths (Å) and angles (°) for **(ZnL1Cl₂)_∞**.

Zn1–Cl1	2.2094(12)
Zn1–Cl2	2.2345(11)
Zn1–N1	2.061(3)
Zn1–N4 ¹	2.061(3)
Cl1–Zn1–Cl2	122.12(6)
N1–Zn1–Cl1	106.01(9)
N1–Zn1–Cl2	105.16(9)
N1–Zn1–N4 ¹	107.83(13)
N4 ¹ –Zn1–Cl1	109.39(10)
N4 ¹ –Zn1–Cl2	105.59(10)
Py [^] Py	134.5(6)

Symmetry codes: $1/2-x, -1/2+y, 3/2-z$

Table S125: Crystal data and refinement parameters for $(\mathbf{1}\cdot\mathbf{L1})_{\infty}$ and $(\mathbf{1}\cdot\mathbf{L2})_2$.

	$(\mathbf{1}\cdot\mathbf{L1})_{\infty}$	$(\mathbf{1}\cdot\mathbf{L2})_2$
Formula	C ₁₆ H ₂₀ CdN ₄ O ₄ P ₂ S ₅	C ₃₂ H ₄₀ Cd ₂ N ₈ O ₈ P ₄ S ₁₀
$D_{calc.}/\text{g cm}^{-3}$	1.743	1.730
μ/mm^{-1}	1.426	1.416
Formula Weight	667.02	1334.04
Colour	Colourless	Colourless
Shape	plate	slab
Size/mm ³	0.05×0.10×0.20	0.20×0.20×0.08
T/K	120(2)	120(2)
Crystal System	Triclinic	Triclinic
Space Group	<i>Pnna</i>	<i>P2₁/c</i>
$a/\text{Å}$	9.6094(2)	14.0414(4)
$b/\text{Å}$	14.2535(4)	15.3357(4)
$c/\text{Å}$	18.5625(5)	12.9456(4)
$\alpha/^\circ$	90.00	90.00
$\beta/^\circ$	90.00	113.2910(10)
$\gamma/^\circ$	90.00	90.00
$V/\text{Å}^3$	2542.46	2560.47
Z	4	2
Z'	0.5	0.5
Wavelength/Å	0.71075	0.71075
Radiation type	MoK α	MoK α
$\theta_{min}/^\circ$	3.37	3.06
$\theta_{max}/^\circ$	27.48	27.48
Measured Refl's.	16542	25433
Indep't Refl's	2892	5847
Refl's $I \geq 2\sigma(I)$	2672	5144
R_{int}	0.039	0.037
Parameters	167	287
Restraints	6	0
Largest Peak	0.48	0.61
Deepest Hole	-0.37	-0.56
GooF	1.201	1.056
wR_2 (all data)	0.0802	0.0984
wR_2	0.0777	0.0945
R_1 (all data)	0.0411	0.0485
R_1	0.0365	0.0408

Table S126: Crystal data and refinement parameters for $[\text{AgL3}(\text{OTf})((\text{CH}_3)_2\text{CO})_{2.5}]_x$.

$[\text{AgL3}(\text{OTf})((\text{CH}_3)_2\text{CO})_{2.5}]_\infty$	
Formula	$\text{C}_{42.5}\text{H}_{29}\text{Ag}_2\text{F}_6\text{N}_4\text{O}_{7.5}\text{S}_4$
$D_{\text{calc.}}/\text{g cm}^{-3}$	1.613
μ/mm^{-1}	1.058
Formula Weight	1173.68
Colour	colourless
Shape	lath
Size/ mm^3	0.28×0.06×0.02
T/K	100(2)
Crystal System	monoclinic
Space Group	$P2_1/n$
$a/\text{\AA}$	16.2185(4)
$b/\text{\AA}$	10.3900(2)
$c/\text{\AA}$	29.0177(7)
$\alpha/^\circ$	90
$\beta/^\circ$	98.740(2)
$\gamma/^\circ$	90
$V/\text{\AA}^3$	4833.00(19)
Z	4
Z'	1
Wavelength/ \AA	0.71075
Radiation type	Mo K_α
$\theta_{\text{min}}/^\circ$	1.960
$\theta_{\text{max}}/^\circ$	27.485
Measured Refl's.	57151
Indep't Refl's	11089
Refl's $I \geq 2\sigma(I)$	8067
R_{int}	0.0496
Parameters	616
Restraints	33
Largest Peak	0.852
Deepest Hole	-0.647
Goof	1.013
wR_2 (all data)	0.1154
wR_2	0.1031
R_1 (all data)	0.0756
R_1	0.0489

Table S127: Selected bond lengths (Å) and angles (°) for [AgL3(OTf)((CH₃)₂CO)_{2.5}]_∞.

Ag1–O1A	2.895(4)	O1A–Ag1–O6	164.79(15)
Ag1–O1B	2.843(14)	O1B–Ag1–O6	144.9(8)
Ag1–N1	2.136(3)	N1–Ag1–O1A	89.36(14)
Ag1–N2 ¹	2.142(3)	N1–Ag1–O1B	80.5(5)
Ag1–O6	3.005(5)	N1–Ag1–N2 ¹	175.84(12)
Ag2–O2A	3.09(4)	N1–Ag1–O6	89.68(12)
Ag2–O2B	2.822(6)	N2 ¹ –Ag1–O1A	88.26(13)
Ag2–N3	2.165(3)	N2 ¹ –Ag1–O1B	96.1(5)
Ag2–N4 ¹	2.172(3)	N2 ¹ –Ag1–O6	91.72(12)
Ag2–O5	2.636(3)	N3–Ag2–O2A	92.3(8)
S3–O1A	1.468(5)	N3–Ag2–O2B	83.59(16)
S3–O1B	1.325(15)	N3–Ag2–N4 ¹	169.18(12)
S3–O2A	1.461(19)	N3–Ag2–O5	99.79(12)
S3–O2B	1.423(5)	N4 ¹ –Ag2–O2A	84.5(8)
S3–O9	1.423(3)	N4 ¹ –Ag2–O2B	94.57(17)
S3–C37	1.807(6)	N4 ¹ –Ag2–O5	87.17(12)
F1A–C37	1.373(7)	O5–Ag2–O2A	154.8(5)
F1B–C37	1.324(10)	O5–Ag2–O2B	149.91(19)
F2A–C37	1.355(8)	Py1 [^] Py2	172.36(13)
F2B–C37	1.249(12)	Py3 [^] Py4	169.35(13)
F3A–C37	1.312(8)	Py1 [^] Tph1 [^] Py2	152.47(4)
F3B–C37	1.381(12)	Py3 [^] Tph2 [^] Py4	152.38(4)
S4–O4	1.418(3)		
S4–O5	1.424(4)		
S4–O6	1.424(4)		
S4–C38	1.819(5)		
F4–C38	1.354(7)		
F5–C38	1.314(6)		
F6–C38	1.319(6)		
O7–C39	1.220(9)		
C39–C40 ²	1.482(7)		
C39–C40	1.481(7)		
O8–C41	1.183(10)		
C41–C42	1.481(10)		
C41–C43	1.563(11)		

Symmetry codes: ¹ 1/2+x,-y,-1/2+z; ² 3/2-x,+y,3/2-z

Py1 = N1-C1-C2-C3-C4-C5; Py2 = N2-C14-C15-C16-C17-C18; Py3 = N3-C19-C20-C21-C22-C23; Py4 = N4-C32-C33-C34-C35-C36; Tph1 = S1-C8-C9-C10-C11; Tph2 = S2-C26-C27-C28-C29.

Table S128: Crystal data and refinement parameters for $[\text{CdL3}(\text{NO}_3)_2(\text{H}_2\text{O})_2 \cdot 1.5\text{H}_2\text{O}]_\infty$.

<u>$[\text{CdL3}(\text{NO}_3)_2(\text{H}_2\text{O})_2 \cdot 1.5\text{H}_2\text{O}]_\infty$</u>	
Formula	$\text{C}_{18}\text{H}_{13}\text{CdN}_4\text{O}_8\text{S}$
$D_{\text{calc.}} / \text{g cm}^{-3}$	1.677
μ / mm^{-1}	1.135
Formula Weight	557.78
Colour	colourless
Shape	block
Size/ mm^3	$0.07 \times 0.02 \times 0.01$
T / K	100(2)
Crystal System	orthorhombic
Space Group	$Pccn$
$a / \text{\AA}$	28.0579(9)
$b / \text{\AA}$	22.2561(7)
$c / \text{\AA}$	7.0747(6)
$\alpha / ^\circ$	90
$\beta / ^\circ$	90
$\gamma / ^\circ$	90
$V / \text{\AA}^3$	4417.9(4)
Z	8
Z'	1
Wavelength/ \AA	0.71073
Radiation type	Mo K_α
$\theta_{\text{min}} / ^\circ$	2.336
$\theta_{\text{max}} / ^\circ$	27.483
Measured Refl's.	40927
Indep't Refl's	5062
Refl's $I \geq 2 \sigma(I)$	4064
R_{int}	0.0673
Parameters	316
Restraints	206
Largest Peak	1.508
Deepest Hole	-1.599
Goof	1.161
wR_2 (all data)	0.1583
wR_2	0.1495
R_1 (all data)	0.0877
R_1	0.0683

Table S129: Selected bond lengths (Å) and angles (°) for [CdL3(NO₃)₂(H₂O)₂·1.5H₂O]_x.

Cd1–O1	2.571(5)	O2–Cd1–O1	50.30(15)
Cd1–O2	2.506(5)	O2–Cd1–O6B	139.2(3)
Cd1–O4	2.330(5)	O4–Cd1–O1	124.1(2)
Cd1–O5	2.316(5)	O4–Cd1–O2	75.3(2)
Cd1–N1	2.285(4)	O4–Cd1–O6B	64.4(3)
Cd1–N2 ¹	2.271(4)	O5–Cd1–O1	70.04(16)
Cd1–O6A	2.320(8)	O5–Cd1–O2	119.04(15)
Cd1–O6B	2.532(10)	O5–Cd1–O4	165.7(2)
O1–N3	1.250(7)	O5–Cd1–O6A	95.0(3)
O2–N3	1.266(6)	O5–Cd1–O6B	101.3(3)
O3–N3	1.230(6)	N1–Cd1–O1	97.23(16)
N4A–O6A	1.250(7)	N1–Cd1–O2	85.63(16)
N4A–O7A	1.005(3)	N1–Cd1–O4	89.59(17)
N4A–O8A	1.241(6)	N1–Cd1–O5	91.01(16)
N4B–O6B	1.240(9)	N1–Cd1–O6A	87.2(5)
N4B–O7B	1.253(2)	N1–Cd1–O6B	87.9(4)
N4B–O8B	1.250(3)	N2 ¹ –Cd1–O1	87.22(16)
N1…N2	14.701(6)	N2 ¹ –Cd1–O2	96.79(16)
		N2 ¹ –Cd1–O4	87.37(17)
		N2 ¹ –Cd1–O5	91.11(16)
		N2 ¹ –Cd1–N1	175.51(15)
		N2 ¹ –Cd1–O6A	88.6(5)
		N2 ¹ –Cd1–O6B	87.8(4)
		O6A–Cd1–O1	164.4(3)
		O6A–Cd1–O2	145.3(3)
		O6A–Cd1–O4	70.7(3)
		O6B–Cd1–O1	169.9(4)
		Py1 [^] Py2	170.9(2)
		Py1–Tph1–Py2	159.37(5)

Symmetry code: ¹ -1/2+x, 1/2+y, -z

Table S130: Crystal data and refinement parameters for $[\text{CuL3}(\text{NO}_3)_2 \cdot \text{CH}_3\text{CN}]_2 \cdot 2\text{CH}_3\text{CN}$.

$[\text{CuL3}(\text{NO}_3)_2 \cdot \text{CH}_3\text{CN}]_2 \cdot 2\text{CH}_3\text{CN}$	
Formula	$\text{C}_{24}\text{H}_{19}\text{CuN}_7\text{O}_6\text{S}$
$D_{\text{calc.}} / \text{g cm}^{-3}$	1.511
μ / mm^{-1}	0.965
Formula Weight	597.06
Colour	clear green
Shape	(cut) block
Size/ mm^3	0.23×0.14×0.06
T/K	100(2)
Crystal System	triclinic
Space Group	$P-1$
$a/\text{\AA}$	9.0135(3)
$b/\text{\AA}$	9.6883(4)
$c/\text{\AA}$	15.8659(4)
$\alpha/^\circ$	82.499(3)
$\beta/^\circ$	74.076(2)
$\gamma/^\circ$	81.673(3)
$V/\text{\AA}^3$	1312.27(8)
Z	2
Z'	1
Wavelength/ \AA	0.71075
Radiation type	Mo K_α
$\theta_{\text{min}}/^\circ$	2.365
$\theta_{\text{max}}/^\circ$	27.483
Measured Refl's.	58370
Indep't Refl's	6032
Refl's $I \geq 2 \sigma(I)$	5640
R_{int}	0.0322
Parameters	415
Restraints	8
Largest Peak	0.464
Deepest Hole	-0.512
GooF	1.107
wR_2 (all data)	0.0771
wR_2	0.0758
R_1 (all data)	0.0350
R_1	0.0318

Table S131: Selected bond lengths (Å) and angles (°) for [CuL3(NO₃)₂·CH₃CN]₂·2CH₃CN.

Cu1–O1	1.9952(12)
Cu1–N1	2.0064(15)
Cu1–N2 ¹	2.0104(14)
Cu1–N4	2.2567(17)
Cu1–O4A	1.977(3)
Cu1–O4B	2.041(2)
O1–Cu1–N1	89.64(6)
O1–Cu1–N2 ¹	91.04(5)
O1–Cu1–N4	81.72(6)
O1–Cu1–O4B	158.83(7)
N1–Cu1–N2 ¹	162.18(6)
N1–Cu1–N4	98.71(6)
N1–Cu1–O4B	98.27(8)
N2 ¹ –Cu1–N4	99.01(6)
N2 ¹ –Cu1–O4B	87.35(8)
O4A–Cu1–O1	152.72(9)
O4A–Cu1–N1	78.36(9)
O4A–Cu1–N2 ¹	93.23(8)
O4A–Cu1–N4	124.00(9)
O4B–Cu1–N4	77.69(8)

Symmetry code: ¹ 2-x, 1-y, 1-z.

Table S132 Crystal data and refinement parameters for $(\text{Co}(\text{L4})_2\text{Cl}_2)_\infty$.

$[\text{Co}(\text{L4})_2\text{Cl}_2]_\infty$	
Formula	$\text{C}_{18}\text{H}_{10}\text{Cl}_2\text{Co}_1\text{N}_2\text{S}$
$D_{\text{calc.}} / \text{g cm}^{-3}$	1.449
μ / mm^{-1}	0.861
Formula Weight	401.72
Colour	pale orange
Shape	(cut) irregular block
Size/ mm^3	0.22×0.08×0.04
T / K	100(2)
Crystal System	monoclinic
Flack Parameter	0.50(7)
Hooft Parameter	0.487(11)
Space Group	$P2_1$
$a / \text{Å}$	11.1956(3)
$b / \text{Å}$	10.3305(3)
$c / \text{Å}$	28.3629(9)
$\alpha / ^\circ$	90
$\beta / ^\circ$	100.726(3)
$\gamma / ^\circ$	90
$V / \text{Å}^3$	3223.03(17)
Z	8
Z'	4
Wavelength/Å	0.71073
Radiation type	Mo K_α
$\theta_{\text{min}} / ^\circ$	1.851
$\theta_{\text{max}} / ^\circ$	27.484
Measured Refl's.	73759
Indep't Refl's	14795
Refl's $I \geq 2 \sigma(I)$	12831
R_{int}	0.0880
Parameters	766
Restraints	848
Largest Peak	3.144
Deepest Hole	-1.182
Goof	1.051
wR_2 (all data)	0.3534
wR_2	0.3438
R_1 (all data)	0.1408
R_1	0.1290

Table S133 Selected bond lengths (Å) and angles (°) for **(Co·(L4)₂Cl₂)_∞**.

Co1-Cl1	2.430(4)	Cl1-Co1-Cl3	179.09(17)
Co1-Cl3	2.437(4)	N1-Co1-Cl1	89.5(4)
Co1-N1	2.137(12)	N1-Co1-Cl3	90.3(4)
Co1-N3	2.198(14)	N1-Co1-N3	93.6(5)
Co1-N5	2.121(13)	N1-Co1-N81	88.3(5)
Co1-N81	2.154(14)	N3-Co1-Cl1	88.1(4)
Co2-Cl2	2.451(6)	N3-Co1-Cl3	91.1(4)
Co2-Cl4	2.430(6)	N5-Co1-Cl1	88.7(4)
Co2-N22	2.249(16)	N5-Co1-Cl3	91.5(4)
Co2-N4	2.113(19)	N5-Co1-N1	178.1(6)
Co2-N63	2.212(18)	N5-Co1-N3	85.8(5)
Co2-N7	2.222(17)	N5-Co1-N81	92.2(6)
		N81-Co1-Cl1	88.0(4)
		N81-Co1-Cl3	92.9(4)
		N81-Co1-N3	175.6(5)
		Cl4-Co2-Cl2	178.5(2)
		N22-Co2-Cl2	89.4(5)
		N22-Co2-Cl4	91.9(5)
		N4-Co2-Cl2	90.0(6)
		N4-Co2-Cl4	89.3(6)
		N4-Co2-N22	90.0(7)
		N4-Co2-N63	88.6(7)
		N4-Co2-N7	178.1(8)
		N63-Co2-Cl2	88.9(5)
		N63-Co2-Cl4	89.9(5)
		N63-Co2-N22	177.7(6)
		N63-Co2-N7	92.8(6)

Table S134 Crystal data and structure refinement parameters for **L5**

L5	
Formula	C ₂₄ H ₁₆ N ₂
<i>D</i> _{calc.} / g cm ⁻³	1.307
μ /mm ⁻¹	0.077
Formula Weight	368.42
Colour	yellow
Shape	lath
Size/mm ³	0.58×0.35×0.25
<i>T</i> /K	173(2)
Crystal System	Monoclinic
Space Group	<i>C</i> 2/ <i>c</i>
<i>a</i> /Å	11.7347(8)
<i>b</i> /Å	14.4591(10)
<i>c</i> /Å	11.6934(9)
<i>a</i> /°	90
<i>b</i> /°	109.302(8)
<i>g</i> /°	90
<i>V</i> /Å ³	1872.5(2)
<i>Z</i>	4
<i>Z</i> '	0.5
Wavelength/Å	0.71075
Radiation type	Mo K α
<i>Q</i> _{min} /°	2.555
<i>Q</i> _{max} /°	28.200
Measured Refl's.	3287
Indep't Refl's	1866
Refl's I \geq 2 σ (I)	1.557
<i>R</i> _{int}	0.0198
Parameters	133
Restraints	0
Largest Peak	0.204
Deepest Hole	-0.146
GooF	1.041
<i>wR</i> ₂ (all data)	0.1025
<i>wR</i> ₂	0.0955
<i>R</i> ₁ (all data)	0.0481
<i>R</i> ₁	0.0383

Table S135 Crystal data and structure refinement parameters for **3**.

3	
Formula	C ₃₆ H ₄₈ Cd ₂ N ₀ O ₈ P ₄ S ₈
<i>D</i> _{calc.} / g cm ⁻³	1.710
μ /mm ⁻¹	1.439
Formula Weight	1213.90
Colour	colourless
Shape	block
Size/mm ³	0.18×0.15×0.12
<i>T</i> /K	120(2)
Crystal System	Monoclinic
Space Group	<i>P2</i> ₁ / <i>c</i>
<i>a</i> /Å	14.8963(2)
<i>b</i> /Å	15.0128(3)
<i>c</i> /Å	10.5525(2)
<i>a</i> /°	90
<i>b</i> /°	92.3350(10)
<i>g</i> /°	90
<i>V</i> /Å ³	2357.95(7)
<i>Z</i>	2
<i>Z</i> '	0.5
Wavelength/Å	0.71073
Radiation type	Mo K α
<i>Q</i> _{min} /°	3.56
<i>Q</i> _{max} /°	27.49
Measured Refl's.	36946
Indep't Refl's	5396
<i>R</i> _{int}	0.0364
Parameters	294
Restraints	0
Largest Peak	0.529
Deepest Hole	-0.517
GooF	1.026
<i>wR</i> ₂ (all data)	0.0520
<i>wR</i> ₂	0.0498
<i>R</i> ₁ (all data)	0.0289
<i>R</i> ₁	0.0229

Table S136 Selected bond lengths (Å) and angles (°) for compound **3**, HAHDEA, MERXUD and QIDKOG.

	3	HAHDEA	MERXUD	QIDKOG			
Cd1-S1	2.6417(5)	Cd1-S1	2.6610(7)	Cd1-S1	2.9877(7)	Cd1-S1	2.6470(11)
Cd1-S2	2.5246(5)	Cd1-S2	2.5249(8)	Cd1-S2	2.5755(8)	Cd1-S2	2.5155(15)
Cd1-S3	2.5508(5)	Cd1-S3	2.5767(9)	Cd1-S3	2.6880(7)	Cd1-S3	2.5249(14)
Cd1-S4	2.5402(5)	Cd1-S4	2.5210(7)	Cd1-S4	2.5161(8)	Cd1-S4	2.5689(18)
P1-S1	2.0030(6)	P1-S1	1.9964(10)	P1-S1	2.0423(11)	P1-S1	1.989(2)
P1-S2	2.0216(6)	P1-S2	2.0239(9)	P1-S2	2.0019(10)	P1-S2	2.0046(18)
P2-S3	2.0174(6)	P2-S3	1.9990(9)	P2-S3	1.9974(11)	P2-S3	2.027(2)
P2-S4	2.0036(6)	P2-S4	2.0409(11)	P2-S4	2.0202(10)	P2-S4	1.9844(18)
P1-O1	1.5959(13)	P1-O1	1.5905(17)	P1-O1	1.5803(18)	P1-O1	1.583(5)
P2-O3	1.5913(13)	P2-O3	1.5842(16)	P2-O3	1.5860(19)	P2-O2	1.578(4)
P1-C3	1.7908(18)	P1-C1	1.796(2)	P1-C8	1.790(2)	P1-C1	1.787(5)
P2-C12	1.7872(18)	P2-C11	1.785(2)	P2-C19	1.805(2)	P2-C11	1.784(4)
S1-Cd1-S2	79.688(14)	S1-Cd1-S2	79.46(3)	S1-Cd1-S2	75.58(2)	S1-Cd1-S2	79.39(4)
S3-Cd1-S4	100.101(15)	S3-Cd1-S4	100.75(3)	S3-Cd1-S4	134.00(3)	S3-Cd1-S4	102.03(5)
S1-P1-S2	110.70(3)	S1-P1-S2	111.15(3)	S1-P1-S2	111.75(4)	S1-P1-S2	111.37(7)
S3-P1-S4	112.86(3)	S3-P1-S4	111.62(4)	S3-P1-S4	111.38(4)	S3-P1-S4	112.70(9)
O1-P1-C3	97.95(8)	O1-P1-C1	100.01(9)	O1-P1-C3	99.30(9)	O1-P1-C1	99.5(2)
O3-P2-C12	99.50(8)	O3-P2-C11	100.25(9)	O3-P2-C19	106.17(10)	O3-P2-C11	100.9(2)

Table S137 Crystal data and refinement parameters for $(2\cdot\text{L5}\cdot\text{CHCl}_3)_\infty$ and $(3\cdot\text{L5})_\infty$.

	$(2\cdot\text{L5}\cdot\text{CHCl}_3)_\infty$	$(3\cdot\text{L5})_\infty$
Formula	$\text{C}_{44}\text{H}_{37}\text{CdCl}_3\text{N}_2\text{O}_4\text{P}_2\text{S}_4$	$\text{C}_{45}\text{H}_{40}\text{N}_2\text{O}_4\text{P}_2\text{S}_4\text{Cd}$
$D_{\text{calc}}/\text{g cm}^{-3}$	1.553	1.496
m/mm^{-1}	0.952	0.817
Formula Weight	1066.68	975.37
Colour	colourless	colourless
Shape	(cut) plate	lath
Size/ mm^3	$0.12\times 0.10\times 0.02$	$0.45\times 0.20\times 0.03$
T/K	100(2)	100(2)
Crystal System	monoclinic	monoclinic
Flack Parameter	-0.041(10)	-
Hooft Parameter	-0.017(7)	-
Space Group	Cc	$P2_1/c$
$a/\text{\AA}$	16.2914(2)	16.0709(4)
$b/\text{\AA}$	23.0504(3)	22.3910(4)
$c/\text{\AA}$	12.7021(2)	12.5602(3)
$a/^\circ$	90	90
$b/^\circ$	106.962(2)	106.696(3)
$g/^\circ$	90	90
$V/\text{\AA}^3$	4562.43(12)	4329.17(18)
Z	4	4
Z'	1	1
Wavelength/ \AA	0.71075	0.71075
Radiation type	MoK_α	MoK_α
$Q_{\text{min}}/^\circ$	1.577	1.819
$Q_{\text{max}}/^\circ$	27.485	27.483
Measured Refl's.	69700	33966
Indep't Refl's	10475	9480
Refl's $I\geq 2\sigma(I)$	9963	7875
R_{int}	0.0585	0.0405
Parameters	553	535
Restraints	2	0
Largest Peak	0.434	0.760
Deepest Hole	-0.229	-0.773
Goof	1.020	1.023
wR_2 (all data)	0.0589	0.0842
wR_2	0.0578	0.0779
R_1 (all data)	0.0329	0.0473
R_1	0.0292	0.0351

Table S138 Crystal data and refinement parameters for **R2** and **R3**

	R2	R3
Formula	C ₃₆ H ₂₈ B ₂ F ₂ O ₄ Si ₂	C ₃₆ H ₂₆ B ₂ F ₄ O ₄ Si ₂
<i>D</i> _{calc.} / g cm ⁻³	1.286	1.380
μ /mm ⁻¹	0.157	0.172
Formula Weight	640.38	676.37
Colour	colourless	colourless
Shape	block	block
Size/mm ³	0.30x0.25x0.15	0.30x0.20x0.20
<i>T</i> /K	173(2)	173(2)
Crystal System	triclinic	triclinic
Space Group	<i>P</i> -1	<i>P</i> -1
<i>a</i> /Å	8.5686(6)	8.7686(3)
<i>b</i> /Å	9.8331(10)	12.6193(5)
<i>c</i> /Å	11.3579(8)	15.6914(7)
α /°	112.478(8)	71.173(4)
β /°	108.622(6)	82.544(3)
γ /°	91.091(7)	89.851(3)
<i>V</i> /Å ³	827.02(13)	1628.09(12)
<i>Z</i>	1	2
<i>Z</i> '		
Wavelength/Å	0.71075	0.71075
Radiation type	MoK α	MoK α
θ_{min} /°	3.124	2.958
θ_{max} /°	25.022	25.023
Measured Refl.	4382	8704
Independent Refl.	2890	5686
<i>R</i> _{int}	0.0164	0.0201
Parameters	208	433
Restraints	-	-
Largest Peak	0.229	0.462
Deepest Hole	-0.297	-0.451
Goof	1.026	1.048
<i>wR</i> ₂ (all data)	0.1018	0.1209
<i>wR</i> ₂	0.0941	0.1085
<i>R</i> ₁ (all data)	0.0714	0.0832
<i>R</i> ₁	0.0467	0.0498

Table S139 Crystal data and refinement parameters for **(L1)₂·R3**, **(L3·R2)_∞**, **(L3·R3)_∞** and **(L5·R2)_∞**.

	(L1)₂·R3	(L3·R2)_∞	(L3·R3)_∞	(L5·R2)_∞
Formula	C ₆₀ H ₄₂ B ₂ F ₄ N ₈ O ₄ S ₂ Si ₂	C ₅₄ H ₃₆ B ₂ F ₄ N ₂ O ₄ SSi ₂	C ₅₄ H ₃₈ B ₂ F ₂ N ₂ O ₄ SSi ₂	C ₆₃ H ₄₄ B ₂ F ₂ N ₂ O ₄ Si ₂
<i>D</i> _{calc.} / g cm ⁻³	1.451	1.391	1.349	1.322
<i>μ</i> /mm ⁻¹	1.961	1.690	0.183	1.126
Formula Weight	1156.93	962.71	926.72	1008.80
Colour	colourless	pale yellow	colourless	pale yellow
Shape	plate	block	prism	tablets
Size/mm ³	0.20×0.08×0.01	0.19×0.16×0.06	0.06×0.05×0.025	0.4×0.15×0.06
<i>T</i> /K	100(2)	100(2)	100(2)	173(2)
Crystal System	triclinic	tetragonal	tetragonal	triclinic
Flack Parameter		-0.005(7)	-0.06(4)	
Hoof Parameter		-0.014(5)	-0.07(4)	
Space Group	<i>P</i> -1	<i>P</i> 4 ₃	<i>P</i> 4 ₃ 2 ₁ 2	<i>P</i> -1
<i>a</i> /Å	9.4015(2)	19.62160(10)	13.8634(2)	10.5710(6)
<i>b</i> /Å	11.6706(2)	19.62160(10)	13.8634(2)	11.3304(7)
<i>c</i> /Å	13.9100(4)	23.8883(2)	23.7340(4)	11.5981(9)
<i>α</i> /°	111.746(2)	90	90	83.092(6)
<i>β</i> /°	101.394(2)	90	90	84.864(6)
<i>γ</i> /°	101.696(2)	90	90	66.844(6)
<i>V</i> /Å ³	1324.33(6)	9197.17(12)	4561.53(15)	1267.28(15)
<i>Z</i>	1	8	4	1
<i>Z</i> '	0.5	2	0.5	0.5
Wavelength/Å	1.54178	1.54178	0.71075	1.54178
Radiation type	CuK _α	CuK _α	MoK _α	CuK _α
<i>θ</i> _{min} /°	3.586	2.252	1.701	3.843
<i>θ</i> _{max} /°	68.225	68.246	27.484	73.423
Measured Refl.	23623	49836	52919	7340
Independent Refl.	4811	16155	5236	4787
Reflections with <i>I</i> > 2(<i>I</i>)	4646	15953	4550	3655
<i>R</i> _{int}	0.0283	0.0270	0.0773	0.0306
Parameters	404	1312	334	397
Restraints	83	444	582	0
Largest Peak	0.343	0.365	0.259	0.279
Deepest Hole	-0.329	-0.219	-0.220	-0.292
GooF	1.055	1.021	1.028	1.022
<i>wR</i> ₂ (all data)	0.0733	0.0883	0.0837	0.1236
<i>wR</i> ₂	0.0727	0.0879	0.0794	0.1076
<i>R</i> ₁ (all data)	0.0295	0.0330	0.0474	0.0630
<i>R</i> ₁	0.0287	0.0326	0.0368	0.0444

Table S140 Selected bond lengths (Å) for compounds **(L1)₂R3**, **(L3R2)_∞**, **(L3R3)_∞** and **(L5R2)_∞**.

(L1)₂R3		(L3R2)_∞		(L3R3)_∞		(L5R2)_∞	
Si1-O1	1.6076(9)	Si1-O1	1.6067(17)	Si1-O1	1.6000(3)	Si3-O2	1.6119(16)
Si1-O2	1.6126(12)	Si1-O2	1.6179(16)	Si1-O2	1.623(3)	Si3-O4	1.6184(15)
				Si2-O3	1.611(3)		
				Si2-O4	1.612(3)		
				Si61-O61	1.619(3)		
				Si61-O62	1.605(3)		
				Si62-O63	1.617(3)		
				Si62-O64	1.614(3)		
Si1-C7	1.8733(12)	Si1-C7	1.865(2)	Si1-C13	1.857(5)	Si3-C32	1.871(3)
Si1-C13	1.8709(16)	Si1-C13	1.877(2)	Si1-C19	1.862(5)	Si3-C38	1.873(18)
				Si2-C25	1.878(4)		
				Si2-C31	1.874(5)		
				Si61-C73	1.864(5)		
				Si61-C79	1.864(5)		
				Si62-C85	1.877(5)		
				Si62-C91	1.875(5)		
B1-O1	1.4304(19)	B1-O1	1.424(3)	B1-O1	1.415(6)	B1-O2	1.429(3)
B1-O2	1.432(2)	B1-O2	1.440(3)	B1-O4	1.447(6)	B1-O4	1.436(3)
B1-C13	1.623(2)	B1-C1	1.623(4)	B2-O2	1.415(6)	B1-C26	1.613(3)
B1-N21	1.6881(14)	B1-N21	1.697(3)	B2-O3	1.436(6)	B1-N5	1.704(2)
				B61-O61	1.413(6)		
				B61-O64	1.439(6)		
				B62-O62	1.410(6)		
				B62-O63	1.448(6)		
				B1-C1	1.623(7)		
				B2-C7	1.644(7)		
				B61-C61	1.636(7)		
				B62-C67	1.610(7)		
				B1-N41	1.690(6)		
				B2-N102	1.713(6)		
				B61-N42	1.704(6)		
				B62-N101	1.694(6)		
F1-C3	1.365(2)	F1-C4	1.368(2)	F1-C3	1.356(5)	F29-C29	1.359(3)
F2-C5	1.3581(19)			F2-C5	1.363(5)		
				F3-C9	1.369(5)		
				F4-C11	1.362(5)		
				F61-C63	1.376(5)		
				F62-C65	1.373(5)		
				F63-C69	1.365(5)		
				F64-C71	1.344(6)		

Table S141 Selected bond angles (°) for compounds **(L1)₂R3**, **(L3·R2)_∞**, **(L3·R3)_∞** and **(L5·R2)_∞**.

(L1)₂R3		(L3·R2)_∞		(L3·R3)_∞		(L5·R2)_∞	
O1-Si1-O2	113.33(6)	O1-Si1-O2	115.65(9)	O1-Si1-O2	115.36(17)	O2-Si3-O4	112.58(9)
				O3-Si2-O4	115.01(17)		
				O61-Si61-O62	114.37(17)		
				O63-Si62-O64	114.37(17)		
O1-Si1-C7	109.46(6)	O1-Si1-C7	108.78(10)	O1-Si1-C13	107.3(2)	O2-Si3-C32	107.22(9)
O1-Si1-C13	107.68(5)	O1-Si1-C13	104.62(9)	O1-Si1-C19	105.87(19)		
O2-Si1-C7	110.29(6)	O2-Si1-C7	108.11(10)	O2-Si1-C13	109.07(19)	O2-Si3-C38	111.79(9)
O2-Si1-C7	107.76(6)	O2-Si1-C13	107.18(10)	O2-Si1-C19	106.97(19)	O4-Si3-C32	106.31(9)
						O4-Si3-C38	109.47(8)
				O3-Si2-C25	103.30(18)		
				O3-Si2-C31	108.59(18)		
				O4-Si2-C25	109.0(2)		
				O4-Si2-C31	108.59(18)		
				O61-Si61-C73	107.04(19)		
				O61-Si61-C79	107.88(19)		
				O62-Si61-C73	105.44(18)		
				O62-Si61-C79	109.18(19)		
				O63-Si62-C85	107.99(18)		
				O63-Si62-C91	107.5(2)		
				O64-Si62-C85	107.7(2)		
				O64-Si62-C91	104.71(18)		
C1-Si1-C7	108.15(7)	C7-Si1-C13	112.58(10)	C13-Si1-C19	112.3(2)	C32-Si3-C38	109.25(10)
				C25-Si2-C31	112.68(19)		
				C73-Si61-C79	107.88(19)		
				C85-Si62-C91	113.0(2)		
O1-B1-O2	117.53(11)	O1-B1-O2	117.6(2)	O1-B1-O4	116.8(4)	O2-B1-O4	116.60(17)
				O2-B2-O3	118.7(4)		
				O61-B61-O64	118.6(4)		
				O62-B62-O63	117.1(4)		
O1-B1-C1	112.68(13)	O1-B1-C1	112.70(19)	O1-B1-C1	113.9(4)	O2-B1-C26	113.86(19)
O2-B1-C1	110.76(12)	O2-B1-C1	110.9(2)	O4-B1-C1	110.5(4)	O4-B1-C26	112.12(16)
				O2-B2-C7	111.7(4)		
				O3-B2-C7	112.1(4)		
				O61-B61-C61	111.4(4)		
				O64-B61-C61	111.6(4)		
				O62-B62-C67	113.3(4)		
				O63-B62-C67	110.0(4)		
O1-B1-N21	103.1(2)	O1-B1-N21	102.36(19)	O1-B1-N41	102.6(4)	O2-B1-N5	102.50(14)
O2-B1-N21	105.48(11)	O2-B1-N21	104.83(17)	O4-B1-N41	104.8(4)	O4-B1-N5	105.19(17)
				O2-B2-N102	106.8(4)		
				O3-B2-N102	100.9(3)		
				O61-B61-N42	106.6(4)		
				O64-B61-N42	101.3(4)		
				O62-B62-N101	102.9(3)		
				O63-B62-N101	104.8(4)		
B1-O1-Si1	141.63(9)	B1-O1-Si1	142.59(15)	B1-O1-Si1	145.2(3)	B1-O2-Si3	141.79(12)
B1-O2-Si1	145.25(10)	B1-O2-Si1	141.45(16)	B2-O2-Si1	142.8(3)	B1-O4-Si3	137.71(14)
				B2-O3-Si2	140.1(3)		
				B1-O4-Si2	141.4(3)		
				B61-O61-Si61	141.8(3)		
				B62-O62-Si61	141.2(3)		
				B62-O63-Si62	141.8(3)		
				B61-O64-Si62	139.6(3)		

Table S142 Crystal data and refinement parameters for **(L7·H₂TER)_∞**.

	(L7·H₂TER)_∞
Formula	C ₂₈ H ₁₈ N ₂ O ₄
<i>D</i> _{calc.} / g cm ⁻³	1.398
<i>m</i> /mm ⁻¹	0.772
Formula Weight	446.44
Colour	colourless
Shape	(cut) lath
Size/mm ³	0.07×0.04×0.02
<i>T</i> /K	100(2)
Crystal System	monoclinic
Space Group	<i>P</i> 2 ₁ / <i>m</i>
<i>a</i> /Å	3.7952(3)
<i>b</i> /Å	46.928(3)
<i>c</i> /Å	5.9562(4)
<i>a</i> °	90.00
<i>b</i> °	91.936(7)
<i>g</i> °	90.00
<i>V</i> /Å ³	1060.20(13)
<i>Z</i>	2
<i>Z</i> '	0.5
Wavelength/Å	1.54178
Radiation type	CuK _α
<i>Q</i> _{min} /°	3.77
<i>Q</i> _{max} /°	68.20
Measured Refl's.	8765
Indep't Refl's	1968
Refl's I ≥ 2 σ(I)	1733
<i>R</i> _{int}	0.0561
Parameters	160
Restraints	1
Largest Peak	0.411
Deepest Hole	-0.390
GooF	1.180
<i>wR</i> ₂ (all data)	0.2895
<i>wR</i> ₂	0.2846
<i>R</i> ₁ (all data)	0.1077
<i>R</i> ₁	0.0993

Table S143 Crystal data and refinement parameters for **(L2·1,4-DITFB)_∞**

	(L2·1,4-DITFB)_∞
Formula	C ₁₈ H ₈ F ₄ I ₂ N ₄ S
<i>D</i> _{calc.} / g cm ⁻³	2.175
<i>μ</i> /mm ⁻¹	3.363
Formula Weight	642.14
Colour	colorless
Shape	prism
Size/mm ³	0.40×0.09×0.07
<i>T</i> /K	173
Crystal System	triclinic
Space Group	<i>P</i> -1
<i>a</i> /Å	5.6690(4)
<i>b</i> /Å	12.3300(9)
<i>c</i> /Å	14.1339(9)
<i>α</i> /°	91.644(6)
<i>β</i> /°	96.314(6)
<i>γ</i> /°	92.400(6)
<i>V</i> /Å ³	980.54(12)
<i>Z</i>	2
<i>Z</i> '	1
Wavelength/Å	0.71073
Radiation type	MoK _α
<i>θ</i> _{min} /°	2.163
<i>θ</i> _{max} /°	31.865
Measured Refl's.	12113
Indep't Refl's	6062
Refl's I ≥ 2 σ(I)	4599
<i>R</i> _{int}	0.0296
Parameters	262
Restraints	0
Largest Peak	3.299
Deepest Hole	-1.328
Goof	1.092
<i>wR</i> ₂ (all data)	0.1660
<i>wR</i> ₂	0.1504
<i>R</i> ₁ (all data)	0.0728
<i>R</i> ₁	0.0516

Table S144 Selected bond lengths (Å) and angles (°) for **(L2·1,4-DITFB)_∞**.

I1–C13	2.098(5)
I2–C16	2.087(6)
F1–C14	1.345(6)
F2–C15	1.331(7)
F3–C18	1.331(7)
F4–C17	1.342(7)
N1–I1	2.801(5)
N4 ¹ –I2	2.951(5)
C13–I1…N1	177.64(19)
C16–I2…N4 ¹	168.06(19)

Symmetry code: ¹ -2-x, 1+y, 1+z

Table S145 Crystal data and refinement parameters for **(H₂L3Br₄)(Br)(Br₃)·0.5 CHCl₃**

(H₂L3Br₄)(Br)(Br₃)·0.5 CHCl₃	
Formula	C _{18.5} H _{12.5} Br ₈ Cl _{1.5} N ₂ S
<i>D</i> _{calc.} / g cm ⁻³	2.406
<i>μ</i> /mm ⁻¹	16.253
Formula Weight	987.32
Colour	red
Shape	(cut) block
Size/mm ³	0.14×0.12×0.07
<i>T</i> /K	100(2)
Crystal System	triclinic
Space Group	<i>P</i> -1
<i>a</i> /Å	13.4627(2)
<i>b</i> /Å	13.8136(2)
<i>c</i> /Å	14.7325(2)
<i>α</i> /°	92.0550(10)
<i>β</i> /°	90.9260(10)
<i>γ</i> /°	95.3640(10)
<i>V</i> /Å ³	2725.50(7)
<i>Z</i>	4
<i>Z</i> '	2
Wavelength/Å	1.54184
Radiation type	Cu K _α
<i>θ</i> _{min} /°	3.002
<i>θ</i> _{max} /°	68.244
Measured Refl's.	49620
Indep't Refl's	9914
Refl's I ≥ 2 σ(I)	9589
<i>R</i> _{int}	0.0235
Parameters	625
Restraints	125
Largest Peak	1.233
Deepest Hole	-1.294
GooF	1.088
<i>wR</i> ₂ (all data)	0.0733
<i>wR</i> ₂	0.0726
<i>R</i> ₁ (all data)	0.0309
<i>R</i> ₁	0.0297

Table S146 Selected bond lengths (Å) and angles (°) for **(H₂L3Br₄)(Br)(Br₃)·0.5 CHCl₃**.

Br1–C6	1.886(4)
Br2–C7	1.899(4)
Br3–C12	1.893(4)
Br4–C13	1.883(4)
Br5–C24	1.900(4)
Br6–C25	1.896(4)
Br7–C30	1.901(4)
Br8–C31	1.891(4)
Br11–Br12	2.6507(7)
Br12–Br13	2.4795(7)
Br14–Br15	2.5187(15)
Br15–Br16	2.5744(9)
Br15–Br17	2.529(16)
Br15–Br18	2.538(13)
Br19–Br20	2.493(18)
Br19–Br21	2.640(18)
Br13–Br12–Br11	177.57(2)
Br14–Br15–Br16	175.43(8)
Br17–Br15–Br18	173.1(9)
Br20–Br19–Br21	177.4(17)

Table S147 Crystal data and refinement parameters for **L11** and **(L11·I₂)·0.5I₂**

	L11	(L11·I₂)·0.5I₂
Formula	C ₃₀ H ₁₄ N ₄	C ₃₀ H ₁₄ I ₃ N ₄
<i>D</i> _{calc.} / g cm ⁻³	1.340	1.939
<i>μ</i> /mm ⁻¹	0.637	3.400
Formula Weight	430.45	811.15
Colour	purple	clear red
Shape	needle	block
Size/mm ³	0.20×0.02×0.01	0.04×0.02×0.02
<i>T</i> /K	100(2)	297(2)
Crystal System	monoclinic	triclinic
Space Group	<i>P</i> 2 ₁ / <i>c</i>	<i>P</i> -1
<i>a</i> /Å	7.0164(2)	8.2475(6)
<i>b</i> /Å	28.2624(6)	9.0038(6)
<i>c</i> /Å	11.2725(3)	19.5017(13)
<i>α</i> /°	90	102.047(2)
<i>β</i> /°	107.350(3)	93.103(2)
<i>γ</i> /°	90	99.802(2)
<i>V</i> /Å ³	2133.63(10)	1389.55(17)
<i>Z</i>	4	2
<i>Z</i> '	1	1
Wavelength/Å	1.54178	0.71073
Radiation type	Cu K _α	MoK _α
<i>θ</i> _{min} /°	3.127	2.354
<i>θ</i> _{max} /°	68.242	27.510
Measured Refl's.	17137	79891
Indep't Refl's	3904	6379
Refl's I≥2 σ(I)	3213	3928
<i>R</i> _{int}	0.0573	0.0640
Parameters	307	335
Restraints	0	0
Largest Peak	0.476	1.165
Deepest Hole	-0.219	-1.682
GooF	1.036	1.127
<i>wR</i> ₂ (all data)	0.1540	0.1967
<i>wR</i> ₂	0.1447	0.1455
<i>R</i> ₁ (all data)	0.0637	0.1023
<i>R</i> ₁	0.0538	0.0532

Table S148 Selected bond lengths (Å) and angles (°) for **(L11·I₂)·0.5I₂**

I1–I2	2.7375(9)
I3– I3 ¹	2.7053(15)
N1–C1	1.323(11)
N1–C5	1.340(10)
N2–C26	1.311(13)
N2–C27	1.322(11)
N3–C30	1.145(10)
N4–C29	1.131(9)
C6–C7	1.154(10)
C30–C28–C29	114.0(6)
N4–C29–C28	179.3(9)
N3–C30–C28	177.5(8)

Symmetry code: ¹-x,1-y,-z

Table S149 Crystal data and structure refinement for **(HL12)I·2.5I₂** and **(HL12s)I·2.5I₂**

	(HL12)I·2.5I₂	(HL12s)I·2.5I₂
Formula	C ₁₀ H ₉ I ₆ N ₂ Se ₂	C ₁₀ H ₉ I ₆ N ₂ S ₂
<i>D</i> _{calc.} / g cm ⁻³	3.265	3.064
<i>μ</i> /mm ⁻¹	11.829	8.938
Formula Weight	1076.51	982.74
Colour	black	dark brown
Shape	chip	plate (cut)
Size/mm ³	0.18×0.15×0.02	0.24×0.22×0.08
<i>T</i> /K	125(2)	120(2)
Crystal System	monoclinic	monoclinic
Space Group	<i>P</i> 2 ₁ / <i>n</i>	<i>P</i> 2 ₁ / <i>n</i>
<i>a</i> /Å	9.2950(2)	9.2956(11)
<i>b</i> /Å	18.2721(4)	18.1444(17)
<i>c</i> /Å	12.8944(2)	12.6314(11)
<i>α</i> /°	90	90
<i>β</i> /°	90.458(2)	90.629(9)
<i>γ</i> /°	90	90
<i>V</i> /Å ³	2189.90(8)	2130.3(4)
<i>Z</i>	4	4
<i>Z</i> '	1	1
Wavelength/Å	0.71073	0.71073
Radiation type	MoK _α	MoK _α
<i>θ</i> _{min} /°	1.933	2.93
<i>θ</i> _{max} /°	28.831	27.50
Measured Refl's.	18078	16996
Indep't Refl's	4993	4867
Refl's I≥2 σ(I)	4537	4624
<i>R</i> _{int}	0.0198	
Parameters	185	183
Restraints	0	0
Largest Peak	0.651	
Deepest Hole	-0.710	
GooF	1.218	1.256
<i>wR</i> ₂ (all data)	0.0381	0.01704
<i>wR</i> ₂	0.0372	0.01691
<i>R</i> ₁ (all data)	0.0236	0.0561
<i>R</i> ₁	0.0192	0.0538

Table S150 Crystal data and refinement parameters for **HPyTeI₂**, **HPyTeBr₂** and **HPyTeBr₄**

	HPyTeI₂	HPyTeBr₂	HPyTeBr₄
Formula	C ₅ H ₅ I ₂ NTe	C ₅ H ₅ Br ₂ NTe	C ₅ H ₅ Br ₄ NTe
<i>D</i> _{calc.} / g cm ⁻³	3.417	2.943	3.309
<i>μ</i> /mm ⁻¹	10.145	13.172	17.888
Formula Weight	460.50	366.52	526.34
Colour	dark red	red	light yellow
Shape	plate	(cut) block	block
Size/mm ³	0.05×0.04×0.03	0.14×0.12×0.08	0.03×0.02×0.01
<i>T</i> /K	100(2)	100(2)	293(2)
Crystal System	monoclinic	monoclinic	monoclinic
Space Group	<i>P</i> 2 ₁ / <i>n</i>	<i>P</i> 2 ₁ / <i>c</i>	<i>P</i> 2 ₁ / <i>c</i>
<i>a</i> /Å	6.76010(10)	9.19180(10)	12.8016(4)
<i>b</i> /Å	9.3390(2)	10.8048(2)	10.2160(3)
<i>c</i> /Å	14.1776(3)	16.8899(3)	8.0776(3)
<i>α</i> /°	90	90	90
<i>β</i> /°	90.583(2)	99.5110(10)	90.343(3)
<i>γ</i> /°	90	90	90
<i>V</i> /Å ³	895.02(3)	1654.37(5)	1056.38(6)
<i>Z</i>	4	8	4
<i>Z</i> '	1	2	1
Wavelength/Å	0.71075	0.71075	0.71075
Radiation type	MoK _α	Mo K _α	Mo K _α
<i>θ</i> _{min} /°	2.612	2.445	2.551
<i>θ</i> _{max} /°	27.485	27.484	27.484
Measured Refl's.	19265	62542	32194
Indep't Refl's	2033	3786	2425
Refl's I≥2 <i>σ</i> (I)	1953	3651	2333
<i>R</i> _{int}	0.0335	0.0503	0.0639
Parameters	85	163	100
Restraints	1	0	0
Largest Peak	0.713	0.541	2.374
Deepest Hole	-0.729	-0.633	-1.201
Goof	1.138	1.243	1.309
<i>wR</i> ₂ (all data)	0.0354	0.0443	0.0956
<i>wR</i> ₂	0.0350	0.0438	0.0945
<i>R</i> ₁ (all data)	0.0163	0.0234	0.0524
<i>R</i> ₁	0.0152	0.0216	0.0493

Table S151 Selected bond lengths (Å) and angles (°) for **HPyTeI₂**, **HPyTeBr₂** and **HPyTeBr₄**.

HPyTeI₂		HPyTeBr₂		HPyTeBr₄	
C1-Te1	2.143(2)	C1-Te1	2.140(3)	C1-Te1	2.171(9)
		C6-Te2	2.141(3)		
I1-Te1	2.9886(2)	Br1-Te1	2.7655(3)	Br1-Te1	2.6793(10)
I2-Te1	2.9070(2)	Br2-Te1	2.6902(3)	Br2-Te1	2.6677(10)
		Br3-Te2	2.6987(3)	Br3-Te1	2.6600(10)
		Br4-Te2	2.7404(4)	Br4-Te1	2.6669(10)
I1-Te1-I2	176.383(7)	Br1-Te1-Br2	178.192(12)	Br1-Te1-Br2	89.96(3)
		Br3-Te2-Br4	177.517(12)	Br1-Te1-Br3	89.95(3)
				Br1-Te1-Br4	170.95(4)
				Br2-Te1-Br3	171.26(4)
				Br2-Te1-Br4	88.78(3)
				Br3-Te1-Br4	90.04(3)
Py^(I1-Te1-I2)	46.48(6)	Py1^(Br1-Te1-Br2)	50.7(5)		
		Py2^(Br3-Te2-Br4)	29.0(4)		

Table S152 Crystal data and refinement parameters for **HL14Cl·2H₂O** and **[(HL14)I₂Cl]₃·0.5I₂**.

	HL14Cl·2H₂O	[(HL14)I₂Cl]₃·0.5I₂
Formula	C ₁₄ H ₁₆ ClNO ₂ Se	C _{10.5} H ₉ Cl _{0.75} I _{1.75} N _{0.75} Se _{0.75}
<i>D</i> _{calc.} / g cm ⁻³	1.577	2.401
<i>μ</i> /mm ⁻¹	5.176	6.697
Formula Weight	344.69	453.57
Colour	colourless	dark red
Shape	lath	(cut) block
Size/mm ³	0.09×0.04×0.01	0.13×0.06×0.05
<i>T</i> /K	100(2)	100(2)
Crystal System	triclinic	triclinic
Space Group	<i>P</i> -1	<i>P</i> -1
<i>a</i> /Å	7.3040(2)	11.76310(10)
<i>b</i> /Å	9.1476(2)	14.0582(2)
<i>c</i> /Å	11.7026(2)	16.4528(2)
<i>α</i> /°	70.419(2)	94.0460(10)
<i>β</i> /°	80.430(2)	95.4730(10)
<i>γ</i> /°	88.427(2)	111.1560(10)
<i>V</i> /Å ³	726.09(3)	2509.62(5)
<i>Z</i>	2	8
<i>Z</i> '	1	4
Wavelength/Å	1.54184	0.71073
Radiation type	Cu K _α	Mo K _α
<i>θ</i> _{min} /°	4.066	1.563
<i>θ</i> _{max} /°	68.225	27.483
Measured Refl's.	13289	115623
Indep't Refl's	2632	11505
Refl's I≥2 <i>σ</i> (I)	2466	10395
<i>R</i> _{int}	0.0296	0.0361
Parameters	185	556
Restraints	4	3
Largest Peak	0.559	0.995
Deepest Hole	-0.409	-1.234
GooF	1.057	1.117
<i>wR</i> ₂ (all data)	0.0731	0.0638
<i>wR</i> ₂	0.0721	0.0622
<i>R</i> ₁ (all data)	0.0307	0.0321
<i>R</i> ₁	0.0284	0.0271

Table S153 Selected bond lengths (Å) and angles (°) for **HL14Cl·2H₂O** and **[(HL14)I₂Cl]₃·0.5I₂**

HL14Cl·2H₂O		[(HL14)I₂Cl]₃·0.5I₂	
Se1-C5	1.857(2)	Se1-C5	1.865(3)
Se1-C7	1.908(2)	Se1-C7	1.903(3)
		Se2-C19	1.859(3)
		Se2-C21	1.903(3)
		Se3-C33	1.862(3)
		Se3-C35	1.906(3)
N1-C1	1.345(3)	N1-Cl1	1.348(4)
N1-C5	1.352(3)	N1-C5	1.345(4)
		N2-C15	1.340(4)
		N2-C19	1.348(4)
		N3-C29	1.350(4)
		N3-C33	1.343(4)
		I1-I2A	2.7969(15)
		I1-I2B	2.784(6)
		I1-Cl1	2.6947(9)
		I3-I4A	2.825(3)
		I3-I4B	2.7097(15)
		I3-Cl2	2.7779(9)
		I5-I6A	2.830(6)
		I5-I6B	2.792(4)
		I5-Cl3	2.7018(9)
		I7-I7 ¹	2.7432(11)
		Cl1-I1-I2A	178.91(4)
		Cl1-I1-I2B	175.8(4)
		I4B-I3-Cl2	172.9(2)
		Cl2-I3-I4A	172.57(14)
		Cl3-I5-I6A	175.2(2)
		Cl3-I5-I6B	175.32(16)
C5-Se1-C7	85.51(10)	C5-Se1-C7	85.85(14)
		C19-Se2-C21	85.92(14)
		C33-Se3-C35	85.82(14)
C1-N1-C5	120.9(2)	C5-N1-C1	121.5(3)
		C15-N2-C19	121.7(3)
		C33-N3-C29	121.2(3)

Table S154 Crystal data and refinement parameters for **L16** and **H4L17**.

	L16	H4L17
Formula	C ₂₉ H ₂₀ Br ₄	C ₃₃ H ₂₄ O ₈
<i>D</i> _{calc.} / g cm ⁻³	1.896	1.454
μ /mm ⁻¹	6.695	0.864
Formula Weight	688.09	548.52
Colour	colourless	colourless
Shape	cut block	block
Size/mm ³	0.340×0.230×0.120	0.09×0.06×0.03
<i>T</i> /K	100(2)	100(2)
Crystal System	monoclinic	triclinic
Space Group	<i>P</i> 2 ₁ / <i>c</i>	<i>P</i> -1
<i>a</i> /Å	8.79840(10)	7.9080(6)
<i>b</i> /Å	16.7929(2)	9.8092(5)
<i>c</i> /Å	16.4790(2)	17.5752(9)
α /°	90	86.930(4)
β /°	98.0820(10)	78.372(5)
γ /°	90	69.784(6)
<i>V</i> /Å ³	2410.60(5)	1252.89(14)
<i>Z</i>	4	2
<i>Z</i> '	1	1
Wavelength/Å	0.71075	1.54184
Radiation type	MoK α	Cu K α
θ _{min} /°	2.338	2.567
θ _{max} /°	27.483	68.251
Measured Refl.	54497	18130
Independent Refl.	5543	4549
Reflections with <i>I</i> > 2(<i>I</i>)	5047	3563
<i>R</i> _{int}	0.0550	0.0316
Parameters	300	385
Restraints	0	4
Largest Peak	0.648	0.257
Deepest Hole	-0.451	-0.259
GooF	1.050	1.062
<i>wR</i> ₂ (all data)	0.0509	0.1535
<i>wR</i> ₂	0.0497	0.1451
<i>R</i> ₁ (all data)	0.0247	0.0673
<i>R</i> ₁	0.0208	0.0528

Table S155 Selected bond lengths (Å) and angles (°) in $[(\text{Cd}_2\text{L17}\cdot 3\text{H}_2\text{O})\cdot 3\text{H}_2\text{O}]_n$.

Cd1–O5	2.408(14)	O5–Cd1–O5 ¹	71.4(6)	O1–Cd3–O1 ²	79.0(5)
Cd1–O7	2.432(14)	O5–Cd1–O7	95.1(5)	O2–Cd3–O1	54.0(4)
Cd1–O8	2.323(10)	O5–Cd1–O7 ¹	163.4(4)	O2–Cd3–O1 ²	107.4(5)
Cd1–O12	2.345(14)	O7–Cd1–O7 ¹	96.5(6)	O2–Cd3–O2 ²	88.5(7)
Cd2–O3	2.253(11)	O8–Cd1–O5 ¹	128.0(6)	O3–Cd3–O1 ²	162.6(5)
Cd2–O10	2.15(4)	O8–Cd1–O5	78.9(5)	O3–Cd3–O1	99.2(4)
Cd2–O11	2.236(14)	O8 ¹ –Cd1–O7	117.6(5)	O3–Cd3–O2	84.5(4)
Cd2–O12 ³	2.411(19)	O8–Cd1–O7	55.2(5)	O3–Cd3–O2 ²	140.9(4)
Cd3–O1	2.443(11)	O8–Cd1–O8 ¹	87.8(5)	O3 ² –Cd3–O2 ²	84.5(4)
Cd3–O2	2.365(15)	O8–Cd1–O12	134.2(3)	O3 ² –Cd3–O2	77.3(5)
Cd3–O3	2.329(12)	O12–Cd1–O5	84.8(5)	O3–Cd3–O9	83.3(5)
Cd3–O9	2.33(2)	O12–Cd1–O7	84.4(4)	O9–Cd3–O1	79.4(5)
Cd4–O1	2.420(12)	O3–Cd2–O3 ²	80.5(6)	O9–Cd3–O2	128.8(4)
Cd4–O5	2.594(17)	O3–Cd2–O12 ³	86.7(4)	O1 ⁴ –Cd4–O1 ⁵	79.9(5)
Cd4–O6	2.296(12)	O10–Cd2–O3	91.1(6)	O1 ⁵ –Cd4–O5	76.5(5)
Cd4–O13	2.39(3)	O10–Cd2–O11	89.8(6)	O1 ⁴ –Cd4–O5	117.5(4)
O1–C1	1.28(2)	O10–Cd2–O12 ³	177.0(8)	O5–Cd4–O5 ¹	65.6(5)
O2–C1	1.24(2)	O11–Cd2–O3 ²	87.6(6)	O6–Cd4–O1 ⁴	159.1(4)
O3–C22	1.274(19)	O11–Cd2–O3	168.1(6)	O6–Cd4–O1 ⁵	79.5(4)
O4–C22	1.28(2)	O11–Cd2–O11 ²	104.3(10)	O6–Cd4–O5	53.7(4)
O5–C12	1.27(2)	O11–Cd2–O12 ³	92.1(5)	O6–Cd4–O5 ¹	110.4(4)
O6–C12	1.26(3)			O6 ¹ –Cd4–O6	120.8(6)
O7–C30	1.23(2)			O6–Cd4–O13	93.1(6)
O8–C30	1.27(3)			O13–Cd4–O1 ⁵	90.5(8)
				O13–Cd4–O5	145.7(4)

Symmetry codes: ¹2-x,+y,+z; ²1-x,+y,+z; ³-1/2+x,-1/2+y,+z; ⁴1/2+x,3/2-y,-1/2+z; ⁵3/2-x,3/2-y,-1/2+z.

Table S156 Selected bond lengths (Å) and angles (°) in $[(\text{Cd}_2\text{L17}\cdot 5\text{H}_2\text{O})\cdot 3\text{H}_2\text{O}]_n$.

Cd1–O1	2.488(3)	O2–Cd1–O1	55.10(10)	O3–Cd2–O7 ²	145.49(10)
Cd1–O2	2.272(3)	O2–Cd1–O5 ¹	159.40(11)	O4–Cd2–O3	55.11(10)
Cd1–O5 ¹	2.390(3)	O2–Cd1–O6 ¹	144.61(11)	O4–Cd2–O7 ²	92.24(10)
Cd1–O6 ¹	2.322(3)	O2–Cd1–O9	90.08(12)	O4–Cd2–O8 ²	145.70(10)
Cd1–O9	2.318(3)	O2–Cd1–O10	82.07(10)	O4–Cd2–O13	129.88(11)
Cd1–O10	2.379(3)	O2–Cd1–O11	86.79(12)	O8 ² –Cd2–O3	158.20(11)
Cd1–O11	2.375(3)	O5 ¹ –Cd1–O1	144.79(10)	O8 ² –Cd2–O7 ²	53.50(10)
Cd2–O3	2.444(3)	O6 ¹ –Cd1–O1	89.83(10)	O8 ² –Cd2–O13	84.13(11)
Cd2–O4	2.330(3)	O6 ¹ –Cd1–O5 ¹	55.95(10)	O12–Cd2–O3	87.66(11)
Cd2–O7 ²	2.528(3)	O6 ¹ –Cd1–O10	133.14(10)	O12–Cd2–O4	92.81(11)
Cd2–O8 ²	2.344(3)	O6 ¹ –Cd1–O11	94.16(11)	O12–Cd2–O7 ²	82.71(10)
Cd2–O12	2.290(3)	O9–Cd1–O1	88.37(11)	O12–Cd2–O8 ²	85.07(11)
Cd2–O13	2.371(3)	O9–Cd1–O5 ¹	86.18(12)	O12–Cd2–O13	98.42(11)
Cd2–O14	2.258(3)	O9–Cd1–O6 ¹	93.79(11)	O13–Cd2–O3	76.64(10)
O2–Cd1–O1	55.10(10)	O9–Cd1–O10	88.49(11)	O13–Cd2–O7 ²	137.49(10)
O2–Cd1–O5 ¹	159.40(11)	O9–Cd1–O11	170.17(11)	O14–Cd2–O3	97.88(13)
O2–Cd1–O6 ¹	144.61(11)	O10–Cd1–O1	137.03(10)	O14–Cd2–O4	86.24(12)
O2–Cd1–O9	90.08(12)	O10–Cd1–O5 ¹	77.59(10)		90.08(12)
O2–Cd1–O10	82.07(10)	O11–Cd1–O1	97.43(11)		82.07(10)
O2–Cd1–O11	86.79(12)	O11–Cd1–O5 ¹	93.49(12)		86.79(12)
O5 ¹ –Cd1–O1	144.79(10)	O11–Cd1–O10	81.86(10)		144.79(10)

Symmetry codes: 1 -x, -y, 1-z; 2 1-x, 2-y, -z.

Table S157 Crystal data and refinement parameters of **(H₄L17·Py₂Et)_∞**.

(H₄L17·Py₂Et)_∞	
Formula	C ₄₅ H ₃₈ N ₂ O ₉
<i>D</i> _{calc.} / g cm ⁻³	1.412
<i>μ</i> /mm ⁻¹	0.810
Formula Weight	750.77
Colour	colourless
Shape	plate
Size/mm ³	0.11×0.09×0.01
<i>T</i> /K	100(2)
Crystal System	monoclinic
Space Group	<i>P</i> 2 ₁ / <i>c</i>
<i>a</i> /Å	11.4011(2)
<i>b</i> /Å	23.9412(6)
<i>c</i> /Å	13.1639(2)
<i>α</i> /°	90
<i>β</i> /°	100.700(2)
<i>γ</i> /°	90
<i>V</i> /Å ³	3530.69(12)
<i>Z</i>	4
<i>Z</i> '	1
Wavelength/Å	1.54184
Radiation type	Cu K _α
<i>θ</i> _{min} /°	3.692
<i>θ</i> _{max} /°	68.247
Measured Refl's.	32615
Indep't Refl's	6439
Refl's I ≥ 2 σ(I)	5077
<i>R</i> _{int}	0.0688
Parameters	519
Restraints	0
Largest Peak	0.411
Deepest Hole	-0.265
Goof	1.045
<i>wR</i> ₂ (all data)	0.1606
<i>wR</i> ₂	0.1501
<i>R</i> ₁ (all data)	0.0765
<i>R</i> ₁	0.0600

Table S158 Crystal data and refinement parameters for $[(\text{Co}_2\text{L}_3\text{L}_{17}\cdot\text{H}_2\text{O})\cdot 2\text{DMF}]_\infty$ and $[(\text{Zn}_2\text{L}_3\text{L}_{17}\cdot 3\text{H}_2\text{O}\cdot\text{DMF})\cdot 3.5\text{DMF}]_\infty$.

	$[(\text{Co}_2\text{L}_3\text{L}_{17}\cdot\text{H}_2\text{O})\cdot 2\text{DMF}]_\infty$	$[(\text{Zn}_2\text{L}_3\text{L}_{17}\cdot 3\text{H}_2\text{O}\cdot\text{DMF})\cdot 3.5\text{DMF}]_\infty$
Formula	$\text{C}_{69}\text{H}_{42}\text{Co}_2\text{N}_4\text{O}_9\text{S}_2$	$\text{C}_{57}\text{H}_{50}\text{N}_4\text{O}_{13}\text{SZn}_2$
$D_{\text{calc.}}/\text{g cm}^{-3}$	1.249	1.355
μ/mm^{-1}	4.946	0.872
Formula Weight	1253.25	1161.81
Colour	pale orange	light yellow
Shape	needle	prism
Size/ mm^3	$0.23\times 0.06\times 0.04$	$0.05\times 0.02\times 0.01$
T/K	100(2)	100(2)
Crystal System	monoclinic	triclinic
Flack Parameter	0.485(7)	
Hooft Parameter	0.4814(15)	
Space Group	$C2$	$P-1$
$a/\text{\AA}$	20.4960(2)	10.0380(3)
$b/\text{\AA}$	17.9454(2)	16.0930(4)
$c/\text{\AA}$	18.3095(2)	18.6155(5)
$\alpha/^\circ$	90	107.834(2)
$\beta/^\circ$	98.2720(10)	90.116(2)
$\gamma/^\circ$	90	95.541(2)
$V/\text{\AA}^3$	6664.33(12)	2847.71(14)
Z	4	2
Z'	1	1
Wavelength/ \AA	1.54184	0.6889
Radiation type	Cu K_α	synchrotron
$\theta_{\text{min}}/^\circ$	3.288	1.952
$\theta_{\text{max}}/^\circ$	68.239	25.493
Measured Refl's.	32767	37671
Indep't Refl's	11723	11512
Refl's $I\geq 2\sigma(I)$	11197	5328
R_{int}	0.0384	0.0808
Parameters	905	705
Restraints	2936	19
Largest Peak	0.349	0.963
Deepest Hole	-0.361	-0.996
GooF	1.039	0.837
wR_2 (all data)	0.1636	0.1603
wR_2	0.1616	0.1505
R_1 (all data)	0.0691	0.1049
R_1	0.0666	0.0592

Table S159 Selected bond lengths (Å) for [(Co₂L₃L₁₇·H₂O)·2DMF]_∞.

Co1–O9	2.158(4)	Co2–O10	2.077(4)
Co1–N1	2.097(8)	Co2–N2 ²	2.086(7)
Co1–N4 ¹	2.281(7)	Co2–N3	2.177(7)
Co1–O1B	2.24(4)	Co2–O3B ¹	2.19(4)
Co1–O2B ²	1.79(4)	Co2–O7B ¹	2.31(5)
Co1–O6B ²	1.93(4)	Co2–O8B	1.92(5)
Co1–O1A	1.943(7)	Co2–O3A ¹	2.037(10)
Co1–O2A ²	2.132(7)	Co2–O7A ¹	2.148(13)
Co1–O6A ²	2.233(7)	Co2–O8A	2.155(8)

Symmetry codes: ¹ 1-x, +y, -z; ² -x, +y, 1-z.**Table S160** Selected bond angles (°) for [(Co₂L₃L₁₇·H₂O)·2DMF]_∞.

O9–Co1–N4 ¹	83.5(2)	O10–Co2–N2 ²	90.6(3)
O9–Co1–O1B	83.8(13)	O10–Co2–N3	176.6(3)
O9–Co1–O6A ²	87.0(2)	O10–Co2–O3B ¹	85.3(10)
N1–Co1–O9	175.2(2)	O10–Co2–O7B ¹	89.6(12)
N1–Co1–N4 ¹	92.0(3)	O10–Co2–O7A ¹	92.2(3)
N1–Co1–O1B	94.7(13)	O10–Co2–O8A	90.6(4)
N1–Co1–O2A ²	91.5(3)	N2 ² –Co2–N3	92.8(3)
N1–Co1–O6A ²	94.2(3)	N2 ² –Co2–O3B ¹	96.5(13)
O2B ² –Co1–O9	94.1(15)	N2 ² –Co2–O7B ¹	168.6(14)
O2B ² –Co1–N1	90.6(15)	N2 ² –Co2–O7A ¹	173.9(4)
O2B ² –Co1–O1B	102.2(18)	N2 ² –Co2–O8A	89.9(4)
O6B ² –Co1–O9	94.6(10)	N3–Co2–O3B ¹	94.7(10)
O6B ² –Co1–N1	86.4(10)	N3–Co2–O7B ¹	87.2(12)
O6B ² –Co1–O1B	172.5(18)	O8B–Co2–O10	93.1(19)
O1A–Co1–O9	89.4(3)	O8B–Co2–N3	87(2)
O1A–Co1–N1	89.0(4)	O8B–Co2–O7A ¹	95(2)
O1A–Co1–N4 ¹	87.7(4)	O3A ¹ –Co2–O10	92.9(3)
O1A–Co1–O2A ²	103.3(4)	O3A ¹ –Co2–N2 ²	89.9(4)
O1A–Co1–O6A ²	174.1(4)	O3A ¹ –Co2–N3	87.5(3)
O2A ² –Co1–O9	93.2(3)	O3A ¹ –Co2–O3B ¹	10.1(12)
O2A ² –Co1–N4 ¹	168.5(4)	O3A ¹ –Co2–O7B ¹	78.8(14)
O2A ² –Co1–O6A ²	81.6(4)	O3A ¹ –Co2–O7A ¹	84.6(4)
O6A ² –Co1–N4 ¹	87.2(3)	O3A ¹ –Co2–O8A	176.5(5)
O10–Co2–N2 ²	90.6(3)	O7A ¹ –Co2–N3	84.4(4)
O10–Co2–N3	176.6(3)	O7A ¹ –Co2–O3B ¹	78.4(13)
O10–Co2–O3B ¹	85.3(10)	O7A ¹ –Co2–O7B ¹	6.6(16)
O10–Co2–O7B ¹	89.6(12)	O7A ¹ –Co2–O8A	95.4(5)
O10–Co2–O7A ¹	92.2(3)	O8A–Co2–N3	89.0(5)
O10–Co2–O8A	90.6(4)	O8A–Co2–O3B ¹	172.4(12)
N2 ² –Co2–N3	92.8(3)	O8A–Co2–O7B ¹	101.4(15)

Symmetry codes: ¹ 1-x, +y, -z; ² -x, +y, 1-z.

Table S161 Selected bond lengths (Å) and angles (°) for [(Zn₂L3L17·3H₂O·DMF)·3.5DMF]_∞.

Zn1-O2	2.001(3)	O2-Zn1-O5 ¹	172.06(12)	O3 ² -Zn2-C14 ²	29.39(14)
Zn1-O5 ¹	2.232(3)	O2-Zn1-O6 ¹	113.74(11)	O4 ² -Zn2-O3 ²	59.51(12)
Zn1-O6 ¹	2.187(3)	O2-Zn1-O11	88.84(12)	O4 ² -Zn2-O9	87.78(13)
Zn1-O11	2.086(3)	O2-Zn1-O12	90.93(12)	O4 ² -Zn2-O10	88.75(14)
Zn1-O12	2.093(3)	O2-Zn1-N1	94.25(13)	O4 ² -Zn2-N2	148.11(15)
Zn1-N1	2.130(4)	O2-Zn1-C15 ¹	143.39(13)	O4 ² -Zn2-C14 ²	30.15(15)
Zn1-C15 ¹	2.547(4)	O5 ¹ -Zn1-C15 ¹	29.91(11)	O8-Zn2-O3 ²	178.39(15)
Zn2-O3 ²	2.306(3)	O6 ¹ -Zn1-O5 ¹	59.60(10)	O8-Zn2-O4 ²	121.40(14)
Zn2-O4 ²	2.094(3)	O6 ¹ -Zn1-C15 ¹	29.72(11)	O8-Zn2-O9	92.06(15)
Zn2-O8	1.972(3)	O11-Zn1-O5 ¹	86.85(11)	O8-Zn2-O10	90.81(15)
Zn2-O9	2.123(4)	O11-Zn1-O6 ¹	89.69(12)	O8-Zn2-N2	90.26(14)
Zn2-O10	2.133(4)	O11-Zn1-O12	176.94(11)	O8-Zn2-C14 ²	151.47(17)
Zn2-N2	2.107(4)	O11-Zn1-N1	91.61(13)	O9-Zn2-O3 ²	86.63(13)
Zn2-C14 ²	2.532(5)	O11-Zn1-C15 ¹	88.85(13)	O9-Zn2-O10	176.31(13)
		O12-Zn1-O5 ¹	93.01(11)	O9-Zn2-C14 ²	85.91(15)
		O12-Zn1-O6 ¹	87.61(11)	O10-Zn2-O3 ²	90.53(14)
		O12-Zn1-N1	91.45(12)	O10-Zn2-C14 ²	90.46(15)
		O12-Zn1-C15 ¹	89.51(12)	N2-Zn2-O3 ²	88.93(14)
		N1-Zn1-O5 ¹	92.54(12)	N2-Zn2-O9	95.32(15)
		N1-Zn1-O6 ¹	152.00(12)	N2-Zn2-O10	86.98(16)
		N1-Zn1-C15 ¹	122.33(14)	N2-Zn2-C14 ²	118.28(17)

Symmetry codes: ¹ 1-x, 2-y, 1-z; ² -x, 1-y, 2-z.

Appendix 7: Supplementary Information

Characterization of 2,7-bis(pyridin-3-ylethynyl)fluoren-9-one (L9)

Figure S162 Asymmetric unit of the crystal structure of **L9**. Thermal ellipsoids are drawn at 50 % probability level.

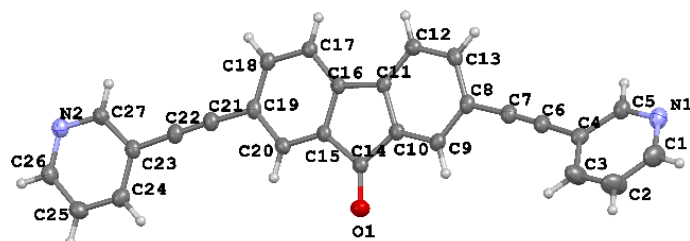
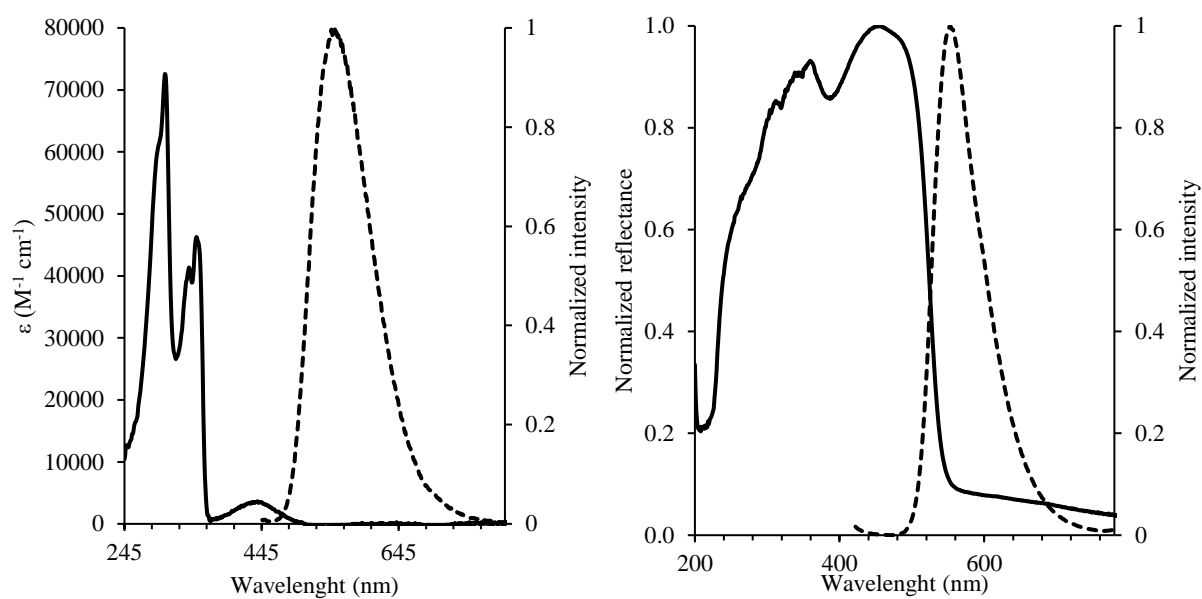


Table S163 Crystal data and refinement parameters for **L9**.

L9	
Formula	C ₂₇ H ₁₄ N ₂ O
<i>D</i> _{calc.} / g cm ⁻³	1.344
μ /mm ⁻¹	0.653
Formula Weight	382.40
Colour	pale yellow
Shape	block
Size/mm ³	0.10×0.06×0.02
<i>T</i> /K	100(2)
Crystal System	monoclinic
Space Group	<i>P</i> 2 ₁ / <i>c</i>
<i>a</i> /Å	6.61900(10)
<i>b</i> /Å	13.71150(10)
<i>c</i> /Å	22.1683(3)
α /°	90
β /°	110.0800(10)
γ /°	90
<i>V</i> /Å ³	1889.62(4)
<i>Z</i>	4
<i>Z</i> '	1
Wavelength/Å	1.54184
Radiation type	Cu K α
θ _{min} /°	3.860
θ _{max} /°	68.232
Measured Refl's.	57856
Ind't Refl's	3441
Refl's with <i>I</i> > 2(<i>I</i>)	3308
<i>R</i> _{int}	0.0247
Parameters	271
Restraints	0
Largest Peak	0.222
Deepest Hole	-0.216
Goof	1.090
<i>wR</i> ₂ (all data)	0.1204
<i>wR</i> ₂	0.1196
<i>R</i> ₁ (all data)	0.0473
<i>R</i> ₁	0.0459

Figure S164 Absorption (solid line) and emission (dashed line) spectra for **L9** measured in CHCl_3 (left) ($C_{L9} = 10^{-5} - 10^{-6}$ M, $\lambda_{\text{ex}} = 436$ nm) and in the solid state (right) ($\lambda_{\text{ex}} = 400$ nm).



^1H , ^{13}C NMR and FT-IR spectra of **L9** are reported in Appendix 1: NMR spectra and Appendix 2: FT-IR spectra, respectively.

Characterization of 2-bromo-7-(pyridin-4-ylethynyl)-9H-fluoren-9-one (L10mono)

Figure S165 ^1H NMR (CDCl_3 , 600 MHz) of L10mono.

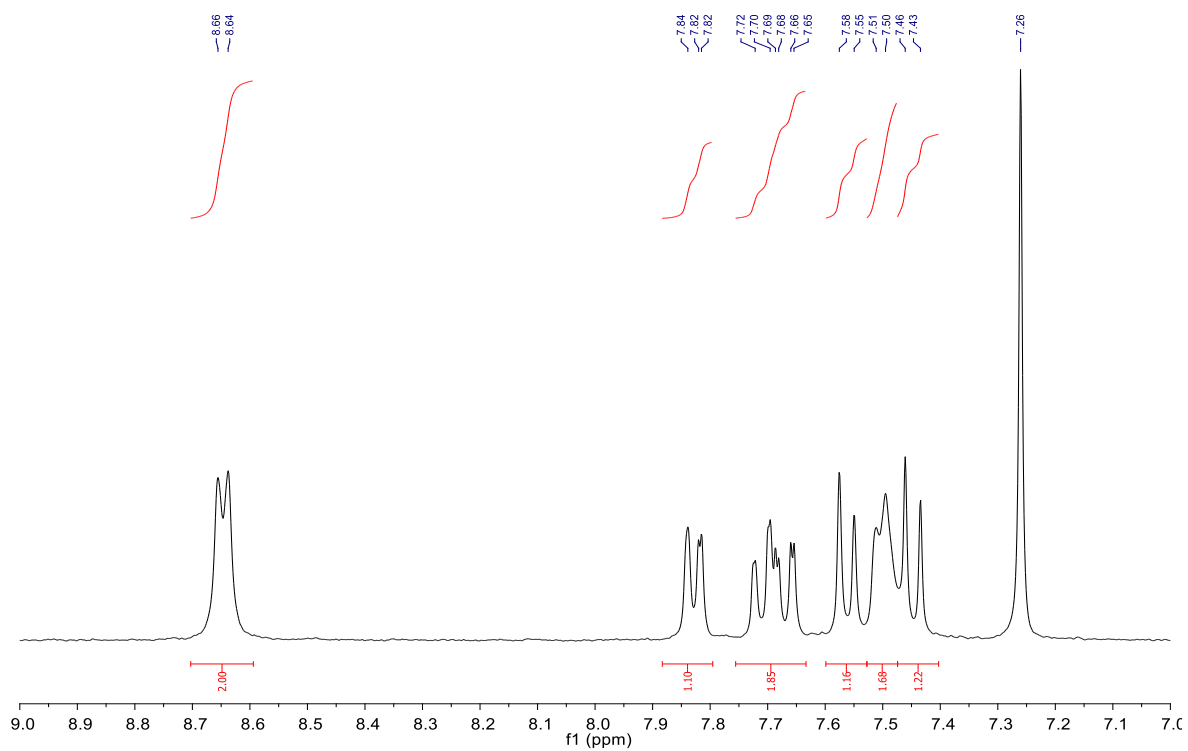


Figure S166 Asymmetric unit of the preliminary crystal structure for L10mono.

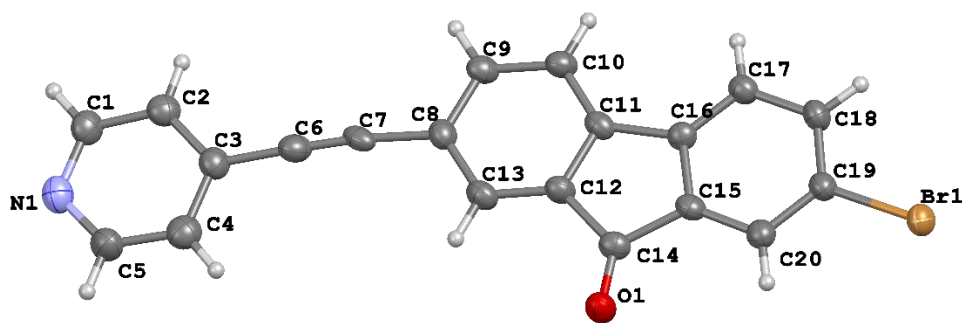


Table S167 Crystal data for the preliminary structure of **L10mono**.

Formula	C ₂₀ H ₁₀ BrNO
<i>D</i> _{calc.} / g cm ⁻³	1.654
μ /mm ⁻¹	3.895
Formula Weight	360.20
Colour	yellow
Shape	lath
Size/mm ³	0.15×0.04×0.02
Crystal System	monoclinic
Space Group	<i>P</i> 2 ₁ / <i>c</i>
<i>a</i> /Å	3.79710(10)
<i>b</i> /Å	15.6274(3)
<i>c</i> /Å	24.3785(4)
α /°	90
β /°	88.566(2)
γ /°	90
<i>V</i> /Å ³	1446.14(5)
<i>Z</i>	4
<i>Z</i> '	1